Springer Series in Reliability Engineering

Series Editor

Hoang Pham

For further volumes:
http://www.springer.com/series/6917

Izuru Takewaki · Abbas Moustafa
Kohei Fujita

Improving the Earthquake Resilience of Buildings

The Worst Case Approach

Springer

Izuru Takewaki
Department of Architecture
and Architectural Engineering
Kyoto University
Kyotodaigaku-Katsura
Kyoto 615-8540
Japan

Kohei Fujita
Department of Architecture
and Architectural Engineering
Kyoto University
Kyotodaigaku-Katsura
Kyoto 615-8540
Japan

Abbas Moustafa
Department of Civil Engineering
Minia University
Minia 61111
Egypt

ISSN 1614-7839
ISBN 978-1-4471-4143-3 ISBN 978-1-4471-4144-0 (eBook)
DOI 10.1007/978-1-4471-4144-0
Springer London Heidelberg New York Dordrecht

Library of Congress Control Number: 2012938947

Printed on acid-free paper

Springer is part of Springer Science+Business Media (www.springer.com)

Preface

Engineers are always interested in the worst-case scenario. The seismic design of buildings should ensure structural safety against the worst possible future earthquakes. The features of this monograph are:

(1) Consideration of elastic–plastic behavior of building structures in the critical excitation method for improved building-earthquake resilience,
(2) Consideration of uncertainties of structural parameters in structural control and base-isolation for improved building-earthquake resilience, and
(3) New insights into structural design of super high-rise buildings under long-period ground motions (case study on tall buildings in mega cities in Japan during the 2011 off the Pacific coast of Tohoku earthquake on March 11).

This book consists of two parts. The first part deals with the characterization and modeling of worst or critical ground motions on inelastic structures. The second part of the book focuses on investigating the worst-case scenario for passively controlled and base-isolated buildings.

Chapter 1 provides an overview of the effects of historic and recent strong earthquake ground motions on building structures and associated life loss.

Chapter 2 provides comprehensive information about the most recent and devastating Tohoku earthquake of moment magnitude 9.0 which hit off the pacific coast of eastern Japan on 11 March 2011. This earthquake and the tsunami following it left severe damage to building structures and caused nearly 20,000 of losses of life.

As is well known, the robust design of buildings for future earthquake loads requires reliable understanding of the ground motion characteristics. Accordingly, Chaps. 3 and 4 report on the characteristics of near-field (near-fault) ground motions with pulse-like acceleration. Furthermore, these two chapters provide simple mathematical models for this class of ground motions and associated structural response. Chapter 3 deals with the simulation of near-field ground motions with pulse-like acceleration while a critical excitation of multiple sequences for inelastic responses is discussed in Chap. 4.

Chapters 5–7 deal with the characterization and modeling of earthquake ground motion of multiple sequences. Recently, this class of ground motions was clearly observed during the 2011 off the Pacific coast of Tohoku earthquake on March 11. This research subject is new and has not received adequate attention from researchers. For instance, most seismic codes specify design ground motions as single events. However, moderate ground motion with repeated acceleration sequences could lead to more severe damage to structures than a single sequence of strong ground motion. The worst-case scenario is studied within the deterministic and probabilistic frameworks. Characteristics of earthquake ground motion of repeated sequences are made clear in Chap. 5 while critical ground motion sequences are discussed in Chap. 6. In Chap. 7, responses of elastic–plastic structures to nonstationary random acceleration sequences are investigated and the reliability of such structures is evaluated.

A practical problem always arises in the design of buildings against earthquake loads. It is always difficult to select a suite of suitable earthquake records from a large set of records as input to the nonlinear time-history analysis of structures. Chapter 8 provides deterministic and probabilistic measures that can be used to identify unfavorable accelerograms. This chapter provides simple concepts which can be utilized to select a suit of appropriate earthquake records for nonlinear time-history analysis of structures.

Chapters 9 and 10 deal with the worst-scenario of earthquake loads on inelastic structures with special emphasis on the type of seismic waves of the ground motion and damage quantification using damage indices.

Chapter 11 deals with the worst-case scenario for bidirectional ground motions. Most of the current seismic-resistant design codes are based on the simulation of building response under uni-directional earthquake input. However, bidirectional input is inevitable for the reliable design of columns.

Chapters 12 and 13 tackle the worst-case scenario for passively controlled buildings. The structural member stiffness and strength of buildings are uncertain due to various factors resulting from randomness, material deterioration, temperature dependence, etc. The passive damper systems are also uncertain depending on various sources. The concept of sustainable building design under such uncertain structural-parameter environment may be one of the most challenging issues to be tackled recently. By predicting the response variability accurately, the elongation of service life of buildings may be possible.

Chapter 14 focuses on the worst-case scenario for base-isolated buildings. The stiffness and damping of the base-isolation system and the stiffness of the superstructure are selected as uncertain parameters. An efficient methodology is explained to evaluate the robustness (variability of response) of an uncertain base-isolated building.

The book closes with Chap. 15 on current challenges and future directions on design of building structures with greater earthquake resilience.

The importance of the worst-scenario approach for improved earthquake resilience of buildings and nuclear reactor facilities has been recognized and demonstrated by the recent great earthquake (March 11, 2011) in Japan. Such understanding is of extreme significance especially for large or important structures.

The word ‘unexpected incident’ is often used in Japan after the 2011 great earthquake. It may be true that the return period of this class of earthquakes at the same place could be 500–1,000 years and the use of this word may be acceptable to some extent from the viewpoint of the balance between the construction cost and the safety level. However, the critical excitation method is expected or has a potential for enhancing the safety level of building structures against undesirable incidents drawn from this irrational concept in the future. One of the most important and challenging missions of structural engineers may be to narrow the range of such unexpected incidents in building structural design. Redundancy, robustness, and resilience are expected to play important roles in such circumstances.

Izuru Takewaki
Abbas Moustafa
Kohei Fujita

Contents

Chapter 1
Introduction

1.1 Background and Review

The 1994 Northridge earthquake and the 1995 Kobe earthquake have remained as two of the most destructive earthquakes in the world and have changed thinking of earthquake and structural engineers for many years. Modern seismic codes have been revised taking into account lessons learned from these earthquakes. Notwithstanding this, the two recent devastating earthquakes in Japan (11 March 2011) and in Haiti (12 January 2010) have raised significant concerns within the earthquake engineering community [1, 2]. Perhaps these two quakes are the strongest earthquakes during the last 100 years. These earthquakes have brought to our attention the challenges still facing the developing as well as the developed countries. The 2011 Tohoku earthquake has caused massive structural damage and enormous economic loss off the Pacific coast of Tohoku in Japan. On the other hand, the 2010 Haiti earthquake has killed about 250,000 people and left a long-term suffer for the residents of the country. The signature of these two earthquakes will remain for a long time in the minds of earthquake and structural engineers. These earthquakes bring to our attention the worst-case scenario or what is also known as the critical excitation.

As is well known, engineers are always interested in the worst-case scenario. This is because engineering structures must resist static and dynamic loads during their service life without loss of safety and functionality. In the field of earthquake-resistant design, seismic design of buildings should ensure structural safety against the possible worst future earthquakes. The features of this monograph are:

(1) Consideration of elastic–plastic behavior of building structures in the critical excitation method for improved building earthquake resilience.
(2) Consideration of uncertainties of structural parameters in structural control and base isolation for improved building earthquake resilience.

I. Takewaki et al., *Improving the Earthquake Resilience of Buildings*,
Springer Series in Reliability Engineering, DOI: 10.1007/978-1-4471-4144-0_1,

(3) New insights into structural design of super high-rise buildings under long period ground motions (case study on tall buildings in megacities in Japan during the 2011 off the Pacific coast of Tohoku earthquake on March 11).

It is well recognized and widely accepted that earthquake ground motions are uncertain even with the up-to-date cutting-edge knowledge and it does not appear easy to predict forthcoming earthquake events precisely at a specific site both in time and frequency contents [3–5]. It is therefore strongly desirable to develop a *robust* structural design method taking into account these uncertainties, enabling the design of safer structures to a broader class of design earthquakes. This also enables structural engineers to narrow the range of 'out of Scenario' and to enhance the structural safety. The concept of "critical excitation" or "worst-case input" is promising and seems to enable the realization of a rational design concept. As the limit states of structures play an important role in setting allowable structural capacity and alternative performance levels of structures during disturbances, the clarification of critical excitations for a given structure or a group of structures appears to provide the structural designers with useful information in determining excitation parameters in a reasonable and reliable way.

The method of the critical excitation was proposed in earthquake engineering by Drenick in 1970 [3] for linear elastic single-degree-of-freedom (SDOF) systems in order to take into account inherent uncertainties in the ground motions. The critical excitation that produces the maximum response from a class of allowable inputs defines the critical excitation for the given structure.

By using the Cauchy–Schwarz inequality, Drenick [3] showed that the critical excitation for a linear elastic SDOF system is its impulse response function reversed in time. This implies that the critical envelope function for linear elastic SDOF systems in deterministic problems can be represented by an increasing exponential function and the critical excitation must be defined from the time at minus infinity. This result may be unrealistic and of only theoretical significance. However, Drenick's paper in 1970 is pioneering in the field of critical excitation since it paved way for developing a new concept. It was often suggested that the critical response by Drenick's model (1970) is conservative. To remedy this point, Shinozuka [4] discussed the same problem in the frequency domain and proved that, if an envelope function of Fourier amplitude spectra can be specified, a narrower upper bound of the maximum response can be derived.

After the works of Drenick and Shinozuka, many useful theories and methods have been proposed on critical excitation including the work of Iyengar [6] and Iyengar and Manohar [7]. The interested readers can refer some of the recent review articles e.g., [5, 8]. The works of Takewaki [5, 8] and Abbas and Manohar [9] tackle the probabilistic modeling of critical excitations in the frequency domain. Abbas and Manohar [9] and Abbas [10], Moustafa [11, 12] tackled the deterministic modeling of critical excitations.

1.2 Input Ground Motion and Worst-Case Scenario

The structural response under random or uncertain loads, such as wind or strong ground motion, depends primarily on how accurate the mathematical models adopted in describing the structural behavior and in predicting possible future earthquake events at the site. In general, the earthquake load can be specified as input to the structure using the response spectrum method, the recorded ground accelerations, or using the theory of random vibration. Each of these methods accounts for uncertainty involved in the earthquake load in a different way. As is well known, the uncertainty involved in the dynamic load, resulting from the fault properties, travel path, and local soil condition, represents the main source of uncertainty arising in the structural response compared to the uncertainty resulting from the variability in the structure's parameters (e.g., cross-section dimensions and capacity). For instance, it is difficult to predict the future ground motion that can cause maximum damage to the structure during its lifetime. This difficulty includes the time, location, and ground motion characteristics (e.g., total duration, energy, frequency content, peak acceleration, etc.). On the other hand, the structural behavior can be accurately described using mathematical models with relatively lower uncertainty.

Structural engineers are required to design safe structures against possible future earthquake events on one hand, and to achieve optimum use of the construction material on the other hand. This implicitly implies that one has to model the worst future ground motion capable of causing the largest damage in the structure. The preface of the recent book by Elishakoff and Ohsaki [13] provides a historic review on the development of the worst-case scenario or what is also known as the critical excitation. The senior author communicated with Drenick (Drenick, 2002, "Private communication") and was informed that the work by Prof. Drenick was motivated by his communication with Japanese researchers in the late 1960s.

In short, the worst-case scenario is an asymptotic scenario in which the maximum response of the structure under possible worst future earthquakes is estimated. Theoretically, the predicted future seismic load represents the worst earthquake load that can happen at the site and the associated response, i.e., the worst response. In this case, the worst ground motion is mathematically obtained using constrained optimization techniques. The constraints associated with the optimization problem involve the main characteristics of the earthquake loads estimated from the seismic data available at the site or from other sites with similar geological soil conditions.

1.3 Organization of the Book

This book consists of two parts. The first part deals with the characterization and modeling of worst or critical ground motions on inelastic structures. The second part of the book focuses on investigating the worst-case scenario for passively controlled and base-isolated buildings.

This chapter provides an overview on the effects of historic and recent strong earthquake ground motions on building structures and associated life loss.

Chapter 2 provides a comprehensive information on the most recent and devastating Tohoku earthquake of moment magnitude 9.0 which hit off the pacific coast of eastern Japan on 11 March 2011. This earthquake and the tsunami following it left severe damage to building structures and caused nearly 20,000 life loss [1].

As is well known the robust design of buildings for future earthquake loads requires reliable understanding of the ground motion characteristics. Accordingly, Chaps. 3 and 4 report on the characteristics of near-fault ground motions with pulse-like acceleration. Furthermore, these two chapters provide simple mathematical models for this class of ground motions and associated structural response [14, 15].

Chapters 5–7 deal with the characterization and modeling of earthquake ground motion of multiple sequences [16–18]. This research subject is new and has not received adequate attention from researchers. For instance, most seismic codes specify design ground motions as single events. However, moderate ground motion with repeated acceleration sequences could lead to severe damage to structures than strong ground motion of a single sequence. The worst-case scenario is studied within the deterministic and the probabilistic frameworks.

A practical problem always arises in the design of buildings against earthquake loads. It is always difficult to select a suite of suitable earthquake records from a large set of records as input to the nonlinear time-history analysis of structures. Chapter 8 provides deterministic and probabilistic measures that can be used to identify unfavorable accelerograms [19]. This chapter provides simple concepts which can be utilized to select a suite of appropriate earthquake records for nonlinear time-history analysis of structures.

Chapters 9 and 10 deal with the modeling worst scenario of earthquake loads on inelastic structures with special emphasis on the type of seismic waves of the ground motion and structural damage quantification using damage indices [12, 20, 21].

Chapter 11 deals with the mathematical modeling of the worst-case scenario for bidirectional ground motions [22]. In this context, it may be recalled that, most of current seismic-resistant design codes are based on the simulation of building response under unidirectional earthquake input. However, bidirectional input is inevitable for the reliable design of columns.

Chapters 12 and 13 tackle the modeling of the worst-case scenario for passively controlled buildings. The structural properties such as the member stiffness and strength of buildings are modeled as uncertain due to various factors resulting from randomness, material deterioration, temperature dependence, etc. [23, 24]. The passive damper systems could also contain uncertain parameters depending on various sources. The concept of sustainable building design under such uncertain structural-parameter environment may be one of the most challenging issues to be tackled recently. By predicting the response variability accurately, extending the service life of buildings may be possible.

Chapter 14 focuses on the worst-case scenario for base-isolated buildings [25]. The stiffness and damping parameters of the base-isolation system and the stiffness of the super structure are modeled as random variables. An efficient methodology is explained to evaluate the robustness (variability of response) of an uncertain base-isolated building.

This book closes with Chap. 15 on current challenges and future directions on design of building structures with greater earthquake resilience.

The importance of the worst scenario approach for improved earthquake resilience of buildings and nuclear reactor facilities has been recognized and demonstrated by the recent great earthquake in Japan. Such understanding is of extreme significance especially for important structures and critical facilities.

The word 'unexpected scenario' is often used in Japan after the 2011 great earthquake. In fact, this quake reminds us of the 1923 Great Kanto earthquake that killed more than 140,000 people in Tokyo and surrounding area and left massive damage to structures. It may be true that the return period of this class of earthquakes at the same place could be 500–1,000 years and the use of this word may be acceptable to some extent from the viewpoint of the balance between the construction cost and the safety. However, the critical excitation method is expected or has a potential for narrowing the range of 'unexpected scenario' and enhancing the safety of building structures against undesirable incidents drawn from this irrational concept in the future.

References

1. Takewaki I, Murakami S, Fujita K, Yoshitomi S, Tsuji M (2011) The 2011 off the Pacific coast of Tohoku earthquake and response of high-rise buildings under long-period ground motions. Soil Dyn Earthq Eng 31(11):1511–1528
2. USGS/EERI Advance reconnaissance team, The Mw 7.0 Haiti earthquake of 12 January 2010
3. Drenick RF (1970) Model-free design of aseismic structures. J Eng Mech Div, ASCE 96(EM4):483–493
4. Shinozuka M (1970) Maximum structural response to seismic excitations. J Eng Mech ASCE 96:729–738
5. Takewaki I (2007) Critical excitation methods in earthquake engineering. Elsevier, New York
6. Iyengar RN (1970) Matched inputs. Report 47, Series J, Center of Applied Stochastics, Purude University, West Lafayette, Ind
7. Iyengar RN, Manohar CS (1987) Nonstationary random critical excitations. J Eng Mech; ASCE 133:529–541
8. Takewaki I (2002) Seismic critical excitation method for robust design: a review. J Struct Eng ASCE 128:665–672
9. Abbas M, Manohar CS (2002) Investigations into critical earthquake excitations within deterministic and probabilistic frameworks. Earthq Eng Struct Dynam 31:813–832
10. Abbas AM (2006) Critical seismic load inputs for simple inelastic structures. J Sound Vib 296:949–967
11. Moustafa A (2009) Discussion of the effect of energy concentration of earthquake ground motions on the nonlinear response of RC structures. Soil Dyn Earthq Eng 29:1181–1183

12. Moustafa A (2011) Damage-based design earthquake loads for single-degree-of-freedom inelastic structures. J Struct Eng, ASCE 137(3):456–467
13. Elishakoff I, Ohsaki M (2010) Optimization and anti-optimization of structures under uncertainties. Imperial College Press, Singapore
14. Moustafa A, Takewaki I (2010) Critical characterization and modeling of pulse-like near-fault strong ground motion. Struct Eng Mech 34(6):755–778
15. Moustafa A, Takewaki I (2010) Deterministic and probabilistic representation of near-field pulse-like ground motion. Soil Dyn Earthq Eng 30(5):412–422
16. Moustafa A, Takewaki I (2010) Modeling critical ground-motion sequences for inelastic structures. Adv Struct Eng 13(4):665–679
17. Moustafa A, Takewaki I (2011) Response of nonlinear single-degree-of-freedom structures to random acceleration sequences. Eng Struct 33:1251–1258
18. Moustafa A, Takewaki I (2012) Earthquake ground motion of multiple sequences and associated structural response. Earthq Struct 3(3) (in press)
19. Moustafa A, Takewaki I (2009) The use of probabilistic and deterministic measures to identify unfavorable earthquake records. J Zhejiang Univ-Sci A 10(5):619–634 (Also from Springer)
20. Moustafa A, Ueno K, Takewaki I (2010) Critical earthquake loads for SDOF inelastic structures considering evolution of seismic waves. Earthq Struct 1(2):147–162
21. Ueno K, Moustafa A, Fujita K, Takewaki I (2011) Critical input for inelastic structures under evolving seismic waves. J Struct Constr Eng, AIJ 659:79–87 (in Japanese)
22. Fujita K, Takewaki I (2010) Critical correlation of bi-directional horizontal ground motions. Eng Struct 32(1):261–272
23. Fujita K, Moustafa A, Takewaki I (2010) Optimal placement of viscoelastic dampers and supporting members under variable critical excitations. Earthq Struct 1(1):43–67
24. Fujita K, Takewaki I (2011) Sustainable building design under uncertain structural-parameter environment in seismic-prone countries. Sustain Cities Soc 1(3):142–151
25. Fujita K, Takewaki I (2011) Earthquake response bound analysis of uncertain base-isolated buildings for robustness evaluation. J Struct Constr Eng AIJ 666:1453–1460 (in Japanese)

Chapter 2
Earthquake Resilience of High-Rise Buildings: Case Study of the 2011 Tohoku (Japan) Earthquake

2.1 Introduction

Accumulated data and experiences are very important in the reliable seismic design of structures. However, it is also true that theoretical expectations and predictions are also of significance for the design of extremely important structures and facilities which are influential for the society and wide district. This was demonstrated in the past earthquakes which are very rare from the viewpoint of return period in the same area.

The most devastating earthquake in Japan after the 1923 Great Kanto earthquake hit eastern Japan in the afternoon of March 11, 2011 (see [1], Takewaki [2, 3], Takewaki et al. [4]). The moment magnitude 9.0 earthquake is one of the five most powerful earthquakes in the world since modern record-keeping began in 1900. It was made clear afterward that the recording system for low-frequency and large-amplitude ground motions was not sufficient in Japan and the first preliminary Japan Meteorological Agency (JMA) magnitude was smaller than 8 (7.9 exactly). The JMA magnitude was updated immediately as 8.4. Records of earthquake ground motions outside Japan were then used to determine the exact moment magnitude of 9.0 (intermediate announcement was 8.8). The earthquake resulted from the thrust faulting near the subduction zone plate boundary between the Pacific and North America Plates (AIJ [1], NIED [5], USGS [6]).

Nearly 20,000 people were killed or are still missing by this great earthquake and the ensuing monster tsunami as of November 1, 2011. The principal cause of this devastating result is due to the great tsunami following the large earthquake. Table 2.1 and Fig. 2.1 show the human and economic loss in recent major natural disasters (data from Asahi newspaper [7]). It can be observed that the economic loss in the 2011 off the Pacific coast of Tohoku earthquake is extremely large.

The maximum height (run-up height) of the tsunami was reported to have attained almost 40 m (Miyako City, Iwate Prefecture) and this was observed in the

I. Takewaki et al., *Improving the Earthquake Resilience of Buildings*,
Springer Series in Reliability Engineering, DOI: 10.1007/978-1-4471-4144-0_2,

Table 2.1 Human and economic loss in recent major natural disasters (data from Asahi newspaper [7])

	Number of victims	Economic loss (Billion dollars)
East Japan great earthquake disaster (2011)	20,631	309
Hurricane Katrina (2005)	1,833	135
Hyogoken–Nanbu earthquake (Kobe EQ 1995)	6,437	100
China (2008)	87,476	85
Chile earthquake (2010)	562	30
New Zealand earthquake (2011)	181	13
Haiti earthquake (2010)	222,570	7.8
North Pakistan earthquake (2005)	73,338	5.2
Sumatra earthquake (2004)	165,708	4.5
Cyclone Nargis (Myanmar 2008)	138,366	4.0

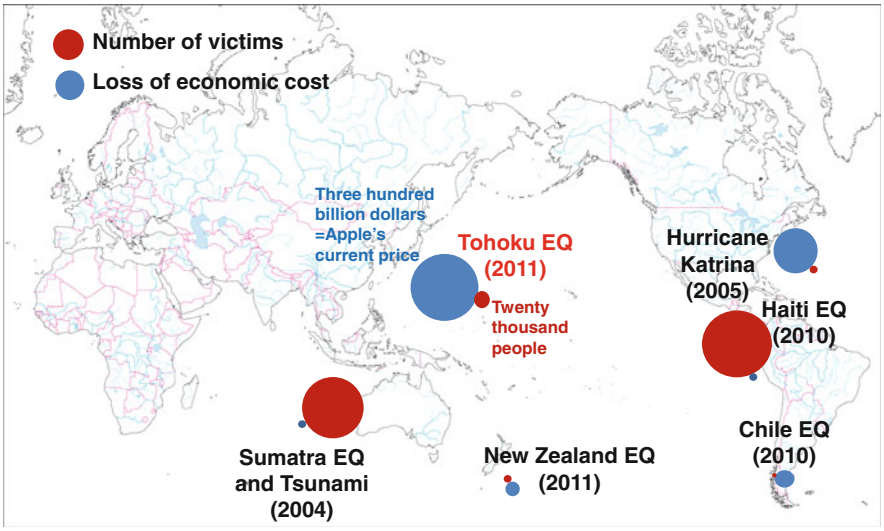

Fig. 2.1 Human and economic loss in recent major natural disasters (data from Asahi newspaper [7])

bay area with complex coast line shapes. It was also reported that the tsunami arrived at the third or fourth story in some buildings and invaded over 5 km from the coastline (Natori City, Miyagi Prefecture). It should be remarked that the number of collapsed (or damaged) buildings and houses remains not clear because most of the damages resulted from the tsunami and a clear record was not left. More detailed data on this earthquake can be obtained from the National Research Institute for Earth Science and Disaster Prevention (NIED) of Japan.

Because super high-rise buildings in mega cities in Japan have never been shaken by the so-called long-period ground motions with high intensities, the response of high-rise buildings to such long-period ground motions is now one of the most controversial issues in the field of earthquake-resistant design in Japan [8]. The issue of long-period ground motion and its effect on building structural design was initially brought up in Mexico, the USA, and Japan during 1980–1990s (for example [9–10]). Some clear observations have actually been reported recently (most famous one is the severe sloshing in oil tanks during the Tokachioki earthquake, Japan in 2003 [11]) and the earthquake ground motions in Tokyo, Yokohama, and Osaka during the March 11, 2011 earthquake are regarded to be extremely influential for super high-rise buildings. In December 2010, just before this earthquake, a set of simulated long-period ground motions was constructed and provided by the Japanese Government [8] for the retrofit of existing high-rise buildings and as a design guideline for new high-rise buildings.

In this chapter, we describe first the characteristics of this 2011 earthquake and discuss the properties of long-period ground motions from the viewpoint of critical excitation, i.e., the phenomenon of resonance characterized by the coincidence of the predominant period of ground motions with the fundamental natural period of high-rise buildings. It is shown that the criticality of the long-period ground motions can be investigated based on the theory of critical excitation [12–14]. This theory is intended to overcome the difficulty resulting from the uncertainty of earthquake ground motions (for example Geller et al. [15]). The credible bounds of input energy responses are obtained using the critical excitation method with the constraints on acceleration and velocity powers. It is demonstrated that the long-period ground motions can be controlled primarily by the velocity power and the ground motion recorded in Tokyo during the 2011 off the Pacific coast of Tohoku earthquake actually included fairly large long-period wave components.

Furthermore, tentatively designed 40- and 60-story steel buildings are subjected to such long-period ground motion as recorded in Shinjuku, Tokyo during the 2011 off the Pacific coast of Tohoku earthquake. It is shown that high-hardness rubber dampers, a kind of viscoelastic dampers with low temperature and frequency dependency, are able to damp the building vibration during long-period ground motions in an extremely shorter duration than in case of the building without those dampers. It is reported recently that this high-hardness rubber damper has a damping performance comparable with oil dampers. Two assumed 40-story steel buildings are also subjected to a set of simulated long-period ground motions taken from a December 2010 document of the Japanese Government [8] for the detailed investigation of response characteristics of super high-rise buildings under many simulated long-period ground motions in various areas.

2.2 General Characteristics of the 2011 Off the Pacific Coast of Tohoku Earthquake

The general characteristics of the 2011 off the Pacific coast of Tohoku earthquake are explained first. The source inversion and slip distribution using near-source strong ground motions are shown in Fig. 2.2a [16]. Since it is necessary to understand the size of the 2011 earthquake, the comparison of slipped fault size is shown in Fig. 2.2b among the 2004 Sumatra earthquake ($M = 9.1$), the 1923 Great Kanto earthquake ($M = 7.9$), the 1995 Hyogoken-Nanbu (Kobe) earthquake ($M = 7.3$), and the 2011 off the Pacific coast of Tohoku earthquake ($M = 9.0$) [17]. Due to the large magnitude and the distance from the source to the Honshu island of Japan, fairly wide areas in the eastern Japan were influenced and shaken by this earthquake.

The representative near-source ground motions along the Pacific coast in the eastern Japan are illustrated from north to south in Fig. 2.3a [18]. It can be found that two or more series (or groups) of waves exist in some areas and most ground motions continue for over 2 min. This implies the repeated occurrence of the fault slips in wide areas. This phenomenon has been pointed out by many researchers (for example Elnashai et al. [19], Hatzigeorgiou and Beskos [20], Moustafa and Takewaki [21]). It was reported afterwards that three main fault slips were observed in this series of events, i.e., the first at the eastern side of Sendai City (off Miyagi Prefecture), the second at the southern (off Miyagi and Fukushima Prefectures) and northern (off Iwate Prefecture) parts of the first one, and the third at the further southern side of the second slip (off Ibaragi Prefecture).

Figure 2.3b presents a more detailed description of those recorded ground motions (Yellow star indicates the epicenter). The following is the interpretation by NIED of Japan [22]. In Tohoku area (from Iwate Prefecture through Fukushima Prefecture), two wave groups (pink and yellow colors) can be observed from the vicinity of the epicenter (star mark). This means that main fault ruptures occurred twice in the vicinity of the epicenter one after another. In Fukushima Prefecture, a wave group (blue color) can be observed around 200 s toward the north. There are intensive waves between the yellow and the blue arrows. In Ibaragi Prefecture, a wave group (blue color arrow downward) can be seen. These results imply that a fault rupture occurred around the epicenter and this rupture induced many subsequent ruptures.

It is believed that the data of ground motions in Fig. 2.3 are very useful for the investigation of the accuracy of methods for constructing the ground motions from several sources. The distributions of the maximum ground accelerations and the maximum ground velocities determined from K-NET and KiK-net (NIED) data are shown in Fig. 2.4 [23].

Table 2.2 shows the top ten largest observed peak ground accelerations during this earthquake [18]. It is found that the maximum ground acceleration over 2.9 g was recorded at the K-NET station of Tsukidate in Kurihara City of Miyagi Prefecture. However, it is reported that the predominant period of this ground

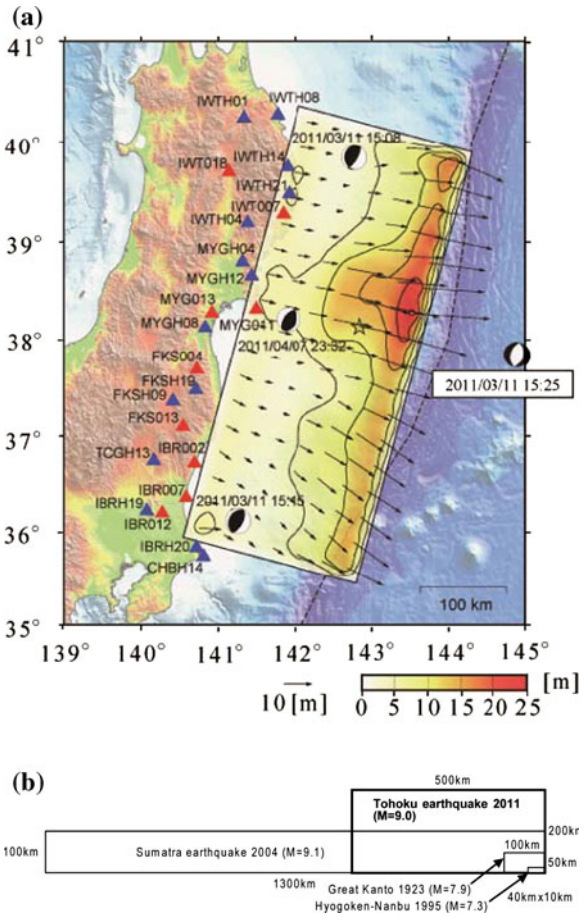

Fig. 2.2 **a** Source inversion and slip distribution using near-source strong ground motions [16], **b** Fault size of 2004 Sumatra earthquake ($M = 9.1$), 1923 Great Kanto earthquake ($M = 7.9$), 1995 Hyogoken-Nanbu (Kobe) earthquake ($M = 7.3$), and 2011 off the Pacific coast of Tohoku earthquake ($M = 9.0$) (data from Asahi newspaper [17]) (Reproduced from Takewaki et al. [4] with kind permission from © Elsevier)

motion is shorter than 0.3 s and this ground motion did not affect most buildings so much. These ground motion characteristics are common in almost all the areas along the Pacific coast in eastern Japan and the damage to buildings is not so large in spite of the tremendous magnitude of 9.0. The damages of most buildings are thought to result from the monster tsunami.

Other peculiar points observed in this 2011 earthquake may be a wide spread of liquefaction and settlement of land along the Pacific coast in Miyagi and Iwate Prefectures. It was reported that remarkable liquefaction occurred in many places on soft grounds including sands (over 42 km^2 even in Tokyo bay area) and the settlement over 1 m of land in Miyagi and Iwate Prefectures may result from the movement of plates near the epicenter. It is understood that the unexpected wide spread of liquefaction in spite of not so high level of maximum ground acceleration results from the long duration of shaking (over 2 min and four times longer than the Hyogoken-Nanbu earthquake). It is thought that this long duration of

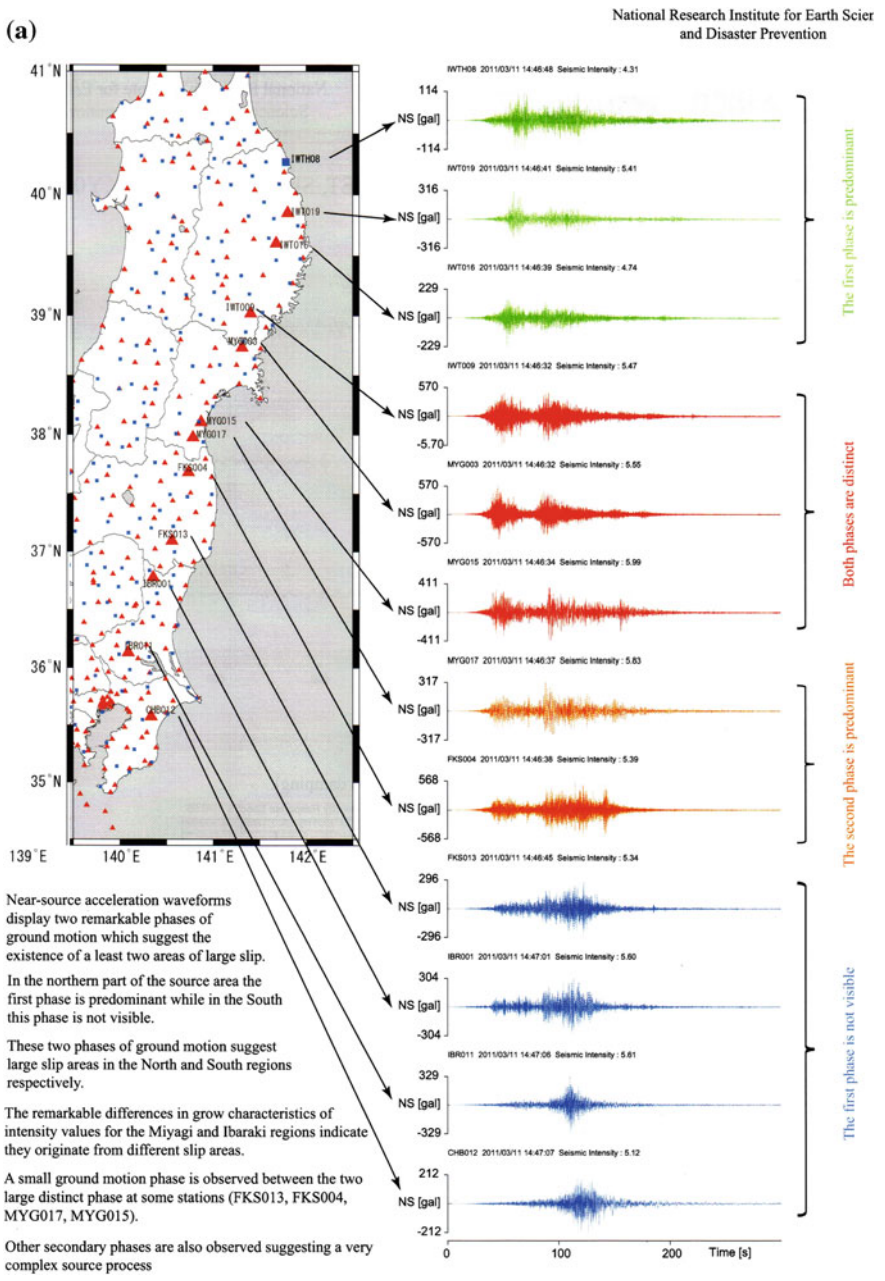

Fig. 2.3 **a** Characteristics of near-source ground motions along Pacific coast in East Japan [18], **b** Relation among fault rupture, wave propagation, and ground motion sequences (*Yellow star* indicates the epicenter) [22]

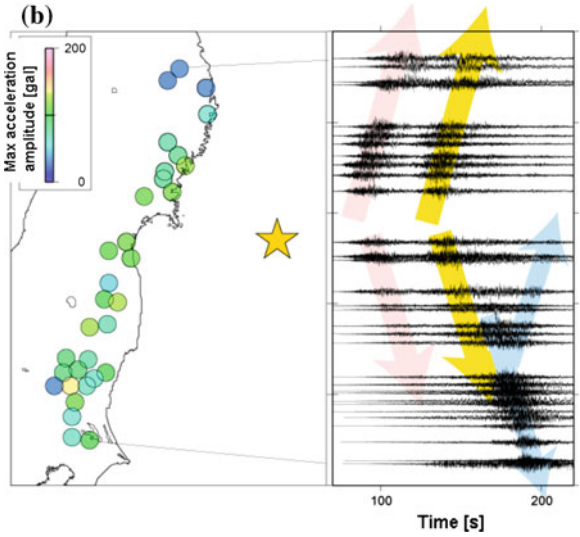

Fig. 2.3 (Continued)

shaking caused a rapid increase of excess pore water pressure. The liquefaction was also observed in Tokyo bay area and it was reported that 14.5 km^2 experienced liquefaction in Urayasu City in Chiba prefecture (one of Tokyo bay area cities).

As stated above, one of the most important issues in mega cities like Tokyo, Osaka, and Nagoya during this 2011 earthquake is the occurrence of long-period ground motions which could affect severely most super high-rise buildings through the resonant phenomenon. It is often reported that many super high-rise buildings in Tokyo and Osaka were severely shaken by those long-period ground motions. This issue will be discussed in the following sections in detail.

2.3 Seismic Response Simulation of Super High-Rise Buildings in Tokyo

2.3.1 Properties of Ground Motions in Tokyo

Figure 2.5a shows the acceleration waveforms of the long-period ground motion recorded at K-NET, Shinjuku station (TKY007) [18] and Fig. 2.5b presents the corresponding velocity wave forms [18]. It can be observed that the maximum ground velocity attains about 0.25 m/s and the ground shaking continues for over several minutes. The velocity response spectra for 1 and 5 % damping are shown in Fig. 2.6 [18]. The corresponding ones of Japanese seismic design code for 5 %

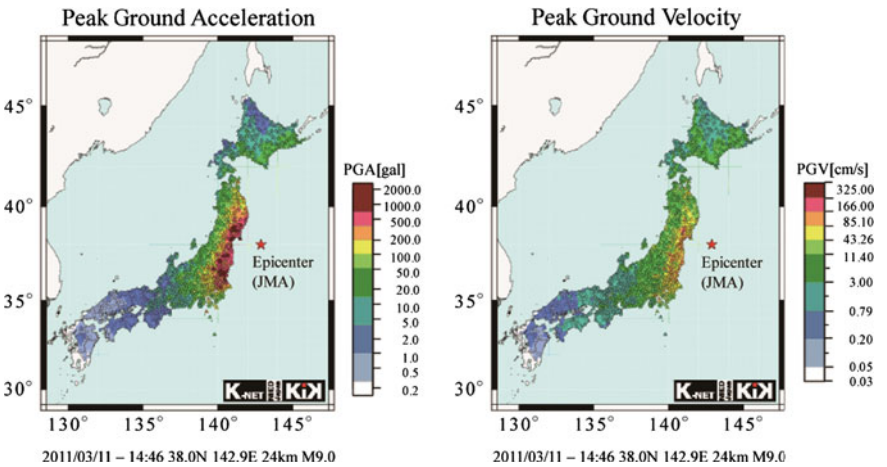

Fig. 2.4 Maximum ground accelerations and maximum ground velocities determined from K-NET and KiK-net data [23]

Table 2.2 List of 10 largest observed peak ground accelerations [18]

	Station name	PGA (gal)	JMA instrumental intensity[a]
1	MYG004	2,933	6.6
2	MYG012	2,019	6.0
3	IBR003	1,845	6.4
4	MYG013	1,808	6.3
5	IBR013	1,762	6.4
6	FKSH10	1,335	6.0
7	TCGH16	1,305	6.5
8	TCG014	1,291	6.3
9	IBRH11	1,224	6.2
10	MYGH10	1,137	6.0

[a] *JMA* Japan Meteorological Agency

MYG Miyagi prefecture, *IBR* Ibaragi prefecture, *FKS* Fukushima prefecture, *TCG* Tochigi prefecture. This list is based on information obtained by March 13, 2011 from 276 K-NET and 112 KiK-net sites

damping are also plotted in Fig. 2.6. It is understood that these ground motions include long-period components up to 10 s. The duration of records at K-NET stations is 300 s and it was found that this duration is not sufficient for the investigation of long-period ground motions.

For investigating further the long-period characteristics of that record, the Fourier amplitude spectra of both acceleration and velocity records have been obtained. Figure 2.7 shows the Fourier amplitude spectra of accelerations of Fig. 2.5a and Fig. 2.8 illustrates those of velocities of Fig. 2.5b [2].

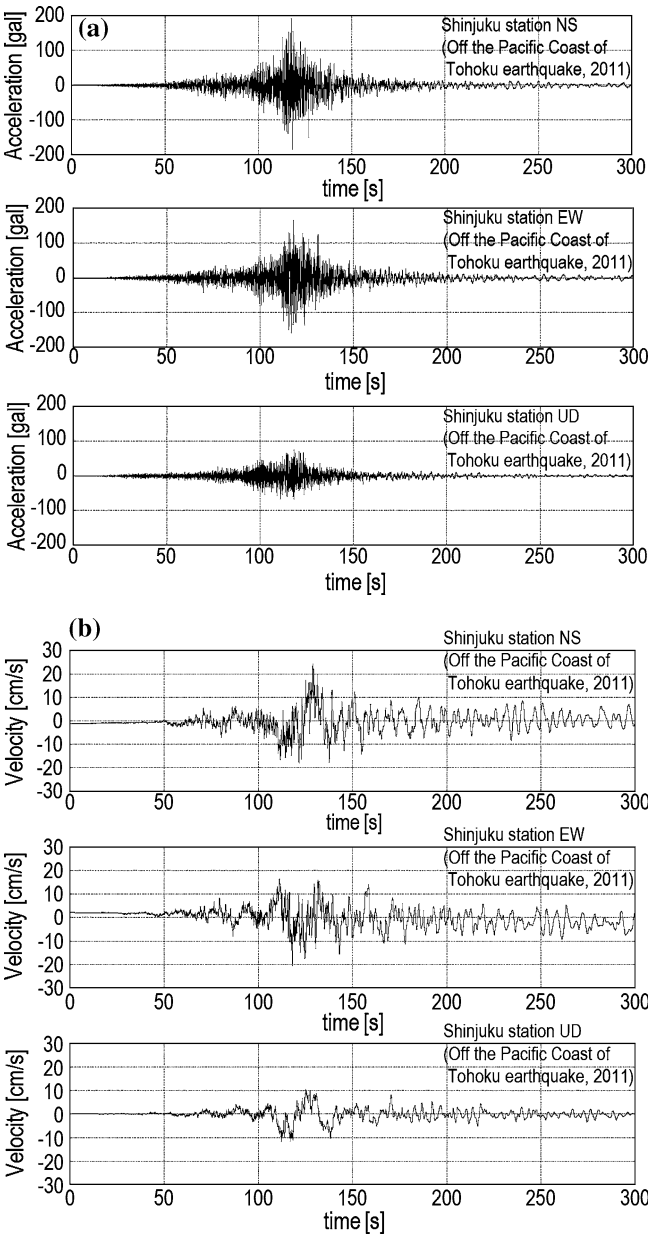

Fig. 2.5 **a** Long-period acceleration ground motion recorded at K-NET, Shinjuku station (TKY007) (Reproduced from Takewaki et al. [4] with kind permission from © Elsevier), **b** Long-period velocity ground motion recorded at K-NET, Shinjuku station (TKY007) (Reproduced from Takewaki et al. [4] with kind permission from © Elsevier)

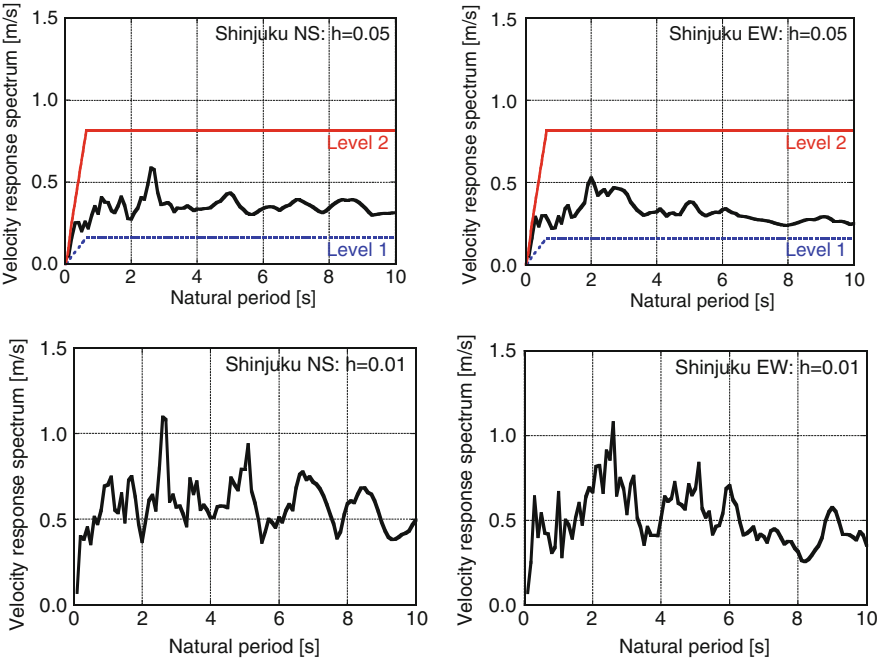

Fig. 2.6 Velocity response spectra (5 and 1 % damping) of ground motions at Shinjuku station (TKY007) and the corresponding ones of Japanese seismic design code for 5 % damping (Reproduced from Takewaki et al. [4] with kind permission from © Elsevier)

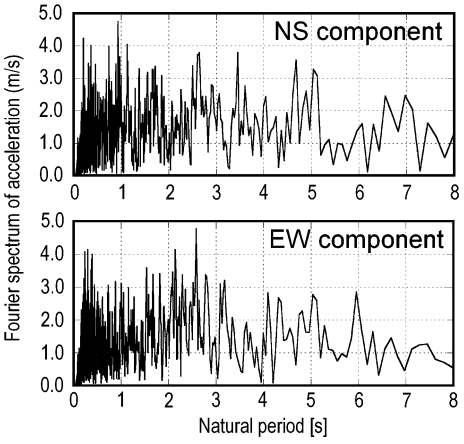

Fig. 2.7 Fourier amplitude spectra of acceleration ground motion at K-NET, Shinjuku station (TKY007) (Reproduced from Takewaki et al. [4] with kind permission from © Elsevier)

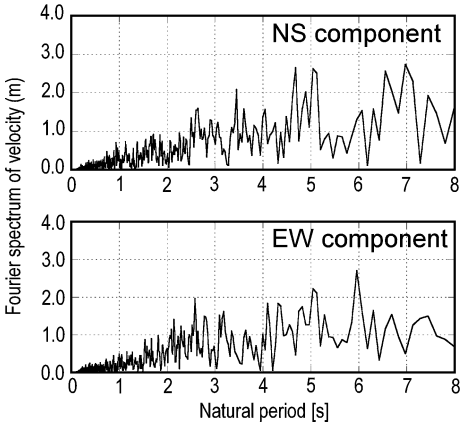

Fig. 2.8 Fourier amplitude spectra of velocity ground motion at K-NET, Shinjuku station (TKY007) (Reproduced from Takewaki et al. [4] with kind permission from © Elsevier)

2.3.2 Measure of Criticality in Long-Period Ground Motions

The critical excitation method [12, 24] is one of the methods for disclosing the level of criticality of ground motions. In the early stage, the maximum displacement was employed as the criticality measure. Then earthquake input energy was introduced to measure the criticality from the view point of input energy [24].

Figure 2.9 explains the schematic diagram for computing credible bounds of the input energy per unit mass E_I/m to a single degree-of-freedom (SDOF) model for acceleration and velocity constraints [13, 14, 24]. The function $F(\omega)$ in the diagram indicates the energy transfer function defined by

$$F(\omega) = \frac{2h\Omega\omega^2}{\pi\{(\Omega^2 - \omega^2)^2 + (2h\Omega\omega)^2\}} \tag{2.1}$$

where Ω: natural circular frequency of the SDOF model, h: damping ratio and ω: the excitation frequency. The input energy per unit mass E_I/m to the SDOF model can then be expressed by

$$E_I/m = \int_0^\infty |A(\omega)|^2 F(\omega)\mathrm{d}\omega \tag{2.2a}$$

or

$$E_I/m = \int_0^\infty |V(\omega)|^2 \omega^2 F(\omega)\mathrm{d}\omega \tag{2.2b}$$

where $A(\omega)$ and $V(\omega)$ are the Fourier transforms of the ground motion acceleration and ground motion velocity, respectively. It can be observed from Fig. 2.9 that the region of short natural period can be controlled by the credible bound for the

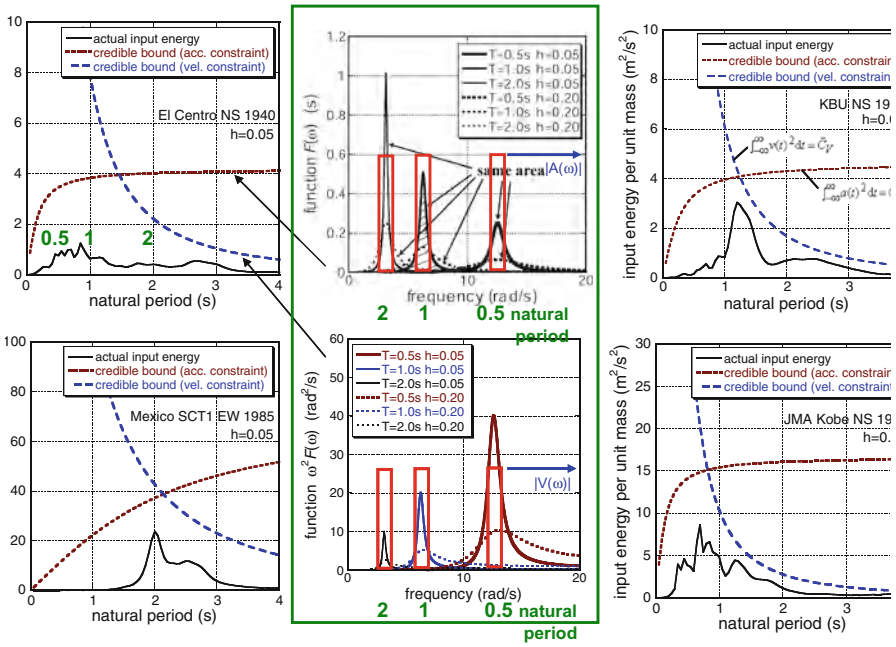

Fig. 2.9 Schematic diagram for computing credible bounds for acceleration and velocity constraints (Reproduced from Takewaki et al. [4] with kind permission from © Elsevier)

acceleration constraint and the region of long period can be controlled by the credible bound for the velocity constraint as explained in [13, 24]. It may be concluded that the introduction of both credible bounds enables the construction of the credible bound with uniform risk in all the natural period range. The word of 'uniform risk' is used in the meaning that the ratio of the actual input energy to the corresponding credible bound is almost constant in some ground motions regardless of the natural period of the model.

Figure 2.10a presents the comparison of the actual input energies (5 % damping), the credible bounds [13, 14, 24] for acceleration constraints (acceleration power in Housner and Jennings [25]) and the credible bounds for velocity constraints (velocity power in Housner and Jennings [25]) for NS and EW components [2]. The intersection point implies the predominant period from the viewpoint of input energy. The periods of 4 and 6 s are such predominant periods of ground motions and this implies that the ground motion recorded at K-NET, Shinjuku station (TKY007) actually included fairly large long-period wave components. For comparison, Fig. 2.10b shows the corresponding figures for El Centro NS 1940 and JMA Kobe NS 1995 (Hyogoken-Nanbu earthquake) [2, 13, 24]. The intersection point corresponds to rather shorter period ranges.

It may be concluded that the credible bound for the velocity constraint can control the bound of input energy from the long-period ground motion and this

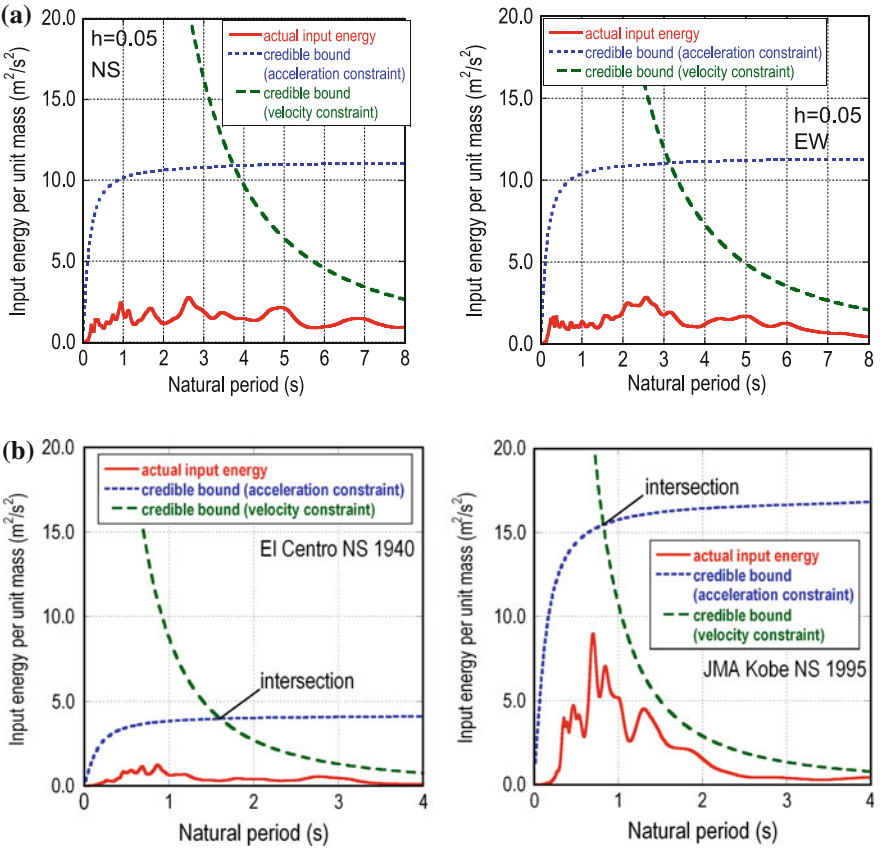

Fig. 2.10 **a** Actual input energies per unit mass (5 % damping), the credible bounds for acceleration constraints and the credible bounds for velocity constraints for the ground motions at K-NET, Shinjuku station (TKY007), **b** Actual input energies per unit mass (5 % damping), the credible bounds for acceleration constraints and the credible bounds for velocity constraints for El Centro NS (1940) and JMA Kobe NS (1995) (Reproduced from Takewaki et al. [4] with kind permission from © Elsevier)

bound plays a role for overcoming the difficulties caused by uncertainties of long-period ground motions (predominant period and intensity level).

2.3.3 *Seismic Response Simulation of Super High-Rise Buildings in Tokyo*

The 2011 off the Pacific coast of Tohoku earthquake may be the first earthquake to have occurred between tectonic plates and have affected super high-rise buildings

Table 2.3 Cross-sections of members

Story	Column (mm)	Beam (mm)
31–40	600 × 600 × 20 × 20	850 × 300 × 15 × 25
21–30	800 × 800 × 25 × 25	850 × 300 × 15 × 25
11–20	1,000 × 1,000 × 35 × 35	850 × 300 × 20 × 30
1–10	1,000 × 1,000 × 45 × 45	1,000 × 300 × 20 × 40

in mega cities. In order to investigate the influence of the recorded long-period ground motions on high-rise buildings, two steel moment-resisting building frames of 40 and 60 stories have been studied in [2]. The 40-story building has a fundamental natural period of $T_1 = 4.14$ s and the 60-story building has a corresponding one of $T_1 = 5.92$ s.

The buildings have a plan of 40 × 40 m (equally spaced 36 columns; span length = 8 m) and one planar frame is taken as the object frame. The uniform story height is 4 m. The floor mass per unit area is assumed to be 800 kg/m^2. The damping ratio is taken as 0.01 in accordance with the well-accepted database [26]. The variability of damping ratio is large depending on amplitude, building usage, etc. and most of the data exist in 0.5–3.0 % in high-rise steel buildings [26]. Therefore, 1 % damping (most credible one) has been used here. The cross-sectional properties of the 40-story steel building frame are shown in Table 2.3. The composite beam action (stiffening by floor slabs) has been taken into account. The stiffness of beams has been set as 1.5 times the original stiffness. The yield stress of the steel members is 235 N/mm^2. The rigid part of members is introduced at each beam–column connection.

It is well accepted that the passive dampers are very effective in the reduction of earthquake response in high-rise buildings. For the purpose of clarifying the merit of viscoelastic dampers (high-hardness rubber dampers [27]) (see Fig. 2.11), the buildings of 40 and 60 stories without and with these high-hardness rubber dampers have been subjected to the long-period ground motion recorded at K-NET, Shinjuku station (TKY007). The outline of the high-hardness rubber dampers is shown in Fig. 2.11. One damper unit consists of rubber thickness = 15 mm and rubber area = 0.96 m^2. The frame includes four damper units at every story.

Figure 2.12 shows the maximum story displacements and interstory drifts of the 40-story building of $T_1 = 4.14$ s without or with high-hardness rubber dampers to ground motion at Shinjuku station (TKY007) (frame response: elastic or elastic–plastic) [2]. It can be understood that linear and nonlinear analyses provide nearly the same results in this case. On the other hand, Fig. 2.13 illustrates the maximum story displacements and interstory drifts of the 60-story building of $T_1 = 5.92$ s without or with high-hardness rubber dampers to ground motion at Shinjuku station (TKY007) (frame response: elastic–plastic, 'four dampers per story' corresponds to 'damper double') [2]. Only nonlinear analyses have been performed. It can be observed that high-hardness rubber dampers are effective for the reduction of displacements.

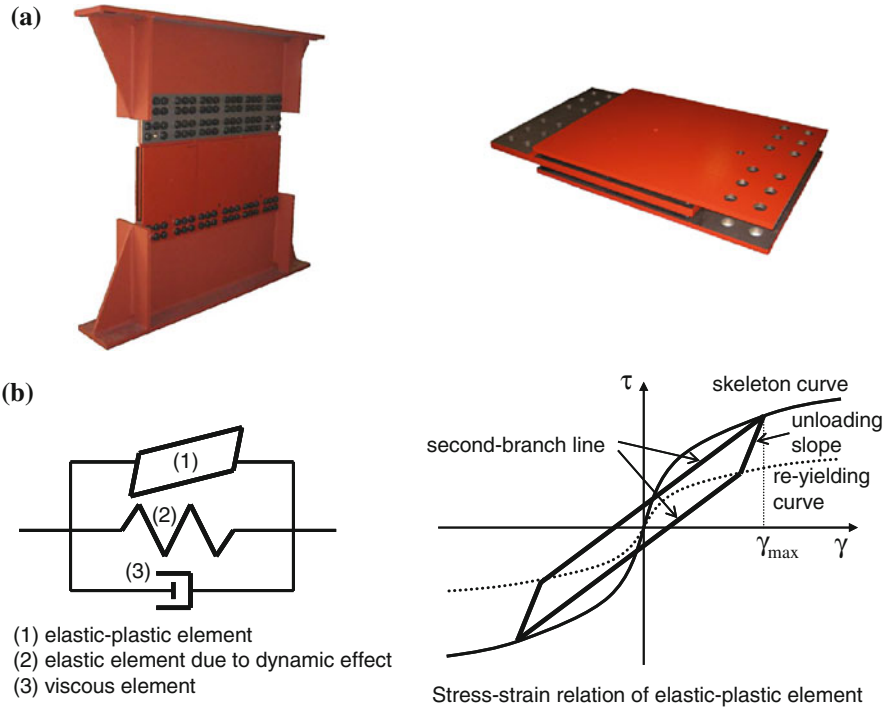

Fig. 2.11 High-hardness rubber dampers **a** Overview, **b** Modeling into three elements (Reproduced from Takewaki et al. [4] with kind permission from © Elsevier)

Table 2.4 shows the comparison of the maximum absolute accelerations at the top between the 60-story buildings without and with high-hardness rubber dampers under three recorded ground motions (EW component of TKY007, EW component at Chiyoda-ku station near Shinjuku station and NS component at Osaka WTC) during the 2011 off the Pacific coast of Tohoku earthquake. It can be seen that the top acceleration is reduced by the introduction of the high-hardness rubber dampers.

Figure 2.14a presents the comparison of time histories of top-story displacements of the assumed 60-story building of $T_1 = 5.92$ s to ground motion at Shinjuku station (EW component of TKY007) during the 2011 off the Pacific coast of Tohoku earthquake (frame response: elastic–plastic, without or with high-hardness rubber dampers) [2]. It can be understood that the high-hardness rubber dampers can damp the building vibration in an extremely short duration. It should be remarked that this ground motion was recorded for 300 s (records at K-NET stations are recorded for 300 s as a rule) and the response after 300 s is a free vibration in this case. Figure 2.14b shows a similar comparison to ground motion (EW component) at Chiyoda-ku station near Shinjuku station during the 2011 off the Pacific coast of Tohoku earthquake. It can be understood that the longer ground

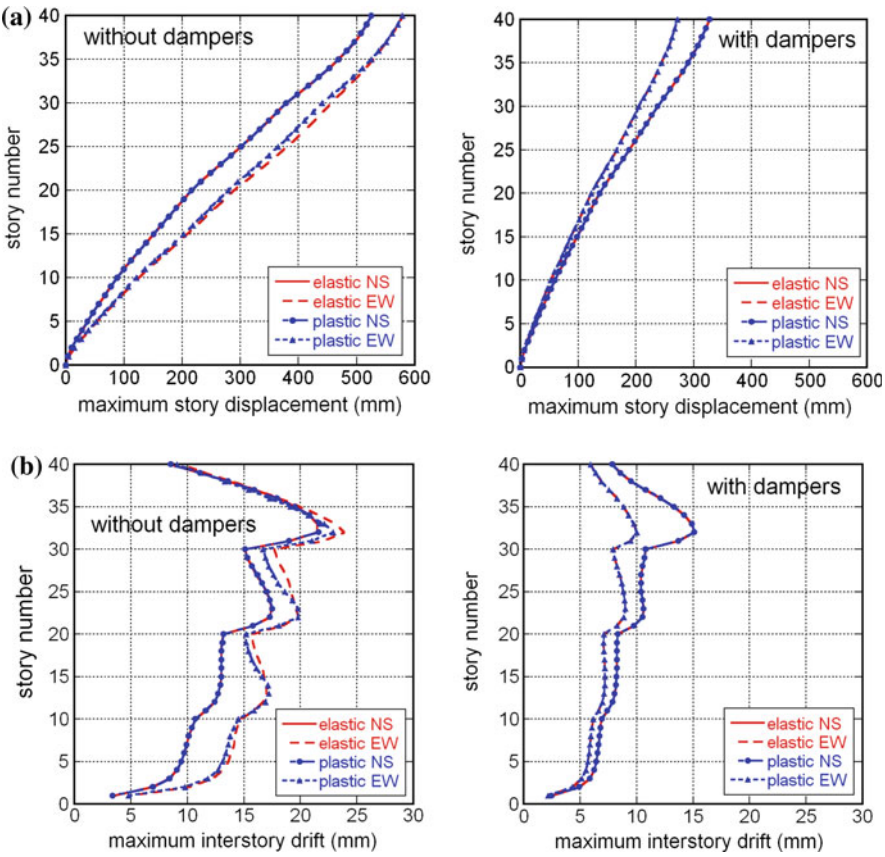

Fig. 2.12 **a** Maximum story displacement and **b** maximum interstory drift of a 40-story building of $T_1 = 4.14$ s without or with high-hardness rubber dampers to ground motion at Shinjuku station (TKY007) during the 2011 off the Pacific coast of Tohoku earthquake (frame response: elastic or elastic–plastic) (Reproduced from Takewaki et al. [4] with kind permission from © Elsevier)

motion duration of 600 s can demonstrate well the damping performance of the high-hardness rubber dampers.

It has been reported [28] that a 54-story building [height = 223 m: fundamental natural period = 6.2 s (short-span direction), 5.2 s (long-span direction)] retrofitted with passive oil dampers including the supporting bracing system in Shinjuku, Tokyo experienced a top displacement of 0.54 m during the 2011 off the Pacific coast of Tohoku earthquake. The vibration duration has been reported to be over 13 min. It has also been found that the building would have attained a top displacement of 0.7 m if the passive dampers had not been installed. This fact corresponds well to the result explained above.

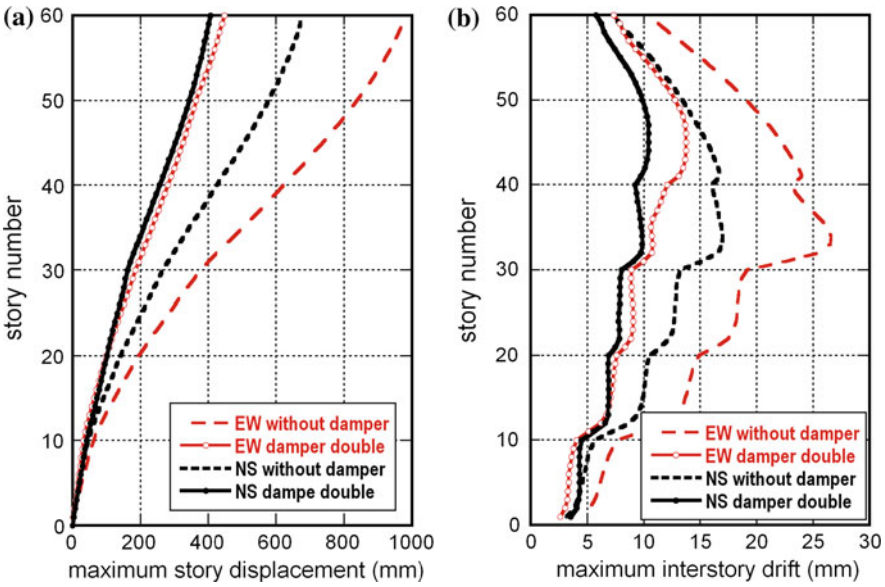

Fig. 2.13 **a** Maximum story displacement and **b** maximum interstory drift of a 60-story building of $T_1 = 5.92$ s without or with high-hardness rubber dampers to ground motion at Shinjuku station (TKY007) during the 2011 off the Pacific coast of Tohoku earthquake (frame response: elastic–plastic, '4 dampers per story' corresponds to 'damper double') (Reproduced from Takewaki et al. [4] with kind permission from © Elsevier)

Table 2.4 Reduction of top acceleration via high-hardness rubber dampers (m/s^2)

60-story building	EW component of TKY007	EW component at Chiyoda-ku station	NS component at Osaka WTC
No damper	1.79	1.54	0.933
With damper	1.65	1.21	0.667

There is another report that a 55-story super high-rise building in Osaka [height = 256 m: fundamental natural period = 5.8 s (long-span direction), 5.3 s (short-span direction)] was shaken severely regardless of the fact that Osaka is located far from the epicenter (about 800 km) and the JMA instrumental intensity was three in Osaka. It should be pointed out that the level of velocity response spectra of ground motions observed here (first floor) is almost the same as that at the Shinjuku station (K-NET) in Tokyo and the top-story displacement are about 1.4 m (short-span direction) and 0.9 m (long-span direction). Figure 2.15a shows the ground acceleration, ground velocity and top-story displacement. It can be observed that a clear resonant phenomenon occurs during about eight cycles. The corresponding velocity response spectra of the ground motion are shown in Fig. 2.15b. The resonance phenomenon can be explained by using the structure of

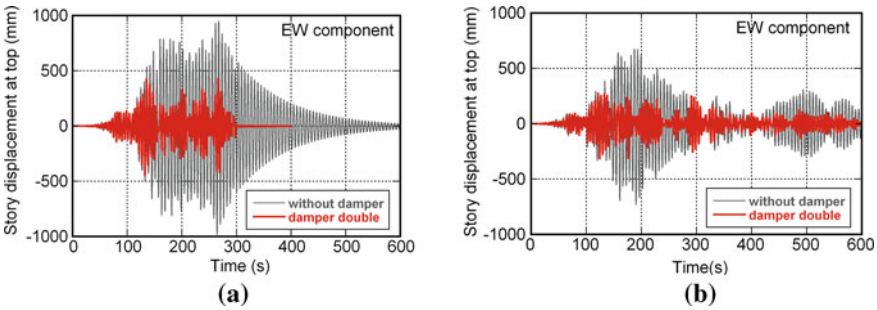

Fig. 2.14 **a** Comparison of time histories of top-story displacement of an assumed 60-story building of $T_1 = 5.92$ s without or with high-hardness rubber dampers to ground motion at Shinjuku station (EW component of TKY007) during the 2011 off the Pacific coast of Tohoku earthquake (frame response: elastic–plastic) (Reproduced from Takewaki et al. [4] with kind permission from © Elsevier), **b** Comparison of time histories of top-story displacement of an assumed 60-story building of $T_1 = 05.92$ s without or with high-hardness rubber dampers to ground motion (EW component) at Chiyoda-ku station near Shinjuku station during the 2011 off the Pacific coast of Tohoku earthquake (frame response: elastic–plastic) (Reproduced from Takewaki et al. [4] with kind permission from © Elsevier)

the surface ground in Fig. 2.15c. Figure 2.15d illustrates the comparison of the actual input energies (5 % damping), the credible bounds [13, 14, 24] for acceleration constraints (acceleration power in Housner and Jennings [25]) and the credible bounds for velocity constraints (velocity power in Housner and Jennings [25]) for NS and EW components [2]. It can be seen that the ground motion recorded here in Osaka bay area actually included fairly large long-period wave components. These facts imply the need of consideration of long-period ground motions in the seismic resistant design of super high-rise buildings in mega cities even though the site is far from the epicenter. The seismic retrofit using hysteretic steel dampers and oil dampers is being planned.

Figure 2.16 illustrates the comparison of the sensitivity of the response amplification in the resonant case and nonresonant case with respect to damping reduction. It may be useful to note that the amplification by damping can be expressed by

$$1/2h \quad \text{for resonant long-period ground motion} \tag{2.3a}$$

$$1.5/(1+10h) \text{ for non-resonant conventional ground motion} (\text{ratio to } h = 0.05) \tag{2.3b}$$

This implies that the high sensitivity of the response to damping in resonant long-period ground motions. Since the damping ratio in super high-rise buildings is usually small (smaller than 0.02), this high sensitivity may be kept in mind in their structural design.

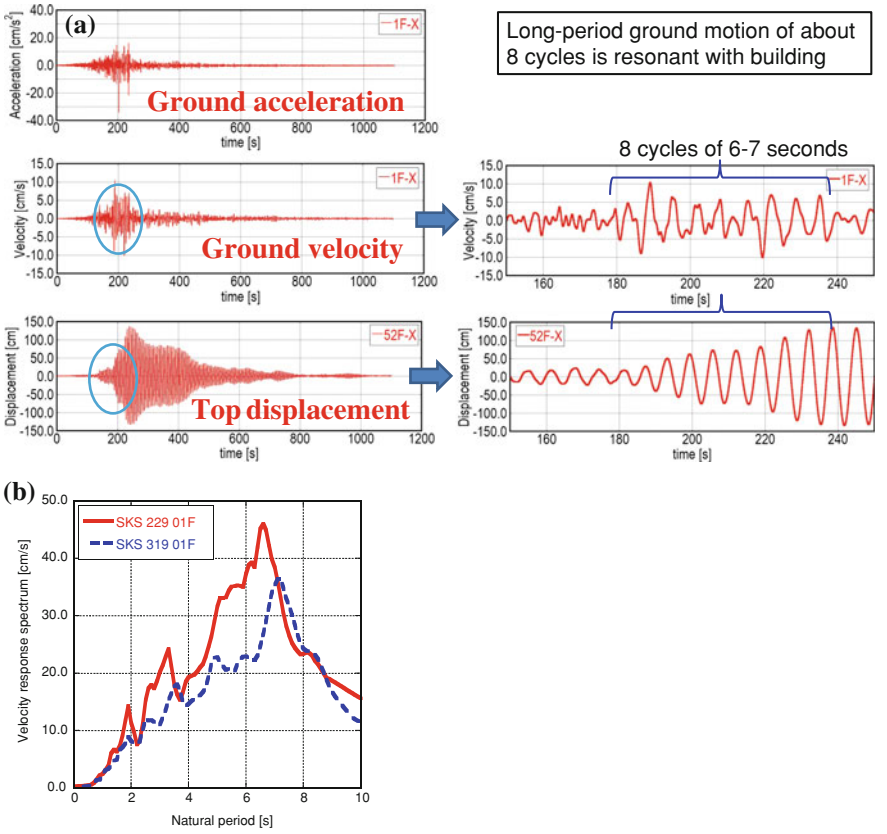

Fig. 2.15 **a** Ground acceleration, ground velocity and top-story displacement of a 55-story building in Osaka during the 2011 off the Pacific coast of Tohoku earthquake, **b** Velocity response spectra of ground motion (horizontal two directions, 229: NS, 319: EW), **c** Shear wave velocity distribution of surface ground, **d** Actual input energies per unit mass (5 % damping), the credible bounds for acceleration constraints and the credible bounds for velocity constraints for the ground motions in Osaka bay area

2.4 Seismic Response of High-Rise Buildings to Simulated Long-Period Ground Motions (Japanese Government Action)

2.4.1 Characteristics of Simulated Long-Period Ground Motions

On December 21, 2010, the Japanese Government made a press release to upgrade the regulation for high-rise buildings under long-period ground motions. The Ministry of Land, Infrastructure, Transport and Tourism (MLIT) of Japan specified

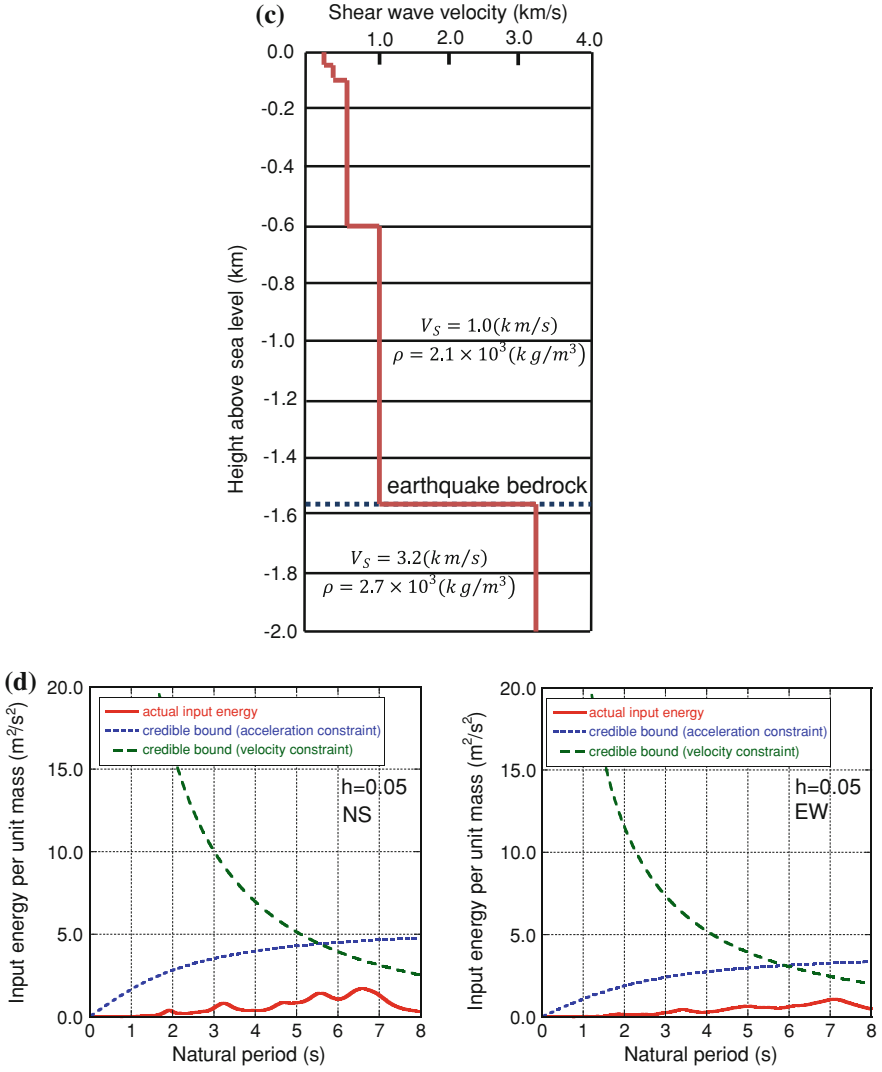

Fig. 2.15 (Continued)

nine areas in Tokyo, Nagoya, and Osaka (see Fig. 2.17) [8]. Areas 1–4 exist in Tokyo, Areas 5–7 in Nagoya, and Areas 8, 9 in Osaka.

Figure 2.18a shows the acceleration and velocity records of simulated ground motions in those nine areas specified in Fig. 2.17. These simulated ground motions were generated by using the acceleration response spectra (5 %) at the bedrock and the group delay time (mean and standard deviation) for the phase property [8]. It can be observed that large velocity waves appear in later times.

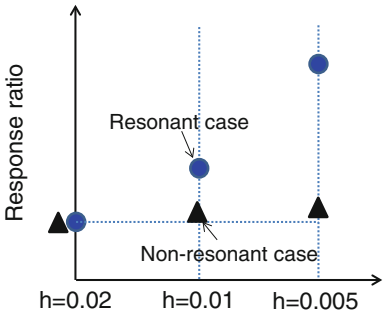

Fig. 2.16 Comparison of sensitivities of the response amplification in the resonant case and nonresonant case with respect to damping reduction

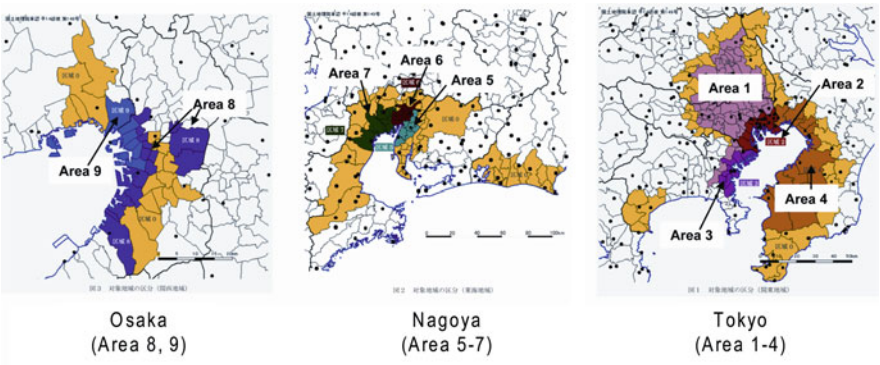

Fig. 2.17 Nine areas in Osaka, Nagoya, and Tokyo specified by the MLIT of Japan MLIT [8] (Reproduced from Takewaki et al. [4] with kind permission from © Elsevier)

Figure 2.18b presents the pseudo velocity response spectra and velocity response spectra of the simulated acceleration ground motions specified by the MLIT. It can be seen that the velocity spectra in 2–8 s have relatively large magnitudes.

Figure 2.18c shows the actual input energies per unit mass [13, 24, 23], the credible bounds for acceleration constraints [13, 24] and the credible bounds for velocity constraints [13, 24] for the simulated ground motions specified by the MLIT. As stated before, the intersection point indicates the predominant period of the ground motion. As in the ground motion recorded at K-NET, Shinjuku station (TKY007), 3–8 s are such predominant periods and this implies that the simulated ground motions actually include fairly large long-period wave components.

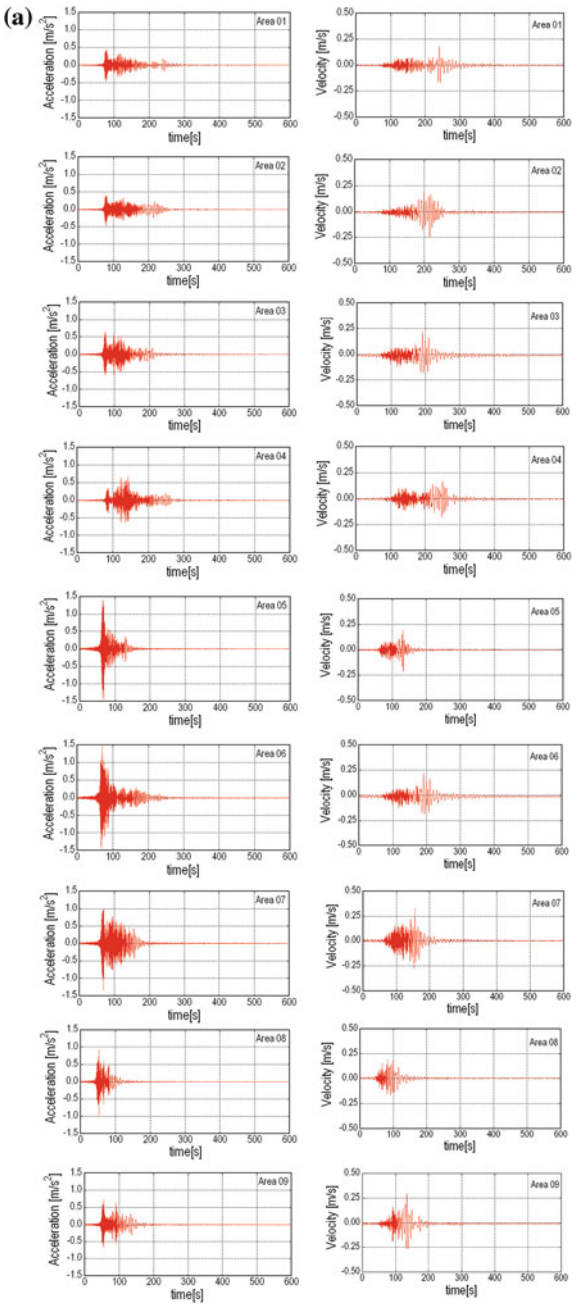

Fig. 2.18 **a** Acceleration and velocity ground motion records at nine areas specified by the MLIT of Japan (data from MLIT [8]) (Reproduced from Takewaki et al. [4] with kind permission from © Elsevier), **b** Pseudo velocity response spectra (5 % damping) and velocity response spectra of the simulated acceleration ground motions specified by the MLIT of Japan MLIT [8] (Reproduced from Takewaki et al. [4] with kind permission from © Elsevier), **c** Actual input energies per unit mass (5 % damping), the credible bounds for acceleration constraints and the credible bounds for velocity constraints for the simulated ground motions specified by the MLIT of Japan (Reproduced from Takewaki et al. [4] with kind permission from © Elsevier)

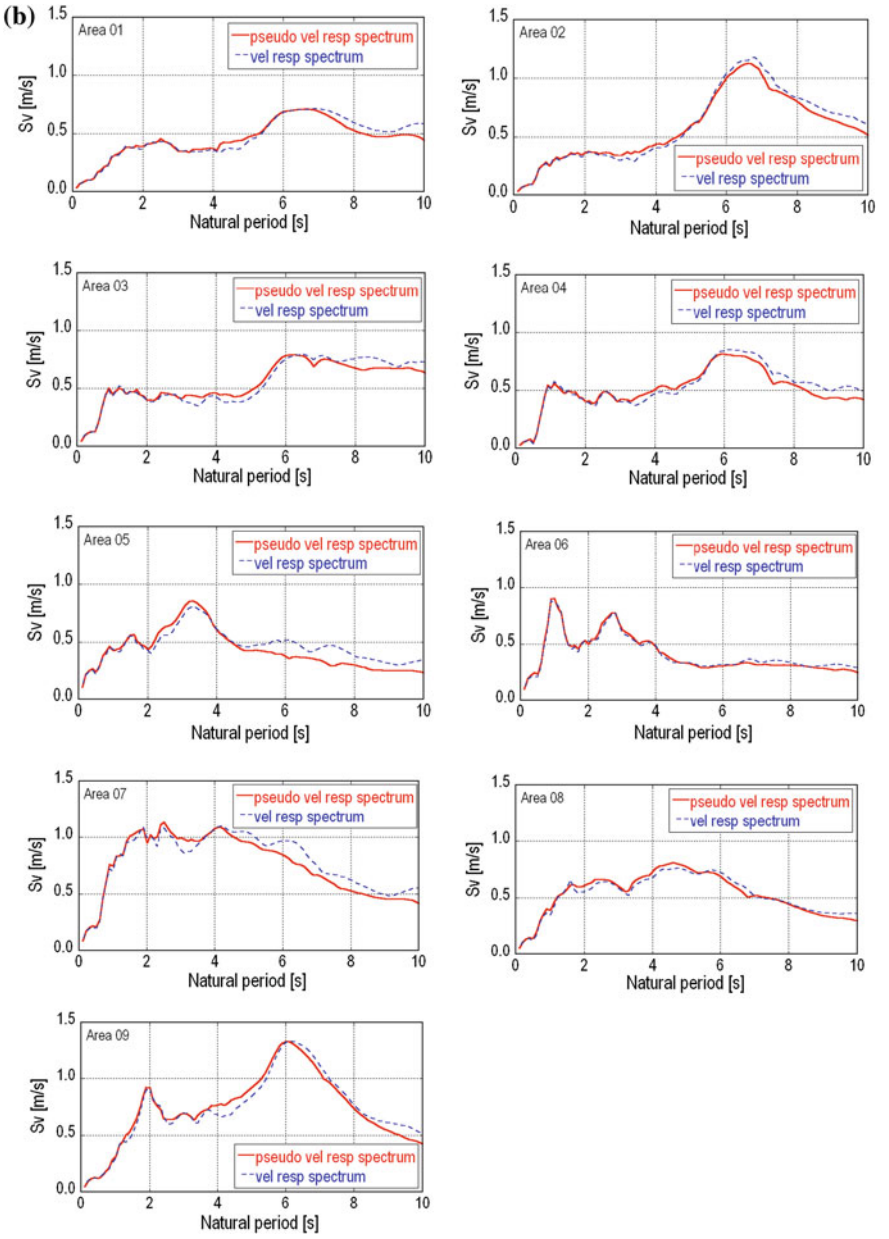

Fig. 2.18 (Continued)

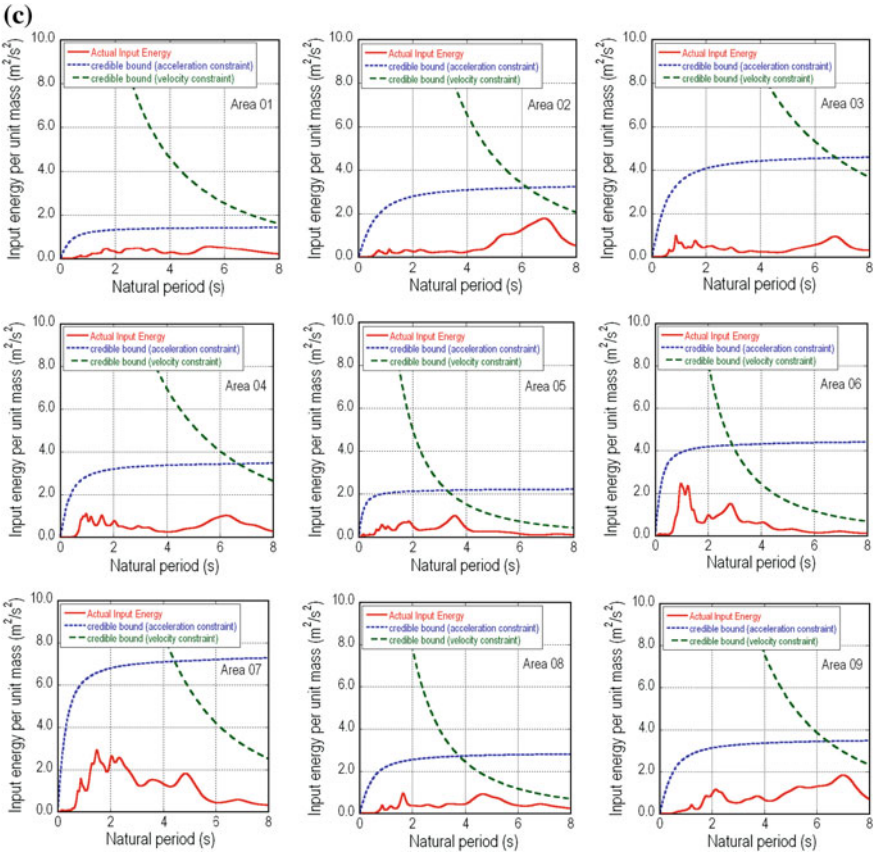

Fig. 2.18 (Continued)

2.4.2 *Response Simulation of Super High-Rise Buildings Without and With High-Hardness Rubber Dampers*

In order to investigate the influence of the simulated ground motions in Areas 1–9 on the response of high-rise buildings, two buildings of 40 stories have been assumed. The parameters of the buildings are the same as those stated in Sect. 2.3.3. The stiffness of beams has been evaluated as double the original stiffness for the building frame of $T_1 = 3.6$ s and as 1.5 times the original stiffness for the building frame of $T_1 = 4.14$ s. Judging from the database on the relationship of the building height with its fundamental natural period in Japan, the model of $T_1 = 3.6$ s is a slightly stiff building model for 40-story steel buildings and the model of $T_1 = 4.14$ s is a slightly flexible steel building model. Only the latter has been treated in Sect. 2.3. For the purpose of clarifying the merit of viscoelastic dampers [high-hardness rubber dampers [27] as in the previous case], the buildings

of 40 stories without and with these high-hardness rubber dampers have been subjected to the simulated long-period ground motions. One damper unit consists of rubber thickness = 15 mm and rubber area = 0.96 m^2. 'Damper single' includes two damper units at every story and 'damper double' includes four damper units at every story.

Figure 2.19a illustrates the comparison of the time histories of the top displacement of the 40-story buildings of $T_1 = 3.6$ s without and with high-hardness rubber dampers (frame response; elastic) under a simulated long-period ground motion in Area 5 (Nagoya area). It can be observed that the high-hardness rubber dampers are able to damp the building vibration during long-period ground motions in an extremely shorter duration compared to the building without those dampers.

Figure 2.19b explains the mechanism of response amplification under long-period ground motion. It can be found that remarkable building response amplification begins almost after the end of input acceleration and such amplification corresponds well with the velocity wave.

Figure 2.20 presents the time histories of the top displacement of the 40-story buildings of $T_1 = 3.6$ s without and with high-hardness rubber dampers (frame response; elastic) under simulated long-period ground motions in nine areas. It can be found that the responses in Areas 5 and 7 (Nagoya area) are large. Figure 2.21 shows the maximum interstory drifts of the 40-story buildings of $T_1 = 3.6$ s without and with high-hardness rubber dampers (frame response; elastic). It can also be understood that the maximum response of the damper double is not different much from that of the damper single and the damper single is sufficient for the maximum response reduction in this case. However, as for the reduction rate of the vibration, the damper double is better than the damper single.

Figure 2.22 illustrates the time histories of the top displacement of the 40-story buildings of $T_1 = 4.14$ s without and with high-hardness rubber dampers (frame response; elastic). It can be seen that the responses are quite different from those of $T_1 = 3.6$ s shown in Fig. 2.20. This characteristic may depend on the relation of the fundamental natural period of the building with the predominant period of ground motions in nine areas. Figure 2.23 shows the maximum interstory drifts of the 40-story buildings of $T_1 = 4.14$ s without and with high-hardness rubber dampers (frame response; elastic). Different from the case for $T_1 = 3.6$ s shown in Fig. 2.21, the maximum response of the damper double is much smaller than that of the damper single especially in Area 7 which shows the maximum response. This indicates the superiority of the increase of damper quantity in the reduction of the maximum response in addition to the reduction rate of the vibration.

Figure 2.24 presents the comparison of the top displacements of the 40-story buildings of $T_1 = 3.6$ s (elastic or elastic–plastic, without or with dampers) under the simulated long-period ground motion in Area 5. It can be observed that the elastic–plastic response of the building frame decreases the response level to some extent. However, it can also be seen that the high-hardness rubber dampers can damp the vibration so quickly. It has been confirmed that this quick vibration reduction rate can be achieved also by viscous dampers like oil dampers so long as

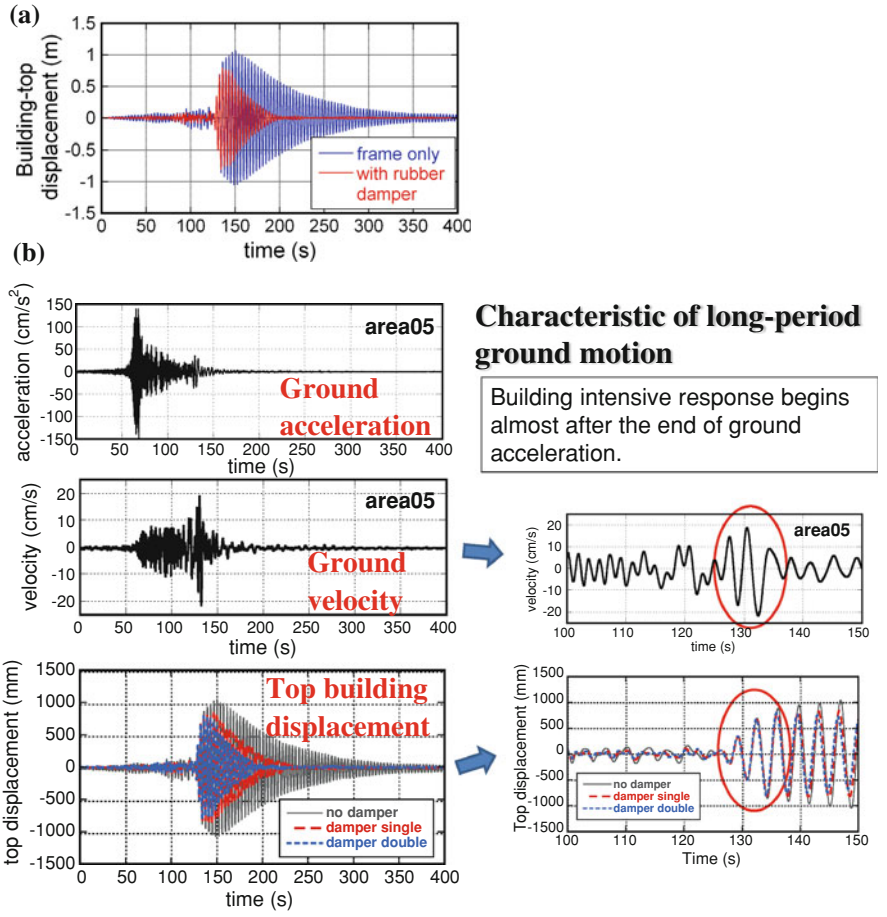

Fig. 2.19 **a** Comparison of the time histories of the top displacement of the 40-story buildings of $T_1 = 3.6$ s without and with high-hardness rubber dampers (frame response; elastic) under a simulated long-period ground motion in Area 5 (Reproduced from Takewaki et al. [4] with kind permission from © Elsevier) **b** Mechanism of response amplification under long-period ground motion

an appropriate amount of dampers is provided. Figure 2.25 shows the maximum interstory drifts of 40-story buildings of $T_1 = 3.6$ s (Area 5) and $T_1 = 4.14$ s (Area 7) without high-hardness rubber dampers (elastic or elastic–plastic). As in Fig. 2.24, it can be seen that the elastic–plastic response of the building frame decreases the response level to some extent. Since the plastic deformation may cause some problems in the beam–column connections (as observed during Northridge and Hyogoken–Nanbu earthquakes) and member plastic deformation capacities, a more detailed investigation will be necessary on the overall characteristics of this property. Figure 2.26 illustrates the plastic hinge formation

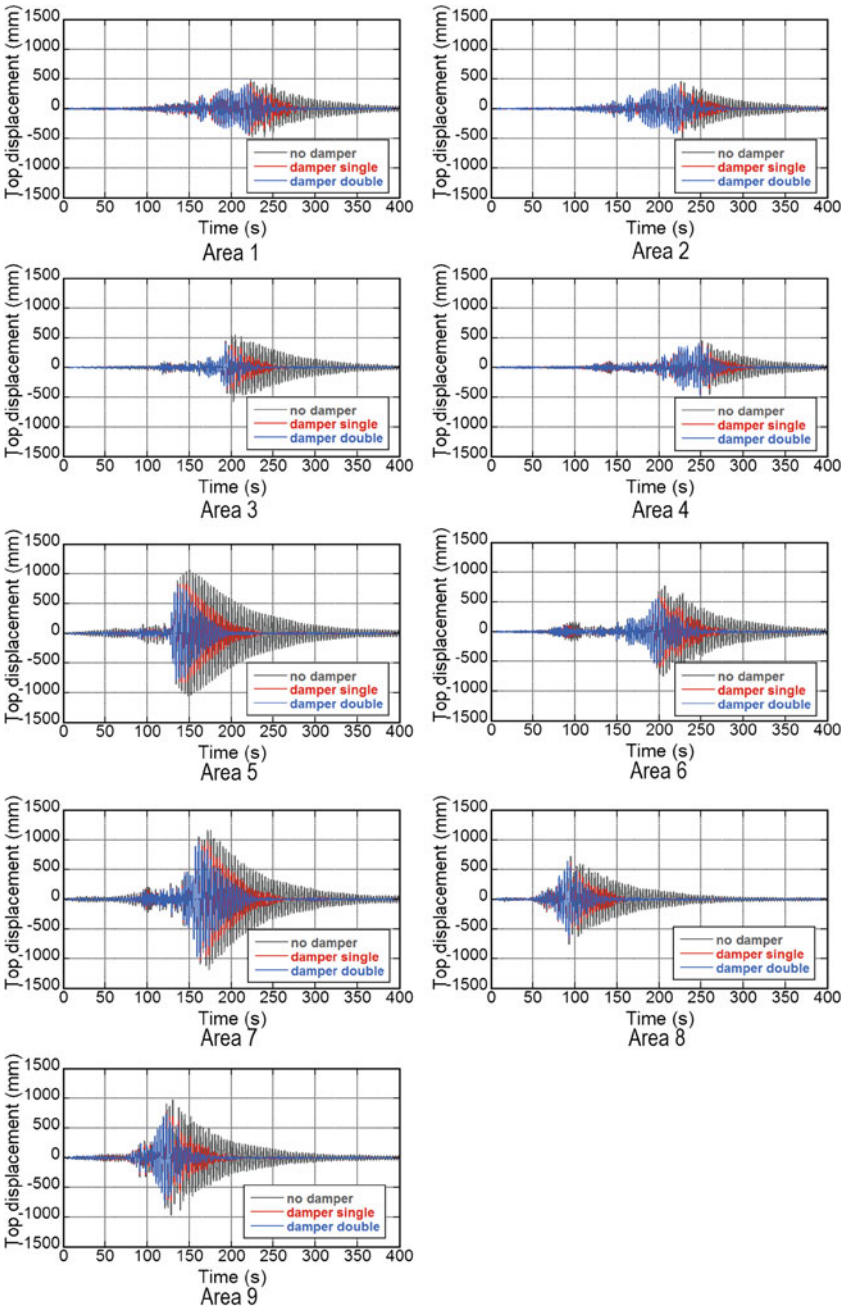

Fig. 2.20 Time histories of top displacement of 40-story buildings of $T_1 = 3.6$ s without and with high-hardness rubber dampers (frame response; elastic) (Reproduced from Takewaki et al. [4] with kind permission from © Elsevier)

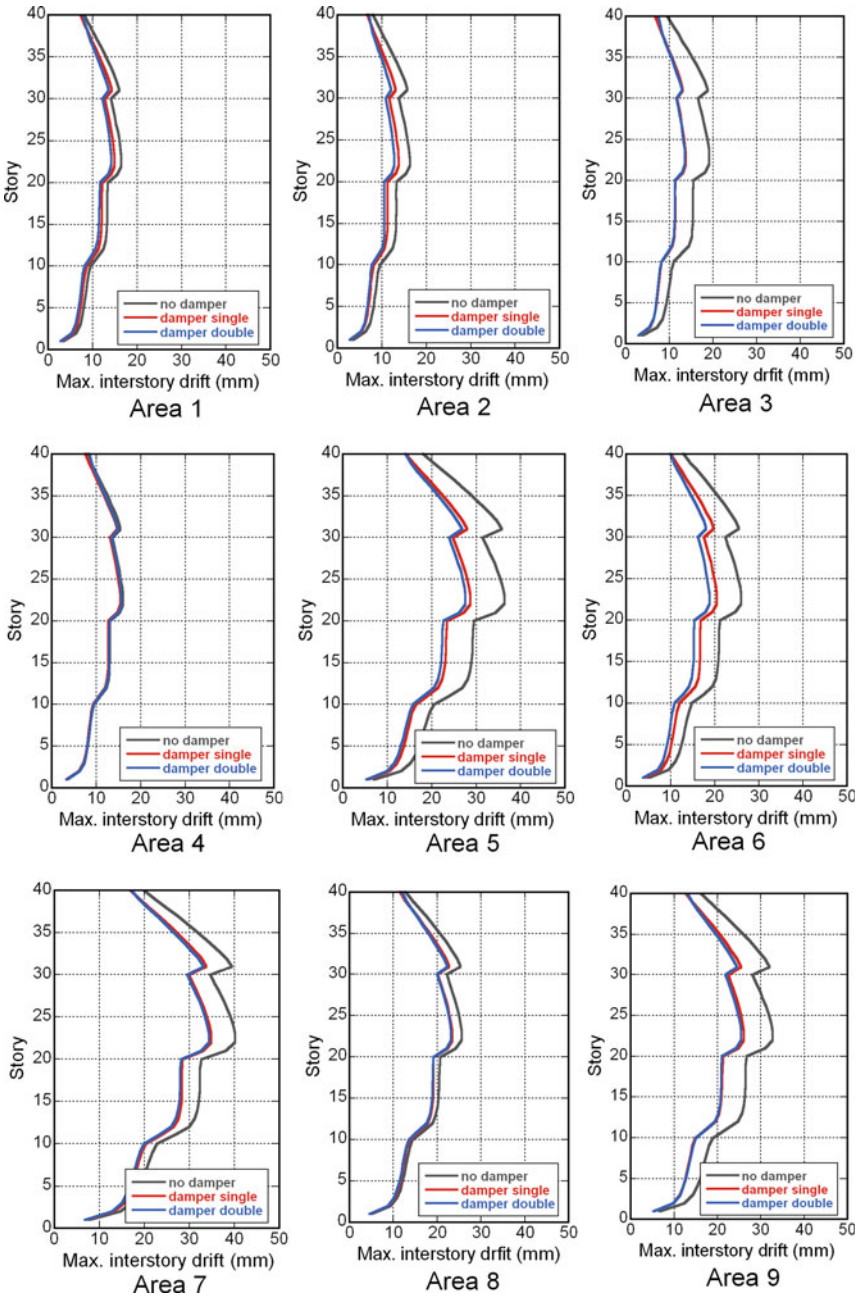

Fig. 2.21 Maximum interstory drifts of 40-story buildings of $T_1 = 3.6$ s without and with high-hardness rubber dampers (frame response; elastic) (Reproduced from Takewaki et al. [4] with kind permission from © Elsevier)

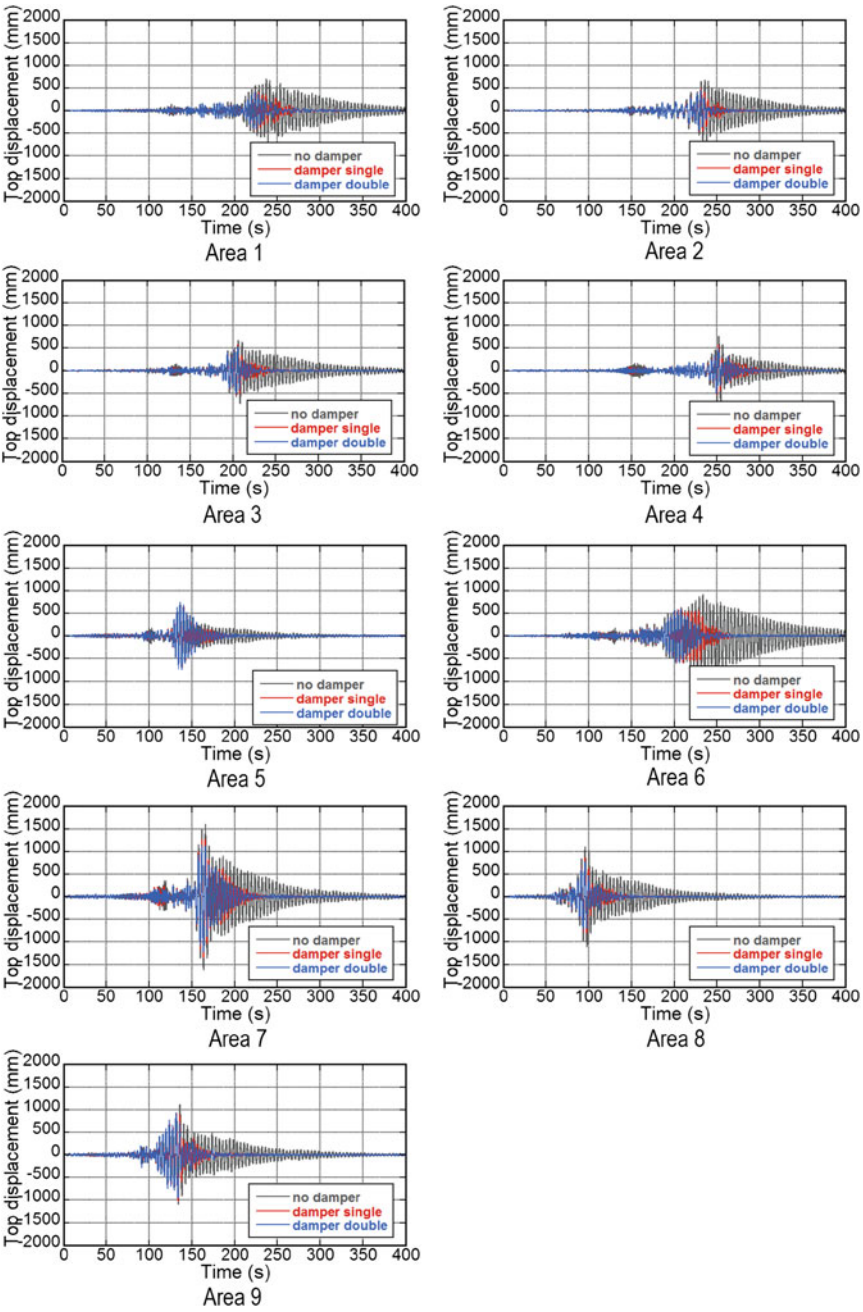

Fig. 2.22 Time histories of top displacement of 40-story buildings of $T_1 = 4.14$ s without and with high-hardness rubber dampers (frame response; elastic) (Reproduced from Takewaki et al. [4] with kind permission from © Elsevier)

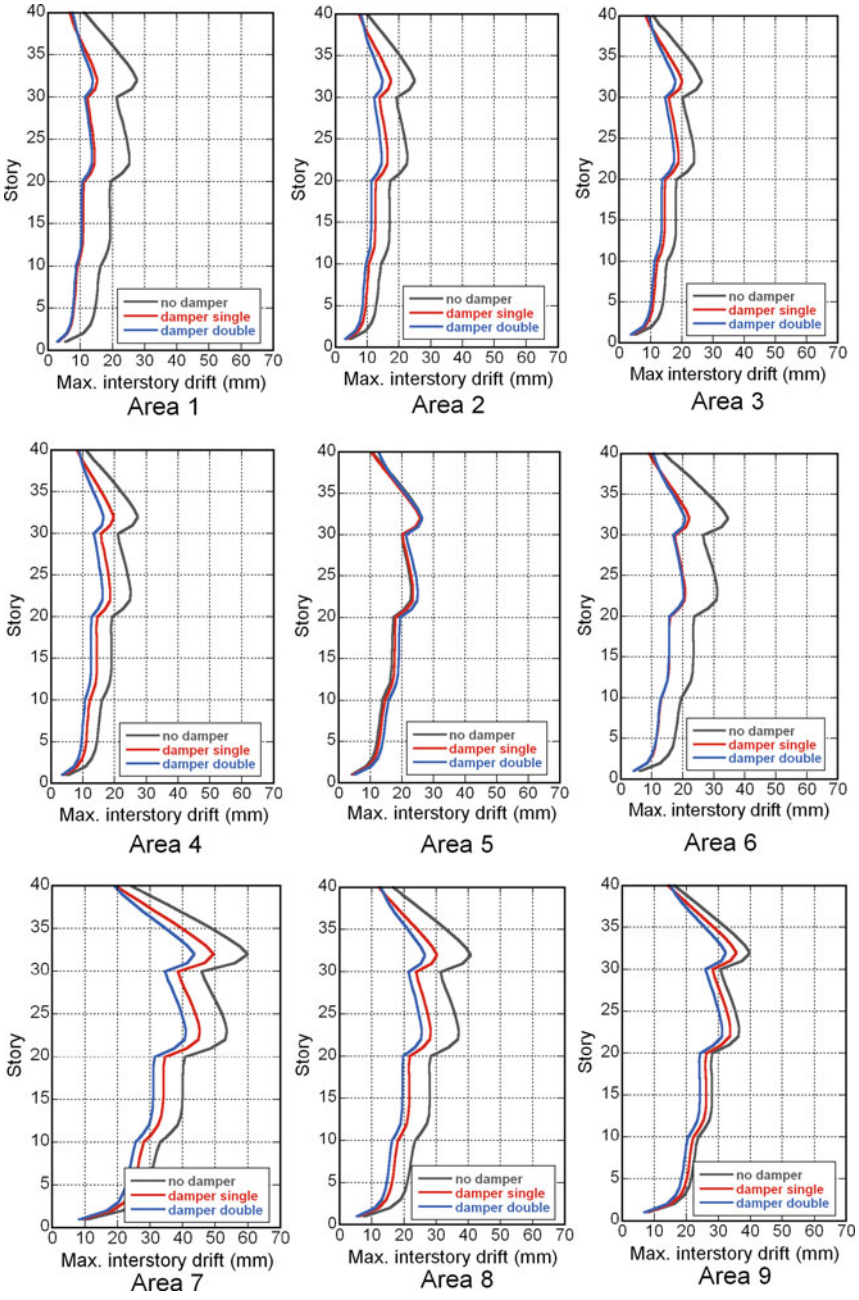

Fig. 2.23 Maximum interstory drifts of 40-story buildings of $T_1 = 4.14$ s without and with high-hardness rubber dampers (frame response; elastic) (Reproduced from Takewaki et al. [4] with kind permission from © Elsevier)

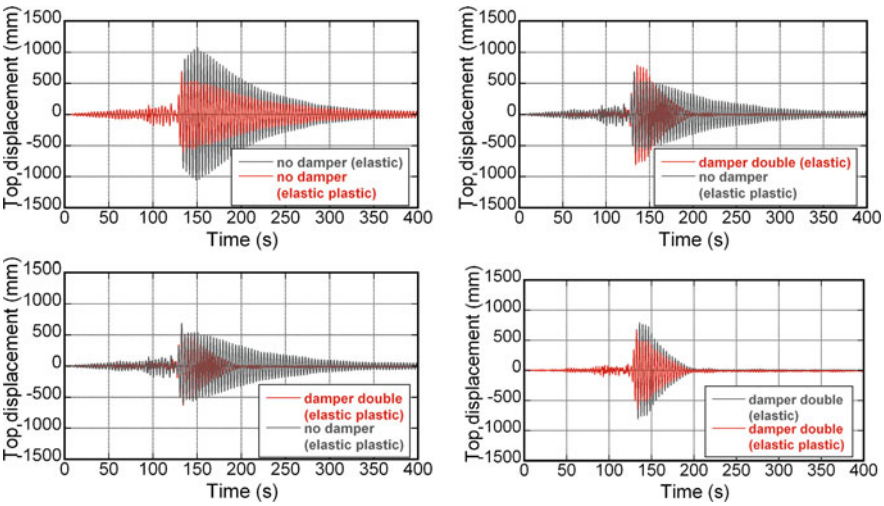

Fig. 2.24 Top displacement of 40-story buildings of $T_1 = 3.6$ s without and with high-hardness rubber dampers (frame response: elastic or elastic–plastic) (Area 5) (Reproduced from Takewaki et al. [4] with kind permission from © Elsevier)

diagram of the building frames without and with dampers. The nonlinear analyses performed take into account both material and geometrical nonlinearities.

The purposes of this chapter (Sect. 2.4) are to disclose the general properties of the effect of simulated long-period ground motions on the responses of high-rise buildings and to investigate the effect of high-hardness rubber dampers in the vibration reduction of high-rise buildings under long-period ground motions. For these purposes only elastic responses have been investigated comprehensively at first (Figs. 2.20, 2.21, 2.22, 2.23). This treatment is valid when high strength steels are used (this is often the case now in Japan), because the response will be almost within the elastic limit. However, since it seems to be also useful to investigate the effect of elastic–plastic behavior on the resonant phenomenon, the comparison between elastic and elastic–plastic responses have been conducted for the model of $T_1 = 3.6$ s in Area 5 and that of $T_1 = 4.14$ s in Area 7 as representative ones. As can be seen from Fig. 2.20, most of the responses are within the elastic limit except in a few cases including Areas 5 and 7. Furthermore, it was made clear that most responses of high-rise buildings in Japan (Tokyo and Osaka) during the 2011 off the Pacific coast of Tohoku earthquake are within the elastic limit. It seems reasonable to a limited extent also from these viewpoints to deal with the elastic response of high-rise buildings under simulated long-period ground motions.

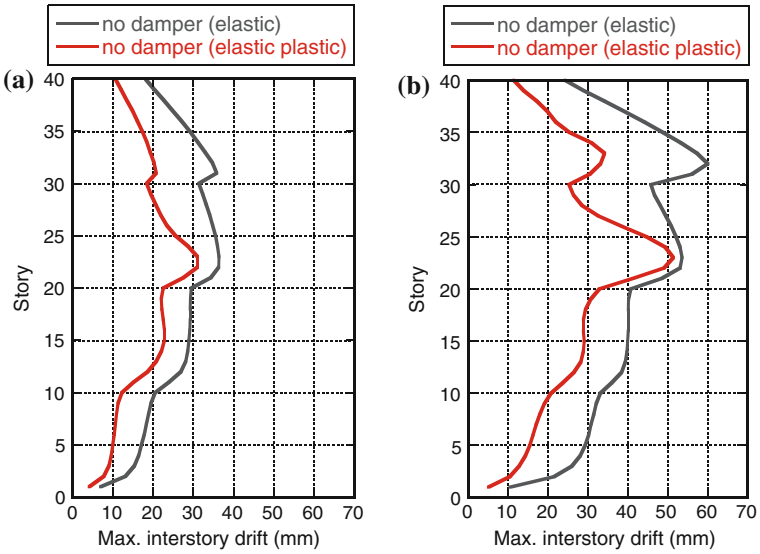

Fig. 2.25 Maximum interstory drifts of 40-story buildings of $T_1 = 3.6$ s and $T_1 = 4.14$ s without high-hardness rubber dampers (frame response; elastic or elastic–plastic), **a** 40-story building of $T_1 = 3.6$ s in area 5, **b** 40-story building of $T_1 = 4.14$ s in area 7 (Reproduced from Takewaki et al. [4] with kind permission from © Elsevier)

2.4.3 AIJ's Research Result

Architectural Institute of Japan (AIJ) made a press release on March 4, 2011 just 1 week before the March 11, 2011 earthquake on the result of their research on the response of high-rise buildings under long-period ground motions [29]. The conclusions in this press release may be summarized as follows:

1. High-rise buildings in Tokyo, Nagoya, and Osaka may experience long-duration vibration under simulated long-period ground motions obtained as a sequence of Tokai, Tonankai, and Nankai earthquakes [30]. However, the collapse will not occur (the possibility may be very low).
2. The long-period ground motions exhibit different properties in different areas. The high-rise buildings also have different properties depending on their heights and constructed periods. The relation of the structural properties of high-rise buildings with the properties of long-period ground motions plays a key role in the evaluation of seismic response of high-rise buildings.
3. The damage to non-structural components, facilities, and furniture may be caused easily. Such damage can be reduced effectively by introducing appropriate steps.
4. Passive dampers will be able to damp the building vibration remarkably and reduce the damage to structural members.

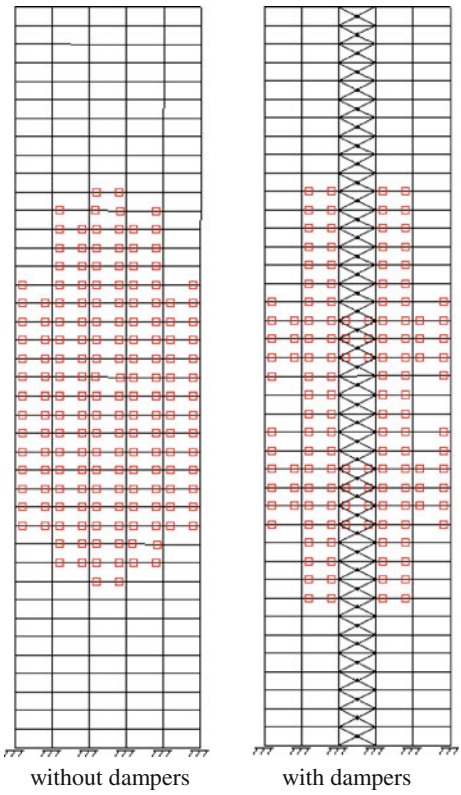

Fig. 2.26 Plastic hinge formation in 40-story buildings of $T_1 = 3.6$ s without and with high-hardness rubber dampers (Area 5) (Reproduced from Takewaki et al. [4] with kind permission from © Elsevier)

2.5 Summary

1. The 2011 off the Pacific coast of Tohoku earthquake is the most devastating earthquake in Japan after the 1923 Great Kanto earthquake in terms of the damaged area and loss cost. This earthquake may be the largest interplate earthquake which attacked mega cities after the construction of super high-rise buildings. However, it is reported that this earthquake may not be the most influential one to be taken into account because the influence depends on the plate (including epicenter) on which mega cities lie and on the soil condition supporting buildings. This fact has been confirmed from the comparison with the result using the simulated ground motions provided by the Japanese Government in December 2010.
2. The ground motion recorded at K-NET, Shinjuku station (TKY007), Tokyo during the 2011 off the Pacific coast of Tohoku earthquake contains fairly large long-period wave components and has a frequency content of broad band (2–6 s). This can be observed from not only the velocity response spectra (and Fourier spectra) but also the earthquake input energy spectra taking into account of the concept of critical excitation. This characteristic has also been

demonstrated by the simulated ground motions provided by the Japanese Government in December 2010.

3. The region of short natural period in the input energy spectrum can be controlled by the credible bound for the acceleration constraint and the region of long period can be controlled by the credible bound for the velocity constraint as demonstrated in the references [13, 14]. The introduction of both credible bounds enables the construction of the credible bound with uniform risk (almost constant ratio of the input energy to its credible bound) in all the natural period range in some ground motions. The credible bound introduced in the references [13, 14] for the velocity constraint can control the bound of input energy from the long-period ground motion and this bound plays a key role for overcoming the difficulties induced by uncertainties of long-period ground motions.
4. Viscoelastic dampers, such as high-hardness rubber dampers, and viscous dampers, such as oil dampers, are able to reduce the building vibration during long-period ground motions in an extremely shorter duration compared to the building without those dampers. It has been made clear from this March 11, 2011 earthquake that the safety is not the only target and the functionality together with the consideration of psychologic aspects (relief) of residents has to be maintained appropriately.
5. The word 'unexpected incident' is often used in Japan after this great earthquake. It may be true that the return period of this class of earthquakes at the same place could be 500–1000 years and the use of this word may be acceptable to some extent from the viewpoint of the balance between the construction cost and the safety level. However, the critical excitation method is expected to enhance the safety level and earthquake resilience of building structures against undesirable incidents drawn from this irrational concept in the future.

References

1. Architectural Institute of Japan (2011) Preliminary reconnaissance report on the 2011 off the Pacific coast of Tohoku earthquake, 6 April 2011 (in Japanese)
2. Takewaki I (2011) Preliminary report of the 2011 off the Pacific coast of Tohoku earthquake. J Zhejiang Univ-SCI A 12(5):327–334
3. Takewaki I (2011) The 2011 off the Pacific coast of Tohoku earthquake and its impact on building structural design, keynote paper (Plenary speaker) at the ASEM11+Congress, in Seoul, Korea, 18–23 Sept 2011
4. Takewaki I, Murakami S, Fujita K, Yoshitomi S, Tsuji M (2011) The 2011 off the Pacific coast of Tohoku earthquake and response of high-rise buildings under long-period ground motions. Soil Dyn Earthq Eng 31(11):1511–1528
5. NIED (2011) National research institute for earth science and disaster prevention. 2011 Off the Pacific Coast of Tohoku earthquake. (in Japanese) Available from http://www.hinet.bosai.go.jp/topics/off-tohoku110311/. Accessed on 3 May 2011
6. USGS (2011) Magnitude 9.0—Near the East coast of Honshu, Japan. Available from http://earthquake.usgs.gov/earthquakes/eqinthenews/2011/usc0001xgp/#summary. Accessed on 3 May 2011

7. Asahi newspaper (2011) 7 Aug 2011 (in Japanese)
8. Ministry of Land, Infrastructure, Transport and Tourism (MLIT) (2011) Code draft for the retrofit of existing high-rise buildings and design guideline for new high-rise buildings. 21 Dec 2010 (in Japanese) Available from http://www.mlit.go.jp/report/press/house05_hh_000218.html. Accessed on 11 Jan 2011
9. Heaton T, Hall J, Wald D, Halling M (1995) Response of high-rise and base-isolated buildings to a hypothetical M 7.0 blind thrust earthquake. Science 267:206–211
10. Ariga T, Kanno Y, Takewaki I (2006) Resonant behavior of base-isolated high-rise buildings under long-period ground motions. Struct Des Tall Spec Buildings 15(3):325–338
11. Zama S, Nishi H, Yamada M, Hatayama K (2008) Damage of oil storage tanks caused by liquid sloshing in the 2003 Tokachi Oki earthquake and revision of design spectra in the long-period range. In: Proceedings of the 14th world conference on earthquake engineering, Beijing, China, 12–17 Oct 2008
12. Drenick RF (1970) Model-free design of aseismic structures. J Eng Mech Div, ASCE 96(EM4):483–493
13. Takewaki I (2004) Bound of earthquake input energy. J Struct Eng, ASCE 130(9):1289–1297
14. Takewaki I (2008) Critical excitation methods for important structures, invited as a semi-plenary speaker. EURODYN 2008, Southampton, England, 7–9 July 2008
15. Geller RJ, Jackson DD, Kagan YY, Mulargia F (1997) Earthquakes cannot be predicted. Science 275:1616
16. NIED (2011) National research institute for earth science and disaster prevention. 2011 off the Pacific Coast of Tohoku earthquake. Source inversion and slip distribution using near-source strong ground motions. (in Japanese) (revised version in 12 April 2011 by Suzuki W, Aoi M and Sekiguchi H) Available from http://www.kyoshin.bosai.go.jp/kyoshin/topics/TohokuTaiheiyo_20110311/inversion/. Accessed on 3 May 2011
17. Asahi newspaper (2011) 10 April 2011 (in Japanese)
18. NIED (2011) National research institute for earth science and disaster prevention. 2011 Off the Pacific Coast of Tohoku earthquake, strong ground motion, emergency meeting of headquarters for earthquake research promotion, 13 March 2011. Available from http://www.k-net.bosai.go.jp/k-net/topics/TohokuTaiheiyo_20110311/nied_kyoshin2e.pdf. Accessed on 20 April 2011
19. Elnashai A, Bommer JJ, Martinez-Pereira A (1998) Engineering implications of strong motion records from recent earthquakes. In: Proceedings of 11th European conference on earthquake engineering. CD-ROM, Paris
20. Hatzigeorgiou GD, Beskos DE (2009) Inelastic displacement ratios for SDOF structures subjected to repeated earthquakes. Eng Struct 31(13):2744–2755
21. Moustafa A, Takewaki I (2011) Response of nonlinear single-degree-of-freedom structures to random acceleration sequences. Eng Struct 33:1251–1258
22. NIED (2011) National research institute for earth science and disaster prevention. 2011 off the Pacific Coast of Tohoku earthquake: overview (in Japanese). Available from http://www.hinet.bosai.go.jp/topics/off-tohoku110311/. Accessed on 3 May 2011
23. NIED (2011) National research institute for earth science and disaster prevention. 2011 off the Pacific coast of Tohoku earthquake, strong ground motion. (in Japanese) Available from http://www.kyoshin.bosai.go.jp/kyoshin/topics/html20110311144626/main_20110311144626.html. Accessed on 20 April 2011
24. Takewaki I (2006) Critical excitation methods in earthquake engineering. Elsevier, Amsterdam
25. Housner GW, Jennings PC (1975) The capacity of extreme earthquake motions to damage structures. In: Hall WJ (ed) Structural and geotechnical mechanics. Prentice-Hall, Englewood Cliff, pp 102–116
26. Satake N, Suda K, Arakawa T, Sasaki A, Tamura Y (2003) Damping evaluation using full-scale data of buildings in Japan. J Struct Eng, ASCE 129(4):470–477

27. Tani T, Yoshitomi S, Tsuji M, Takewaki I (2009) High-performance control of wind-induced vibration of high-rise building via innovative high-hardness rubber damper. Struct Des Tall Spec Buildings 18(7):705–728
28. Asahi newspaper (2011) evening edition of 19 April 2011 (in Japanese)
29. Architectural Institute of Japan (AIJ) (2011) Report at the open research meeting on design guide for super high-rise buildings under long-period ground motions. 4 March 2011 (in Japanese)
30. Kamae K, Kawabe H, Irikura, K (2004) Strong ground motion prediction for huge subduction earthquakes using a characterized source model and several simulation techniques. In: Proceedings of the 13th WCEE, Vancouver

Chapter 3
Simulation of Near-Field Pulse-Like Ground Motion

3.1 Introduction

The accurate prediction of ground motions from possible future earthquakes is the first step towards the robust assessment and mitigation of structural damage against earthquake hazards. The modeling of critical or resonant ground motions has been developed by the present authors in several studies [1–7]. These studies showed that the resonant ground motion has its energy in a narrow frequency range and produces larger damage in the structure compared to ordinary records. Resonant or pulse-like ground motion has been observed in near-field records with directivity focusing or fling effects. Such ground motion is influenced by the rupture mechanism and possesses the following characteristics (e.g. [8]): (1) large peak ground velocities and displacements, (2) concentration of energy in a single or a few pulses, and (3) unusual response spectra shapes. These features have been recently studied by these authors [8].

The first seismological evidence of the near-field phenomenon was observed in the 1952 Kern County (California) earthquake [9]. The propagation of the fault rupture as a moving source was shown to lead to different types of ground motions at opposite ends of the rupture. Housner and Hudson reported the first engineering evidence of near-field ground motions in the 1957 Port Hueneme earthquake [10, 11]. They showed that this earthquake consisted of a single pulse and attributed the unusual damage caused by such moderate earthquake to the concentration of the energy in one pulse. They further concluded that if a pulse-like earthquake of larger magnitude could occur, it would require a revision of engineering thinking with possible intensities of ground motions. Similarly, the 1966 Parkfield earthquake measured 61 m from the fault was shown to consist of three pulses [12]. The severity of the impulsive nature of near-field ground motions on the damage of structures was observed in the 1971 San Fernando earthquake [13, 14]. In fact, the 1966 Parkfield and the 1971 San Fernando earthquakes represent historical milestones related to near-source ground motions [15]. Near-field velocity pulses were represented by different types of idealized pulses to

I. Takewaki et al., *Improving the Earthquake Resilience of Buildings*,
Springer Series in Reliability Engineering, DOI: 10.1007/978-1-4471-4144-0_3,

examine their effects on the performance of various structures systematically [16–20]. Near-field effects became a focus of research after the 1994 Northridge (California), the 1995 Kobe (Japan), and the 1999 Izmit (Turkey) earthquakes [8–35]. These earthquakes caused widespread damage to the urban infrastructure in the near-field region. Near-field ground motions with high PGV/PGA ratios were shown to have wide acceleration-sensitive regions in the response spectra that increase the base shear, inter-story drift, and ductility demand of high-rise buildings [21]. Extensive reviews on the historical development and characterization of near-fault ground motions can be found in [8]. Several studies have investigated the factors that influence near-source ground motions [22–26]. The implications of this class of ground motion on the design of the engineering structures in the near-fault region have been studied by many researchers [27–31].

The literature on modeling earthquake ground motions is vast. In the context of near-field ground motion, several authors have modeled this class of ground motion. Two kinds of models have been developed, namely, seismological and engineering models. The seismological (also known as physical or predictive) models account for the source properties (fault dimension, rupture velocity, attenuation, stress drop, density of intervening medium), epicentral distance, earthquake magnitude, and local soil condition [32–34]. The engineering models replicate the gross features observed in earthquake records in the near-field region [15, 16]. The seismological models require specifying information on the source properties. The engineering models, on the other hand, can be used when information on the source properties is not available or difficult for the engineer to prescribe. Some of the engineering models represent the ground motion with an equivalent main pulse (e.g. [15, 35]). A few studies have accounted for the multiple pulses in modeling near-field ground motions. For instance, several studies developed deterministic engineering models using triangular or sinusoidal half pulse, single pulse, or multiple pulses for this class of ground motion [16–20]. They showed that multiple pulses can produce larger displacements in linear structures than half and single pulses. Suzuki and Asano [34] used the Green's functions and seismological models to simulate near-source records. The study has also attempted to include higher frequencies using regression techniques. Mavroeidis and Papageorgiou [15] developed a simple analytical model that accounts for the observed qualitative and quantitative characteristics of the impulsive nature in the ground displacement, velocity, and, in some cases, acceleration. Baker [32, 33] used the signal processing (the wavelet transform) to extract the pulse-like signals from 3,500 near-field records. The literature on near-field earthquakes is vast and all previous works cannot be reported here. Readers can refer Moustafa and Takewaki [8] for a comprehensive review on this subject.

The above discussion reveals that the characterization and modeling of near-field pulse-like ground motions is of essential importance in seismic-resistant design of engineering structures in the near-field region. The objective of this chapter is to develop simple deterministic and probabilistic models for near-field pulse-like ground motions that account for nonstationarity and multiple-pulses in the velocity signal, and, to examine the implication of this class of ground motions

on the response of structures. The next sections develop the representation of this class of ground motions using deterministic and probabilistic approaches.

3.2 Characterization and Representation of Near-field Pulse-Like Ground Motions

This section discusses the main features of near-field pulse-like ground motion and develops the mathematical representation of this class of ground motions. Table 3.1 lists 27 near-field ground motion records from 15 earthquakes. The table contains information on earthquake magnitude, duration, Aria's intensity (square root of the area under the square of the ground acceleration), site-source distance, and peak values of ground acceleration (PGA), velocity (PGV), and displacement (PGD) [36]. The local soil condition and the ratios of the PGV/PGA and PGD/PGA are also reported in the table. Figure 3.1 depicts the time history and the Fourier amplitude spectra of the ground velocity for 20 of these records. Similar plots for the ground accelerations of the same records are shown in Fig. 3.2. Regardless of the soil type, the pulse-like tendency and large velocity amplitude are evident from the plots of Fig. 3.1 and from the ratio of PGV/PGA in Table 3.1. This feature is particularly obvious in some records, such as, H-E06230, TAB-TR, YPT060, LCN275, ERZ-NS, and DZC-NS. These records have most of the energy of the ground velocity contained in very narrow frequency band. This observation is not easily remarkable in the plots of the ground accelerations. The average dominant frequency of the ground motion ω_{ef} is also reported in Table 3.1 [8]. The numerical value of ω_{ef} is reasonably small for the records that have high impulsive characteristics. It may be emphasized that the value of ω_{ef} depends on the source properties, local soil type, and path effects [8].

Referring to the plots of the velocity and acceleration of the near-field ground motions shown in Figs. 3.1 and 3.2, the following observations can be made:

1. The frequency content of the ground velocities is about (0–5) Hz.
2. The frequency content of the ground accelerations is about (0–10) Hz.

Therefore, the frequency content of the ground acceleration is wider compared to the frequency content of the ground velocity. The representation of near-field ground motions using deterministic sine or cosine function of a single pulse may fail to capture the aforementioned feature. This is particularly obvious for records, such as, C02065, RRS228, TCU078 W, CPM000, and DZC180 (see Figs. 3.1 and 3.2). Single pulse representation does not account for the relatively wide frequency content of the ground acceleration compared to the narrow frequency content of the ground velocity. This is of essential importance since the ground acceleration, not the ground velocity, is always used in estimating the structural response through numerical integration of the equations of motion. A few researchers observed this feature and showed that multiple pulses produce larger maximum

Table 3.1 Information on near-field ground motion records [41, 42]

Event, station and record	Site consdition[a]	M_W	Epicentral distance (km)	PGA (g)	PGV (m/s)	PGD (m)	r_1 (s)	r_2 (s^2)	Duration (s)	Intensity ($m/s^{1.5}$)	ω_{ef}[b]
1940 El Centro, ELC#9, H-180	Medium	7.0	12.99	0.31	0.30	0.13	0.10	0.04	40.00	10.64	0.26
1940 El Centro, ELC#9, H-270	Medium	7.0	12.99	0.22	0.30	0.24	0.14	0.11	40.00	7.46	0.13
1966 Parkfield, Chol.#2, C02065	Medium	6.1	31.04	0.48	0.75	0.23	0.16	0.05	43.69	11.13	0.17
1971 San Fernando, LA HW, PCD164	Medium	6.6	11.86	0.21	0.19	0.12	0.10	0.06	28.00	4.06	0.16
1978 Tabas, Tabas, TAB-LN	Medium	7.4	55.24	0.84	0.98	0.37	0.12	0.05	32.84	8.49	0.13
1978 Tabas, Tabas, TAB-TR	Medium	7.4	55.24	0.85	1.22	0.95	0.15	0.11	32.84	8.48	0.11
1979 Imperial Valley, H-AEP045	Medium	6.5	2.47	0.33	0.43	0.10	0.13	0.03	11.15	7.15	0.35
1979 Imperial Valley, H-E06230	Medium	6.5	27.47	0.44	1.10	0.66	0.26	0.15	39.04	3.31	0.08
1981 Westmorland, WSM-090	Medium	5.8	7.02	0.37	0.49	0.11	0.14	0.03	40.00	10.96	0.14
1989 Loma Prieta, LGP000	Rock	6.9	18.46	0.56	0.95	0.41	0.17	0.08	24.97	49.12	0.17
1992 Erzincan, ERZ-NS	Medium	6.9	8.97	0.52	0.84	0.27	0.17	0.05	21.31	9.42	0.19
1992 Landers, LCN-275	Rock	7.3	44.02	0.72	0.98	0.70	0.14	0.10	48.13	43.46	0.06
1992 Landers, JOS-090	Stiff	7.3	13.67	0.28	0.43	0.15	0.16	0.06	44.00	14.67	0.17
1992 Cape Mendocino, CPM000	Rock	7.1	10.36	**1.50**	1.27	0.41	0.09	0.03	30.00	27.19	0.16
1994 Northridge, Rinaldi, RRS228	Medium	6.7	10.91	0.84	1.66	0.29	0.20	0.04	14.95	46.03	0.31
1994 Northridge, Sylmar, SCS052	Medium	6.7	13.11	0.61	1.17	0.54	0.20	0.09	40.00	36.42	0.21
1995 Kobe, Takatori-000	Soft	6.9	13.12	0.61	1.27	0.36	0.21	0.06	40.96	54.31	0.17
1995 Kobe, Takatori-090	Soft	6.9	13.12	0.62	1.21	0.33	0.20	0.06	40.96	7.13	0.20
1995 Kobe, KJM-000	Stiff	6.9	18.27	0.82	0.81	0.18	0.10	0.02	48.00	7.24	0.21
1995 Kobe, KJM-090	Stiff	6.9	18.27	0.60	0.74	0.20	0.13	0.03	48.00	5.83	0.21
1999 Kocaeli, YPT060	Medium	7.4	19.30	0.27	0.66	0.57	0.25	0.22	35.00	1.36	0.06
1999 Chichi, TCU068-N	Medium	7.6	47.86	0.46	**2.63**	**4.30**	**0.58**	**0.95**	90.00	20.06	0.02

(continued)

Table 3.1 (continued)

Event, station and record	Site consdition[a]	M_W	Epicentral distance (km)	PGA (g)	PGV (m/s)	PGD (m)	r_1 (s)	r_2 (s^2)	Duration (s)	Intensity ($m/s^{1.5}$)	ω_{ef}[b]
1999 Chichi, TCU068-W	Medium	7.6	47.86	0.57	1.77	3.24	0.32	0.58	90.00	20.62	0.02
1999 Chichi, ALS-E	Stiff	7.6	37.83	0.18	0.39	0.10	0.22	0.06	59.00	6.00	0.12
1999 Chichi, TCU078W	Medium	7.6	4.96	0.44	0.39	0.31	0.09	0.07	90.00	36.15	0.07
1999 Chichi, TCU089N	Stiff	7.6	7.04	0.25	0.31	0.32	0.13	0.13	79.00	9.64	0.07
1999 Duze, DZC180	Medium	7.1	1.61	0.35	0.60	0.42	0.18	0.12	25.89	16.83	0.09

[a] Soft soil: $v_s < 180\,\mathrm{m/s}$, medium soil: $180 \le v_s \le 360\,\mathrm{m/s}$, stiff soil: $360 \le v_s \le 750\,\mathrm{m/s}$, rock soil: $v_s > 750$ m/s. $r_1 = \mathrm{PGV/PGA}$, $r_2 = \mathrm{PGD/PGA}$

[b] $a = 0.01$, $b = 0.01$, $(\Omega_0, \Omega_u) = (0, 100\pi)$ rad/s (Alavi and Krawinkler [16])

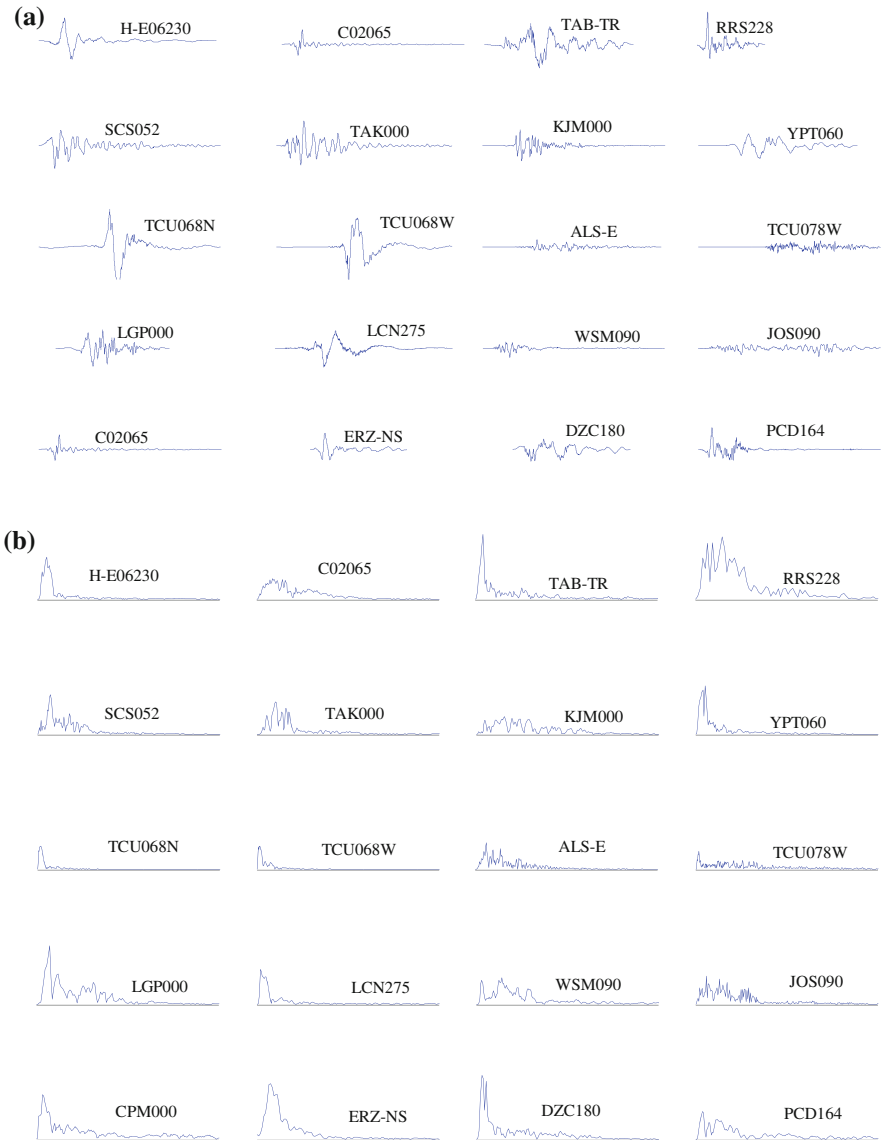

Fig. 3.1 Near-field strong ground motion with distinct velocity pulses: **a** velocity time history, **b** velocity Fourier amplitude spectra [41]

response in linear structures compared to half and single pulses [11, 16–20]. Thus, the problem in modeling near-field ground motions with a single equivalent pulse is the incapability of the model to include amplitudes from lower and higher frequencies other than the dominant pulse [11]. This gets automatically encapsulated in the ground acceleration leading to underestimation or overestimation of

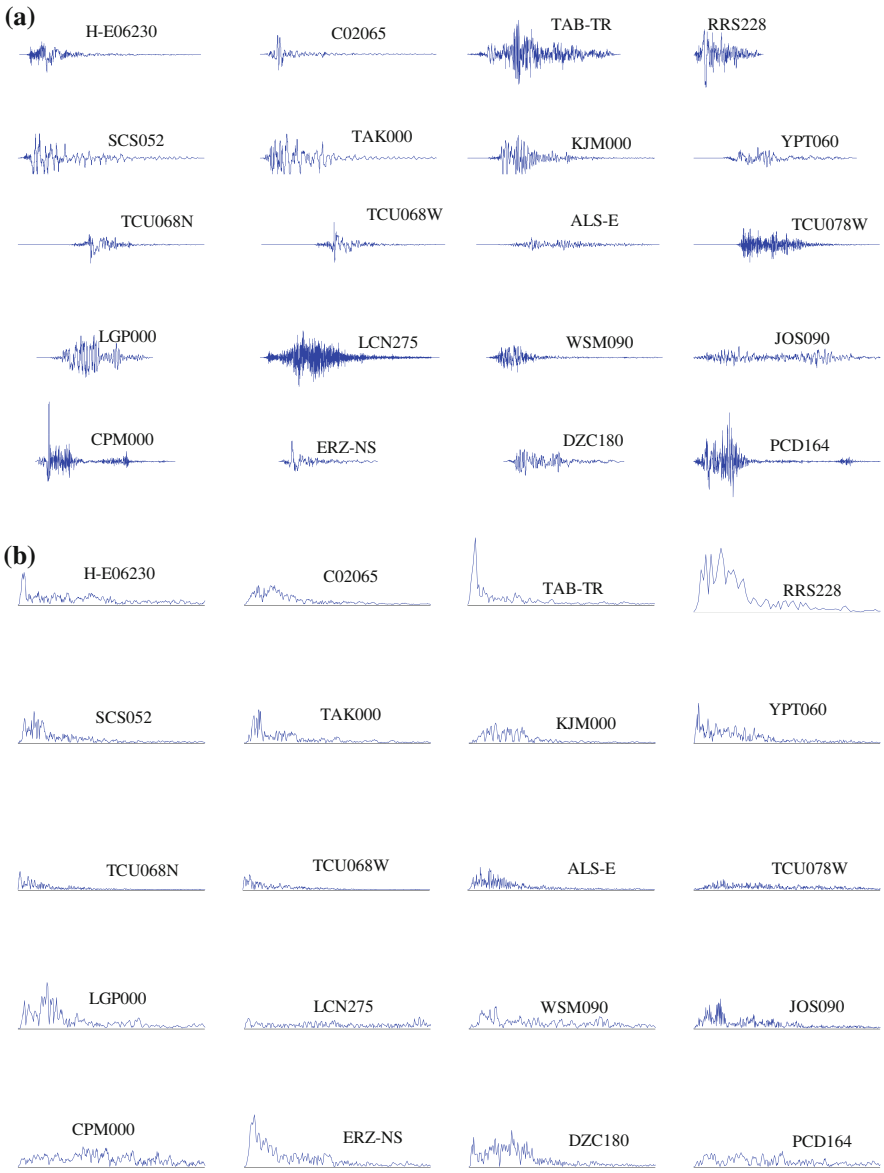

Fig. 3.2 Near-field ground motion with distinct velocity pulses: **a** acceleration time history, **b** acceleration Fourier amplitude spectra [41]

the structural response. For instance, some records, such as, H-E06230, TAB-TR, and TCU068N could be modeled with a single pulse. On the other hand, multiple pulses can be seen in other records, such as, RRS228, TAK000, YPT060, and DZC-NS. This problem can be overcome by the accurate representation of all the pulses contained in the ground motion. An alternative, in which the ground

displacement is used instead of the ground acceleration in estimating the structural response, has been recently proposed [11, 37]. This alternative, however, could be computationally expensive and may introduce additional errors to the solution if not used carefully.

To investigate the contribution of each time segment to the total energy of the ground motion, it is first noted that the scaled Arias intensity is given as [36]:

$$I_{\mathrm{t}} = \left[\int_0^t \left[\ddot{x}_{\mathrm{g}}(t) \right]^2 dt \right]^{1/2}, \tag{3.1}$$

where $\ddot{x}_{\mathrm{g}}(t)$ is the ground acceleration. Similarly, the contribution to the earthquake total energy from each frequency range can also be estimated in the frequency domain by making use of the Parseval's theorem $\left(\int_{-\infty}^{\infty} [\ddot{x}_{\mathrm{g}}(t)]^2 dt = (1/2\pi) \int_{-\infty}^{\infty} |y(\omega)|^2 d\omega \right)$ as follows:

$$E_{\Omega} = \left[\int_{-\infty}^{\Omega} |y(\omega)|^2 d\omega \right]^{1/2} = \left[\int_{-\infty}^{\Omega} y(\omega) y^*(-\omega) d\omega \right]^{1/2}. \tag{3.2}$$

Herein, $y(\omega)$ is the Fourier transform of $\ddot{x}_{\mathrm{g}}(t)$ and $y^*(-\omega)$ is the complex conjugate function of $y(\omega)$. Therefore, we use Eq. (3.2) to estimate the contribution of each frequency range to the total energy of the ground velocity by replacing $\ddot{x}_{\mathrm{g}}(t)$ with $\dot{x}_{\mathrm{g}}(t)$.

Table 3.2 summarizes the percentage contribution of each frequency range to the total energy of the ground velocity for the records of Table 3.1. For most of the records, the contribution from the frequency range (0–1) Hz is about 70–90 % of the total energy of the signal. The contributions from the frequency ranges between (1–2) and (2–3) Hz are about 6–18 and 1–8 %, respectively. The average value of energy in each frequency range across the set of records is also summarized in Table 3.2. The total average value of the velocity intensity from (0–5) Hz is about 97 % of the total intensity. These numerical results reveal that the ground velocity of near-field pulse-like ground motions can be represented with a velocity function that has most of the energy contained in the frequency range (0–1) Hz and the remaining of the energy being located in the frequency range of (1–3) Hz. These numerical results confirm the observation made by some researchers on the presence of multiple pulses in the near-field records [16–20]. For example, the 1940 El Centro and the 1966 Parkfield records contain multiple pulses.

In this chapter, we represent the ground velocity as follows:

$$\dot{x}_{\mathrm{g}}(t) = e(t) \dot{u}_{\mathrm{g}}(t), \tag{3.3}$$

where $e(t)$ is a modulating envelope function that imparts the transient trend to the ground motion, $\dot{u}_{\mathrm{g}}(t)$ is a steady-state function (a stationary component), and dot indicates differentiation with respect to time. This representation belongs to the

Table 3.2 Percentage of Arias intensity in different frequency ranges to the total intensity for near-field ground motion [41]

Event, station and record	% Intensity to total intensity				
	(0–1) Hz	(1–2) Hz	(2–3) Hz	(3–4) Hz	(4–5) Hz
1940 El Centro, ELC#9, H-180	82.03	13.27	2.70	1.22	0.49
1940 El Centro, ELC#9, H-270	63.11	18.36	8.02	3.51	1.98
1966 Parkfield, Chol.#2, C02065	72.51	15.03	6.47	2.32	1.20
1971 San Fernando, LA HW, PCD164	77.79	11.84	6.00	1.43	1.03
1978 Tabas, Tabas, TAB-LN	91.37	6.36	1.24	0.40	0.10
1978 Tabas, Tabas, TAB-TR	82.73	9.33	2.70	1.66	0.96
1979 Imperial Valley, H-AEP045	68.78	14.28	6.48	4.65	1.58
1979 Imperial Valley, H-E06230	89.86	6.09	1.71	0.96	0.62
1981 Westmorland, WSM-090	94.47	3.66	0.80	0.35	0.15
1989 Loma Prieta, LGP000	65.57	8.56	6.13	3.01	2.61
1992 Erzincan, ERZ-NS	78.13	12.83	5.27	1.44	0.95
1992 Landers, LCN-275	67.43	20.11	6.41	2.13	0.79
1992 Landers, JOS-090	95.11	3.54	0.90	0.35	0.10
1992 Cape Mendocino, CPM000	86.75	8.30	1.98	1.03	0.60
1994 Northridge, Rinaldi, RRS228	83.43	10.93	2.98	1.37	0.55
1994 Northridge, Sylmar, SCS052	79.03	13.53	4.55	1.27	0.81
1995 Kobe, Takatori-000	67.06	25.15	4.29	1.50	0.69
1995 Kobe, Takatori-090	68.43	24.13	3.60	1.63	0.74
1995 Kobe, KJM-000	91.43	6.02	1.40	0.58	0.21
1995 Kobe, KJM-090	87.98	6.91	1.75	1.24	0.49
1999 Kocaeli, YPT060	85.46	7.23	3.61	1.50	0.89
1999 Chichi, TCU068-N	74.44	17.49	4.15	1.65	0.81
1999 Chichi, TCU068-W	34.44	24.50	12.49	8.87	5.55
1999 Chichi, ALS-E	53.52	16.41	8.95	6.37	4.01
1999 Chichi, TCU078 W	92.71	5.19	1.31	0.40	0.18
1999 Chichi, TCU089 N	69.05	16.61	6.11	3.27	1.57
1999 Duze, DZC180	72.65	16.72	5.83	2.01	0.95
Average value (total % = 97.12)	76.86	12.68	4.36	2.08	1.13

class of uniformly modulated ground motions. Several models can be used to describe the envelope function, such as, exponential, Gamma, Beta, and piecewise linear models. In this study, we use two models of the exponential form which are given as follows:

$$e_1(t) = A[\exp(-\alpha t) - \exp(-\beta t)]; \quad \beta > \alpha > 0, \tag{3.4}$$

$$e_2(t) = A\exp\{-[2\pi(t - t_0)/\gamma]^2\}. \tag{3.5}$$

Here, the parameters of the envelope function α, β and λ control the nonstationarity of the ground motion, A is a scaling constant and t_0 is the time instant of the peak pulse amplitude. Note that in the second model, the time instant of the peak velocity t_0 can be directly controlled. The plots of the envelope functions of Eqs. (3.4) and (3.5) are shown in Fig. 3.3. Note that the value of the parameter λ

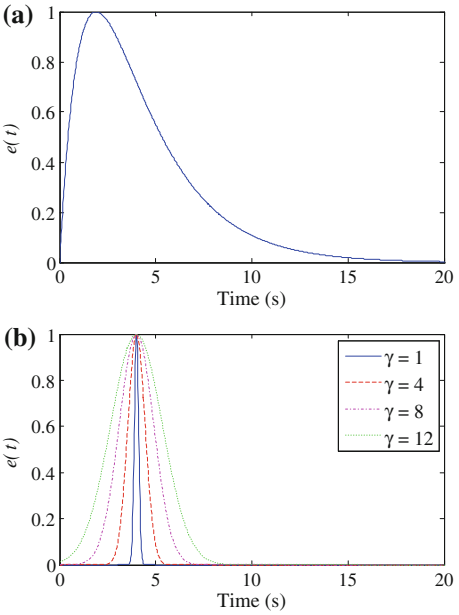

Fig. 3.3 Envelope function: **a** Eq. (3.4), **b** Eq. (3.5) for $t_0 = 4$ s [41]

can be used to control the envelope shape, and, thus the shape of the velocity pulse. Based on the framework of analysis to be adopted (deterministic or probabilistic), the ground velocity $\dot{u}_g(t)$ can be modeled as a deterministic steady-state function or a stationary random process. The next sections develop the simulation of near-field ground motions using deterministic and probabilistic models.

3.3 Representation of Near-field Pulse-Like Ground Motions Using Deterministic Models

A simple, yet, realistic model for the velocity signal of near-field ground motions with multiple pulses can be represented as [see Eq. (3.3)]:

$$\dot{x}_g(t) = e(t)\dot{u}_g(t) = e(t)\sum_{i=1}^{n} v_{pi}\sin[2\pi f_{pi}(t - t_i)], \tag{3.6}$$

where v_{pi}, f_{pi} are the ith amplitude and pulse frequency ($f_{pi} = \omega_{pi}/2\pi$) and t_i is the associated time instant of peak amplitude. Based on the discussion presented in the previous section, typical values of n are $n \geq 1$. Note that, when $n = 1$, the model reduces to similar models developed before, e.g. [15, 35]. To proceed further, the ground acceleration can be obtained by differentiating Eq. (3.6) as follows:

$$\ddot{x}_g(t) = e(t)\ddot{u}_g(t) + \dot{e}(t)\dot{u}_g(t). \tag{3.7}$$

Thus, for the envelope functions of Eqs. (3.4) and (3.5), the ground acceleration is given as:

$$\begin{aligned}\ddot{x}_g(t) = A[\beta\exp(-\beta t) - \alpha\exp(-\alpha t)]\sum_{i=1}^{n} v_{pi}\sin[2\pi f_{pi}(t-t_i)] \\ + 2\pi e_1(t)\sum_{i=1}^{n} v_{pi}f_{pi}\cos[2\pi f_{pi}(t-t_i)],\end{aligned} \tag{3.8}$$

$$\begin{aligned}\ddot{x}_g(t) = 2\pi\, e_2(t)\sum_{i=1}^{n} v_{pi}f_{pi}\cos[2\pi f_{pi}(t-t_i)] \\ - \frac{8\pi^2(t-t_0)}{\gamma^2}e_2(t)\sum_{i=1}^{n} v_{pi}\sin[2\pi f_{pi}(t-t_i)].\end{aligned} \tag{3.9}$$

Hence, the ground acceleration is given in a closed form eliminating numerical techniques.

To examine the realism of the proposed model of Eqs. (3.6–3.9), we use these equations to simulate the time history of the ground velocity. For the first exponential model [Eqs. (3.4) and (3.8)], the envelope parameters are taken as $\alpha = 0.35$, $\beta = 0.75$ and A is selected such that the envelope function has a peak value of unity. The number of velocity pulses n is taken as 1, 2, and 3, and the total duration of the earthquake signal is adopted as 20 s. The pulse frequencies are taken as 0.15, 0.35 and 0.60 Hz, and the associated amplitudes as 0.7, 1.0, and 0.5 m/s, respectively. Note that, the main pulse amplitude is taken at 0.35 Hz while the other two secondary amplitudes are considered at 0.15 and 0.60 Hz. The ground velocities are normalized to the same intensity using the Arias intensity measure [36]. Figure 3.4 shows the plots of the time history of the ground velocity and associated Fourier spectrum for different values of the model parameters. It can be seen that, the shape of the ground velocity and the amplitude at the main pulse frequency depend significantly on the number of velocity pulses.

The simulated ground velocity using the second envelope function [Eqs. (3.5) and (3.9)] is shown in Fig. 3.5. Herein, $n = 1$ and the pulse frequency $= 0.35$ Hz. The value of the parameter γ is varied to control the shape of the velocity pulse. Again, it can be observed that the shape of the velocity signal and the associated amplitude depend on the number of pulses adopted.

This section examined the representation of near-field pulse-like ground motion using deterministic engineering models. The next section develops the representation of near-field pulse-like ground motions using probabilistic models.

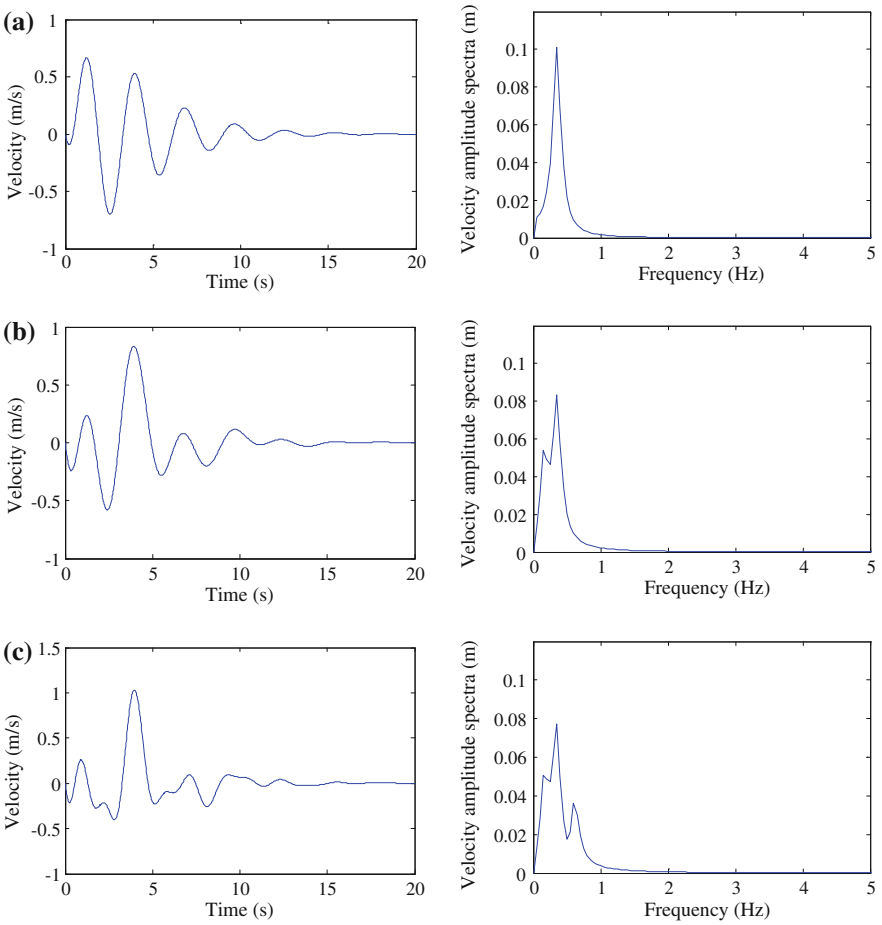

Fig. 3.4 Ground velocity and associated Fourier amplitude spectra with envelope function from Eqs. (3.4), (3.8): **a** Single pulse $f_b = 0.35$ Hz, **b** Two pulses $f_{b1} = 0.15$, $f_{b2} = 0.35$ Hz, **c** Three pulses $f_{b1} = 0.15$, $f_{b2} = 0.35$, $f_{b3} = 0.60$ Hz [41]

3.4 Representation of Near-Field Pulse-Like Ground Motions Using Probabilistic Models

In this section, the ground motion is modeled as a nonstationary Gaussian random process of zero mean. The ground velocity is again taken to be represented by Eq. (3.3) but with $\dot{u}_g(t)$ modeled as a stationary random process. Referring to Eq. (3.6) and considering the velocity amplitudes $v_{pi}, i = 1, 2, \ldots, n$ to be modeled as a set of uncorrelated normal random variables of zero mean that satisfy the following conditions:

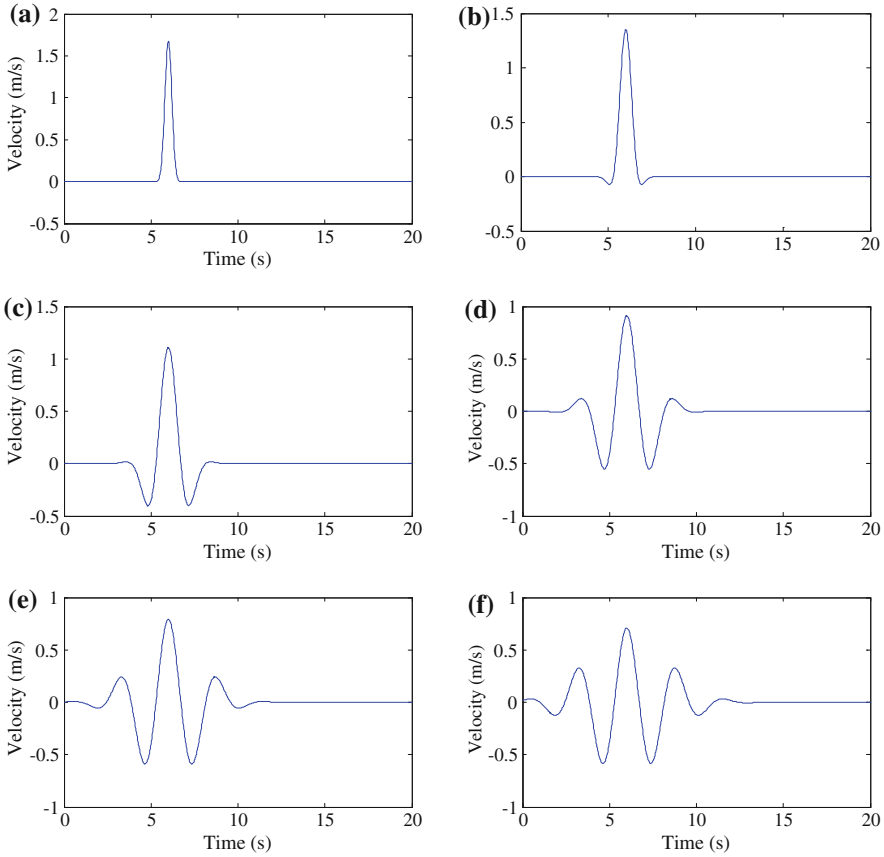

Fig. 3.5 Ground velocity with envelope function from Eqs. (3.5) and (3.9), and $n = 1$: **a** $\gamma = 2$, **b** $\gamma = 4$, **c** $\gamma = 8$, **d** $\gamma = 12$, **e** $\gamma = 16$, **f** $\gamma = 20$ [41]

$$\begin{aligned} <v_{\mathrm{p}i}v_{\mathrm{p}j}> &= \sigma_i^2\delta_{ij}; \quad i = 1, 2, \ldots, n, \\ \delta_{ij} &= 1 \quad \forall\, i = j;\ \delta_{ij} = 0;\ \forall\, i \neq j, \end{aligned} \tag{3.10}$$

where $<.>$ denotes the mathematical expectation, δ_{ij} is the Kronecker delta, and σ_i^2 is the variance of the ith amplitude $v_{\mathrm{p}i}$. Under these conditions, $\dot{u}_{\mathrm{g}}(t)$ is a stationary Gaussian random process, and $\dot{x}_{\mathrm{g}}(t)$ is a nonstationary Gaussian random process. Note that, $e(t)$ is a deterministic envelope function [see Eqs. (3.4) and (3.5)]. The one-sided power spectral density function (PSDF) of the ground velocity $\dot{u}_{\mathrm{g}}(t)$ can be shown to be given as [see Eq. (3.6)]:

$$S_{\dot{u}}(\omega) = 2\sum_{i=1}^{n} \sigma_i^2 \delta(\omega - \Omega_i) \tag{3.11}$$

Fig. 3.6 Power spectral density function for near-field ground velocity [41]

where Ω_i is the frequency of the ith pulse.

Figure 3.6 shows the PSDF for the set of records shown in Fig. 3.1. The PSDFs for the stationary ground velocity $\dot{u}_g(t)$ obtained from Eq. (3.11), for alternative values of the number of velocity pulses n, are shown in Fig. 3.7. Herein, the PSDF of the ground acceleration is obtained as $S_{\ddot{u}}(\omega) = \omega^2 S_{\dot{u}}(\omega)$ [38]. The plots of this figure reveal that the proposed velocity pulse model is capable of representing near-field pulse-like ground motion of multiple pulses. Multiple pulses observed in recorded ground motions, such as, H-E06230, YPT060, ALS-E, LCN275, and DZC180 can be represented by the model.

Simulated realizations for the time history of the ground velocity from the PSDFs of Fig. 3.7 are shown in Fig. 3.8. This stochastic model when combined with structural reliability methods (e.g. FORM/SORM) facilitates carrying out probabilistic applications for near-field pulse-like ground motions, such as, reliability assessment of elastic, and inelastic structures to this class of ground motion [4, 39, 40]. The next section provides numerical demonstrations on the use of deterministic and probabilistic models for response assessment of structures to near-field ground motion.

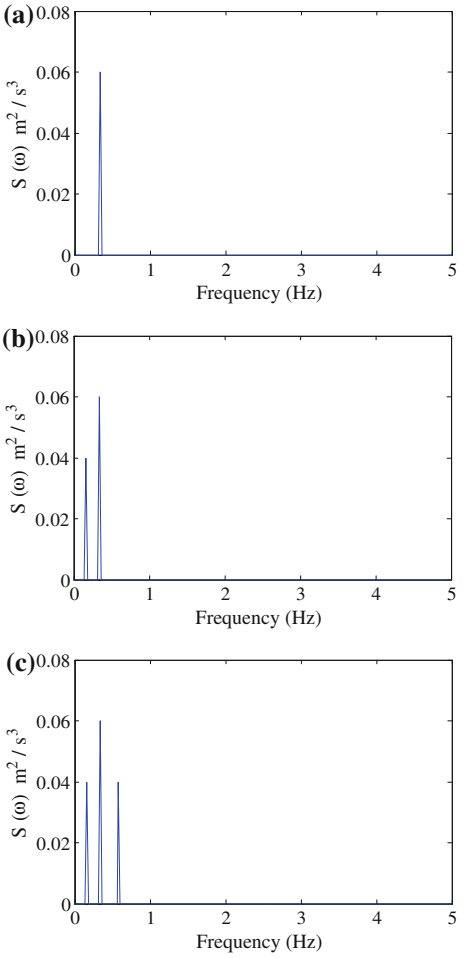

Fig. 3.7 Power spectral density function for the stationary velocity component of near-field ground motion: **a** $n = 1$, **b** $n = 2$, **c** $n = 3$ [41]

3.5 Numerical Applications

The deterministic model is considered first. The maximum displacement response for single-degree-of-freedom (SDOF) elastic–plastic structures to the simulated ground motions with different number of velocity pulses developed above is computed. Figure 3.9a shows the inelastic response spectra for elastic–plastic SDOF systems with damping ratio $= 0.05$ and yield strength $= 4 \times 10^4$ N. It can be seen that the first secondary pulse at 0.15 Hz has a very significant effect on the structural response in the lower frequency range (0–2.0 Hz). This effect decreases at higher frequencies. The second pulse at 0.60 Hz has minor effect on the structural response. This could be attributed to the shift caused by this pulse to the energy of the ground velocity in the frequency domain. The figure reveals also that

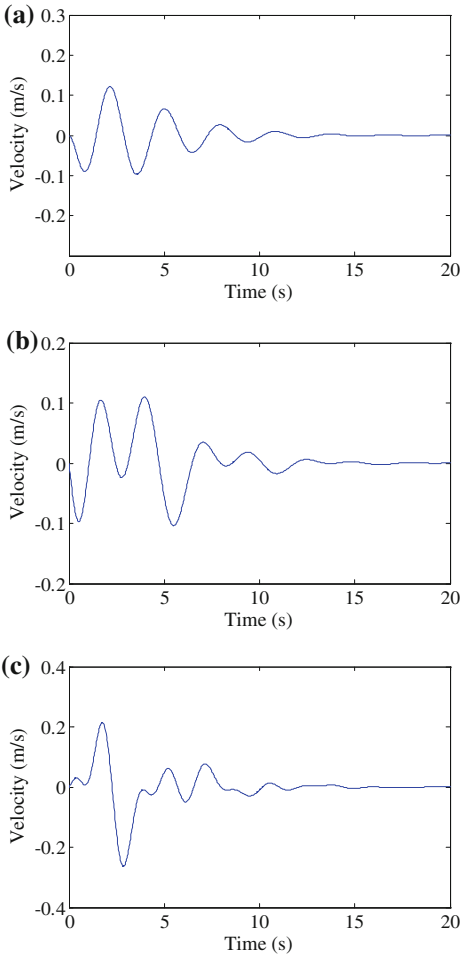

Fig. 3.8 Simulated ground velocity from power spectral density function: **a** $n = 1$, **b** $n = 2$, **c** $n = 3$ [41]

the structure response is overly high, especially for inelastic structures of lower initial frequencies.

To examine the reduction of the structural response of engineering structures in the near-field region, we estimate the structure's responses after adding supplemental dampers. Figure 3.9a depicts the displacement spectra for elastic–plastic SDOF structures with 0.05 damping ratio under different number of pulses from the deterministic model of Sect. 3.3. Similar plots with added viscous damping of 0.15 (i.e., total damping ratio = 0.20) are shown in Fig. 3.9b. Added viscous damping reduces the maximum response significantly for structures of natural frequency higher than about 1.0 Hz. The response in the lower frequency range of (0–1.0) Hz is reduced by about 25 %. A slight difference in the structural response for frequencies higher than about 5.0 Hz can be observed.

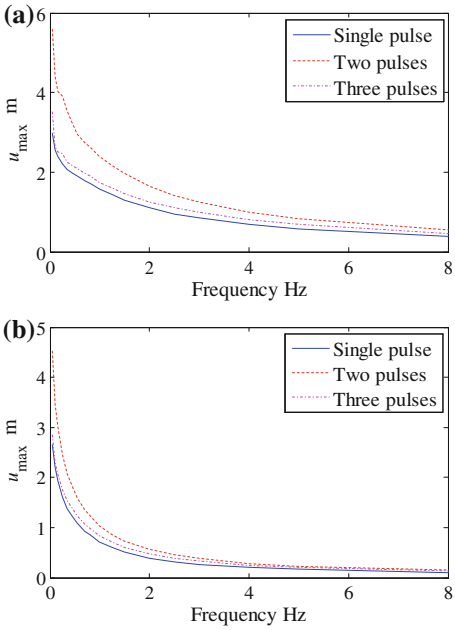

Fig. 3.9 Effect of secondary pulses on maximum inelastic response: **a** $\zeta = 0.05$, **b** $\zeta = 0.20$ [41]

The pseudo velocity spectra are also computed and plotted in Fig. 3.10a for the ground motion for different number of pulses and damping ratio = 0.20. It can be seen that the pseudo acceleration is higher and reaches a steady state for larger number of pulses, particularly for frequencies larger than about 2.0 Hz. The hysteretic energy dissipated by yielding is also estimated and shown in Fig. 3.10b. The effect of the secondary pulses is seen to be substantially different from their effect on the structural inelastic response. The difference in dissipated energy from single and two pulses is seen to be in the lower frequency range of about (0–1.0) Hz. The dissipated energy by yielding is almost constant for frequencies higher than 2.0 Hz. The presence of the third frequency pulse causes the dissipated energy by yielding to decrease.

In order to demonstrate the application of the stochastic model in assessing the structural reliability, we consider a one-storey frame structure of storey stiffness $k = 4.50 \times 10^5\,\mathrm{N/m}$ and mass $= 4.50 \times 10^5$ kg (natural frequency = 1.0 Hz). Since the input ground motion is a Gaussian random process and the structure is linear, any response quantity of the structure, such as, the displacement, or a linear transformation of the displacement (e.g. stress component or stress resultant) will also be a Gaussian random process. Following the standard reliability terminology, the structural response $L(t)$ is denoted as the load effect that is a time-variant quantity. The associated capacity of the structure (e.g. the maximum permissible displacement or stress) is denoted by R. The determination of the structural failure probability constitutes a time-variant reliability problem and is given as [39] (Fig. 3.11):

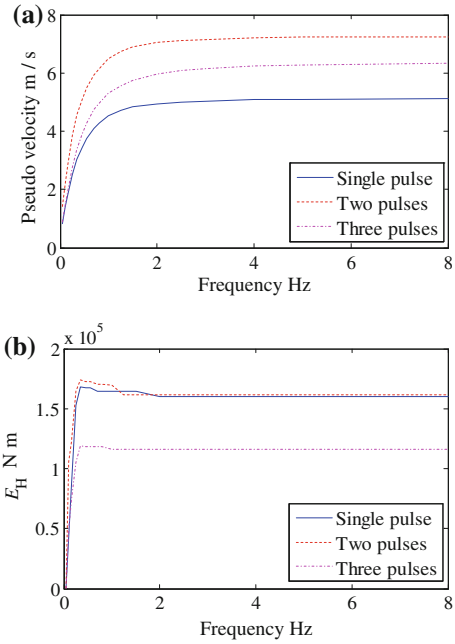

Fig. 3.10 Effect of secondary pulses on maximum inelastic response: **a** $\zeta = 0.05$, **b** $\zeta = 0.20$ [41]

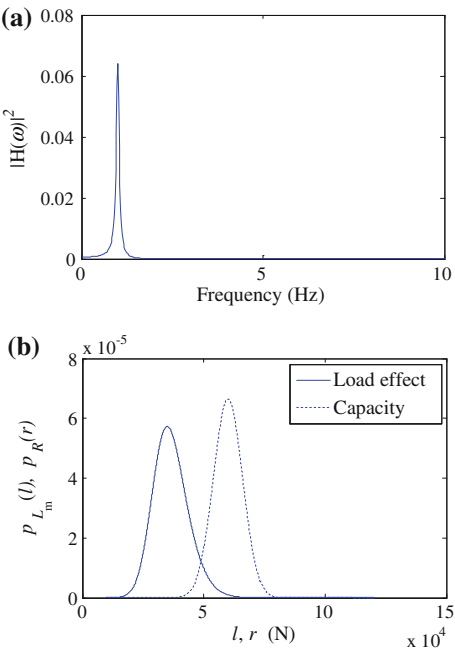

Fig. 3.11 **a** Frequency transfer function ($f = 1.0$ Hz) **b** Probability density function for load effect and capacity for SDOF structure [41]

$$P_f = \int_0^{\infty} P_R(l)\, p_{L_m}(l)\, dl \tag{3.12}$$

where $P_R(r)$ is the probability distribution function of the capacity R and $p_{L_m}(l)$ is the probability density function of the load effect $L_m = \max_{0<t<T_d} |L(t)|$ (T_d is the total duration of the ground motion). Let the load effect be taken as the shear force in the columns $L_m = ku(t)$ where $u(t)$is the displacement. The structural capacity R is defined as the maximum permissible yield force in the columns, modeled as a normal random variable with $\mu_R = 6.0 \times 10^4$ N and $\sigma_R = 6.0 \times 10^3$ N. Assuming that the ground motion is modeled by Eq. (3.11) with the envelope function taken as unity and making use of extreme value distribution of stationary normal random processes, $p_{L_m}(l)$ can be shown to be given as [39]:

$$p_{L_m}(l) = \frac{N_0^+ l T_d}{k^2 \sigma_{0L}^2} \exp\left[-\frac{l^2/k^2 + 2N_0^+ T_d \sigma_{0L}^2 \exp(-l^2/(2k^2\sigma_{0L}^2))}{2\sigma_{0L}^2} \right]; \quad 0 \le l \le \infty \tag{3.13}$$

Herein, N_0^+ is the average rate of zero crossing of the response process $L(t)$ given as $N_0^+ = \sqrt{\sigma_{2L}^2/\sigma_{0L}^2}/(2\pi)$, in which, σ_{0L}^2 and σ_{2L}^2 are the zeroth and the second spectral moments of $L(t)$. These moments are given in terms of the PSDF of the ground acceleration as:

$$\sigma_{iL}^2 = \int_0^{\infty} \omega^i |H_L(\omega)|^2 S_{\ddot{x}_g}(\omega)\, d\omega; \quad i = 0, 2 \tag{3.14}$$

where $H_L(\omega)$ is the frequency response function of the response quantity $L(t)$. The probability of failure from three pulses, two pulses, and one pulse was computed to be 1.10×10^{-2}, 2.0×10^{-3}, and 3.0×10^{-3}, respectively. This confirms the same results obtained from the deterministic model.

Finally, it may be emphasized that, the probabilistic model can be combined with standard reliability methods (e.g. FORM, SORM, importance sampling technique, and response surface method) to assess the safety of inelastic structures under near-field pulse-like ground motion. In this case, the exact evaluation of the structure's failure probability is not available in a closed form, but the theory of reliability indices is used to provide an estimate of the notional safety of the structure [4, 40].

3.6 Summary

Despite the lessons learned from the past damaging earthquakes, and despite the large strong ground motion database accumulated worldwide during the last 76 years, the accurate prediction of future strong ground motions remains one of

the major challenges for engineers to build a safe environment. This is particularly of importance for engineering structures to be constructed in the near-fault region. The widespread damage and inadequate performance of code-designed structures during the 1994 Northridge (California) and the 1995 Kobe (Japan) earthquakes have prompted seismologists and engineers of the essential importance of characterizing and modeling near-field ground motions with impulsive nature. The large velocity pulses associated with these two earthquakes have resulted from the rupture directivity and the tectonic displacement (fling effect).

This chapter investigated the features of near-field ground motions with distinct velocity pulses. Deterministic and probabilistic models for the representation of this class of ground motions have been developed. These models belong to the class of engineering models which aim to replicate some of the gross features observed in strong ground motions at the near-field region. Both models account for nonstationarity and multiple pulses in the ground velocity. The deterministic model can be used for simulating pulse-like ground motion as inputs to time history analysis of elastic and inelastic structures. The probabilistic model combined with standard reliability methods (e.g. FORM, SORM, importance sampling technique, and response surface method) can be used for reliability assessment of elastic and inelastic structures. This model facilitates handling uncertainties in the ground motion and variability in the structure properties. This chapter has also studied the reduction of the structural responses using added supplemental dampers.

References

1. Abbas AM (2002) Deterministic/reliability-based critical earthquake load models for linear/nonlinear engineering structures. PhD. Thesis, Indian Institute of Science, Bangalore
2. Abbas AM, Manohar CS (2002) Investigations into critical earthquake excitations within deterministic and probabilistic frameworks. Earthq Eng Struct Dynam 31:813–832
3. Abbas AM (2006) Critical seismic load inputs for simple inelastic structures. J Sound Vib 296:949–967
4. Abbas AM, Manohar CS (2007) Reliability-based vector nonstationary random critical earthquake excitations for parametrically excited systems. Struct Saf 29:32–48
5. Takewaki I (2002) Seismic critical excitation method for robust design: a review. J Struct Eng 128:665–672
6. Takewaki I (2004) Bound of earthquake input energy. J Struct Eng 130:1289–1297
7. Takewaki I (2006) Probabilistic critical excitation method for earthquake energy input rate. J Eng Mech 132(9):990–1000
8. Moustafa A, Takewaki I (2010) Critical characterization of pulse-like near-fault strong ground motion. Struct Eng Mech 34(6):755–778
9. Benioff H (1955) Mechanism and strain characteristics of the white wolf fault as indicated by aftershocks sequence, earthquakes in Kern County, California during 1952. Calif Dept Nat Res Div Mines Bull 171:199–202
10. Housner GW, Hudson DE (1958) The Port Hueneme earthquake of March 18, 1957. Bull Seismol Soc Am 48(2):163–168

11. Moustafa A (2010) Discussion of analytical model of ground motion pulses for the design and assessment of seismic protective systems. J Struct Eng 136:229–230
12. Anderson JC, Bertero VV (1987) Uncertainties in establishing design earthquakes. J Struct Eng 113(8):1709–1724
13. Sasani M, Bertero VV (1978) Importance of severe pulse-like ground motions in performance-based engineering: historical and critical review. In: Proceedings of the twelfth world conference on earthquake engineering, Aukland, New Zealand
14. Bertero VV, Mahin SA, Herrera RA (1978) Aseismic design implications of near-fault San Fernando earthquake records. Earthq Eng Struct Dynam 6:31–41
15. Mavroeidis GP, Papageorgiou AS (2003) A mathematical representation of near-fault ground motions. Bull Seismol Soc Am 93(3):1099–1131
16. Alavi B, Krawinkler H (2004) Behavior of moment-resisting frame structures subjected to near-fault ground motions. Earthq Eng Struct Dynam 33:687–706
17. Huang CT (2003) Considerations of multimode structural response for near-field earthquakes. J Struct Eng 129:458–467
18. Makris N (1997) Rigidity–plasticity–viscosity: can electrorheological dampers protect base-isolated structures from near-source ground motions? Earthq Eng Struct Dynam 26:571–591
19. Makris N, Chang SP (2000) Response of damped oscillators to cycloid pulses. J Eng Mech 126:123–131
20. Zhang J, Makris N (2001) Rocking of free-standing blocks under cycloidal pulses. J Eng Mech 127(5):473–483
21. Malhotra PK (1999) Response of building to near-field pulse-like ground motions. Earthq Eng Struct Dynam 28:1309–1326
22. Bray JD, Rodriguez-Marek A (2004) Characterization of forward-directivity ground motions in the near-fault region. Soil Dyn Earthq Eng 24:815–828
23. Hall JH, Heaton TH, Halling MW, Wald DJ (1995) Near-source ground motion and its effect on flexible buildings. Earthq Spectra 11:569–605
24. Iwan W (1997) Drift spectrum: measure of demand for earthquake ground motions. J Struct Eng 123(4):379–404
25. Kalkan E, Kunnath SK (2007) Effective cyclic energy as a measure of seismic demand. J Earthq Eng 11:725–751
26. Mavroeidis GP, Dong G, Papageorgiou AS (2004) Near-source ground motions, and the response of elastic and inelastic single-degree-of-freedom (SDOF) systems. Earthq Eng Struct Dynam 33:1023–1049
27. Cao H, Friswell MI (2009) The effect of energy concentration of earthquake ground motions on the nonlinear response of RC structures. Soil Dyn Earthq Eng 29:292–299
28. Krawinkler H, Alavi B, Zareian F (2005) Impact of near-fault pulses on engineering design: directions in strong motion instrumentation In: Gulkan P, Anderson JG (eds) Springer, Dordrecht
29. Mavroeidis GP, Papageorgiou AS (2002) Near-source strong ground motion: characteristics and design issues. In: Proceedings of the seventh US national conference on earthquake engineering, Boston, Massachusetts, 21–25 July 2002
30. Moustafa A (2009) Discussion of the effect of energy concentration of earthquake ground motions on the nonlinear response of RC structures. Soil Dyn Earthq Eng 29:1181–1183
31. Somerville PG, Smith N, Graves R, Abrahamson N (1997) Modification of empirical strong ground motion attenuation relations to include the amplitude and duration effects of rupture directivity. Seismol Res Lett 68(1):199–222
32. Baker JW (2007) Quantitative classification of near-fault ground motions using wavelet analysis. Bull Seismol Soc Am 97(5):1486–1501
33. Baker JW (2008) Identification of near-fault velocity pulses and prediction of resulting response spectra. In: Proceedings of the geotechnical earthquake engineering and structural dynamics IV, Sacramento, CA, 18–22 May 2008
34. Suzuki S, Asano K (2000) Simulation of near source ground motion and its characteristics. Soil Dyn Earthq Eng 20:125–136

35. He WL, Agrawal AK (2008) Analytical model of ground motion pulses for the design and assessment of seismic protective systems. J Struct Eng 134(7):1177–1188
36. Arias A (1970) A measure of earthquake intensity. In seismic design of nuclear power plants. MIT press, Cambridge, pp 438–468
37. Wilson EL (2002) Three-dimensional static and dynamic analysis of structures: a physical approach with emphasis on earthquake engineering, 3rd edn. Computers & Structures Inc., CA
38. Clough RW, Penzien J (2003) Dynamics of structures, 3rd edn. Computers & Structures Inc, CA
39. Abbas AM, Manohar CS (2005) Reliability-based critical earthquake load models. Part 1: linear structures. J Sound Vib 287:865–882
40. Abbas AM, Manohar CS (2005) Reliability-based critical earthquake load models. Part 2: nonlinear structures. J Sound Vib 287:883–900
41. Moustafa A, Takewaki I (2010) Deterministic and probabilistic representation of near-field pulse-like ground motion. Soil Dyn Earthq Eng 30(5):412–422
42. PEER. Pacific Earthquake Engineering Research Center (2005). http://peer.berkeley.edu/smcat/search.html

Chapter 4
Critical Characterization and Modeling of Pulse-Like Near-Field Strong Ground Motion

4.1 Introduction

Pulse-like (also known as resonant, cycloidal pulses, or impulse-like) ground motion has been observed in near-field (also near-fault or near-source) records with directivity focusing or fling effects. This class of ground motion is significantly influenced by the rupture mechanism, substantially different from ordinary ground motion records, and can be characterized by the following features [1–8, among others]: (1) long period and large amplitudes, (2) high peak ground velocity (PGV)/peak ground acceleration (PGA) and peak ground displacement (PGD)/PGA ratios, (3) unusual response spectra shapes, and (4) concentration of energy in one or very few pulses.

Pulse-like ground motions occurring close to urban and metropolitan regions can place severe demands on buildings and other facilities in the near-fault region. The 1923 Kanto earthquake is a striking example of a great earthquake occurring close to a heavily populated city killing about 140,000 persons (59,000 in Tokyo) and causing structural damage of more than $2.0 billion [9]. Near-field effects have been known for many years and became a focus of research after the 1994 Northridge and the 1995 Kobe earthquakes. The 1957 Port Hueneme earthquake of magnitude 4.7 was the first earthquake that consisted of a single pulse [5]. Since the energy was concentrated in one pulse, the damage caused by this earthquake was unusual for a moderate earthquake. Similarly, the 1966 Parkfield earthquake measuring 61 m from the source consisted of three pulses [1].

Table 4.1 summarizes information of 27 near-fault records from 15 earthquakes [10]. Figure 4.1 shows the acceleration, velocity, and displacement of three pulse-like records and one ordinary record (1940 El Centro) from Table 4.1. The resonance and large velocity and displacement amplitudes of pulse-like motions are evident from Fig. 4.1. For instance, the 1999 Chi-Chi record exhibits unusual high PGV and PGD (see Fig. 4.1d and Table 4.1).

I. Takewaki et al., *Improving the Earthquake Resilience of Buildings*,
Springer Series in Reliability Engineering, DOI: 10.1007/978-1-4471-4144-0_4,

Table 4.1 Information on near-fault ground motion [10] (Moustafa and Takewaki [46] with permission from Techno Press)

Event, station and record	Site condition[a]	M_W	Source-site Dist. (km)	PGA (g)	PGV (m/s)	PGD (m)	r_1 (s)	r_2 (s^2)	Duration (s)	Intensity (m/$s^{1.5}$)	$\bar{\omega}_{ef}$[b]	$\bar{\omega}_s$[c]
1940 El Centro, ELC#9, H180	medium	7.0	12.99	0.31	0.30	0.13	0.10	0.04	40.00	10.64	0.26	0.66
1940 El Centro, ELC#9, H270	medium	7.0	12.99	0.22	0.30	0.24	0.14	0.11	40.00	7.46	0.13	0.70
1966 Parkfield, Chol.#2, C02065	medium	6.1	31.04	0.48	0.75	0.23	0.16	0.05	43.69	11.13	0.17	0.68
1971 San Fernando, LA HW, PCD164	medium	6.6	11.86	0.21	0.19	0.12	0.10	0.06	28.00	4.06	0.16	0.70
1978 Tabas, Tabas, TAB-LN	medium	7.4	55.24	0.84	0.98	0.37	0.12	0.05	32.84	8.49	0.13	0.61
1978 Tabas, Tabas, TAB-TR	medium	7.4	55.24	0.85	1.22	0.95	0.15	0.11	32.84	8.48	0.11	0.62
1979 Imperial Valley, H-AEP045	medium	6.5	2.47	0.33	0.43	0.10	0.13	0.03	11.15	7.15	0.35	0.68
1979 Imperial Valley, H-E06230	medium	6.5	27.47	0.44	1.10	0.66	0.26	0.15	39.04	3.31	0.08	0.76
1981 Westmorland, WSM-090	medium	5.8	7.02	0.37	0.49	0.11	0.14	0.03	40.00	10.96	0.14	0.74
1989 Loma Prieta, LGP000	rock	6.9	18.46	0.56	0.95	0.41	0.17	0.08	24.97	49.12	0.17	0.77
1992 Erzincan, ERZ-NS	medium	6.9	8.97	0.52	0.84	0.27	0.17	0.05	21.31	9.42	0.19	0.89
1992 Landers, LCN-275	rock	7.3	44.02	0.72	0.98	0.70	0.14	0.10	48.13	43.46	0.06	0.61
1992 Landers, JOS-090	stiff	7.3	13.67	0.28	0.43	0.15	0.16	0.06	44.00	14.67	0.17	0.69
1992 Cape Mendocino, CPM000	rock	7.1	10.36	**1.50**	1.27	0.41	0.09	0.03	30.00	27.19	0.16	0.63
1994 Northridge, Rinaldi, RRS228	medium	6.7	10.91	0.84	1.66	0.29	0.20	0.04	14.95	46.03	0.31	0.78
1994 Northridge, Sylmar, SCS052	medium	6.7	13.11	0.61	1.17	0.54	0.20	0.09	40.00	36.42	0.21	0.78
1995 Kobe, Takatori-000	soft	6.9	13.12	0.61	1.27	0.36	0.21	0.06	40.96	54.31	0.17	0.75
1995 Kobe, Takatori-090	soft	6.9	13.12	0.62	1.21	0.33	0.20	0.06	40.96	7.13	0.20	0.72
1995 Kobe, KJM-000	stiff	6.9	18.27	0.82	0.81	0.18	0.10	0.02	48.00	7.24	0.21	0.69
1995 Kobe, KJM-090	stiff	6.9	18.27	0.60	0.74	0.20	0.13	0.03	48.00	5.83	0.21	0.69
1999 Kocaeli, YPT060	medium	7.4	19.30	0.27	0.66	0.57	0.25	0.22	35.00	1.36	0.06	0.85
1999 Chichi, TCU068-N	medium	7.6	47.86	0.46	**2.63**	**4.30**	**0.58**	**0.95**	90.00	20.06	0.02	0.83

(continued)

Table 4.1 (continued)

Event, station and record	Site condition[a]	M_W	Source-site Dist. (km)	PGA (g)	PGV (m/s)	PGD (m)	r_1 (s)	r_2 (s^2)	Duration (s)	Intensity (m/$s^{1.5}$)	$\bar{\omega}_{ef}$[b]	$\bar{\omega}_s$[c]
1999 Chichi, TCU068-W	medium	7.6	47.86	0.57	1.77	3.24	0.32	0.58	90.00	20.62	0.02	0.87
1999 Chichi, ALS-E	stiff	7.6	37.83	0.18	0.39	0.10	0.22	0.06	59.00	6.00	0.12	0.77
1999 Chichi, TCU078W	medium	7.6	4.96	0.44	0.39	0.31	0.09	0.07	90.00	36.15	0.07	0.73
1999 Chichi, TCU089N	stiff	7.6	7.04	0.25	0.31	0.32	0.13	0.13	79.00	9.64	0.07	0.73
1999 Duze, DZC180	medium	7.1	1.61	0.35	0.60	0.42	0.18	0.12	25.89	16.83	0.09	0.84

[a] *Soft soil* $v_s < 180$ m/s, *medium soil* $180 \leq v_s < 360$ m/s, *stiff soil* $360 \leq v_s < 750$ m/s, *rock soil* $v_s \geq 750$ m/s. r_1 = PGV/PGA, r_2 = PGD/PGA

[b] $a = 0.01$, $b = 0.01$

[c] $(\Omega_0, \Omega_u) = 2\pi \times (0, 50)$rad/s.

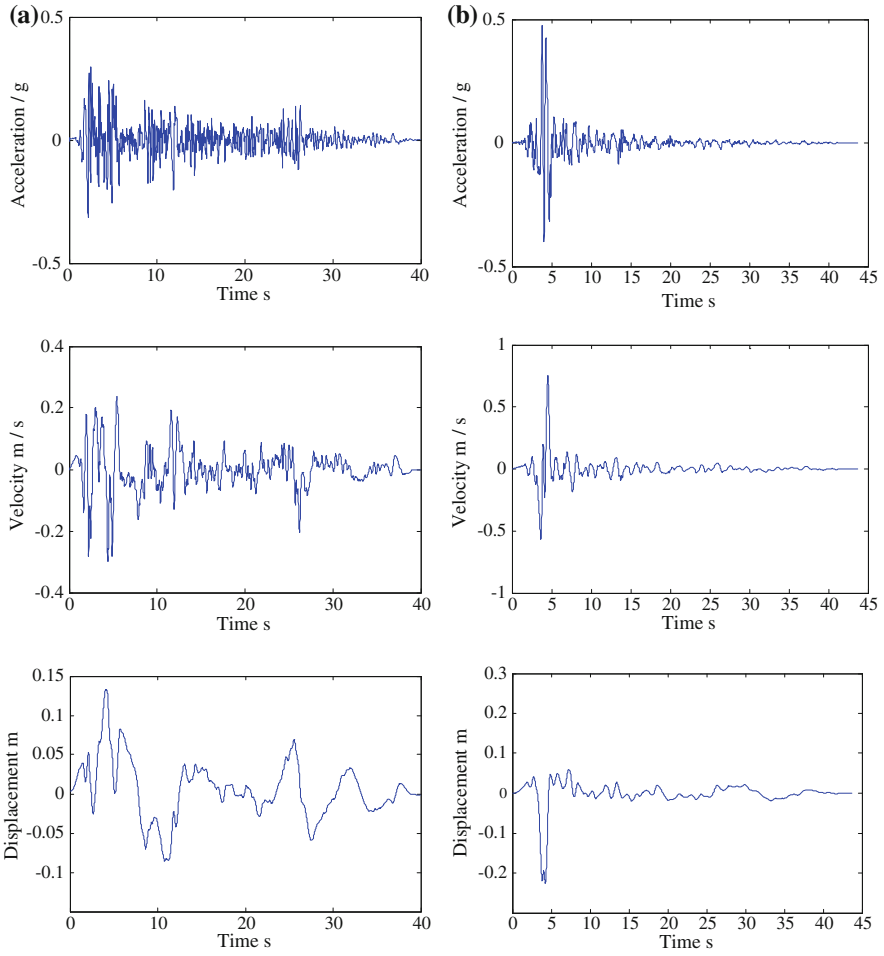

Fig. 4.1 Near-fault ground motion; **a** 1940 El Centro #9, H180, **b** 1966 Parkfield earthquake (Cholame # 2, C02065). **c** The 1995 Kobe earthquake (Takatori, TAK000), **d** The 1999 Chi-Chi earthquake (TCU068-N) (Moustafa and Takewaki [46] with permission from Techno Press)

The widespread damage caused to code designed structures during the 1994 Northridge and the 1995 Kobe earthquakes have motivated engineers and researchers for better and deeper understanding of near-fault strong ground motions of impulsive characteristics. Meanwhile, the increasing availability of strong ground motion data (e.g., from Japan, California, Taiwan, Turkey, India, and Iran) and the ease in accessing these data facilitate studying this class of ground motions and their effects on structures. With this in mind, the objectives of this chapter are: (1) to demonstrate the distinctive features of near-fault pulse-like ground motions and their differences from ordinary records in addition to those

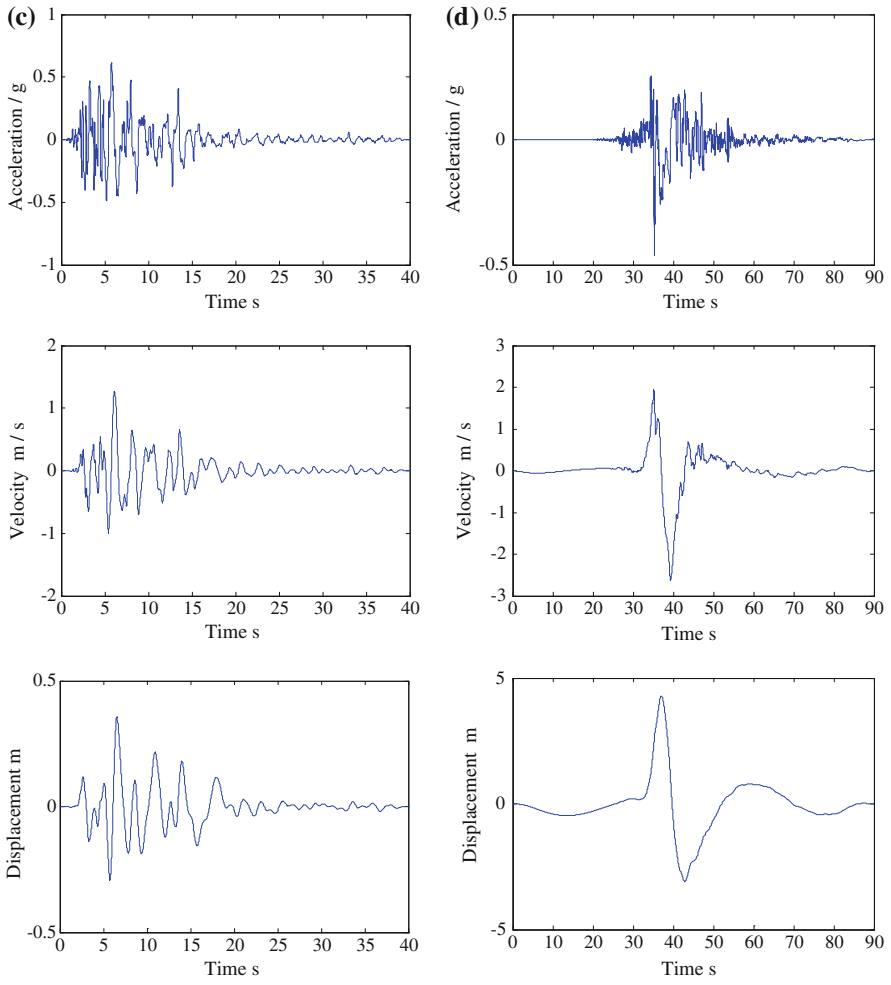

Fig. 4.1 (continued)

explained in Sect 3.2, (2) to investigate the structural performance to this class of ground motions using energy concepts and damage indices, and (3) to provide simple mathematical models for pulse-like ground motion using optimization techniques, energy concepts, and damage indices for sites having limited earthquake data. In order to facilitate the formulation, the next section summarizes various measures for characterizing near-fault ground motions.

4.2 Characteristics of Near-Field Pulse-Like Strong Ground Motion From Another Viewpoint

The characterization of near-field pulse-like ground motions was made in Sect 3.2 and some features of near-field pulse-like ground motion were explained. In this section, the representation of near-field pulse-like ground motions is provided from another viewpoint.

The potential of strong ground motions to damage structures can be quantified in terms of measures of the recorded free-field ground motion or in terms of measures that are based on the structure performance during ground shaking. These measures can be described as follows:

1. Free-field measures: These are parameters based on the ground motion records, such as magnitude, energy, PGA, PGV, PGD, frequency content, duration, and epicentral distance. These parameters do not depend on the structure's properties, and, therefore have limited capability in quantifying the earthquake potential to damage structures.
2. Elastic response spectra: These include response spectra, spectrum intensity, and drift spectra. Such parameters do not account for inelastic structural behavior including effects from amplitude and number of cycles of inelastic stress reversals.
3. Inelastic response spectra: These parameters are based on the maximum inelastic response of single-degree-of-freedom (SDOF) structures, such as displacement, ductility, interstory drift, and design spectra. These parameters do not include effects from the duration of the ground motion and cumulative energy dissipated by the structure.
4. Energy spectra: This includes the cumulative energy dissipated by damping and yielding mechanisms. These parameters account for fundamental features of inelastic response and cumulative effects of repeated cycles of inelastic deformation and duration of ground motion. These measures require normalization with respect to the structure's energy dissipation capacity.
5. Damage spectra: These measures represent the variation of a damage index versus the natural period of structures. By definition, damage indices contain contribution from maximum deformation excursion and cumulative energy dissipated by the structure, and thus, are expected to be robust measures for the earthquake potential to damage the structures.

In this chapter, we utilize the above measures and develop new measures for the frequency content of the ground acceleration to characterize pulse-like strong ground motion for the set of records listed in Table 4.1. The two horizontal components of the 1940 Imperial Valley earthquake (ordinary records) of $M_W = 6.9$ are also included in the set of records for comparison. The following sections provide details on the above measures.

4.2.1 Measures Based on Recorded Free-Field Ground Motion

A distinct pattern of near-fault pulse-like ground motion can be observed in the time histories of the ground velocity and displacement, and also in the large ratios of PGV/PGA and PGD/PGA (see Fig. 4.1 and Table 4.1). For example, such pulse-like records exhibit large velocity and displacement amplitudes compared with other ordinary records. An example can be found in the TCU068 NS component of the 1999 Chi-Chi earthquake. The ratios of PGV/PGA and PGD/PGA are substantially large for these records compared with other ordinary records.

Figure 4.2 illustrates the Fourier amplitude spectra for the earthquake accelerations presented in Fig. 4.1. Each acceleration record is scaled to unit Arias intensity [11] as an acceleration power. In other words, the square root of the area under the square of the ground acceleration is set to unity. Note that, although this scaling affects the amplitude of the ground acceleration, this procedure does not alter the frequency content. It can be seen that most of the near-fault records (e.g., 1995 Kobe and 1999 Chi-Chi earthquakes) possess narrow frequency contents compared with other ordinary ones, e.g., the 1940 El Centro records. It is also remarkable that the peak Fourier amplitude of the Kobe and Chi-Chi records are higher than those of ordinary records. We present a new measure for quantifying the frequency content of the ground acceleration below.

The Arias intensity of the ground acceleration is given as [11]:

$$E_{\mathrm{t}} = \left[\int_{-\infty}^{\infty} [\ddot{x}_{\mathrm{g}}(\tau)]^2 \mathrm{d}\tau \right]^{1/2} \tag{4.1}$$

Equation (4.1) provides a measure of the acceleration energy (or power) computed in time domain. Let $\ddot{X}_{\mathrm{g}}(\omega) = \int_{-\infty}^{\infty} \ddot{x}_{\mathrm{g}}(t) e^{-i\omega t} \mathrm{d}t$ denote the Fourier transform of the ground acceleration. Recalling Parseval's theorem expressed by

$$\int_{-\infty}^{\infty} [\ddot{x}_{\mathrm{g}}(t)]^2 \mathrm{d}t = \frac{1}{2\pi} \int_{-\infty}^{\infty} |\ddot{X}_{\mathrm{g}}(\omega)|^2 \mathrm{d}\omega, \tag{4.2}$$

a similar measure can be obtained in frequency domain:

$$E_{\Omega} = \left[\int_{-\infty}^{\infty} |\ddot{X}_{\mathrm{g}}(\omega)|^2 \mathrm{d}\omega \right]^{1/2} = \left[\int_{-\infty}^{\infty} \ddot{X}_{\mathrm{g}}(\omega) \ddot{X}_{\mathrm{g}}^{*}(-\omega) \mathrm{d}\omega \right]^{1/2} \tag{4.3}$$

In Eq. (4.3), $\ddot{X}_{\mathrm{g}}^{*}(-\omega)$ is the complex conjugate function of $\ddot{X}_{\mathrm{g}}(\omega)$. The introduced new measure for the frequency content of the ground motion is taken as (ω_a, ω_b). Herein, ω_a and ω_b express the frequencies at which a and $(1 - b)$ times the Fourier energy E_{Ω} are attained, respectively. Thus, the frequency bandwidth is

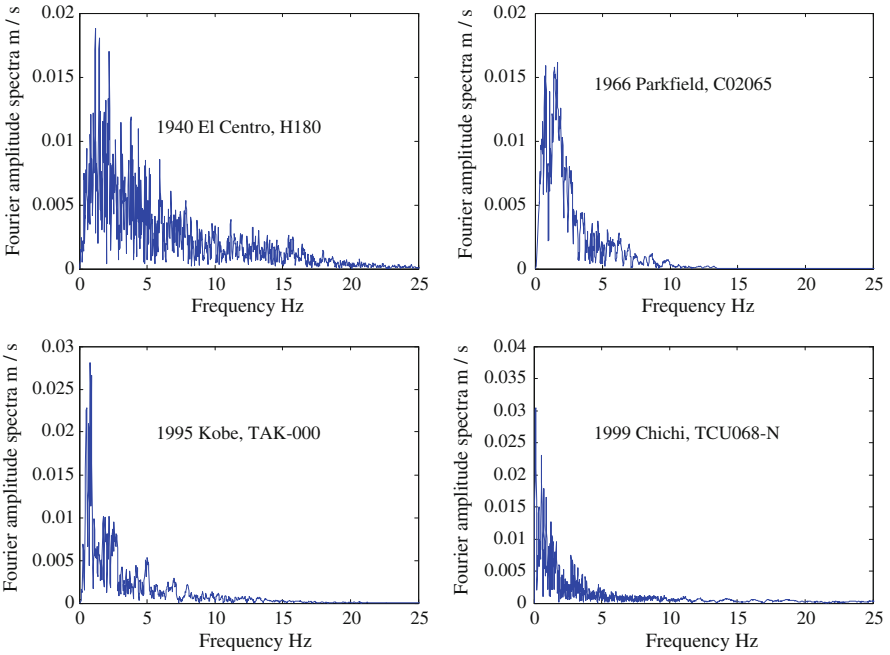

Fig. 4.2 Fourier amplitude of some of the ground accelerations in Fig. 4.1 (Moustafa and Takewaki [46] with permission from Techno Press)

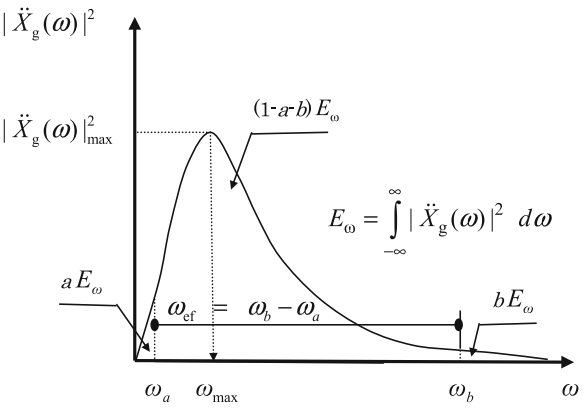

Fig. 4.3 Measures of frequency bandwidth of recorded ground accelerations (Moustafa and Takewaki [46] with permission from Techno Press)

taken to be given as $\omega_{ef} = \omega_b - \omega_a$ (see Fig. 4.3). Typical values of a and b can be taken as $a = b = 0.05$ or any reasonable values (e.g. 0.01 or 0). When $a = b = 0.05$, ω_{ef} can be understood as a measure of the frequencies contributing to the strong phase of the ground motion [12]. Furthermore, the bandwidth ω_{ef} can be normalized to provide a measure bounded between zero and one:

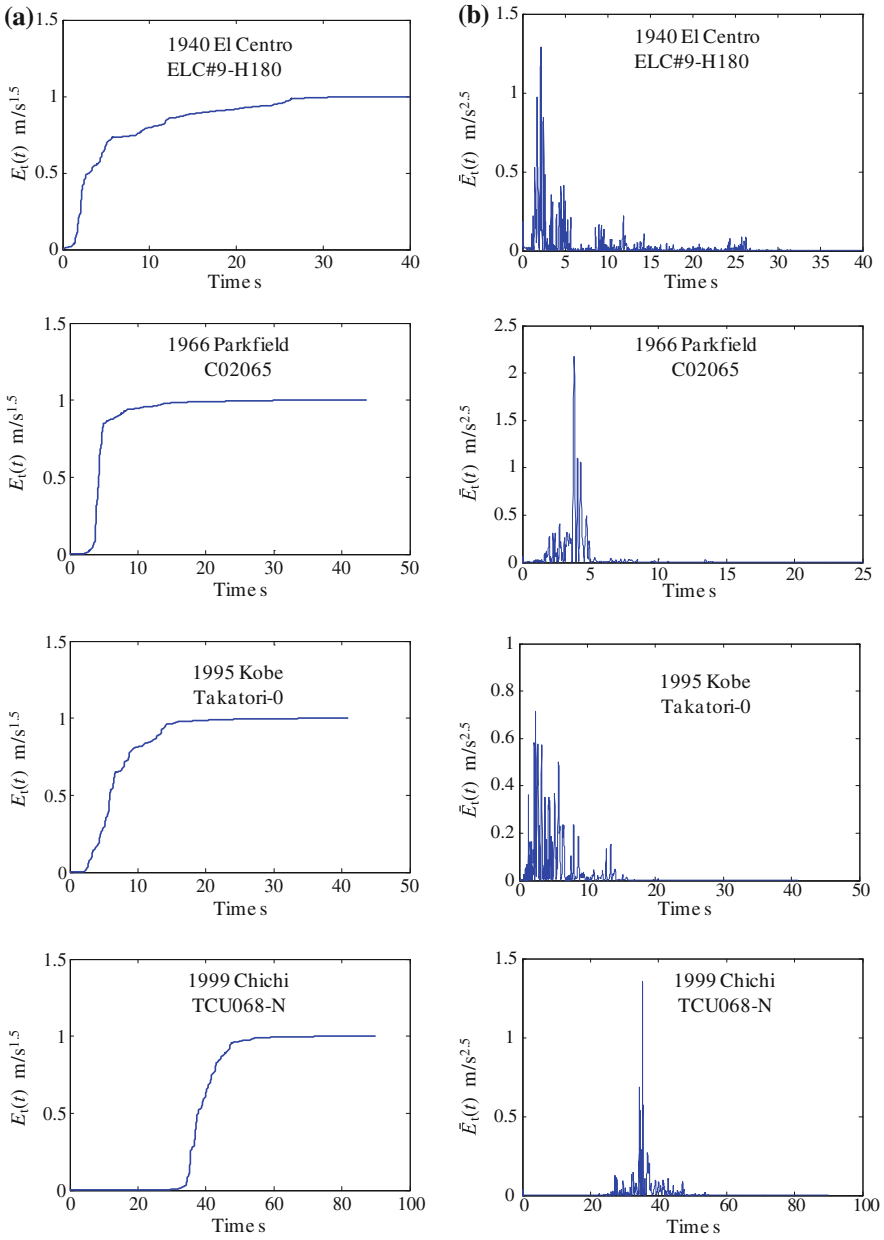

Fig. 4.4 Energy and energy rate in time domain (Moustafa and Takewaki [46] with permission from Techno Press)

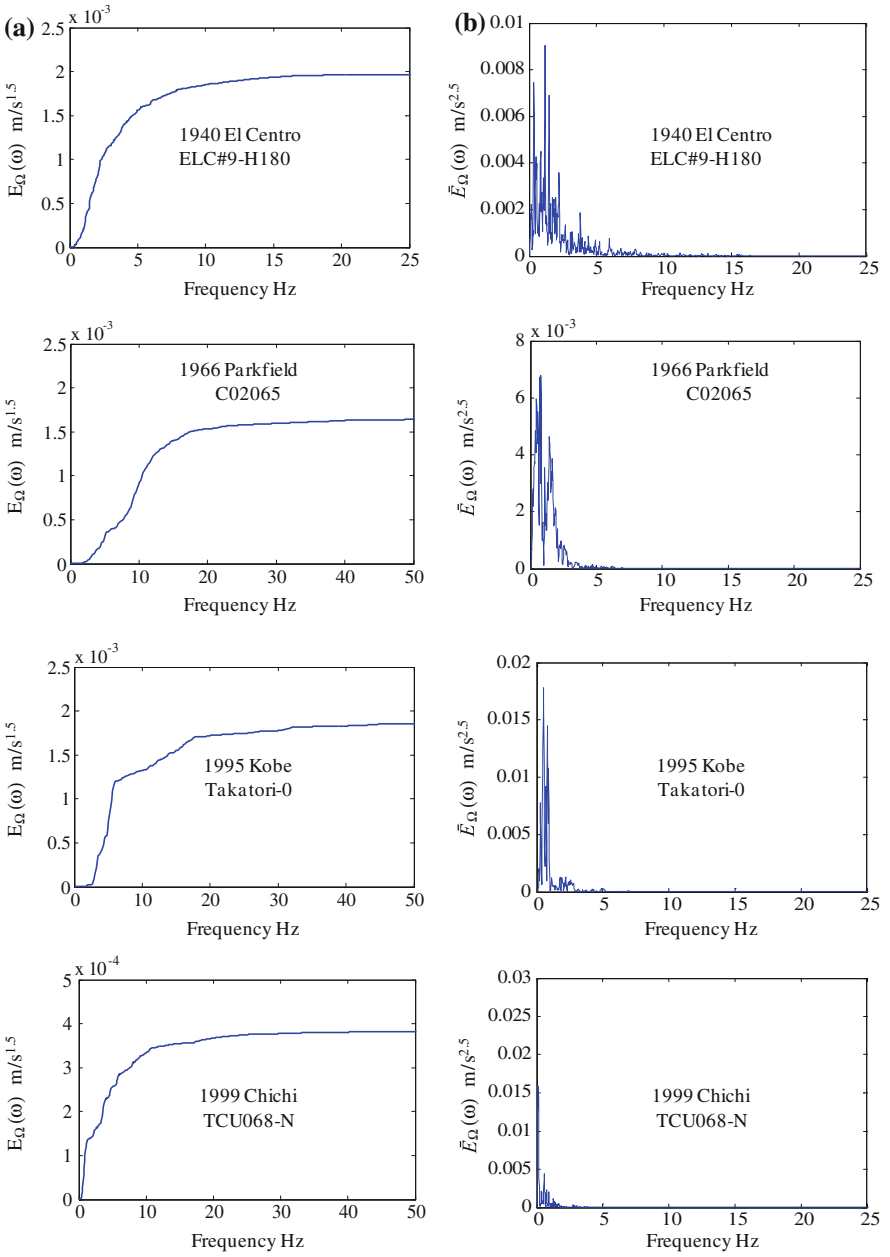

Fig. 4.5 Energy and energy rate in frequency domain (Moustafa and Takewaki [46] with permission from Techno Press)

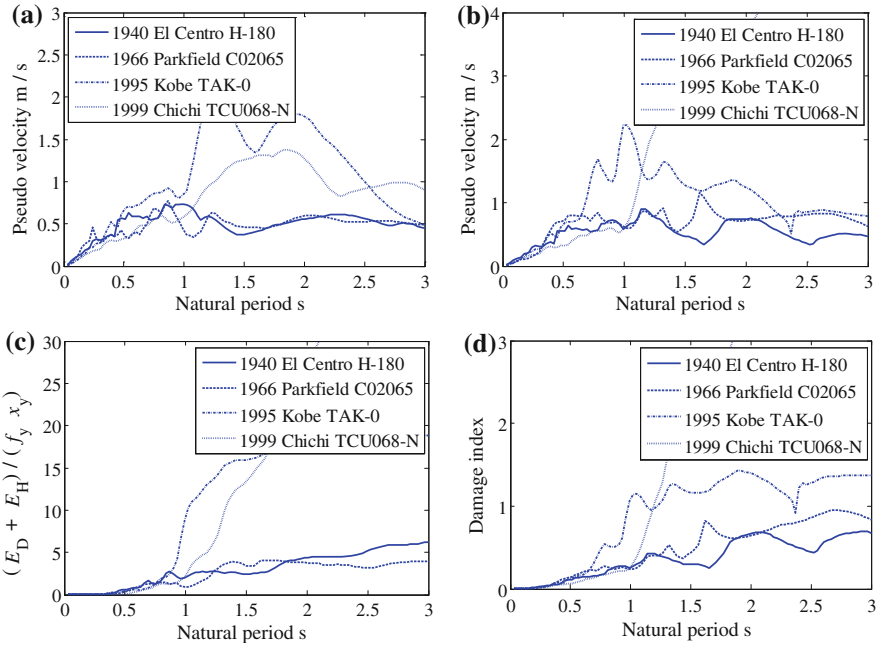

Fig. 4.6 Pseudo velocity spectra: **a** elastic spectra, **b** inelastic spectra, **c** energy spectra, **d** damage spectra (Moustafa and Takewaki [46] with permission from Techno Press)

$$\bar{\omega}_{ef} = \frac{\omega_b - \omega_a}{\Omega_u - \Omega_0} \tag{4.4}$$

The frequency content (Ω_0, Ω_u) is generally defined in the range of $2\pi \times (0.5 \sim 50)$ rad/s depending on the site soil condition and the fault-rupture properties. When $\bar{\omega}_{\text{ef}}$ is close to zero, the ground motion resembles the resonance phenomenon or pulse-like trend. An example of this scenario is a harmonic signal of a single or a few frequencies. For example, it is expressed by $\ddot{x}_{\text{g}}(t) = A\sin(\omega_{\text{g}} t)$, where A, ω_{g} are the acceleration amplitude and dominant frequency, respectively. When $\bar{\omega}_{\text{ef}}$ is significantly larger than zero, the ground acceleration will be rich in frequencies. The frequency bandwidth of the ground motion can also be quantified based on the random vibration theory. That is expressed by

$$\omega_{\text{s}} = \sqrt{\omega_2^2 - \omega_1^2}; \quad \omega_i = \int_{-\infty}^{\infty} \omega^i |\ddot{X}_{\text{g}}(\omega)|^i d\omega \Big/ \int_{-\infty}^{\infty} |\ddot{X}_{\text{g}}(\omega)|^2 d\omega \tag{4.5}$$

In Eq. (4.5), ω_1 is the central frequency of the ground acceleration and ω_{s} is the radius of gyration as a measure of the dispersion of the center of mass of the Fourier spectrum function from the central frequency. This measure comes from the work of Vanmarcke [13, 14] that he used for quantifying the frequency

bandwidth of stationary random processes in terms of the moments of the power spectral density (PSD) function. In this chapter, the Fourier spectrum is used for the ground acceleration instead of the PSD function. The frequency ω_s can also be normalized with respect to ω_2 to provide a measure $\bar{\omega}_s$ that is bounded between zero and one.

The quantified values of $\bar{\omega}_{ef}$ and $\bar{\omega}_s$ for the 27 earthquake records of Table 4.1 are shown in the same table. The parameters a and b are taken as $a = b = 0.01$. The values of $\bar{\omega}_{ef}$ are understood to correlate well with the frequency bandwidth of the ground accelerations. Note here that $\bar{\omega}_s$ is inversely proportional to the frequency bandwidth. These results clearly reveal that $\bar{\omega}_{ef}$ is an accurate descriptor for the frequency content of the ground acceleration.

The energy of the ground acceleration is an important parameter for characterizing earthquake ground motions [11, 12, 15, 16]. For example, the expressions of the acceleration energy in time and frequency domains are given by Eqs. (4.1) and (4.3), respectively. The time and frequency variations of the energy of the ground motion can be useful indicators of the potential of earthquake ground motions to damage structures. For instance, near-fault ground motion can cause severe damage to structures due to the large input energy in a short duration to the structure. This feature can be well captured by examining the time variation of the acceleration energy and the relation between the structure fundamental natural frequency and the dominant frequency of the ground motion [15, 17]. The computation and quantification of the energy of the ground motion in the frequency domain are essential for this purpose since it reflects clearly the acceleration energy at various frequencies. For this purpose, two energy measures are used for characterizing the earthquake properties. The first measure is the energy rate in time domain [18, 19] which represents the instantaneous incremental energy of the ground motion in time domain per unit time. The second measure is a new measure and is the incremental energy of the ground motion in frequency domain per unit frequency. These measures are given as:

$$\bar{E}_t(t_i) = \frac{E_t(t_{i+1}) - E_t(t_i)}{t_{i+1} - t_i} = \frac{\Delta E_t(t_i)}{\Delta t_i}; \quad \bar{E}_\Omega(\omega_i) = \frac{E_\Omega(\omega_{i+1}) - E_\Omega(\omega_i)}{\omega_{i+1} - \omega_i} = \frac{\Delta E_\Omega(\omega_i)}{\Delta \omega_i} \tag{4.6a, b}$$

where

$$E_t(t) = \left[\int_{-\infty}^{t} [\ddot{x}_g(\tau)]^2 d\tau\right]^{1/2}; \quad E_\Omega(\omega) = \left[2\int_{0}^{\omega} |\ddot{X}_g(\gamma)|^2 d\gamma\right]^{1/2} \tag{4.7a, b}$$

Many years ago, Trifunac and Brady [12] proposed an energy measure for the ground acceleration by normalizing the energy with respect to the total duration of the ground motion. Note that $\bar{E}_t(t)$ in Eq. (4.6a, b) provides a robust measure of the acceleration energy at discrete time instants.

The plots of the two measures of Eq. (4.6a, b) for the records presented in Fig. 4.1 are shown in Figs. 4.4b and 4.5b. Figures 4.4a and 4.5a illustrate the plots of the energies given by Eq. (4.7a, b). Note that all records are normalized to unit Arias intensity. The effectiveness of the energy measures $\bar{E}_{\mathrm{t}}(t)$ and $\bar{E}_{\Omega}(\omega)$ in characterizing pulse-like ground motion records is evident from the plots shown in Figs. 4.4 and 4.5. For instance, the Chi-Chi record has most of its energy at about 38 s. In frequency domain, the energies of the Kobe and Chi-Chi records are concentrated in a narrow frequency range. It can also be seen that the peak amplitude of the Chi-Chi and Kobe records are substantially higher than other records. It is believed that the measures $\bar{\omega}_{\mathrm{ef}}, \bar{E}_{\mathrm{t}}(t)$ and $\bar{E}_{\Omega}(\omega)$ provide important and useful information on the nature of the ground motion. However, the use of these measures alone for quantifying possible damage of the structure without the inclusion of the structural parameters is inadequate. The following section tackles this limitation by considering measures by paying attention to the structural responses.

4.2.2 Measures Based on the Structural Response

Figures 4.6a and b show the elastic and inelastic response spectra for the records in Fig. 4.1. These plots represent the maximum elastic and inelastic pseudo velocity of an SDOF system versus the natural period of the system, respectively. A viscous damping model of damping ratio = 0.05 is adopted for elastic and inelastic systems. For the inelastic case, the material nonlinearity is modeled by an elastic–plastic force-deformation law. The yield displacement and strength are assumed to be $x_{\mathrm{y}} = 0.10\,\mathrm{m}$ and $f_{\mathrm{y}} = 10^4\,\mathrm{N}$. All records are normalized to the PGA of 0.30 g. The significant differences in the maximum responses of pulse-like records from ordinary records are remarkable. Kobe and Chi-Chi records produce significantly higher responses compared with ordinary records.

The energy spectrum of the ground acceleration represents the plot of the maximum energy with respect to the natural period of a structure. In order to do this, we consider the equation of motion of an elastic–plastic SDOF system driven by a single component of the ground acceleration $\ddot{x}_{\mathrm{g}}(t)$:

$$m\ddot{x}(t) + c\dot{x}(t) + f_{\mathrm{s}}(t) = -m\ddot{x}_{\mathrm{g}}(t) \tag{4.8}$$

In Eq. (4.8), m and c are the mass and damping coefficient of the structure and $f_{\mathrm{s}}(t)$ is its hysteretic restoring force. Integrating Eq. (4.8), we get the following relation [17, 20–25]:

$$E_{\mathrm{K}} + E_{\mathrm{D}} + E_{\mathrm{S}} = E_{\mathrm{I}} \tag{4.9}$$

where $E_{\mathrm{K}}, E_{\mathrm{D}}, E_{\mathrm{S}}, E_{\mathrm{I}}$ are the relative kinetic energy (although physically not exact), the energy absorbed by damping, the strain energy, and the earthquake input energy to the structure, respectively. $E_{\mathrm{K}}(t) = m\dot{x}^2(t)/2$ and $E_{\mathrm{S}}(t)$ is

composed of the cumulative unrecoverable hysteretic energy $E_H(t)$ and elastic recoverable energy $E_e(t) = kx^2(t)/2$, where k is the initial stiffness.

We construct the spectra $(E_D + E_H)$ of dissipated energy for the acceleration records shown in Fig. 4.1. These results are presented in Fig. 4.6c. The distinct differences in the energy spectra of pulse-like records are evident. The pulse-like records are seen to produce higher energy demands than ordinary records.

Structural damage under strong ground motions occurs not only due to the maximum deformation or ductility, but also due to the hysteretic cumulative energy dissipated by the structure. The literature on structural damage measures of buildings under strong ground motion is versatile [26–28]. Damage indices are based on either a single or combination of structural response parameters. Measures that are based on a single response parameter, such as the maximum ductility or the maximum energy dissipated during the ground shaking, neither incorporates information on how the earthquake input energy is imparted on the structure nor how this energy is dissipated. Therefore, the definition of the structural damage in terms of a single response parameter is inadequate. Damage indices can be established by comparing the response parameters demanded by the earthquake with the corresponding structural capacities. The damage index developed by Park and co-workers is the well-known and most commonly used damage index due to its simplicity and extensive experimental calibration with the field observations in earthquakes. That damage index is given by the following form [29]:

$$DI_{PA} = \frac{x_{max}}{x_u} + \lambda \frac{E_H}{f_y x_u} = \frac{\mu_{max}}{\mu_u} + \lambda \frac{E_H}{f_y x_y \mu_u} \tag{4.10}$$

In Eq. (4.10), x_{max} and E_H are the maximum absolute displacement and maximum dissipated hysteretic energy under the earthquake, respectively. In addition, μ_u is the ultimate yield ductility capacity under a monotonic loading and λ is a positive constant weighting the effect of cyclic loading on structural damage. The state of the structural damage is defined in the following form:

(a) Repairable damage, when $DI_{PA} < 0.40$,
(b) Damaged beyond repair, when $0.40 \leq DI_{PA} < 1.0$, and
(c) Total or complete collapse, when $DI_{PA} \geq 1.0$.

These criteria are based on calibration of DI_{PA} for experimental results and field observations after earthquakes [29]. Equation (4.10) demonstrates that both the maximum ductility and hysteretic energy dissipation contribute to the structural damage during ground motion. Here, the damage is expressed as a linear combination of the damage caused by excessive deformation and that contributed by repeated cyclic loading effect. It should be noted that the quantities x_{max}, E_H depend on the loading history, while the quantities λ, x_u, f_y are determined only from experimental tests. The numerical results on DI_{PA} are plotted in Fig. 4.6d. Herein, μ_u is assumed to be 6 and $\lambda = 0.15$. From the numerical results, it is evident that pulse-like records produce more damage than ordinary records for

structures having natural period greater than 0.70 s. However, the examination is narrow and more elaborated discussion should be necessary.

Near-field ground motions were characterized in this section using measures that are based on the recorded free-field ground motion and those that are based on the structural responses and damage indices. It has been shown that near-fault pulse-like earthquake ground motions possess distinctive features compared with ordinary records, and also produce large structural responses and damage indices. The following section provides simple analytical expressions for modeling near-fault pulse-like earthquake ground motions.

4.3 Modeling Near-Field Pulse-Like Ground Motion

It was noted in the introduction section that real recorded ground motions exhibit the resonance nature when the energy of the earthquake ground motion is concentrated in a narrow frequency range. The concept and method of critical excitation may provide a useful tool for modeling such a pulse-like or resonant ground motion for a given structure. This discussion has been made frequently [18, 20, 30–33]. The damage caused by the critical ground motions can be larger (sometimes significantly) than those from ordinary ground motions, since such a ground motion is tailor-made to produce the maximum response. In this section, a simple analytical representation of this class of ground motion is made using optimization techniques and simple procedures are provided for solving the optimization problem. These simple analytical expressions can be easily and effectively used by the structural engineer to assess the structural safety in a simple, but reliable manner without numerical integration of the equation of motion to obtain the structural response.

4.3.1 Representation of Pulse-Like Ground Motion Using Trigonometric Functions

A simple functional representation of concerned pulse-like ground motion can be expressed as:

$$\begin{aligned} \ddot{x}_g(t) &= A\sin(\omega_p t) \\ \dot{x}_g(t) &= A[1-\cos(\omega_p t)]/\omega_p \\ x_g(t) &= A[t-\sin(\omega_p t)/\omega_p]/\omega_p; \quad 0<t\le T_p = 2\pi/\omega_p \end{aligned} \tag{4.11}$$

In Eq. (4.11), A is a constant representing the acceleration amplitude and ω_p is the pulse frequency of the ground motion.

This simple representation has been used earlier for modeling near-fault pulse-like ground motions [7]. In that reference, the velocity record is used to derive the

pulse frequency ω_p and the acceleration amplitude as $A = (\omega_p \dot{x}_{p_{max}})/2$. An improved analytical model for near-fault pulse-like ground motions was developed by He and Agrawal [34]. In that reference, the velocity pulse is represented as a sinusoidal function modulated by an exponential decaying envelope function. In this model the velocity is expressed by

$$\dot{x}_g(t) = Ct^n e^{-at} \sin(\omega_p t + \upsilon);\ t \geq t_0 \tag{4.12}$$

In Eq. (4.12), ω_p is the pulse frequency, C is an amplitude scaling factor, υ is a phase angle, a is a constant that controls the modulation function, n is a non-negative integer parameter controlling the skewness of the pulse envelope in time, and t_0 is the starting time point of the pulse. These authors derived the analytical expressions for the ground acceleration and displacement together with those for the displacement response of SDOF systems. This model is used for the seismic performance-based design of passive energy dissipation structures [35].

In this section, a resonant or pulse-like ground motion is modeled for linear structures. For this modeling, the parameters ω_p and A of the ground motion are computed by optimization techniques so that the structural response is maximized. Assume that the ground motion is given by Eq. (4.11) and the structure exhibits linear elastic behavior with zero initial conditions. The displacement response of the SDOF structure can then be given by

$$x(t) = \frac{-mA}{k\sqrt{(1-r^2)^2 + 4\eta^2 r^2}} \sin(\omega_p t - \theta); \quad \theta = \tan^{-1}\left(\frac{2\eta r}{1-r^2}\right) \tag{4.13}$$

where r is the ratio of the pulse frequency ω_p to the structure natural frequency, ω_n, θ is a phase angle of response, and η is the structural damping ratio. Hence, the displacement response is given in a closed-form and thus numerical integration of the equation of motion is eliminated. In addition, the errors associated with the numerical integration are also eliminated.

It can be shown that the clear resonance of the displacement, velocity, and acceleration responses occur at $\omega_n\sqrt{1-2\eta^2}$, ω_n, $\omega_n/\sqrt{1-2\eta^2}$, respectively. For viscous damping model of $\eta = 0.03$, these values are $0.9991\omega_n$, ω_n, $1.0009\omega_n$, respectively. Similarly, the resonant frequencies for $\eta = 0.05$ are $0.9975\omega_n$, ω_n, $1.0025\omega_n$. For practical applications the resonance frequency can be taken equal to ω_n.

It may be noted that the representation of ground motion discussed above does not account for the nonstationarity or the transient nature of the ground motion. The representation of the ground motion developed here can be utilized for preliminary analysis and design of structures. The optimization problem is solved in two steps. First, the dominant frequency of the ground motion is taken to coincide with the structure natural frequency. Subsequently, the acceleration amplitude is determined so that the structure response is maximized subject to predefined constraints. These procedures will be demonstrated below.

4.3.1.1 Energy Constraint

Arias intensity was introduced originally to measure the power of acceleration [11]. Arias intensity is recognized as the most commonly used measure of earthquake energy or power. Mathematically, this constraint is given by the following form (see Eq. (4.1)):

$$I_{\mathrm{A}} = \left[\int_0^{\infty} [\ddot{x}_{\mathrm{g}}(t)]^2 \mathrm{d}t \right]^{1/2} \tag{4.14}$$

Using Eq. (4.11), the parameter A can be shown to be given by

$$A = I_{\mathrm{A}} / \sqrt{\int_0^{\infty} [\sin(\omega_{\mathrm{p}} t)]^2 \mathrm{d}t} \tag{4.15}$$

After this process, the problem reduces to computing the value of the parameter A from the above equation, while the pulse frequency is taken to coincide with the structure fundamental natural frequency.

4.3.1.2 PGV Constraint

In earlier works, the parameters characterizing the pulse model are estimated so that the model possesses the pulse frequency and peak velocity amplitude observed in previous recorded ground motions. Implicit constraints on the peak values of acceleration and displacement and the ground motion energy are automatically considered and included due to the closed-form representation adopted [36]. In this case, $\dot{x}_{\mathrm{g}}(t)$ is explicitly constrained to its peak value N. Then the parameter A leads to

$$A = \omega_{\mathrm{p}} N / |1 - \cos(\omega_{\mathrm{p}} t)|_{\max} \tag{4.16}$$

Now, the problem reduces to finding the value of the parameter A from Eq. (4.16). The velocity constraint is known and recognized to be more effective than the acceleration constraint [15].

The model considered here is called Model I in the numerical analysis. The representation of a pulse-like ground motion presented above does not account for the nonstationarity of the ground motion. Since the nonstationarity of the ground motion is very important in the proper characterization of ground motions, the following section tackles this limitation.

4.3.2 Representation of Pulse-Like Ground Motion Using Trigonometric Functions Modulated by Envelope Function

The nonstationarity of ground motion can be well accounted for by modulating the sine signal of Eq. (4.11) with an exponential envelope function as follows:

$$\ddot{x}_g(t) = e(t)\ddot{u}_g(t) = A[\exp(-\alpha t) - \exp(-\beta t)]\sin(\omega_p t) \tag{4.17}$$

In Eq. (4.17) the parameters α and β are introduced to control the nonstationarity of the ground acceleration. These parameters can be calculated so that they make the expression of Eq. (4.17) match the nonstationarity trend of past recorded ground accelerations [18, 20, 30–33]. The displacement response of the SDOF structure to this input can be shown to be given by

$$\begin{aligned} x(t) = {} & [B_\alpha \exp(-\alpha t) + B_\beta \exp(-\beta t)]\cos(\omega_p t) \\ & + [D_\alpha \exp(-\alpha t) + D_\beta \exp(-\beta t)]\sin(\omega_p t) \end{aligned} \tag{4.18}$$

where the coefficients B_α and D_α are given by

$$\begin{aligned} B_\alpha &= \frac{-2A\omega_p(\alpha - \eta\omega_n)}{4\omega_p^2(\alpha - \eta\omega_n)^2 + (\alpha^2 - \omega_p^2 - 2\eta\omega_n\alpha + \omega_n^2)^2} \\ D_\alpha &= \frac{-A(\alpha^2 - \omega_p^2 - 2\eta\omega_n\alpha + \omega_n^2)^2}{4\omega_p^2(\alpha - \eta\omega_n)^2 + (\alpha^2 - \omega_p^2 - 2\eta\omega_n\alpha + \omega_n^2)^2} \end{aligned} \tag{4.19}$$

The parameters B_β, D_β can be obtained from the above expressions by replacing α with β. The advantages of this expression are (1) the elimination of the numerical integration in calculating the structural response and also the error involved in the numerical integration, (2) the exclusion of nonlinear optimization techniques. The model considered here is called Model II in the numerical analysis.

The numerical results for Models I and II are summarized in Table 4.3. The energy and PGV constraints are taken as 3.26 m/s$^{1.5}$ and 0.30 m/s, respectively. These values are determined to reflect the intensity and PGV of the 1940 El Centro NS record. The elastic and elastic–plastic responses of the same structural model to El Centro 1940 NS component are also included in Table 4.3. The parameters of the elastic–plastic structural models are taken as given in Sect. 2.2. It can be seen that the energy constraint (case 1) provides realistic response quantities compared with those produced with the PGV constraint (case 2). It is also noticeable that the elastic linear model is not sufficient especially when dealing with the extreme loads of pulse-like trend.

Since inelastic responses are important in the seismic design of structures, the following section accounts for inelastic structural behavior in modeling pulse-like ground motions.

4.4 Damage-Based Critical Earthquake Ground Motion for Inelastic Structures

4.4.1 Problem Formulation

As seen and discussed in the introduction and the previous sections, ground motions in near-fault regions affected by directivity focusing or fling effects possess a peculiar pulse-like trend. It may be possible that the dominant frequency of such ground motion coincides with the structure fundamental natural frequency. In such a case, the ground motion is sometimes termed 'critical excitation' and produces the largest response in the structure under certain conditions or frameworks. Comprehensive reviews of previous works on this topic can be found in the references [18, 20, 30–33]. The use of critical excitation methods is generally associated with safety assessment of important structures to be constructed in seismically active regions having limited or sparse earthquake data. The method provides a rational answer to the question on the worst-case scenario that can (or may) happen to the structure under uncertain situations. This worst-case scenario represents one of the main concerns for structural engineers. The method relies on the high uncertainty associated with earthquake occurrence and its properties. Since inelastic responses are important in the seismic design of structures, this section characterizes pulse-like ground motions for inelastic structures.

Most of the theories for critical excitations deal with elastic structures and displacement and (or) acceleration as critical measures except a few works. The historical sketch can be found in [33]. Unlike earlier work in which the critical earthquake is defined as that to produce the maximum response, we develop earthquake loads that cause the maximum damage in the structure using energy concepts and damage indices. The ground acceleration is represented by

$$\begin{aligned}\ddot{x}_{\mathrm{g}}(t) &= e(t)\sum_{i=1}^{N_{\mathrm{f}}} R_i \cos(\omega_i t - \phi_i) \\ &= A_0[\exp(-\alpha t) - \exp(-\beta t)]\sum_{i=1}^{N_{\mathrm{f}}} R_i \cos(\omega_i t - \phi_i)\end{aligned} \tag{4.20}$$

In Eq. (4.20), A_0 is a scaling constant and the parameters α and β represent the transient trend in $\ddot{x}_{\mathrm{g}}(t)$. R_i and ϕ_i are $2N_{\mathrm{f}}$ unknown amplitudes and phase angles, respectively, and $\omega_i, \quad i = 1, 2, \ldots, N_{\mathrm{f}}$ are the frequencies presented in the ground acceleration that are selected to span satisfactorily the frequency content of $\ddot{x}_{\mathrm{g}}(t)$. In constructing critical ground accelerations, the envelope function is introduced to be a known one. The information on energy E, PGA M_1, PGV M_2, and PGD M_3 are also assumed to be available. This enables one to define the following constraints [20, 30]:

$$\begin{aligned}
&\left[\int_0^\infty [\ddot{x}_g(t)]^2 dt\right]^{1/2} \le E;\\
&\max_{0<t<\infty} |\ddot{x}_g(t)| \le M_1;\\
&\max_{0<t<\infty} |\dot{x}_g(t)| \le M_2;\\
&\max_{0<t<\infty} |x_g(t)| \le M_3;\\
&M_5(\omega) \le |\ddot{X}_g(\omega)| \le M_4(\omega)
\end{aligned} \tag{4.21}$$

In Eq. (4.21), $\ddot{X}_g(\omega)$ is the Fourier transform of $\ddot{x}_g(t)$. From Eq. (4.20), the constraints of Eq. (4.21) can be expressed in terms of the unknown variables $R_i, \phi_i, \quad i = 1, 2, \ldots, N_f$. Those expressions can be summarized as

$$\begin{aligned}
&\left[A_0^2 \sum_{m=1}^{N_f}\sum_{n=1}^{N_f} R_m R_n \int_0^\infty [\exp(-\alpha t) - \exp(-\beta t)]^2 \cos(\omega_m t - \phi_m)\cos(\omega_n t - \phi_n) dt\right]^{\frac{1}{2}} \le E\\
&\max_{0<t<\infty} |A_0[\exp(-\alpha t) - \exp(-\beta t)] \sum_{n=1}^{N_f} R_n \cos(\omega_n t - \phi_n)| \le M_1\\
&\max_{0<t<\infty} |A_0 \sum_{n=1}^{N_f} \int_0^t R_n[\exp(-\alpha\tau) - \exp(-\beta\tau)]\cos(\omega_n\tau - \phi_n) d\tau\\
&\quad -A_0 \sum_{n=1}^{N_f} \int_0^\infty R_n[\exp(-\alpha\tau) - \exp(-\beta\tau)]\cos(\omega_n\tau - \phi_n) d\tau| \le M_2\\
&\max_{0<t<\infty} |A_0 \sum_{n=1}^{N_f} \int_0^t R_n[\exp(-\alpha\tau) - \exp(-\beta\tau)](t-\tau)\cos(\omega_n\tau - \phi_n) d\tau\\
&\quad -A_0 t \sum_{n=1}^{N_f} \int_0^\infty R_n[\exp(-\alpha\tau) - \exp(-\beta\tau)]\cos(\omega_n\tau - \phi_n) d\tau| \le M_3\\
&M_5(\omega) \le |A_0 \sum_{n=1}^{N_f} \int_0^\infty R_n\{\exp[-(\alpha + i\omega)t] - \exp[-(\beta + i\omega)t]\}\cos(\omega_n t - \phi_n) dt| \le M_4(\omega)
\end{aligned} \tag{4.22}$$

where $i = \sqrt{-1}$. The bounds $M_4(\omega)$ and $M_5(\omega)$ are introduced to replicate the Fourier spectra of past records on the critical ground acceleration [37, 38] and are given by

$$M_4(\omega) = E \max_{1 \le i \le N_r} |\bar{V}_{g_i}(\omega)|; \quad M_5(\omega) = E \min_{1 \le i \le N_r} |\bar{V}_{g_i}(\omega)| \tag{4.23}$$

In Eq. (4.23) the function $\bar{V}_{g_i}(\omega), \quad i = 1, 2, \ldots, N_r$ represents the Fourier transform of the ith normalized accelerogram $\ddot{v}_{g_i}(t)$ computed using the Fast Fourier Transform.

Now, the problem of deriving critical earthquake loads can be posed as determining the variables $\mathbf{y} = \{R_1, R_2, \ldots, R_{N_f}, \phi_1, \phi_2, \ldots, \phi_{N_f}\}^T$ such that DI_{PA} given by Eq. (4.10) is maximized under the constraints of Eq. (4.22).

It may be emphasized that, the ground energy rate is a more effective measure than the energy constraint in influencing the structural responses. A few

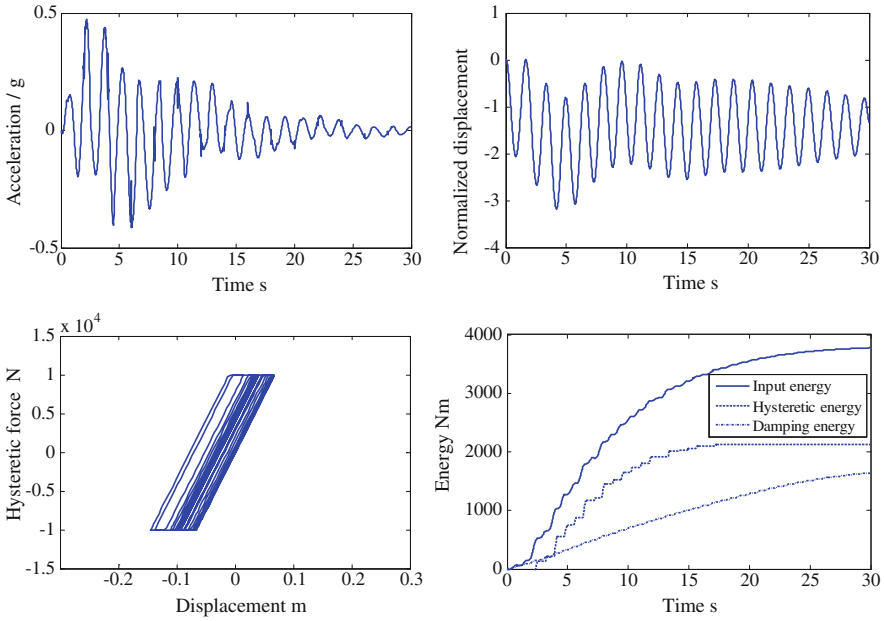

Fig. 4.7 Critical earthquake accelerations and associated critical responses for case 1 (Moustafa and Takewaki [46] with permission from Techno Press)

researchers have confirmed the effectiveness of the energy rate of the ground motion in producing larger structural responses [39, 40]. Note, however, that the energy of the ground motion indicates the earthquake magnitude and can be easily estimated from the time histories of the ground motion. The energy rate of the ground motion, on the other hand, is a time-dependent function. Constraining the energy rate of the ground motion requires imposing this constraint at discrete points of time which will increase the computational loads. This constraint can be implemented in the same way as the Fourier amplitude spectra constraints have been imposed (see Eqs. (4.21) and (4.22)). An alternative is to derive the critical ground velocity by maximizing the energy rate of the ground motion. Takewaki [18] has discussed the earthquake input energy rate to the structure in modeling the critical earthquake loads.

4.4.2 Solution Procedures

The nonlinear constrained optimization problem stated above is solved using the sequential quadratic programming (SQP) method [41]. In the numerical method, the following convergence criteria are adopted:

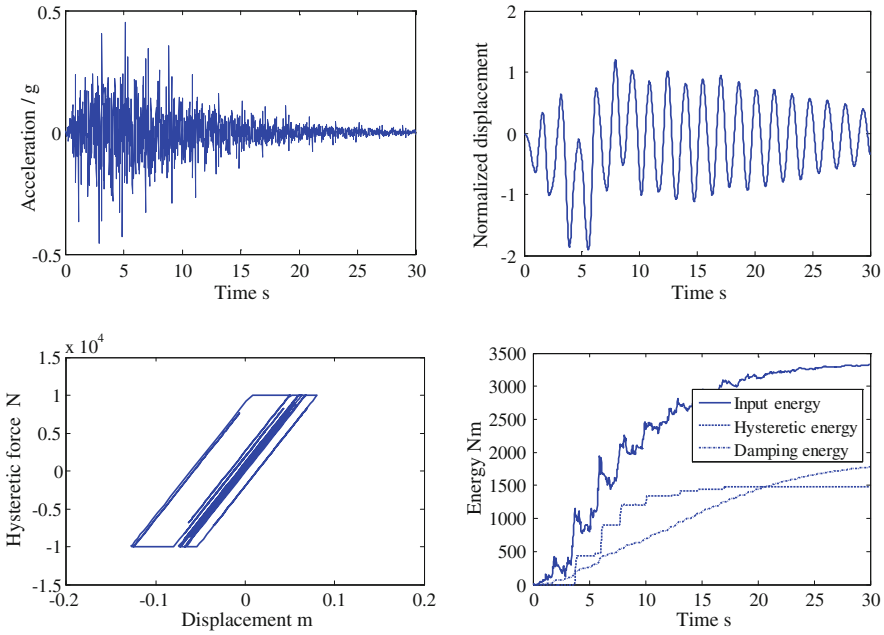

Fig. 4.8 Critical earthquake accelerations and associated critical responses for case 4 (Moustafa and Takewaki [46] with permission from Techno Press)

$$|f_j - f_{j-1}| \leq \varepsilon_1; \quad |y_{i,j} - y_{i,j-1}| \leq \varepsilon_2 \tag{4.24}$$

In Eq. (4.24), the function f_j is the objective function at the jth iteration, $y_{i,j}$ is the ith optimization variable at the jth iteration and $\varepsilon_1, \varepsilon_2$ are small quantities to be specified. The inelastic deformation of the structure is estimated by solving the equation of motion in the incremental form [20]. In distributing the frequencies of Eq. (4.20), it was found to be advantageous to place more frequencies within the half bandwidth of the natural frequency of the elastic structure and to select one of these frequencies to coincide exactly with this frequency. It seems that this enables the energy of the ground motion to get distributed around the structure fundamental natural frequency and to facilitate rapid convergence of the optimization procedure. In the numerical analyses, several initial guesses were examined and it was found that the optimization procedure converges to the same optimal solution.

It may be emphasized that the quantities $\mu(t) = u_{\max}/u_y$ and $E_H(t)$ do not reach their respective maxima at the same time. In this case, the optimization problem is solved at discrete time steps and the optimal solution $\mathbf{y}^* = [R_1^*, R_2^*, \ldots, R_{N_f}^*, \phi_1^*, \phi_2^*, \ldots, \phi_{N_f}^*]^T$ is the one that produces the maximum index DI_{PA} across all time points. The critical earthquake loads are then characterized by the accelerations and associated damage indices, inelastic deformations and energy dissipated by the structure. This model is called Model III in the numerical analysis.

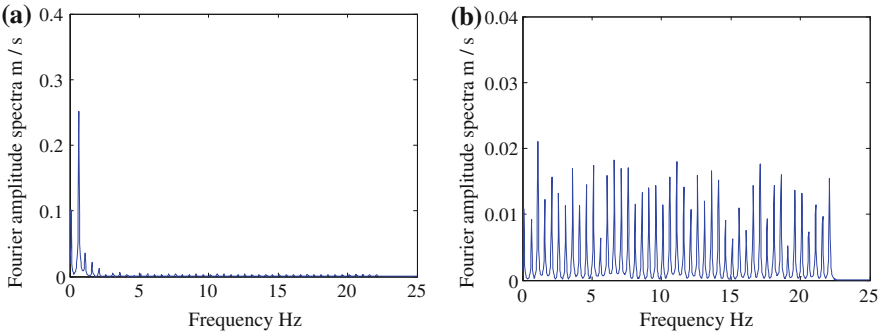

Fig. 4.9 Fourier amplitude of critical acceleration: **a** case 1, **b** case 4 (Moustafa and Takewaki [46] with permission from Techno Press)

Table 4.2 Nomenclature of constraint scenarios for Models I, II, and III (Moustafa and Takewaki [46] with permission from Techno Press)

Case	Models I and II	Model III
1	Energy	Energy and PGA
2	PGV	Energy, PGA, PGV, and PGD
3	–	Energy, PGA and UBFS
4	–	Energy, PGA, UBFS, and LBFS

UBFS: upper bound of Fourier spectrum, *LBFS*: lower bound of Fourier spectrum

Table 4.3 Response parameters of SDOF ($\omega_n = 4.10$ rad/s) to alternative acceleration inputs (Moustafa and Takewaki [46] with permission from Techno Press)

Response quantity	Earthquake input load						
	El Centro NS record	Critical input (model I)		Critical input (model II)		Critical input (model III)	
		Case 1	Case 2	Case 1	Case 2	Case 1	Case 4
Max. displ.[a] (m)	0.7518	1.1601	4.8370	2.04	3.85	–	–
Max. displ.[b] (m)	0.0918	0.0839	0.1653	0.1145	0.1655	0.16	0.13
Ductility	1.37	1.25	2.46	1.71	2.47	3.18	2.10
DI_{PA}	0.26	0.72	3.84	0.66	1.31	0.97	0.39

[a] Linear elastic analysis
[b] Elastic–plastic analysis

4.4.3 Illustrative Example

Illustrative examples are discussed in this section. Consider an elastic–plastic SDOF building frame with mass $= 9 \times 10^3$ kg, initial stiffness $k = 1.49 \times 10^5$ N/m, and viscous damping model of 0.03 damping ratio. The initial natural circular

Table 4.4 Sensitivity analysis of the critical damage index to the constraints parameters (Moustafa and Takewaki [46] with permission from Techno Press)

Parameter	E	M_1	M_2	M_3	$M_4(\omega)$	$M_5(\omega)$	α	β
ℓ_1	0.51	0.18	0.14	0.23[a]	0.16[a]	0.13	0.04	0.06
ℓ_2	4.52	1.60	1.71	2.04[a]	1.42[a]	1.15	0.36	0.53

[a] these values represent ℓ_1, ℓ_2, at the frequency at which $M_4(\omega)$, $M_5(\omega)$ reach their maximum values

frequency is about 4.10 rad/s and the yield force $f_y = 10^4$N and the yield displacement $u_y = 0.07$ m. The structure is assumed to start vibrating from rest.

The constraint quantities are set as $E = 4.17$ m/s$^{1.5}$, $M_1 = 4.63$ m/s^2 (0.47 g), $M_2 = 0.60$ m/s, and $M_3 = 0.15$ m. The envelope parameters are set as $A_0 = 2.17$, $\alpha = 0.13$, and $\beta = 0.50$. The upper and lower constraint values on the Fourier spectra are evaluated from the set of past records in Table 4.1 measured at a medium soil. The convergence limits $\varepsilon_1, \varepsilon_2$ are set as 10^{-6}. The frequency content of $\ddot{x}_g(t)$ is defined as $2\pi \times (0 \sim 25)$ rad/s.

The nonlinear constrained optimization problem is solved using the SQP method through the Matlab optimization toolbox [42]. To select the number of frequency terms N_f, a parametric study was carried out and the number $N_f = 51$ was found to give satisfactory results.

The constraint cases considered in obtaining critical earthquake loads are listed in Table 4.2. The numerical results obtained are presented in Figs. 4.7, 4.8, 4.9, Tables 4.3, and 4.4. Figure 4.7 shows the results for 'constraint scenario 1' and similar results for case 4 are presented in Fig. 4.8. Each figure shows the time history of the critical ground acceleration, the inelastic structural deformation, the hysteretic force, and the energy, dissipated by the structure. Based on extensive analyses of the numerical results, the following observations are induced:

1. The frequency content and Fourier amplitude of the critical earthquake ground motion are strongly dependent on the constraints imposed (see Table 4.3). If available information on earthquake ground motion data is limited to the total energy and PGA, the critical input is resonant to the structure natural frequency or of pulse-like nature and the structure deformation is conservative (see Fig. 4.7 and Table 4.3). Furthermore, most of the power of the Fourier amplitude is concentrated at a frequency close to the natural frequency of the elastic structure while the amplitudes at other frequencies are low and uniformly distributed (see Fig. 4.9a). It appears that the results for case 1 coincide well with earlier works reported by Abbas [20] and Takewaki [38]. These results, however, are substantially different from those of the elastic structure where all energy of the acceleration is centered around ω_0 [30]. Additional constraints on the Fourier amplitude spectra (see Table 4.3) require the Fourier amplitude of the critical acceleration to get distributed across other frequencies (see Fig. 4.9b). The critical acceleration possesses a dominant frequency close to the average frequency of past records. It should be noted that the realism of

the critical earthquake input is also evident from the maximum damage index it produces. For instance, the damage index for case 4 is 0.39 which is substantially smaller than 0.97 for case 1.

2. To study the influence of the damping ratio on the computed critical earthquake ground motion, limited studies were further carried out. The damping ratio is changed (namely, 0.01, 0.03, and 0.05) while all other parameters are kept unchanged. The critical earthquake ground motion is computed by solving a new optimization problem for each case. The value of the damping ratio does not seem to significantly influence the frequency content of the earthquake acceleration. It was observed, however, that the ductility ratio and the maximum inelastic deformation for the structure decrease toward higher damping ratios. Thus, the ductility ratio decreases to 1.98 for the damping ratio of 0.05, while the ductility ratio increases to 2.95 for damping ratio = 0.01. It is also observed that the inelastic structure with higher damping ratio dissipates more energy through damping compared to that with lower damping ratio. The damage index also reduces when the damping ratio becomes large.
3. The sensitivity of the critical damage index with respect to variation in values of the constraint values E, M_1, M_2, M_3, $M_4(\omega)$, $M_5(\omega)$ and the envelope parameters α, β are studied using numerical methods. To examine the sensitivity of DI_{PA} with respect to a specific parameter, the value of this parameter is changed by 1 % while all other parameters are held unchanged, and the optimization problem is solved again. This leads to the calculation of the percentage change in the optimal damage index ℓ_1, and also the ratio of change in the optimal damage index DI_{PA} to the change in the parameter value ℓ_2. Table 4.4 summarizes the results of these calculations for case 4. For the bounds $M_4(\omega)$, $M_5(\omega)$ of constraints, the change of 1 % is taken to be uniform across all frequencies. Table 4.4 reveals that the changes in energy E and PGD $M_4(\omega)$ alter the optimum solution considerably compared with similar changes in other parameters. The optimum solution is less sensitive to changes in the envelope parameters.

It may be noted that models I and II represent near-field pulse-like ground motions with an equivalent main pulse. Model III accounts for the multi-pulses in the ground velocity. It is well known that this class of ground motion may contain several pulses. Furthermore, the earthquake ground motion has been treated as deterministic in nature. The modeling of this class of ground motion using the probabilistic approach facilitates handling uncertainties in the ground motion, variability in the structure's parameters, and assessing the structure's reliability. These aspects have been recently investigated by the present authors [43]. Furthermore, the reduction of the structural responses under strong ground motion including critical ones by passive dampers has also been studied [44, 45].

4.5 Summary

This chapter investigates the distinctive characteristics of near-field pulse-like strong ground motions. This class of ground motion can be characterized using measures based on analyses of the free-field earthquake records or based on the associated structural response. A new measure of the effective frequency content of the ground acceleration has also been developed. An additional measure for the frequency content of the ground motion that is based on the work of Vanmarcke [13, 14] has also been examined. It has been shown that these two measures successfully identify resonant or pulse-like ground motions. The energy rate of the ground acceleration in time and frequency domains were also employed for the same purpose. Pulse-like ground motions have also been characterized in terms of measures of the structural performance during the ground shaking (response, energy, and damage spectra). This chapter also provides simple analytical models for near-fault pulse-like ground motion which can be used by the structural engineer to assess the safety of linear structures without the need for numerical integration of the equations of motion.

Given the central importance of considering nonlinear behavior of structures under strong ground motion, the mathematical modeling of near-field pulse-like ground motions has also been investigated for inelastic structures using the critical excitation method and nonlinear sequential optimization techniques and damage indices. It has been shown that the proposed method can successfully model pulse-like ground motions at sites having limited earthquake data.

References

1. Anderson J, Bertero V (1987) Uncertainties in establishing design earthquakes. J Struct Eng 113(8):1709–1724
2. Bray JD, Rodriguez-Marek A (2004) Characterization of forward-directivity ground motions in the near-fault region. Soil Dyn Earthquake Eng 24:815–828
3. Hall JH, Heaton TH, Halling MW, Wald DJ (1995) Near-source ground motion and its effect on flexible buildings. Earthquake Spectra 11:569–605
4. Heaton TH, Hall JH, Wald DJ, Halling MW (1995) Response of high-rise and base-isolated buildings in a hypothetical MW 7·0 blind thrust earthquake. Science 267:206–211
5. Housner GW, Hudson DE (1958) The Port Hueneme earthquake of March 18, 1957. Bull Seismol Soc Am 48(2):163–168
6. Housner GW, Trifunac MD (1967) Analysis of accelerograms-Parkfield earthquake. Bull Seismol Soc Am 57(6):1193–1220
7. Makris N (1997) Rigidity-plasticity-viscosity: Can electrorheological dampers protect base-isolated structures from near-source ground motions? Earthquake Eng Struct Dynam 26:571–591
8. Zhang J, Makris N (2001) Rocking of free-standing blocks under cycloidal pulses. J Eng Mech 127(5):473–483
9. Hough SE, Bilham RG (2006) After the earthquakes: elastic rebound on an urban planet. Oxford University Press, NY

10. Pacific Earthquake Engineering Research Center (2005) http://peer.berkeley.edu
11. Arias A (1970) A measure of earthquake intensity: seismic design of nuclear power plants. MIT press, Cambridge, pp 438–468
12. Trifunac MD, Brady AG (1975) A study on the duration of strong earthquake ground motion. Bull Seismol Soc Am 65(3):581–626
13. Vanmarcke EH (1972) Properties of spectral moments with applications to random processes. J Eng Mech 42:215–220
14. Vanmarcke EH (1976) Structural response to earthquakes. In: Lomnitz C, Rosenbluth E (eds) Seismic risk and engineering decisions. Elsevier, NY
15. Housner GW (1970) Strong ground motion. In: Wiegel RL (ed) Earthquake engineering. Prentice Hall, NJ
16. Housner GW, Jennings PC (1977) The capacity of extreme earthquake motions to damage structures. In: Hall WJ (ed) Structural and geotechnical mechanics: A volume honoring N. M. Newmark. Prentice-Hall, Englewood Cliff, NJ, pp 102–116
17. Takewaki I (2004) Bound of earthquake input energy. J Struct Eng 130:1289–1297
18. Takewaki I (2006) Probabilistic critical excitation method for earthquake energy input rate. J Eng Mech 132(9):990–1000
19. Yamamoto K, Fujita K, Takewaki I (2011) Instantaneous earthquake input energy and sensitivity in base-isolated building. J Struct Des Tall Spec Buildings 20(6):631–648
20. Abbas AM (2006) Critical seismic load inputs for simple inelastic structures. J Sound Vib 296:949–967
21. Akiyama H (1985) Earthquake-resistant limit-state design for buildings. University of Tokyo Press, Tokyo
22. Chai YH, Fajfar P (2000) A procedure for estimating input energy spectra for seismic design. J Earthquake Eng 4(4):39–561
23. Moustafa A (2009) Critical earthquake load inputs for multi-degree-of-freedom inelastic structures. J Sound Vib 325(3):532–544
24. Uang C-M, Bertero VV (1990) Evaluation of seismic energy in structures. Earthquake Eng Struct Dynam 19:77–90
25. Zahrah TF, Hall WJ (1984) Earthquake energy absorption in sdof structures. J Struct Eng 110:1757–1772
26. Cosenza C, Manfredi G, Ramasco R (1993) The use of damage functionals in earthquake engineering: a comparison between different methods. Earthquake Eng Struct Dynam 22:855–868
27. Ghobara A, Abou-Elfath H, Biddah A (1999) Response-based damage assessment of structures. Earthquake Eng Struct Dynam 28:79–104
28. Powell GH, Allahabadi R (1988) Seismic damage predictions by deterministic methods: concepts and procedures. Earthquake Eng Struct Dynam 16:719–734
29. Park YJ, Ang AH-S, Wen YK (1985) Seismic damage analysis of reinforced concrete buildings. J Struct Eng 111(4):740–757
30. Abbas AM, Manohar CS (2002) Investigations into critical earthquake excitations within deterministic and probabilistic frameworks. Earthquake Eng Struct Dynam 31:813–832
31. Abbas AM, Manohar CS (2007) Reliability-based vector nonstationary random critical earthquake excitations for parametrically excited systems. Struct Saf 29:32–48
32. Takewaki I (2002) Seismic critical excitation method for robust design: a review. J Struct Eng 128:665–672
33. Takewaki I (2007) Critical excitation methods in earthquake engineering. Elsevier, Amsterdam
34. He WL, Agrawal AK (2008) Analytical model of ground motion pulses for the design and assessment of seismic protective systems. J Struct Eng 134(7):1177–1188
35. Tan P, Agrawal AK, Pan Y (2005) Near-field effects on seismically excited highway bridge equipped with nonlinear viscous dampers. Bridge Struct 1(3):307–318
36. Moustafa A (2010) Discussion of analytical model of ground motion pulses for the design and assessment of seismic protective systems. J Struct Eng 136(2):229–230

37. Shinozuka M (1970) Maximum structural response to seismic excitations. J Eng Mech 96:729–738
38. Takewaki I (2001) Probabilistic critical excitation for MDOF elastic-plastic structures on compliant ground. Earthquake Eng Struct Dynam 30:1345–1360
39. Trifunac MD (2005) Power design method. In: Proceedings of earthquake engineering in the 21st century to mark 40th anniversary of IZIIS-Skopje, key note lecture, 28 Aug–1 Sept 2005, Skopje and Ohrid, Macedonia
40. Trifunac MD (2008) Energy of strong motion at earthquake source. Soil Dyn Earthquake Eng 28:1–6
41. Arora JS (2004) Introduction to optimum design. Elsevier Academic Press, San Diego
42. Caleman T, Branch MA, Grace A (1999) Optimization toolbox for the use with Matlab, user's guide. The Math Works Inc., USA
43. Moustafa A, Takewaki I (2010) Deterministic and probabilistic representation of near-field pulse-like ground motion. Soil Dyn Earthquake Eng 30(5):412–422
44. Fujita K, Moustafa A, Takewaki I (2010) Optimal placement of viscoelastic dampers and supporting members under variable critical excitations. Earthquakes Struct 1(1):43–67
45. Takewaki I (2009) Building control with passive dampers: optimal performance-based design for earthquakes. Wiley, Singapore
46. Moustafa A, Takewaki I (2010) Critical characterization and modeling of pulse-like near-fault strong ground motion. Struct Eng Mech 34(6):755–778

Chapter 5
Characteristics of Earthquake Ground Motion of Repeated Sequences

5.1 Introduction

Ground acceleration sequences separated by short time intervals have been observed at several parts of the world, including Japan, Mexico, Turkey, Italy, and California. However, such ground motion data is not available in catalogues for easy access to structural engineers. It should be emphasized that the 2011 off the Pacific coast of Tohoku earthquake had multiple sources and exhibited multiple sequences (see Fig. 2.3a, b). Ground motion sequences can create significant damage in structures due to the accumulation of the inelastic deformation from the repeated sequences before any structural repair is possible. Additionally, the low-frequency content in secondary sequences may cause resonance in lower modes of the damaged structure leading to further damage to the structure (see Chap. 10). Accordingly, the verification of the structure adequacy to withstand multiple acceleration sequences without collapse is of essential concern in earthquake engineering, especially since current seismic codes do not account for their effects.

Elnashai et al. [1] shed lights on this subject and reported significant increase in the force demand of ductile structures to multiple acceleration sequences. The dynamic analysis of inelastic structures under acceleration sequences has been studied by Amadio et al. [2] and Das et al. [3]. Simulated acceleration sequences have been used as input to inelastic structures. Extensive investigations on the displacement ratio of SDOF inelastic structures driven by repeated earthquakes have been carried out by Hatzigeorgiou and Beskos [4]. 112 ordinary accelerograms recorded at four different soil sites have been used to produce two and three repeated sequences. More recently, Hatzigeorgiou [5, 6] studied the properties of near-fault and far-fault repeated acceleration sequences using ordinary recorded accelerograms for different soil types. He derived analytical expressions for the inelastic displacement ratio and the ductility demand in terms of the period of vibration, the viscous damping ratio, the strain-hardening ratio, the force reduction factor, and the soil class. Most research

I. Takewaki et al., *Improving the Earthquake Resilience of Buildings*,
Springer Series in Reliability Engineering, DOI: 10.1007/978-1-4471-4144-0_5,

carried out so far has focused on the effect of the repeated earthquake shakings on SDOF systems. However, a few studies have dealt with multi-degree-of-freedom (MDOF) systems (e.g. [7–9]). These studies have shown that repeated acceleration sequences can produce large deformations in the structures. It may be emphasized that the characteristics of recorded earthquakes of multiple sequences have not been studied before. In other words, the structural response to repeated ground motions have been extensively studied but the characteristics of strong ground motion of multiple sequences have not been studied.

Given the drastic growth in strong ground motion data worldwide over the last 76 years, it is of interest to investigate the characteristics of repeated acceleration sequences. This aspect is of relevance to (a) the mathematical modeling and simulation of ground motion acceleration sequences, (b) the selection of earthquake ground motion records as input to the time-history analysis of inelastic (or loading-history dependent) structures, and (c) the performance-based seismic design of structures. The objectives of this chapter are (1) to provide a list of recorded earthquake ground motions with multiple sequences, (2) to explain the characteristics of ground motion sequences using actual recorded data, (3) to examine if such ground motion occurs at the near-fault region or at the far-fault region, and whether it is limited to certain soil condition, and (4) to discuss the inelastic structural response to recorded earthquake ground motions of multiple sequences. It is emphasized in this chapter that it is needed to consider repeated acceleration sequences in seismic design of structures beyond its elastic limit or with loading history-dependent properties. It may be recalled that the 1994 Northridge and the 1995 Hyogoken-Nanbu earthquakes have motivated modern seismic codes to introduce modification factors to design spectra in the near-fault regions [10–15]. The characteristics of recorded ground motion sequences are discussed in the next section.

5.2 Characteristics of Earthquake Records of Repeated Sequences

The horizontal and vertical components of the ground accelerations of a set of 54 ground accelerations are adopted from 18 earthquakes recorded in seven countries. Table 5.1 summarizes information on these records. This information includes the moment magnitude, the observed number of sequences, the site-source distance, the total duration, the peak ground acceleration (PGA), and the Arias intensity (square root of the area under the square of the ground acceleration) [16]. The Arias intensity was discussed in Chap. 4. The earthquake date, time of occurrence, the site, the recording station, and the local soil condition beneath the recording station are also included in the table. The digitized accelerations data have been accessed from the COSMOS database Center [17], the Kyoshin-Network [18], the Kiban Kyoshin-Network [19], and the Pacific Earthquake Engineering Research Center [20]. These records cover a variety of earthquake magnitude, duration, soil condition, site-source distance, and PGA. These records represent strong ground motion in the

range of M $\geq$ 5.0 or PGA $\geq$ 0.05 g. The selection criterion of these records was not based on the site-source distance, the duration, or the soil class. Each record is reported as a single accelerogram of multiple acceleration sequences. Note also that, some of the secondary sequences represent aftershocks following the mainshock. Some of the secondary sequences of a few earthquakes represent foreshocks preceding the mainshock. In fact, it is difficult to explain the silence time separating the acceleration sequences unless they are interpreted as mainshock/aftershock events. Further investigations from seismologists and engineers may provide deeper understanding of the multiple acceleration sequences in future.

Table 5.1 summarizes also information on the three acceleration components of two ordinary earthquakes without sequences. The first one is the 1940 Imperial Valley (El Centro) earthquake recorded at El Centro array #9 and the second one is the 1995 Hyogoken-Nanbu (Kobe) earthquake recorded at the Kobe university recording station for comparison. Figure 5.1 shows the three acceleration components for earthquakes having two and three sequences (see Table 5.1). Based on analyses of these records, the following remarks can be made.

1. **Source-site distance**: Most records (except Katsurao and Bhuj earthquakes) represent strong ground motion measured in the near-fault region with site-source distance less than about 23 km. The three acceleration records of each earthquake contain distinct sequences. The sequence trend is also observable in the velocity and the displacement waves. The acceleration records of the Katsurao earthquake (site-source distance = 39 km) have two sequences. The vertical acceleration only of Bhuj earthquake contains two sequences which could be attributed to the local soil effects [17]. Thus, multiple sequences can often be observed at the near-fault and the far-fault regions.
2. **Influence of source mechanism**: Most earthquake ground motion records of repeated sequences are measured at sites with various soil conditions. A few records, however, are reported at sites with rock condition. This implies that the occurrence of repeated acceleration sequences is independent of the local soil condition beneath the recording station. For this reason, such ground motion is primarily influenced by the source mechanism, where the energy at the source is released in sequences separated by short-intervals of time.
3. **Number of acceleration sequences**: The observed number of acceleration sequences is generally two or three (see Table 5.1 and Fig. 5.1). On the other hand, a larger number of sequences have been observed in a few records. For instance, the vertical acceleration of the 2004 Niigata-ken Chuetsu earthquake recorded at Ojiya (NIG019) contains five sequences (see Table 5.1). Note that, the number of acceleration sequences depends on the records considered. Note also that, a clear criterion for defining the effective number of acceleration sequences does not exist, and is introduced in the next section.
4. **Total duration and duration of sequences**: The total duration of acceleration records listed in Table 5.1 is remarkably larger than those of ordinary records and ranges between about 1.0 and 10.0 min. Some records, however, have shorter durations than 1.0 min (see Table 5.1). The duration of individual

Table 5.1 Information on strong ground-motions with multiple acceleration sequences (Moustafa and Takewaki [32] with permission from Techno Press)

Earthquake	Date	Time	Soil type	Site (station)	N_s	M	D_{ss} (km)	t_d (s)	PGA (g)			E (m/s$^{3/2}$)		
									H_1	H_2	UD	H_1	H_2	UD
Helena aftershock	11.28.1935	14:41:48	Rock	Helena Federal Bldg (HFB)	2	5.0	6.3	45	0.09	0.08	0.03	1.47	1.76	0.58
San Francisco	03.22.1957	19:44:21	Alluvium	350 McAllister (USGS1080)	2	5.3	17.0	41	0.10	0.07	0.05	0.64	0.47	0.44
San Fernando	02.09.1971	14:02:24	Rock	Pacoima dam (CSMIP24207)	2	3.9	10.9	31	0.12	0.13	0.05	0.70	0.57	0.29
Victoria	06.09.1980	03:28:19	Alluvium	Chihuahua, Mexico (6621)	2	6.4	5.7	56	0.19	0.15	0.17	1.89	1.77	1.13
New Zealand	06.18.1994	03.25.15	medium	Arthurs Pass (GNS505A)	3	6.8	16.0	160	0.44	0.34	0.37	5.49	3.47	3.24
Katsurao	02.20.1997	05:22:00	Soft soil	Katsurao (FKS006)	2	5.3	39.0	67	0.12	0.12	0.06	0.87	0.86	0.45
Kocaeli	08.17.1999	00:01:40	Soft soil	Yarimca (KOER772)	2	7.4	22.7	136	0.23	0.32	0.24	3.14	3.17	2.74
Chi-Chi	09.20.1999	17:47:16	Stiff soil	Taichung (TCU071)	2	7.6	4.9	160	0.53	0.65	0.42	6.30	9.62	5.06
Chi-Chi	09.20.1999	18:03:00	Stiff soil	Taichung (TCU078)	2	6.2	7.6	65	0.28	0.47	0.24	2.28	3.66	1.20
Bhuj	01.26.2001	03:16:40	NA	Ahmd abad (IITR)	2[a]	7.0	239.0	134	0.11	0.08	0.07	1.31	1.01	0.80
Niigata-ken Chuetsu	10.23.2004	17:56:00	Soft soil	Ojiya (NIG019)	2	6.8	7.0	299	1.17	1.33	0.84	9.83	11.64	6.97
Niigata-ken Chuetsu	10.23.2004	17:56:00	NA	Nagaoka-shisho (NIG028)	2	6.8	15.0	580	0.89	0.72	0.44	9.70	7.84	4.72
Niigata-ken Chuetsu	10.23.2004	18:03:00	Soft soil	Ojiya (NIG019)	2[b]	6.3	18.0	299	0.20	0.23	0.10	1.95	2.40	1.03
Niigata-ken Chuetsu	10.23.2004	18.07:00	Soft soil	Koide (NIG020)	3	5.7	15.0	299	0.12	0.12	0.04	0.76	0.76	0.36
Niigata-ken Chuetsu	10.23.2004	18:34:00	Soft soil	Koide (NIG020)	2	6.5	09.0	299	0.54	0.53	0.34	5.65	4.07	2.51
Niigata-ken Chuetsu	10.23.2004	19:46:00	Soft soil	Koide (NIG020)	3	5.7	10.0	299	0.15	0.13	0.06	1.23	1.15	0.61
Niigata-ken Chuetsu	10.27.2004	10:40:00	Soft soil	Koide (NIG020)	2	6.1	9.0	299	0.53	0.40	0.54	3.51	2.53	2.16
Honshu	04.15.2007	19:47:00	Soft soil	Kohga (SIG012)	2	5.4	13.0	120	0.26	0.11	0.05	2.05	0.53	0.41
Niigata-ken Chuetsu-oki	08.16.2007	04:15:00	Soft soil	Hasunuma (CHBH19)	2	5.3	17.0	147	0.10	0.03	0.04	0.55	0.42	0.27
Iwate-Miyagi	06.14.2008	09:20:00	Soft soil	Ichinoseeki-w (IWTH25)	2	5.7	22.0	212	0.80	0.21	0.47	2.61	1.20	1.73
El Centro[c]	05.19.1940	04:37:00	Soft soil	117 El Centro array # 9	0	7.0	12.99	40	0.22	0.31	0.21	3.27	3.57	1.79
Hyogoken-Nanbu[c]	01.16.1995	20:46:00	NA	Kobe University	0	6.9	0.90	32	0.31	0.29	0.38	2.26	2.76	2.03

NA not available, N_s number of acceleration sequences, M magnitude, D_{ss} site-source distance, t_d total duration

[a] UD component only has two acceleration sequences, [b] UD component has five acceleration sequences, [c] ordinary records without acceleration sequences

H_1 first horizontal acceleration component, H_2 second horizontal acceleration component, *UD* vertical acceleration component

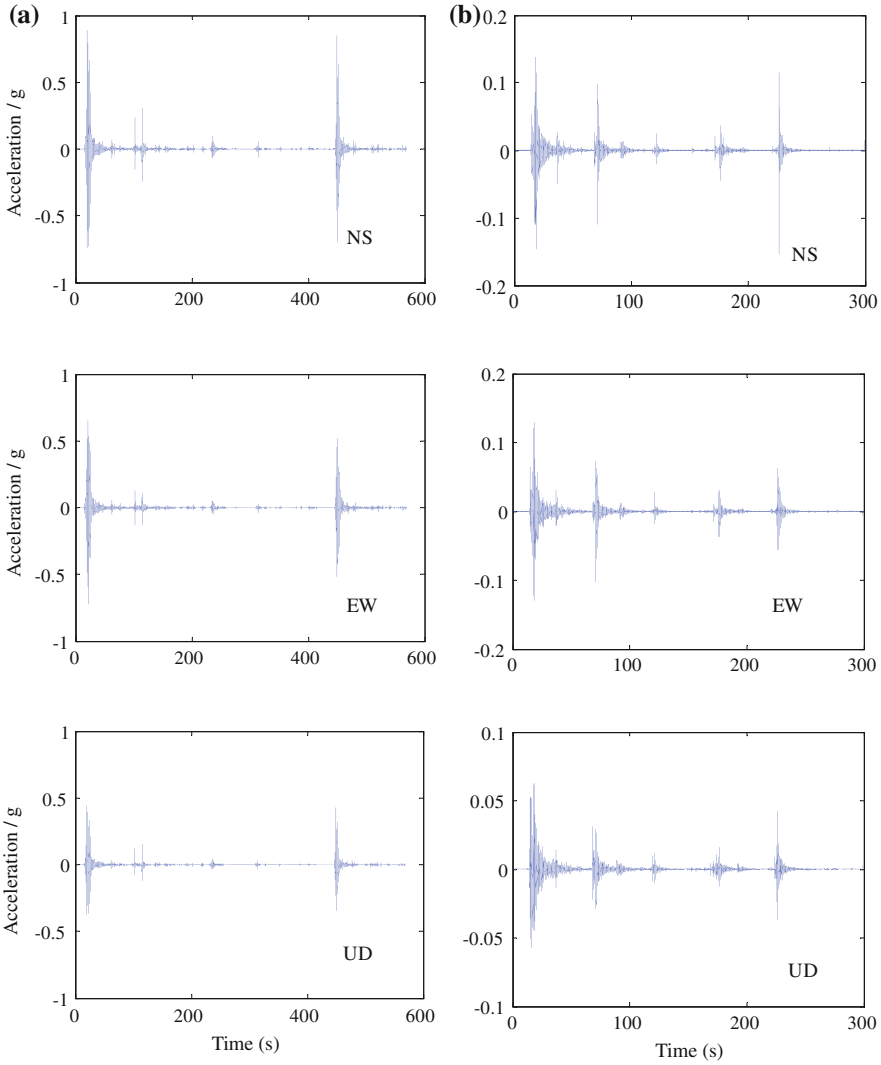

Fig. 5.1 Ground accelerations with multiple sequences. **a** 2004 Niigata-ken Chuetsu earthquake at Nagaoka-shisho (NIG028). **b** 2004 Niigata-ken Chuetsu earthquake at Koide (NIG020) (Moustafa and Takewaki [32] with permission from Techno Press)

sequences (duration between 5 and 95 % of the sequence energy) known as bracketed duration [21] is significantly small, typically about 5–30 s. The individual sequences of most records have sharp build up, short strong-phase and sudden decay. The time-intervals separating the acceleration sequences are about 1–3 times the duration of the individual sequences. Note that, the earthquake total duration depends on the triggering mechanism of the seismic instrument, the processing methodology of the ground motion adopted by each

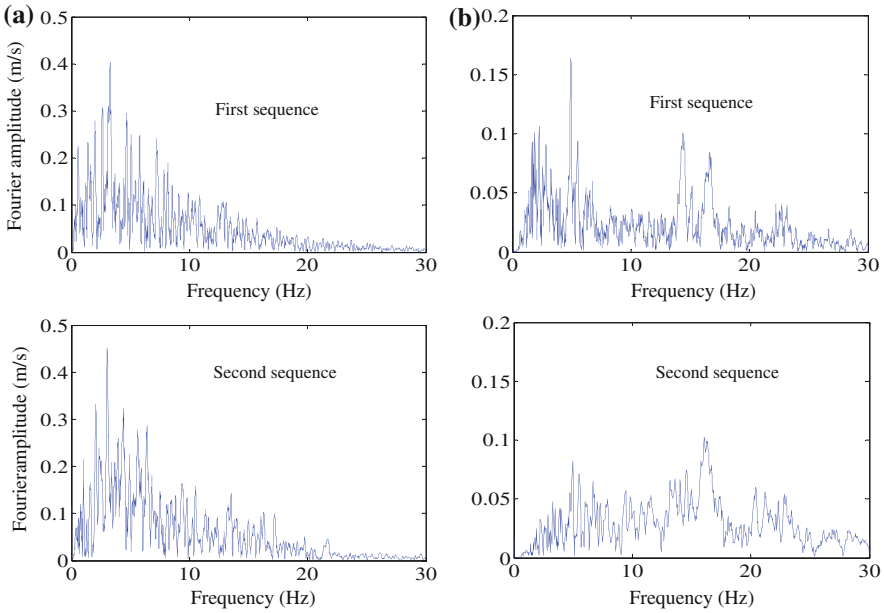

Fig. 5.2 Fourier amplitude spectra for individual sequences. **a** 2004 Niigata-ken Chuetsu (NIG028-NS). **b** 2007 Honshu (SIG012-NS) (Moustafa and Takewaki [32] with permission from Techno Press)

agency and the criterion adopted for selecting earthquake ground motion records of multiple sequences. For instance, if aftershock records are included, the total duration could increase remarkably.

5. **Frequency content of sequences**: Figure 5.2 shows the Fourier amplitude spectra for each sequence of the NS acceleration components of the 2004 Niigata-ken Chuetsu and the 2007 Honshu earthquakes (Table 5.1). These plots show that the frequency content and the amplitude for the individual sequences of the same record could be significantly different. Hence, in simulating repeated acceleration sequences, the consideration of identical sequences may not be accurate.
6. **Distribution of energy in individual sequences**: In general, the individual sequences of the same record have different energies and durations. The first sequence (mainshock) of most records has larger energy and longer duration than secondary sequences in general. In addition, the individual sequences have sharp build up of energy (see Figs. 5.3 and 5.4).
7. **PGA**: The PGA is generally contained in the first sequence (mainshock) and the largest observed PGA is 1.33 g. In this study, we limited our attention to ground motions with the minimum PGA of about 0.05 g. Some records, however, have PGA slightly less than 0.05 g but the magnitude is $M \geq 5.0$.
8. **Magnitude range**: The earthquake magnitude corresponding to the ground motions reported in this chapter ranges between 5.0 and 7.4 (see Table 5.1). One earthquake, however, has magnitude $= 3.9$, but the associated PGAs are larger than 0.05 g.

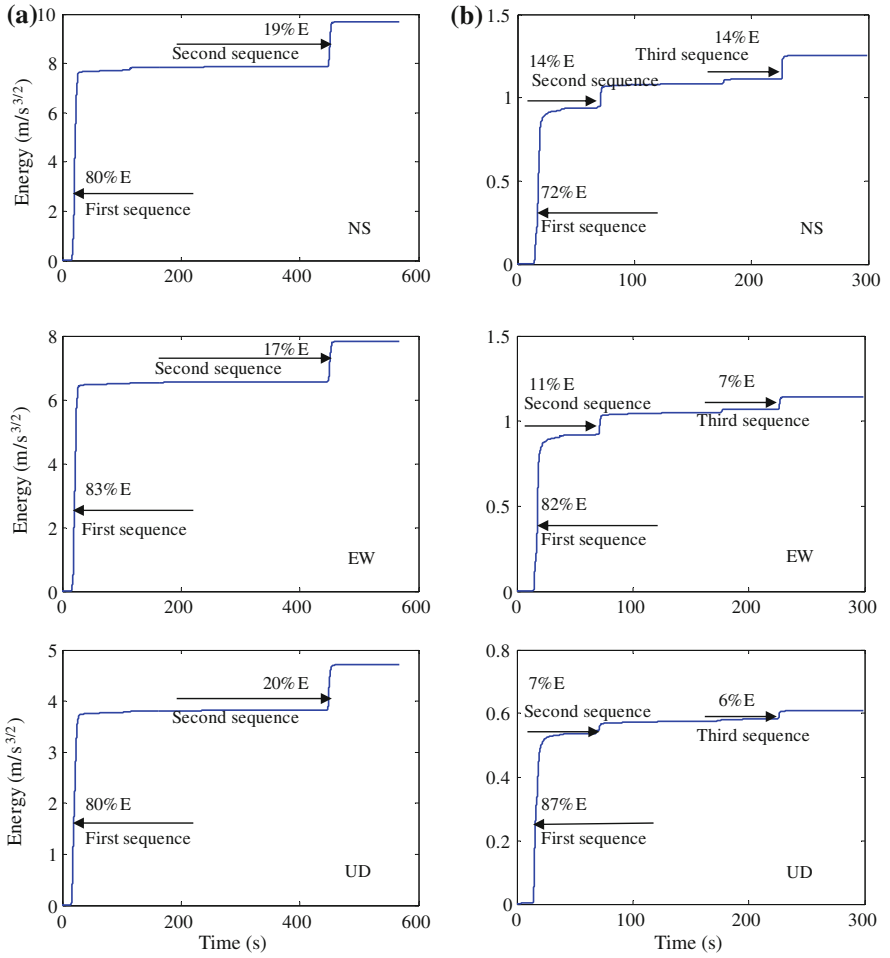

Fig. 5.3 Time-variation of energy for acceleration sequences estimated from Eq. (5.1). **a** 2004 Niigata-ken Chuetsu at Nagaoka-shisho (NIG028). **b** 2004 (19:46:00) Niigata-ken Chuetsu at Koide (NIG020) (Moustafa and Takewaki [32] with permission from Techno Press)

9. **Correlation of acceleration components**: Three acceleration components of each earthquake exhibit significant correlations (Fig. 5.1). The corresponding sequences in the three records of the same earthquake have similar durations and time instants of initial build up, strong-phase and decay. Therefore, as expected, the cross-correlation functions of the acceleration components are significant during the strong shaking durations (Fig. 5.5).
10. **Mainshock and aftershocks**: The 2004 Niigata-ken Chuetsu earthquakes represent a series of earthquake events containing the mainshock and 16 aftershocks occurring during about 3 weeks. The first six aftershocks occurred in the same day of the mainshock. Each event contains distinct acceleration

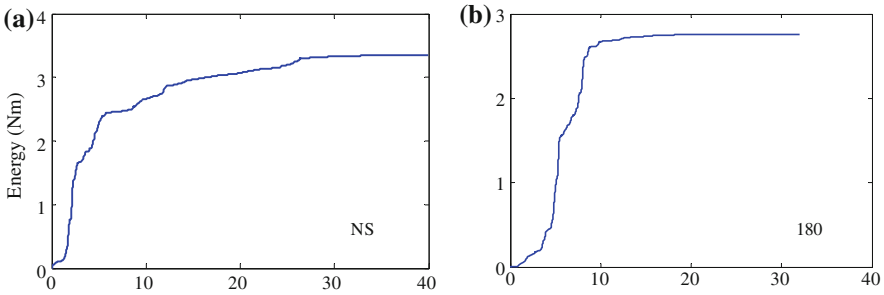

Fig. 5.4 Time-variation of energy for ordinary earthquakes. **a** 1940 Imperial valley earthquake (El Centro array #9). **b** 1995 Hyogoken-Nanbu earthquake (Kobe University) (Moustafa and Takewaki [32] with permission from Techno Press)

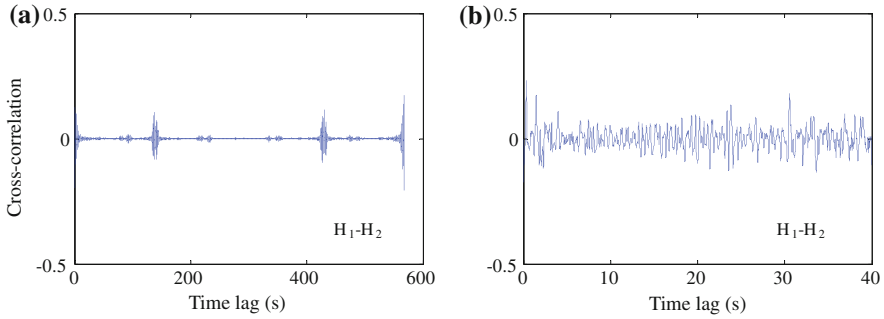

Fig. 5.5 Cross-correlation functions of ground accelerations. **a** 2004 Niigata-ken Chuetsu earthquake (NIG028). **b** 1940 El Centro (El Centro #9) (Moustafa and Takewaki [32] with permission from Techno Press)

sequences. Note, however, that some earthquakes have foreshock and aftershocks but the individual records do not have acceleration sequences. These earthquakes are not included here.

Section 5.3 investigates the earthquake characteristics, such as, the energy, frequency content, and effective number of sequences and effective duration of repeated acceleration sequences.

5.3 Characteristics of Free-Field Acceleration Records of Repeated Sequences

In this section, the time variation of the energy is examined of strong earthquake ground motion of repeated sequences. The definition of the effective number of sequences is introduced for later convenience. The acceleration energy (or power) is defined in terms of the Arias intensity as follows [16].

$$E(t) = \left[\int_0^t [\ddot{x}(\tau)]^2 d\tau \right]^{1/2}, \tag{5.1}$$

where $\ddot{x}(t)$ is the ground acceleration and τ is a dummy time variable. It is well-known that the total input energy can be estimated by replacing t with t_d (t_d = total duration) in the above equation.

Figure 5.3 illustrates the time variation of earthquake ground motion energy estimated using Eq. (5.1) for three acceleration components for the earthquake records shown in Fig. 5.1. Figure 5.4 shows the ground motion energy for one of the horizontal accelerations (H1 in Table 5.1) for the two ordinary earthquakes without sequences. The multiple sequences have repeated build up of energy during each sequence and no significant contribution from the time-intervals separating sequences. This feature is more remarkable in the Niigata-ken Chuetsu accelerograms recorded at Nagaoka-shisho (Fig. 5.3a). It can be seen that the contribution to the total energy from the first sequence is remarkably high (72–87 %) while that from the secondary sequences is small (6–20 %). Note that, minor secondary sequences of low amplitude exist in some records. These sequences have small build up of energy (Fig. 5.3b). The contribution from these secondary sequences to the total energy is very small. This observation is used to define the effective number of sequences in earthquake ground motion records of multiple sequences below.

It is proposed and discussed here that the effective number N_{ef} of ground motion acceleration sequences be defined based on the contribution of the individual sequence energy to the total energy of the ground acceleration. Let the total energy of the ground motion acceleration signal be described by Eq. (5.1) with $t = t_d$. The effective number of sequences is defined as those sequences that contribute by a minimum of a % to the total acceleration energy where a is a positive quantity to be specified. For instance, if $a = 5$, the earthquake acceleration records of Fig. 5.1a have two sequences while those of Fig. 5.1b have three sequences. The ratio of the PGA in each sequence to that of the entire record can also be used as a criterion for defining N_{ef}. This criterion, however, excludes important information, such as, the duration and the energy of each sequence. Similarly, the definition of the effective acceleration duration t_{ef} can also be introduced. Herein, t_{ef} is defined as the sum of individual effective durations of all acceleration sequences excluding the time intervals separating sequences. This duration reflects the actual duration of strong shaking of the ground. Based on this, the effective duration for the 2004 Niigata-ken Chuetsu earthquake recorded at Nagaoka-shisho is about 50 s. This definition can be used in comparing the effective duration of ground shaking of ordinary records with records of multiple sequences. As for the effective duration, there are several definitions, e.g. the bracketed duration [21] as mentioned above.

To examine the frequency content and amplitude of repeated acceleration sequences, the short-time Fourier transform (STFT) is effective and used. Herein, the Fourier transform is estimated for snapshots or a sliding window of the original acceleration signal as follows:

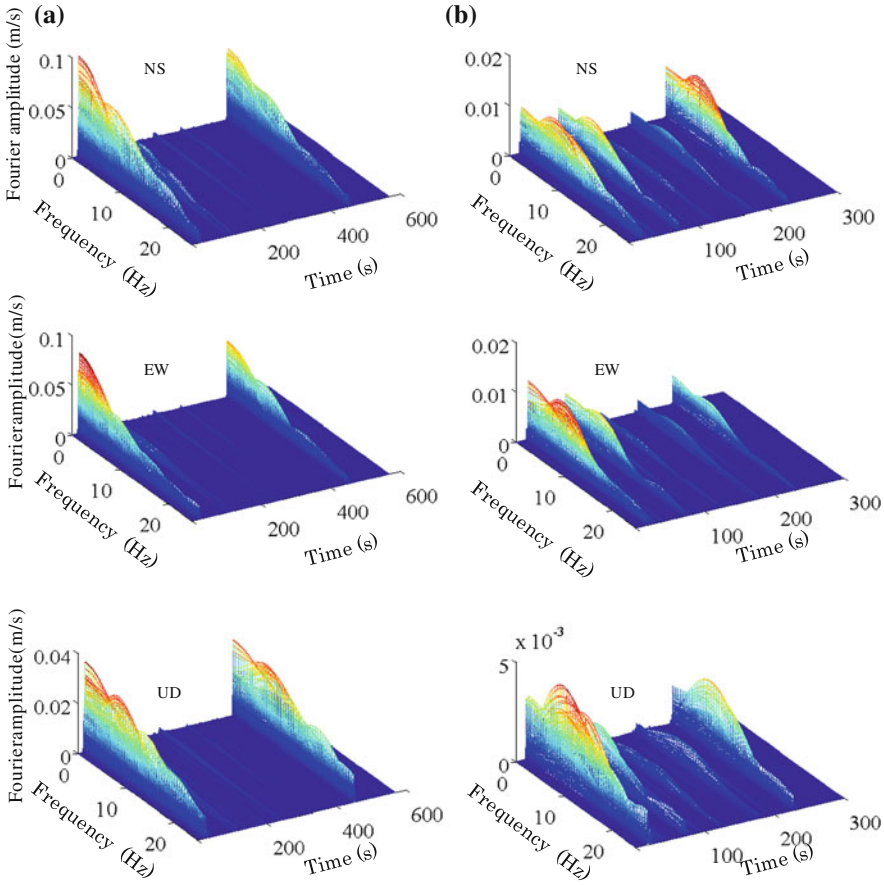

Fig. 5.6 Short-Time Fourier amplitude spectra for repeated earthquake sequences. **a** 2004 Niigata-ken Chuetsu earthquake at Nagaoka-shisho (NIG028). **b** 2004 Niigata-ken Chuetsu earthquake at Koide (NIG020) (Moustafa and Takewaki [32] with permission from Techno Press)

$$X(\omega, t) = \int_{-\infty}^{\infty} \ddot{x}(\tau) g(\tau - t) e^{-i\omega\tau} d\tau \tag{5.2}$$

In Eq. (5.2) $X(\omega, t)$ is the Fourier transform of the acceleration at time t, $g(\tau)$ is a sliding rectangular window of unit intensity and $i = \sqrt{-1}$. Thus, for a fixed time $t = t_j$, $X(\omega, t_j)$ represents the local spectral content of the ground acceleration as a function of the frequencies near t_j.

Figure 5.6 shows the STFT for the three records of the 2004 Niigata-ken Chuetsu earthquake recorded at Nagaoka-shisho (NIG028) and those recorded at Koide (NIG020) (see Table 5.1). These plots clearly reflect the non-stationarity of the acceleration sequences in time and frequency domains. Note that, the records of Fig. 5.6a have peak amplitudes at the frequency range (0–4) Hz, while those of

Fig. 5.6b have peak amplitudes near 8.0 Hz. The frequency content of the ground accelerations is seen to be distributed around (0–30) Hz. It can also be observed that the vertical accelerations are richer in frequency content compared to the horizontal components within the frequency range of (0–20) Hz. Note that, the STFT may lead to smooth spectra compared to the ordinary Fourier spectra when the length of the window function $g(\tau - t)$ is small. The inelastic response of SDOF structures to repeated acceleration sequences is examined in the next section.

5.4 Response Quantities of Inelastic Structures to Acceleration Sequences

Let us examine the displacement response, the input and dissipated energies, and the damage of SDOF inelastic structures to strong ground motions with multiple acceleration sequences. Let $\ddot{x}(t)$ be the multiple acceleration sequences. It is first noted that the equation of motion for the SDOF inelastic structure is given by [22]

$$m\,\ddot{u}(t) + c\,\dot{u}(t) + f_s(t) = -m\,\ddot{x}(t) \tag{5.3}$$

where m, c are the mass and the damping coefficient of the system, $f_s(t)$ is the nonlinear hysteretic restoring force, $u(t)$ is the displacement response, and dot indicates differentiation with respect to time. Herein, $u(t)$ is estimated using numerical integration techniques. The input energy per unit mass for the SDOF structure is given as follows [23].

$$E_i(t) = -\int_0^t \ddot{x}(\tau)\dot{u}(\tau)d\tau \tag{5.4}$$

The kinetic energy (pseudo because relative velocity is used) and elastic strain energy are given, respectively, by

$$E_K(t) = \dot{u}^2(t)/2; E_S(t) = f_s^2(t)/(2k_0) \tag{5.5}$$

In Eq. (5.5) k_0 is the initial elastic stiffness. The hysteretic and damping energies are given by

$$E_H(t) = \int_0^t \dot{u}(\tau) f_s(\tau)d\tau - E_S(t); E_D(t) = \int_0^t c\dot{u}^2(\tau)d\tau \tag{5.6}$$

The literature on damage of structures during earthquakes and the use of damage indices to quantify the associated damage level are vast. Moustafa [29] and Khashaee [24] presented extensive reviews on this subject. Several mathematical expressions for quantifying the damage level of SDOF inelastic structures

have been developed by many researchers. It may be meaningful to review some representative ones. The first damage index is given in terms of the maximum ductility demanded by the ground motion $\mu_{\max}$ [25]:

$$DI_{\mu} = \frac{\mu_{\max} - 1}{\mu_{\mathrm{u}} - 1} \tag{5.7}$$

In Eq. (5.7) μ_{u} is the ultimate ductility capacity of the structure under monotonic loading estimated from experimental tests. The second damage index is given in terms of the normalized hysteretic energy demanded by the earthquake ground motion [26]:

$$DI_{\mathrm{H}} = \frac{E_{\mathrm{H}}/(f_{\mathrm{y}} u_{\mathrm{y}})}{\mu_{\mathrm{u}} - 1} \tag{5.8}$$

where E_{H}, f_{y}, u_{y} are the hysteretic energy demand, the yield strength, and the yield displacement, respectively. Park and coworkers expressed damage as a linear combination of the maximum ductility and the hysteretic energy [27, 28]. That is given by

$$DI_{\mathrm{PA}} = \frac{\mu_{\max}}{\mu_{\mathrm{u}}} + \beta \frac{E_{\mathrm{H}}/(f_{\mathrm{y}} u_{\mathrm{y}})}{\mu_{\mathrm{u}}} \tag{5.9}$$

In Eq. (5.9) β is a positive constant that weights cyclic loading effects on structural damage. The parameter β ranges typically between 0 and 0.30. The quantities $\mu_{\max}$, E_{H} depend on the loading history while β, μ_{u}, f_{y} are determined from experimental tests. Note that, the first damage index does not account for energy dissipation while the second damage index is dependent on the hysteretic energy. The third damage index accounts for both effects from maximum ductility and cyclic loadings. This damage index, although has some limitations, has been widely used by many researchers due to its simplicity and extensive experimental calibrations for structures during earthquakes [29]. Due to this damage index, the structure's damage state is defined as (a) repairable damage ($DI_{\mathrm{PA}} < 0.40$), (b) damaged beyond repair ($0.40 \leq DI_{\mathrm{PA}} < 1.0$), and (c) total collapse ($DI_{\mathrm{PA}} \geq 1.0$) [28].

To investigate the effect of the acceleration sequences on the structural inelastic response, the response is estimated of an elastic-perfectly plastic (simply elastic–plastic) SDOF structure of initial period = 2.0 s to the NS acceleration of the 2004 Niigata-ken Chuetsu earthquake recorded at Nagaoka-shisho. A viscous damping of 0.03 damping ratio is adopted. The yield strength and initial stiffness are taken as 5×10^3 N and 1.49×10^5 N/m, respectively. These parameters are modified later to examine their influence on the structure's response. The dynamic analysis is carried out using the Newmark-β linear acceleration method with time step = 0.005 s.

Figure 5.7 shows the displacement, the input energy, the hysteretic energy, the damping energy, the force–displacement hysteretic loops, and the damage indices (Eqs. (5.7)–(5.9)). The displacement response reveals clearly that each acceleration sequence drives the structure to a new equilibrium position (see Fig. 5.7a) and

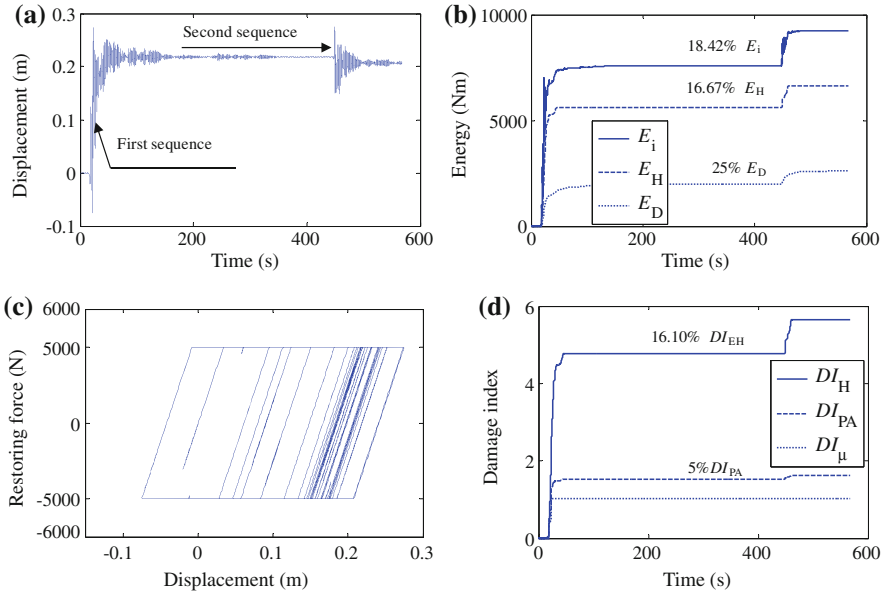

Fig. 5.7 Time-variation of input energy and response quantities for elastic–plastic structure ($f_y = 510^3$ N, $T_0 = 2.0$ s) under 2004 Niigata-ken Chuetsu NS record (Nagaoka-shisho). **a** Displacement response. **b** Input, hysteretic and damping energies. **c** Force–displacement hysteretic loops. **d** Damage indices (Moustafa and Takewaki [32] with permission from Techno Press)

that a significant permanent deformation remains at the end of the overall ground shaking. The second sequence slightly increases the maximum displacement (secondary sequences of other records increase the maximum displacement by up to 20 %) but has a substantial effect on the input, hysteretic, and damping energies (see Fig. 5.7b). It can be observed that most of the input energy (about 82 %) results from the first sequence. However, the maximum displacement response is attained during the second sequence.

The influences of the second acceleration sequence on the force–displacement hysteretic loops and on the hysteretic energy demand for two different yield strength values are shown in Fig. 5.8. The second sequence causes more yielding events to the structure (see Fig. 5.8 and Table 5.2). The force–displacement hysteretic loops, the hysteretic energy, and damping energy are significantly influenced by the second acceleration sequence. For instance, EH increases by about 17 % and ED increases by about 25 % due to the second acceleration sequence. Furthermore, the input energy and the displacement response can be observed to be larger for the lower yield strength. This observation is confirmed by the hysteretic loops shown in Figs. 5.8a, b. The structure with a larger yield strength has small damage indices while that with a lower yield strength exhibits large damage indices. Thus, $DI_{PA} = 1.62$ (total collapse) for $f_y = 5 \times 10^3$ N, $DI_{PA} = 0.55$ (damaged beyond repair) for $f_y = 1 \times 10^4$ N and $DI_{PA} = 0.27$

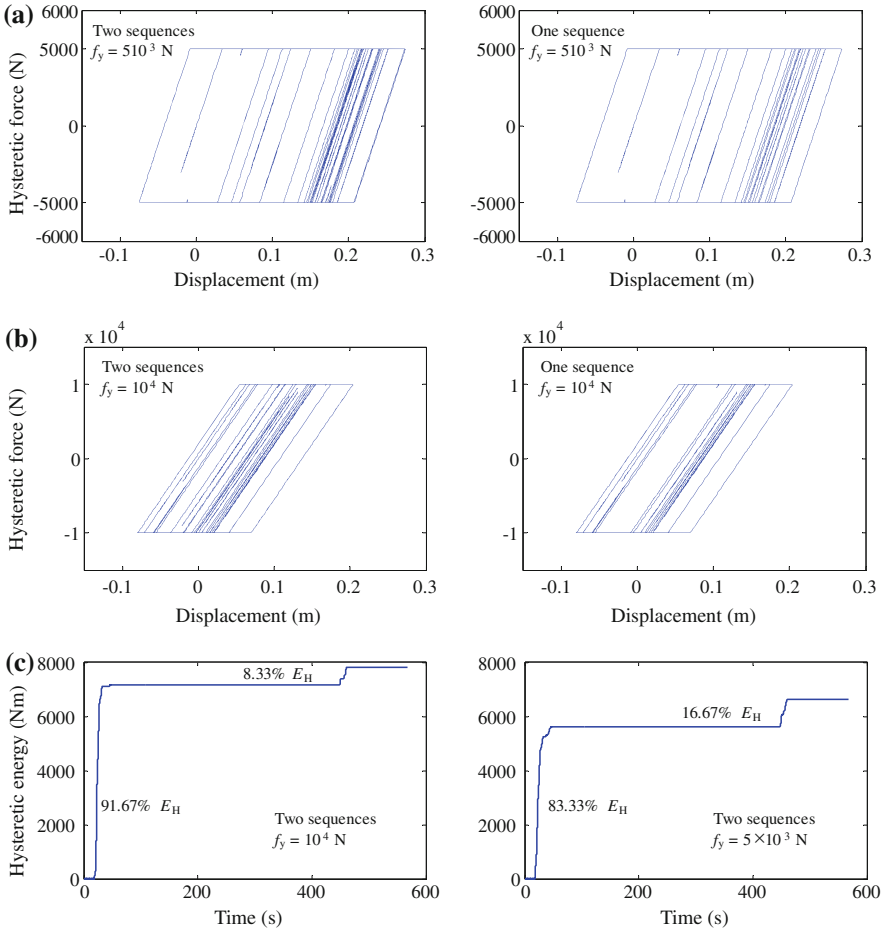

Fig. 5.8 Influence of number of sequences and yield strength on the hysteretic energy and hysteretic loops for elastic–plastic structure ($T_0 = 2.0$ s) under 2004 Niigata-ken Chuetsu NS record (Nagaoka-shisho) (Moustafa and Takewaki [32] with permission from Techno Press)

(repairable damage) for $f_y = 2 \times 10^4$ N ($\beta = 0.12$, $\mu_u = 8.0$). The associated ductility demands (8.19, 3.04, and 1.82) correspond to high, moderate, and low ductility levels, respectively. It appears that the effect of the second sequence on the Park and Ang damage index is small (about 5 %). However, the damage index in Eq. (5.8) increases by about 16 % due to the effect of the second sequence. When the yield strength decreases from 1×10^4 N to 5×10^3 N, the maximum ductility demand increases 2.7 times, the maximum hysteretic energy decreases by about 70 %, the number of yield points doubles, the permanent plastic deformation increases 5 times, DI_{PA} increases 2.9 times (the damage state changes from 'damaged beyond repair' to 'total collapse'), and DI_{μ} increases about 3.5 times (see Table 5.2). Hence, the structural response depends on the yield parameters of

Table 5.2 Influence of secondary acceleration sequences on the response quantities of SDOF elastic–plastic structure ($T_0 = 2.0$ s) (Moustafa and Takewaki [32] with permission from Techno Press)

Yield strength f_y	First acceleration sequence only								First and second acceleration sequences							
	$D_{F\max}$	$E_{H\max}$ (Nm)	$E_{D\max}$ (Nm)	N_y	DI_{PA}	DI_H	DI_μ	$\lvert u_p \rvert$ (m)	$DF_{\max}$	$E_{H\max}$ (Nm)	$E_{D\max}$ (Nm)	N_y	DI_{PA}	DI_H	DI_μ	$\lvert u_p \rvert$ (m)
5×10^3 (N)	8.16	5608	1908	1447	1.52	4.78	1.02	0.19	8.19	6643	2615	1947	1.62	5.66	1.03	0.21
1×10^4 (N)	3.01	7157	3107	723	0.54	1.52	0.29	0.08	3.04	7821	4270	893	0.55	1.67	0.29	0.04
2×10^4 (N)	1.82	8220	5654	326	0.27	0.44	0.12	0.03	1.82	8220	7440	326	0.27	0.44	0.12	0.02

T_0 initial natural period, $D_{F\max}$ maximum ductility, $E_{H\max}$ maximum hysteretic energy, $E_{D\max}$ maximum damping energy, N_y number of yield reversals, u_p permanent deformation, DI_{PA}, DI_H, DI_μ damage indices (Eqs. 5.7–5.9)

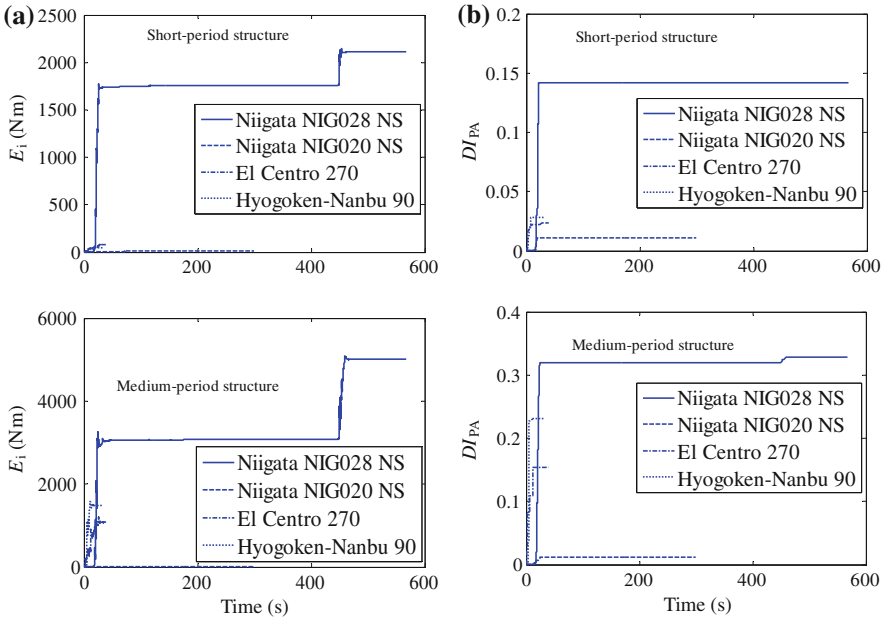

Fig. 5.9 Time-variation of input energy and Park and Ang damage index for elastic–plastic structures under different earthquake inputs. **a** Input energy. **b** Damage index (Moustafa and Takewaki [32] with permission from Techno Press)

the structural model. The structural response under the earthquake records listed in Table 5.1 has been computed and the general feature was found to be the same.

To examine the influence of the structure's initial natural period on the inelastic response to different acceleration sequences, the responses of three inelastic structures with three different initial natural periods $T_0 = 0.3$, 1.0, and 3.0 s are estimated under the horizontal acceleration (H1) of the earthquake records shown in Table 5.1. These natural periods represent typical structures of short-period (<0.5 s), medium-period (0.5–1.5 s), and long-period (>1.5 s). The same response quantities are also determined for the two ordinary records. Elastic–plastic and bilinear inelastic force–deformation laws have been considered ($f_y = 1 \times 10^4$ N and $\varsigma = 0.03$).

The results of these analyses are presented in Fig. 5.9 and Table 5.3. Figure 5.9 shows the time variation of the input energy and the damage index DI_{PA} for SDOF elastic–plastic structures to two earthquake records with two sequences and for the ordinary records. It can be observed that the input energy and the damage indices depend on the structure's fundamental natural period and the dominant period and intensity of the input acceleration. For instance, the NS component of the 2004 Niigata-ken Chuetsu earthquake (NIG028) produces the maximum input energy and the maximum damage index for the structures with short- and medium-periods. The NS record of the 2004 Niigata-ken Chuetsu earthquake (NIG020)

Table 5.3 Response and damage parameters for short-, medium-, and long-period SDOF elastic–plastic structures to ground motion with repeated sequences (H_1 acceleration component in Table 5.1). Moustafa and Takewaki [32] with permission from Techno Press)

Input $(f_0 - f_c)$Hz	Record	Short-period structure ($T_0 = 0.30$ s)						Medium-period structure ($T_0 = 1.0$ s)						Long-period structure ($T_0 = 3.0$ s)					
		μ_{max}	E_{max} (Nm)	N_y	$\|u_p\|$ (m)	DI_{PA}	DL	μ_{max}	E_{max} (Nm)	N_y	$\|u_p\|$ (m)	DI_{PA}	DL	μ_{max}	E_{max} (Nm)	N_y	$\|u_p\|$ (m)	DI_{PA}	DL
Helena aft.	(0-22)	1.44	838.65	20	0.08	0.15	RD	0.44	71.68	0	0.01	0.04	ND	0.05	1.30	0	0	0.01	ND
San Francisco	(0-15)	0.20	55.06 s	0	0.01	0.03	ND	0.11	9.05	0	0	0.01	ND	0.08	5.68	0	0	0.01	ND
San Fernando	(0-30)	0.10	50.84	0	0	0.01	ND	0.06	9.82	0	0	0	ND	0.11	9.40	0	0	0.01	ND
Victoria	(0-19)	2.28	7944.5	777	0	0.30	RD	0.55	504.91	0	0	0.06	ND	0.27	70.52	0	0	0.03	ND
New Zealand	(0-25)	0.06	28.53	0	0	0.01	ND	0.14	17.73	0	0	0.01	ND	0.06	5.16	0	0	0.01	ND
Katsurao	(0-35)	0.03	10.63	0	0	0	ND	0.03	3.41	0	0	0	ND	0.07	4.62	0	0	0.01	ND
Kocaeli	(0-10)	6.58	21183	1562	0.33	0.94	TC	1.66	2180.7	73	0.04	0.17	RD	0.23	87.22	0	0	0.02	ND
Chi-Chi	(0-12)	2.51	4722.4	245	0.09	0.28	RD	2.05	4794	209	0.06	0.24	RD	0.59	609.08	0	0	0.06	ND
Chi-Chi	(0-20)	0.65	489.65	0	0	0.07	ND	0.78	628.24	0	0	0.08	ND	0.29	94.9	0	0	0.03	ND
Bhu	(0-25)	0.92	787.68	0	0	0.09	ND	0.70	480.8	0	0	0.07	RD	0.13	29.41	0	0	0.01	ND
Niigata	(0-20)	3.23	20393	362	0.07	0.51	DBR	2.72	15405	237	0.05	0.44	DBR	1.16	1201.8	3	0.01	0.11	ND
Niigata	(0-25)	2.34	15089	905	0.05	0.38	RD	2.29	6474.4	198	0.08	0.28	RD	0.76	1590.2	0	0	0.08	ND
Niigata	(0-20)	1.10	1725.9	10	0	0.11	RD	0.88	920.08	0	0	0.09	ND	0.15	71.65	0	0	0.02	ND
Niigata	(0-32)	0.12	15.31	0	0	0.01	ND	0.08	9.26	0	0	0.01	ND	0.03	1.36	0	0	0.01	ND
Niigata	(0-21)	1.53	1921.7	32	0.04	0.16	RD	0.78	655.58	0	0	0.08	ND	0.55	491.44	0	0	0.06	ND
Niigata	(0-30)	0.17	43.07	0	0	0.017	ND	0.08	16.87	0	0	0.01	ND	0.11	10.72	0	0	0.01	ND
Niigata	(0-23)	2.04	3032.2	59	0.06	0.22	RD	1.41	1835.7	18	0.03	0.15	RD	0.79	485.2	0	0	0.08	ND
Honshu	(0-34)	0.17	60.83	0	0	0.02	ND	0.27	90.92	0	0	0.03	ND	0.13	32.37	0	0	0.01	ND
Niigata-ken	(0-26)	0.11	27.93	0	0	0.01	ND	0.14	32.45	0	0	0.01	ND	0.05	3.17	0	0	0.01	ND
Iwate-Miyagi	(0-32)	0.28	394.87	0	0	0.03	ND	0.29	114.65	0	0	0.03	ND	0.17	20.82	0	0	0.02	ND
El Centro	(0-18)	3.11	4980.3	121	0.14	0.35	RD	1.44	2333.6	44	0.01	0.16	RD	0.27	112.12	0	0	0.03	ND
Hyog.-Nanbu	(0-12)	2.30	8762	168	0.09	0.32	RD	3.67	5690.0	138	0.12	0.43	DBR	0.27	.30	0	0	0.03	ND

T_0 initial natural period, μ_{max} maximum ductility, E_{Hmax} maximum hysteretic energy, N_y number of yield reversals, u_p permanent deformation, DI_{PA}, DI_μ damage indices (Eqs. 5.7–5.9), *DL* damage level, *ND* nondamaged (linear behavior), *RD* repairable damage, *DBR* damaged beyond repair, *TC* total collapse

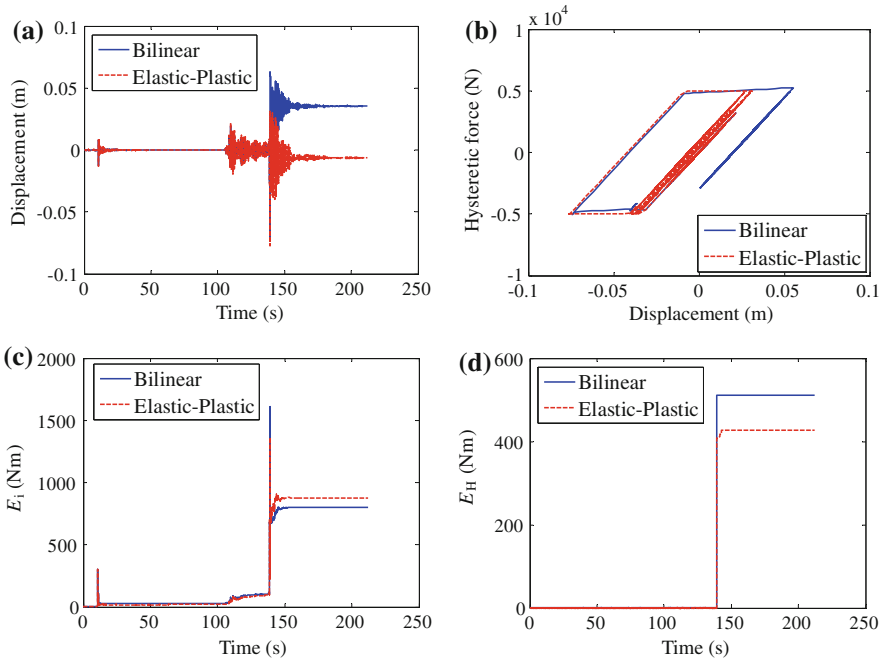

Fig. 5.10 Response of elastic–plastic and bilinear inelastic SDOF structures to the horizontal acceleration H_1 of the 2007 Iwate-Miyagi earthquake. **a** Displacement. **b** Hysteretic loops. **c** Input energy. **d** Hysteretic energy ([32] with permission from Techno Press)

results in the least input energy and damage index. The 1940 El Centro record provides the largest input energy and damage indices for the structure with long-period (this record has large amplitude near $T_0 = 3.0$ s). The structures with short- and medium-periods are either damaged with the level of repairable damage ($DI_{PA} < 0.40$) or behave elastically (see Fig. 5.9 and Table 5.3). The long-period structure behaves elastically under the 2004 Niigata-ken Chuetsu (NIG020) record and is damaged beyond repair ($DI_{PA} > 0.40$) under other earthquake records. Note that, the influence of the repeated sequences is more obvious in the plots of the input energy to the structure compared to the plots of the damage index (Fig. 5.9). Accordingly, it can be concluded that, the ground acceleration with multiple sequences need not always produce the maximum response and/or damage in the structure. In other words, although can be understood without much difficulty, the structural inelastic response depends on the structure's initial natural period, the yield parameters and the associated dominant period, and intensity of the ground motion. Tables 5.1 and 5.3 summarize the intensity Eq. (5.1) and the average frequency content ($f_0 - f_c$) of the ground acceleration (the frequency range that contains 90 % of the acceleration intensity) [30, 31]. The numerical values of these parameters confirm clearly that the structure's response depends on the characteristics of the input acceleration sequences and the structure's properties.

To compare the structural responses of elastic–plastic and bilinear structures, two SDOF systems are considered of initial natural period = 1.0 s, initial stiffness = 1.49×10^5 N/m, viscous damping ratio = 0.03, and yield strength in tension and compression = 5×10^3 and -5×10^3 N, respectively. The strain-hardening ratio of the bilinear structure is taken as 0.05. The two structures are assumed to be driven by the horizontal acceleration H_1 (see Table 5.1) of the Iwate-Miyagi earthquake with PGA = 1.0 g. The responses of the two structures are illustrated in Fig. 5.10. The maximum input energy to the elastic–plastic structure is seen to be slightly smaller than that for the bilinear inelastic structure (Fig. 5.10c). However, the maximum displacement of the elastic–plastic structure is larger than that for the bilinear structure by about 10 % (Fig. 5.10a). In addition, it appears that the elastic–plastic structure yields more frequently ($N_y = 33$) than the bilinear structure ($N_y = 8$) (Fig. 5.10b). The maximum hysteretic energy dissipated by the bilinear structure is 16 % larger than the hysteretic energy dissipated by the elastic–plastic structure. These results reveal that the elastic–plastic structure is more vulnerable to the acceleration sequences compared with the bilinear structure (see e.g. [2]).

5.5 Summary

Repeated acceleration sequences separated by short time intervals have been observed in many parts of the world, such as, Japan, Mexico, Italy, Turkey, California. This ground motion results from mainshock preceded by foreshocks or followed by aftershocks. This chapter has investigated the characteristics of this class of ground motion. Specifically, the number, the duration, PGA, and energy of the individual sequences are studied. Similarly, properties of the entire record (e.g., duration, PGA, Fourier amplitude and frequency content, and site-source distance) have also been studied. The definitions of the effective number of sequences and the effective duration of recorded acceleration sequences have also been introduced. The two horizontal and the vertical accelerations of 20 strong-motion earthquakes have been used in the numerical investigation. These records are measured in several different countries covering a variety of earthquake magnitude, duration, site-source distance, PGA, and local soil condition.

It has been found that (1) multiple acceleration sequences are greatly influenced by the source mechanism, (2) have longer effective durations compared to ordinary records, and (3) can be observed at the near-fault and the far-fault regions. The first sequence (mainshock) possesses most of the acceleration energy. The secondary sequences (aftershocks) have shorter durations and lower energy compared to the main sequence. The individual sequences have short duration, sharp build up, short strong-phase, and sudden decay. These characteristics should be considered in simulating acceleration sequences. In this chapter, the general characteristics of the ground motion of multiple sequences that are commonly relevant to engineers have been explained. The modeling of acceleration sequences including the

discontinuity of the released energy at the source and associated attenuation due to path and local soil effects is of future concern.

The structural response to recorded acceleration sequences has been investigated. Each sequence drives the structure to a new equilibrium position. Secondary sequences increase the ductility demand, the number of yield points, and the input, hysteretic, and damping energies. Their influences on damage indices based on maximum ductility are seen to be small, but have substantial effect on damage indices that are based on hysteretic energy demand. In this chapter, elastic–plastic and bilinear SDOF inelastic structures have been studied. It is also of interest to examine the structural behavior of inelastic MDOF structures with degrading stiffness and/or strength which can describe the formation of plastic hinges and the time-dependent damage of the structure. Moreover, accelerograms that are reported as single records with multiple sequences were considered. If aftershocks are also included, the ground motion characteristics, such as, the total duration, the number of sequences, the input, and dissipated energies, will change. In both cases, the inclusion of repeated acceleration sequences in the nonlinear design of the structure remains necessary.

References

1. Elnashai A, Bommer JJ, Martinez-Pereira A (1998) Engineering implications of strong-motion records from recent earthquakes. In: Proceedings of 11th European conference on earthquake engineering, Paris, CD-ROM
2. Amadio C, Fragiacomo M, Rajgelj S (2003) The effects of repeated earthquake ground motions on the non-linear response of SDOF systems. Earthq Eng Struct Dyn 32:291–308
3. Das S, Gupta VK, Srimahavishnu V (2007) Damage-based design with no repair for multiple events and its sensitivity to seismicity model. Earthq Eng Struct Dyn 36:307–325
4. Hatzigeorgiou GD, Beskos DE (2009) Inelastic displacement ratios for SDOF structures subjected to repeated earthquakes. Eng Struct 31:2744–2755
5. Hatzigeorgiou GD (2010) Ductility demand spectra for multiple near- and far-fault earthquakes. Soil Dyn Earthq Eng 30:170–183
6. Hatzigeorgiou GD (2010) Behavior factors for nonlinear structures subjected to multiple near-fault earthquakes. Comput Struct 88:309–321
7. Fragiacomo M, Amadio C, Macorini L (2004) Seismic response of steel frames under repeated earthquake ground motions. Eng Struct 26:2021–2035
8. Li Q, Ellingwood BR (2007) Performance evaluation and damage assessment of steel frame buildings under main shock–aftershock earthquake sequences. Earthq Eng Struct Dyn 36:405–427
9. Nour SD, Barbuta M, Mihul A (1992) Analysis of the behaviour of some historical consolidated buildings made of brick masonry to repeated earthquakes. In: Proceedings of the 10th world conference on earthquake engineering, Balkema, Rotterdam, pp 5327–5331
10. Architecture Institute of Japan (2005) Recommendations for loads on buildings, Tokyo
11. Bray JD, Rodriguez-Marek A (2004) Characterization of forward-directivity ground motions in the near-fault region. Soil Dyn Earthq Eng 24:815–828
12. European Committee for Standardization (2003) Eurocode 8: design of structures for earthquake resistance, Brussels
13. International Building Code (2009) International code council, inc. First printing, IL

14. Kalkan E, Kunnath SK (2006) Effects of fling step and forward directivity on seismic response of buildings. Earthq Spectra 22(2):367–390
15. Krawinkler H, Alavi B, Zareian F (2005) Imapct of near-fault pulses on engineering design. In: Gulkan P, Anderson JG (eds) Directions in strong motion instrumentation. Springer, Dordrecht
16. Arias A (1970) A measure of earthquake intensity: seismic design of nuclear power plants. MIT press, Cambridge, pp 438–468
17. COSMOS (2009) Consortium organizations for strong-motion observation systems. http://db.cosmos-eq.org/scripts/default.plx
18. Kyoshin-Network (2009) National research institute for earth science and disaster prevention. http://www.k-net.bosai.go.jp/
19. Kiban-Kyoshin Network (2009) National research institute for earth science and disaster prevention. http://www.kik.bosai.go.jp/
20. PEER (2009) Pacific earthquake engineering research center. http://peer.berkeley.edu/smcat/search.html
21. Trifunac MD, Brady AG (1975) A study on the duration of strong earthquake ground motion. Bull Seismol Soc Am 65(3):581–626
22. Chopra AK (2007) Dynamics of structures, 3rd edn. Prentice Hall, NJ
23. Takewaki I (2004) Bound of earthquake input energy. J Structural Eng 130:1289–1297
24. Khashaee P (2005) Damage-based seismic design of structures. Earthq Spectra 21(2): 371–387
25. Powell GH, Allahabadi R (1988) Seismic damage predictions by deterministic methods: concepts and procedures. Earthq Eng Struct Dyn 16:719–734
26. Cosenza C, Manfredi G, Ramasco R (1993) The use of damage functionals in earthquake en-gineering: a comparison between different methods. Earthq Eng Struct Dyn 22:855–868
27. Park YJ, Ang AH-S (1985) Mechanistic seismic damage model for reinforced concrete. J Struct Eng 111(4):722–739
28. Park YJ, Ang AH-S, Wen YK (1987) Damage-limiting aseismic design of buildings. Earthq Spectra 3(1):1–26
29. Moustafa A (2011) Damage-based design earthquake loads for SDOF inelastic structures. J Struct Eng 137(3):456–467
30. Moustafa A, Takewaki I (2010) Deterministic and probabilistic representation of near-field pulse-like ground motion. Soil Dyn Earthq Eng 30:412–422
31. Moustafa A, Takewaki I (2010) Characterization and modeling of near-fault pulse-like strong ground motion via damage-based critical excitation method. Struct Eng Mech 34(6):1–24
32. Moustafa A, Takewaki I (2012) Earthquake ground motion of multiple sequences and associated structural response. Earthquakes and Structures 3(3) (in press)

Chapter 6
Modeling Critical Ground-Motion Sequences for Inelastic Structures

6.1 Introduction

Earthquake loads are usually specified as inputs to engineering structures using the seismic coefficient method, the response or hazard spectra of the site, or in terms of the time history of the ground acceleration [1–3]. On the other hand, the nonlinear time history analysis is compulsory in cases of important structures, critical facilities, structures having irregularities in plan or elevation, structures designed for high ductility levels, structures in which higher modes can get excited, and special structures containing seismic isolation or energy dissipation devices [4]. This is because the time history analysis provides the most accurate means for dynamic analysis of structures [5].

Some ground-motion sequences separated by short intervals of time have been observed in regions of medium–strong seismicity, such as, Italy, Mexico, Japan, Turkey, California, and other parts of the world. Some characteristics of earthquake records of repeated sequences were explained in Sect. 5.2. Figure 6.1 shows three acceleration components for the 23 October 2004 Niigata-ken Chuetsu earthquake of Mw = 6.5 recorded at the Niigata-ken Chuetsu station at 28.7 km from the source [6]. These records contain two sequences of about 30 s duration each, separated by time interval of about 400 s, with peak ground acceleration (PGA) of 0.89, 0.72, and 0.44 g in NS, EW and UD components, respectively. The foreshock of this earthquake was followed by 16 aftershocks, 7 of which occurred on the same day of the foreshock. Figure 6.2 illustrates three acceleration components for the 15 April 2007 Western Honshu earthquake of $M_b = 5.4$ recorded at the Kohga-SIG012 station at 21.0 km from the source. These records contain two sequences of about 100 s total duration and PGA of 0.26, 0.11, and 0.05 g for EW, NS, and UD components, respectively.

Multiple earthquake ground-motion sequences may not be an important issue in dynamic analysis of linear structures since linear structures with damping return to their initial equilibrium position by the start of each subsequent sequence. Such

I. Takewaki et al., *Improving the Earthquake Resilience of Buildings*,
Springer Series in Reliability Engineering, DOI: 10.1007/978-1-4471-4144-0_6,

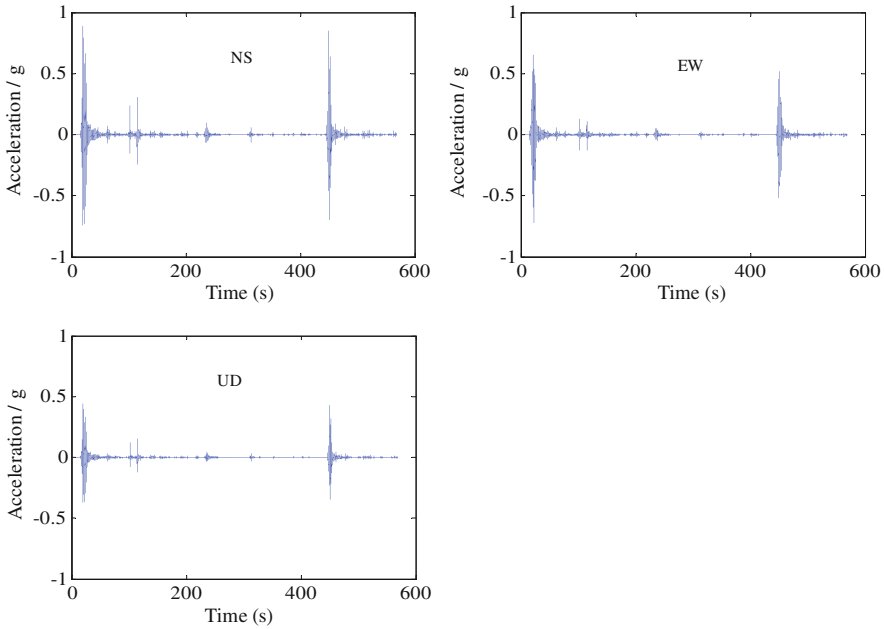

Fig. 6.1 Ground accelerations for the 23 October 2004 Niigata-ken Chuetsu earthquake sequences recorded at Nagaoka-Shisho station [6] (Moustafa and Takewaki [49] with permission from Multi-Science Publishing)

ground motion, however, can create severe damage in inelastic structures (or structures with loading history-dependent properties) due to accumulation of inelastic deformations and (or damage) from all sequences before any structural repair is possible. In addition, the low-frequency content in secondary sequences may cause resonance in lower modes of the damaged structure leading to further damage or total collapse to the structure (see [7], also Chap. 10). Accordingly, the verification of the structure's adequacy to withstand earthquakes with multiple sequences without collapse or instability is of essential concern to structural engineers. For instance, a series of moderate earthquakes separated by short periods of time could cause larger damage to the structure compared to a single severe event. This aspect is of interest in performance-based seismic design of structures in earthquake-prone countries.

Dynamic analysis of inelastic structures under multiple sequences of ground motion has received limited research attention. This may result from the fact that the effect of such events on the structural damage has never been clear. Elnashai et al. [8] emphasized the implication of multiple earthquake ground-motion sequences on the response of structures and reported an increase of up to 30 % in the force demand of ductile structures due to acceleration sequences. The effect of repeated ground-motion sequences on the inelastic response of single degree-of-freedom (SDOF) systems has been studied recently by Amadio et al. [9] and

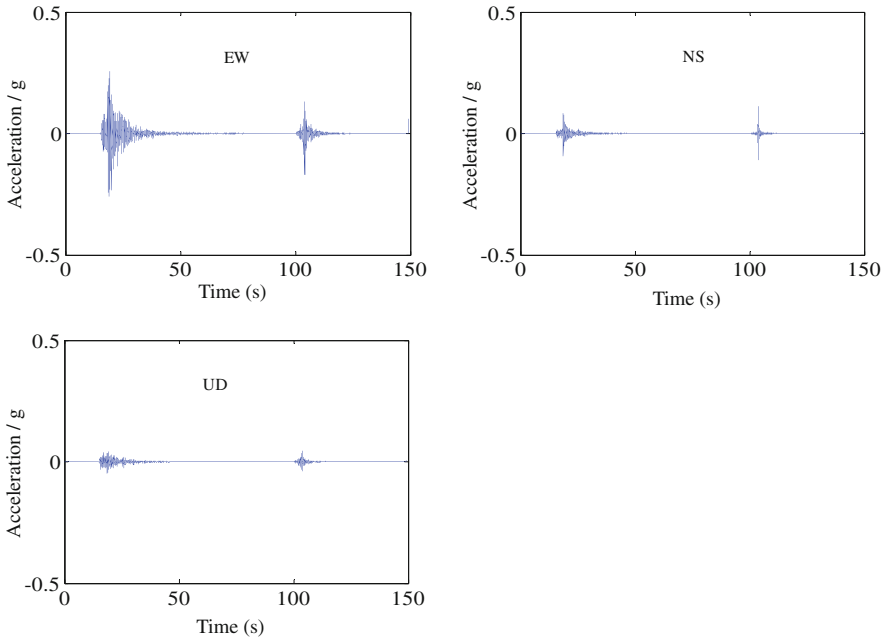

Fig. 6.2 Ground accelerations for the 15 April 2007 western honshu earthquake sequences recorded at Kohga-SIG012 station [6] (Moustafa and Takewaki [49] with permission from Multi-Science Publishing)

Das et al. [10]. These studies employ simulated acceleration sequences as representative inputs to inelastic structures. More recently, an extensive parametric investigation on the displacement ratios of SDOF inelastic structures subjected to repeated earthquakes was carried out by Hatzigeorgiou and Beskos [11]. In their paper, 112 accelerograms of single shocks recorded at four different soil sites were used to produce two and three identical sequences. All these studies have clearly shown that repeated earthquake sequences could produce larger deformations in structures compared with ordinary earthquakes and the consideration of such a scenario is important for the construction of a framework of more reliable seismic resistant designs.

The specification of earthquake loads (or demands) as inputs to inelastic structures is a crucial task in earthquake engineering. Transformed static loads, demands based on inelastic response spectra, and time history data are examples of various load representations. There are cases, however, where the site under consideration has limited or scarce seismic data, making this process a difficult task. Meanwhile, given the high uncertainty involved in the earthquake phenomenon (see for example [12]), structural engineers are often concerned with the worst-case scenario that can happen to the structure during its service life under possible future earthquakes. This scenario is of further interest in cases of important structures and critical facilities in which collapse or severe damage is

absolutely prohibited. The critical excitation method has been developed as a counterpart to other methods of seismic load specification and provides reliable solutions to such situations. An overview on this method can be found in Takewaki [12–14] and Abbas and Manohar [15–17]. The critical input to a given structure is derived by solving an inverse dynamic problem so that the structure response is maximized while the input is constrained to a group qualified based on available earthquake information at the site.

In the context of the potential of ground motions to damage structures, several authors have attempted to identify the characteristics of the critical earthquake records. One of the early studies on this subject has been carried out by Housner and Jennings [18]. These authors have attempted to identify the maximum credible ground motion that can be used in seismic design of the structure by developing a simple intensity measure similar to the Arias measure [19]. They also introduced a velocity power which can be derived by replacing the acceleration wave with the velocity wave. This concept was followed by Takewaki [12, 14] for identification of critical inputs in the context of earthquake input energy. (PGA), the effective PGA, the peak ground velocity (PGV), the effective PGV, the energy, the intensity, the duration, and the number of cycles of the ground accelerations have been used for this purpose (see e.g. [20, 21]). However, damage of structures is contributed by several parameters of the ground motion, and thus there is no single parameter for identifying critical ground motions.

Naeim and Anderson [21] used the earthquake magnitude and PGA (limited to $M \geq 5.0$ and $\mathrm{PGA} \geq 0.05$ g) to select 1,157 horizontal accelerations from a set of about 5,000 accelerograms recorded during 1933–1992. Subsequently, 30 records that have the highest PGA, EPGA, PVA, EPGV, PGD, IV, and ID have been selected from the 1,157 records. A set of 84 records was further selected based on the 'bracketed duration' (see [22], also Chap. 5) and a subset of 36 records with long durations was identified. This led to a database of 120 records. This study provided simple procedures for identifying the most severe real seismic design ground motions. More recently, the critical excitation concept has been used in identifying resonant or unfavorable earthquake records [23–25]. Thus, Zhai and Xie [25] considered a database of 852 records from 34 earthquakes measured during 1940–2001 and classified it into four groups based on the site soil type. This database was further divided into three groups based on the region (mainland China, Taiwan of China, and regions outside China). The most unfavorable records were then determined for each of these three groups by considering their damage potential in terms of the parameters of the ground motion and the associated structural damage criteria, such as, deformation, hysteretic energy, and damage indices.

This chapter explains the mathematical modeling of critical earthquake loads composed of multiple sequences and its effects on inelastic structures. This theme was motivated by the high level of uncertainty involved with ground motions and the uncompromised safety requirements of important structures against earthquake loads. The following section provides a brief overview on damage assessment in inelastic structures using damage indices.

6.2 Damage Assessment in Inelastic Structures Using Damage Indices

Several methods of damage assessment for inelastic structures were explained in Chaps. 4 and 5. For deeper understanding of such concepts and technical merit, the main part will be explained again here.

As explained in Chap. 5, damage indices are estimated by comparing structural responses demanded by the earthquake with the structure capacities. For example, the ductility capacity μ_u and the ductility demand $\mu_{\max}$ are used to quantify damage as follows [26]:

$$DI_\mu = \frac{\mu_{\max} - 1}{\mu_u - 1}. \tag{6.1}$$

This damage index does not incorporate hysteretic energy dissipation. Another damage index [27, 28] based on the hysteretic energy E_H, yield strength f_y, and yield displacement x_y is given by

$$DI_H = \frac{E_H/(f_y x_y)}{\mu_u - 1}. \tag{6.2}$$

Park and Ang [29–31] expressed damage as a linear combination of maximum ductility and cumulative energy dissipation by

$$DI_{\mathrm{PA}} = \frac{\mu_{\max}}{\mu_u} + \beta \frac{E_H/(f_y x_y)}{\mu_u} \tag{6.3}$$

where $\mu_{\max}$ and E_H are the maximum ductility and dissipated hysteretic energy, respectively, demanded by the earthquake. The parameter μ_u is the ultimate ductility capacity under monotonic loading and β is a positive constant that weights the effect of cyclic loading on structural damage. The quantities $\mu_{\max}, E_H$ depend on the loading history while β, μ_u, f_y are independent of the loading history and are determined from experimental tests. The estimation methods and its results of hysteretic energy dissipated by inelastic structures under earthquake loads can be found in many Ref. [32–34].

Equation (6.3) can be used to compute the damage index for SDOF structures or a member in a multi-degree-of-freedom (MDOF) structure. On the other hand, the global damage index for MDOF structures can be estimated as a weighted sum of member's local damage indices as follows [30]:

$$DI_g = \sum_{i=1}^{N} \lambda_i DI_i = \sum_{i=1}^{N} \frac{E_i}{E_t} DI_i \tag{6.4}$$

where N is the number of the structure's members, E_i is the energy absorbed by the ith member, and E_t is the total energy absorbed by the structure. The structure's damage state is defined based on calibration of Park and Ang damage index against experimental tests and field observations during earthquakes [29]. The damage state consists of (a) repairable damage $(DI_{\mathrm{PA}} < 0.40)$, (b) damaged beyond repair $(0.40 \leq DI_{\mathrm{PA}} < 1.0)$, and (c) total or complete collapse $(DI_{\mathrm{PA}} \geq 1.0)$.

In this chapter, the damage indices expressed by Eqs. (6.3) and (6.4) are used in modeling critical earthquake sequences for inelastic structures. As discussed above, DI_{PA} is more robust than those of Eqs. (6.1) and (6.2) because it accounts for damage from the maximum deformation and hysteretic energy. This damage index, however, has some limitations [35, 36], namely, (a) the weak cumulative component given the dominance of peak displacement over accumulated energy, (b) the use of linear combination of deformation and energy despite the nonlinearity of the problem, (c) the lack of considering loading sequence effect in the cumulative energy term, (d) for elastic behavior, DI_{PA} is greater than zero, and (e) when the system reaches its maximum deformation, Eq. (6.3) leads to $DI_{\mathrm{PA}} > 1.0$. A modification to DI_{PA} to correct for the last drawback was proposed by Chai et al. [37]. Notwithstanding this, DI_{PA} has been extensively used by many researchers, due to its simplicity and extensive calibration against experimentally observed structural damage during past earthquakes. The modeling of critical earthquake ground-motion sequences for inelastic structures is explained in the following section.

6.3 Modeling Critical Ground-Motion Sequences for Inelastic Structures

Some important characteristics of earthquake ground accelerations with multiple sequences and their effect on inelastic structures were explained in Chap. 5. However, mathematical modeling of such earthquake ground accelerations with multiple sequences has never been explained. In this section, the mathematical modeling will be provided in detail.

Let the ground acceleration of n sequences be represented as a combination of Fourier series modulated by envelope functions as follows [9, 10]:

$$\ddot{x}_g(t) = \sum_{i=1}^{n} \left\{ e_i[t' + (i-1)T] \sum_{j=1}^{m} R_{ij} \cos[\omega_{ij}\{t' + (i-1)T\} - \varphi_{ij}] \right\} \tag{6.5}$$

In Eq. (6.5) $e_i(t), R_{ij}, \phi_{ij}$ are the envelope function, jth amplitude, and phase angle of the ith sequence. Furthermore, T is a time parameter separating ith and $(i+1)$th sequences, and m is the number of frequencies adopted in each sequence. The time parameter t' is defined in Fig. 6.3a. For identical sequences, the above expression reduces to

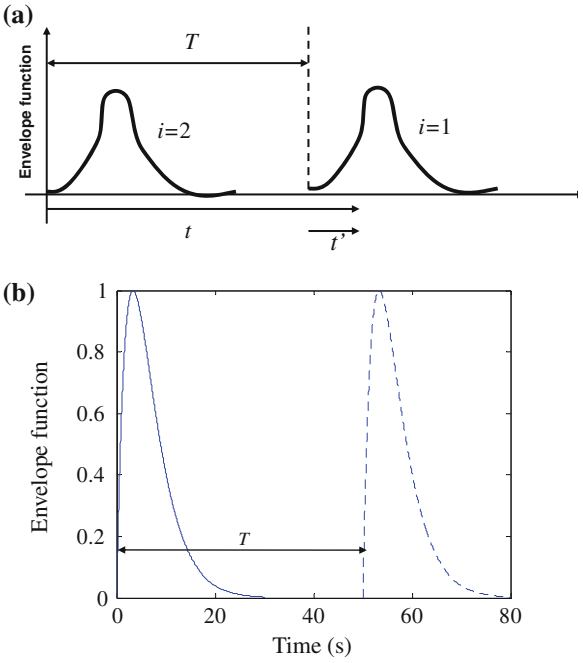

Fig. 6.3 **a** Envelope functions for two acceleration sequences according to Eq. (6.5) **b** Envelope functions for two acceleration sequences with $\alpha_1 = \alpha_2 = 0.30$, $T = 50$ s. The parameters a_1,a_2 are selected so that each envelope has a peak value of unity and the total acceleration duration = 80 s ([49] with permission from Multi-Science Publishing)

$$\ddot{x}_g(t) = e(t') \sum_{j=1}^{m} R_j \cos(\omega_j t' - \varphi_j) + e(t'+T) \sum_{j=1}^{m} R_j \cos\{\omega_j (t'+T) - \varphi_j\} + \cdots \tag{6.6}$$

In constructing critical earthquake inputs, the envelope functions are assumed to be known. A well-known envelope function is used here. The envelope function of the ith sequence is represented by

$$e_i(t) = a_i[t' + (i-1)T]\, e^{-\alpha_i[t'+(i-1)T]} \tag{6.7}$$

Herein $a_1, a_2, \ldots, a_n$, are n scaling constants and $\alpha_1, \alpha_2, \ldots, \alpha_n$ are positive parameters that control the nonstationary trend of each sequence. Figure 6.3b shows the envelope functions for two acceleration sequences with $\alpha_1 = \alpha_2 = 0.30$, $T = 50$ s. The parameters a_1, a_2 are selected so that each envelope has a peak value of unity and the total acceleration duration = 80 s.

In modeling critical earthquake sequences, the information about the total energy E, peak ground acceleration M_1, PGV M_2, peak ground displacement (PGD) M_3, lower bound Fourier amplitude spectra (LBFAS) $M_4(\omega)$, and upper bound Fourier amplitude spectra (UBFAS) $M_5(\omega)$ is assumed to be available. In this case, the constraints lead to the following form [15, 16]:

$$\begin{aligned}
&\left(\int_0^\infty \ddot{x}_g^2(t)\,dt\right)^{1/2} \le E \\
&\max_{0<t<\infty} |\ddot{x}_g(t)| \le M_1 \\
&\max_{0<t<\infty} |\dot{x}_g(t)| \le M_2 \\
&\max_{0<t<\infty} |x_g(t)| \le M_3 \\
&M_4(\omega) \le |X_g(\omega)| \le M_5(\omega)
\end{aligned} \tag{6.8}$$

where $X_g(\omega)$ is the Fourier transform of the ground acceleration. Note that the constraint on the earthquake energy E is related to the Arias intensity [19] explained in Chaps. 4 and 5. The UBFAS and LBFAS constraints are introduced to replicate the frequency content and amplitude observed in past earthquake records on the critical earthquake. The ground velocity and displacement can then be obtained from Eq. (6.5) in the following forms:

$$\begin{aligned}
\dot{x}_g(t) &= \sum_{i=1}^{n} \left\{ \int_0^{t'} e_i[\tau + (i-1)T] \sum_{j=1}^{m} R_{ij} \cos[\omega_{ij}\{\tau + (i-1)T\} - \varphi_{ij}]d\tau \right\} + C_1 \\
x_g(t) &= \sum_{i=1}^{n} \left\{ \int_0^{t'} e_i[\tau + (i-1)T](t'-\tau) \sum_{j=1}^{m} R_{ij} \cos[\omega_{ij}\{\tau + (i-1)T\} - \varphi_{ij}]d\tau \right\} \\
&\quad + C_1 t' + C_2
\end{aligned} \tag{6.9}$$

Substituting the ground-motion conditions $x_g(0) = 0$ and $\lim_{t\to\infty} \dot{x}_g(t) \to 0$, the constants in Eq. (6.9) reduce to the following form [38]:

$$C_2 = 0; C_1 = -\sum_{i=1}^{n} \int_0^{\infty} \left\{ e_i[\tau + (i-1)T] \sum_{j=1}^{m} R_{ij} \cos[\omega_{ij}\{\tau + (i-1)T\} - \varphi_{ij}] \right\} d\tau \tag{6.10}$$

The constraints in Eq. (6.8) can be recast in terms of the variables $R_i, \phi_i, i = 1, 2, \ldots, m$ as:

$$\left[a_0^2\sum_{i=1}^{m}R_i^2\int_0^{\infty}\left\{t^2e^{-2\alpha t}\cos^2(\omega_i t-\varphi_i)+(t+T)^2e^{-2\alpha(t+T)}\cos^2[\omega_i(t+T)-\varphi_i]+\ldots\right\}dt\right]^{\frac{1}{2}}\le E$$

$$\max_{0<t<\infty}\left|a_0e^{-\alpha t}\left\{\sum_{i=1}^{m}R_i\{t\cos(\omega_i t-\varphi_i)+(t+T)e^{-\alpha T}\cos[\omega_i(t+T)-\varphi_i]+\ldots\}\right\}\right|\le M_1$$

$$\max_{0<t<\infty}\left|a_0\sum_{i=1}^{m}R_i\int_0^{t}e^{-\alpha\tau}\{\tau\cos(\omega_i\tau-\varphi_i)+(\tau+T)e^{-\alpha T}\cos[\omega_i(\tau+T)-\varphi_i]+\ldots\}d\tau\right.$$
$$\left.-a_0\sum_{i=1}^{m}R_i\int_0^{\infty}e^{-\alpha\tau}\{\tau\cos(\omega_i\tau-\varphi_i)+(\tau+T)e^{-\alpha T}\cos[\omega_i(\tau+T)-\varphi_i]+\ldots\}d\tau\right|\le M_2$$

$$\max_{0<t<\infty}\left|a_0\sum_{i=1}^{m}R_i\int_0^{t}(t-\tau)e^{-\alpha\tau}\{\tau\cos(\omega_i\tau-\varphi_i)+(\tau+T)e^{-\alpha T}\cos[\omega_i(\tau+T)-\varphi_i]+\ldots\}d\tau\right.$$
$$\left.-a_0t\sum_{i=1}^{m}R_i\int_0^{\infty}(t-\tau)e^{-\alpha\tau}\{\tau\cos(\omega_i\tau-\varphi_i)+(\tau+T)e^{-\alpha T}\cos[\omega_i(\tau+T)-\varphi_i]+\ldots\}d\tau\right|\le M_3$$

$$M_5(\omega)\le\left|a_0\sum_{i=1}^{m}R_i\int_0^{\infty}e^{-\alpha\tau}\{\tau\cos(\omega_i\tau-\varphi_i)+(\tau+T)e^{-\alpha T}\cos[\omega_i(\tau+T)-\varphi_i]+\ldots\}e^{-j\omega\tau}d\tau\right|\le M_4(\omega) \tag{6.11}$$

where $j=\sqrt{-1}$. It is noted that the cross terms in the energy constraint vanish since the envelope functions are not overlapped in this case. The constraints on E, M_1, M_2, and M_3 are introduced to replicate the energy, PGA, PGV and PGD of available seismic data at the site. The bounds on Fourier amplitude can be estimated from past records [15, 16] or using empirical expressions as proposed in Ref. [39]. In this chapter the first alternative is adopted as will be explained in the following section.

Now, the problem of modeling critical earthquake sequences for inelastic structures reduces to estimating the optimization variables $y=\{R_1,R_2,\ldots,R_m,\phi_1,\phi_2,\ldots,\phi_m\}^t$ so that the damage index given by Eq. (6.3) or (6.4) is maximized subjected to the constraints of Eq. (6.11). This constrained nonlinear optimization problem is solved using the sequential quadratic programing method [40]. The convergence criteria $|f_j-f_{j-1}|\le\varepsilon_1$ and $|y_{i,j}-y_{i,j-1}|\le\varepsilon_2$ are adopted, where f_j is the objective function of jth iteration, $y_{i,j}$ is ith optimization variable of jth iteration, and the parameters $\varepsilon_1,\varepsilon_2$ are small quantities to be defined. The inelastic response of the structure is computed using the Newmark-β method built as a subroutine in the optimization program. Note that the quantities $\mu(t)$ and $E_H(t)$ given by Eq. (6.3) attain their maximum values at different time instants. Accordingly, the optimization is performed at discrete time points. The optimal solution is taken as that producing the maximum damage index across all time instants. Numerical illustrations on the formulation developed above will be provided in the following section.

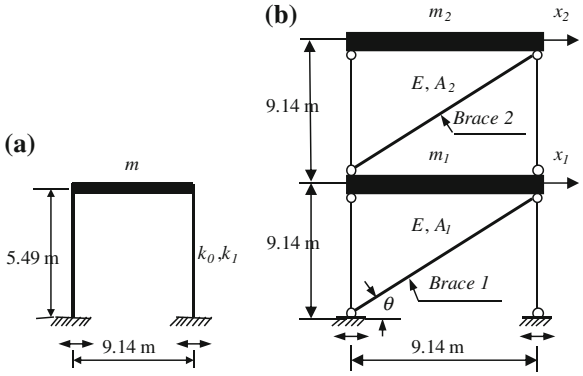

Fig. 6.4 Inelastic structures studied **a** single-story bilinear inelastic frame structure, **b** two-story elastic–plastic frame structure ([49] with permission from Multi-Science Publishing)

Table 6.1 Constraint scenarios considered ([49] with permission from Multi-Science Publishing)

Case	Constraints imposed
1	Energy and PGA
2	Energy, PGA, PGV, and PGD
3	Energy, PGA, and UBFS
4	Energy, PGA, UBFS, and LBFS

6.4 Numerical Illustrations and Discussions

6.4.1 Bilinear Inelastic Single-Story Frame Structure

Consider a single-story frame building with mass $= 9 \times 10^3$ kg, initial stiffness $k_0 = 1.49 \times 10^5$ N/m (initial natural frequency $= 4.1$ rad/s), and viscous damping of 0.05 damping ratio as shown in Fig. 6.4a. The structural parameters are set as the yield displacement $= 0.10$ m and the strain-hardening ratio (ratio of post-yield stiffness to pre-yield stiffness $\gamma = k_1/k_0) = 0.10$. The parameters in Eq. (6.3) are taken as $\beta = 0.15$ and $\mu_u = 8$ [29]. These parameters are changed later to examine their influences on the critical earthquake load and associated structural damage. The parameters in the Newmark-β method are taken as $\delta = 1/2$; $\alpha = 1/6$ and $\Delta t = 0.005$ s.

In this example, the critical scenario is taken into account for the Western Honshu earthquake. Unlike ordinary records, adequate/homogeneous recorded ground-motion sequences reflecting the same number of sequences and local soil conditions are not currently available. The bounds $M_4(\omega)$ and $M_5(\omega)$ on Fourier amplitude are taken as the minimum and maximum Fourier amplitude spectra across the three normalized records scaled by M_1 [41]. The PGA was scaled to 0.40 g to ensure inelastic behavior. Critical earthquake accelerations with two and

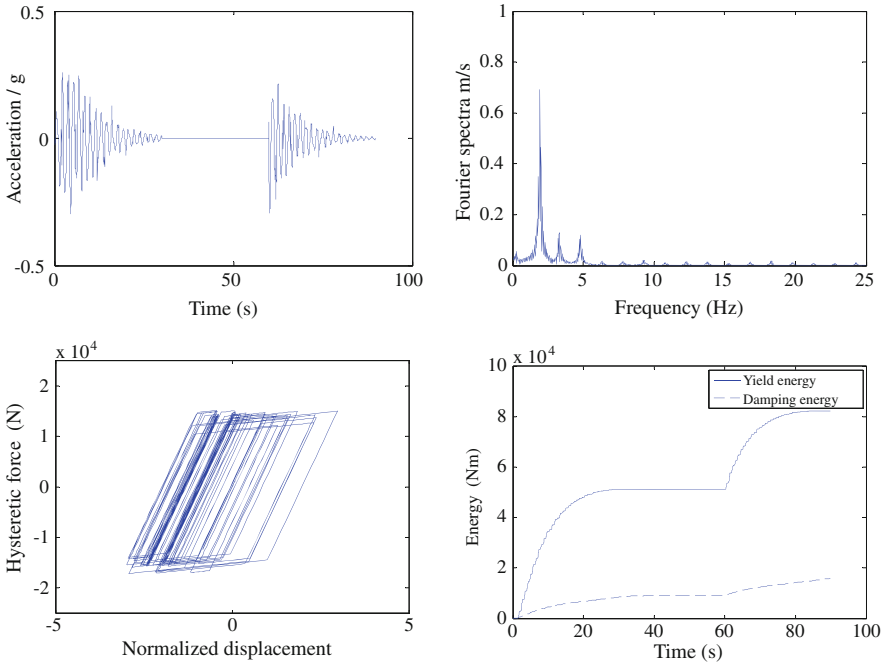

Fig. 6.5 Critical ground acceleration of two sequences and associated response for bilinear inelastic structure (*case 1*) ([49] with permission from Multi-Science Publishing)

three repeated sequences are derived here. The duration of each sequence is taken as 30 s and the time interval separating each two consecutive sequences is also taken as 30 s. The envelope parameters are $a_1 = 1.23$, $a_2 = 1.31$, $\alpha_1 = 0.30$ and $\alpha_2 = 0.28$. This leads to envelope functions having peak values of unity at about 3.5 and 63.5 s. The convergence limits are set as $\varepsilon_1 = \varepsilon_2 = 10^{-6}$ and the frequency content of the ground acceleration is assumed to be (0–25) Hz. The frequencies $\omega_i, i = 1, 2, \ldots, m$ are distributed in the interval (0–25) with some of these frequencies taken to coincide with the initial natural frequency of the structure and more frequencies are placed within the modal half-bandwidth. The constraint scenarios treated here are listed in Table 6.1. The optimization problem is solved using the Matlab optimization toolbox [42]. Several initial guesses, within the feasible region, were examined and found to lead to the same optimal solution. A parametric study on the number of frequencies in Eq. (6.5) is performed and $m = 150$ was found to give satisfactory results.

The numerical results obtained are shown in Figs. 6.5, 6.6, 6.7 and Tables 6.2 and 6.3. The frequency content and Fourier amplitude of the critical acceleration were found to be dependent on the constraints imposed (see Table 6.1 and Figs. 6.4 and 6.5). If information about the critical earthquake is limited to energy and PGA, the critical input is narrow-band and the structural deformation is high

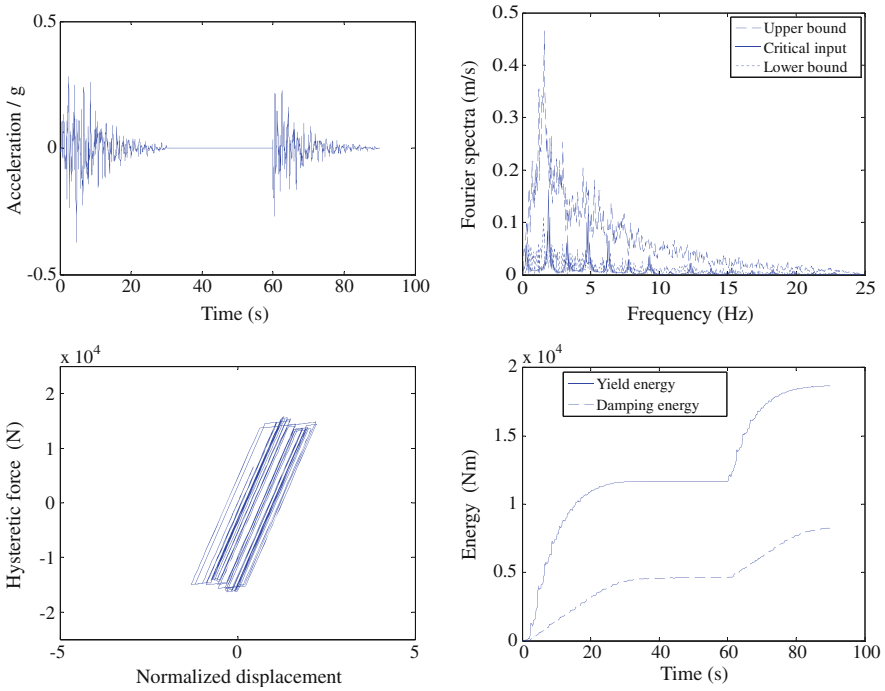

Fig. 6.6 Critical ground acceleration of two sequences and associated response for bilinear inelastic structure (*case 4*) [49] with permission from Multi-Science Publishing)

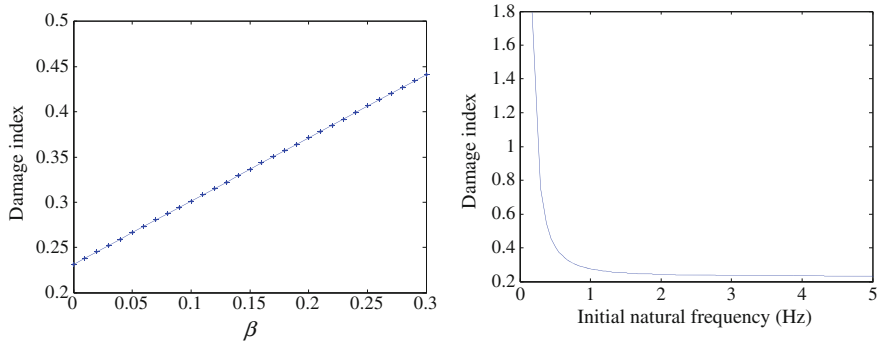

Fig. 6.7 Effect of β and initial natural frequency on the damage index of the single-story structure ([49] with permission from Multi-Science Publishing)

(Table 6.2). Most of the Fourier amplitude is located close to the initial natural frequency of the structure with secondary peaks located at higher frequencies (Fig. 6.5). These amplitudes get redistributed at other frequencies when the

Table 6.2 Response and damage parameters for the single-story frame structure ($\gamma = 0.10$, $\eta = 0.05$) ([49] with permission from Multi-Science Publishing)

Case	x_{max} (m)	μ_{max}	x_p (m)	N_{yp}	DI_{PA}	R_{DI}	Damage status
1	0.43	4.33	0.08	120	1.49	5.73	Total collapse
2	0.37	3.71	0.06		1.29	4.97	Total collapse
3	0.31	3.12	0.04	94	0.93	3.58	Damaged beyond repair
4	0.19	1.85	0.03	50	0.34	1.31	Repairable damage

x_p permanent deformation, N_{yp} number of yield points, R_{DI} ratio of damage index from critical input to that from 2007 Western Honshu NS record

Table 6.3 Effect of number of sequences on damage level for the single-story frame structure (Case 4, $\eta = 0.05$) ([49] with permission from Multi-Science Publishing)

Sequences scenario	μ_{max}	DI_{PA}	Damage status
Zero sequences	1.27	0.25	Repairable damage
Two sequences	1.85	0.34	Repairable damage
Three sequences	2.38	0.57	Damaged beyond repair

constraints on the Fourier amplitude spectra are brought in (Fig. 6.6). These observations are very useful for the seismic resistant design for ground motions with multiple sequences.

Case 1 provides higher input energy to the structure that is mainly dissipated by yielding (Fig. 6.5). The realism of the earthquake input is evident from the frequency content, the inelastic deformation produced, and the value of the associated damage index. For the two sequences scenario, the damage index for constraint case 1 is 1.49 which implies the arrival to total collapse, while that for case 4 is 0.34 implying repairable damage. These quantities are about 5.7 and 1.3 times that produced by the NS component of the Western Honshu record scaled to 0.40 g PGA. The associated maximum ductility is 4.65 and 1.85, respectively (Table 6.2). The constraints on PGV and PGD do not produce realistic earthquake ground motions compared to the Fourier spectra bounds. Note that the resonant ground-motion scenario of case 1 has been observed in actual recorded earthquakes, such as, the 1985 Mexico, the 1995 Kobe, and the 2011 Tohoku (Japan) earthquakes [43]. Resonant ground motions have also been observed in near-field records with directivity or fling effects [44].

Our attention is focused now on the effect of multiple earthquake sequences on the structural damage state and associated inelastic deformations. Table 6.3 summarizes the damage index and corresponding maximum inelastic displacement for the critical ground accelerations with zero, two, and three sequences. The numerical results reveal clearly the substantial effect of multiple earthquake sequences on the structural damage state and associated inelastic deformations. Thus, the values of the damage index and maximum inelastic displacement increase remarkably for the critical acceleration with two and three sequences compared with the case of critical input without sequences. As can be expected, the input energy to the structure increases as the number of acceleration sequences increases. The energy dissipated by yielding is substantially larger than that

dissipated by damping. The kinetic and recoverable elastic strain energies are remarkably small and diminish by the end of the ground-motion duration. This observation agrees with the results obtained by one of the authors on critical earthquake loads for elastic–plastic SDOF structures [41].

To examine effects of the strain-hardening ratio and the damping ratio on the derived critical acceleration, limited parametric studies are carried out. The values of these parameters are changed, each at a time, and the critical acceleration is determined by solving a new optimization problem. Namely, γ is taken as 0.20, 0.10, 0.05, and 0.01 and $\eta = 0.02$, 0.05 and 0.10. It does not appear that the strain-hardening ratio influences the frequency content of the critical input. The structure with lower values of γ yields more frequently compared to that with higher γ values. The cumulative hysteretic energy dissipated during multiple sequences was observed to decrease for higher values of γ, particularly at the end of the earthquake duration. The damping ratio was also not seen to alter the frequency content of the critical ground motion. The inelastic deformation and damage index, however, increase for lower values of the damping ratio. For case 4, the ductility ratio increases from 1.85 to 2.19 when the damping ratio is changed from 0.05 to 0.02. The inelastic structure with higher damping ratios dissipates more energy through damping.

To assess the structure damage level, Eq. (6.3) was used to estimate and evaluate the damage index of the structure subjected to the critical earthquake load. The effect of the parameter β on the damage index is examined. Based on the results of experimental tests, it is reported that β ranges between 0.05 and 0.20 with an average value of 0.15 [5]. Figure 6.7 shows the influence of β on the damage index for case 4 for two acceleration sequences. To study the effect of the initial natural frequency of the structure on the damage index, the structure stiffness was varied while other parameters are kept unchanged and the critical earthquake is computed. The value of DI_{PA} is then calculated. The parameters $\beta = 0.15$ and $\mu_u = 8$ are adopted. The numerical results reveal that the damage index depends significantly on the structure initial natural frequency (Fig. 6.7).

In this chapter, the constraints quantities E, M_1, M_2, M_3, $M_4(\omega)$, and $M_5(\omega)$ are introduced to define the energy, PGA, PGV, PGD, and upper and lower bounds on the Fourier amplitude spectra of past recorded ground motions at the given site or from other sites with similar soil conditions. The critical earthquake ground motion by definition is the one that produces the maximum damage in the structure, and thus it turns out to be the excitation that matches the vibration property of the structure under consideration. For instance, if the energy and PGA constraints are only imposed (case 1: limited information), the optimal (critical) acceleration has most of the energy located in a narrow-frequency band close to the structure initial natural frequency (Fig. 6.5). Thus, the optimal (critical) acceleration, in this case, reflects the resonance nature and produces conservative responses. The influence of including further constraints, such as upper and lower bounds on the Fourier spectra, forces the energy of the ground acceleration to get distributed at frequencies other than the structure frequencies. This leads to the ground acceleration that is rich in frequency content and produces smaller responses (Fig. 6.6).

6.4.2 Two-Story Elastic–Plastic Framed Structure

To demonstrate the formulation developed in this chapter for inelastic MDOF structures, a two-story braced frame building shown in Fig. 6.4b is considered. The braces are assumed to exhibit elastic–plastic behavior. The mass and initial stiffness matrices of the structure are given by

$$\mathbf{M} = \begin{bmatrix} m_1 & 0 \\ 0 & m_2 \end{bmatrix}; \mathbf{K}_{el} = E\cos^2\theta \begin{bmatrix} A_1/L_1 + A_2/L_2 & -A_2/L_2 \\ -A_2/L_2 & A_2/L_2 \end{bmatrix}. \tag{6.12}$$

The values of floor masses are taken as $m_1 = m_2 = 1.75 \times 10^5$ kg, the cross-sectional areas of braces are $A_1 = A_2 = 6.45 \times 10^{-4}$ m^2, and the Young's modulus $E = 2.59 \times 10^{11}$ N/m^2. When both braces behave elastically, the stiffness matrix is $\mathbf{K} = \mathbf{K}_{el}$. On the other hand, if brace 1 yields, the tangential stiffness matrix for incremental analysis is $\mathbf{K} = \mathbf{K}_1$ and if brace 2 yields, the corresponding one is $\mathbf{K} = \mathbf{K}_2$. If both braces yield, the corresponding one becomes $\mathbf{K} = \mathbf{K}_{12}$. These matrices are given by

$$\begin{aligned} &\mathbf{K}_{el} = D\begin{bmatrix} 2 & -1 \\ -1 & 1 \end{bmatrix}; \mathbf{K}_1 = D\begin{bmatrix} 1 & -1 \\ -1 & 1 \end{bmatrix}; \mathbf{K}_2 = D\begin{bmatrix} 1 & 0 \\ 0 & 0 \end{bmatrix}; \\ &\mathbf{K}_{12} = \begin{bmatrix} 0 & 0 \\ 0 & 0 \end{bmatrix}; D = \frac{AE}{L}\cos^2\theta. \end{aligned} \tag{6.13}$$

The first two natural frequencies of the elastic structure are computed as 6.2 and 16.2 rad/s. A proportional damping $\mathbf{C} = a\mathbf{M} + b\mathbf{K}$ with $a = 0.2683$, $b = 0.0027$ is adopted (equivalent viscous damping ratio is 0.03 in the first two modes). The yield strain of braces ε_y is taken as 0.002 for both tension and compression. The braces yield at a displacement $x_y = L\varepsilon_y/\cos\theta = 0.04$ m. Brace 1 yields when $|x_1| = 0.04$m and brace 2 yields when $|x_2 - x_1| = 0.04$ m. The global damage index of Eq. (6.4) with $\mu_u = 10$ and $\beta = 0.15$ is taken as the objective function. In this example, we model the critical ground motion for the 2004 Niigata-ken Chuetsu earthquake with two and three sequences. The constraint bounds of Eq. (6.11) are quantified across the three records with $M_1 = 0.45$ g. The same envelope functions and time durations of the previous example are adopted here.

The numerical results of this example are shown in Figs. 6.8 and 6.9 and Table 6.4. The general features of critical ground-motion sequences observed in the previous example were generally the same. Again, constraint scenario 1 produces higher damage than other cases since the input energy to the structure is remarkably high (Figs. 6.8 and 6.9). Furthermore, the ground motion tends to have more frequencies compared with the previous example due to influence of the second vibration mode. The damage index and the maximum inelastic displacement increase as the number of acceleration sequences increases. For constraint case 4, two and three repeated sequences produce damage indices that are respectively about 1.5 and 2.4 times that of the critical input without sequences

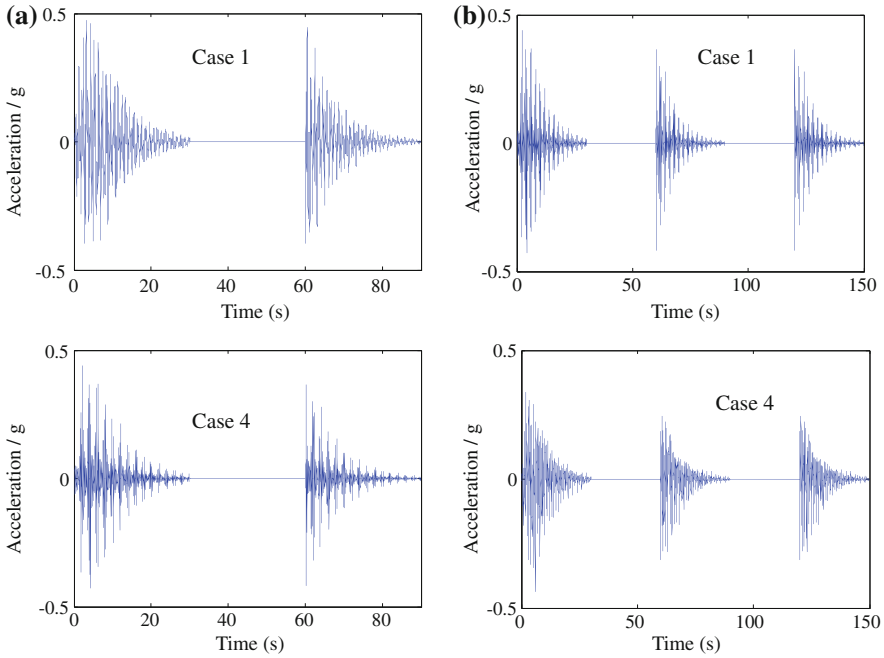

Fig. 6.8 Critical ground acceleration sequences for the two-story elastic–plastic structure **a** two sequences, **b** three sequences ([49] with permission from Multi-Science Publishing)

(see Table 6.4 and Fig. 6.9). The maximum ductility factors for cases 1 and 4 are 2.8 and 1.5 times those produced by the Niigata NS record with PGA = 0.45 g. Similarly, the damage index from the critical input for cases 1 and 4 are about 6.5 and 1.6 times that from the 2004 Niigata NS acceleration.

6.5 Summary

Repeated sequences of earthquake ground motions separated by short time intervals have the potential of causing severe damage to structures due to accumulation of inelastic deformations from multiple sequences and impossibility of repairing the structure before the end of all sequences. This class of ground motion has been observed in Japan and other parts of the world. Critical earthquake loads of repeated sequences were modeled in this chapter for inelastic structures at sites having limited earthquake data and (or) information. The method of critical excitation and subsequent procedures provide a reliable tool for modeling possible future earthquake loads as inputs to important and influential structures. New damage descriptors using energy concepts and damage indices have been employed in deriving the critical earthquake loads. The quantification of the structure's damage

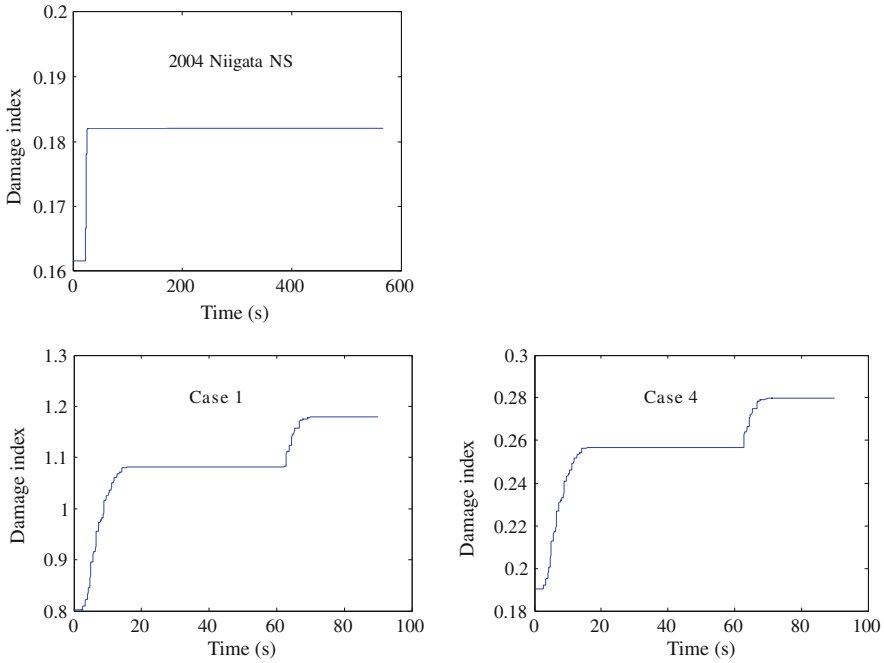

Fig. 6.9 Damage index for the two-story elastic–plastic structure from recorded ground motion and critical earthquake load ([49] with permission from Multi-Science Publishing)

Table 6.4 Response and damage parameters for the two-story frame structure ($\eta = 0.03$) ([49] with permission from Multi-Science Publishing)

Case	x_{max} (m)	μ_{max}	x_p(m)	DI_{PA}	R_{DI}	Damage status
1	0.21	5.25	0.06	1.18	6.48	Total collapse
2	0.18	4.40	0.04	0.89	4.89	Damaged beyond repair
3	0.15	3.75	0.03	0.76	4.18	Damaged beyond repair
4	0.11	2.74	0.03	0.28	1.54	Repairable damage

μ_{max} is computed for displacement at second floor level, DI_{PA} represents weighted damage in the braces, R_{DI} = ratio of damage index from critical input to that from 2004 Niigata NS record

using damage indices facilitates assessing the structure's performance by quantifying its damage level. Critical repeated earthquake ground-motion sequences for inelastic structures have been estimated by solving inverse dynamic problems using nonlinear time history response analysis and nonlinear optimization techniques. It has been explained that repeated sequences of critical ground motions produce larger structural damage than critical ground motions without sequences. Several aspects of the problem have been studied, such as, influences of the available earthquake information, number of acceleration sequences, strain-hardening ratio, and damping ratio on the derived critical earthquake loads and associated structural

responses. Finally, the modeling of random critical acceleration sequences for inelastic structures is also of great interest and is currently under investigation. In this investigation, it seems that evolutionary power spectral density models can be used along with stochastic equivalent linearization and nonlinear optimization techniques to tackle the problem.

The formulation developed in this chapter has been explained for simple structures with bilinear and elastic–plastic force–deformation laws. The application of the explained method to more complex structures and the use of detailed degradation models need to be investigated. Critical earthquake loads maximizing the structural damage have been obtained using deterministic methods. Critical earthquake loads can also be estimated based on hazard analysis using the probability of occurrence. Furthermore, the critical earthquake sequences explained in this chapter belong to the class of engineering models that are consistent with ground motion models commonly used by engineers. These models are introduced to replicate gross features of recorded motions, such as, amplitude, frequency content, non-stationarity trend, and local soil effects. Predictive ground-motion models that account for several details, such as, fault dimension and orientation, rupture velocity, earthquake magnitude, attenuation, stress drop, density of the intervening medium, local soil condition, and epicentral distance, are also of great interest and have been developed mainly by seismologists [26, 45–48]. Critical earthquake ground motions can be formulated based on seismological models where the model parameters can be optimized to produce the least favorable conditions. In this case the class of admissible functions becomes additionally constrained by the physical model adopted. In this sense, the approach explained in this chapter is nonparametric in nature.

References

1. IBC (2009) International Building Code. International Code Council Inc, USA
2. Architectural Institute of Japan (2004) Recommendations for loads on buildings. AIJ, Tokyo
3. European Committee for Standardization (2003) Eurocode 8: design of structures for earthquake resistance, Brussels
4. Bommer JJ, Acevedo AB (2004) The use of real earthquake accelerograms as design input to dynamic analysis. J Earthq Eng 8(1):43–91
5. Pinho R (2007) Nonlinear dynamic analysis of structures subjected to seismic action. In: Pecker A (ed) Advanced earthquake engineering analysis. Springer, NY
6. Kyoshin-Net (2009) National research institute for earth science and disaster prevention. Available at http://www.k-net.bosai.go.jp/
7. Moustafa A, Ueno K, Takewaki I (2010) Critical earthquake loads for SDOF inelastic structures considering evolution of seismic waves. Earthq Struct 1(2):147–162
8. Elnashai A, Bommer JJ, Martinez-Pereira A (1998) Engineering implications of strong-motion records from recent earthquakes. In: Proceedings of 11th European conference on earthquake engineering, Paris, CD-ROM
9. Amadio C, Fragiacomo M, Rajgelj S (2003) The effects of repeated earthquake ground motions on the non-linear response of SDOF systems. Earthq Eng Struct Dyn 32:291–308

10. Das S, Gupta VK, Srimahavishnu V (2007) Damage-based design with no repair for multiple events and its sensitivity to seismicity model. Earthq Eng Struct Dyn 36:307–325
11. Hatzigeorgiou GD, Beskos DE (2009) Inelastic displacement ratios for SDOF structures subjected to repeated earthquakes. Eng Struct 31(11):2744–2755
12. Takewaki I (2007) Critical excitation methods in earthquake engineering. Elsevier Science, Amsterdam
13. Takewaki I (2002) Seismic critical excitation method for robust design: a review. J Struct Eng 128:665–672
14. Takewaki I (2004) A comprehensive review of seismic critical excitation methods for robust design. Adv Struct Eng 8(4):349–364
15. Abbas AM, Manohar CS (2002) Investigations into critical earthquake load models within deterministic and probabilistic frameworks. Earthq Eng Struct Dyn 31:813–832
16. Abbas AM, Manohar CS (2005) Reliability-based critical earthquake load models. Part 2: nonlinear structures. J Sound Vib 287:883–900
17. Abbas AM, Manohar CS (2007) Reliability-based vector nonstationary random critical earthquake excitations for parametrically excited systems. Struct Saf 29:32–48
18. Housner GW, Jennings PC (1977) The capacity of extreme earthquake motions to damage structures. In: Hall WJ (ed) Structural and geotechnical mechanics, a volume honoring Newmark NM. Prentice-Hall, Englewood Cliffs, pp 102–116
19. Arias A (1970) A measure of earthquake intensity: seismic design of nuclear power plants. MIT press, Cambridge, pp 438–468
20. Amiri GG, Dana FM (2005) Introduction to the most suitable parameter for selection of critical earthquakes. Comput Struct 83(8–9):613–626
21. Naeim F, Anderson JC (1993) Classification and evaluation of earthquake records for design. The NEHRP Professional Fellowship Report to EERI and FEMA
22. Trifunac MD, Brady AG (1975) A study on the duration of strong earthquake ground motion. Bull Seismol Soc Am 65(3):581–626
23. Moustafa A (2009) Discussion of a new approach of selecting real input ground motions for seismic design: the most unfavourable real seismic design ground motions. Earthq Eng Struct Dyn 38:1143–1149
24. Moustafa A, Takewaki I (2009) Use of probabilistic and deterministic measures to identify unfavorable earthquake records. J Zhejiang Univ: Sci A 10(5):619–634
25. Zhai C-H, Xie L–L (2007) A new approach of selecting real input ground motions for seismic design: the most unfavourable real seismic design ground motions. Earthq Eng Struct Dyn 36:1009–1027
26. Powell GH, Allahabadi R (1988) Seismic damage predictions by deterministic methods: concepts and procedures. Earthq Eng Struct Dyn 16:719–734
27. Cosenza C, Manfredi G, Ramasco R (1993) The use of damage functionals in earthquake engineering: a comparison between different methods. Earthq Eng Struct Dyn 22:855–868
28. Fajfar P (1992) Equivalent ductility factors, taking into account low-cyclic fatigue. Earthq Eng Struct Dyn 21:837–848
29. Park YJ, Ang AH-S, Wen YK (1987) Damage-limiting aseismic design of buildings. Earthq Spectra 3(1):1–26
30. Park YJ, Ang AH-S (1985) Mechanistic seismic damage model for reinforced concrete. J Struct Eng 111(4):722–739
31. Park YJ, Ang AH-S, Wen YK (1985) Seismic damage analysis of reinforced concrete buildings. J Struct Eng 111(4):740–757
32. Zahrah TF, Hall WJ (1984) Earthquake energy absorption in sdof structures. J Struct Eng 110:1757–1772
33. Akiyama H (1985) Earthquake-resistant limit-state design for buildings. University of Tokyo Press, Tokyo
34. Uang CM, Bereto VV (1990) Evaluation of seismic energy in structures. Earthq Eng Struct Dyn 19:77–90

35. Mehanny SS, Deierlein GG (2000) Modeling of assessment of seismic performance of composite frames with reinforced concrete columns and steel beams, Report No. 135, The John Blume earthquake research center, Stanford University
36. Bozorgenia Y, Bertero VV (2003) Damage spectra: characteristics and applications to seismic risk reduction. J Struct Eng 129(4):1330–1340
37. Chai YH, Romstad KM, Bird SM (1995) Energy-based linear damage model for high-intensity seismic loading. J Struct Eng 121(5):857–864
38. Shinozuka M, Henry L (1965) Random vibration of a beam column. J Eng Mech 91:123–143
39. Shinozuka M (1970) Maximum structural response to seismic excitations. J Eng Mech 96:729–738
40. Arora JS (2004) Introduction to optimum design. Elsevier Academic Press, San Diego
41. Abbas AM (2006) Critical seismic load inputs for simple inelastic structures. J Sound Vib 296:949–967
42. Caleman T, Branch MA, Grace A (1999) Optimization toolbox for the use with Matlab, user's guide. Math Works Inc, USA
43. Takewaki I, Murakami S, Fujita K, Yoshitomi S, Tsuji M (2011) The 2011 off the Pacific coast of Tohoku earthquake and response of high-rise buildings under long-period ground motions. Soil Dyn Earthq Eng 31(11):1511–1528
44. Moustafa A (2009) Discussion of the effect of energy concentration of earthquake ground motions on the nonlinear response of RC structures. Soil Dyn Earthq Eng 29:1181–1183
45. Quek ST, Teo YP, Balendra T (1990) Non-stationary structural response with evolutionary spectra using seismological input model. Earthq Eng Struct Dyn 19:275–288
46. Boore DM (1983) Stochastic simulation of high-frequency ground motions based on seismological models of the radiated spectra. Bull Seismol Soc Am 73:1865–1894
47. Brune JN (1970) Tectonic stress and the spectra of seismic shear waves from earthquakes. J Geophys Res 75:4997–5009
48. Hanks TG, McGuire RK (1981) The character of high frequency ground motions based on seismic shear waves. Bull Seismol Soc Am 71:2071–2095
49. Moustafa A, Takewaki I (2010) Modeling critical ground-motion sequences for inelastic structures. Adv Struct Eng 13(4):665–679

Chapter 7
Response of Nonlinear SDOF Structures to Random Acceleration Sequences

7.1 Introduction

In performance-based design, the structure is designed to behave linearly elastic without damage under a moderate frequent earthquake and to undergo repairable damage under a rare strong earthquake [1, 2]. Design earthquakes are specified in current seismic codes as single events [3–5]. However, the structure may experience repeated accelerations in a short period of time. Ground accelerations of multiple sequences could result in more damage to the structure than a single ordinary event. This is because the structure gets damaged from the first sequence and additional damage accumulates from secondary sequence before any repair is possible. The evidence from recent earthquakes confirms this scenario. For example, the 2004 Niigata earthquake recorded at Ojiya (NIG019) consisted of two acceleration sequences (see Fig. 7.1). Multiple acceleration sequences result from mainshock–aftershock earthquakes. For instance, the 2010 Haiti earthquake had mainshock of 7.0 Mw followed by about 14 aftershocks of 5.0–6.1 magnitude [6]. Repeated acceleration sequences separated by short-time intervals have also been observed at other regions of the world as shown in Table 7.1 [7, 8]. Thus, ground accelerations of repeated sequences represent a real situation that requires special treatment in seismic design.

Elnashai et al. [9] reported the first evidence of repeated acceleration sequences in the 1997 Umbria-Marche Italy earthquake. The response of inelastic steel structures to simulated acceleration sequences was studied in [10, 11]. Das and Gupta [12] used the spectrum of the force ratio in designing single-degree-of-freedom (SDOF) structures to survive all possible earthquakes during their service life without undergoing repairs. Recently, recorded accelerograms were used to investigate the implication of repeated acceleration sequences on the inelastic displacement ratio and the ductility demand of SDOF and MDOF structures [13–16]. Extensive parametric studies were conducted in these studies to derive expressions for the inelastic displacement ratio and the ductility demand in terms

I. Takewaki et al., *Improving the Earthquake Resilience of Buildings*,
Springer Series in Reliability Engineering, DOI: 10.1007/978-1-4471-4144-0_7,

of the period of vibration, the viscous damping ratio, the strain-hardening ratio, the force reduction factor, and the soil class. More recently, the characteristics of strong ground motion of multiple sequences were studied by Moustafa and Takewaki [17]. The definitions of the effective number of sequences and the effective strong duration were also introduced.

Dunbar and Charlwood [18] reported the significant difference in the frequency content for the M6.2 earthquake and the M4.9 aftershock recorded at the C-00 of the SMART array in Taiwan. The statistical properties of aftershock sequences were studied in [19]. The study showed that aftershocks are associated with three empirical scaling relations, namely, (1) Gutenberg-Richter frequency-magnitude scaling, (2) Bath's law for the magnitude of the largest aftershock, and (3) the modified Omori's law for the temporal decay of aftershocks. The probabilistic seismic hazard analysis (PSHA) of aftershocks following a mainshock was studied by Yeo and Cornell [20]. The study showed that aftershock occurrence rates decrease with increased elapsed time from the initial occurrence of the mainshock, and that the aftershock ground motion hazard at a site depends on the magnitude and location of the causative mainshock. The same authors introduced a decision analysis methodology based on the stochastic dynamic programming in the post-quake aftershock environment by studying the damage sustained by the building due to the mainsheet, time-varying aftershock rates and the potential for further damage progression [21].

The modeling of strong ground motion is a crucial problem in earthquake engineering. A state-of-the-art review on modeling random earthquake loads using engineering models can be found in [22–28]. The Kanai-Tajimi model represents one of the widely used models [30, 31]. The engineering models replicate observed feature of acceleration records. The predictive (also known as physical or seismological) models require information on the source properties and have been developed by seismologists [32–34]. From a seismological perspective, the reason for the occurrence of multiple acceleration sequences is that: the mainshock increases the regional stresses resulting in the subsequent aftershocks [18]. The strain accumulation and release produces regions of stress increase which also contribute to the occurrence of repeated acceleration sequences. Furthermore, the local stress concentrations resulting from asperities and barriers also contribute to the generation of aftershocks in the vicinity of the mainshock rupture. Note that, the simulation of repeated acceleration sequences using seismological models has not been studied before.

This chapter proposes a simple model for representing random acceleration sequences. Given that, most previous studies deal with the response analysis of inelastic structures to deterministic acceleration sequences, this paper investigates the response of nonlinear structures to random acceleration sequences using the proposed model. Furthermore, the theory of statistical linearization is integrated with structural reliability analysis to assess the structural safety under repeated acceleration sequences. The next section provides a brief overview on the characteristics of ground accelerations with repeated sequences.

Table 7.1 Information on earthquake ground motions with multiple acceleration sequences [41]

Earthquake	Date	Time	Soil type	Site (station)	N_s	M	D_{ss} (km)	t_d (s)	PGA (g)			I_A (m/s)		
									H_1	H_2	UD	H_1	H_2	UD
Helena aftershock	11.28.1935	14:41:48	Rock	Helena Federal Bldg (HFB)	2	5.0	6.3	45	0.09	0.08	0.03	1.47	1.76	0.58
San Francisco	03.22.1957	19:44:21	Alluvium	350 McAllister (USGS1080)	2	5.3	17.0	41	0.10	0.07	0.05	0.64	0.47	0.44
San Fernando	02.09.1971	14:02:24	Rock	Pacoima dam (CSMIP24207)	2	3.9	10.9	31	0.12	0.13	0.05	0.70	0.57	0.29
Victoria	06.09.1980	03:28:19	Alluvium	Chihuahua, Mexico (6621)	2	6.4	5.7	56	0.19	0.15	0.17	1.89	1.77	1.13
New Zealand	06.18.1994	03.25.15	medium	Arthurs Pass (GNS505A)	3	6.8	16.0	160	0.44	0.34	0.37	5.49	3.47	3.24
Katsurao	02.20.1997	05:22:00	Soft soil	Katsurao (FKS006)	2	5.3	39.0	67	0.12	0.12	0.06	0.87	0.86	0.45
Kocaeli	08.17.1999	00:01:40	Soft soil	Yarimca (KOER772)	2	7.4	22.7	136	0.23	0.32	0.24	3.14	3.17	2.74
Chi-Chi	09.20.1999	17:47:16	Stiff soil	Taichung (TCU071)	2	7.6	4.9	160	0.53	0.65	0.42	6.30	9.62	5.06
Chi-Chi	09.20.1999	18:03:00	Stiff soil	Taichung (TCU078)	2	6.2	7.6	65	0.28	0.47	0.24	2.28	3.66	1.20
Bhuj	01.26.2001	03:16:40	NA	Ahmd abad (IITR)	2[a]	7.0	239.0	134	0.11	0.08	0.07	1.31	1.01	0.80
Niigata	10.23.2004	17:56:00	Soft soil	Ojiya (NIG019)	2	6.8	7.0	299	1.17	1.33	0.84	9.83	11.64	6.97
Niigata	10.23.2004	17:56:00	NA	Nagaoka-shisho (NIG028)	2	6.8	15.0	580	0.89	0.72	0.44	9.70	7.84	4.72
Niigata	10.23.2004	18:03:00	Soft soil	Ojiya (NIG019)	2[b]	6.3	18.0	299	0.20	0.23	0.10	1.95	2.40	1.03
Niigata	10.23.2004	18.07:00	Soft soil	Koide (NIG020)	3	5.7	15.0	299	0.12	0.12	0.04	0.76	0.76	0.36
Niigata	10.23.2004	18:34:00	Soft soil	Koide (NIG020)	2	6.5	09.0	299	0.54	0.53	0.34	5.65	4.07	2.51
Niigata	10.23.2004	19:46:00	Soft soil	Koide (NIG020)	3	5.7	10.0	299	0.15	0.13	0.06	1.23	1.15	0.61
Niigata	10.27.2004	10:40:00	Soft soil	Koide (NIG020)	2	6.1	9.0	299	0.53	0.40	0.54	3.51	2.53	2.16
Honshu	04.15.2007	19:47:00	Soft soil	Kohga (SIG012)	2	5.4	13.0	120	0.26	0.11	0.05	2.05	0.53	0.41
Niigata-ken	08.16.2007	04:15:00	Soft soil	Hasunuma (CHBH19)	2	5.3	17.0	147	0.10	0.03	0.04	0.55	0.42	0.27
Iwate-Miyagi	06.14.2008	09:20:00	Soft soil	Ichinoseeki-w (IWTH25)	2	5.7	22.0	212	0.80	0.21	0.47	2.61	1.20	1.73

NA not available, N_s Number of acceleration sequences, M Magnitude, D_{ss} Site-source distance, t_d earthquake duration, $I_A = \int_0^\infty [\ddot{x}(t)]^2 dt$,

[a] UD component only has two acceleration sequences, [b] UD component has five acceleration sequences

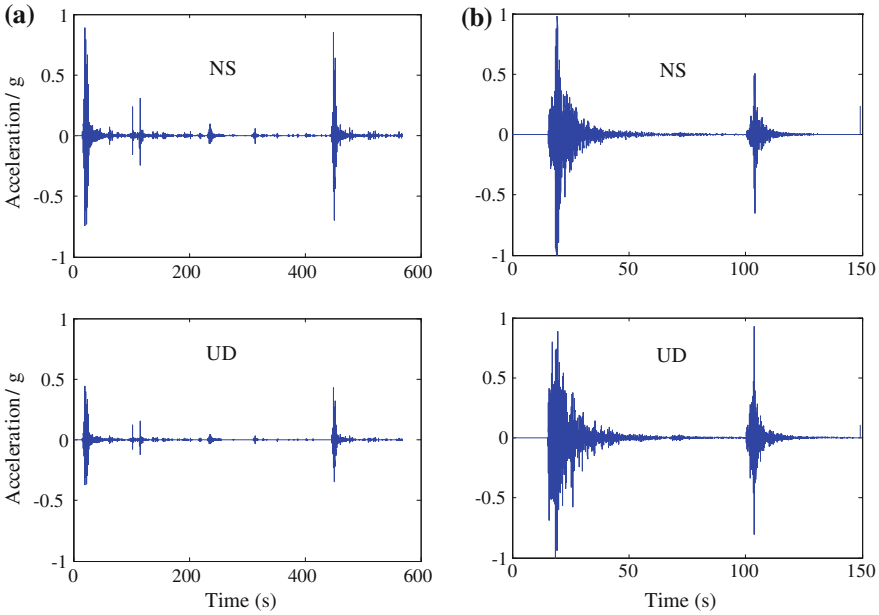

Fig. 7.1 Recorded acceleration sequences for **a** 2004 Niigata (NIG028), **b** 2007 Honshu (SIG012) [41]

7.2 Characteristics of Acceleration Records of Repeated Sequences

Some characteristics of the acceleration records and repeated sequences were explained in Sect. 5.2. The notable points are stated in this section again.

Table 7.1 lists information on 60 records from 17 earthquakes of multiple acceleration sequences. This information includes the soil type beneath the recording station, the magnitude, the epicenter distance, and the total duration for each earthquake. The table contains also the intensity, peak ground acceleration (PGA), and the observed number of acceleration sequences. Figure 7.1 depicts one horizontal and the vertical accelerations for two earthquakes from Table 7.1 [7, 8]. The important characteristics of repeated ground motion sequences can be summarized as follows [17]:

1. Repeated acceleration sequences are recorded at sites with different soil types (see Table 7.1).
2. The frequency content depends on the soil type, epicenter distance, and source characteristics.
3. All the three accelerations have multiple sequences and the observed number of sequences for the records listed in Table 7.1 is either 7.2 or 7.3.

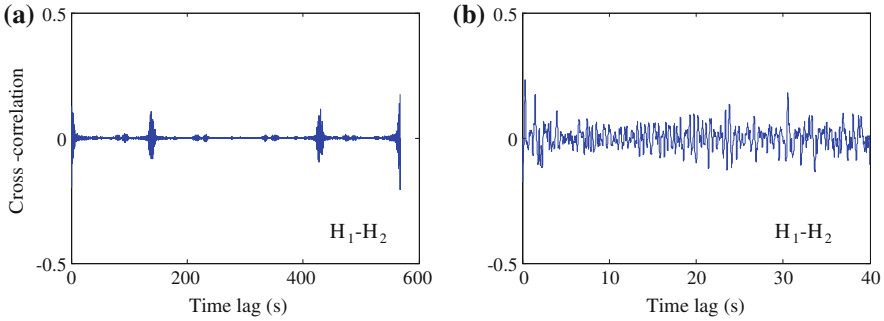

Fig. 7.2 Cross-correlation functions of ground accelerations **a** 2004 Niigata earthquake (NIG028), **b** 1940 El Centro (El Centro #9) [41]

4. The individual sequences generally have sharp build up, short strong phase and fast decay. Furthermore, they have different energy, duration (5–30 s), and PGA ($\leq$1.33 g). In general, the first sequence has the largest energy, PGA, and duration.
5. The total duration of repeated acceleration sequences for the earthquake records listed in Table 7.1 ranges between 30 and 600 s. This duration can change based on the earthquake records adopted. However, repair of the structure due to damage resulting from the strong ground motion sequences reported in Table 7.1 is not possible.
6. The three acceleration components of each earthquake exhibit significant correlations (see Fig. 7.2). The corresponding sequences in the three records of the same earthquake have similar durations and time instants of initial build up, strong phase, and decay. Therefore, as can be expected, the cross-correlation functions of the acceleration components are significant during the strong shaking durations.

An additional important aspect is the frequency content of individual sequences. Figure 7.3 shows the Fourier amplitude spectra for the NS accelerations of the 2004 Niigata and the 2007 Honshu earthquakes (see Table 7.1). The plots in Fig. 7.3b reveal that the frequency content and amplitude for the individual sequences of the same record could be significantly different. This observation agrees with the finding reported in Moustafa and Takewaki [17]. Thus, it may not be accurate to consider that the acceleration sequences have identical frequency content. The above properties need to be considered in modeling repeated acceleration sequences.

Secondary sequences can be viewed as earthquakes that occur due to repeated rupture of the fault or because the fault that ruptured in the first sequence is still readjusting itself. They typically occur within the same zone along a fault that ruptured in the original event. The next section demonstrates the representation of stochastic ground acceleration with repeated sequences.

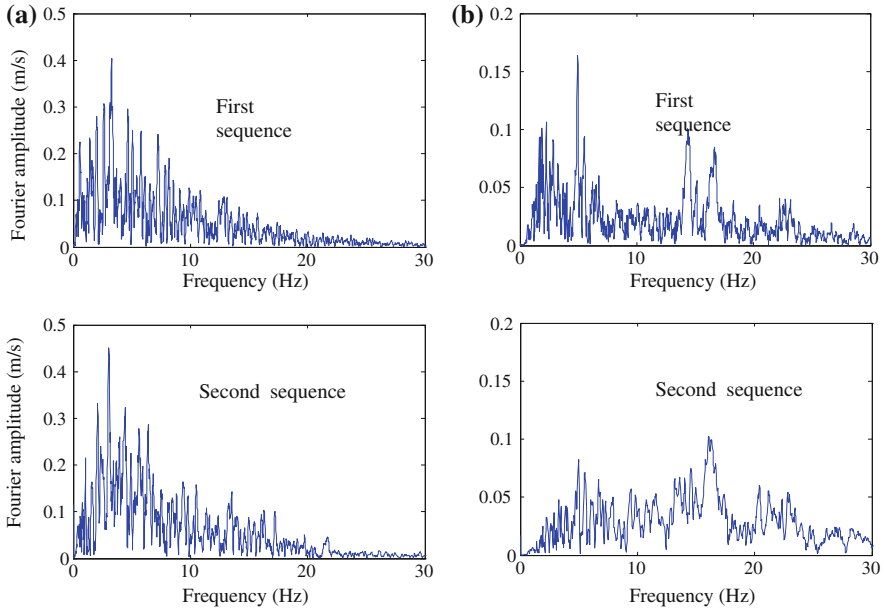

Fig. 7.3 Fourier amplitude spectra for individual sequences **a** 2004 Niigata (NIG028-NS), **b** 2007 Honshu (SIG012-NS) [41]

7.3 Representation of Random Ground Acceleration with Multiple Sequences

Based on the properties of repeated acceleration sequences presented in the previous section, the nonstationary ground acceleration $\ddot{x}(t)$ of n sequences is expressed as follows:

$$\ddot{x}(t) = \begin{cases} e_1(t)\,\ddot{w}_1(t): & 0 \le t \le T_1 \\ 0; & T_1 \le t \le T_1 + T_2 \\ e_2(t - T_1 - T_2)\ddot{w}_2(t); & T_1 + T_2 \le t \le T_1 + T_2 + T_3 \\ 0; & T_1 + T_2 + T_3 \le t \le T_1 + T_2 + T_3 + T_4 \\ \cdots & \\ \cdots & \\ \cdots & \\ e_n(t - \sum_{i=1}^{n+1} T_i)\ddot{w}_n(t); & \sum_{i=1}^{n+1} T_i \le t \le \sum_{i=1}^{n+2} T_i \end{cases} \tag{7.1}$$

where $e_1(t), e_2(t), \ldots, e_n(t)$ are the envelope functions associated with the acceleration sequences 1, 2, …, n, $\ddot{w}_1(t), \ddot{w}_2(t), \ldots, \ddot{w}_n(t)$ are stationary random processes, $T_1, T_3, \ldots, T_{n+2}$ are the time durations of the acceleration sequences and $T_2, T_4, \ldots, T_{n+1}$ are the time intervals separating these sequences. Note that,

$\ddot{x}(t)$ reduces to the stationary case when the envelope functions are replaced with the Heaviside step functions.

The ground acceleration described in Eq. (7.1) belongs to the class of engineering ground motion models. These models aim to replicate the gross features observed in earthquake records and are used when adequate information on the source properties is not available. The seismological models, on the other hand, can be adopted when sufficient information on the source properties (e.g., fault dimension, fault depth, rupture velocity, attenuation, stress drop, density of intervening medium, etc.) is available [32–34]. Note also that, the special scenario of identical repeated acceleration sequences is obtainable from Eq. (7.1) when $e_1(t) = e_2(t) = \cdots = e_n(t)$, $\ddot{w}_1(t) = \ddot{w}_2(t) = \cdots = \ddot{w}_n(t)$ and $T_1 = T_3 = \cdots = T_{n+2}$. Additionally, when $n = 1$, the above expression reduces to the ordinary ground motion without sequences.

To proceed further, the envelope function for the ith sequence is expressed as:

$$e_i(t) = A_i(t - \sum_{i=1}^{n} T_i)\exp[-\alpha_i(t - \sum_{i=1}^{n} T_i)]; \quad \sum_{i=1}^{n+1} T_i \le t \le \sum_{i=1}^{n+2} T_i \tag{7.2}$$

where A_i and α_i are 2n positive constants that control the intensity and the non-stationarity trend of the ith acceleration sequence. The power spectral density function (PSDF) of the ith acceleration sequence can be shown to be given as [29]:

$$S_{\ddot{x}_i}(\omega, t) = e_i^2(t) S_{\ddot{w}_i}(\omega) \tag{7.3}$$

where $S_{\ddot{w}_i}(\omega)$ is the one-sided PSDF of the ith acceleration sequence $\ddot{w}_i(t)$. In this paper, the stationary components $\ddot{w}_i(t)$, $i = 1, 2, \ldots, n$ are modeled as Gaussian random processes, and, thus, the ground acceleration $\ddot{x}(t)$ is a nonstationary Gaussian random process. Therefore, $\ddot{x}(t)$ can be characterized in terms of the first two moments of its PSDF.

Equation (7.1) implies that the ground acceleration $\ddot{x}(t)$ has zero mean when the stationary components $\ddot{w}_i(t)$, $i = 1, 2, \ldots, n$ have zero mean. Moreover, the variance of the ith acceleration sequence $\ddot{x}(t)$ is given by:

$$\sigma_{\ddot{x}_i}^2(t) = e_i^2(t) \int_0^\infty S_{\ddot{w}_i}(\omega)\, d\omega \tag{7.4}$$

Note that, if the stationary components $\ddot{w}_1(t)$, $\ddot{w}_2(t)$, …, $\ddot{w}_n(t)$ have unit variance, the intensity of the sequences $\ddot{x}(t)$ can be controlled through the envelope functions. Alternatively, the envelope functions can be normalized to unit peak values and the variance of $\ddot{x}(t)$ is controlled through the variances of the stationary components. Numerical illustrations on the response of nonlinear SDOF structures to repeated acceleration sequences are provided in the next section.

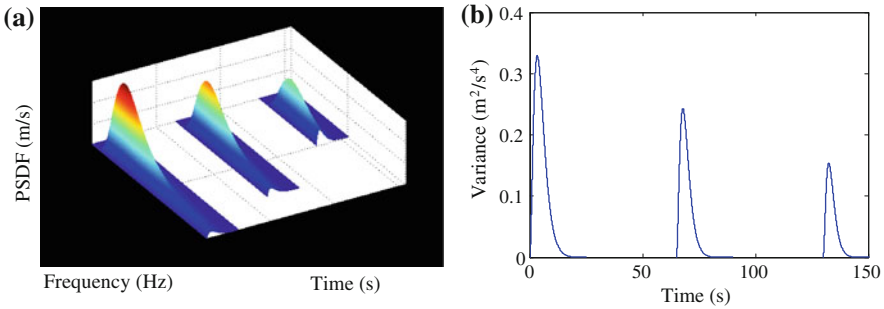

Fig. 7.4 **a** PSDF of $S(\omega, t)$, **b** Variance of $\ddot{x}(t)$ ($\omega_g = 3\pi$ rad/s, $\eta_g = 0.40$, $n = 3$) [41]

7.4 Numerical Examples

Equations (7.1–7.4) define repeated acceleration sequences that can be used as input to the probabilistic response analysis of nonlinear systems. It can also be used for simulating the input acceleration to the deterministic time-history analysis of nonlinear systems. The envelope functions can be adjusted to reflect the nonstationarity trend of past records. The stationary accelerations $\ddot{w}_1(t)$, $\ddot{w}_2(t)$, …, $\ddot{w}_n(t)$ can be adopted to replicate the frequency content and the dominant frequency of the site soil. Without loss of generality, the PSDF of the stationary components is taken to be given by the Kanai-Tajimi model. Thus, the PSDF for the ith acceleration sequence is given by [34, 35]:

$$S_{\ddot{w}_i}(\omega) = s_0 \frac{\omega_g^2 + 4\eta_g^2\omega^2\omega_g^2}{\left(\omega_g^2 - \omega^2\right)^2 + 4\eta_g^2\omega^2\omega_g^2} \tag{7.5}$$

where s_0 is the intensity of the white noise process at the rock level, ω_g is the dominant frequency of the soil site, and η_g is the associated damping ratio of the soil layer.

Figure 7.4 shows the PSDF for the ground acceleration $\ddot{x}(t)$ for medium soil site. The soil parameters are taken as $\omega_g = 3\pi$ rad/s, $\eta_g = 0.40$ and the number of acceleration sequences $n = 3$. The intensities of the acceleration sequences are taken as $s_0 = 0.02$, 0.015 and 0.01 m^2/s^3, and the associated frequency contents are (0–10), (0–8), and (0–5) Hz, respectively. The parameters of the envelope functions are adopted as $\alpha_1 = 0.30$, $\alpha_2 = 0.35$ and $\alpha_3 = 0.40$ (the time duration of the sequences is about 25, 20, and 15 s, respectively) and the separating time interval between the sequences is 40 s. The parameters A_1, A_2 and A_3 are selected so that the envelope functions have peak values of unity [see Eq. (7.2)]. Figure 7.4 shows also the variance of the ground acceleration. Figure 7.5 depicts a sample of the simulated ground acceleration $\ddot{x}(t)$.

The response of nonlinear SDOF structures to random acceleration sequences is studied below.

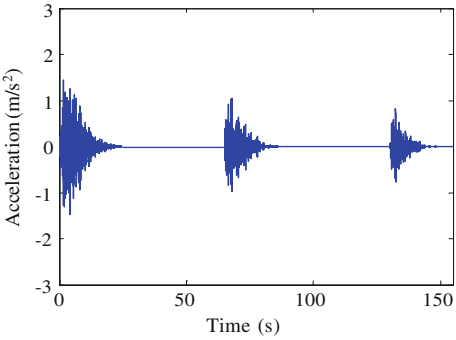

Fig. 7.5 Sample simulated acceleration sequences ($\omega_g = 3\pi\,\text{rad/s}, \eta_g = 0.40, n = 3$) [41]

7.4.1 Response of Elastic–Plastic Structure to Nonstationary Random Acceleration Sequences

The response of an SDOF elastic–plastic structure driven by the ground acceleration $\ddot{x}(t)$ described by the PSDF shown in Fig. 7.4a is studied. The first two sequences are only considered. The structure parameters are taken as $m = 9 \times 10^4$ kg, $k_0 = 9 \times 10^4$ N/m, the yield force $= 1 \times 10^4$ N, and the yield displacement $= 0.11$ m. A viscous damping of 0.03 damping ratio is adopted. Given that, the structure is inelastic and that the input acceleration is a Gaussian random process of zero mean, the structural response $u(t)$ is a non-Gaussian random process of nonzero mean. The structural inelastic response is computed using the Newmark integration technique and the Monte Carlo Simulation with 2,000 samples. The structural response is characterized in terms of the earthquake input energy E_I, the hysteretic yield energy E_H, the ductility demand μ and the Park and Ang damage index D_{PA}. These quantities are given as [36–38]:

$$E_I(t) = -\int_0^t m\ddot{x}(\tau)\dot{u}(\tau)d\tau \tag{7.6a}$$

$$E_H(t) = \int_0^t \dot{u}(\tau)f_s(\tau)d\tau - [f_s(t)]^2 \tag{7.6b}$$

$$D_{PA} = \frac{\mu_{max}}{\mu_u} + \beta\frac{E_H/(f_y u_y)}{\mu_u} \tag{7.6c}$$

where m is the mass, $\ddot{x}(t)$ is the external acceleration, $\dot{u}(t)$ is the velocity response, $f_s(t)$ is the restoring force in the spring. Furthermore, f_y, u_y are the yield force and yield displacement, μ_u is the ultimate ductility capacity under monotonic loading, and β is a positive constant that weights the effect of cyclic loading on structural

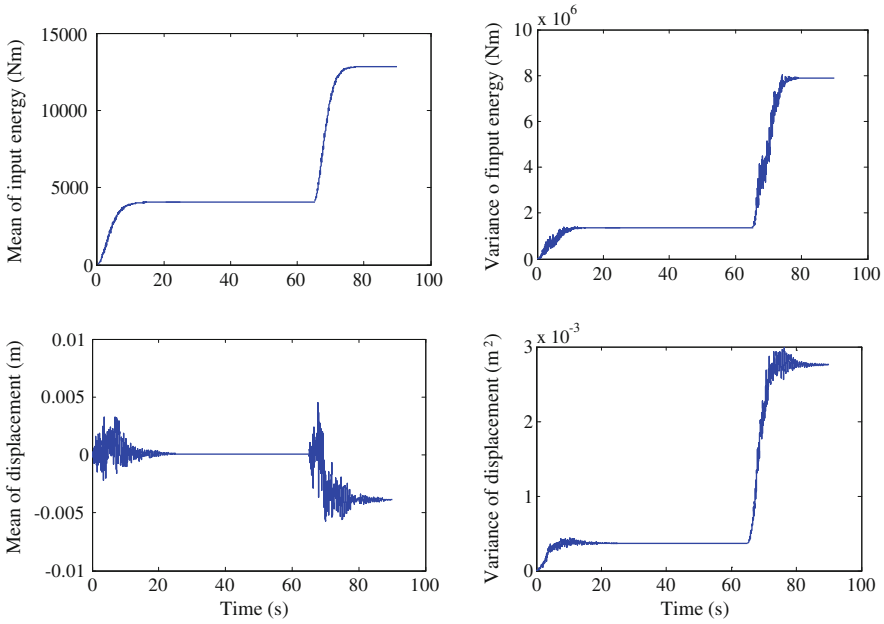

Fig. 7.6 Mean of response quantities for elastic–plastic structure to ground acceleration of three sequences [41]

damage. Note that, $\beta = 0$ implies that the contribution to DPA from cyclic loading is omitted.

Figure 7.6 shows the mean and variance of the input energy and displacement response. The mean of the damage index and hysteretic energy dissipated by damping is shown in Fig. 7.7. These plots reveal the significant influence of the secondary sequence on the structural response. For example, the mean of the maximum displacement response increases by about 25 % while that for the damage index increases from 0.24 (repairable damage) to about 1.0 (total collapse) due to the presence of the second sequence [39]. Similar effects on the input and hysteretic energy can be observed (see Fig. 7.7).

7.4.2 Reliability of Nonlinear SDOF System to Random Acceleration Sequences

This example investigates the response of SDOF nonlinear systems with cubic force-deformation relation to random earthquake sequences. The ground acceleration is modeled as a stationary random process of two repeated sequences. The structure's response is estimated using the equivalent linearization method [34].

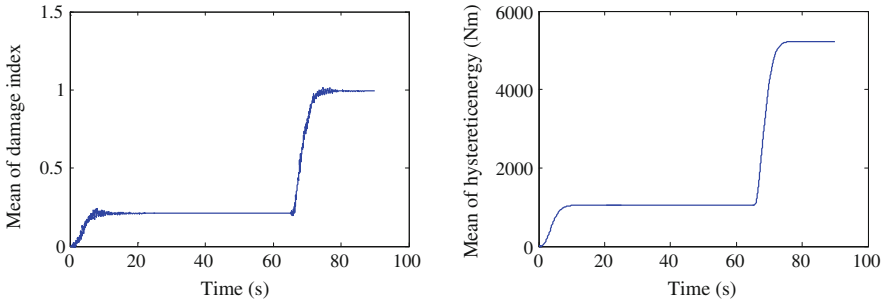

Fig. 7.7 Mean of response quantities for elastic–plastic structure to ground acceleration of three sequences [41]

To do this, it is first noted that, the equation of motion for the displacement response $u(t)$ is given as:

$$\ddot{u}(t) + 2\eta_{\mathrm{n}}\omega_{\mathrm{n}}\dot{u}(t) + \omega_{\mathrm{n}}^2[u(t) + \gamma u^3(t)] = -\ddot{x}(t) \tag{7.7}$$

where η_{n} and ω_{n} are the damping ratio and the initial natural frequency of the nonlinear system. The equation of motion for the equivalent linear system is given by:

$$\ddot{y}(t) + 2\eta_{\mathrm{eq}}\omega_{\mathrm{eq}}\,\dot{y}(t) + \omega_{\mathrm{eq}}^2\,y(t) = -\ddot{x}(t) \tag{7.8}$$

Herein, η_{eq} and ω_{eq} are the equivalent damping ratio and the equivalent natural frequency for the linear structure. These parameters are obtained by minimizing the mean square error of the responses from Eqs. (7.7) and (7.8) and can be shown to be given by:

$$\omega_{\mathrm{eq}} = \omega_{\mathrm{n}}\sqrt{1 + \frac{6\gamma}{\sqrt{\pi}}\sigma_{\mathrm{y}}^2\Gamma\left(\frac{3}{2}\right)}; \quad \eta_{\mathrm{eq}} = \frac{\omega_{\mathrm{n}}}{\omega_{\mathrm{eq}}}\eta_{\mathrm{n}} \tag{7.9}$$

where σ_y^2 is the response variance and $\Gamma(.)$ is the gamma function. Note that, the estimation of the parameters η_{eq} and ω_{eq} involves iterative calculation of the response variance σ_y^2 until a convergence criterion is satisfied. In the numerical calculation, the intensities of the acceleration sequences are taken as 0.03 and 0.03 $\mathrm{m}^2/\mathrm{s}^3$ and the frequency contents are (0–10) and (0–5) Hz, respectively. The soil type is taken as soft soil with $\omega_{\mathrm{g}} = \pi\,\mathrm{rad/s}$ and $\eta_{\mathrm{g}} = 0.20$.

The parameters of the SDOF structure are taken as $m = 9 \times 10^4$ kg, $\omega_{\mathrm{n}} = 6.28\,\mathrm{rad/s}$. Figure 7.8a shows the PSDF of the displacement response for the linear and the equivalent linear systems from the first acceleration sequence ($\gamma = 1.0$). The influence of the nonlinear parameter γ on the PSDF of the displacement response is shown in Fig. 7.8b. It can be seen that, as γ increases the equivalent natural frequency increases while the peak value of the PSDF decreases. The

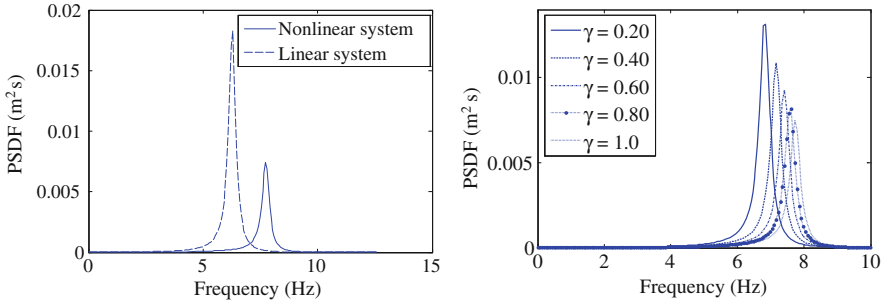

Fig. 7.8 PSDF for the displacement response for SDOF with cubic force-deformation relation under the first sequence of a random ground acceleration [41]

response variance σ_y^2 from the first and the second acceleration sequences is computed as 0.03 and 0.04 m2, respectively.

To assess the reliability of the system considered, the structural failure probability is estimated. Since the input acceleration is a Gaussian process and the nonlinear system is replaced with the equivalent linear system, any response quantity of the structure (e.g., displacement or a linear transformation of the displacement) is approximated by a Gaussian process. Following standard reliability terminology, the structural response $L(t)$ which is a time-variant quantity is denoted as the "load effect." The associated capacity or resistance of the structure (e.g., maximum permissible displacement or stress) is denoted by R. The determination of the structural failure probability constitutes a time-variant reliability problem, given as:

$$P_f = \int_0^\infty P_R(l) p_{L_m}(l) dl \tag{7.10}$$

where $P_R(r)$ is the probability distribution function of the capacity R and $p_{L_m}(l)$ is the probability density function of the load effect $L_m = \max_{0<t<T_d} |L(t)|$ (T_d is the duration of the ground motion).

Let the load effect be the force in the spring of the equivalent linear system $L_m = k_{eq}\, y(t)$ where $y(t)$ is the displacement. The structural capacity R is defined as the maximum permissible yield force in the spring, modeled as a normal random variable with $\mu_R = 6.0 \times 10^4$ N, and $\sigma_R = 6.0 \times 10^3$ N. Assuming that, the ground motion is modeled by Eq. (7.1) with the envelope function taken as the Heaviside step functions $H_1(t)$, $H_2(t)$ and making use of the extreme value distribution for stationary normal random processes, $p_{L_m}(l)$ can be shown to be given as [40]:

$$p_{L_m}(l) = \frac{N_0^+ l T_d}{k^2 \sigma_{0L}^2} \exp\left[-\frac{l^2/k^2 + 2N_0^+ T_d \sigma_{0L}^2 \exp(-l^2/(2k^2\sigma_{0L}^2))}{2\sigma_{0L}^2} \right]; \quad 0 \le l \le \infty \tag{7.11}$$

Herein, N_0^+ is the average rate of zero crossing of the response process $L(t)$ given as $N_0^+ = \sqrt{\sigma_{2L}^2/\sigma_{0L}^2}/(2\pi)$, in which, σ_{0L}^2 and σ_{2L}^2 are the zero and the second spectral moments of $L(t)$. These moments are given in terms of the PSDF of the ground acceleration as:

$$\sigma_{iL}^2 = \int_0^\infty \omega^i |H_L(\omega)|^2 S_{\ddot{x}}(\omega) d\omega; \quad i = 0, 2 \tag{7.12}$$

where $H_L(\omega)$ is the frequency response function for $L(t)$. The probability of failure under the two acceleration sequences was computed to be 3.14 and 4.21 $\times$ 10^{-3}, respectively. Note that, the failure probability from the second sequence is larger than that from the first sequence. This could be attributed to the narrow frequency content of the second sequence compared to the relatively wider frequency content of the first sequence.

Strong ground motion of multiple sequences has been considered in this study. The occurrence of ground accelerations of repeated sequences does not depend on the soil type beneath the recording station or on the site source distance but on the source properties. Accordingly, earthquake records recorded at different soil conditions and site source distance have been considered in this study. It may be noted that recorded ground motion sequences at a site depend on the source properties, the path effects and also on the amplification of the amplitude, and frequency of the seismic waves resulting from the local soil type. Accordingly, the associated structural inelastic response under repeated ground motion sequences could be significantly influenced by the amplification of the seismic waves at sites of soft soils. Finally, it may be emphasized that the stochastic ground motion of Eqs. (7.1–7.4) can be combined with standard reliability methods (e.g., FORM, SORM, importance sampling technique and response surface method) to assess the safety of inelastic structures to repeated acceleration sequences. In this case, the exact evaluation of the structure's failure probability is not obtainable in a closed form as in Eq. (7.10), but the theory of reliability indices can be used to provide an estimate of the notional failure probability for the structure.

7.5 Summary

Most previous studies have focused on the response analysis of inelastic structures to repeated acceleration sequences. This paper has investigated the response of nonlinear SDOF systems to random ground motion of repeated sequences. A novel point of the paper is the combination of the theory of statistical linearization with structural reliability analysis to assess the structural safety of inelastic structures. A simple stochastic model for representing strong ground sequences is proposed in this paper. The ground acceleration is represented as a product of a stationary Gaussian random processes and an envelope function of repeated character.

Numerical examples on the response analysis of nonlinear SDOF structures are provided. The proposed acceleration model combined with structural reliability methods (FORM, SORM, Importance Sampling Techniques, Monte Carlo Simulation, and Response Surface Method) can be used in assessing the safety of engineering structures under repeated ground motion sequences. The model can also be used in simulating the acceleration sequences as input to the nonlinear time history analysis of structures.

The representation of repeated ground accelerations proposed in this paper belongs to the class of engineering models. Seismological models that are based on attenuation of the seismic waves at the source could also be developed when adequate information on the source properties is available.

References

1. Ghobara A (2001) Performance-based design in earthquake engineering: state of development. Review article. Eng Struct 23:878–884
2. SEAOC, Vision Committee (2002) Performance based seismic design engineering. Sacramento, USA: structural engineers association of California (SEAOC) report
3. Architectural Institute of Japan (2004) Recommendations for loads on buildings. AIJ, Tokyo
4. European Committee for Standardization (2003) Eurocode 8: design of structures for earthquake resistance. Brussels
5. International Building Code (2009) International code council Inc, USA
6. Eberhard M, Baldridge S, Marshall J, Mooney W, Rix G (2010) The Mw 7.0 Haiti earthquake of January 12, 2010. USGS/EERI advance reconnaissance team: team report V 1.0
7. Kyoshin-Net (2009) National research institute for earth science and disaster prevention. Available at http://www.k-net.bosai.go.jp/. Accessed June 2009
8. PEER (2005) Pacific earthquake engineering research center. (http://peer.berkeley.edu)
9. Elnashai A, Bommer JJ, Martinez-Pereira A (1998) Engineering implications of strong-motion records from recent earthquakes. In: Proceedings of 11th european conference on earthquake engineering, Paris, CD-ROM
10. Amadio C, Fragiacomo M, Rajgelj S (2003) The effects of repeated earthquake ground motions on the non-linear response of SDOF systems. Earthq Eng Struct Dyn 32:291–308
11. Fragiacomo M, Amadio C, Macorini L (2004) Seismic response of steel frames under repeated earthquake ground motions. Eng Struct 26(2021):2035
12. Das S, Gupta VK, Srimahavishnu V (2007) Damage-based design with no repair for multiple events and its sensitivity to seismicity model. Earthq Eng Struct Dyn 36:307–325
13. Hatzigeorgiou GD, Beskos DE (2009) Inelastic displacement ratios for SDOF structures subjected to repeated earthquakes. Eng Struct 31(11):2744–2755
14. Hatzigeorgiou GD (2010) Ductility demand spectra for multiple near- and far-fault earthquakes. Soil Dyn Earthq Eng 30(4):170–183
15. Hatzigeorgiou GD, Liolios AA (2010) Nonlinear behaviour of RC frames under repeated strong ground motions. Soil Dyn Earthq Eng 30:1010–1025
16. Hatzigeorgiou GD (2010) Damping modification factors for SDOF systems subjected to near-fault, far-fault and artificial earthquakes. Earthq Eng Struct Dyn 39(11):1239–1258
17. Moustafa A, Takewaki I (2012) Earthquake ground motion of multiple sequences and associated structural response. Earthq Struct 3(3) (in press)
18. Dunbar WS, Charlwood RG (1991) Empirical methods for the prediction of response spectra. Earthq Spectra 7(3):333–353

19. Shcherbakov R, Turcotte DL, Rundle JB (2005) Aftershock statistics. Pure Appl Geophys 162:1051–1076
20. Yeo GL, Cornell CA (2009) Post-earthquake decision analysis using dynamic programming. Earthq Eng Struct Dyn 38:79–93
21. Yeo GL, Cornell CA (2009) A probabilistic framework for quantification of aftershock ground-motion hazard in California: methodology and parametric study. Earthq Eng Struct Dyn 38:45–60
22. Lin YK, Yong Y (1987) Evolutionary Kanai-Tajimi earthquake models. J Eng Mech 113(8):1119–1137
23. Shinozuka M, Deodatis G (1988) Stochastic process models for earthquake ground motion. J Prob Eng Mech 3:114–123
24. Spanos PD (1987) Recursive simulation of stationary multivariate random processes—part II. J. Appl Mech ASME 54:681–687
25. Conte JP, Peng BF (1997) Fully nonstationary analytical earthquake ground-motion model. J Eng Mech 123(1):15–24
26. Der Kiureghian A, Crempien J (1989) An evolutionary model for earthquake ground motion. Struct Saf 6:235–246
27. Shinozuka M, Deodatis G (1991) Simulation of stochastic processes by spectral reprezentation. App Mech Rev 44(4):191–204
28. Shinozuka M, Deodatis G (1996) Simulation of multi-dimensional Gaussian stochastic fields by spectral representation. App Mech Rev 49(1):29–53
29. Takewaki I (2007) Critical excitation methods in earthquake engineering. Elsevier, Amsterdam, pp 1–22
30. Kanai K (1957) Semiempirical formula for the seismic characteristics of the ground. Bulletin of Earthquake Research Institute, University of Tokyo 35:309–325
31. Tajimi H (1960) A statistical method of determining the maximum response of a building structure during earthquakes. In: Proceedings second WCEE, Tokyo, 2:781–797
32. Boore DM (1983) Stochastic simulation of high-frequency ground motions based on seismological models of the radiated spectra. Bull Seism So Amer 73:1865–1894
33. Brune JN (1970) Tectonic stress and the spectra of seismic shear waves from earthquakes. J Geoph Res 75:4997–5009
34. Quek ST, Teo YP, Balendra T (1990) Non-stationary structural response with evolutionary spectra using seismological input model. Earthq Eng Struct Dyn 19:275–288
35. Roberts JB, Spanos PD (1990) Random vibration and statistical linearization. Wiley, Chichester
36. Akiyama H (1985) Earthquake-resistant limit-state design for buildings. University of Tokyo Press, Tokyo
37. Zahrah TF, Hall WJ (1984) Earthquake energy absorption in sdof structures. J Struct Eng 110:1757–1772
38. Uang CM, Bereto VV (1990) Evaluation of seismic energy in structures. Earthq Eng Struct Dyn 19:77–90
39. Park YJ, Ang AH-S (1985) Mechanistic seismic damage model for reinforced concrete. J Struct Eng 111(4):722–739
40. Abbas AM, Manohar CS (2005) Reliability-based critical earthquake load models. Part 1: linear structures. J Sound Vib 287:865–882
41. Moustafa A, Takewaki I (2011) Response of nonlinear single-degree-of-freedom structures to random acceleration sequences. Eng Struct 33:1251–1258

Chapter 8
Use of Deterministic and Probabilistic Measures to Identify Unfavorable Earthquake Records

8.1 Introduction

The robust design of structures toward earthquake loads is the key for the mitigation of the structure damage against earthquake hazards. The structural engineer aims to design structures that are safe against possible future earthquakes and economic at the same time. The selection of suitable design earthquake loads for structural design is the first step to achieve this goal. The use of accurate nonlinear model describing the inelastic behavior of the structure is the second step to achieve this goal. Earthquake loads can be specified for seismic design of structures using the response spectrum method, using recorded accelerograms, or using the random vibration theory. The method of the critical excitation has been developed in the literature for specifying mathematical earthquake loads on structures. The works of Takewaki [1, 2] and Abbas [3, 4] provide extensive overviews on this method. The critical or most unfavorable earthquake load for a given structure is derived by solving an inverse dynamic optimization problem subject to predefined constraints reflecting known information on the seismic data at the site. These earthquake loads are tailor-made to produce the maximum structural response and are thus termed critical or worst-case input.

Many studies have attempted to identify unfavorable real ground motion records [5, 6, 7, 8, 9, 10]. For instance, Anderson and Bertero [6] studied implications of adjusted earthquake records on the maximum structural responses produced by near-fault ground motions. Takewaki [8] used the critical excitation method to quantify resonance and criticality of earthquake records for a given structure by comparing the structural response produced by the critical input and that from the earthquake record. Amiri and Dana [5] used the effective peak ground velocity to identify resonant records at a given site. Dhakal et al. [7] utilized probabilistic methods to identify critical earthquake records by relating them to the maximum design earthquake. The study by Zhai and Xie [10] employs the critical excitation concept to identify most unfavorable earthquake records for structures of known frequency

I. Takewaki et al., *Improving the Earthquake Resilience of Buildings*,
Springer Series in Reliability Engineering, DOI: 10.1007/978-1-4471-4144-0_8,

range. A resonant ground motion possesses a narrow frequency content leading to its energy being contained in one or a few pulses. Such an input is capable of producing the highest response among other inputs if the resonant or dominant frequency is close to the structure fundamental frequency. In this chapter, the term "resonant ground motion" implies that the energy of the ground motion is concentrated in a single or a few frequencies. This, in turn, implies that the ground motion has a narrow frequency content or of pulse-like characteristics.

In the context of earthquake engineering, Abbas [3] and Abbas and Manohar [11, 12] examined the significance of incorporating a lower bound on the entropy rate of the ground acceleration in deriving critical random earthquake load models. These authors proved the significance of the entropy rate constraint quantified from actual recorded accelerograms in producing realistic earthquake loads that are rich in frequency content.

In this chapter, the notion of the critical excitation method and the random vibration theory are employed to introduce measures for identifying resonant or unfavorable earthquake records among a set of records. The first measure is based on the concept of the entropy of random processes. The second measure is the dispersion index of the power spectral density function (PSDF) of the ground acceleration and is based on the work of Vanmarcke [13, 14]. Deterministic measures of the frequency content of the ground acceleration are also developed. These measures can provide a basis for the selection of proper design earthquake records for structures. The numerical illustrations demonstrate the identification of resonance in random process and 110 earthquake records at various soil sites.

The following section explains a new measure using the entropy rate for identifying resonance in random processes. Subsequently, the dispersion index and central frequency measures developed by Vanmarcke [13] are discussed. The use of these measures to identify resonant earthquake records is then demonstrated. The development of deterministic measures for identifying frequency content of ground motions is explained. The last section illustrates the use of these measures for the selection of suitable acceleration records for seismic design of structures.

8.2 Use of Entropy as a Measure of Resonance/Criticality of Probabilistic Earthquake Models

The use of entropy to measure the amount of information in random signals sent along a transmission line was proposed by Shannon [15]. This idea has been advocated as being a general principle of statistical inference and has been used in the broad field of science, engineering, and economics. The literature on the use of entropy in engineering is vast (see, e.g., [16, 17]). Entropy in its basic form is a measure of uncertainty or missing information. For example, the entropy of a random variable x is a measure of the uncertainty associated with that random variable, which is given in terms of the probability density function $p(x)$ and is given in the following form [17]:

$$H_x = \int_{-\infty}^{\infty} p(x) \ln p(x) dx \tag{8.1}$$

When the quantity H_x is large, the uncertainty as to the value of x is also large. For instance, the entropy of a normal random variable of 'large coefficient of variation' is also large. Note that, when the coefficient of variation is significantly large, the normal distribution can approximate the uniform distribution that possesses the largest entropy among all distributions. On the other hand, when the coefficient of variation is very small, the distribution may approximate a deterministic quantity which possesses zero entropy.

The use of entropy rate in earthquake engineering to model critical earthquake loads was introduced by Manohar and Sarkar [18], Abbas [3], Abbas and Manohar [11, 12]. These studies proved the crucial role of including the entropy in producing realistic critical earthquake loads. The entropy rate of a zero-mean stationary Gaussian random process $\ddot{u}(t)$ is given as [17]:

$$H = \ln \sqrt{2\pi e} + \frac{1}{2(\omega_u - \omega_0)} \int_{\omega_0}^{\omega_u} \ln S(\omega)\, d\omega \tag{8.2}$$

In Eq. (8.2), (ω_0, ω_u) and $S(\omega)$ define the frequency range and the one-sided PSDF of the ground acceleration. The constant $\ln \sqrt{2\pi e}$ (e: natural number) represents a reference level from which the entropy rate is measured. It can be understood from Eq. (8.2) that the entropy rate of a stationary Gaussian process is constant. Thus, when the entropy rate of $\ddot{u}(t)$ is large, the uncertainty as to the value of $\ddot{u}(t)$ at discrete time instants is also large. On the other hand, the entropy of a harmonic signal with a random amplitude and a single or very few frequencies (e.g., $\ddot{u}(t) = A \sin(\omega_g t)$) is almost zero. In other words, the energy of the signal or the amplitude of the Fourier transform of a sine or a cosine time series of a single or very few frequencies is well ordered in the frequency range (ω_0, ω_u) while a time signal composed of several frequencies will be disordered. Note that two random processes with the same energy (same area under the PSDF) need not possess the same entropy. This is because entropy depends on the frequency bandwidth and the spectral amplitude of the PSDF [Eq. (8.2)]. To gain more insights into the use of entropy in characterizing ground motions, the entropy of probabilistic models of Gaussian ground motion models will be derived in the following sections.

8.2.1 Stationary Narrow-Band White Noise Model

The narrow-band random process has been used extensively as an idealization for random signals, noises, turbulences, and earthquakes (see, for example, [19, 20]). Consider a stationary narrow-band signal of intensity s_0 and central frequency ω_c. Then, Eq. (8.2) leads to:

$$H = \frac{\ln s_0}{2(\omega_u - \omega_0)} \tag{8.3}$$

As seen from Eq. (8.3), the parameters s_0, ω_0, ω_u define the entropy of the narrow-band signal. Note that the term $\ln \sqrt{2\pi e}$ of Eq. (8.2) was omitted.

8.2.2 Stationary Band-Limited White Noise Model

The band-limited white process has been frequently used as an approximation for earthquake and wind loads. This process possesses finite energy, constant spectral amplitude in the frequency range (ω_0, ω_u). Thus, Eq. (8.2) leads to:

$$H = \frac{\ln s_0}{2} \tag{8.4}$$

Therefore, the spectral parameter s_0 defines the entropy of the band-limited process. It can be observed from Eqs. (8.3) and (8.4) that entropy of the band-limited ground acceleration model is significantly larger than that of the narrow-band acceleration model.

8.2.3 Stationary Kanai-Tajimi Model

This model has been widely used in modeling strong ground motions in seismic resistant design of structures and infrastructures [21, 22]. The PSDF of the ground acceleration is obtained by passing a band-limited white noise through a filter that represents the soil layer above the bedrock, given by

$$S(\omega) = s_0 \frac{\omega_g^4 + 4\eta_g^2 \omega_g^2 \omega^2}{\left(\omega_g^2 - \omega^2\right)^2 + 4\eta_g^2 \omega_g^2 \omega^2} \tag{8.5}$$

where s_0, η_g, ω_g are the intensity of the PSDF at the rock level, damping, and frequency of the soil layer, respectively. The entropy of the Kanai-Tajimi model can be estimated numerically instead of integrating Eq. (8.2) analytically.

8.2.4 Nonstationary and Evolutionary PSDF Models

Different earthquake acceleration models have been developed and proposed in the literature to account for nonstationarity in time and frequency content. This class of earthquake models is known as evolutionary PSDF models (see [20]). Herein, the PSDF of the ground acceleration is a function of time and frequency and is represented by

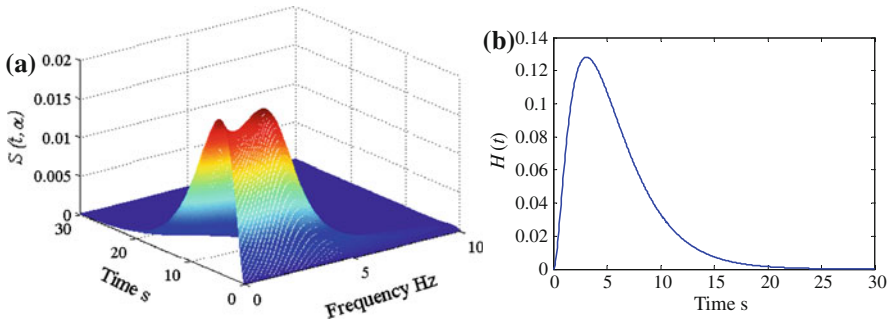

Fig. 8.1 **a** Evolutionary Kanai-Tajimi PSDF, **b** Entropy function (Moustafa and Takewaki [23] with permission from Springer)

$$S(t,\omega) = |A(t,\omega)|^2 S(\omega) \tag{8.6}$$

In Eq. (8.6) $A(t,\omega)$ is a modulating envelope that could be a complex function and $S(\omega)$ is a stationary PSDF. When $A(t,\omega)$ is separable into a time function and a frequency function, the model reduces to the uniformly modulated nonstationary random process which possesses invariable PSDF at all time instants. Accordingly, the entropy is constant and the computation follows the same procedures for stationary acceleration models.

Consider the ground acceleration defined by the Kanai-Tajimi PSDF of Eqs. (8.5) and (8.6) with $A(t,\omega)$ given by

$$A(t,\omega) = e(t)g(t,\omega) = A_0[e^{-\alpha t} - e^{-\beta t}]\, e^{\left(\frac{-r\,\omega\, t}{\omega_m\, t_m}\right)} \tag{8.7}$$

In Eq. (8.7) $A_0, \alpha, \beta, r, \omega_m, t_m$ are constants. Herein, the quantification of the entropy can be carried out using numerical integration of the evolutionary PSDF at discrete points of time. Figure 8.1 shows the evolutionary PSDF of the ground acceleration and the associated entropy function for $A_0 = 2.87$, $\alpha = 0.13$, $\beta = 0.35$, $r = 1.0$, $\omega_m = 5.0$ Hz, and $t_m = 5.0$ s.

The above sections explained the quantification of the entropy rate for probabilistic earthquake models. It is shown that the entropy for stationary and uniformly modulated random processes is constant. Additionally, the entropy rate of the band-limited acceleration is significantly larger than that of the narrow-band acceleration. We explain the quantification of the relative entropy of two random processes in the following section.

8.2.5 Relative Entropy Rate of Two Random Processes

To compare the entropy from alternative acceleration models, we measure the entropy of the random process $\ddot{u}(t)$ with reference to a wide-band signal $\ddot{z}(t)$ of spectral intensity s_0. This is known as the relative entropy of two random

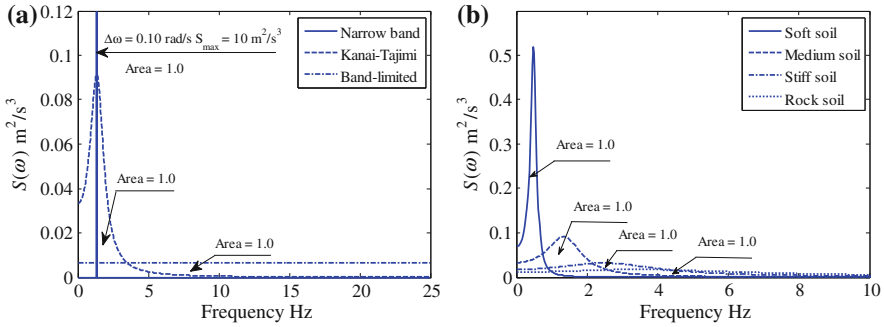

Fig. 8.2 **a** PSD function for ground acceleration models for medium soil, **b** Kanai-Tajimi PSD function for different soil types (Moustafa and Takewaki [23] with permission from Springer)

processes. Thus, under the assumption that $\ddot{u}(t)$ is independent of $\ddot{z}(t)$, the increase in entropy when $\ddot{u}(t)$ is added to $\ddot{z}(t)$ is given by the following expression:

$$\Delta H = \frac{1}{2(\omega_u - \omega_0)} \int_{\omega_0}^{\omega_u} \ln\left[1 + \frac{S(\omega)}{s_0}\right] d\omega \tag{8.8}$$

Let us calculate the entropy index ΔH for the narrow-band, the Kanai-Tajimi and the band-limited acceleration models, described above, from a reference wide-band signal of intensity 0.02 m^2/s^3. The PSDF for each of these three models is normalized so that they possess unit area (see Fig. 8.2). This normalization implies equality of the earthquake energy of the three models [24]. The parameters ω_g, η_g of the Kanai-Tajimi model are taken as π rad/s, 0.20 for soft soil, 3π rad/s, 0.40 for medium soil, 6π rad/s, 0.60 for stiff soil, and 9π rad/s, 0.80 for rock soil (see, Table 8.1). In addition, the spectral intensity at the rock level is taken as $s_0 = 0.02$ m^2/s^3 and the central frequency of the narrow-band signal is taken as $\omega_g = \pi, 3\pi, 6\pi, 9\pi$ rad/s for soft, medium, stiff, and rock soil, respectively. The numerical results are shown in Table 8.1. Based on careful examination of these results, the following observations can be drawn.

1. The narrow-band acceleration possesses the smallest entropy. In other words, the PSDF of this model is well ordered or the acceleration energy is concentrated at a single frequency. Note that the central frequency of the acceleration does not influence the entropy [see Table 8.1 and Eq. (8.3)]. Thus, the entropy of narrow-band signals with the same energy is invariant regardless of the central frequency
2. The band-limited acceleration possesses the highest entropy among all models. This is because the energy of the process is well represented at all frequencies
3. The Kanai-Tajimi acceleration is significantly disordered. This is expected since the PSDF is reasonably distributed across a significant frequency range (see Fig. 8.2a). The entropy for soft soil is small compared with that for rock soil. This is not surprising since the PSDF for soft soil is narrow-band while that for rock soil is distributed across a wider frequency range (see Fig. 8.2b).

Table 8.1 Resonance measures for alternative earthquake models and different soil types (Moustafa and Takewaki [23] with permission from Springer)

Earthquake model	Soil type							
	Soft soil		Medium soil		Stiff soil		Rock soil	
	Entropy index	Bandwidth factor	Entropy index	Bandwidth factor	Entropy index	Bandwidth factor	Entropy index	Bandwidth factor
Narrow-band[a]	0.0294	0.0785	0.0294	0.0785	0.0294	0.0785	0.0294	0.0785
Kanai-Tajimi[b]	0.2122	4.0869	0.4080	14.7227	0.5228	26.2513	0.5704	34.1420
Band-limited	0.6040	45.2997	0.6040	45.2997	0.6040	45.2997	0.6040	45.2997
1992 Cape Mend. (Petrolia)	-	-	0.3215	5.7164	-	-	-	-

[a] $\omega_c = \pi, 3\pi, 6\pi, 9\pi$ for soft, medium, stiff, and rock soil, respectively

[b] $\omega_g = \pi, 3\pi, 6\pi, 9\pi$ and $\eta_g = 0.20, 0.40, 0.60, 0.80$ for soft, medium, stiff, and rock soil, respectively

4. The entropy of the Kanai-Tajimi model is bounded between the entropy of the narrow-band acceleration and that from the band-limited acceleration for all soil conditions (see Table 8.1). This result is interesting since it provides lower and upper bounds on the entropy of the Kanai-Tajimi acceleration model

Earthquake records often possess amplitude distributed across a significant frequency range. This is because the energy released at the source gets amplified and filtered by the soil layer above the rock level due to site and attenuation effects caused by soil damping, geometric spreading, wave scattering, and local soil profile. As discussed above, real accelerograms, however, exhibit the resonance trend. Accordingly, the associated frequency range is narrow which can be characterized in terms of the entropy rate.

This section explained the use of entropy rate as a measure of the frequency content of probabilistic earthquake models. It is shown that the narrow-band and the band-limited signals provide lower and upper bounds on the entropy of the Kanai-Tajimi model. The entropy of recorded accelerograms will be estimated in the following section.

8.3 Dispersion Index and Central Frequency

Vanmarcke [13, 14] introduced important measures for the frequency content of the ground acceleration in terms of the geometric properties or the moments of the PSDF. These measures are briefly outlined here. The ith moment of $S(\omega)$ is given by

$$\lambda_i = 2\int_0^\infty \omega^i S(\omega) d\omega; \quad i = 0, 1, \ldots, n \tag{8.9}$$

The zeroth moment defines the energy and the second moment defines the variance of the velocity process. The ith frequency is defined by

$$\omega_i = \left(\frac{\lambda_i}{\lambda_0}\right)^{\frac{1}{i}}; \quad i = 1, 2, \ldots, n \tag{8.10}$$

Here $\omega_1 = \omega_c$ is the central frequency of the ground acceleration and ω_2 indicates where the spectral mass of the PSDF is located along the frequency range. The radius of gyration of $S(\omega)$ about the frequency origin ω_c is given by the following form [13, 14]:

$$\omega_s = \sqrt{\omega_2^2 - \omega_1^2} \tag{8.11}$$

In Eq. (8.11) ω_s is a measure of dispersion of the PSDF about the central frequency. Thus, when ω_s is small, it implies that the ground acceleration is narrow-band and when ω_s is large, the ground acceleration is broadband or rich in

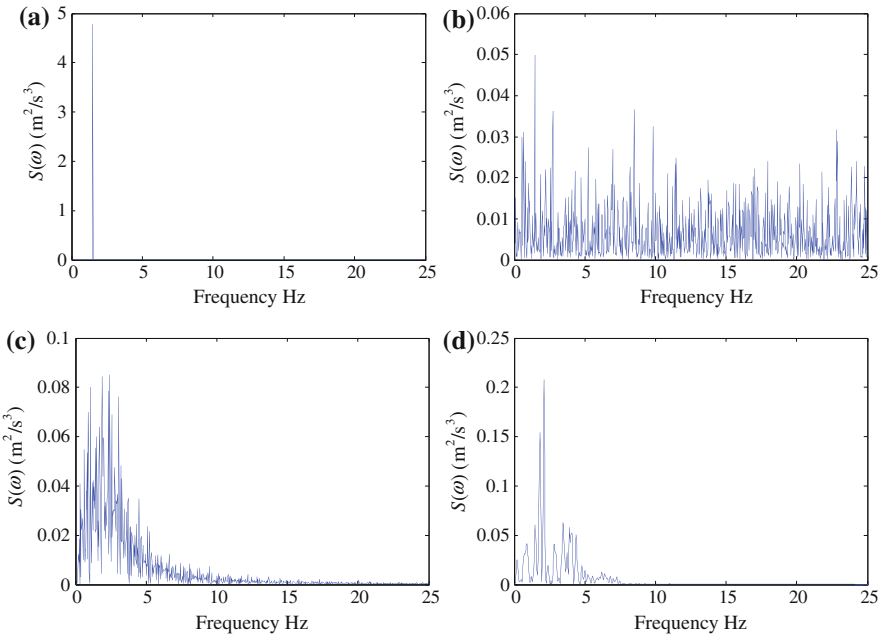

Fig. 8.3 PSD function for ground acceleration **a** narrow-band, **b** band-limited, **c** Kanai-Tajimi, **d** 1992 Cape Mendocino (Petrolia) earthquake (Mostafa and Takewaki [23] with permission from Springer)

frequency content. Table 8.1 summarizes the dispersion index for narrow-band, Kanai-Tajimi, and band-limited random processes defined above. The numerical values of the parameters of these models are given in the same table. It is evident from these results that the narrow-band and the band-limited models provide lower and upper bounds on the dispersion index of the Kanai-Tajimi model. The following section explains how to use the measures developed in this section and the previous section for identifying resonant earthquake records.

8.3.1 Use of Entropy Rate and Dispersion Index to Measure Resonance of Earthquake Records

Consider an actual recorded earthquake acceleration $\ddot{x}(t)$ that is represented by

$$\ddot{x}(t) = e(t)\ddot{u}(t) = A_0[e^{-\alpha t} - e^{-\beta t}]\,\ddot{u}(t) \tag{8.12}$$

Herein $\ddot{u}(t)$ is a steady-state function and $e(t)$ is an envelope function that defines and characterizes the nonstationarity of $\ddot{x}(t)$. The envelope parameters A_0, α and β can be estimated by matching the transient trend of the recorded

earthquake acceleration. Subsequently, the stationary part $\ddot{u}(t)$ can be obtained by dividing $\ddot{x}(t)$ by $e(t)$. The PSDF of $\ddot{u}(t)$ can then be calculated. This is followed by the estimation of the entropy using Eq. (8.8).

Figure 8.3 shows the PSDFs for four ground acceleration models. The first acceleration represents a sample narrow-band pseudo-sinusoidal signal $\ddot{x}(t) = e(t)A \sin \omega_g t$, with random amplitude A, and central frequency $\omega_g = 3\pi$ (medium soil). The second acceleration represents a sample of a band-limited model, $\ddot{x}(t) = e(t) \sum_{i=1}^{N} \{A_i \cos(\omega_i t) + B_i \sin(\omega_i t)\}$, where A_i and B_i are uncorrelated normal random variables of variance s_0. The third signal is an acceleration simulated from the Kanai-Tajimi model of Eq. (8.5) for the medium soil ($\omega_g = 3\pi$ rad/s; $\eta_g = 0.40$). The fourth acceleration represents the first horizontal acceleration of the 1992 Cape Mendocino (Petrolia) earthquake measured at medium soil site [25]. The stationary components $\ddot{u}(t)$ for the first three models are modulated by the envelope function that matches the transient trend of the actual record and all accelerations are normalized to unit intensity.

The relative entropy for these accelerations from a wide-band acceleration of spectral intensity 0.02 m^2/s^3 is determined. The numerical values were found to be 0.03 for the narrow-band acceleration, 0.56 for the band-limited acceleration, 0.19 for the simulated Kanai-Tajimi acceleration, and 0.32 for the Cape Mendocino accelerogram (see Table 8.1). It can be observed from these results that entropy of the Kanai-Tajimi model is bounded by the entropy of the narrow-band acceleration and the entropy of the band-limited acceleration. Interestingly, the entropy of the recorded acceleration is also bounded by the narrow-band and the band-limited signals. Note that the narrow-band signal represents a resonant acceleration that is poor in frequency content. The band-limited signal, on the other hand, represents an acceleration that is rich in frequency content. Based on this observation, it can be expected that the entropy of a resonant or a narrow-band acceleration will be the smallest among a set of records, while the entropy of an acceleration that is rich in frequency content will be large. The following section explains deterministic measures to quantify the frequency content of ground motions.

8.3.2 Use of Deterministic Measures to Identify Resonance in Earthquake Records

Consider an acceleration record of finite energy in time domain satisfying the acceleration energy condition:

$$E_t = \int_{-\infty}^{\infty} [\ddot{x}(t)]^2 dt < \infty \tag{8.13}$$

Under this condition, the Fourier transform of the ground acceleration is given by

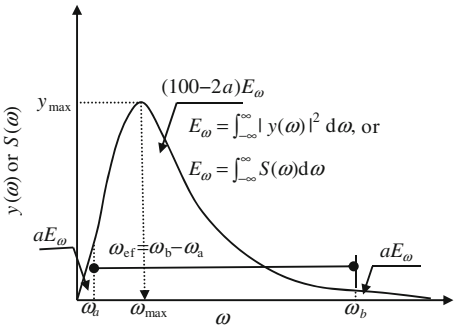

Fig. 8.4 Measures of frequency bandwidth of recorded ground accelerations (Moustafa and Takewaki [23] with permission from Springer)

$$y(\omega) = \int_{-\infty}^{\infty} \ddot{x}(t)\, e^{-i\omega t} dt \tag{8.14}$$

Equation (8.13) provides a measure of the acceleration energy computed in time domain (see [24] and also Chaps. 3–7). Recalling Parseval's theorem ($\int_{-\infty}^{\infty} [\ddot{x}(t)]^2 dt = (1/2\pi) \int_{-\infty}^{\infty} |y(\omega)|^2 d\omega$), a similar measure can be computed in frequency domain:

$$E_\omega = \int_{-\infty}^{\infty} |y(\omega)|^2 d\omega = \int_{-\infty}^{\infty} y(\omega)\, y^*(-\omega)\, d\omega \tag{8.15}$$

Herein, $y^*(-\omega)$ is the complex conjugate of $y(\omega)$. The frequency content, presented in this chapter, is taken within (ω_a, ω_b). The parameters ω_a and ω_b represent the frequencies at which a and b times the Fourier energy are attained, respectively. Thus, the frequency bandwidth is given by $\omega_{ef} = \omega_b - \omega_a$ (see Fig. 8.4). Typical values of a and b can be 0.05 and 0.95 (5 and 95 % of the acceleration energy, see [26]), respectively, or any reasonable values (e.g., 0.01 and 0.99). When $a = 0.05$ and $b = 0.95$, the parameter ω_{ef} can be viewed as a measure of the frequencies contributing to the strong phase of the ground motion (see, e.g. [26]). The effective frequency bandwidth can be further normalized to provide a measure that is bounded between zero and one:

$$\bar{\omega}_{ef} = \frac{\omega_b - \omega_a}{\Omega_u - \Omega_0} \tag{8.16}$$

The frequency range (Ω_0, Ω_u) is generally in the range of 2π (0,10 $\sim$ 50) rad/s depending on the site soil condition. When $\bar{\omega}_{ef}$ is close to zero, the ground acceleration is narrow-band or poor in frequency content. An example of this scenario is a harmonic signal of a single or a few frequencies. For example, $\ddot{x}(t) = A \sin(\omega_g t)$, where A and ω_g are the acceleration amplitude and dominant frequency, respectively. When $\bar{\omega}_{ef}$ is significantly larger than zero, the ground acceleration will be rich in frequencies. The band-limited acceleration model

Table 8.2 Frequency content measures for recorded ground motion (Moustafa and Takewaki [23] with permission from Springer)

Earthquake (station, record)	ω_c(Hz)	ω_{ef} (Hz)	$\bar{\omega}_{ef}$ [a]	$\omega_{\max}$(Hz)
1940 El Centro (El Centro#9, H180)	13.53	43.92	0.88	5.88
1966 Parkfield (Cholame#2, C065)	8.18	28.85	0.58	8.24
1992 Landers (Lucerne, LCN000)	23.05	46.69	0.93	28.52
1995 Kobe (Takatori, TAK000)	6.75	31.49	0.63	4.03
1999 Chi-Chi (ALS, ALS0)	3.83	16.52	0.33	1.74

[a] Eq. (8.16), $\Omega_0 = 0$, $\Omega_u = 50\,\text{Hz}$

(constant amplitude at all frequencies) is an example of this scenario. The average frequency of the ground motion is calculated as $\omega_{av} = (\omega_b - \omega_a)/2$.

The central or dominant frequency of the ground acceleration reflecting the influence of the local soil profile can be computed by

$$\omega_c = \int_{-\infty}^{\infty} \omega |y(\omega)|^2 d\omega \Big/ \int_{-\infty}^{\infty} |y(\omega)|^2 d\omega \tag{8.17}$$

An additional frequency $\omega_{\max}$ that corresponds to the peak amplitude of $y(\omega)$ can also be estimated (see Fig. 8.4). The relevance of $\omega_{\max}$ becomes obvious by comparing $\omega_{\max}$ with the fundamental frequency ω_n of the structure. Thus, when the ratio $\omega_{\max}/\omega_n$ is close to one, it can be expected that the input energy to the structure will be large (see [27]).

It is believed that these measurers provide important information about the nature of the ground motion, and thus, can be adopted in identifying the frequency content of recorded accelerograms. It is proposed in this chapter that these measures be utilized in selecting recorded accelerations as design inputs to important structures. Thus, if a set of n records are available and it is required to select a few records (typically $3 \sim 10$) for seismic design of a new structure of fundamental circular frequency ω_n (obtainable using approximate or empirical expressions), the following procedures can be adopted:

1. Normalize the set of available accelerograms to the same Arias intensity [24].
2. Calculate the central and effective frequencies for each record [Eqs.(8.16), (8.17)].
3. Sort the records based on the central frequency and associated effective frequency.
4. Select those records that have their ω_c close to ω_n and have the smallest $\bar{\omega}_{ef}$.

To demonstrate how to use the measures developed in this chapter in quantifying resonant recorded accelerograms, the acceleration records listed in Table 8.2 [25] are considered. The numerical values of these measures are given in the same table. These results reveal clearly the significant differences between these records. It is seen that $\bar{\omega}_{ef}$ for the Chi–chi record is the smallest and that for the Landers is the largest. The Kobe record would govern the design of buildings of ω_n in the

range (0, 4) Hz. This observation is confirmed by the large Fourier amplitude of the Kobe record that is about twice the amplitude of El Centro record and about four times that of the Chi–chi record.

8.4 Identification of Resonant Accelerations and Selection of Design Records

To examine the applicability of the measures explained in this chapter in identifying resonant accelerograms at a site, four recorded earthquake groups shown in Table 8.3 are considered. These records include accelerograms measured at rock, stiff, medium, and soft soil sites [25]. The selection of these records is based on the site soil classification adopted by the USGS in terms of the shear wave velocity v_s (see Table 8.3). The vertical and the two horizontal accelerations of the record during each earthquake are considered in the numerical analyses. Table 8.3 provides information about magnitude, source-site distance, PGA, Arias intensity, duration, and recording station for these 72 accelerograms considered. In numerical calculations, the dispersion index is normalized by ω_2 and all records are scaled to the same Arias intensity.

The numerical results on entropy and dispersion indices for these records are shown in Table 8.3. The mean and coefficient of variation for the entropy are (0.58, 0.17), (0.52, 0.23), (0.47, 0.14), and (0.50, 0.28) for rock, stiff, medium, and soft soil, respectively. The higher variation can be observed in the entropy for the soft soil site which could be attributed to the differences in the source properties and other characteristics (e.g., duration, magnitude, epicentral distance, fault mechanism, etc.). If these 72 accelerograms are considered, the mean entropy and coefficient of variation are calculated as (0.52, 0.22). Figures 8.5, 8.6, 8.7, 8.8 illustrate the PSDF for the stationary components of the vertical and the two horizontal accelerations, respectively. The results reveal that the entropy and the dispersion indices correlate well and that they successfully identify resonant accelerograms. For instance, the vertical acceleration of the 1979 Imperial Valley earthquake recorded at soft soil (El Centro #3) possesses the lowest entropy among all records. Figure 8.5 confirms this result since the PSDF of this acceleration is narrow-band and resembles a resonant signal with high amplitude at a single frequency. On the other hand, the accelerations that are rich in frequency content (e.g. 1999 Kocaeli (Arcelik) earthquake) possess the largest entropy. It is also evident that three accelerations of the same earthquake have different entropy and dispersion indices. These observations were confirmed by the Fourier transform of these accelerations. The numerical results on the deterministic measures were also seen to successfully identify resonant ground motions.

The numerical results reveal also that the Arias intensity and the peak ground acceleration are not guaranteed as accurate parameters for selecting design ground motions for structures. For instance, the vertical acceleration of the 1992 Landers

Table 8.3 Information about earthquake records and entropy and bandwidth indices for different soil conditions [25] (Moustafa and Takewaki [23] with permission from Springer)

Soil type (v_s m/s)	Earthquake (station)	M [a]	Ep. dis. (km)	PGA (g) V / H_1 / H_2	I_A [b] (m^2/s^3) V / H_1 / H_2	Dur. (s)	Ef. Bandwidth V / H_1 / H_2	Entropy[c] V / H_1 / H_2	Disp. index[d] V / H_1 / H_2
Rock $v_s > 750$	1971 San Fernando (Lake Hug. #9)	6.6	23.10	0.09/0.16/0.13	0.50/0.94/0.67	34.89	0.63/0.57/0.54	0.49/0.70/0.66	1.46/0.83/0.90
	1989 Loma Prieta (Gilory #1)	6.9	28.64	0.21/0.41/0.47	1.85/6.59/10.49	39.95	0.64/0.34/0.42	0.47/0.62/0.60	1.50/1.03/0.98
	1992 Cape Mendocino (CM)	7.1	10.36	0.75/1.50/1.04	8.59/37.19/14.91	30.00	0.44/0.34/0.39	0.42/0.63/0.58	1.64/1.03/0.98
	1992 Landers (Lurcene)	7.3	44.02	0.82/0.72/0.78	51.37/41.10/43.46	48.13	0.79/0.77/0.81	0.62/0.68/0.71	0.29/0.41/0.56
	1999 Kocaeli (ERD)	7.4	47.03	0.20/0.24/0.14	1.16/3.43/2.00	28.00	0.48/0.23/0.24	0.67/0.63/0.58	0.84/1.18/0.89
	1999 Chichi (TAP051)	7.6	152.71	0.04/0.06/0.11	0.27/0.81/1.44	90.00	0.22/0.17/0.17	0.46/0.43/0.49	0.84/0.90/0.81
Stiff soil $360 < v_s \leq 750$	1989 Loma Prieta (Gilory #6)	6.9	35.47	0.10/0.13/0.17	0.61/1.39/2.76	39.96	0.38/0.29/0.19	0.37/0.50/0.43	1.58/1.09/1.21
	1992 Cape Mendocino (Fort. Blvd)	7.1	29.55	0.05/0.12/0.11	0.34/1.63/1.49	44.00	0.33/0.17/0.16	0.34/0.48/0.45	1.53/1.24/1.14
	1992 Landers (DH Springs)	7.3	27.33	0.17/0.17/0.15	3.61/4.41/4.23	50.00	0.40/0.26/0.24	0.64/0.57/0.71	0.82/0.88/0.81
	1995 Kobe (0KJMA)	6.9	18.27	0.34/0.82/0.60	11.66/52.40/33.94	48.00	0.22/0.12/0.14	0.60/0.46/0.46	0.76/0.57/0.63
	1999 Kocaeli (Arcelik)	7.4	53.68	0.09/0.22/0.15	0.50/1.81/1.36	30.00	0.65/0.34/0.37	0.77/0.61/0.63	0.79/0.52/1.10
	1999 Chichi (ALS)	7.6	37.83	0.07/0.18/0.16	1.26/6.00/5.74	59.00	0.24/0.14/0.15	0.48/0.42/0.47	0.94/0.78/0.69

(continued)

Table 8.3 (continued)

Soil type (v_s m/s)	Earthquake (station)	M [a]	Ep. dis. (km)	PGA (g) V / H_1 / H_2	I_A^b (m^2/s^3) V / H_1 / H_2	Dur. (s)	Ef. Bandwidth V / H_1 / H_2	Entropy[c] V / H_1 / H_2	Disp. index[d] V / H_1 / H_2
Medium soil $180 \leq v_s \leq 360$	1942 Borrego (El Centro #9)	6.5	57.79	0.04/0.07/0.10	0.08/0.53/0.39	40.00	0.46/0.24/0.23	0.48/0.40/0.43	1.46/0.74/0.85
	1960 Central Calif. (Hollister CH)	5.0	8.01	0.03/0.04/0.06	0.06/0.12/0.26	40.00	0.17/0.13/0.15	0.33/0.35/0.45	0.49/0.57/0.55
	1992 Big Bear (SBE & H)	6.4	45.51	0.07/0.09/0.10	0.65/1.70/1.83	100.00	0.38/0.23/0.26	0.54/0.45/0.53	0.69/1.03/0.88
	1992 Cape Mendocino (Petrolia)	7.1	4.51	0.16/0.59/0.66	2.46/21.33/23.86	36.00	0.32/0.33/0.33	0.46/0.58/0.53	1.42/0.89/0.90
	1999 Chichi (CHY006)	7.6	40.47	0.20/0.36/0.35	3.98/12.70/9.35	150.00	0.45/0.21/0.17	0.45/0.45/0.44	0.71/0.64/0.66
	1999 Chichi (CHY024)	7.6	24.10	0.15/0.18/0.28	11.41/7.46/4.33	90.00	0.29/0.22/0.19	0.51/0.53/0.49	1.03/0.81/0.73
Soft soil v_s<180	1979 Imperial Valley (El Centro #3)	6.5	28.65	0.13/0.27/0.22	1.32/7.08/4.26	39.55	0.48/0.26/0.25	0.20/0.59/0.58	2.50/0.85/0.92
	1981 Westmorland (SSW Rd.)	5.8	8.62	0.21/0.20/0.18	2.05/3.26/3.20	28.75	0.93/0.33/0.35/	0.70/0.51/0.57	0.67/1.04/0.99
	1989 Loma Prieta (Apeel2 RC)	6.9	63.49	0.08/0.27/0.22	0.58/7.82/4.44	35.83	0.20/0.10/0.10	0.61/0.32/0.31	0.71/1.04/0.57
	1994 Northridge (MB Rd.)	6.7	47.11	0.08/0.18/0.13	0.41/2.02/1.20	21.83	0.26/0.19/0.21	0.59/0.54/0.58	0.46/0.56/0.77
	1995 Kobe (Kakogawa)	6.9	24.20	0.16/0.25/0.35	1.75/6.44/10.54	40.96	0.44/0.23/0.22	0.68/0.54/0.51	0.84/0.82/0.88
	1999 Kocaeli (Ambarli)	7.4	112.26	0.08/0.25/0.18	0.86/6.28/7.74	150.41	0.40/0.10/0.10	0.35/0.37/0.37	1.11/0.90/0.76

[a] M = Richter's magnitude

[b] $I_A = \int_0^\infty [\ddot{x}_g(t)]^2 dt$ (Arias intensity)

[c] Entropy index calculated from Eq. (8.8)

[d] Dispersion index calculated from Eq. (8.11)

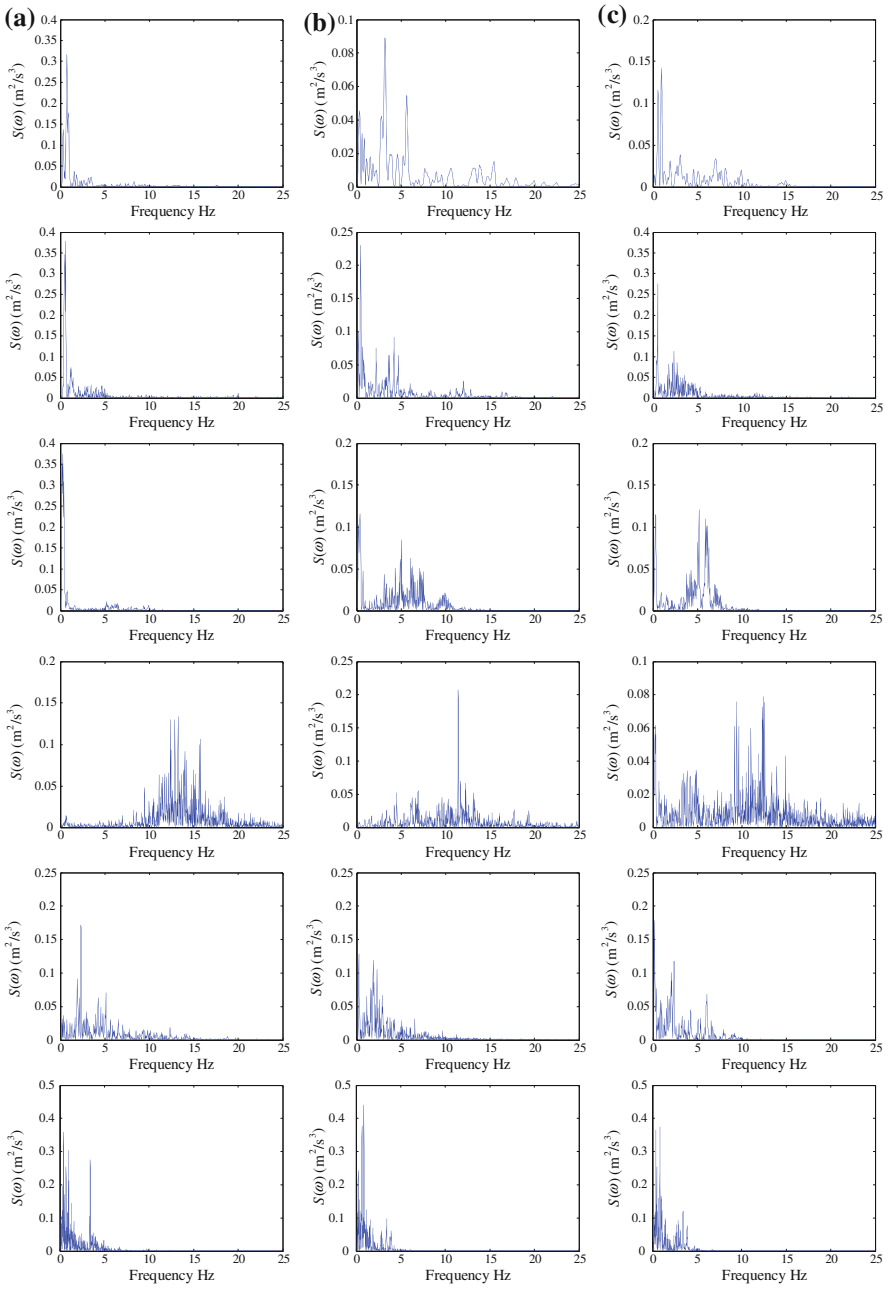

Fig. 8.5 Power spectral density function for records at rock soil site shown in Table 8.3 (Moustafa and Takewaki [23] with permission from Springer)

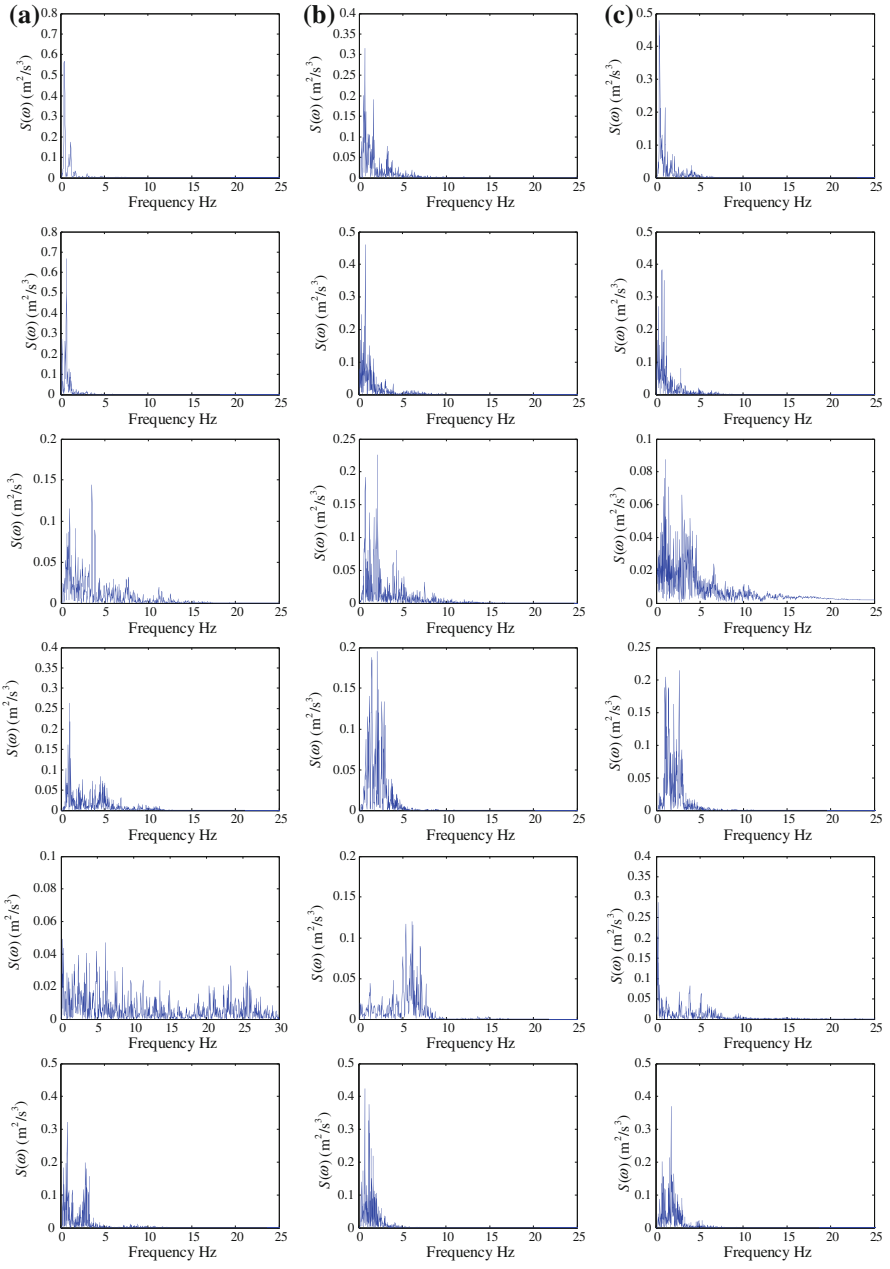

Fig. 8.6 Power spectral density function for records at stiff soil site shown in Table 8.3 (in order from the *top*) **a** Vertical component, **b** First horizontal component, **c** Second horizontal component (Moustafa and Takewaki [23] with permission from Springer)

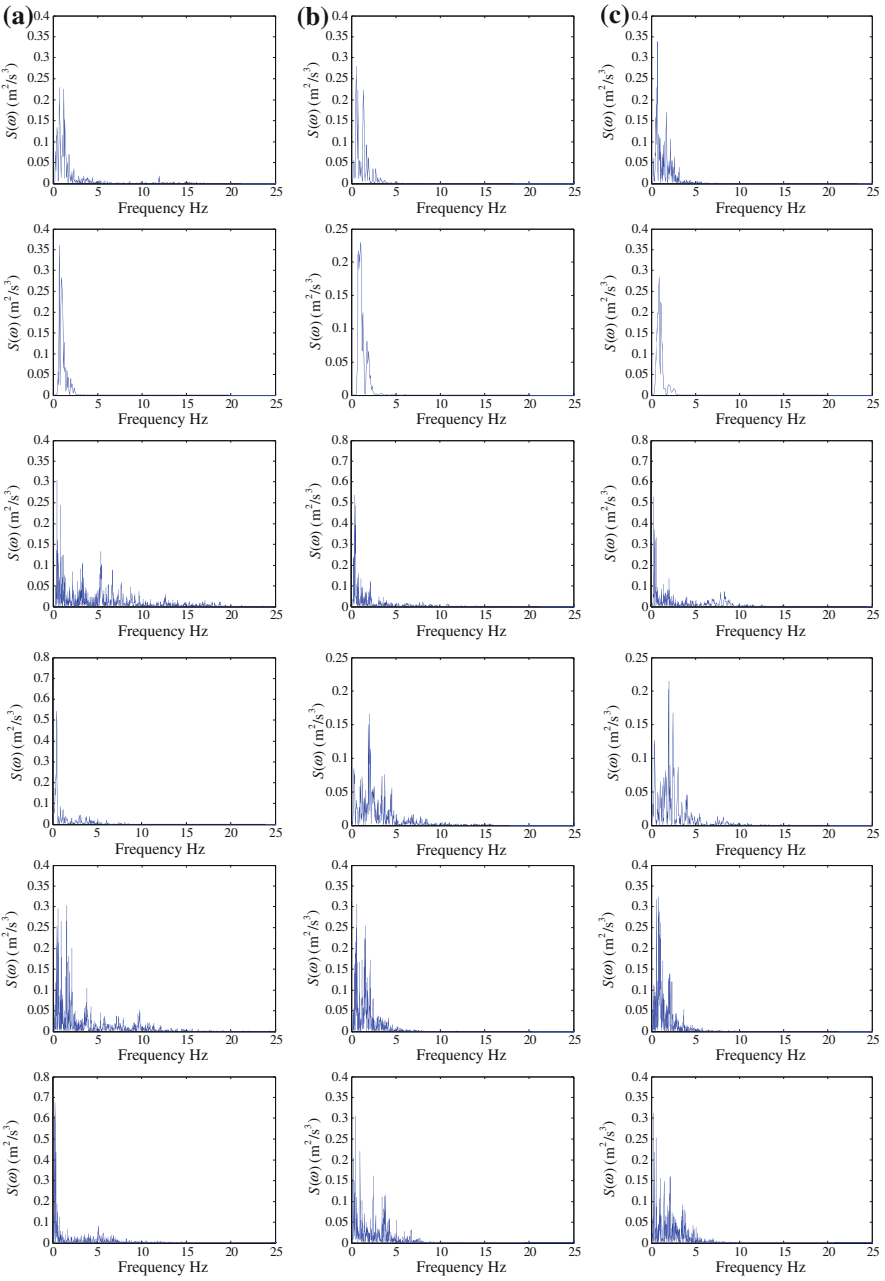

Fig. 8.7 Power spectral density function for records at medium soil site shown in Table 8.3 (in order from the *top*) **a** Vertical component, **b** First horizontal component, **c** Second horizontal component (Moustafa and Takewaki [23] with permission from Springer)

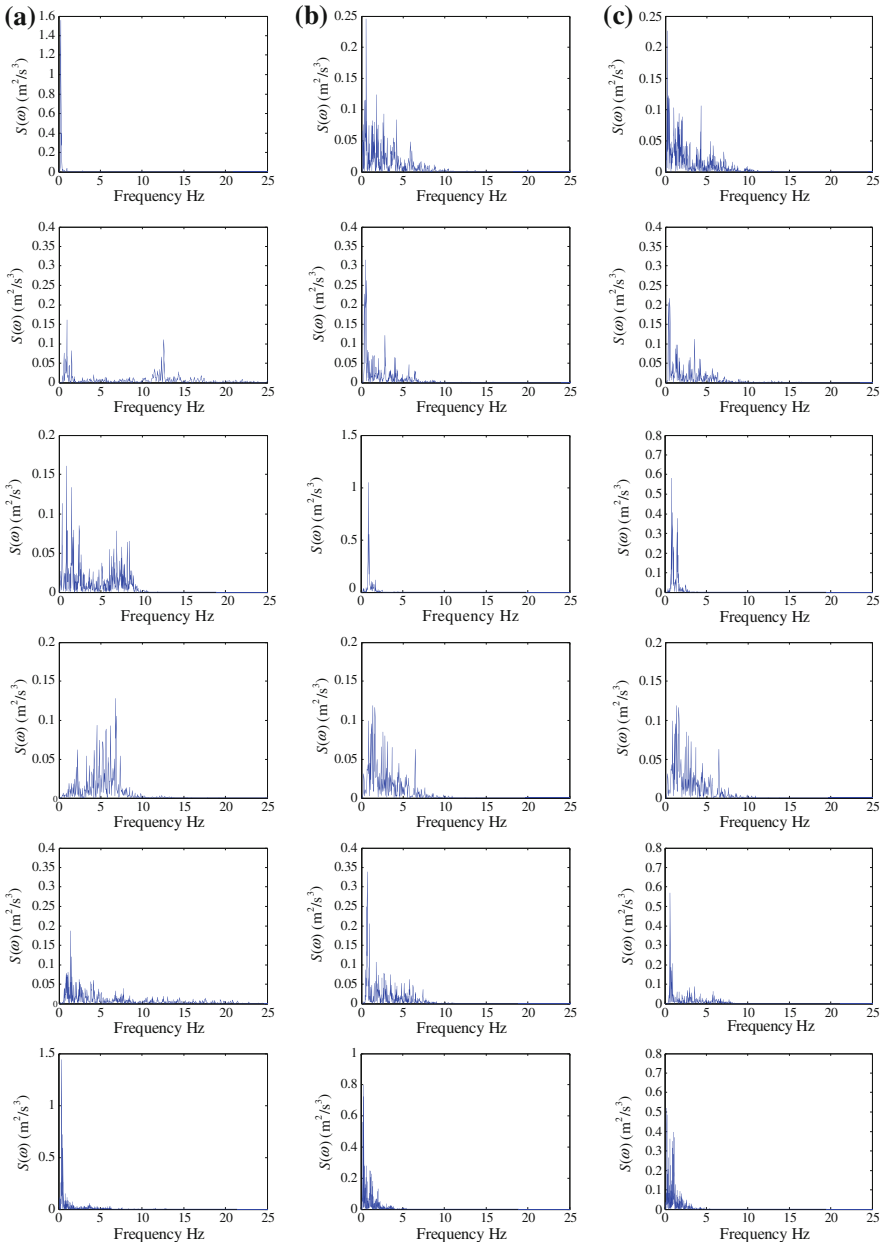

Fig. 8.8 Power spectral density function for records at soft soil site shown in Table 8.3 (in order from the *top*) **a** Vertical component, **b** First horizontal component, **c** Second horizontal component (Moustafa and Takewaki [23] with permission from Springer)

Table 8.4 Ductility factor and damage index for SDOF inelastic structure subjected to ground acceleration (Moustafa and Takewaki [23] with permission from Springer)

Earthquake (station)	Structure fundamental frequency					
	f = 0.13 Hz		f = 0.21 Hz		f = 0.41 Hz	
	Ductility factor	Damage index	Ductility factor	Damage index	Ductility factor	Damage index
1992 Cape Mendocino (CM)	4.39	0.74	7.09	1.05	1.41	0.19
1992 Landers (Lucerne)	0.93	0.12	0.60	0.08	0.43	0.05

earthquake (Lucerne) measured at rock soil possesses high PGA (0.82 g) and high Arias intensity (51.37 m^2/s^3). However, the spectral amplitude of this acceleration is substantially small in the frequency range $2\pi(0, 9)$ rad/s. On the other hand, the vertical acceleration of the 1992 Cape Mendocino (CM) measured at the same soil condition has relatively lower PGA (0.75 g) and substantially smaller intensity (8.59 m^2/s^3), but possesses significantly higher spectral amplitudes in the frequency range $2\pi(0,2)$ rad/s. Thus, it can be expected that this record will produce large deformations in a structure with short to moderate natural period compared to the first acceleration. This observation will be verified below.

Consider three SDOF building models of natural frequency of 0.13, 0.21, and 0.41 Hz. The yield displacement and yield strength of these structures are taken as $u_y = 0.10$ m and $f_y = 10^4$ N and a viscous damping of 0.05 damping ratio is adopted. The material nonlinearity is modeled using an elastic–plastic relation. Nonlinear dynamic analysis is carried out for each structure subjected to a single acceleration using the Newmark-β method ($\alpha = 1/2$, $\beta = 1/6$, $\Delta t = 0.004$). All records were normalized to the same Arias intensity of 6.00 m^2/s^3. The Park and Ang damage index for each structure driven by the ground acceleration is calculated as follows (see [28] and also Chaps. 5, 7):

$$DI_{\mathrm{PA}} = \frac{u_{\max}}{u_{\mathrm{u}}} + \beta \frac{E_{\mathrm{H}}}{f_{\mathrm{y}} u_{\mathrm{u}}} = \frac{\mu_{\max}}{\mu_{\mathrm{u}}} + \beta \frac{E_{\mathrm{H}}}{f_{\mathrm{y}} u_{\mathrm{y}} \mu_{\mathrm{u}}} \tag{8.18}$$

In Eq. (8.18) $u_{\max}$ and E_{H} are the maximum displacement and dissipated hysteretic energy (excluding elastic energy) under the earthquake [4, 28]. The parameter μ_{u} is the ultimate yield ductility capacity under monotonic loading and β is a positive constant that weights the effect of cyclic loading on structural damage (taken as 6 and 0.15). The numerical results on DI_{PA} are provided in Table 8.4. From the numerical results it is evident that the identified resonant acceleration (Cape Mendocino) produces more damage than the Landers acceleration. In fact, these three structures are damaged beyond repair ($DI_{\mathrm{PA}} > 0.40$) by the first acceleration while they sustain the second acceleration with repairable damage ($DI_{\mathrm{PA}} < 0.40$) [28]. The same observation applies to the ductility factor.

Table 8.5 Information about earthquake records and entropy and dispersion indices for different soil conditions [14] (Moustafa and Takewaki [23] with permission from Springer)

Group type	Earthquake (station)	M_W	PGA (g)	I_A^a (m^2/s^3)	Duration (s)	Ef. Bandwidth H_1 / H_2	Entropy index[b] H_1 / H_2	Dispersion index [c] H_1 / H_2
Near-fault (rock)	1992 Landers (Lucerne)	7.2	0.79/ 0.72	41.10/ 43.46	48.13	0.77/0.81	0.68/0.71	27.90/34.85
	1992 Cape Mendocino (CM)	7.0	1.50/ 1.04	37.19/ 14.91	30.00	0.39/0.34	0.63/0.58	21.34/15.93
	1995 Kobe (JMA)	6.9	0.82/ 0.60	52.40/ 33.94	48.00	0.13/0.14	0.46/0.46	7.73/8.30
	1989 Loma Prieta (LG pres. center)	6.9	0.61/ 0.56	49.12/ 19.28	24.97	0.29/0.34	0.48/0.56	17.79/22.29
Near-fault (soil)	1978 Tabas (Tabas)	7.4	0.84/ 0.85	46.03/ 24.74	32.84	0.28/0.26	0.67/0.60	27.64/17.30
	1992 Cape Mendocino (Petrolia)	7.0	0.59/ 0.66	21.33/ 23.86	36.00	0.33/0.32	0.58/0.53	17.51/14.82
	1994 Northridge (Rinaldi)	6.7	0.84/ 0.85	72.09/ 72.01	14.95	0.23/0.35	0.59/0.64	23.01/28.15
	1994 Northridge (Sylmar converter)	6.7	0.61/ 0.90	36.42/ 32.99	40.00	0.22/0.19	0.33/0.37	5.27/9.23
	1979 Imperial valley (Meloland)	6.5	0.31/ 0.30	5.36/6.74	39.99	0.17/0.13	0.48/0.41	9.88/9.71
Short-duration	1983 Caolinga (Anticline Ridge)	5.0	0.67/ 0.58	4.42/3.90	9.84	0.36/0.42	0.55/0.54	18.09/24.87
	1970 Lytle Creek (Devils canyon)	5.4	0.15/ 0.15/	0.65/0.57	13.61	0.34/0.43	0.40/0.46	20.33/24.56
	1986 N. Palm Spring (SR Mountain)	6.0	0.10/ 0.10	0.29/0.39	10.40	0.97/0.99	0.79/0.82	70.27/70.42
	1975 Northern Calif. (CM Petrolia)	5.2	0.18/ 0.12	0.74/0.55	14.61	0.28/0.22	0.58/0.53	15.26/12.53

(continued)

Table 8.5 (continued)

Group type	Earthquake (station)	M_W	PGA (g)	I_A^a (m^2/s^3)	Duration (s)	Ef. Bandwidth H_1 / H_2	Entropy index[b] H_1 / H_2	Dispersion index [c] H_1 / H_2
	1971 San Fernando (Gormon-Oso)	6.6	0.11/0.08	0.37/0.28	9.23	0.21/0.23	0.64/0.70	17.68/13.76
	1984 Morgan Hill (Lick observatory)	6.2	0.05/0.08	0.15/0.50	16.00	0.20/0.18	0.58/0.53	15.93/17.05
Long-duration	1992 Big Bear (SB-E & hospitality)	6.4	0.10/0.10	1.70/1.83	100.00	0.23/0.26	0.45/0.53	11.26/14.12
	1995 Kobe (OSAJ)	6.9	0.08/0.06	1.44/1.22	120.00	0.14/0.16	0.19/0.17	1.89/1.40
	1999 Kocaeli (Maslak)	7.4	0.25/0.19	6.28/7.74	150.41	0.10/0.10	0.37/0.37	5.68/5.10
	1999 Chichi (CHY034)	7.6	0.31/0.25	11.35/9.12	250.00	0.12/0.13	0.38/0.35	4.38/4.16

[a] $I_A = \int_0^\infty [\ddot{x}_g(t)]^2 dt$ (Arias intensity)

[b] Entropy index calculated from Eq. (8.8)

[c] Dispersion index calculated from Eq. (8.11)

Let us further examine the measures developed in this chapter for the four groups of earthquake records listed in Table 8.5. These records include near-fault accelerograms measured at rock and soil sites, and short- and long-duration earthquakes [25]. The selection of records for different soil conditions and for different earthquake durations is meant for examining the robustness of the proposed measures to different earthquake characteristics. The two horizontal accelerations are considered in the numerical analyses. Table 8.5 provides information about these records. Note that all records are scaled to the same Arias intensity.

The numerical results on entropy and dispersion indices for each of these earthquake accelerations are provided in Table 8.5. The results demonstrate that the entropy and the dispersion indices correlate well and that they both successfully identify resonant accelerograms. It is seen that the narrow-band records possess the smallest entropy and dispersion indices (e.g., 1995 Kobe (OSAJ) and 1994 Northridge (Sylmar) earthquakes) while the accelerations that are rich in frequency content (e.g. 1992 Landers and 1986 N. Palm Spring earthquakes) possess the largest entropy and dispersion. It is also evident that the two acceleration components of the same earthquake have different entropy and dispersion indices. This observation is consistent with the findings by Anderson and Bertero [6]. The short-duration earthquakes are seen to possess higher entropy and dispersion indices and sharp energy jump compared to the long-duration earthquakes. It is also remarkable that near-fault records measured on soil site have smaller entropy and dispersion indices compared to near-fault records measured on rock soil. This may be attributed to the site soil effects that can significantly filter the amplitude and frequency content of the ground motion for soil sites. The same observations hold for the effective frequency measure.

8.5 Summary

In seismic design of structures, it is essential to select the design ground motion, among a set of available records, which produces the highest structural response. In this chapter, measures that can be used to identify resonance/criticality of earthquake ground motions are developed. The entropy rate and the dispersion index are shown to identify resonance of probabilistic earthquake models and earthquake records. It is shown that resonant accelerations exist regardless of soil site conditions and source characteristics. In probabilistic earthquake models, it was shown that the bandlimited and the narrow-band signals provide upper and lower bounds on entropy rate and dispersion index of the Kanai-Tajimi acceleration models. Similarly, narrow-band and broadband harmonic functions provide bounds on the frequency content of recorded accelerograms. Measures that are based on the deterministic approach are also shown to be suitable descriptors of resonance of ground motions.

The usefulness of the measures developed in this chapter is demonstrated by identifying resonant acceleration records measured at sites with different soil conditions and with different earthquake characteristics (e.g., total duration, frequency content, site-source-distance, energy, etc.). Resonant ground accelerations are shown to produce large structural response and damage when their dominant frequency is close to the fundamental frequency of the structure. Numerical verifications using nonlinear dynamic analysis and Park and Ang damage indices are also provided.

References

1. Takewaki I (2002) Seismic critical excitation method for robust design: a review. J Struct Eng 128:665–672
2. Takewaki I (2007) Critical excitation methods in earthquake engineering. Elsevier Science, Amsterdam
3. Abbas AM (2002) Deterministic/reliability-based critical earthquake load models for linear/nonlinear structures, Ph.D. thesis, Indian Institute of Science, Bangalore
4. Abbas AM (2006) Critical seismic load inputs for simple inelastic structures. J. Sound Vibr 296:949–967
5. Amiri GG, Dana FM (2005) Introduction to the most suitable parameter for selection of critical earthquakes. Comput Struct 83:613–626
6. Anderson JC, Bertero VV (1987) Uncertainties in establishing design earthquakes. J Struct Eng 113(8):1709–1724
7. Dhakal RP, Mander JB, Mashiko N (2006) Identification of critical ground motions for seismic performance assessment of structures. Earthq Eng Stuct Dyn 35:989–1008
8. Takewaki I (2001) Resonance and criticality measure of ground motions via probabilistic critical excitation method. Soil Dyn Earthq Eng 21:645–659
9. Uang C-M, Bertero VV (1988) Implications of recorded earthquake ground motions on seismic design of building structures. Report No. UCB/EERC-88/13, Earthquake Engineering Research Center, Berkeley, CA
10. Zhai C-H, Xie L–L (2007) A new approach of selecting real input ground motions for seismic design: The most unfavourable real seismic design ground motions. Earthq Eng Struct Dyn 36:1009–1027
11. Abbas AM, Manohar CS (2002) Investigations into critical earthquake excitations within deterministic and probabilistic frameworks. Earthq Eng Stuct Dyn 31:813–832
12. Abbas AM, Manohar CS (2007) Reliability-based vector nonstationary random critical earthquake excitations for parametrically excited systems. Struct Saf 29:32–48
13. Vanmarcke EH (1972) Properties of spectral moments with applications to random vibrations. J Eng Mech 98(2):425–446
14. Vanmarcke EH (1976) Structural response to earthquakes. In: Lomnitz C, Rosenbluth E (eds) Seismic risk and engineering decisions. Elsevier, NY
15. Shannon C (1948) A mathematical theory of communication. Bell Sys Tec J 27: 379–423, 623–656
16. Kapur JN (1993) Maximum entropy models in science and engineering. Wiley Eastern, New Delhi
17. Papoulis A (1991) Probability, random variables and stochastic processes. McGraw-Hill, NY
18. Manohar CS, Sarkar A (1995) Critical earthquake input power spectral density function models for engineering structures. Earthq Eng Struct Dyn 24:1549–1566
19. Lin YK (1967) Probabilistic theory of structural dynamics. McGraw-Hill, NY

20. Nigam NC, Narayana S (1994) Applications of random vibrations. Narosa Publishing House, New Delhi
21. Kanai K (1957) Semi-empirical formula for the seismic characteristics of the ground. Bull Earthq Res Inst Univ Tokyo 35:309–325
22. Tajimi H (1960) A statistical method of determining the maximum response of a building structure during earthquakes. Proc 2nd WCEE Tokyo 2:781–797
23. Moustafa A, Takewaki I (2009) The use of probabilistic and deterministic measures to identify unfavorable earthquake records. J Zhejiang Univ: Sci A. 10(5): 619–634 (also from Springer)
24. Arias A (1970) A measure of earthquake intensity. Seismic design of nuclear power plants. MIT press, Cambridge, pp. 438–468
25. PEER (2005) Pacific Earthquake Engineering Research Center: http://peer.berkeley.edu
26. Trifunac MD, Brady AG (1975) A study on the duration of strong earthquake ground motion. Bull Seismol Soc Am 65(3):581–626
27. Takewaki I (2004) Bound of earthquake input energy. J Struct Eng 130(9):1289–1297
28. Park YJ, Ang AH-S (1985) Mechanistic seismic damage model for reinforced concrete. J Struct Eng 111(4):722–739

Chapter 9
Damage Assessment of Inelastic Structures Under Worst Earthquake Loads

9.1 Introduction

Earthquakes continue to claim thousands of lives and to damage structures every year [1]. In fact, each earthquake brings out new surprises and lessons with it. For instance, the unexpected loss of lives and the severe damage of infrastructures and buildings during past strong earthquakes (e.g., 1994 Northridge, 1995 Kobe, 2010 Haiti and the most recent 2011 Tohoku earthquakes) have raised significant concern and questions on life safety and performance of engineering structures under possible future earthquakes. The occurrence of strong earthquakes in densely populated regions, especially in developing countries with vulnerable building stock and fragile infrastructure, could lead to catastrophic consequences. A notable example is the 2010 Haiti earthquake that killed 250,000 people and left a long-term suffering for the residents of this developing country [2]. On the other hand, the severe damage caused by the 2011 Tohoku earthquake in Japan has raised significant challenges to one of the most developed countries as well [3]. Hence, the assessment of seismic performance of structures under strong ground motions is an important problem in earthquake engineering. Structures need to resist unknown future earthquakes which add more complexity to the problem [4–11]. The consideration of the earthquake inherent uncertainty, the variability in the structure parameters, and modeling the nonlinear behavior of the structure is essential for the accurate prediction of the actual response of the structure. Earthquake uncertainties include time, location, magnitude, duration, frequency content and amplitude, referred to as aleatory uncertainties.

The earthquake-resistant design of structures has been an active area of research for many decades [12]. The structural engineer aims to ensure safe performance of the structure under possible future earthquakes while maintaining optimal use of the construction material. The design objectives in current seismic building codes are to ensure life safety and to prevent damage of the structure in minor and moderate frequent earthquakes, and to control local and global damage (prevent

I. Takewaki et al., *Improving the Earthquake Resilience of Buildings*,
Springer Series in Reliability Engineering, DOI: 10.1007/978-1-4471-4144-0_9,

total collapse) and reduce life loss in a rare major earthquake. This can be achieved through: (1) robust prediction of expected future strong ground motions at the site, (2) accurate modeling of the material behavior under seismic loads, and (3) optimal distribution of the construction material.

Early works on seismic design have dealt with the specification of earthquake loads using the response spectrum method, the time history of the ground acceleration, or using the theory of random vibrations. The nonlinear time-history analysis is recognized as the most accurate tool for dynamic analysis of structures [13]. Many researchers have also established deterministic and probabilistic hazard spectra for the site [14, 15]. The development of mathematical models to describe the hysteretic nonlinear behavior of the structure during earthquakes has also been pursued in several studies [16–18]. New design concepts and methods, such as energy-, performance- and displacement-based design, base isolation, and structural control have been recently developed [19–21]. Similarly, the optimal design of the structures under earthquake loads has been investigated in several studies [19, 22–25]. The evaluation of the current procedures and present new, practical procedures for ground motion selection and modification are provided in the recent special issue on earthquake ground motion selection, and modification for nonlinear dynamic analysis of structures [26]. The two edited books by Papadrakakis et al. [27] and Tsompanakis et al. [28] and the doctoral thesis by Plevris [25] present the state-of-the-art on advances and applications of optimal seismic design of structures considering uncertainties.

The definition of the worst or critical ground motion represents a major challenge in earthquake-resistance design of structures. This is because of the high uncertainty involved in the occurrence of the earthquake phenomenon compared to the relatively low variability in the structure's properties. Strasser and Bommer [29] pose an important question on whether we have seen the worst ground motion yet, and the answer is no. They identify the worst ground motions as those having large amplitude. It may be emphasized that the worst ground motion for a structure may not be the worst input for a different structure. For example, the 2002 earthquake of magnitude 7.9 occurred along Alaska's Denali fault killed no one and did little serious damage, while the 1995 Kobe earthquake of 6.9 magnitude killed 5,100 people and caused billion of dollars in structural damage. Early studies on defining severity of strong ground motion and earthquake capability to create large damage have focused on the earthquake intensity, peak values of ground acceleration, velocity and displacement (PGA, PGV, PGD), effective PGV, and so on [11, 30]. Near-field ground motion with pulse-like characteristic is a phenomenon representing one scenario of severity in the near-field region. Other scenarios of earthquake severity include repeated occurrence of ground motion in sequences [31]. Deep soft soils can also amplify earthquake amplitudes and modify frequency content. Secondary causes include also the travel path effects. In reality, some of these causes could exist together.

To carry out nonlinear time-history analysis, a set of suitable accelerograms need to be selected from available records (see, e.g., [32]). In this context, the criteria based on which records are selected and scaled represent an interesting

subject. A notable effort in this direction and other related subjects has been extensively investigated by several researchers, especially at Stanford University (e.g., [33–39]). If the number of the available records is small, records from other sites with similar soil condition or artificially simulated ground motions could be employed. The critical excitation method provides another alternative in the case of scarce, inhomogeneous, or limited earthquake data for the site. This method has been used to assess the structure's response under mathematically simulated earthquake inputs representing possible worst future earthquakes (e.g., [6, 10, 11]). This method relies on the high uncertainty associated with the occurrence of the earthquake phenomenon, associated characteristics and also on the safety requirements of the important and lifeline structures (nuclear plants, storage tanks, industrial installations, etc.). The critical earthquake input for a given structure is computed by minimizing the structure's performance while satisfying predefined constraints observed in real earthquake records. The structural performance may be described in terms of the structure's response or in terms of reliability measures or damage indices [4, 5, 8, 9]. The optimum design of the structure under varying critical earthquake loads has also been studied (e.g., [40–42]). Several practical applications have evolved from the concept of critical excitation. This includes design of structures to critical excitations, deriving critical response spectra for a site, estimating critical cross power spectral density functions of multi-point and spatially varying ground motions, and reliability analysis of structures to partially specified loads. This method of critical excitations has also been employed in identifying resonant accelerations and in selecting critical recorded accelerograms based on the notion of the entropy principle [5, 8, 9, 43–45]. Comprehensive reviews on these aspects can be found in [6].

This chapter deals with the damage assessment of inelastic structures under worst mathematical future earthquakes obtained using the critical excitations method. The novelty of this research is in combining damage indices, with nonlinear optimization, and nonlinear time-history analysis in assessing the structural performance under possible future ground motions. The use of damage indexes provides a quantitative measure for damage and necessary repair for the structure. Bilinear and elastic–plastic force–displacement relationships are taken to model the material nonlinearity, and thus the present work is limited to nondeteriorating structures. Numerical examples for one-story and two-storys plane frames without irregularities are provided. Future practical applications of the proposed methodology in seismic analysis and design of structures are also discussed.

9.2 Damage Assessment for Inelastic Structures Under Earthquakes

Damage assessment for structures is generally based on the nonlinear response quantities under earthquake loads (see Table 9.1). The bilinear and the elastic–plastic models are shown in Fig. 9.1. The evaluation of the structure's damage is

Table 9.1 Response descriptors for inelastic buildings under earthquake ground motion (Moustafa [6] with permission from ASCE)

Response parameter	Definition
Maximum ductility	$\mu_{\max} = \max_{0 \le t \le t_f} \lvert \frac{x(t)}{x_y} \rvert$
Number of yield reversals	Number of times velocity changes sign
Maximum normalized plastic deformation range	$\Delta \bar{x}_{p,i} = \max_{0 \le t \le t_f} \lvert \frac{\Delta x_{p,i}}{x_y} \rvert$
Normalized cumulative ductility	$\mu_{ac.} = \sum_{i=1}^{N} \frac{\lvert \Delta x_{p,i} \rvert}{x_y} + 1$
Residual (permanent) ductility	$\mu_{res} = \lvert \frac{x(t_f)}{x_y} \rvert$
Normalized earthquake input energy	$\bar{E}_I = \frac{1}{f_y x_y} \int_0^{t_f} E_I(t) dt$
Normalized total hysteretic energy dissipated	$\bar{E}_H = \frac{1}{f_y x_y} \int_0^{t_f} E_H(t) dt$
Ratio of total hysteretic energy to input energy	$r_E = \frac{\bar{E}_H}{\bar{E}_I}$
Maximum rate of normalized input energy	$P_{I,\max} = \frac{1}{f_y x_y} \max_{0 \le t \le t_f} \left[\frac{dE_I(t)}{dt} \right]$
Maximum rate of normalized damping energy	$P_{D,\max} = \frac{1}{f_y x_y} \max_{0 \le t \le t_f} \left[\frac{dE_D(t)}{dt} \right]$
Maximum rate of normalized hysteretic energy	$P_{H,\max} = \frac{1}{f_y x_y} \max_{0 \le t \le t_f} \left[\frac{dE_H(t)}{dt} \right]$

usually carried out using damage indices which are quantified in terms of the structure's response and the associated absorbed energy. Therefore, the quantification of damage indices is carried out after performing nonlinear time-history analysis for the structure. The nonlinear time-history analysis for the structure is performed by solving the equations of motions using numerical integration schemes [5, 8, 9, 46].

9.2.1 Energy Dissipated by Inelastic Structures

The energies dissipated by N multi-degree-of-freedom (MDOF) structures under the ground acceleration $\ddot{x}(t)$ are computed by integrating the equations of motion as follows [16, 47–50]:

$$E_K(t) = \int_0^t \dot{\mathbf{X}}^T(\tau)\mathbf{M}\ddot{\mathbf{X}}(\tau)d\tau = \frac{1}{2}\sum_{i=1}^{N} m_i \dot{x}_i^2(t) \tag{9.1a}$$

$$E_D(t) = \int_0^t \dot{\mathbf{X}}^T(\tau)\mathbf{C}\dot{\mathbf{X}}(\tau)d\tau = \sum_{i=1}^{N} \int_0^t \dot{x}_i(\tau) f_{Di}(\tau) d\tau \tag{9.1b}$$

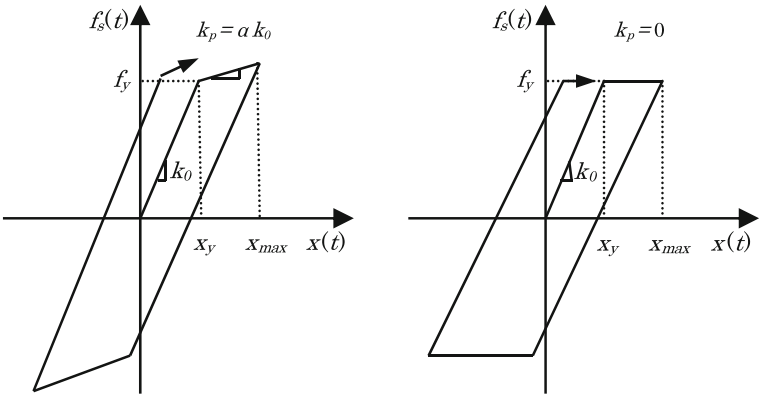

(a) Bilinear model **(b)** Elastic-plastic model

Fig. 9.1 Force–displacement relation for nonlinear materials. **a** Bilinear model. **b** Elastic-platic model (Moustafa [6] with permission from ASCE)

$$E_H(t) = \sum_{i=1}^{N} \int_0^t \dot{x}_i(\tau) f_{si}(\tau) d\tau - E_s(t) \tag{9.1c}$$

where, **M**, **C**, are the mass and damping matrices of the structure, respectively, $f_{si}(t)$is the ith hysteretic restoring force, $X(t)$ is the structure displacement vector and dot indicates differentiation with respect to time. The quantities $E_K(t)$, $E_D(t)$, $E_s(t)$ and $E_H(t)$ represent the kinetic, damping, strain, and hysteretic energies, respectively [5, 8, 9]. For viscous damping models, the damping energy reduces to $\sum_{i=1}^{N} \sum_{j=1}^{N} \int_0^t c_{ij} \dot{x}_i(\tau) \dot{x}_j(\tau) d\tau$.

Note that Eq. (9.1) provides the relative energy terms. Note that, by the end of the earthquake duration the kinetic and elastic strain energies diminish. Thus, the earthquake input energy to the structure is dissipated by hysteretic and damping energies. The next section demonstrates the use of the structure's response and the hysteretic energy in developing damage indices.

9.2.2 Damage Measures for Inelastic Structures

The literature work on damage measures in structures under earthquake loads is enormous (see, e.g., [51, 52]). Damage indices are quantified using a single or a combination of structural response parameters. Table 9.1 lists several damage measures that are based on a single response parameter [51, 53]. For instance, the first measure represents the ultimate ductility produced during the ground shaking. This measure does not incorporate information on how the earthquake input energy is imparted on the structure nor how this energy is dissipated. Earthquake damage occurs due to the

maximum deformation or ductility and the hysteretic energy dissipated by the structure. Therefore, the definition of structural damage in terms of the ductility is inadequate. The last three measures in Table 9.1 indicate the rate of the earthquake input energy to the structure (how fast the input energy E_I is imparted by the earthquake and how fast it gets dissipated). Damage indices can be estimated by comparing the response parameters demanded by the earthquake with the structural capacities.

Essential damage measures were explained in Chaps. 4–6, 8. For clear presentation of such damage measures, the definitions are shown again.

Powell and Allahabadi [53] proposed a damage index in terms of the ultimate ductility (capacity) μ_u and the maximum ductility attained during ground shaking $\mu_{\max}$:

$$DI_\mu = \frac{x_{\max} - x_y}{x_u - x_y} = \frac{\mu_{\max} - 1}{\mu_u - 1} \tag{9.2}$$

However, DI_μ does not include effects from hysteretic energy dissipation. Additionally, this damage index may not be zero for undamaged structures. A damage index that overcomes this problem has been proposed by [54]:

$$DI_K = \frac{1 - \mu_{\max}^{-1}}{1 - \mu_u^{-1}} \tag{9.3}$$

Cosenza et al. [51] and Fajfar [55] quantified damage based on the structure hysteretic energy E_H:

$$DI_H = \frac{E_H/(f_y x_y)}{\mu_u - 1} \tag{9.4}$$

A robust damage measure should include not only the maximum displacement response, but also the effect of repeated cyclic loading in terms of hysteretic energy. Park and co-workers developed a simple damage index [56–58]. The index can be expressed by

$$DI_{PA} = \frac{x_{\max}}{x_u} + \beta \frac{E_H}{f_y x_u} = \frac{\mu_{\max}}{\mu_u} + \beta \frac{E_H}{f_y x_y \mu_u} \tag{9.5}$$

Here, $x_{\max}$ and E_H are the maximum absolute displacement and the dissipated hysteretic energy excluding elastic energy. The parameter x_u is the ultimate deformation capacity under monotonic loading and β is a positive constant that weights the effect of cyclic loading on structural damage. Note that, if $\beta = 0$, the contribution to DI_{PA} from cyclic loading is omitted.

The state of the structure damage is defined as: (a) repairable damage, when $DI_{PA} < 0.40$, (b) damaged beyond repair, when $0.40 \leq DI_{PA} < 1.0$, and (c) total or complete collapse, when $DI_{PA} \geq 1.0$. These criteria of damage state are based on calibration of DI_{PA} against experimental results and field observations in earthquakes [58]. Note that Eq. (9.5) represents that both maximum ductility and hysteretic energy dissipation contribute to the structure's damage during earthquakes. Equation (9.5) expresses damage mathematically as a linear combination of the damage

caused by excessive deformation and that contributed by repeated cyclic loading effect. Note also that the displacement and energy quantities $x_{\max}, E_H$ depend on the loading history while the quantities β, x_u, f_y are independent of the loading history and are determined from experimental tests. It should also be emphasized that Eqs. (9.2–9.5) can be used to estimate damage for a member in a structure which defines the local damage. To estimate the global damage of the structure, a weighted sum of the local damage indices need to estimated [58]. In this chapter, Eq. (9.5) is adopted in quantifying the structural damage. The next section develops the mathematical modeling of critical future earthquake loads.

9.3 Formulation of the Worst Case Scenario

The worst future ground motion acceleration is represented as a product of a Fourier series and an envelope function:

$$\begin{aligned}\ddot{x}_g(t) &= e(t)\sum_{i=1}^{N_f} R_i \cos(\omega_i t - \varphi_i) \\ &= A_0[\exp(-\alpha_1 t) - \exp(-\alpha_2 t)]\sum_{i=1}^{N_f} R_i \cos(\omega_i t - \varphi_i)\end{aligned} \tag{9.6}$$

where, A_0 is a scaling constant and the parameters α_1, α_2 impart the transient trend to $\ddot{x}_g(t)$. The parameters R_i and φ_i are $2N_f$ unknown amplitudes and phase angles, respectively and $\omega_i, i = 1, 2, \ldots, N_f$ are the excitation frequencies presented in the ground acceleration which are selected to span satisfactory the frequency range of the ground motion acceleration $\ddot{x}_g(t)$. In constructing critical seismic inputs, the envelope function is taken to be known. The information on energy E, peak ground acceleration (PGA) M_1, peak ground velocity (PGV) M_2, peak ground displacement (PGD) M_3, upper bound of Fourier amplitude spectra (UBFAS) $M_4(\omega)$, and lower bound of Fourier amplitude spectra (LBFAS) $M_5(\omega)$ are also taken to be available which enables defining the following nonlinear constraints [59, 60]:

$$\begin{aligned}&\left[\int_0^\infty \ddot{x}_g^2(t)\, dt\right]^{\frac{1}{2}} \le E \\ &\max_{0<t<\infty} |\ddot{x}_g(t)| \le M_1 \\ &\max_{0<t<\infty} |\dot{x}_g(t)| \le M_2 \\ &\max_{0<t<\infty} |x_g(t)| \le M_3 \\ &M_5(\omega) \le |X_g(\omega)| \le M_4(\omega)\end{aligned} \tag{9.7}$$

In Eq. (9.7), $X_g(\omega)$ is the Fourier transform of the ground motion acceleration $\ddot{x}_g(t)$. Note that the constraint on the earthquake energy is related to the Arias intensity [61] which was explained before. The spectra constraints aim to replicate the frequency content and amplitude observed in past recorded accelerograms on the future earthquake. Integrating Eq. (9.6) provides the ground velocity and displacement as follows:

$$\begin{aligned}\dot{x}_g(t) &= \sum_{i=1}^{N_f} \int_0^t R_i e(\tau)\cos(\omega_i\tau - \varphi_i)d\tau + C_1; x_g(t) \\ &= \sum_{i=1}^{N_f} \int_0^t R_i e(\tau)(t-\tau)\cos(\omega_i\tau - \varphi_i)d\tau + C_1 t + C_2 \end{aligned} \tag{9.8}$$

Making use of the conditions $x_g(0) = 0$ and $\lim_{t\to\infty} \dot{x}_g(t) \to 0$ [62], the constants C_1 and C_2 can be shown to be given as [60]:

$$C_2 = 0; C_1 = -\sum_{i=1}^{N_f} \int_0^\infty R_i e(\tau)\cos(\omega_i\tau - \varphi_i)d\tau \tag{9.9}$$

The constraints of Eq. (9.7) can be expressed in terms of the variables $R_i, \varphi_i, i = 1, 2, \ldots, N_f$ by

$$\left[A_0^2 \sum_{m=1}^{N_f}\sum_{n=1}^{N_f} R_m R_n \int_0^\infty [\exp(-\alpha_1 t) - \exp(-\alpha_2 t)]^2 \cos(\omega_m t - \varphi_m)\cos(\omega_n t - \varphi_n)\, dt\right]^{\frac{1}{2}} \le E$$

$$\max_{0<t<\infty} |A_0[\exp(-\alpha_1 t) - \exp(-\alpha_2 t)] \sum_{n=1}^{N_f} R_n \cos(\omega_n t - \varphi_n)| \le M_1$$

$$\max_{0<t<\infty} |A_0 \sum_{n=1}^{N_f} \int_0^t R_n[\exp(-\alpha_1\tau) - \exp(-\alpha_2\tau)]\cos(\omega_n\tau - \varphi_n)d\tau$$

$$- A_0 \sum_{n=1}^{N_f} \int_0^\infty R_n[\exp(-\alpha_1\tau) - \exp(-\alpha_2\tau)]\cos(\omega_n\tau - \varphi_n)d\tau| \le M_2$$

$$\max_{0<t<\infty} |A_0 \sum_{n=1}^{N_f} \int_0^t R_n[\exp(-\alpha_1\tau) - \exp(-\alpha_2\tau)](t-\tau)\cos(\omega_n\tau - \varphi_n)d\tau$$

$$- A_0 t \sum_{n=1}^{N_f} \int_0^\infty R_n[\exp(-\alpha_1\tau) - \exp(-\alpha_2\tau)]\cos(\omega_n\tau - \varphi_n)d\tau| \le M_3$$

$$M_5(\omega) \le |A_0 \sum_{n=1}^{N_f} \int_0^\infty R_n\{\exp[-\alpha_1\tau] - \exp[-\alpha_2\tau]\}\cos(\omega_n\tau - \varphi_n)\exp[-i\omega\tau]d\tau| \le M_4(\omega)$$

(9.10)

In Eq. (9.10), $i = \sqrt{-1}$. To quantify the constraints quantities E, M_1, M_2, M_3, $M_4(\omega)$, and $M_5(\omega)$, it is assumed that a set of N_r earthquake records denoted by $\ddot{v}_{gi}(t), i = 1, 2, \ldots, N_r$ are available for the site under consideration or from other sites with similar geological soil conditions. The values of energy, PGA, PGV, and PGD are obtained for each of these records. The highest of these values across all records defines E, M_1, M_2, and M_3. The available records are further normalized so that the Arias intensity of each record is set to unity (i.e.,$[\int_0^\infty \ddot{v}_{gi}^2(t)dt]^{1/2} = 1$, [61]), and are denoted by$\{\ddot{\bar{v}}_{gi}\}_{i=1}^{N_r}$. The bounds $M_4(\omega)$and $M_5(\omega)$ of Fourier amplitude spectra are obtained from

$$M_4(\omega) = E \max_{1 \le i \le N_r} |\bar{V}_{gi}(\omega)|;\ M_5(\omega) = E \min_{1 \le i \le N_r} |\bar{V}_{gi}(\omega)| \tag{9.11}$$

Here $\bar{V}_{gi}(\omega), i = 1, 2, \ldots, N_r$ denotes the Fourier transform of the ith normalized accelerogram $\ddot{v}_{gi}(t)$. It should be noted that the bound $M_4(\omega)$ of Fourier amplitude spectra has been considered earlier [10, 42, 63, 64]. On the other hand, the lower bound was considered by Moustafa [65] and Abbas and Manohar [60] to make the candidates ground motions realistic.

Finally, the problem of deriving critical future earthquake loads on inelastic structures can be posed as follows. Determine the optimization variables $y = \{R_1, R_2, \ldots, R_{N_f}, \varphi_1, \varphi_2, \ldots, \varphi_{N_f}\}^t$ such that the damage index DI_{PA} is maximized subject to the constraints of Eq. (9.10). The solution to this nonlinear constrained optimization problem can be tackled by using the sequential quadratic programming method [66]. For numerical purposes, the following convergence criteria are adopted.

$$|f_j - f_{j-1}| \le \varepsilon_1;\ |y_{i,j} - y_{i,j-1}| \le \varepsilon_2 \tag{9.12}$$

In Eq. (9.12), f_j is the objective function at the jth iteration, $y_{i,j}$ is the ith optimization variable at the jth iteration and the parameters $\varepsilon_1, \varepsilon_2$ are small quantities to be specified. The structure inelastic deformation is estimated using the Newmark-β method which is built as a subroutine inside the optimization program. The details of the optimization procedures involved in the computation of the optimal (critical) earthquake and the associated damage index are shown in Fig. 9.2. Further details can also be found in Abbas [59].

It may be emphasized that the ductility and hysteretic energy quantities $\mu(t)$ and $E_H(t)$do not reach their respective maxima at the same time. Therefore, the optimization is performed at discrete points of time and the optimal solution $y^* = [R_1^*, R_2^*, \ldots, R_{N_f}^*, \varphi_1^*, \varphi_2^*, \ldots, \varphi_{N_f}^*]^t$ is the one that produces the maximum DI_{PA} across all time points. The critical earthquake loads are then characterized in terms of the critical accelerations and associated damage indices, inelastic deformations, and energy dissipated by the structure. The next section provides numerical illustrations for the formulation explained in this section.

As mentioned before, in the numerical analysis, the constraints quantities E, M_1, M_2, M_3, $M_4(\omega)$, and $M_5(\omega)$ are estimated using past recorded earthquake data.

This approach is considered to be consistent with the aspirations of the ground motion models that are commonly used by structural and earthquake engineers, which, aim to replicate the gross features of recorded motions, such as amplitude, frequency content, nonstationarity trend, local soil amplification effects, and duration. It is therefore of interest to note in this context that, predictive or physical models for ground motions, which take into account several details, such as fault dimension, fault orientation, rupture velocity, magnitude of earthquake, attenuation, stress drop, density of the intervening medium, local soil condition and epicentral distance, have also been developed in the existing literature, mainly by seismologists (e.g., [67–70]). The possibility has been explained in references [3, 71]. In these models, one needs to input values for a host of parameters and the success of the model depends on how realistically this is done. It is possible to formulate the optimal earthquake models based on the latter class of models in which one can aim to optimize the parameters of the model so as to realize the least favorable conditions. In this case, the class of admissible functions in estimating the critical inputs, becomes further constrained by the choice of the physical model. In this sense, the approach, adopted in this chapter, is nonparametric in nature. A comparison of results based on this approach with those from 'model-based' approaches is of interest; however, these questions are not considered in this chapter.

9.4 Numerical Example

9.4.1 Bilinear Inelastic Frame Structure

Consider an SDOF frame structure with mass 9×10^3 kg, initial stiffness k_0 = 1.49×10^5 N/m and viscous damping of 0.03 damping ratio (initial natural frequency = 4.07 rad/s). The strain hardening ratio is taken as 0.05. These parameters are changed later to study their influence on the estimated worst earthquake loads and the associated damage. The yield displacement is assumed to be 0.10 m and the structure is assumed to start from rest. The Park and Ang damage index DI_{PA} given by Eq. (9.5) is adopted as the objective function. The parameters of the Newmark-β method are taken as $\delta = 1/2; \alpha = 1/6$ and $\Delta t = 0.005$s.

9.4.1.1 Quantification of Constraints

A set of 20 earthquake records is used to quantify the constraint bounds E, M_1, M_2, M_3, $M_4(\omega)$and $M_5(\omega)$ [72]. Table 9.2 provides data on these records. Based on numerical analysis of these records, the constraints values were computed as E = 4.17 m/s$^{1.5}$, M_1 = 4.63 m/s^2 (0.47 g), M_2 = 0.60 m/s and M_3 = 0.15 m and the average dominant frequency was determined about 1.65 Hz. The envelope

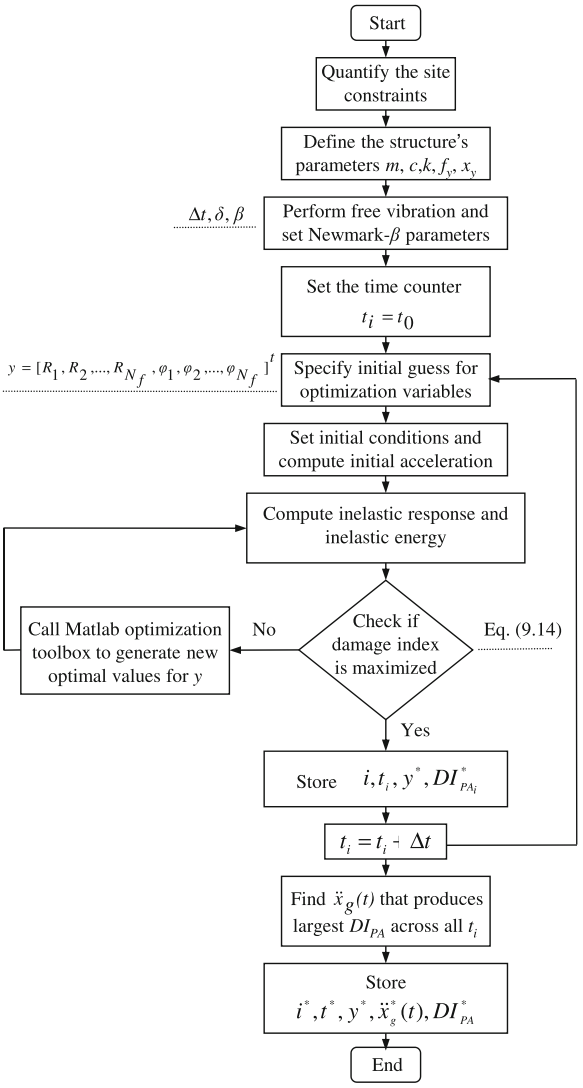

Fig. 9.2 Flowchart for deriving optimal earthquake loads (Moustafa [6] with permission from ASCE)

parameters were specified as $A_0 = 2.17$, $\alpha_1 = 0.13$, and $\alpha_2 = 0.50$. The convergence limits $\varepsilon_1, \varepsilon_2$ were set as 10^{-6} and the convergence criterion on the secant stiffness is taken as 10^{-3} N/m. The frequency content for $\ddot{x}_g(t)$ is defined over (0.1-25) Hz. Additionally, in distributing the frequencies $\omega_i, i = 1, 2, \ldots, N_f$ in the interval $(0.1, 25)$, it was found advantageous to select some of these frequencies ω_i to coincide with the natural frequency of the elastic structure and also to place relatively more points within the modal half-power bandwidth.

The constraint scenarios considered in deriving the worst earthquake inputs are shown in Table 9.3. The constrained nonlinear optimization problem is solved

Table 9.2 Information on past recorded ground motion records for a firm soil site (Moustafa [6] with permission from ASCE)

Earthquake	M	Ds (km)	Component	PGA (m/s^2)	PGV (m/s)	PGD (m)	Energy[a] (m/s$^{1.5}$)	Site
Mamoth lakes	6.2	1.5	W	4.02	0.21	0.05	3.73	Convict Greek
05.25.1980			S	3.92	0.23	0.05	4.01	
Loma prieta	7.0	9.7	W	3.91	0.31	0.07	3.82	Capitola
10.18.1989			S	4.63	0.36	0.11	2.61	
Morgan hill	6.1	4.5	S60E	3.06	0.40	0.07	2.33	Halls valley
04.24.1984			S30 W	1.53	0.30	0.02	1.64	
San Fernando	6.6	27.6	N69 W	3.09	0.17	0.04	2.07	Castaic old ridge
02.09.1971			N21E	2.66	0.28	0.10	2.47	Parkfield fault
Parkfield	5.0	9.1	W	2.88	0.44	0.01	1.33	
12.20.1994			S	3.80	0.10	0.01	1.74	Cantua creek
Caolinga	6.5	30.1	W	2.83	0.26	0.10	2.67	
05.02.1983			N	2.20	0.26	0.10	2.14	Canoga park
Northridge	6.7	5.9	S74E	3.81	0.60	0.12	4.17	
01.17.1994			S16 W	3.43	0.34	0.09	3.50	Petrolia general
Cape Mendocino	7.0	5.4	W	3.25	0.45	0.15	2.44	
04.25.1992			S	2.89	0.24	0.08	2.31	Westmorland fire
Westmorland	5.0	6.6	E	4.35	0.33	0.11	3.26	
04.26.1981			S	3.54	0.44	0.15	3.25	Calexico fire
Imperial valley	6.4	17.4	S45 W	2.68	0.22	0.10	2.30	
10.15.1979			N45 W	1.98	0.19	0.15	2.14	

[a] $E = [\int_0^\infty \ddot{v}_g^2(t)\,dt]^{1/2}$ [61]

Table 9.3 Nomenclature of constraint scenarios considered (Moustafa [6] with permission from ASCE)

Case	Constraints imposed
1	Energy and PGA
2	Energy, PGA, PGV and PGD
3	Energy, PGA and UBFAS
4	Energy, PGA, UBFAS and LBFAS

using the sequential quadratic optimization algorithm 'fmincon' of the Matlab optimization toolbox [73]. In the numerical calculations, alternative initial starting solutions, within the feasible region, were examined and were found to yield the same optimal solution. This was done for checking the local/global optimization. To select the number of frequency terms N_f, a parametric study was carried out and the number $N_f = 51$ was found to give satisfactory results. Figure 9.3 illustrates the influence of N_f on the convergence of the objective function for constraints scenarios 1 and 4 (see Table 9.3).

9.4.1.2 Numerical Results and Discussion

The numerical results obtained are presented in Figs. 9.4, 9.5, 9.6, 9.7, 9.8, 9.9, and Table 9.4. Figure 9.4 shows results for constraint scenario 1 and similar results for case 4 are presented in Fig. 9.5. Each of these figures shows the Fourier amplitude spectrum of the worst ground acceleration, the inelastic deformation, the hysteretic force, and the energy dissipated by the structure. Figure 9.6 presents the time history of the ground acceleration. Based on extensive analysis of the numerical results, the major observations can be summarized as follows.

The frequency content and Fourier amplitude of the worst earthquake ground motion are strongly dependent on the constraints imposed (see Table 9.3). If available information on earthquake data is limited to the total energy and PGA, the worst input is narrow band (highly resonant to the structure natural frequency) and the structure deformation is conservative (see Fig. 9.4 and Table 9.4). Furthermore, most of the power (or intensity) of the Fourier amplitude are concentrated at a frequency close to the natural frequency of the elastic structure. This amplitude gets shifted away from the natural frequency towards a higher frequency when the strain hardening ratio increases. The Fourier amplitudes at other frequencies are low and uniformly distributed. This result is substantially different from that for the elastic structure where all power of the acceleration amplitude is concentrated around ω_0 with no amplitude at other frequencies [60]. Additional constraints on the Fourier amplitude spectra (see Table 9.3) force the Fourier amplitude of the worst acceleration to get distributed across other frequencies. The critical acceleration possesses a dominant frequency that is close to the average dominant frequency observed in past records (see Fig. 9.5). The realism of the earthquake input is also evident from the maximum damage index it produces. For instance, the damage index for case 4 is 0.37 which is substantially smaller than 1.15 for case 1 (Table 9.4). The constraints on PGV and PGD were not found to be significant in producing realistic critical inputs compared to the constraints on UBFAS and LBFAS. Also, the realism of the optimal acceleration for case 4 can be examined by comparing the Fourier amplitude spectra and frequency content of the worst ground motions acceleration (Figs 9.4,9.5) with the Fourier amplitude spectra of past recorded earthquakes (Fig. 9.7). Note that, while the constraint scenario 1 leads to pulse-like ground motion (see Chaps. 3, 4), such scenario is observable past earthquakes (e.g., 1971 San Fernando, 1985 Mexico, and 1995 Kobe earthquakes). Resonant or pulse-like earthquakes are also observable in near-field ground motion with directivity focusing, known as forward- and backward-directivity ground motion (see Chap. 3, 4 and [44, 74–76]). The realism of worst earthquake loads can also be examined by comparing the maximum response from these accelerations with those from past recorded ground motions. Thus, the maximum ductility factor of the structure from the worst earthquake ground motion is about 3.9 (case 1) and 2.6 (case 4) times that from the Kobe earthquake and is 2.7 (case 1) and 1.5 (case 4) times that from the San Fernando earthquake.

To examine the effect of the strain hardening ratio on the derived worst earthquake acceleration, limited studies were carried out. The value of α was

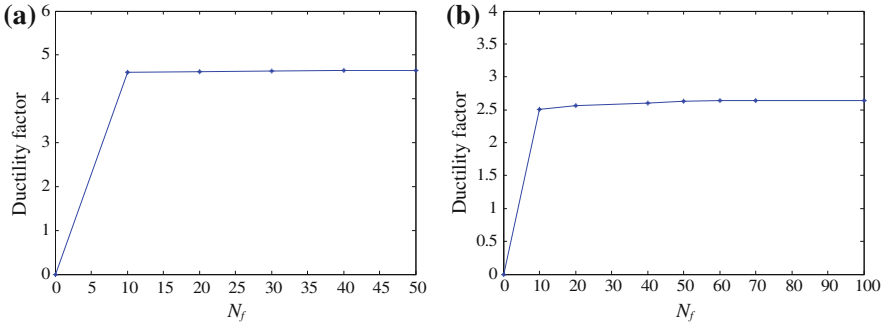

Fig. 9.3 Convergence of objective function in terms of frequency terms N_f (**a**) Case 1, (**b**) Case 4 (Moustafa [6] with permission from ASCE)

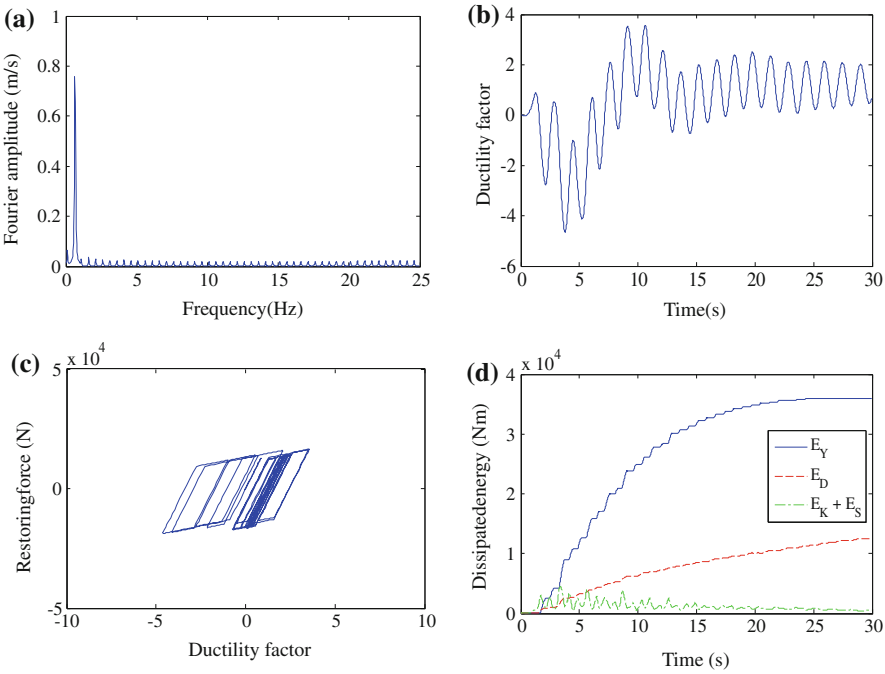

Fig. 9.4 Optimal earthquake input and associated structural responses for case 1 (**a**) fourier amplitude of the ground acceleration, (**b**) normalized inelastic deformation, (**c**) hysteretic restoring force, (**d**) dissipated energy (Moustafa [6] with permission from ASCE)

changed and the critical acceleration was estimated by solving a new optimization problem. Numerically, α was taken as 0.20, 0.10, 0.05, and 0.01. The numerical results showed that the strain hardening ratio does not influence the frequency content of the critical earthquake input significantly. However, the inelastic structure with lower values of α was seen to yield more frequently compared to the

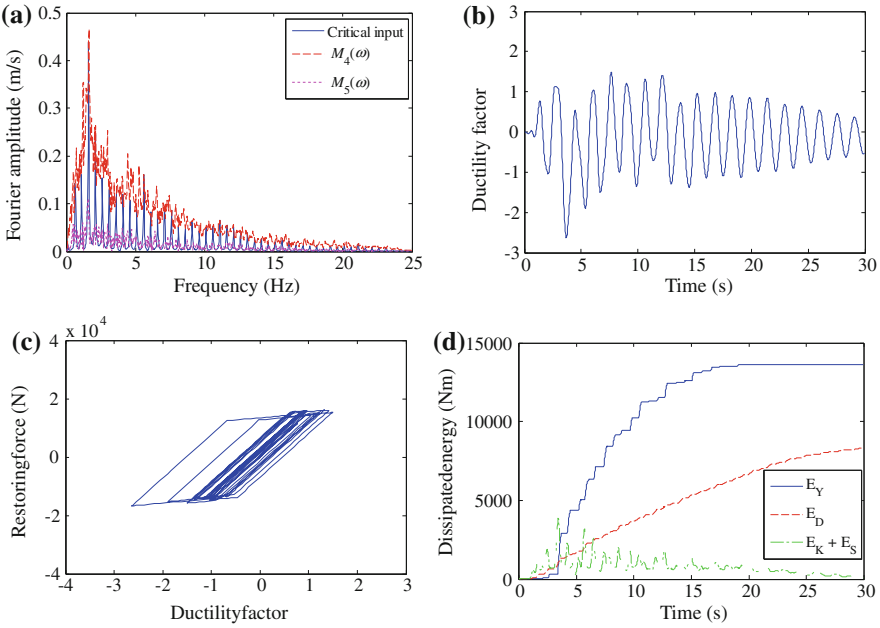

Fig. 9.5 Optimal earthquake input and associated structural responses for case 4 (**a**) fourier amplitude of the ground acceleration, (**b**) normalized inelastic deformation, (**c**) hysteretic restoring force, (**d**) dissipated energy (Moustafa [6] with permission from ASCE)

same structure with higher α. Hence, the cumulative hysteretic energy dissipated was observed to decrease for higher values of α (Fig. 9.8a). This feature was particularly remarkable at the end of the earthquake duration. It was also remarked that the results on critical earthquake accelerations for bilinear inelastic structure with $\alpha = 0.01$ are close to those for the elastic–plastic structure [59].

To examine the effect of the damping ratio on the computed critical earthquake load, limited studies were carried out. The damping ratio was changed and three cases of 0.01, 0.03 and 0.05 were treated, while all other parameters were kept unchanged. The critical earthquake ground motion is computed by solving a new optimization problem for each case. The effect of the change in η_0 was seen to be similar to that due to α. In other words, the value of the damping ratio was not seen to significantly influence the frequency content of the earthquake acceleration. It was observed, however, that the ductility ratio and the maximum inelastic deformation for the structure decrease for higher damping ratios. Thus, the ductility ratio decreases to 2.43 when the damping ratio is changed to 0.05 while the ductility ratio increases to 2.89 when the damping ratio reduces to 0.01. It was also observed that the inelastic structure with higher damping ratio dissipates more energy through damping compared with the same structure with lower damping ratio (see Fig. 9.8b). The damage index also reduces when the damping ratio increases.

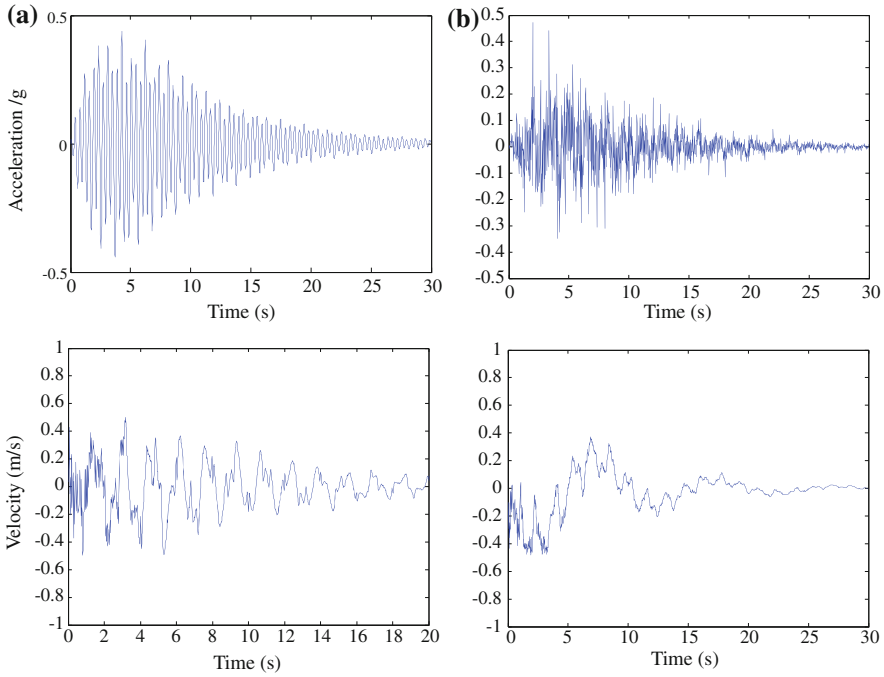

Fig. 9.6 Optimal earthquake acceleration and velocity. **a** Case 1. **b** Case 4 (Moustafa [6] with permission from ASCE)

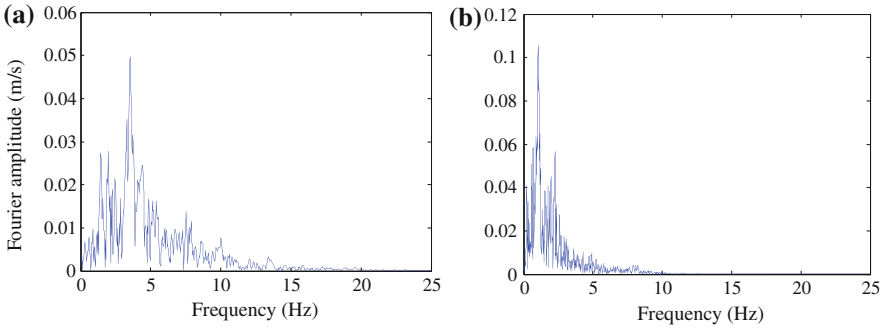

Fig. 9.7 Fourier amplitude of recorded earthquakes (**a**) San Fernando 1971, (**b**) Hyogoken-Nanbu 1995 (Moustafa [6] with permission from ASCE)

Equation (9.7) was used to estimate the damage index of the structure under the critical earthquake load. The influence of the parameter β on the damage index is examined first. Previous experimental tests showed that β ranges between 0.05 and 0.20 with an average value of 0.15 (e.g., [58]). Figure 9.9a shows the effect of β on the damage index. To investigate the influence of the initial natural frequency of

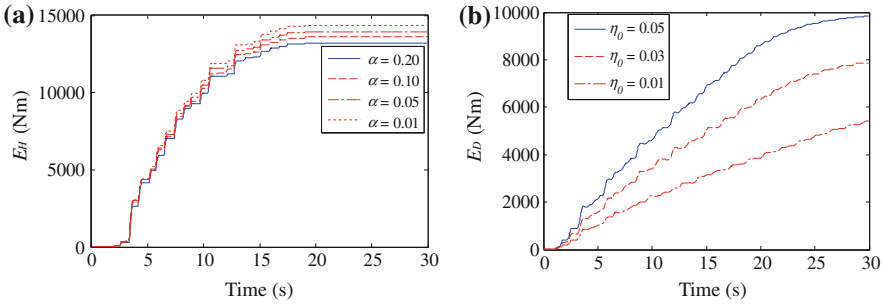

Fig. 9.8 **a** Effect of strain hardening ratio on dissipated yield energy. **b** Effect of damping on dissipated damping energy (Moustafa [6] with permission from ASCE)

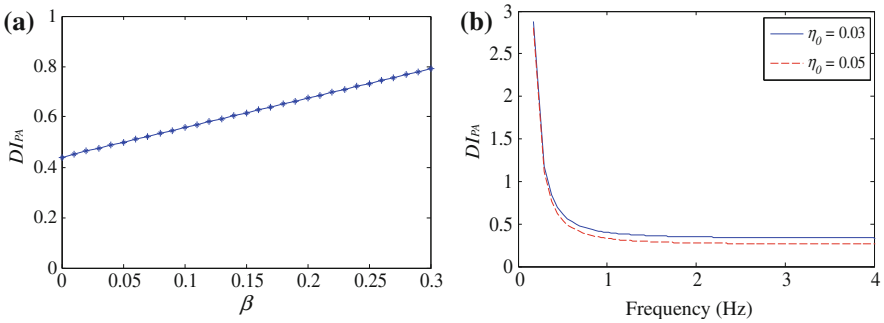

Fig. 9.9 (**a**) Effect of the value of β on the damage index. **b** Damage spectra for inelastic SDOF buildings (Moustafa [6] with permission from ASCE)

Table 9.4 Response parameters for alternative constraint scenarios (α = 0.05, ζ = 0.03) (Moustafa [6] with permission from ASCE)

Case	x_{max} (m)	μ_{max}	x_p (m)	N_{rv}^a	DI_{PA}	Damage status
1	0.47	4.65	0.07	60	1.15	Total collapse
2	0.45	4.53	0.06	54	0.97	Damaged beyond repair
3	0.41	4.14	0.07	49	0.72	Damaged beyond repair
4	0.26	2.64	0.05	44	0.37	Repairable damage

[a] N_{rv} number of yield reversals (see Table 9.1)

the structure on the damage index, the structure stiffness was changed, keeping all other parameters unchanged at their respective values and the critical earthquake load was computed for each case. Subsequently, the value of DI_{PA} was calculated for each case. In the numerical calculations, β was taken as 0.15 and the parameters x_{max}, μ_{max} are set to 0.10 m and 2.64, respectively. The value of μ_u was taken as 6 in Figs. 9.9a and 9.8 and in Fig. 9.9b. It was found that the damage index for the structure with the initial natural frequency smaller than 1.65 is higher than 0.40 and thus either total collapse or damage beyond repair of the structure is expected

in this case. The value of DI_{PA} for the structure with ω_0 greater than about 1.70 Hz is less than 0.40 and thus the structure does not experience total damage but repairable damage in this case. This observation is consistent since the site dominant frequency is around 1.65 Hz and since the Fourier amplitude of the ground acceleration is seen to be located in the stiff side of the initial frequency of the inelastic structure.

The numerical illustrations of the formulation explained in this chapter were demonstrated for simple structures with bilinear and elastic–plastic force–deformation laws. The application of the proposed method to more complex structures and the use of more detailed degradation models (e.g., trilinear degradation, Takeda and Clough models) need to be investigated (see [77]). Additionally, in this chapter the commonly used Park and Ang damage index DI_{PA} has been employed to assess the structure performance. It may be noted that this damage index has some limitations [78, 79], namely: (1) the weak cumulative component for practical cases given the typical dominance of the peak displacement term over the accumulated energy term, (2) the use of a linear combination of deformation and energy in spite of the obvious nonlinearity of the problem and the inter-dependence of the two quantities, and (3) the lack of considering the loading sequence effects in the cumulative energy term. Furthermore, when $E_H = 0$ (elastic behavior), the value of Park and Ang damage index DI_{PA} should be zero. However, the value of DI_{PA} computed from Eq. (9.5) will be greater than zero. Similarly, when the system reaches its maximum monotonic deformation, while DI_{PA} should be 1.0; however, Eq. (9.5) leads to DI_{PA} greater than 1.0. Chai et al. [80] proposed modification to DI_{PA} to correct for the second drawback only. The study, also, examined experimentally the implication of the energy-based linear damage model of DI_{PA}. Despite the drawbacks of DI_{PA}, it has been extensively used by many researchers, mainly due to its simplicity and the extensive calibration against experimentally observed seismic structural damage during earthquakes (mainly for reinforced concrete structures). Bozorgenia and Bertero [78] proposed two improved damage indices to overcome some of the drawbacks associated with DI_{PA}. The interested readers should check this reference.

In this chapter, the worst earthquake loads that maximize the structural damage were obtained using the deterministic approach. The worst earthquake loads can be formulated using stochastic processes, random vibration theory and reliability analysis which provides a powerful alternative to the methodology developed here. Interested readers can refer Abbas and Manohar [4, 81] and others [84, 89, 92, 93, 95, 103] for more details. Energy approaches are discussed in [82, 83, 85, 87, 88, 94, 97, 100, 104, 105, 107, 108] and inelastic design approaches are explained in [86, 91, 101, 102, 106]. As for generation of design earthquake ground motions, see [90, 96, 98, 99].

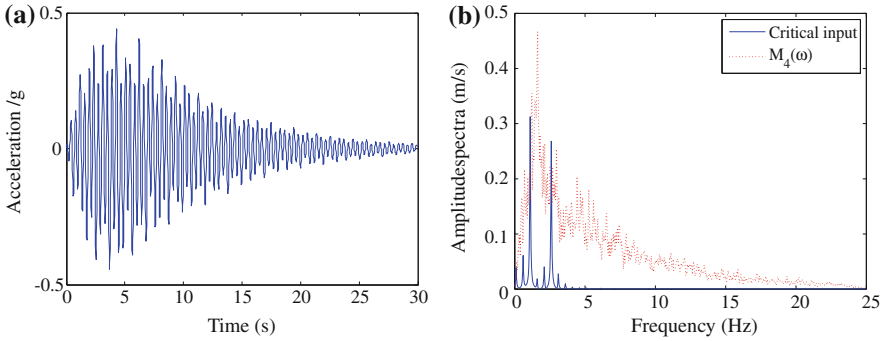

Fig. 9.10 Critical acceleration for inelastic structure for case 1 (**a**) time history, (**b**) Fourier amplitude spectrum

9.4.2 Inelastic Two-Story Frame Structure

A two-story braced building frame is considered to demonstrate the formulation for MDOF inelastic structures [5, 8, 9]. The material behavior of the braces is taken as bilinear ($k_2 = \gamma\, k_1$) as shown in Fig. 9.1a. The floor masses are taken as $m_1 = m_2 = 1.75 \times 10^5$ Ns^2/m, the cross-sectional areas of the braces are $A_1 = A_2 = 6.45 \times 10^{-4}$m^2, the Young's modulus $= 2.59 \times 10^{11}$ N/m^2, and the strain hardening ratio $= 0.10$ (i.e., ratio of the postyield stiffness to the preyield stiffness). When both braces are behaving elastically, the stiffness matrix $\mathbf{K}_s = \mathbf{K}_{el}$, if brace 1 yields $\mathbf{K}_s = \mathbf{K}_1$, if brace 2 yields $\mathbf{K}_s = \mathbf{K}_2$ and if both braces yield $\mathbf{K}_s = \mathbf{K}_{12}$. These matrices are given in Moustafa [5, 8, 9]. The structure is assumed to start from rest. The first two natural frequencies of the elastic structure were computed as $\omega_1 = 6.18$ rad/s and $\omega_2 = 16.18$ rad/s. A Rayleigh proportional damping $\mathbf{C} = a\mathbf{M} + b\mathbf{K}_s$ with $a = 0.2683$, $b = 0.0027$ is adopted. These values are selected such that the damping ratio in the first two modes is 0.03. This implies that the damping forces in braces are nonlinear hysteretic functions of the deformed shape of the structure. Let the yield strain of the braces $\varepsilon_y = 0.002$ for both tension and compression. The braces will yield at a relative displacement $x_y = L\varepsilon_y/\cos\theta = 0.0381$ m. Thus, brace 1 yields when $|x_1| = 0.0381$ m and brace 2 yields when $|x_2 - x_1| = 0.0381$ m. The objective function is taken as the weighted damage indices in braces 1 and 2. In the numerical analysis, the parameters of the Newmark β-method were taken as $\delta = 1/2; \alpha = 1/6$and the time step $\Delta t = 0.005$ s.

The results of this example are shown in Figs. 9.10 and 9.11. In general, the feature observed for the future earthquakes in the previous example was also observed in this example. However, the inelastic deformation and the associated damage were seen to depend on the two vibration modes. Thus, the maximum ductility ratio μ for case 1 is 4.34 while that produced from constraint case 4 is 2.27. Similarly, the maximum response reduces from 0.15 m to 0.08 m when the

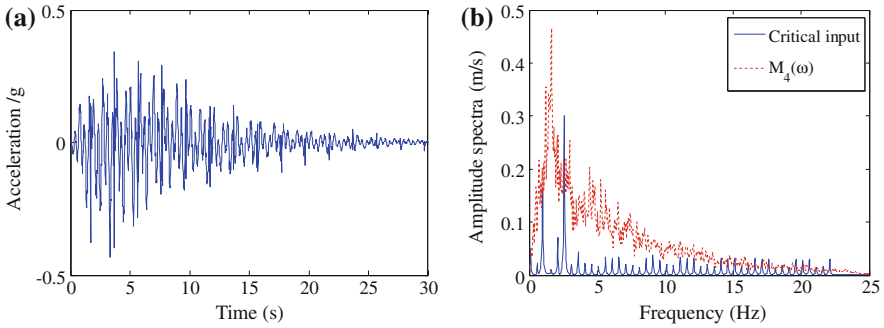

Fig. 9.11 Critical acceleration for inelastic structure for case 2 (**a**) time history, (**b**) Fourier amplitude spectrum

constraints on UBFS and LBFS are brought in. The earthquake input energy to the inelastic system is mainly dissipated by yielding and nonlinear damping of the structure. The hysteretic and damping energies are significantly higher than the recoverable strain and kinetic energy. The kinetic and recoverable strain energies are small and diminish near the end of the ground shaking. The energy dissipated by yielding is significantly higher than that dissipated by damping. It was also observed that the inelastic structure with Rayleigh damping dissipates more energy through damping mechanism compared to the same system with viscous damping. The weighted damage index for case 1 was about 0.96 implying total collapse while for case 4 the damage index was about 0.35 implying repairable damage.

9.5 Summary

Seismic design of structures requires that they resist possible future earthquakes with repairable damage. A methodology for assessing damage in structures under worst future earthquake loads has been explained in this chapter. The novelty of this approach lies in combing damage indices, nonlinear optimization and nonlinear time-history analysis in assessing the structural performance, and making the feature of critical ones clear under future earthquakes. Damage descriptors have been introduced in deriving the worst earthquake ground motion. The structural damage has been quantified in terms of the well-known and commonly used Park and Ang damage indices. The damage indices describe the damage state of the structure and it is well understood that the measure correlates well with the actual damage displayed during earthquakes. The quantification of the structure's damage using such damage indices is of substantial importance in deriving critical earthquake loads for inelastic structures. This is because damage indices imply that the structure is damaged by a combination of repeated stress reversals and high

stress excursions. This also facilitates assessing the safety of the structure by providing a quantitative measure on the necessary repair to the structure.

In this chapter, the worst earthquake load has been derived based on available information using inverse nonlinear dynamic analysis, optimization techniques, and damage indices explained. It was seen that, if available information is limited to the energy and PGA, the resulting earthquake is highly resonant to the structural natural frequency and produces conservative damage. When extra or additional information on the Fourier amplitude spectra is available, more realistic earthquake loads (in terms of frequency content, amplitude, inelastic deformations, and damage indices produce) are obtained. The influences of the strain hardening and damping ratios on the estimated critical design loads were studied. Critical damage spectra for the site were also established. These spectra provide upper bounds on the structural damage and directions of necessary repair under possible future earthquakes. The formulation explained in this chapter was demonstrated for inelastic frame structures modeled with bilinear and elastic–plastic force–deformation laws. In other words, nondeteriorating structures were only considered. Future extension requires the use of nonlinear degradation models that facilitate the development of plastic hinges in the structure (see Chap. 10 and [77]). In this case, the computations will increase considerably due to the complexity in estimating the structural response. Finally, it may be emphasized that the structural properties have been kept unchangeable. It may be possible to apply the explained methodology for optimal design of the structure under future earthquakes. Herein, an initial guess for the dimensions of the structure's members needs to be assumed and an iterative procedure has to be carried out leading to the optimal design of the structure, the system-dependent worst earthquake and the associated damage [11, 40–42].

References

1. Comartin C, Brvez S, Naeim F, Greene M, Blondet M, Cherry S, D'Ayala D, Farsi M, Jain SK, Pantelic J, Sarnant L, Sassu M (2004) A challenge to the earthquake engineering professionals. Earthq Spectra 20(4):1049–1056
2. USGS/EERI Advance Reconnaissance Team (2010) The Mw7.0 Haiti earthquake of January 12, 2010
3. Takewaki I, Murakami S, Fujita K, Yoshitomi S, Tsuji M (2011) The 2011 off the Pacific coast of Tohoku earthquake and response of high-rise buildings under long-period ground motions. Soil Dyn Earthq Eng 31(11):1511–1528
4. Abbas AM, Manohar CS (2007) Reliability-based vector nonstationary random critical earthquake excitations for parametrically excited systems. Struct Saf 29:32–48
5. Moustafa A (2009) Critical earthquake load inputs for multi-degree-of-freedom inelastic structures. J Sound Vib 325:532–544
6. Moustafa A (2011) Damage-based design earthquake loads for SDOF inelastic structures. J Struct Eng (ASCE) 137(3):456–467
7. Moustafa A, Takewaki I (2010) Modeling critical strong ground motion sequences on inelastic structures. Adv Struct Eng 13(4):665–679

8. Moustafa A (2009) Discussion of the effect of energy concentration of earthquake ground motions on the nonlinear response of RC structures. Soil Dyn Earthq Eng 29:1181–1183
9. Moustafa A (2009) Discussion of a new approach of selecting real input ground motions for seismic design: the most unfavourable real seismic design ground motions. Earthq Eng Struct Dyn 38:1143–1149
10. Takewaki I (2002) Seismic critical excitation method for robust design: a review. J Struct Eng (ASCE) 128:665–672
11. Takewaki I (2007) Critical excitation methods in earthquake engineering. Elsevier Science, The Netherlands
12. Penelis GG, Kappos AJ (1997) Earthquake-resistant concrete structures. E & FN SPON, London
13. Pinho R (2007) Nonlinear dynamic analysis of structures subjected to seismic action. In: Pecker A (ed) Advanced earthquake engineering analysis. Springer Wien, NY
14. McGuire RK (1995) Probabilistic seismic hazard analysis and design earthquake: closing the loop. Bull Seism Soc Am 85:1275–1284
15. Reiter L (1990) Earthquake hazard analysis. Columbia University Press, NY
16. Akiyama H (1985) Earthquake-resistant limit-state design for buildings. University of Tokyo Press, Tokyo
17. Otani S (1981) Hysteretic models of reinforced concrete for earthquake response analysis. J Fac Eng Univ Tokyo 36(2):407–441
18. Takeda T, Sozen MA, Nielsen N (1970) Reinforced concrete response to simulated earthquakes. J Struct Div 96(ST12):2557–2573
19. Fardis MN (ed) (2010) Advances in performance-based earthquake engineering. Springer, NY
20. Priestely MJN, Calvi GM, Kowalsky MJ (2007) Displacement-based seismic design of structures. IUSS Press, Pavia
21. Takewaki I (2009) Building control with passive dampers. Wiley, Singapore
22. Elishakoff I, Ohsaki M (2010) Optimization and anti-optimization of structures under uncertainty. Imperial College Press, Singapore
23. Haldar A (ed) (2006) Recent developments in reliability-based civil engineering. World Scientific Publishing Co. Pt. Ltd, Singapore
24. Liang QQ (2005) Performance-based optimization of structures. Spon Press, NY
25. Plevris V (2009) Innovative computational techniques for the optimum structural design considering uncertainties. Ph. D. dissertation, Institute of Structural Analysis and Seismic Research, National Technical University of Athens, June 2009
26. Kalkan E, Luco N (eds) (2011) Earthquake ground motion selection and modification for nonlinear dynamic analysis of structures. J Struct Eng 137(3):277–467
27. Papadrakakis M, Charmpis DC, Lagaros ND, Tsompanakis Y (eds) (2009) Computational structural dynamics and earthquake engineering. Taylor and Francis, London
28. Tsompanakis Y, Lagaros ND, Papadrakakis M (eds) (2008) Structural design optimization considering uncertainties. Taylor and Francis, London
29. Strasser FO, Bommer JJ (2009) Review: strong ground motions—Have we seen the worst? Bull Seismol Soc Am 99(5):2613–2637
30. Housner GW, Jennings PC (1975) The capacity of extreme earthquake motions to damage structures. Structural and geotechnical mechanics: A volume honoring N.M. Newmark. In: WJ Hall (ed). Prentice-Hall Englewood Cliff, NJ, pp 102–116
31. Elnashai A, Bommer JJ, Martinez-Pereira A (1998) Engineering implications of strong-motion records from recent earthquakes. In: Proceedings of 11th European Conference on Earthquake Engineering, Paris, CD-ROM
32. Pacific Earthquake Engineering Research Center (2011) (http://peer.berkeley.edu/peer_ground_motion_database)
33. Baker JW, Cornell CA (2006) Spectral shape, epsilon and record selection. Earthq Eng Struct Dyn 35:1077–1095
34. Baker JW (2011) Conditional Mean Spectrum: Tool for ground motion selection. J Struct Eng 137(3):322–331

35. Baker JW, Lin T, Shahi SK, Jayaram N (2011) New ground motion selection procedures and selected motions for the PEER transportation research program. PEER Tech Rep 2011(03):106p
36. Bommer JJ, Acevedo AB (2004) The use of real earthquake accelerograms as input to dynamic analysis. J Earthq Eng 1:43–91
37. Buratti N, Stafford PJ, Bommer JJ (2011) Earthquake accelerogram selection and scaling procedures for estimating the distribution of drift response. J Struct Eng 137(3):345–357
38. Haselton C, Baker JW, Liel AB, Deierlein GG (2011) Accounting for ground motion spectral shape characteristics in structural collapse assessment through an adjustment for epsilon. J Struct Eng 137(3):332–344
39. Moustafa A, Ueno K, Takewaki I (2010) Critical earthquake loads for SDOF inelastic structures considering evolution of seismic waves. Earthq Struct 1(2):147–162
40. Fujita K, Moustafa A, Takewaki I (2010) Optimal placement of viscoelastic dampers and supporting members under variable critical excitations. Earthq Struct 1(1):43–67
41. Saikat S, Manohar CS (2005) Inverse reliability based structural design for system dependent critical earthquake loads. Probab Eng Mech 20:19–31
42. Takewaki I (2002) Robust building stiffness design for variable critical excitations. J Struct Eng (ASCE) 128(12):1565–1574
43. Moustafa A (2010) Identification of resonant earthquake ground motion. Indian Acad Sci 35(3):355–371
44. Moustafa A (2010) Discussion of analytical model of ground motion pulses for the design and assessment of seismic protective systems. J Struct Eng 137(1):229–230
45. Moustafa A (2010) Closure to discussion of critical earthquake load inputs for multi-degree-of-freedom inelastic structures. J Sound Vib 330:356–360
46. Hart GC, Wong K (2000) Structural dynamics for structural engineers. Wiley, NY
47. Kalkan E, Kunnath SK (2008) Relevance of absolute and relative energy content in seismic evaluation of structures. Adv Struct Eng 11(1):1–18
48. Uang C-M, Bertero VV (1990) Evaluation of seismic energy in structures. Earth Eng Struct Dyn 19:77–90
49. Takewaki I (2004) Bound of earthquake input energy. J Struct Eng (ASCE) 130:1289–1297
50. Zahrah TF, Hall WJ (1984) Earthquake energy absorption in sdof structures. J Struct Eng 110:1757–1772
51. Cosenza C, Manfredi G, Ramasco R (1993) The use of damage functionals in earthquake engineering: a comparison between different methods. Earthq Eng Struct Dyn 22:855–868
52. Ghobara A, Abou-Elfath H, Biddah A (1999) Response-based damage assessment of structures. Earthq Eng Struct Dyn 28:79–104
53. Powell GH, Allahabadi R (1988) Seismic damage predications by deterministic methods: concept and procedures. Earthq Eng Struct Dyn 16(5):719–734
54. Khashaee P (2004) Damage-based seismic design of structures. Earthq Spectra 21(2):371–387
55. Fajfar P (1992) Equivalent ductility factors, taking into account low-cyclic fatigue. Earthq Eng Struct Dyn 21:837–848
56. Park YJ, Ang AH-S (1985) Mechanistic seismic damage model for reinforced concrete. J Struct Eng 111(4):722–739
57. Park YJ, Ang AH-S, Wen YK (1985) Seismic damage analysis of reinforced concrete buildings. J Struct Eng 111(4):740–757
58. Park YJ, Ang AH-S, Wen YK (1987) Damage-limiting aseismic design of buildings. Earthq Spec 3(1):1–26
59. Abbas AM (2006) Critical seismic load inputs for simple inelastic structures. J Sound Vib 296:949–967
60. Abbas AM, Manohar CS (2002) Investigations into critical earthquake load models within deterministic and probabilistic frameworks. Earthquake Eng Struct Dyn 31:813–832
61. Arias A (1970) A measure of earthquake intensity: seismic design of nuclear power plants. MIT press, Cambridge, pp 438–468

62. Shinozuka M, Henry L (1965) Random vibration of a beam column. J Eng Mech 91: 123–143
63. Shinozuka M (1970) Maximum structural response to seismic excitations. J Eng Mech 96:729–738
64. Takewaki I (2001) Probabilistic critical excitation for MDOF elastic-plastic structures on compliant ground. Earthq Eng Struct Dyn 30:1345–1360
65. Moustafa A (2002). Deterministic/reliability-based critical earthquake load models for linear/nonlinear engineering structures. Doctoral dissertation, Department of Civil Engineering, Indian Institute of Science, Bangalore, India
66. Arora JS (2004) Introduction to optimum design. Elsevier Academic Press, San Diego
67. Boore DM (1983) Stochastic simulation of high-frequency ground motions based on seismological models of the radiated spectra. Bull Seismol Soc Am 1983(73):1865–1894
68. Brune JN (1970) Tectonic stress and the spectra of seismic shear waves from earthquakes. J Geoph Res 75:4997–5009
69. Hanks TG, McGuire RK (1981) The character of high frequency ground motions based on seismic shear waves. Bull Seismol Soc Am 71:2071–2095
70. Quek ST, Teo YP, Balendra T (1990) Non-stationary structural response with evolutionary spectra using seismological input model. Earthq Eng Struct Dyn 19:275–288
71. Takewaki I (2008) Critical excitation methods for important structures, invited as a Semi-Plenary Speaker. EURODYN 2008, 7–9 July 2008, Southampton, England
72. COSMOS (2005) Consortium organizations for strong-motion observation systems. http://db.cosmos-eq.org/scripts/default.plx
73. Caleman T, Branch MA, Grace A (1999) Optimization toolbox for the use with Matlab: user's guide. The Math Works Inc., USA
74. Housner GW, Hudson DE (1958) The Port Hueneme earthquake of March 18, 1957. Bull Seism Soc Am 48:163–168
75. He WL, Agrawal AK (2008) Analytical model of ground motion pulses for the design and assessment of seismic protective systems. J Struct Eng 134(7):1177–1188
76. Kalkan E, Kunnath SK (2006) Effects of fling step and forward directivity on seismic response of buildings. Earthq Spectra 22(2):367–390
77. Ueno K, Fujita K, Moustafa A, Takewaki I (2011) Critical input for inelastic structures under evolving seismic waves. J Struct Constr Eng AIJ 659:79–87 (in Japanese)
78. Bozorgenia Y, Bertero VV (2003) Damage spectra: Characteristics and applications to seismic risk reduction. J Struct Eng 129(4):1330–1340
79. Mehanny SS, Deierlein GG (2000) Modeling of assessment of seismic performance of composite frames with reinforced concrete columns and steel beams. In: Report no. 135, the John Blume earthquake research center, Stanford University
80. Chai YH, Romstad KM, Bird SM (1995) Energy-based linear damage model for high-intensity seismic loading. J Struct Eng 121(5):857–864
81. Abbas AM, Manohar CS (2005) Reliability-based critical earthquake load models. Part 2: nonlinear structures. J Sound Vib 287:883–900
82. Bozorgenia Y, Bertero VV (eds) (2004) Earthquake engineering. CRC Press, NY
83. Choi H, Kim J (2006) Energy-based design of buckling-restrained braced frames using hysteretic energy spectrum. Eng Struct 28:304–311
84. Conte JP, Peng BF (1997) Fully nonstationary analytical earthquake ground motion model. J Eng Mech 123:15–24
85. Decanini LD, Mollaioli F (2001) An energy-based methodology for the assessment of seismic demand. Soil Dyn Earthq Eng 21:113–137
86. Drenick RF (1977) The critical excitation of nonlinear systems. J Appl Mech 44(2):333–336
87. Fajfar P, Krawinkler H (1997) Seismic design methodologies for the next generation of codes. Balkema, Rotterdam
88. Goel RK (1997) Seismic response of asymmetric systems: energy-based approach. J Struct Eng 123(11):1444–1453

89. Iyengar RN (1972) Worst inputs and a bound on the highest peak statistics of a class of nonlinear systems. J Sound Vib 25:29–37
90. Der Kiureghian A, Crempien J (1989) An evolutionary model for earthquake ground motion. Struct Saf 6:235–246
91. Mahin SA, Bertero VV (1981) An evaluation of inelastic seismic design spectra. J Struct Div 107(ST9):1777–1795
92. Moustafa A, Takewaki I (2011) Response of nonlinear SDOF structures to random acceleration sequences. Eng Struct 33(4):1251–1258
93. Moustafa A, Takewaki I (2010) Deterministic and probabilistic representation of near-field pulse-like ground motion. Soil Dyn Earthq Eng 30:412–422
94. Moustafa A, Takewaki I (2010) Characterization and modeling of near-fault pulse-like strong ground motion via damage-based critical excitation method. Struct Eng Mech 34(6):755–778
95. Moustafa A, Mahadevan S (2010) Probabilistic critical earthquake excitations using earthquake response spectra. Asian J Civil Eng (Build Hous) 11(3):295–319
96. Moustafa A, Takewaki I, Wijeyewickrema (2010) Selection of earthquake records for time-history analysis of structures. In: Joint 7th international conference on urban earthquake engineering and 5th international conference on earthquake engineering, 3–5 March, Tokyo, Japan
97. Nakashima M, Saburi K, Tsuji B (1996) Energy input and dissipation behavior of structures with hysteretic dampers. Earth Eng Struct Dyn 25:483–496
98. Newmark NM, Hall WJ (1982). Earthquake spectra and design, Monograph. Earthq Eng Res Inst (EERI)
99. Pecker A (ed) (2007) Advanced earthquake engineering analysis. Springer, Udine
100. Priestley MJN, Kowalsky MJ (2007) Displacement-based seismic design of structures. IUSS Press, Pavia
101. Riddell F (1995) Inelastic design spectra accounting for soil conditions. Earthq Eng Struct Dyn 24:1491–1510
102. Philippacopoulos AJ, Wang PC (1984) Seismic inputs for nonlinear structures. J Eng Mech 110:828–836
103. Sarkar A (2003) Linear stochastic dynamical system under uncertain load: inverse reliability analysis. J Eng Mech 129(6):665–671
104. SEAOC, Vision Committee (2002) Performance based seismic design engineering. Structural Engineers Association of California (SEAOC) Report, Sacramento, USA
105. Takewaki I (2011) The 2011 off the Pacific coast of Tohoku earthquake and its impact on building structural design. In: Keynote paper (plenary speaker) at the ASEM11+ congress, 18–23 Sept 2011 in Seoul, Korea, pp 36–61
106. Westermo BD (1985) The critical excitation and response of simple dynamic systems. J Sound Vib 100:233–242
107. Wong KKF, Yong R (2002) Earthquake response and energy evaluation of inelastic structures. J Eng Mech 128(3):308–317
108. Yamaguchi H, El-Abd A (2003) Effect of energy input characteristics on hysteretic damper efficiency. Earthq Eng Struct Dyn 32:827–843

Chapter 10
Critical Earthquake Loads for SDOF Inelastic Structures Considering Evolution of Seismic Waves

10.1 Introduction

The damage of structures induced by earthquake ground motions depends primarily on three parameters: (1) the characteristics of earthquake source properties and ground motions (magnitude, epicentral distance, duration, frequency content, amplitude and local soil type), (2) the properties of the structure (natural frequencies, mode shapes, damping properties, material of construction, structural system and ductility capacity), and (3) how close the structure's fundamental natural frequency to the dominant frequency of the ground motion (see [1, 2]). The 2011 off the Pacific coast of Tohoku earthquake has demonstrated these facts clearly [3–5]. In general, the ground motion characteristics involve large inherent uncertainties and cannot be controlled while the structure's properties have smaller variability and can be managed to some extent in general [6]. For instance, the material and members of construction can be selected and the seismic-resistance of the structure can be improved to fairly high levels through member detailing for enhancement of ductility capacity.

The seismic waves arriving at a specific site depend on the source mechanism, the travel path (site-source distance) and the local soil condition [7]. The ground motion hitting the structure's foundations is known to be composed of several waves that have different phase velocities, arrival times, amplitudes, and frequency contents [8]. Body waves consist of P (primary) and S (shear or secondary) waves that have higher frequency components and arrive at the site first. Surface waves, on the other hand, are composed of Rayleigh (R) and Love (L) waves which have lower phase velocities, lower frequency components and reach the site next. P-waves are compression waves while S-waves are transverse waves. Surface waves result in rolling motion that constitutes the most destructive waves to structures and infrastructures. Some of these waves could be of more damage to the structure depending on their dominant frequency, amplitude and relation with the structure's natural frequencies (for example [3–5]). The attenuation of the seismic waves that

I. Takewaki et al., *Improving the Earthquake Resilience of Buildings*,
Springer Series in Reliability Engineering, DOI: 10.1007/978-1-4471-4144-0_10,

propagate at the source gives rise to variation of the ground motion in time and space. Seismic waves attenuate due to natural causes (local soil amplification, reflection, transmittance, refraction and energy dissipation of travelling waves) and man-made obstacles, such as, cavities and underground structures [9]. Surface waves are known to attenuate slower than body waves. Attenuation of seismic waves depends largely on soil conditions. For instance, soft soils can significantly amplify the amplitude and modify the frequency content of the ground motion. This characteristic has been confirmed clearly during Mexico earthquake (1985) and Tohoku/Japan (2011) earthquake. Attenuation modeling of the ground motion is an attractive and active field of research in engineering seismology [10]. The influence of the high-frequency components of the ground motion on the damage of masonry structures has been investigated by Meyer et al. [11]. High frequencies can cause vertical interstone vibrations resulting in irreversible relative displacements of the stones, which may ultimately lead to collapse. The partial fluidification and densification of the loose, granular inner core of some unreinforced masonry walls may also increase the outward thrust.

The modeling of strong ground motion has been an interesting problem in the field of earthquake engineering for many decades. A state of the art review on modeling stationary/non-stationary deterministic/stochastic ground motion can be found in the researches of He and Agrawal [12], Takewaki [6], Conte and Peng [13], Der Kiureghian and Crempien [14], Lin and Yong [15]. This aspect is of importance in seismic analysis and design of engineering structures. The well-known Kanai-Tajimi model represents one of the most widely used ground motion models [15]. The parameters of the ground motion model are usually estimated by matching the model parameters with recorded accelerograms. Der Kiureghian and Crempien [14] decomposed the 1971 Orion earthquake into seven acceleration components of different frequency bands. On the other hand, Conte [16] employed the ARMA stochastic models to study the effect of the frequency nonstationarity of the ground motion on the response of inelastic structures. Furthermore Conte and Peng [13] developed a fully non-stationary stochastic model for earthquake accelerations that is composed of several seismic waves.

Strong ground motion involves several uncertainties including occurrence time, location, duration, magnitude, frequency content, etc. (see [6]). On the other hand, the structural engineer is often concerned with the worst case scenario that can happen to the structure. This may result from many unexpected phenomena in the former earthquake observations. The modeling of critical earthquake loads for structures has attracted many researchers. Early research thoughts on this subject have been provided by Drenick [17], Shinozuka [18] and Iyengar [19]. Extensive reviews on modeling critical earthquake loads on elastic and inelastic structures have been reported by Takewaki [6, 20, 21], Abbas and Manohar [22, 23], Abbas [24] and Moustafa [25]. The notion of critical excitation has been employed recently in identifying critical recorded accelerograms [26–30]. Mathematically, the critical input for a given structure is computed by solving an inverse dynamic problem such that a measure of the structural damage is maximized while the input is constrained to predefined bounds that aim to replicate observed characteristics of

recorded ground motions on the input. A sophisticated critical excitation method for structures with variable parameters has also been developed [6, 31].

In this chapter, critical ground motion inputs are modeled for inelastic structures considering evolution of seismic waves in time and frequency. It is well-recognized that inelastic responses of structures depend sensitively on the complex combination of time and frequency contents. It is therefore meaningful to discuss the effects of this complex combination on critical inelastic deformation. The ground acceleration is represented as a combination of seismic waves that have different characteristics. The amplitudes and phase angles of these waves are optimized (or determined) to produce the highest damage in the structure subject to constraints on the peak ground acceleration (PGA) and energy. The constraints include restrictions on the non-stationary shape and the frequency content of each wave, and bounds on the energy and PGA of the total acceleration. The material nonlinearity is modeled using bilinear inelastic relation. The next section explains the dynamic analysis of SDOF inelastic structures to earthquake loads.

10.2 Dynamic Analysis and Energies Dissipated by Inelastic Structures

The displacement $u(t)$ of a one-storey structure modeled as an SDOF inelastic system, relative to the ground, driven by the ground acceleration $\ddot{u}_g(t)$ is derived from the equation of motion:

$$m\,\ddot{u}(t) + c\,\dot{u}(t) + f_s(t) = -m\,\ddot{u}_g(t) \tag{10.1}$$

where m and c are the mass and the damping coefficient of the SDOF system and $f_s(t)$ is the inelastic restoring force in the spring which is a nonlinear function of $u(t)$. In other words, the force–deformation relation is no longer a single valued function. Thus, for a displacement $u(t_i)$, the restoring force depends upon prior history of motion of the system and whether the velocity response $\dot{u}(t_i)$ is increasing or decreasing. The above equation can be reduced to the following normalized one:

$$\ddot{u}(t) + 2\varsigma\omega\,\dot{u}(t) + \omega^2 u_y \bar{f}_s(t) = -\ddot{u}_g(t) \tag{10.2}$$

where, ς is the damping ratio, ω is the initial natural circular frequency for the inelastic system and u_y is the yield displacement. The function $\bar{f}_s(t)$ is the spring restoring force in a dimensionless form. Referring to Eq. (10.2), the inelastic response of the system for a given acceleration $\ddot{u}_g(t)$ depends on the initial natural circular frequency ω of the system, the damping ratio ς and the yield displacement $u_y (u_y = f_y/k, f_y =$ yield strength and $k =$ initial stiffness). The maximum ductility demand (ductility response) is obtained by normalizing the maximum absolute displacement by the yield displacement. The inelastic dynamic response is obtained by solving the incremental equation of motion numerically (see [32]).

The earthquake input energy and the energies stored or dissipated in the structure have been investigated for a long time and can be quantified by integrating Eq. (10.1). Thus, the energy balance for the structure is well known [24, 33–36] and given as:

$$\int_0^u m\,\ddot{u}(t)\mathrm{d}u + \int_0^u c\,\dot{u}(t)\mathrm{d}u + \int_0^u f_s(t)\mathrm{d}u = -\int_0^u m\,\ddot{u}_g(t)\mathrm{d}u \tag{10.3}$$

The right hand side of Eq. (10.3) represents the total input energy to the structure. Uang and Bertero [34] introduced a concept of relative kinetic energy (pseudo work) and absolute kinetic energy (real work). The right hand side of Eq. (10.3) corresponds to the former pseudo work. The first term in the left side is the kinetic energy $E_K(t)$:

$$E_K(t) = \int_0^u m\,\ddot{u}(t)\mathrm{d}u = \int_0^t m\,\ddot{u}(\tau)\dot{u}(\tau)\mathrm{d}\tau = m\frac{[\dot{u}(t)]^2}{2} \tag{10.4}$$

The second term in the left side of Eq. (10.3) is the energy $E_D(t)$ dissipated by damping:

$$E_D(t) = \int_0^u c\,\dot{u}(t)\mathrm{d}u = \int_0^t c[\dot{u}(\tau)]^2\mathrm{d}\tau \tag{10.5}$$

The third term in the left side of Eq. (10.3) is the sum of the recoverable elastic strain energy $E_S(t)$ and the unrecoverable accumulated hysteretic energy $E_H(t)$ dissipated by yielding. These quantities can be described by

$$E_S(t) = \frac{[f_s(t)]^2}{2k} \tag{10.6a}$$

$$E_H(t) = \int_0^u f_s(t)\mathrm{d}u - E_S(t) = \int_0^t \dot{u}(\tau)f_s(\tau)\mathrm{d}\tau - E_S(t) \tag{10.6b}$$

The next section explains the use of maximum ductility and hysteretic energy demands in developing damage indices.

10.3 Quantification of Structural Damage Using Damage Indices

The literature on damage measures of structures under strong ground motions is versatile [37, 38]. Damage measures are often referred to as damage indices and such damage indices are estimated by comparing the response parameters demanded by

the earthquake with the corresponding structural ultimate capacities. Powell and Allahabadi [39] proposed a damage index in terms of the ultimate ductility (capacity) μ_u and the maximum ductility μ_{max} demanded by the ground motion:

$$D_\mu = \frac{\mu_{max} - 1}{\mu_u - 1} \tag{10.7}$$

On the other hand, Cosenza et al. [37] and Fajfar [40] proposed another damage index based on the structure hysteretic energy E_H:

$$D_H = \frac{E_H/(f_y u_y)}{\mu_u - 1} \tag{10.8}$$

As a combined version, Park and co-workers introduced a damage index based on maximum ductility and hysteretic energy dissipated by the structure [41, 42]:

$$D_{PA} = \frac{\mu_{max}}{\mu_u} + \beta \frac{E_H/(f_y u_y)}{\mu_u} \tag{10.9}$$

Here, μ_{max} and E_H are the maximum ductility and hysteretic energy demands (excluding elastic energy). μ_u is the ultimate ductility capacity under monotonic loading and β is a positive constant that weights the effect of cyclic loading on structural damage ($\beta = 0$ implies that the contribution to D_{PA} from cyclic loading is omitted). It should be remarked that the damage index by Park and co-workers is a combination of ductility and hysteretic energy and can well simulate actual damage states.

The state of the structure's damage is defined as: (a) repairable damage ($D_{PA} < 0.40$), (b) damage beyond repairable limit ($0.40 \le D_{PA} < 1.0$), and (c) total or complete collapse ($D_{PA} \ge 1.0$). These criteria are based on calibration of D_{PA} against experimental results and field observations after earthquakes [42]. Equation (10.9) expresses damage as a linear combination of the damage caused by excessive deformation and that contributed by repeated cyclic loading effects. Note that the quantities μ_{max}, E_H depend on the loading history while the parameters β, μ_u, f_y are independent of the loading history and are determined from experimental data. The next section explains critical earthquake loads for inelastic structures.

10.4 Critical Earthquake Loads Considering Evolution of Seismic Waves

In this chapter, the ground acceleration is represented by a combination of N_s seismic waves:

$$\ddot{u}_g(t) = \sum_{i=1}^{N_s} e_i(t)\ddot{u}_i(t) = \sum_{i=1}^{N_s} e_i(t) \sum_{j=1}^{N_f} R_{ij} \cos(\omega_{ij} t - \phi_{ij}) \tag{10.10}$$

Herein, R_{ij} and ϕ_{ij} are unknown amplitudes and phase angles, ω_{ij} is the jth circular frequency of the ith seismic wave and N_f is the number of frequencies considered in each signal. Following Conte and Peng [13], the envelope function of the ith seismic wave is taken to be given as:

$$e_i(t) = \alpha_i (t - \zeta_i)^{\beta_i} e^{-\lambda_i (t-\zeta_i)} \tag{10.11}$$

where α_i and λ_i are positive constants, β_i is a positive integer, ζ_i is the arrival time of the ith seismic wave. In view of realistic situations, the ground acceleration is taken here to be composed of body waves and surface waves ($N_\mathrm{s} = 2$).

In deriving critical earthquake loads, the envelope functions are taken to be known while the amplitudes and phase angles [Eq. (10.10)] are treated as unknowns. The treatment of the envelope functions as unknowns is challenging and may open another door for general critical excitation problems. This problem will be discussed elsewhere. The information on energy E and PGA (M) are also assumed to be known, thus, defining the following constraints [22, 25]:

$$\left[\int_0^\infty \ddot{u}_\mathrm{g}^2(t) \mathrm{d}t \right]^{\frac{1}{2}} \leq E \tag{10.12a}$$

$$\max_{0<t<\infty} \left| \ddot{u}_\mathrm{g}(t) \right| \leq M \tag{10.12b}$$

Note that the constraint on the earthquake energy, i.e. Eq. (10.12a), is related to the Arias intensity [43]. It is also interesting to remark that the earthquake energy related directly to the ground motion only has strong relationship with the earthquake input energy related to both the structure and the ground motion [6, 44].

The constraints of Eq. (10.12a) are further expressed in terms of the variables $R_{ij}, \phi_{ij}; \quad i = 1, 2, \ldots, N_s, \quad j = 1, 2, \ldots, N_f$ as:

$$\left[\sum_{i=1}^{N_\mathrm{s}} \sum_{j=1}^{N_\mathrm{f}} \sum_{m=1}^{N_\mathrm{s}} \sum_{n=1}^{N_\mathrm{f}} R_{ij} R_{mn} \int_0^\infty e_i(t) e_m(t) \cos(\omega_{ij} t - \phi_{ij}) \cos(\omega_{mn} t - \phi_{mn}) \, \mathrm{d}t \right]^{\frac{1}{2}} \leq E \tag{10.13a}$$

$$\max_{0<t<\infty} \left| \sum_{i=1}^{N_\mathrm{s}} e_i(t) \sum_{j=1}^{N_\mathrm{f}} R_{ij} \cos(\omega_{ij} t - \phi_{ij}) \right| \leq M \tag{10.13b}$$

To quantify the constraints quantities E and M, it is assumed here that a set of acceleration records are available for the given site or from other sites with similar soil conditions. The values of energy and PGA are obtained for each of these records. The highest of these values across all records are taken to define E and M. It may be noted that the constraints on the Fourier amplitude spectra developed by Abbas and Manohar [22] require more information on recorded earthquakes at the site and have not been considered here.

The problem of deriving critical earthquake loads for inelastic structures can be posed as determining the variables $\mathbf{y} = \{R_{11}, R_{12}, \ldots, R_{N_s N_f}, \phi_{11}, \phi_{12}, \ldots, \phi_{N_s N_f}\}^T$ in the optimization problem such that D_{PA} [Eq. (10.9)] is maximized subject to the constraints of Eq. (10.13a). This nonlinear constrained optimization problem is solved using the sequential quadratic programming method [45]. The following convergence criteria are adopted:

$$|f_j - f_{j-1}| \leq \varepsilon_1 \tag{10.14a}$$

$$|y_{i,j} - y_{i,j-1}| \leq \varepsilon_2 \tag{10.14b}$$

Herein, f_j is the objective function value at the jth iteration, $y_{i,j}$ is the ith optimization variable at the jth iteration and $\varepsilon_1, \varepsilon_2$ are small positive quantities to be specified. The structure inelastic deformation is estimated using the Newmark-β method which is built as a subroutine inside the optimization program.

It may be emphasized that the quantities $\mu(t)$ and $E_H(t)$ do not reach their respective maxima at the same time. Hence, the damage index of Eq.(10.9) is maximized at discrete points of time and the optimal solution $\mathbf{y}^* = \{R_{11}^*, R_{12}^*, \ldots, R_{N_s N_f}^*, \phi_{11}^*, \phi_{12}^*, \ldots, \phi_{N_s N_f}^*\}^T$ is the one that produces the maximum structural damage at all time points. The next section provides numerical illustrations for the formulation explained above.

10.5 Numerical Results and Discussions

Consider a one-storey frame structure. The columns' initial stiffness (storey stiffness) is taken as 4×10^6 N/m and the girder carries a total load of 1×10^5 kg (initial natural frequency = 1.0 Hz). The columns are assumed to behave elastic-plastically (bilinear inelastic) with strain-hardening ratio $\gamma = 0.05$. The yield strength in tension and compression are taken as 6 and -6×10^4 N, respectively (yield displacements are 0.02 and -0.02 m). A viscous damping model with 0.02 damping ratio is adopted. The constraints of Eq. (10.13a) have been quantified using a set of 20 earthquake records [25]. These records have been recorded at sites with a firm soil condition. Specifically, the PGA and the energy are specified as $M = 4.63$ m/s^2 and $E = 4.16$ m/s$^{1.5}$ [Eq. (10.12a)]. The envelope functions adopted, i.e. Eq. (10.11), are shown in Fig. 10.1 [13]. The numerical values of the parameters of these envelope functions are taken as $\alpha_1 = 2.0$, $\zeta_1 = 5.0$, $\beta_1 = 8$, $\lambda_1 = 0.60$ for body waves and $\alpha_2 = 8.0$, $\zeta_2 = 2.0$, $\beta_2 = 6$, $\lambda_2 = 0.45$ for surface waves. These envelope functions are normalized to unit peak values. Note that the numerical values of the parameters $\zeta_i (i = 1, 2)$ are used to control the arrival time of each seismic wave. The numerical values of these parameters are changed later to study the influence of the arrival time of the seismic waves on the derived critical acceleration and the associated inelastic response. Note that the envelope functions can be treated as unknowns and the optimal values of the

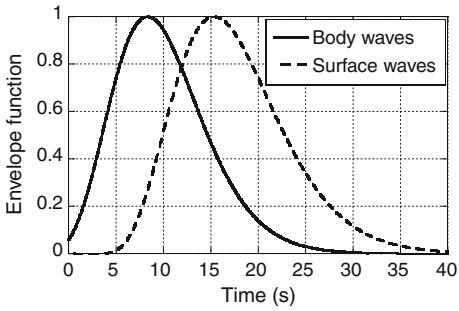

Fig. 10.1 Envelope funtions of body waves and surface waves showing different arrival times (Moustafa et al. [49] with permission from Techno Press)

envelopes parameters can be estimated using optimization techniques. In that case, upper and lower bounds and other positivity constraints on these parameters need to be specified. To quantify these constrains, the numerical values of these parameters has to be calculated for each of the available records to match their non-stationarity trends. The lowest and the highest values of these parameters define the lower and the upper bound constraints. This approach, however, may lead to an overly constrained optimization problem or could result in unrealistic non-stationarity trend for the seismic waves, especially with the form of the envelope functions adopted in this chapter (large number of envelope parameters). Such approach can be considered for simple envelope functions as has been carried out in some of our previous studies [46, 24]. In this chapter, the envelope functions are taken to reflect the average nonstationarity trend of the past recorded accelerograms at the site.

The frequency content of the surface waves is defined in the range (0–1.0) Hz and that for the body waves is defined in the range (1.0–10.0) Hz [47]. These frequency ranges are discretized by the increment 0.10 Hz resulting in a total of 204 optimization variables [$N_f = 102$, see Eq. (10.10)]. The influence of the frequency contents of the seismic waves on the estimated critical acceleration and the associated structural response are also studied later. The structure's inelastic response is computed using the Newmark numerical integration scheme ($\alpha = 0.50$, $\delta = 0.25$, $\Delta t = 0.005$s). The parameters β and μ_u of Eq. (10.9) are taken as 0.15 and 6.0, respectively. The input energy and the hysteretic, damping, kinetic and elastic strain energies dissipated by the structure are calculated using Eqs. (10.3–10.6a) and the damage indices are computed using Eqs. (10.7–10.9).

The numerical results are shown in Figs. 10.2, 10.3, 10.4, 10.5, 10.6, 10.7, 10.8, and 10.9 and Tables 10.1, 10.2 and 10.3. Based on thorough investigations of the numerical results obtained, the following observations are made:

1. **Non-stationarity trend and effect of arrival time of seismic waves**: The body waves have different non-stationarity trend and different arrival time compared with the surface waves (Fig. 10.2a, c). Body waves build up faster, have relatively narrow strong phase (duration) and decay faster. Surface waves build up at about 8.0 s, have longer strong phase (duration) and decay slower. These features were observed clearly during the 2011 off the Pacific coast of Tohoku

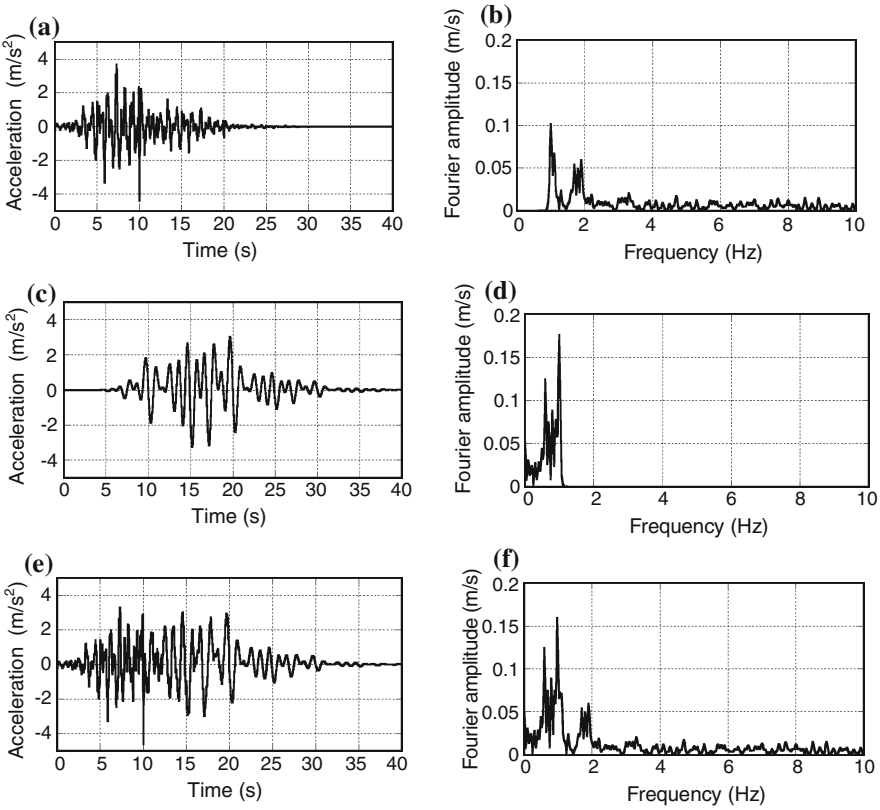

Fig. 10.2 Critical ground acceleration for bilinear inelastic structure **a** Body waves in time domain, **b** Body waves in frequency domain, **c** Surface waves in time domain, **d** Surface waves in frequency domain, **e** Total acceleration in time domain, **f** Total acceleration in frequency domain (Moustafa et al. [49] with permission from Techno Press)

earthquake [48] and match well the assumed modulating envelope functions and arrival times (see Fig. 10.1). The two acceleration components result in a total acceleration that has broader strong phase of about 20.0 s. The PGA is attained at the overlap time-interval region between the peaks of the body waves and the surface waves (see Fig. 10.2e). To examine the influence of the arrival times on the derived critical acceleration and associated structural response, ζ_2 in Eq. (10.11), that controls the arrival time of the surface waves, has been changed to 2.5, shifting the arrival time and the peak amplitude by about 2.0 s. This was seen to reduce the maximum ductility, the number of yield reversals and the Park and Ang's damage index from 1.91, 79 and 4.54 to 1.35, 64 and 2.43, respectively. This implies that, when the arrival times of the different seismic waves are close, more energies are superposed. This results in larger structural responses (e.g. case of near-field shallow ground motion).

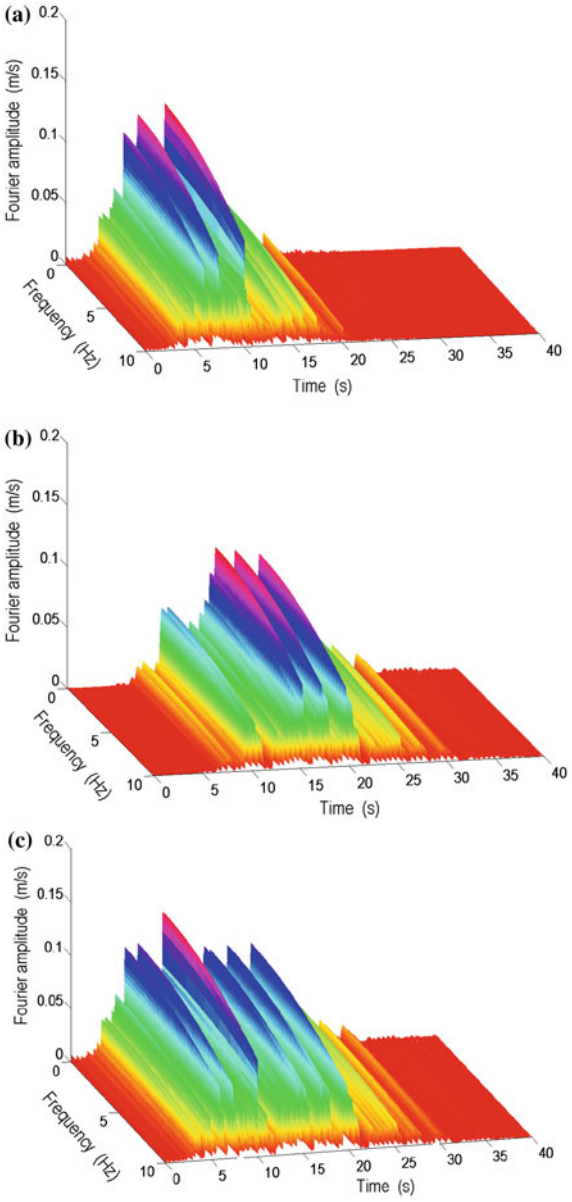

Fig. 10.3 Short-time Fourier amplitude spectra for critical ground acceleration **a** Body waves, **b** Surface waves, **c** Total acceleration (Moustafa et al. [49] with permission from Techno Press)

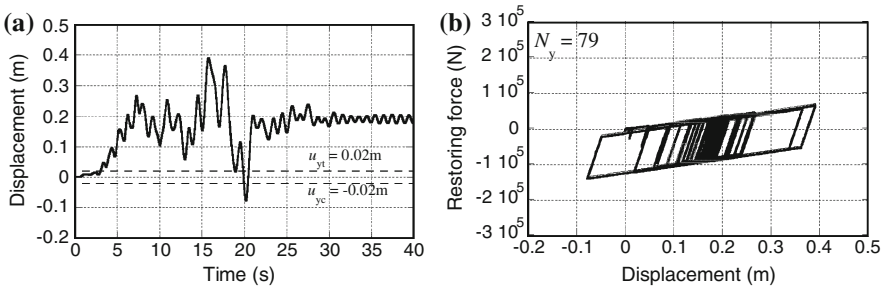

Fig. 10.4 Critical response of the inelastic structure under the critical acceleration **a** Inelastic displacement, **b** Force–displacement hysteretic loops (Moustafa et al. [49] with permission from Techno Press)

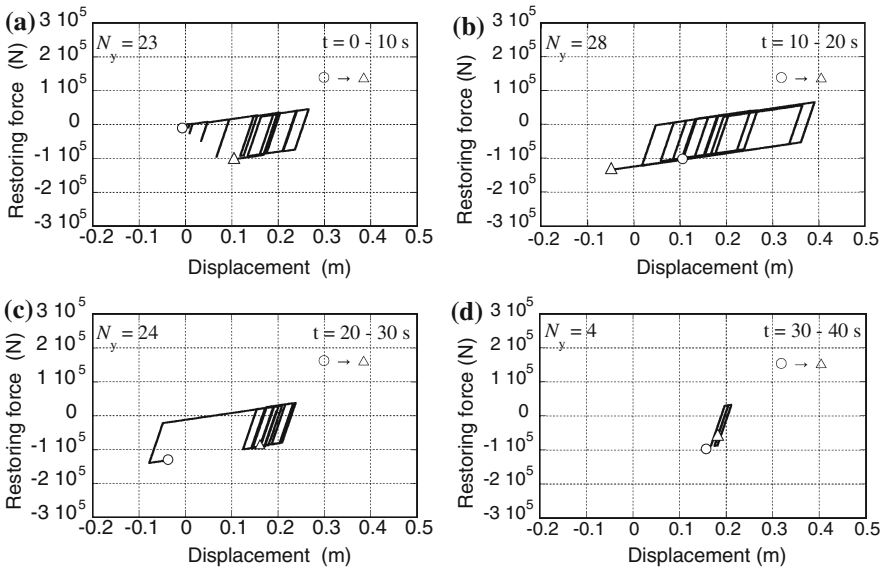

Fig. 10.5 Force-displacement hysteretic loops for different time intervals **a** t = 0–10 s, **b** t = 10–20 s, **c** t = 20–30 s, **d** t = 30–40 s (*circle* and *triangle* represent the extreme points of the hysteretic loops) (Moustafa et al. [49] with permission from Techno Press)

When the arrival times are much different, the energy provided by the total acceleration is distributed across a wider time duration (e.g. case of far-field deep earthquakes). This leads to smaller responses.

2. **Frequency content and effect of frequency range of seismic waves**: The frequency content of the body waves covers a broad frequency range with large energy concentrated close to the initial fundamental natural frequency of the structure. Lower energy is also distributed over higher frequencies (Fig. 10.2b). A similar feature can also be observed in the surface waves where large energy

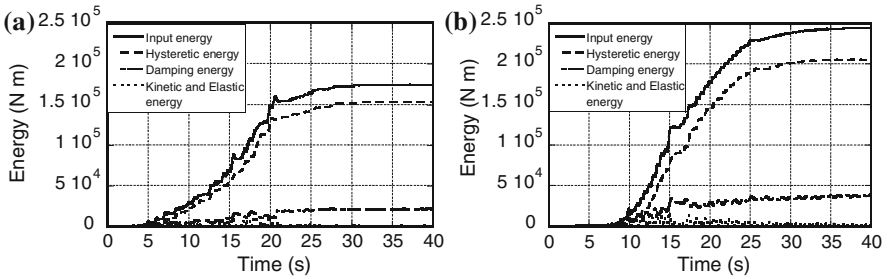

Fig. 10.6 Input and dissipated energies for inelastic structures under critical acceleration **a** $f_y = 6.0 \times 10^4$ N, **b** $f_y = 12 \times 10^4$ N (Moustafa et al. [49] with permission from Techno Press)

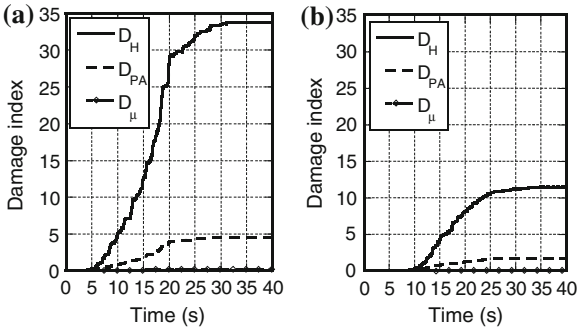

Fig. 10.7 Damage indices [Eqs. (10.7–10.9)] for inelastic structures under critical acceleration **a** $f_y = 6.0 \times 10^4$ N, **b** $f_y = 12 \times 10^4$ N (Note that D_μ in Fig. 10.7b coincides with the x-axis) (Moustafa et al. [49] with permission from Techno Press)

is located close to the initial natural frequency of the structure and smaller energy is located at the low frequency range of 0–0.5 Hz (Fig. 10.2d). The resulting ground acceleration is fairly rich in the frequency content which resembles actual recorded accelerograms (Fig. 10.2f). A peak amplitude is observed at the system initial natural frequency and large amplitudes are located at frequencies lower and higher than the system initial natural frequency (at about half and twice of ω). Figure 10.3 shows the short-time Fourier transform of the body waves, the surface waves and the overall acceleration. The transient trend of the ground motion both in time and frequency domains is remarkable. To examine the effect of the frequency contents of the seismic waves on the derived critical acceleration and corresponding structural responses, the frequency contents of the surface and body waves have been changed to (0–1.50) Hz and (0.50–10.0) Hz, respectively, keeping all other parameters unchanged. This overlap in the frequency contents of the seismic waves has been found to lead to ground acceleration richer in the frequency content compared with the case studied above. The structural responses have also been found to increase due to the overlap in the frequency contents of the seismic waves.

3. **Structural responses**: The maximum inelastic response of about 0.39 m is attained at about 16.0 s (Fig. 10.4a). The corresponding force–displacement

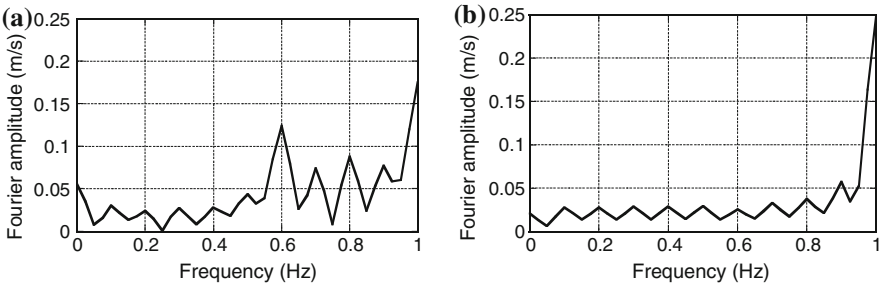

Fig. 10.8 Influence of yield strength on the frequency content of the surface waves **a** $f_y = 6.0 \times 10^4$ N, **b** $f_y = 12 \times 10^4$ N (Moustafa et al. [49] with permission from Techno Press)

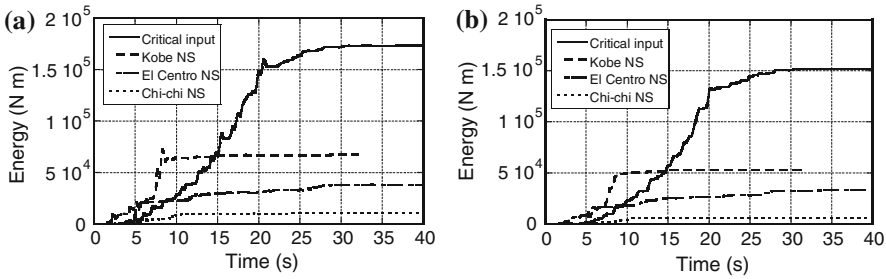

Fig. 10.9 Input and hysteretic energies from critical acceleration and recorded ground accelerations (all records are scaled to the same PGA of 4.63 m/s^2) **a** Input energy, **b** Hysteretic energy (Moustafa et al. [49] with permission from Techno Press)

hysteretic loops are shown in Fig. 10.4b. In order to disclose the detail of the transient response, the relation is further divided into four time intervals (0–10, 10–20, 20–30 and 30–40 s). The relations in the four time intervals (0–10, 10–20, 20–30 and 30–40 s) are shown in Fig. 10.5a–d (the end of each interval is marked in these plots). It can be seen that the number of yield reversals is larger for the period 10–20 s ($N_y = 28$). The number of yield reversals decreases remarkably at the end of the ground motion ($N_y = 4$ for $t = 30$–40 s). Note also that the hysteretic loops are wider during the interval $t = 10$–20 s and that the maximum displacement is also attained during the same time period. Most of the input energy to the structure (around 80 %) is provided during this period and the maximum value is attained at about 25 s (Fig. 10.6). It may also be noted that most of the input energy is dissipated by the hysteretic energy and that the damping energy is significantly smaller (Fig. 10.6). The kinetic and elastic strain energies are substantially small and diminish at the end of the ground motion. The damage indices reveal that they increase during the strong phase of the ground motion (Fig. 10.7). Park and Ang's damage index reflects that the structure is damaged beyond repair ($D_{PA} = 4.54$). The damage index D_H demanded by the critical input [Eq. (10.8)] is significantly higher than other

Table 10.1 Influence of the strain-hardening ratio on the response of the inelastic structure (Moustafa et al. [49] with permission from Techno Press)

Strain-hardening ratio	μ_{max}	N_y	u_p (m)	D_{PA}	D_H	D_μ
0.01	1.33	111	0.72	3.24	24.2	0.07
0.05	1.91	79	0.18	4.54	33.8	0.18
0.10	5.77	92	0.11	5.70	37.9	0.95
0.50	11.20	55	0.01	3.90	16.3	2.03

μ_{max} maximum ductility demand, N_y number of yield reversals, u_p residual defomration after ground stops shaking, D_{PA} Park and Ang damage index [Eq. (10.9)], D_H Damage index based on hysteretic energy dissipation [Eq. (10.8)], D_μ damage index based on ductility [Eq. (10.7)]

Table 10.2 Influence of the initial natural frequency on the response of the inelastic structure (Moustafa et al. [49] with permission from Techno Press)

Initial natural frequency(Hz)	μ_{max}	N_y	U_p (m)	D_{PA}	D_H	D_μ
0.5	2.43	66	0.22	5.23	38.6	0.29
1.0	1.91	79	0.18	4.54	33.8	0.18
2.0	1.78	56	0.08	0.36	0.50	0.16

two damage indices. The damage index based on ductility is the smallest among the three damage indices (0.18).

4. **Influences of the yield parameters ($\mathbf{f}_y$ and γ)**: The yield strength is seen to influence the frequency content of the surface waves of the critical acceleration and also the input and hysteretic energies of the structure. The frequency content of the critical acceleration for the structure with lower yield strength (6×10^4 N) is observed to get shifted towards the lower frequency range (Fig. 10.8a). The structure with higher yield capacity (12×10^4 N) is seen to have higher input energy demand and hysteretic energy demand (Fig. 10.6), lower ductility demand and lower damage indices (Fig. 10.7). For instance, when the yield strength increases from 6 to 12×10^4 N, Park and Ang's damage index decreases from 4.54 to 1.50. Similarly, the strain-hardening ratio was seen to influence the critical input and the associated inelastic responses. Table 10.1 summarizes the response quantities for $\gamma = 0.01, 0.05, 0.10$ and 0.50. It can be seen that, as the strain-hardening ratio decreases, the structure yields more frequently and the maximum displacement decreases.
5. **Effect of initial natural frequency of the structure**: In order to examine the influence of the structure's initial natural frequency on the critical excitation and the associated inelastic response, a parametric study has been carried out. The structure's initial natural frequency is varied, keeping all other parameters unchanged, and the critical input was re-estimated by solving a new optimization problem. Table 10.2 shows the response parameters of the structure under the critical excitation for three models of different initial natural frequencies (0.50, 1.0 and 2.0 Hz) having the same yield characteristics and damping ratio. It can be observed that the initial natural frequency has a

Table 10.3 Response quantities for the inelastic structure under the critical acceleration and past recorded ground motions (Moustafa et al. [49] with permission from Techno Press)

Input acceleration	μ_{max}	N_y	u_p (m)	D_{PA}	D_H	D_μ
Critical acceleration	1.91	79	0.18	4.54	33.8	0.18
1995 Kobe NS (Kobe University)	1.71	26	0.29	1.76	11.8	0.14
1940 El Centro NS (array #9)	1.98	65	0.08	1.24	7.26	0.20
1999 Chi-chi NS (TCU078)	1.03	21	0.15	0.34	1.33	0.01

significant effect on the critical responses. The structure with smaller initial natural frequency produces larger ductility demand and damage indices.

6. **Comparison with recorded accelerations**: To examine the realism of the critical accelerations, the structural responses have been estimated using the critical acceleration and past recorded ground motions. All acceleration inputs have been scaled to the same PGA of 4.63 m/s^2. Figure 10.9 and Table 10.3 summarize the numerical results. The input energy from the critical input is around 2.5, 4.6 and 16.6 times the associated values from Kobe (1995), El Centro (1940) and Chi-chi (1999) earthquake records, respectively. On the other hand, the hysteretic energy demand from the critical input is 2.8, 4.7 and 25.6 times those from Kobe (1995), El Centro (1940) and Chi-chi (1999) records, respectively. It should be remarked that the input energy rate (input energy per unit time) from the critical input is found to be substantially higher than those from the actual earthquake records [21].

10.6 Summary

In this chapter it was assumed that strong ground motions are composed of seismic waves that have different characteristics, such as, phase velocity, arrival time, non-stationarity trend, duration, frequency content, energy and amplitude. The modeling of critical earthquake loads has been explained for inelastic structures taking into account the different characteristics of the seismic wave components of the ground acceleration. The critical earthquake loads have been calculated by solving inverse dynamic problems using a nonlinear optimization technique, inelastic time-history response analysis and damage indices. The critical acceleration is expressed in terms of superposition of seismic waves with unknown amplitudes and phase angles. These unknown parameters have been computed so that a measure of the structure's damage (damage index) is maximized subject to the constraints on predefined bounds on the ground motion.

Several specific aspects relating to the present problem have been explained. The effects of non-stationarity trend, arrival time and frequency content of the seismic waves on the critical ground acceleration and the associated inelastic responses have been examined and discussed in detail. Similarly, the influences of the structural parameters, such as, the initial fundamental natural frequency, the yield strength and the strain-hardening ratio on the structural responses have also

been studied. The structural response and performance have been characterized in terms of the maximum ductility, input and hysteretic energies and damage indices. It may be concluded that damage indices are accurate response descriptors because they can account for structural damage due to repeated stress reversals and high stress excursions. The critical earthquake load is found to possess large energy around the structure's initial natural frequency. Significant energy has also been concentrated at lower frequencies than the natural frequency of the elastic structure. This is because the structure's equivalent natural frequency decreases due to its plastic deformation. When the seismic waves have comparable arrival times, the critical acceleration has been found to produce larger damage in the structure. The structure with lower strain-hardening ratio has been shown to yield more frequently than the same structure with higher strain-hardening ratio. The hysteretic energy has also been found to increase for lower values of the strain-hardening ratio. In other words, the elastic–plastic structure may be the most vulnerable one. It should be remarked that the input energy rate (input energy per unit time) from the critical input is found to be substantially higher than those from actual records.

It was presumed that the ground acceleration is composed of two seismic components, namely, body waves and surface waves. Implicit constraints on the frequency contents and the arrival times of the seismic waves have been imposed. Explicit constraints on the energy and PGA of the overall ground motion have also been imposed. No constraint was imposed on the energies or the amplitudes of the individual components of the seismic waves. Such constraints can be easily incorporated in the formulation, but this information is not easily available. The structures considered have been approximated using single-degree-of freedom systems and the nonlinear behavior has been modeled using a bilinear force–displacement relation. The application of the methodology explained in this chapter to multi-degree-of-freedom structures and the use of nonlinear degrading models are of interest and will be discussed elsewhere.

References

1. Dowrick DJ (2003, 2009) Earthquake resistant design and risk reduction. Wiley, London
2. Bangash MYH (2011) Earthquake resistant buildings. Springer, London
3. Takewaki I (2011) Preliminary report of the 2011 off the Pacific coast of Tohoku earthquake. J Zhejiang University Sci A 12(5):327–334
4. Takewaki I (2011) The 2011 off the Pacific coast of Tohoku earthquake and its impact on building structural design, Keynote paper (Plenary speaker) at The ASEM11 + Congress, 18–23 Sept 2011 in Seoul, Korea
5. Takewaki I, Murakami S, Fujita K, Yoshitomi S, Tsuji M (2011) The 2011 off the Pacific coast of Tohoku earthquake and response of high-rise buildings under long-period ground motions. Soil Dyn Earthq Eng 31(11):1511–1528
6. Takewaki I (2007) Critical excitation methods in earthquake engineering. Elsevier, Amsterdam, pp 1–22

7. Der Kiureghian A (1996) A coherency model for spatially varying ground motions. Earthq Eng Struct Dyn 25:99–111
8. Hudson JA (1969) A quantitative evaluation of seismic signals at teleseismic distances-II: body waves and surface waves from an extended source. Geophys J R Astr Soc 18:353–370
9. Wang ZL, Konietzky H, Shen RF (2010) Analytical and numerical study of P-wave attenuation in rock shelter layer. Soil Dyn Earthq Eng 30(1–2):1–7
10. Elnashai AS, Sarno LD (2008) Fundamentals of earthquake engineering, Chapter 3: Earthquake input motion. Wiley, England
11. Meyer P, Ochsendorf J, Germaine J, Kausel E (2007) The impact of high-frequency/low-energy seismic waves on unreinforced masonry. Earthq Spec 23:77–94
12. He W-L, Agrawal AK (2008) Analytical model of ground motion pulses for the design and assessment of seismic protective systems. J Struct Eng 134(7):1177–1188
13. Conte JP, Peng BF (1997) Fully nonstationary analytical earthquake ground-motion model. J Eng Mech 123(1):15–24
14. Der Kiureghian A, Crempien J (1989) An evolutionary model for earthquake ground motion. Struct Saf 6:235–246
15. Lin YK, Yong Y (1987) Evolutionary Kanai-Tajimi earthquake models. J Eng Mech 113(8):1119–1137
16. Conte JP (1992) Effects of earthquake frequency nonstationarity on inelastic structural response. In: Proceedings of the 10th world conference on earthquake engineering, A.A. Balkema, Rotterdam
17. Drenick RF (1970) Model-free design of aseismic structures. J Eng Mech 96:483–493
18. Shinozuka M (1970) Maximum structural response to seismic excitations. J Eng Mech 96:729–738
19. Iyengar RN (1970) Matched inputs report 47, series J, center for applied stochastics, Purdue University, West Lafayete, Indiana
20. Takewaki I (2002) Seismic critical excitation method for robust design: a review. J Struct Eng 128(5):665–672
21. Takewaki I (2006) Probabilistic critical excitation method for earthquake energy input rate. J Eng Mech 132:990–1000
22. Abbas AM, Manohar CS (2002) Investigations into critical earthquake load models within deterministic and probabilistic frameworks. Earthq Eng Struct Dyn 31(4):813–832
23. Abbas AM, Manohar CS (2007) Reliability-based vector nonstationary random critical earthquake excitations for parametrically excited systems. Struct Saf 29:32–48
24. Abbas AM (2006) Critical seismic load inputs for simple inelastic structures. J Sound Vib 296:949–967
25. Moustafa A (2009) Critical earthquake load inputs for multi-degree-of-freedom inelastic structures. J Sound Vib 325:532–544
26. Takewaki I (2005) Resonance and criticality measure of ground motions via probabilistic critical excitation method. Soil Dyn Earthq Eng 21(8):645–659
27. Amiri GG, Dana FM (2005) Introduction to the most suitable parameter for selection of critical earthquakes. Comput Struct 83(8–9):613–626
28. Zhai C-H, Xie L–L (2007) A new approach of selecting real input ground motions for seismic design: the most unfavourable real seismic design ground motions. Earthq Eng Struct Dyn 36:1009–1027
29. Moustafa A (2009) Discussion of a new approach of selecting real input ground motions for seismic design: the most unfavorable real seismic design ground motions. Earthq Eng Struct Dyn 38:1143–1149
30. Moustafa A, Takewaki I (2009) Use of probabilistic and deterministic measures to identify unfavorable earthquake records. J Zhej Uni: Sci A 10(5):619–634
31. Takewaki I (2002) Robust building stiffness design for variable critical excitations. J Struct Eng ASCE 128(12):1565–1574
32. Chopra AK (2007) Dynamics of structures, 3rd edn. Prentice-Hall, NJ
33. Takewaki I (2004) Bound of earthquake input energy. J Struct Eng 130:1289–1297

34. Uang C-M, Bertero VV (1990) Evaluation of seismic energy in structures. Earthq Eng Struct Dyn 19:77–90
35. Akiyama H (1985) Earthquake-resistant limit-state design for buildings. University of Tokyo Press, Tokyo
36. Zahrah TF, Hall WJ (1984) Earthquake energy absorption in SDOF structures. J Struct Eng 110:1757–1772
37. Cosenza C, Manfredi G, Ramasco R (1993) The use of damage functionals in earthquake engineering: a comparison between different methods. Earthq Eng Struc Dyn 22:855–868
38. Ghobara A, Abou-Elfath H, Biddah A (1999) Response-based damage assessment of structures. Earthq Eng Struc Dyn 28:79–104
39. Powell GH, Allahabadi R (1988) Seismic damage predictions by deterministic methods: concepts and procedures. Earthq Eng Struc Dyn 16:719–734
40. Fajfar P (1992) Equivalent ductility factors, taking into account low-cyclic fatigue. Earthq Eng Struc Dyn 21:837–848
41. Park YJ, Ang AH-S (1985) Mechanistic seismic damage model for reinforced concrete. J Struct Eng 111(4):722–739
42. Park YJ, Ang AH-S, Wen YK (1987) Damage-limiting aseismic design of buildings. Earthq Spec 3(1):1–26
43. Arias A (1970) A measure of earthquake intensity: seismic design of nuclear power plants. MIT press, Cambridge, pp 438–468
44. Housner GW, Jennings PC (1975) The capacity of extreme earthquake motions to damage structures. In: Hall WJ (ed) Structural and geotechnical mechanics: a volume honoring Newmark NM. Prentice-Hall, Englewood Cliff, pp 102–116
45. Arora JS (2004) Introduction to optimum design. Elsevier Academic Press, San Diego
46. Takewaki I (2004) Critical envelope functions for non-stationary random earthquake input. Comput Struct 82(20–21):1671–1683
47. Okada K, Shibata T (2008) Geomechanics. University of Tokyo Press, Tokyo (in Japanese)
48. Takewaki I, Fujita K, Yoshitomi (2012) Uncertainties of long-period ground motion and its impact on building structural design. In: Proceedings of One Year after 2011 Great east Japan earthquake, international symposium on engineering lessons learned from the giant earthquake, Tokyo, 3–4 March 2012
49. Moustafa A, Ueno K, Takewaki I (2010) Critical earthquake loads for SDOF inelastic structures considering evolution of seismic waves. Earthq Struct 1(2):147–162

Chapter 11
Critical Correlation of Bidirectional Horizontal Ground Motions

11.1 Introduction

The ground motion is a realization in space and simultaneous consideration of multiple components of ground motion is realistic and inevitable in the reliable design of structures [1, 2]. It is often assumed practically that there exists a set of principal axes in the ground motions [3, 4]. It is well recognized in the literature that the principal axes are functions of time and change their directions during the ground shaking. In the current structural design practice, the effect of the multi-component ground motions is often taken into account by use of the SRSS method (square root of the sum of the squares) or the CQC3 method (extended Complete Quadratic Combination rule [5]).

In the SRSS method, the maximum responses under respective ground motions are combined by the rule of SRSS. The SRSS method assumes the statistical independence among the respective ground motions. However, the multi-component ground motions have some statistical dependence.

On the other hand, the CQC3 rule is well known as a response spectrum method which can take into account the effect of correlation between the components of ground motions. Although an absolute value of a cross power spectral density (PSD) function has been described by the correlation coefficient, the CQC3 rule cannot treat directly, in the sense of direct treatment of both real and imaginary parts, the cross PSD functions of multi-component ground motions. Menun and Der Kiureghian [6] and Lopez et al. [7] employed the CQC3 method as the response evaluation method and discussed the critical states, e.g., a critical loading combination or a critical incident angle. Athanatopoulou [8] investigated the effect of incident angle of ground motions on structural response without use of the Penzien–Watabe model [3] and pointed out the significance of considering multiple inputs in the practical seismic design. The approach is applicable only to a set of recorded motions. In this chapter, the cross PSD function in terms of both real and imaginary parts will be discussed in more detail from the viewpoint of critical excitation.

I. Takewaki et al., *Improving the Earthquake Resilience of Buildings*,
Springer Series in Reliability Engineering, DOI: 10.1007/978-1-4471-4144-0_11,

A problem of critical excitation is considered in this chapter for a one-story one-span moment resisting three-dimensional (3-D) frame subjected to bidirectional horizontal ground motions (2DGM). Because the horizontal ground motions are known to be influential to most of ordinary building structures, only horizontal ground motions are treated here. The two horizontal ground accelerations are modeled as nonstationary random processes whose auto PSD functions are known. A critical excitation problem is formulated such that the worst cross PSD function of the 2DGM is determined for the maximum mean-squares extreme-fiber stress of the column at the top. It is found that the real part (co-spectrum, e.g., see Nigam [9]) and the imaginary part (quad-spectrum) of the worst cross PSD function can be obtained by a devised algorithm including the interchange of the double maximization procedure in the time and frequency domains.

The critical excitation problems have been treated extensively by many researchers, e.g., Drenick [10], Shinozuka [11], Iyengar and Manohar [12], Manohar and Sarkar [13], Abbas and Manohar [14–16], Takewaki [17–22]. The works by Sarkar and Manohar [23, 24], Abbas and Manohar [15, 16] are concerned with the content of this chapter. Sarkar and Manohar [23, 24] and Abbas and Manohar [15] formulated interesting problems and solved the problems via sophisticated mathematical insights. In particular, they revealed that the critical correlation occurs under the condition of perfect coincidence of the multiple-support inputs with the corresponding transfer functions. Furthermore, Abbas and Manohar [15] discussed a critical excitation problem of a stack-like structure subjected to horizontal and vertical simultaneous inputs with the reliability index as the objective function. They determined the critical PSD matrix using response surface models. This chapter formulates a similar problem for a different model (multi-component input) with different variables in the complex plane of the cross PSD function of ground motions. Especially the relationship of the building principal axes with the ground-motion principal axes produces an interesting aspect.

11.2 Penzien–Watabe Model and Extended Penzien–Watabe Model

11.2.1 Penzien–Watabe Model

The CQC3 rule is based on the Penzien–Watabe model (P–W model; [3]). The P–W model assumes the existence of the principal axes Z_1 and Z_2 along which the correlation coefficient of ground motions is zero. One principal axis in the horizontal plane is directed to the fault and the other is perpendicular to the former one.

Although the CQC3 rule is a known method of response analysis for 2DGM, the correlation between 2DGM is fixed rigidly. In order to generalize the correlation

between the 2DGM in a feasible complex plane of the cross PSD function, a new ground input model is explained in this chapter. Then, the CQC3 rule can be regarded as a special case of response evaluation using the input model explained in this chapter. This will be explained later in Sect. 11.5. A brief explanation is shown in Fig. 11.1 in the form of flow chart.

Consider a one-story, one-span 3 D frame. It is assumed that two axes X_1 and X_2 are perpendicular to each other and along the building structural axes. Let $S_{Z_1}(\omega)$ and $S_{Z_2}(\omega)$ denote the auto PSD functions along the principal axes Z_1, Z_2 of ground motions, respectively. According to the P–W model, 2DGM along Z_1, Z_2 are regarded to be completely uncorrelated. The auto PSD functions of ground motions along X_1, X_2 are determined from the auto PSD functions of 2DGM along Z_1, Z_2. The auto PSD functions along X_1, X_2 are described by $S_{11}(\omega)$ and $S_{22}(\omega)$, respectively.

It can be shown (see Appendix 1) that the sum of $S_{Z_1}(\omega)$ and $S_{Z_2}(\omega)$ is to be equal to the sum of $S_{11}(\omega)$ and $S_{22}(\omega)$. Furthermore, the coherence function between 2DGM along X_1 and X_2 is also denoted as

$$\rho_{12}(\gamma_{\text{org}}, \theta) = \frac{(1-\gamma_{\text{org}})\sin 2\theta}{\sqrt{(1+\gamma_{\text{org}})^2 - (1-\gamma_{\text{org}})^2 \cos^2 2\theta}}, \tag{11.1}$$

where $\gamma_{\text{org}} = S_{Z_2}(\omega)/S_{Z_1}(\omega)$. θ is the angle of rotation (incident angle) between the two horizontal axes Z_1, X_1. Figure 11.2 shows the coherence function expressed by Eq. (11.1) with various values of γ_{org} for varied rotation (incident) angle. In Fig. 11.2, when γ_{org} is zero, the coherence function ρ_{12} is reduced to 1 at any θ except $\theta = 0$ and $\theta = \pi/2$. This means that the components along X_1 and X_2 have perfect correlation under unidirectional ground motion along the major principal axis of ground motion.

11.2.2 Extended Penzien–Watabe Model

The P–W model is often used in the modeling of multi-component ground motions. Although the coherence function of 2DGM along X_1 and X_2 can be given in terms of γ_{org} and θ as shown in Eq. (11.1), the cross PSD function cannot be treated directly in the CQC3 rule. For that reason, it is supposed in this chapter that the cross PSD function between 2DGM along X_1 and X_2 can take any value in the feasible complex plane. From the definition of the coherence function, the co-spectrum (real part of cross PSD) $C_{12}(\omega)$ and quad-spectrum (imaginary part of cross PSD) $Q_{12}(\omega)$ must satisfy the following relation.

$$C_{12}(\omega)^2 + Q_{12}(\omega)^2 \leq \left\{\rho_{12}(\gamma_{\text{org}}, \theta)\right\}^2 S_{11}(\omega) S_{22}(\omega) \tag{11.2}$$

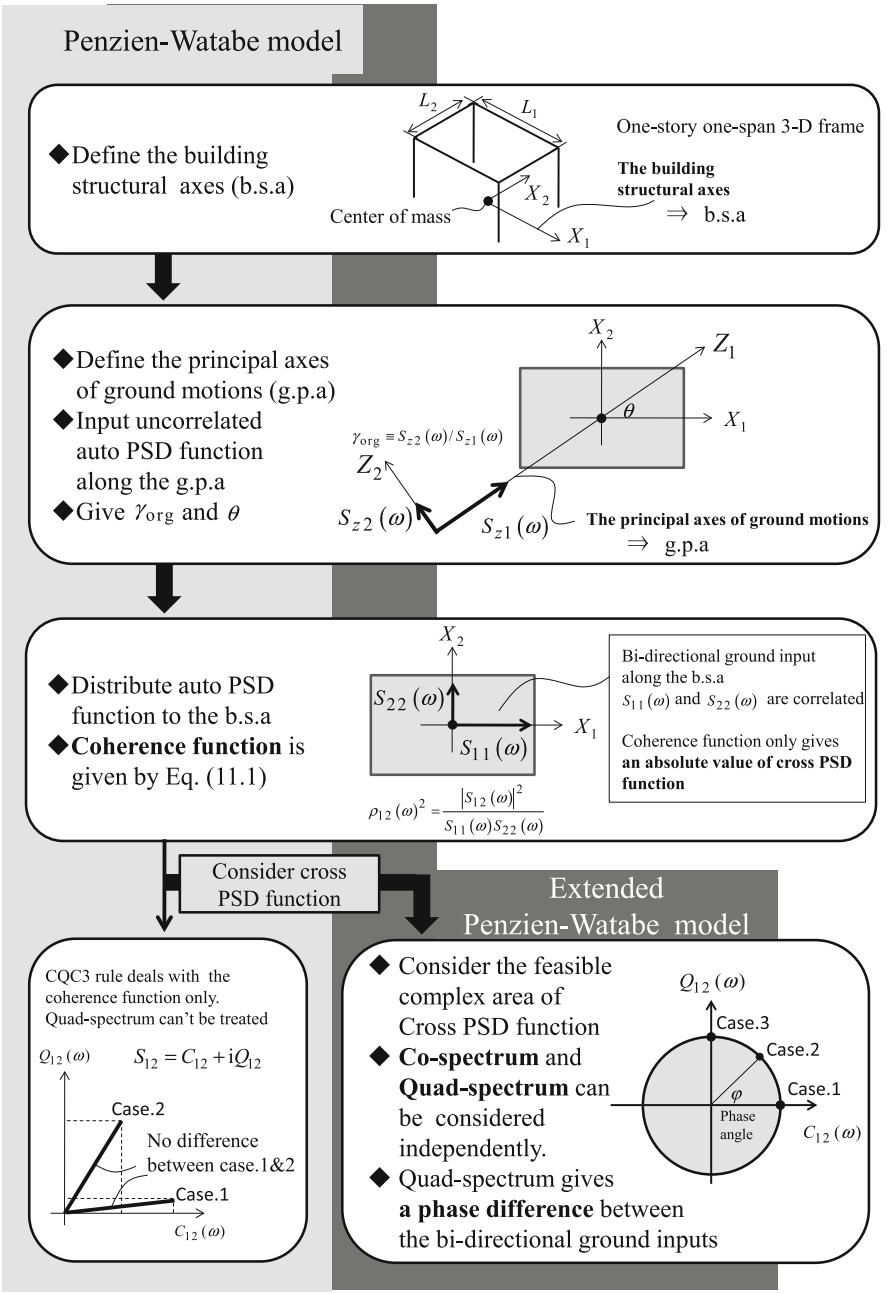

Fig. 11.1 Comparison of extended P–W model with P–W model [25]

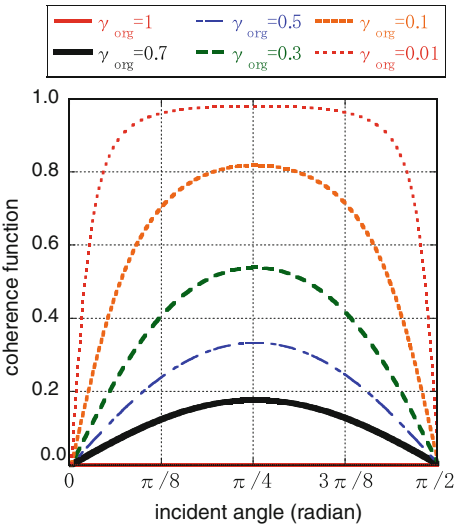

Fig. 11.2 Coherence function of 2DGM with various auto PSD ratios with respect to various incident angles in the Penzien–Watabe model [25]

This model is called the extended P–W model hereafter. It may be possible to incorporate the extended P–W model into the stochastic response evaluation method. In that case, a new critical excitation problem can be constructed in which the critical cross PSD function is searched in the feasible complex plane represented by Eq. (11.2). This method can be regarded as an extended method of the CQC3 rule based on the P–W model.

11.3 Stochastic Response to 2DGM Described by Extended Penzien–Watabe Model

11.3.1 Definition of Nonstationary Ground Motion

It is assumed here that the one-directional horizontal motions can be described by the following uniformly modulated nonstationary model.

$$\ddot{u}_{gi}(t) = c_i(t) w_i(t) \quad (i = 1, 2) \tag{11.3}$$

where $c_i(t)$ is an envelope function and $w_i(t)$ is a stationary random process. The envelope function is given by

$$\begin{aligned} c_i(t) &= (t/t_0)^2 \quad (0 \le t \le t_0) \\ c_i(t) &= 1.0 \quad (t_0 \le t \le t_1) \\ c_i(t) &= e^{-0.24(t-t_1)} \quad (t_1 \le t \le t_f) \end{aligned} \tag{11.4}$$

The auto PSD function of $w_i(t)$ in Eq. (11.3) is assumed to be given by

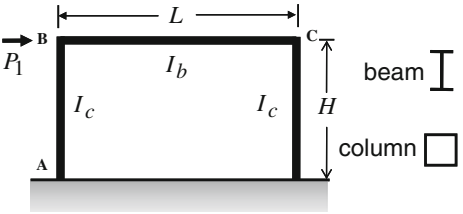

Fig. 11.3 One-story one-span plane frame consisting of beam of wide-flange cross-section and column of square-tube cross-section [25]

$$S_{ii}(\omega) = S_{V,h=0}^{(i)^2} / \left\{ 2\pi T |c_i(t)|_{\max} \right\} \quad (i = 1, 2), \tag{11.5}$$

where T is the time duration and h is the damping ratio. $S_{V,h=0}^{(i)}$ is the velocity response spectrum for null damping ratio.

11.3.2 Stochastic Response Evaluation in Frequency Domain

11.3.2.1 Structure Model

Consider a 3D frame subjected to 2DGM $\ddot{u}_{g1}, \ddot{u}_{g2}$ along the building structural axes X_1 and X_2. It is assumed that the center of mass is coincident with the center of stiffness and the torsional response does not occur so long as there is no rotational input. The columns have a square-tube cross-section and the beams have a wide-flange cross-section as shown in Fig. 11.3. The story height is H and the span length of the plane frame of interest in the first part of this section is L_1. The span length in the other direction is denoted by L_2. Let E, I_b, I_c, Z_c denote the Young's modulus of beam and column, the second moment of area of beam, that of column and the section modulus of column, respectively. The mass on one plane frame is denoted by m_1.

Assume that each plane frame of the 3D model can be expressed by an SDOF model. The equivalent horizontal stiffness of the SDOF model is expressed by (see Appendix 2)

$$k_1 = \frac{12EI_c\{1 + 6(I_b/I_c) \cdot (H/L_1)\}}{H^3\{2 + 3(I_b/I_c) \cdot (H/L_1)\}} \tag{11.6}$$

The extreme-fiber stress at the top of the column under one-directional horizontal motion may be expressed by (see Appendix 2)

$$\sigma_{BA}^1(t) = \{6EI_b/(Z_c L_1)\}\theta_B = A_{\sigma 1} u_1(t), \tag{11.7}$$

where $A_{\sigma 1} \equiv 18EI_b/[HL_1 Z_c\{2 + 3(I_b/I_c) \cdot (H/L_1)\}]$.

Let $\omega_1 = \sqrt{k_1/m_1}$ denote the fundamental natural circular frequency in the horizontal vibration of the SDOF model. The horizontal displacement of the floor can be derived as

$$u_1(t) = \int_0^t \{-\ddot{u}_{g1}(\tau)\} g_1(t-\tau) d\tau, \tag{11.8}$$

where $g_1(t)$ is the well-known unit impulse response function.

Using Eqs. (11.7) and (11.8), $\sigma^1_{BA}(t)$ can be expressed as

$$\sigma^1_{BA}(t) = A_{\sigma 1} \int_0^t \{-\ddot{u}_{g1}(\tau)\} g_1(t-\tau) d\tau \tag{11.9}$$

Let $\sigma^2_{BA}(t)$ denote the extreme-fiber stress at the top of the column under another horizontal motion $\ddot{u}_{g2}$. The same equations as those in the direction X_1 can be used only by replacing L_1 by L_2 and other parameters in the direction X_1 by those in the direction X_2. The sum of the extreme-fiber stresses at the top of the column under 2DGM may be expressed by

$$f(t) = \sigma^1_{BA}(t) + \sigma^2_{BA}(t) \tag{11.10}$$

11.3.2.2 Stochastic Response Evaluation in Frequency Domain

The auto-correlation function of $f(t)$ defined in Eq. (11.10) can be expressed by

$$\begin{aligned} E[f(t_1)f(t_2)] =& E\left[\sigma^1_{BA}(t_1)\sigma^1_{BA}(t_2)\right] + E\left[\sigma^1_{BA}(t_1)\sigma^2_{BA}(t_2)\right] \\ &+ E\left[\sigma^2_{BA}(t_1)\sigma^1_{BA}(t_2)\right] + E\left[\sigma^2_{BA}(t_1)\sigma^2_{BA}(t_2)\right] \end{aligned}, \tag{11.11}$$

where $E[\,\cdot\,]$ denotes the ensemble mean. The mean-squares extreme-fiber stresses in directions X_1 and X_2 derived from Eq. (11.11) may be expressed by (see Appendix 3)

$$E[\sigma^1_{BA}(t)^2] = A^2_{\sigma 1} \int_{-\infty}^{\infty} \{B_c(t;\omega)^2 + B_s(t;\omega)^2\} S_{11}(\omega) d\omega \tag{11.12}$$

$$E[\sigma^2_{BA}(t)^2] = A^2_{\sigma 2} \int_{-\infty}^{\infty} \{C_c(t;\omega)^2 + C_s(t;\omega)^2\} S_{22}(\omega) d\omega \tag{11.13}$$

$B_c(t;\omega), B_s(t;\omega), C_c(t;\omega), C_s(t;\omega)$ are defined in Appendix 3.

The cross terms in Eq. (11.11) can be transformed into (see Appendix 4)

$$E[\sigma_{BA}^1(t)\sigma_{BA}^2(t)] + E[\sigma_{BA}^2(t)\sigma_{BA}^1(t)] = 2A_{\sigma 1}A_{\sigma 2}\int_{-\infty}^{\infty}\{f_1(t;\omega)C_{12}(\omega) + f_2(t;\omega)Q_{12}(\omega)\}d\omega, \tag{11.14}$$

where C_{12} and Q_{12} are the co-spectrum and quad-spectrum of the cross PSD function and

$$f_1(t;\omega) = B_c(t;\omega)C_c(t;\omega) + B_s(t;\omega)C_s(t;\omega) \tag{11.15a}$$

$$f_2(t;\omega) = B_c(t;\omega)C_s(t;\omega) - B_s(t;\omega)C_c(t;\omega) \tag{11.15b}$$

Finally, the mean-squares of the sum of extreme-fiber stresses at the top of the column under 2DGM may be expressed by

$$\begin{aligned} E[\{\sigma_{BA}^1(t) + \sigma_{BA}^2(t)\}^2] &= \mathrm{A}_{\sigma 1}^2\int_{-\infty}^{\infty}\{\mathrm{B_c}(t;\omega)^2 + \mathrm{B_s}(t;\omega)^2\}\mathrm{S}_{11}(\omega)\mathrm{d}\omega \\ &+ 2\mathrm{A}_{\sigma 1}\mathrm{A}_{\sigma 2}\int_{-\infty}^{\infty}\{\mathrm{f}_1(t;\omega)\mathrm{C}_{12}(\omega) + \mathrm{f}_2(t;\omega)\mathrm{Q}_{12}(\omega)\}\mathrm{d}\omega \\ &+ \mathrm{A}_{\sigma 2}^2\int_{-\infty}^{\infty}\{\mathrm{C_c}(t;\omega)^2 + \mathrm{C_s}(t;\omega)^2\}\mathrm{S}_{22}(\omega)\mathrm{d}\omega \end{aligned} \tag{11.16}$$

11.4 Critical Excitation Method for Worst Cross PSD Function Between 2DGM

The critical excitation problem may be stated as: find the cross PSD function of 2DGM

$$S_{12}(\omega) = C_{12}(\omega) + \mathrm{i}Q_{12}(\omega) \tag{11.17a}$$

so as to achieve

$$\max_{S_{12}(\omega)}\max_{t} E[\{\sigma_{BA}^1(t) + \sigma_{BA}^2(t)\}^2] \tag{11.17b}$$

When the time t is fixed and the frequency ω is specified, the transfer functions $f_1(t;\omega)$ and $f_2(t;\omega)$ defined in Eqs. (11.15a, b) can be regarded as coefficients, not functions of t and ω. Therefore, the integrand in the second term of Eq. (11.16) can be regarded as the function $z(C_{12}, Q_{12})$ of C_{12} and Q_{12}.

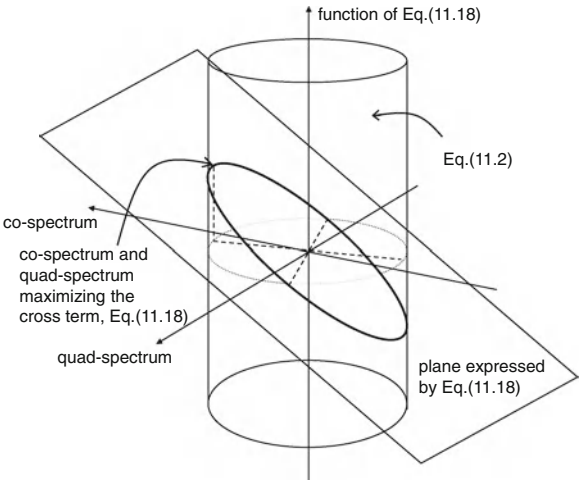

Fig. 11.4 Schematic illustration of the present critical excitation problem [25]

$$z(C_{12}, Q_{12}) = f_1(t;\omega)C_{12}(\omega) + f_2(t;\omega)Q_{12}(\omega) \tag{11.17c}$$

Figure 11.4 illustrates the structure of the critical excitation problem. The critical excitation problem is to maximize

$$z^*(C_{12}, Q_{12}) = 2A_{\sigma 1}A_{\sigma 2}\{f_1(t;\omega)C_{12}(\omega) + f_2(t;\omega)Q_{12}(\omega)\} \tag{11.18}$$

under the constraint Eq. (11.2). The critical co-spectrum and quad-spectrum can then be obtained analytically as

$$C_{12}(\omega) = \rho_{12}(\gamma_{\text{org}}, \theta) f_1(t;\omega) \frac{\sqrt{S_{22}(\omega)S_{11}(\omega)}}{\sqrt{f_1(t;\omega)^2 + f_2(t;\omega)^2}} \tag{11.19a}$$

$$Q_{12}(\omega) = \rho_{12}(\gamma_{\text{org}}, \theta) f_2(t;\omega) \frac{\sqrt{S_{22}(\omega)S_{11}(\omega)}}{\sqrt{f_1(t;\omega)^2 + f_2(t;\omega)^2}} \tag{11.19b}$$

It should be noted that Eqs. (11.19a, b) include the coherence function $\rho_{12}(\gamma_{\text{org}}, \theta)$ and are different from the equations derived in the reference (Fujita et al. [26]). Abbas and Manohar [15] had obtained a similar result for a different problem of multiple inputs.

Figure 11.5 indicates the solution algorithm. Substitution of Eqs. (11.19a, b) into Eq. (11.14) leads to the expression of the cross term.

$$\begin{aligned} &E\left[\sigma^1_{BA}(t)\sigma^2_{BA}(t)\right] + E\left[\sigma^2_{BA}(t)\sigma^1_{BA}(t)\right] \\ &= 2\rho_{12}(\gamma_{\text{org}}, \theta)A_{\sigma 1}A_{\sigma 2} \int_{-\infty}^{\infty} \sqrt{f_1(t;\omega)^2 + f_2(t;\omega)^2}\sqrt{S_{22}(\omega)S_{11}(\omega)}d\omega \end{aligned} \tag{11.20}$$

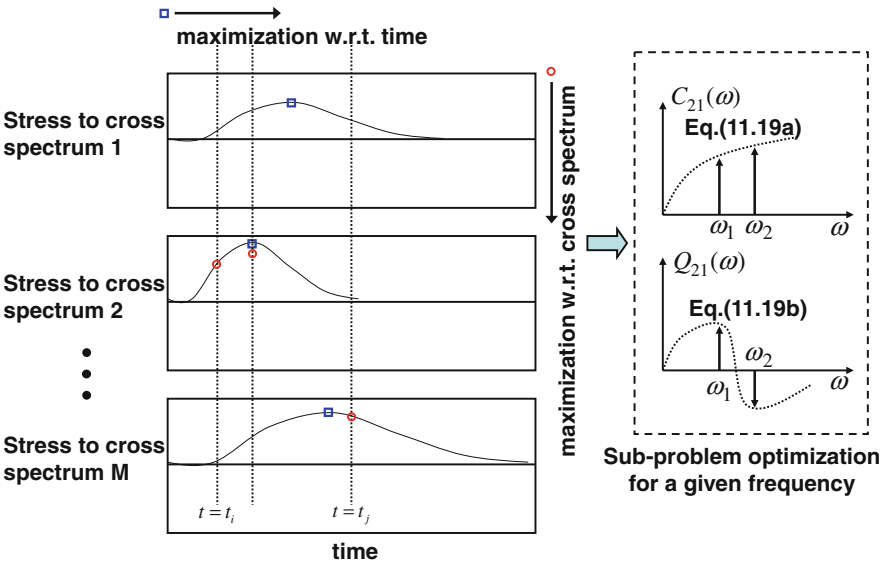

Fig. 11.5 Schematic diagram of the proposed procedure (order interchange of double maximization procedure including subproblem optimization) [25]

11.5 Numerical Example

11.5.1 Response to 2DGM with the Constraint of Sum of Auto PSD Functions

In most of the current structural design practice, safety and functionality checks are made with respect to one-directional earthquake input. This is because the ground motion model for multi-component inputs is complicated and a well-accepted model of practical use has never been presented except a few (e.g., Eurocode, IBC International Code). In addition, it may be understood that an approximate safety margin is incorporated in the magnitude of one-directional input. In this section, the effect of bidirectional input on the seismic response is investigated through the comparison with the response by CQC3 rule (perfectly correlated; although CQC3 does not correspond to the perfectly correlated case, this terminology is used symbolically) or SRSS rule (uncorrelated). The effect of correlation of 2DGM on the response is also clarified. Figure 11.6 shows the flow chart of the aim in this section and the relationship with Sect. 11.5.2. The given structural parameters are shown in Tables 11.1 and 11.2.

Consider the case where the auto PSD function ratio in two directions X_1, X_2 is varied under the condition that the sum of the auto PSD functions in two directions is constant. This is because the intensity of the unidirectional input as the combined component of two-directional input should be regarded to be constant. For

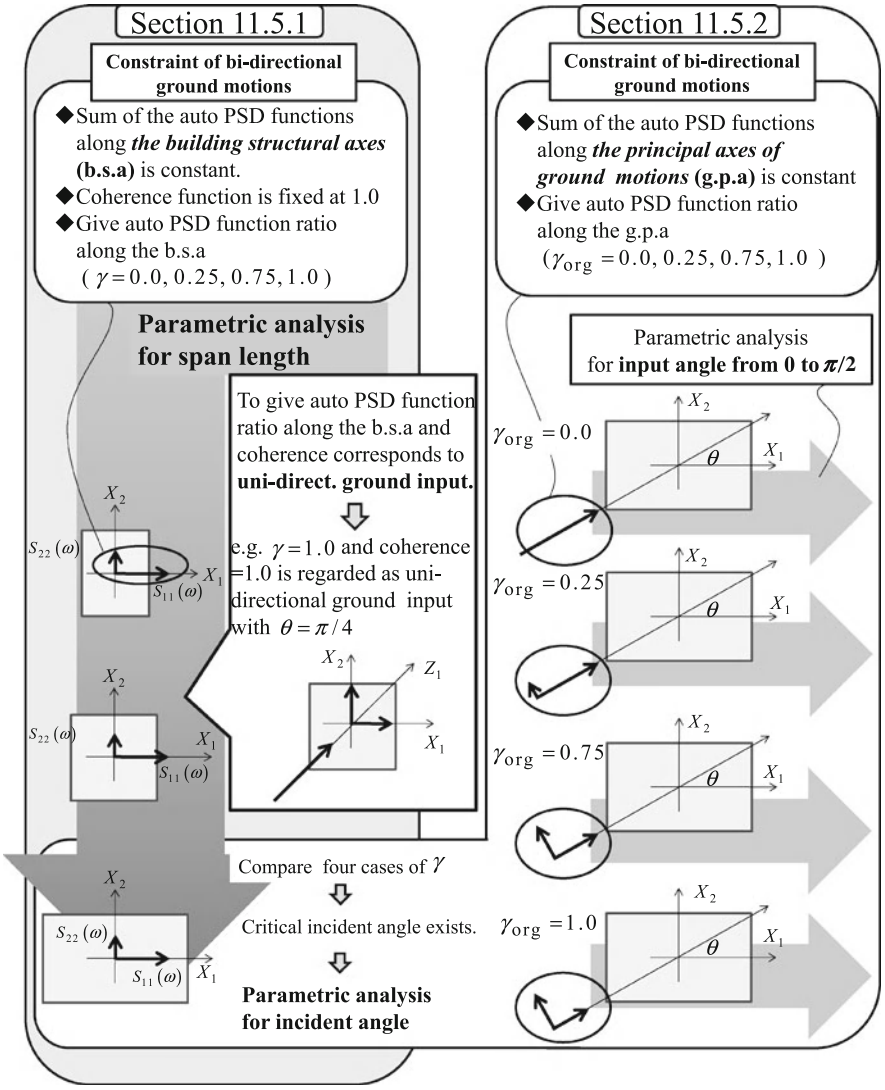

Fig. 11.6 Relationship between numerical analysis of Sects. 11.5.1 and 11.5.2 [25]

unidirectional input ($\gamma_{org} = 0$) along the major principal axis of ground motion, the coherence function between the ground motions along the building structural axes is fixed to 1.0 [see Eq. (11.1)]. The auto PSD function ratios along the building structural axes are chosen as $\gamma = S_{22}/S_{11} = 0$, 0.25, 0.75 and 1.0. The 2DGM along the building structural axes with the auto PSD function ratio of 1.0 and coherence = 1.0 coincides with the unidirectional input along the major ground principal axis of $\theta = \pi/4$. The common envelope function $c_1(t), c_2(t)$ is shown in Fig. 11.7. The parameters in Eq. (11.4) are taken as $c_0 = 3$ s, $c_1 = 12.5$ s and

Table 11.1 Structural member properties [25]

	Column	Beam
Cross-section (mm)	□– 1,500 × 1,500 × 50	H – 1,200 × 600 × 40 × 32
Cross-sectional area (mm^2)	2.90×10^5	8.57×10^4
Second moment of area (mm^4)	1.02×10^{11}	1.99×10^{10}
Mass per unit length (kg/m)	2273	673

Table 11.2 Geometrical and structural parameters [25]

Span length (m)	$L_2 = 15.0$
Horizontal stiffness k_1 (N/mm)	7.62×10^8
Horizontal stiffness k_2 (N/mm)	7.62×10^8
Mass m_1 (kg)	3.87×10^6
Mass m_2 (kg)	3.87×10^6
Horizontal natural period T_1 (s)	0.448
Horizontal natural period T_2 (s)	0.448

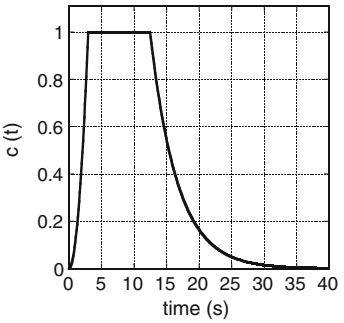

Fig. 11.7 Envelope function of horizontal ground motion [25]

$c_f = 40.0$ s here. Figure 11.8a–c indicate the auto PSD functions of $w_1(t), w_2(t)$ for various γ with the constraint of sum of auto PSD functions. The simulated ground acceleration using this PSD functions has the maximum value of about 1G. The span length L_2 is specified as 15 m and the span length L_1 has been varied continuously from 10 to 30 m.

Figure 11.9 shows the comparison of the response to critically correlated 2DGM along the building structural axes with the response to uncorrelated bidirectional input. The curve indicated as 'uncorrelated' corresponds to the SRSS response and the curve indicated as 'critically correlated' presents the critical response derived in this chapter. In addition, the responses to 2DGM which have fixed correlation functions, i.e. $C_{12} = \sqrt{S_{11}S_{22}}$ and $Q_{12} = 0$ ("Perfectly correlated" without phase delay), $C_{12} = Q_{12} = \sqrt{S_{11}S_{22}}/\sqrt{2}$ (case 2), $C_{12} = 0$ and $Q_{12} = \sqrt{S_{11}S_{22}}$ (case 3), are also plotted. It can be seen that the critical response and the response to the input model with $C_{12} = \sqrt{S_{11}S_{22}}$ and $Q_{12} = 0$ almost coincide in the model with the span of $L_1 = 15$ m.

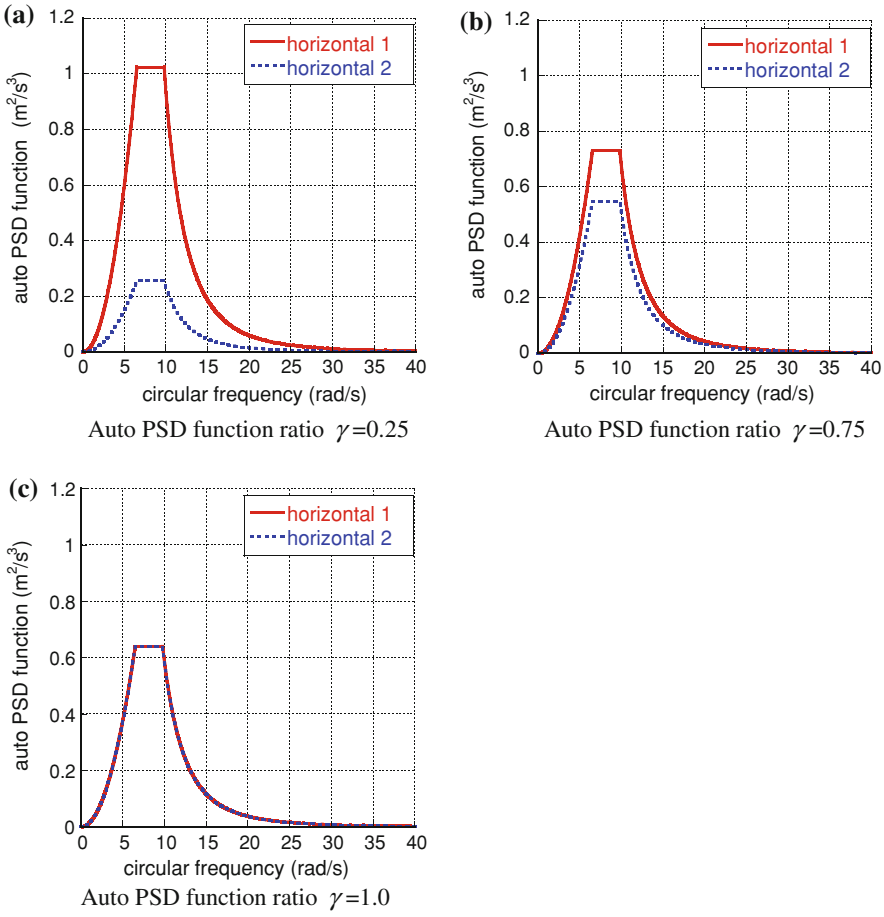

Fig. 11.8 Three combinations of the auto PSD functions of 2DGM along the building structural axes with the constraint of sum of the auto PSD functions. **a** Auto PSD function ratio $\gamma = 0.25$. **b** Auto PSD function ratio $\gamma = 0.75$. **c** Auto PSD function ratio $\gamma = 1.0$ [25]

It can be observed from Fig. 11.9 that the critical response is amplified around $L_1 = 15$ m where the lengths of span in two directions are equal and the natural frequencies of the model in two directions are equal. It can also be observed that, as the span length L_1 becomes longer than 15 m, the critical response for the input model of $\gamma = 0.25$ becomes larger than those for $\gamma = 0.75, 1.0$. This is because, as the span becomes longer, a horizontal stiffness along the long span decreases. It can be concluded that the critical incident angle of multi-component ground motions may exist depending on the combination of structural stiffnesses due to difference in span lengths.

Figure 11.10 shows the increased ratio of the critical response to 2DGM of various auto PSD function ratios from the SRSS response. In this case, the increased ratio is about 40 % at $L_1 = 15$ m. This implies that most of the present

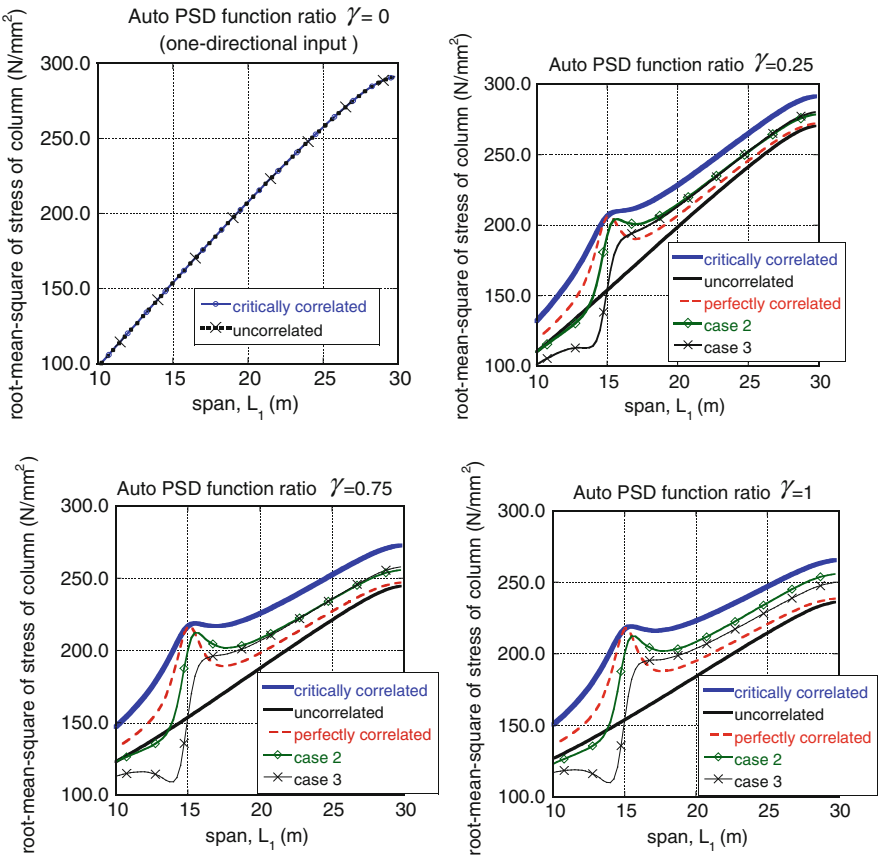

Fig. 11.9 Comparison of the response to the critically correlated 2DGM of various auto PSD function ratios with the responses to other inputs [25]

design code using only one-directional input ($\gamma = 0$) for safety check are not sufficient for extreme loading.

Figure 11.11 shows the co-spectrum and quad-spectrum of the critical cross PSD function for $\gamma = 1$ and $L_1 = 25$ m.

11.5.2 Response to 2DGM Described by Extended Penzien–Watabe Model: Analysis From the Viewpoint of Critical Incident Angle

Since the analytical solution has been obtained as Eqs. (11.19a, b) the critical incident angle can be searched parametrically in an efficient manner for which the response quantity can be maximized for each combination of span length. The right figure in Fig. 11.6 shows the flow chart indicating the aim in this section.

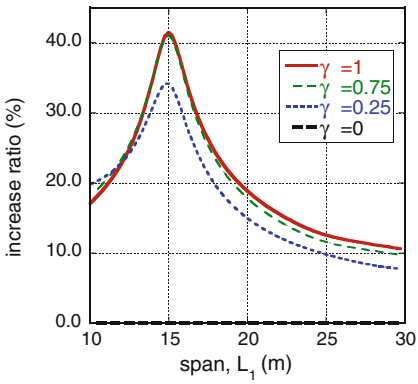

Fig. 11.10 Increase ratio of critical response from SRSS response [25]

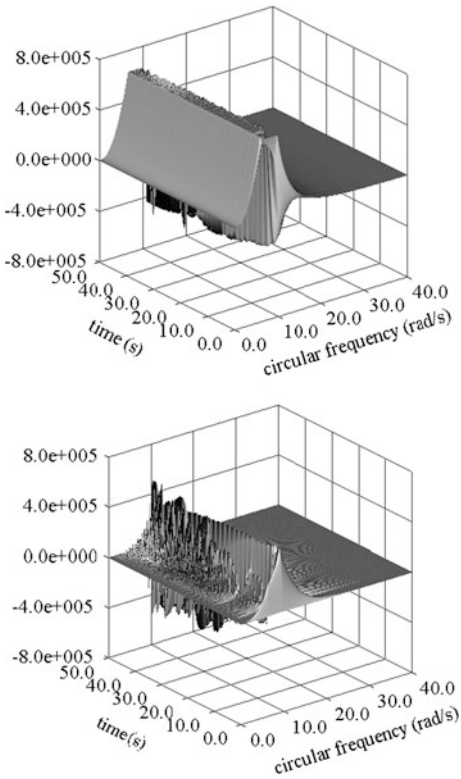

Fig. 11.11 Co-spectrum and quad-spectrum for $\gamma = 1$ and $L_1 = 25$ m [25]

While the auto PSD function ratio along the building structural axes has been treated directly in Sect. 11.5.1, the auto PSD functions along the principal axes of ground motions are treated directly in this section. In other words, the physical meaning of ground motions is taken into account in detail in this section.

Consider the case where the ratio γ_{org} of the auto PSD functions along the principal axes of ground motions is assumed to be fixed to 0.0, 0.05, 0.10, 0.25,

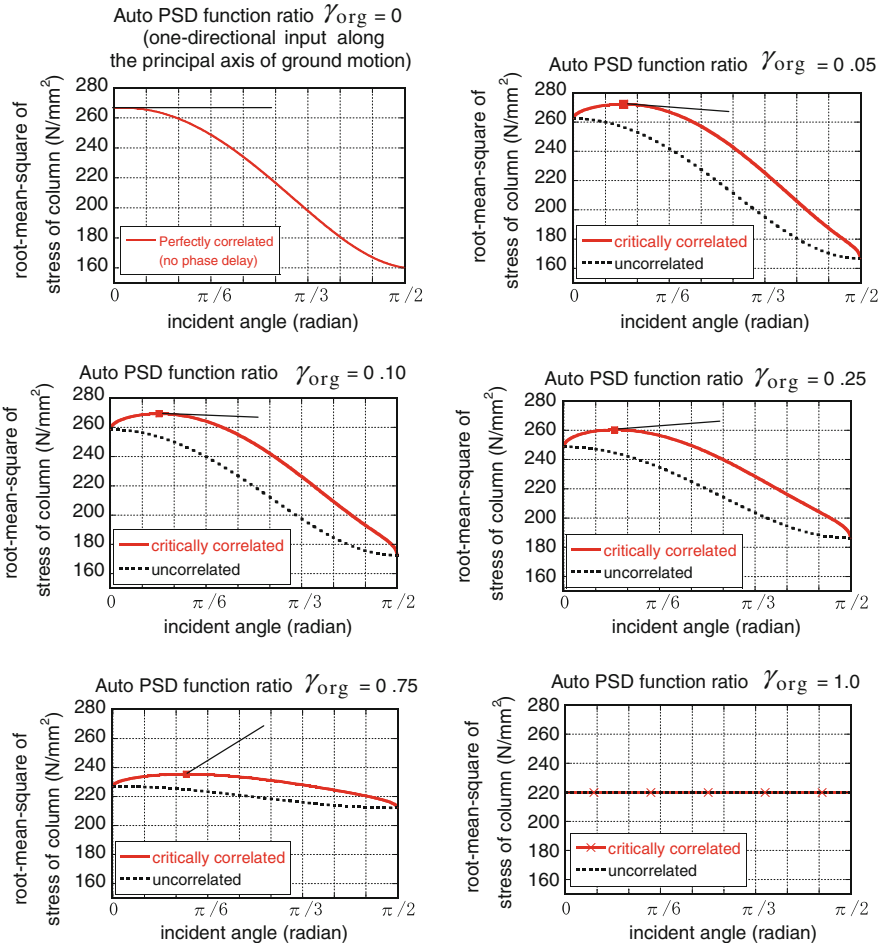

Fig. 11.12 Root-mean-square extreme-fiber stress of column with respect to the angle between the two sets of axes to the critically correlated 2DGM and to the uncorrelated 2DGM (various auto PSD function ratios along the principal axes of ground motions) [25]

0.75, 1.0, and the angle between the two sets of axes is varied continuously from 0 rad to $\pi/2$ rad. The structural plan is given as $L_1 = 15$ m, $L_2 = 25$ m.

Figure 11.12a–f show the comparison of the critical response with the corresponding SRSS response in the case of six ratios γ_{org} under various incident angles. The auto PSD functions along the building structural axes are determined from those along the principal axes of ground motions in terms of θ and γ_{org} (See Appendix 1). Since the case of $\gamma_{org} = 0.0$ shown in Fig. 11.12a can be regarded as the unidirectional input along the ground major principal axis, the coherence function $\rho_{12}(\gamma_{org}, \theta)$ is 1.0 for any incident angle θ. Furthermore, it can be regarded that there is no phase delay between 2DGM along the building structural

axes. For this reason, the critical excitation method presented in this chapter provides the perfectly correlated one without phase delay in this case.

From Fig. 11.12b–e, it can be understood that there exists a critical incident angle which maximizes the response quantity by considering the effect of critical correlation between 2DGM along the building structural axes. It should be noted that, while Lopez et al. [7] used the P–W model, this chapter introduced the extended P–W model and took into account the critical cross PSD function between 2DGM. The critical response and the corresponding SRSS response have the same value at $\theta = 0.0$ and $\theta = \pi/2$ in Fig. 11.12b–e. This is because, in the case of $\gamma_{\mathrm{org}} \neq 0.0$, the coherence function $\rho_{12}(\gamma_{\mathrm{org}}, \theta)$ based on the P–W model is 0.0 at $\theta = 0.0$ or $\theta = \pi/2$ and the cross term of Eq. (11.11) does not exist. In Fig. 11.12f, there is no differences between the two lines. This is because 2DGM along the building structural axes are uncorrelated due to $\rho_{12}(\gamma_{\mathrm{org}}, \theta) = 0.0$ for $\gamma_{\mathrm{org}} = 1.0$. It can also be observed that the maximum value of the response considering the critical correlation is large for the small value of γ_{org}. This may result from the fact that (1) the coherence is 1.0 in Fig. 11.12a and is smaller than 1.0 in Fig. 11.12b–d, and (2) the concentrated unidirectional input is more effective in maximizing the extreme-fiber stress. Furthermore, comparing Fig. 11.12a with Fig. 11.12b, c, the maximum value of the response to the 2DGM along the principal axes of ground motions exceeds that to the unidirectional input shown in Fig. 11.12a. From these results, it can be concluded that a larger upper bound of the structural response can be evaluated by the proposed critical excitation method for bidirectional ground motions based on the extended P–W model.

Under the constraint of sum of auto PSD functions along the principal axes of ground motions, it may be concluded that the general response evaluation to the unidirectional input along the principal axes of ground motions ($\gamma_{\mathrm{org}} = 0.0$) is not sufficient as far as the maximum value of response quantity is concerned.

11.5.3 Comparison of Response to Critically Correlated 2DGM with that to Perfectly Correlated 2DGM

In order to understand the property of the critically correlated ground motions more deeply, the comparison with the perfectly correlated ground motions without time delay has been made. The structural plan is given as $L_1 = 15$ m, $L_2 = 25$ m. Figure 11.13a shows two horizontal ground motions with the critical correlation for input model of $\gamma_{\mathrm{org}} = 0$ and $\theta = 0.106\pi[\mathrm{rad}](= 19.0^\circ)$ (critical incident angle shown in Fig. 11.12a). This set has been generated by using random numbers. On the other hand, Fig. 11.13b indicates two horizontal ground motions with the perfect correlation without time delay for $\gamma_{\mathrm{org}} = 0$ and $\theta = 0.106\pi[\mathrm{rad}](= 19.0^\circ)$. Figure 11.14 illustrates the root-mean-square of column-end extreme-fiber stress to these two sets of horizontal ground motions. It can be observed that the response to the critically correlated ground motions could become about 1.5 times larger than that to the perfectly correlated ground motions without time delay.

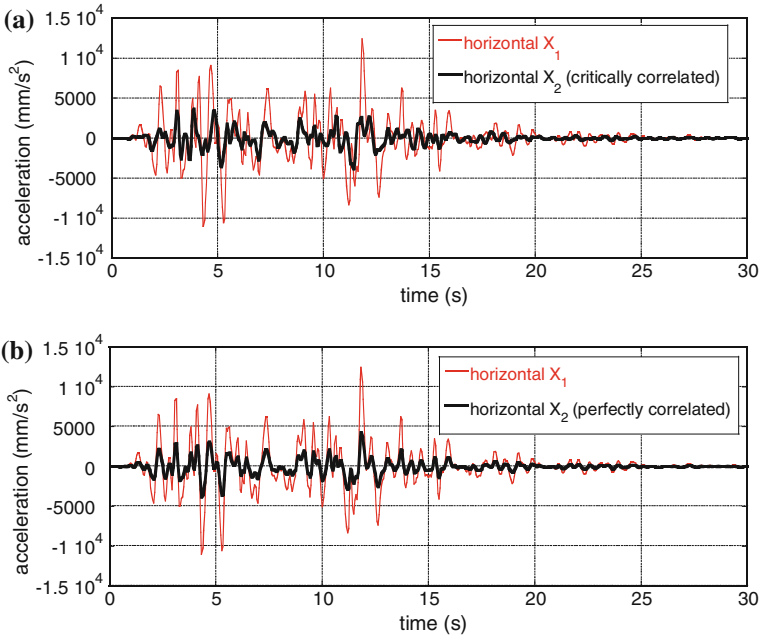

Fig. 11.13 One sample set of Monte Carlo simulation of the 2DGM; **a** critically correlated, **b** perfectly correlated [25]

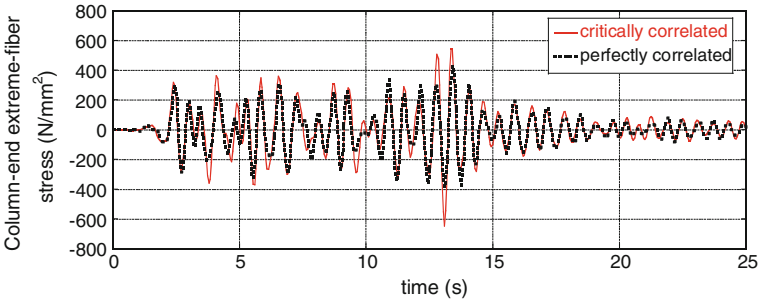

Fig. 11.14 Comparison of the column-end extreme-fiber stress to the critically correlated 2DGM with that to the perfectly correlated ones [25]

11.5.4 Analysis of Recorded 2DGM

The correlation between recorded 2DGM should be compared with the result of the critical excitation method developed in this chapter. In this section, the coherence function between the recorded 2DGM (El Centro NS and EW during Imperial Valley 1940, SCT1 NS and EW during Mexico Michoacan 1985) is calculated.

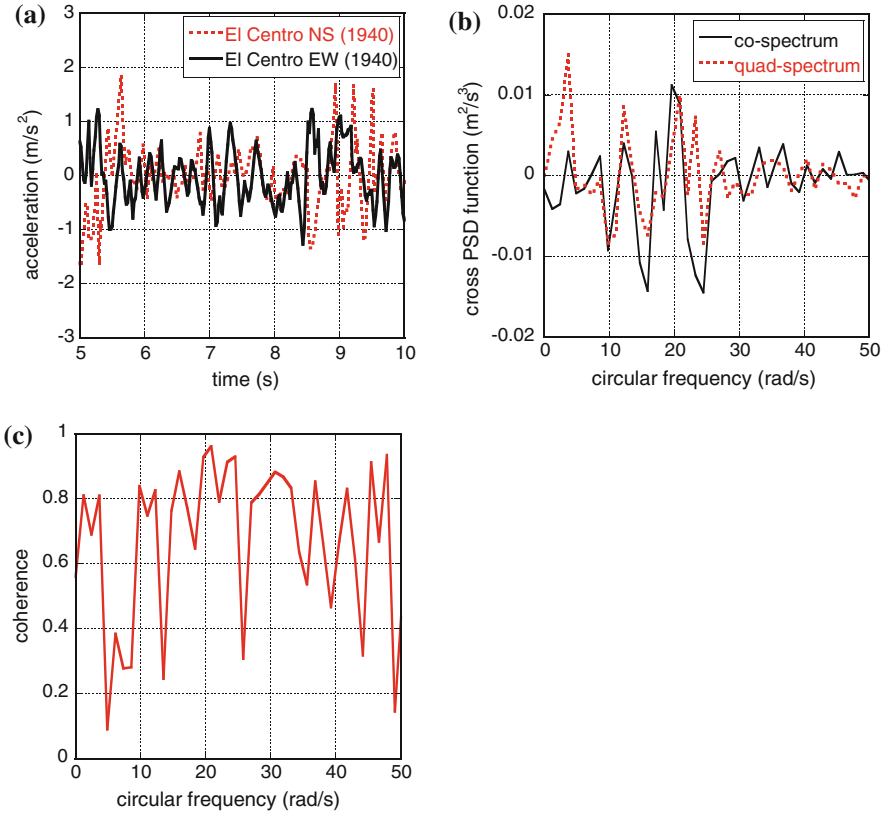

Fig. 11.15 **a** Acceleration records of El Centro NS and EW during imperial valley 1940, **b** Cross PSD function (co-spectrum and quad-spectrum), **c** Coherence function [25]

The auto PSD functions and cross PSD functions have been calculated from the Fourier transforms by using the Welch-Bartlett's method. The starting time of the window with the duration T (5 s in El Centro and 10 s in SCT1) was changed successively (time-lag of 0.02 s) and the corresponding set of data for the 100 windows was chosen to represent candidates of the ensemble mean. Then the procedure of ensemble mean was taken of the functions computed from the Fourier transforms.

Figure 11.15a shows the representative acceleration records of El Centro NS and EW and Fig. 11.15b illustrates the cross PSD function of both motions. For these data, Fig. 11.15c indicates the coherence function. It has been understood from several parametric analyses that the coherence function is affected significantly by the portion of ground motions. On the other hand, Fig. 11.16a–c illustrate the corresponding ones for SCT1 NS and EW. It can be seen that the cross PSD function of SCT1 NS and EW has a peculiar characteristic due to the predominant period of these motions. In Fig. 11.16c, the cases of the numbers 200

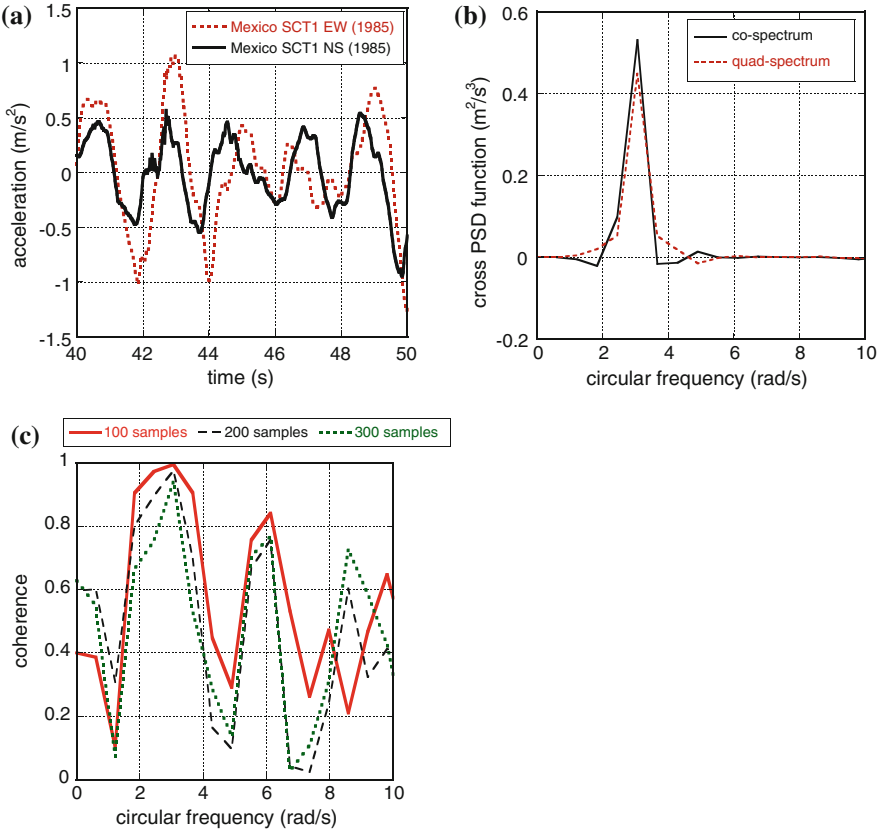

Fig. 11.16 **a** Acceleration records of SCT1 EW and NS during Mexico Michoacan 1985, **b** Cross PSD function (co-spectrum and quad-spectrum), **c** Coherence function [25]

and 300 of windows have also been examined in using the Welch-Bartlett's method. It can be observed that the coherence strongly depends on the type of earthquake ground motions. Furthermore, as stated, the coherence also depends on the portion of ground motions (these data are not shown here due to page limit). The prediction of the coherence function before its occurrence is quite difficult and the critical excitation method will provide a meaningful insight even in these circumstances.

As for the reality of critical excitation methods, a severe ground motion attacked recently (July 16, 2007) the city of Kashiwazaki, Niigata Prefecture in Japan, and many old wood houses were destroyed. It has been reported that a peculiar ground motion as shown in Fig. 11.17a has been observed and the ground motion had a predominant period of 2.5 s. This period is thought to be resonant with the natural period of old wood houses with heavy roofs. This ground motion is very similar to one, shown in Fig. 11.17b, predicted in Ref. [19]. It should be

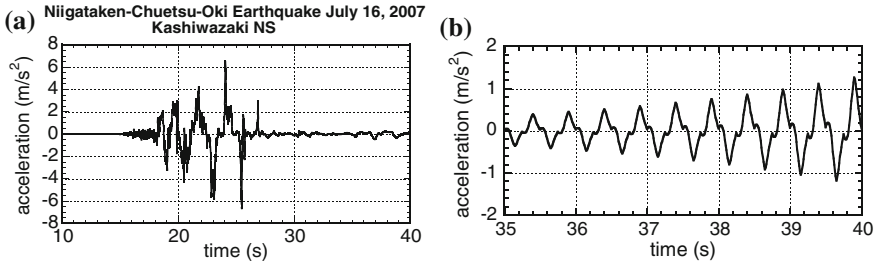

Fig. 11.17 **a** Critical-type ground motion in recent earthquake near nuclear reactor facilities, **b** Corresponding theoretical one predicted before its occurrence [25]

noted that a large nuclear reactor facility is located in the city of Kashiwazaki and that facility had relatively minor damage. Further damage investigation is being conducted even now. This ground motion strongly supports the importance of introducing the critical excitation methods especially for important structures.

11.6 Summary

An extended Penzien–Watabe (P–W) model has been explained in which the cross PSD function of 2DGM can be treated in a more relaxed manner. While only the coherence function, i.e., the absolute value of the cross PSD function, can be treated in the P–W model, the direct treatment of the cross PSD function has been made possible in the extended P–W model. The contents explained in this chapter may be summarized as follows.

1. A critical excitation problem has been formulated for a one-story one-span moment resisting 3D frame subjected to the 2DGM obeying the proposed extended P–W model. The objective function is the corner-fiber stress at the column-end. The extended P–W model is an extended version of the P–W model including additional information on the cross PSD function as a complex function.
2. The mean-squares corner-fiber stress at the column-end has been shown to be the sum of the term due to the 2DGM and that due to their correlation. Since the auto PSD functions of 2DGM are given and prescribed, the maximization in the critical excitation problem means the maximization of the correlation term of 2DGM.
3. The real part (co-spectrum) and the imaginary part (quad-spectrum) of the worst cross PSD function can be obtained by a devised algorithm including the interchange of the double maximization procedure in the time and cross PSD function dual domains.
4. Numerical examples indicate that the explained algorithm can work very well. The root-mean-square corner-fiber stress at the column-end to the critical

combination of the 2DGM becomes more than 10 % larger than that by the SRSS estimate of corner-fiber stress at the column-end due to the 2DGM. When the horizontal stiffnesses along the building structural axes coincide with each other, the response to the critical excitation becomes about 40 % ($\simeq \sqrt{2}$) larger than that by the SRSS estimate.

5. Analytical solutions, Eqs. (11.19a, b), have enabled the efficient parametric analysis of critical incident angle (see Fig. 11.12).
6. The coherence function between the 2DGM of recorded earthquakes has been calculated. The coherence strongly depends on the type of earthquake ground motions and the prediction of the coherence function before its occurrence is quite difficult. The critical excitation method will provide a meaningful insight even in these circumstances.

Appendix 1: Computation of Coherence Function and Transformation of PSD Matrices

Let $\ddot{u}_{g1}$ and $\ddot{u}_{g2}$ denote the ground-motion accelerations along the building structural axes X_1 and X_2, respectively. Under the 2DGM along the principal axes of ground motions in the P–W model, $\ddot{u}_{g1}$ and $\ddot{u}_{g2}$ are described by

$$\begin{Bmatrix} \ddot{u}_{g1} \\ \ddot{u}_{g2} \end{Bmatrix} = \begin{bmatrix} \cos\theta & \sin\theta \\ -\sin\theta & \cos\theta \end{bmatrix} \begin{Bmatrix} \ddot{u}_{z1} \\ \ddot{u}_{z2} \end{Bmatrix}, \tag{11.21}$$

where $\ddot{u}_{z1}$ and $\ddot{u}_{z2}$ are the ground-motion accelerations along the principal axes of ground motions. θ denotes the angle between two sets of horizontal axes (= incident angle).

Let $\mathbf{S}_{\ddot{Z}\ddot{Z}}(\omega)$ denote the auto PSD matrix of the components along the principal axes of ground motions. Then the PSD matrix, consisting of S_{11}, S_{22}, S_{12}, S_{21}, of the components along the building structural axes may be described as

$$\mathbf{S}_{\ddot{X}\ddot{X}}(\omega) = \begin{bmatrix} \cos\theta & \sin\theta \\ -\sin\theta & \cos\theta \end{bmatrix} \mathbf{S}_{\ddot{Z}\ddot{Z}}(\omega) \begin{bmatrix} \cos\theta & -\sin\theta \\ \sin\theta & \cos\theta \end{bmatrix} \tag{11.22}$$

$$\mathbf{S}_{\ddot{Z}\ddot{Z}}(\omega) = \begin{bmatrix} S_{\ddot{Z}_1\ddot{Z}_1}(\omega) & 0 \\ 0 & S_{\ddot{Z}_2\ddot{Z}_2}(\omega) \end{bmatrix} \tag{11.23}$$

The coherence function between the components of ground motions along the building structural axes is defined by

$$\rho_{12} = \frac{E\left[\ddot{u}_{g1}\ddot{u}_{g2}\right]}{\sqrt{E\left[\ddot{u}_{g1}^2\right]E\left[\ddot{u}_{g2}^2\right]}}, \tag{11.24}$$

where $E[\ \cdot\ ]$ denotes the ensemble mean. It is assumed in the P–W model that there is no correlation between the 2DGM along the principal axes of ground motions (i.e. $E[\ddot{u}_{z1}\ddot{u}_{z2}] = 0$). Let γ_{org} denote the ratio of the auto PSD functions $S_{\ddot{Z}_2\ddot{Z}_2}(\omega)/S_{\ddot{Z}_1\ddot{Z}_1}(\omega)$ along the principal axes of ground motions. Substitution of $\ddot{u}_{g1}$ and $\ddot{u}_{g2}$ in Eq. (11.21) into Eq. (11.24) and some manipulations provide

$$\rho_{12}(\gamma_{\text{org}}, \theta) = \frac{(1-\gamma_{\text{org}})\sin 2\theta}{\sqrt{(1+\gamma_{\text{org}})^2 - (1-\gamma_{\text{org}})^2 \cos^2 2\theta}} \tag{11.25}$$

Appendix 2: Horizontal Stiffness of Frame

Let u_1 and ϕ_{AB} denote the horizontal displacement of the upper node in the frame and the angle of member rotation of column, respectively. When the horizontal force is denoted by P_1, the horizontal stiffness of the plane frame can be expressed as

$$k_1 = P_1/u_1 = P_1/(H \cdot \phi_{AB}) \tag{11.26}$$

The extreme-fiber stress at the top of the column under one-directional horizontal input may be expressed by

$$\sigma_{BA}^1(t) = \{6EI_b/(Z_c L_1)\}\theta_B \tag{11.27}$$

From the moment equilibrium around the node B, the angle of rotation of the node B can be expressed by

$$\theta_B = 3\phi_{AB}/[2 + 3(I_b/I_c) \cdot (H/L_1)] \tag{11.28}$$

Equation (11.28) and the equation of story equilibrium provide

$$\phi_{AB} = \frac{P_1 H^2 \{2 + 3(I_b/I_c) \cdot (H/L_1)\}}{12EI_c\{1 + 6(I_b/I_c) \cdot (H/L_1)\}} \tag{11.29}$$

Then the story stiffness can be expressed by

$$k_1 = \frac{12EI_c\{1 + 6(I_b/I_c) \cdot (H/L_1)\}}{H^3\{2 + 3(I_b/I_c) \cdot (H/L_1)\}} \tag{11.30}$$

Appendix 3: Stochastic Response 1

The auto-correlation function of $\sigma_{BA}^{1}(t)$ can be expressed by

$$E\left[\sigma_{BA}^{1}(t_1)\sigma_{BA}^{1}(t_2)\right] = A_{\sigma 1}^{2}\int_0^{t_1}\int_0^{t_2}[c_1(\tau_1)c_1(\tau_2)g_1(t_1-\tau_1)g_1(t_2-\tau_2)E[w_1(\tau_1)w_1(\tau_2)]]d\tau_1 d\tau_2 \tag{11.31}$$

The auto-correlation function of $w_1(t)$ can be described in terms of the auto PSD function $S_{11}(\omega)$ by

$$E[w_1(\tau_1)w_1(\tau_2)] = \int_{-\infty}^{\infty} S_{11}(\omega)e^{\mathrm{i}\omega(\tau_1-\tau_2)}d\omega \tag{11.32}$$

Equation (11.31) can then be modified to

$$\begin{aligned} &E\left[\sigma_{BA}^{1}(t_1)\sigma_{BA}^{1}(t_2)\right] \\ &= \int_{-\infty}^{\infty}\left[\begin{array}{l} \mathrm{A}_{\sigma 1}\int_0^{t_1}\mathrm{c}_1(\tau_1)\mathrm{g}_1(t_1-\tau_1)(\cos\omega\tau_1 + \mathrm{i}\sin\omega\tau_1)\mathrm{d}\tau_1 \\ \times\mathrm{A}_{\sigma 1}\int_0^{t_2}\mathrm{c}_1(\tau_2)\mathrm{g}_1(t_2-\tau_2)(\cos\omega\tau_2 - \mathrm{i}\sin\omega\tau_2)\mathrm{d}\tau_2 \end{array}\right]\mathrm{S}_{11}(\omega)\mathrm{d}\omega \end{aligned} \tag{11.33}$$

By substituting $t_1 = t_2 = t$, $\tau_1 = \tau_2 = \tau$ in Eq. (11.33), the mean-squares $E[\sigma_{BA}^{1}(t)^2]$ can be derived as

$$E[\sigma_{BA}^{1}(t)^2] = A_{\sigma 1}^{2}\int_{-\infty}^{\infty}\{B_c(t;\omega)^2 + B_s(t;\omega)^2\}S_{11}(\omega)d\omega \tag{11.34}$$

where

$$B_c(t;\omega) \equiv \int_0^t c_1(\tau)g_1(t-\tau)\cos\omega\tau d\tau \tag{11.35a}$$

$$B_s(t;\omega) \equiv \int_0^t c_1(\tau)g_1(t-\tau)\sin\omega\tau d\tau \tag{11.35b}$$

On the other hand, the component in the direction X_2 may be transformed into

$$E\left[\sigma_{BA}^{2}(t_1)\sigma_{BA}^{2}(t_2)\right] = A_{\sigma 2}^{2}\int_0^{t_1}\int_0^{t_2}[c_2(\tau_1)c_2(\tau_2)g_2(t_1-\tau_1)g_2(t_2-\tau_2)E[w_2(\tau_1)w_2(\tau_2)]]\,d\tau_1 d\tau_2 \tag{11.36}$$

The auto-correlation function of $w_2(t)$ can be described in terms of the auto PSD function $S_{22}(\omega)$ by

$$E[w_2(\tau_1)w_2(\tau_2)] = \int_{-\infty}^{\infty} S_{22}(\omega)e^{i\omega(\tau_1-\tau_2)}d\omega \tag{11.37}$$

The mean-squares $E[\sigma_{BA}^2(t)^2]$ can be derived as

$$E[\sigma_{BA}^2(t)^2] = A_{\sigma 2}^2 \int_{-\infty}^{\infty} \{C_c(t;\omega)^2 + C_s(t;\omega)^2\}S_{22}(\omega)d\omega, \tag{11.38}$$

where

$$C_c(t;\omega) \equiv \int_0^t c_2(\tau)g_2(t-\tau)\cos\omega\tau d\tau \tag{11.39a}$$

$$C_s(t;\omega) \equiv \int_0^t c_2(\tau)g_2(t-\tau)\sin\omega\tau d\tau \tag{11.39b}$$

Appendix 4: Stochastic Response 2

The cross-correlation function of $\sigma_{BA}^1(t)$ and $\sigma_{BA}^2(t)$ can be expressed as

$$E\left[\sigma_{BA}^1(t_1)\sigma_{BA}^2(t_2)\right] = A_{\sigma 1}A_{\sigma 2}\int_0^{t_1}\int_0^{t_2}[c_1(\tau_1)c_2(\tau_2)g_1(t_1-\tau_1)g_2(t_2-\tau_2)E[w_1(\tau_1)w_2(\tau_2)]]d\tau_1 d\tau_2 \tag{11.40}$$

The cross-correlation function of $w_1(t)$ and $w_2(t)$ can be described in terms of the cross PSD function $S_{12}(\omega)$ by

$$E[w_1(\tau_1)w_2(\tau_2)] = \int_{-\infty}^{\infty} S_{12}(\omega)e^{i\omega(\tau_1-\tau_2)}d\omega \tag{11.41}$$

Let us introduce the definition of the cross PSD function $S_{12}(\omega) = C_{12}(\omega) + iQ_{12}(\omega)$.

Then Eq. (11.41) can be expressed by

$$E[w_1(\tau_1)w_2(\tau_2)] = \int_{-\infty}^{\infty} \{C_{12}(\omega) + iQ_{12}(\omega)\}e^{i\omega(\tau_1-\tau_2)}d\omega \tag{11.42}$$

The cross-term can be modified into

$$
\begin{aligned}
&E\left[\sigma_{BA}^{1}(t)\sigma_{BA}^{2}(t)\right] \\
&= A_{\sigma 1}A_{\sigma 2}\int_{-\infty}^{\infty}\left[\begin{array}{l}\displaystyle\int_{0}^{t} c_1(\tau)g_1(t-\tau)(\cos\omega\tau+\mathrm{i}\sin\omega\tau)d\tau \\ \displaystyle\times\int_{0}^{t} c_2(\tau)g_2(t-\tau)(\cos\omega\tau-\mathrm{i}\sin\omega\tau)d\tau\{C_{12}(\omega)+\mathrm{i}Q_{12}(\omega)\}\end{array}\right]d\omega \\
&= A_{\sigma 1}A_{\sigma 2}\int_{-\infty}^{\infty}\left[\{B_c(t;\omega)+\mathrm{i}B_s(t;\omega)\}\{C_c(t;\omega)-\mathrm{i}C_s(t;\omega)\}\{C_{12}(\omega)+\mathrm{i}Q_{12}(\omega)\}\right]d\omega
\end{aligned}
\tag{11.43}
$$

Another cross-correlation function $E[\sigma_{BA}^{2}(t_1)\sigma_{BA}^{1}(t_2)]$ may be described by

$$
\begin{aligned}
&E[\sigma_{BA}^{2}(t)\sigma_{BA}^{1}(t)] \\
&= A_{\sigma 2}A_{\sigma 1}\int_{-\infty}^{\infty}\left[\{C_c(t;\omega)+\mathrm{i}C_s(t;\omega)\}\{B_c(t;\omega)-\mathrm{i}B_s(t;\omega)\}\{C_{12}(\omega)-\mathrm{i}Q_{12}(\omega)\}\right]d\omega
\end{aligned}
\tag{11.44}
$$

By combining both cross terms, the corresponding term can be expressed finally by

$$
\begin{aligned}
&E[\sigma_{BA}^{1}(t)\sigma_{BA}^{2}(t)]+E[\sigma_{BA}^{2}(t)\sigma_{BA}^{1}(t)] \\
&= 2A_{\sigma 1}A_{\sigma 2}\mathrm{Re}\left[\int_{-\infty}^{\infty}\left[\{B_c(t;\omega)+\mathrm{i}B_s(t;\omega)\}\{C_c(t;\omega)-\mathrm{i}C_s(t;\omega)\}\{C_{12}(\omega)+\mathrm{i}Q_{12}(\omega)\}\right]d\omega\right] \\
&= 2A_{\sigma 1}A_{\sigma 2}\int_{-\infty}^{\infty}\{f_1(t;\omega)C_{12}(\omega)+f_2(t;\omega)Q_{12}(\omega)\}d\omega
\end{aligned}
\tag{11.45}
$$

References

1. Rigato AB, Medina RA (2007) Influence of angle of incidence on seismic demands for inelastic single-storey structures subjected to bi-directional ground motions. Eng Struct 29(10):2593–2601
2. Ghersi A, Rossi PP (2001) Influence of bi-directional ground motions on the inelastic response of one-storey in-plan irregular systems. Eng Struct 23(6):579–591
3. Penzien J, Watabe M (1975) Characteristics of 3-dimensional earthquake ground motion. Earthq Eng Struct Dyn 3:365–374
4. Clough RW, Penzien J (1993) Dynamics of structures, 2nd edn. Prentice Hall, Englewood Cliffs
5. Smeby W, Der Kiureghian A (1985) Modal combination rules for multicomponent earthquake excitation. Earthq Eng Struct Dyn 13:1–12

6. Menun C, Der Kiureghian A (1998) A replacement for the 30 %, 40 %, and SRSS rules for multicomponent seismic analysis. Earthq Spectra 14(1):153–163
7. Lopez OA, Chopra AK, Hernandez JJ (2000) Critical response of structures to multicomponent earthquake excitation. Earthq Eng Struct Dyn 29:1759–1778
8. Athanatopoulou AM (2005) Critical orientation of three correlated seismic components. Eng Struct 27:301–312
9. Nigam NC (1983) Introduction to random vibrations. MIT Press, London
10. Drenick RF (1970) Model-free design of aseismic structures. J Engrg Mech Div, ASCE 96(EM4):483–493
11. Shinozuka M (1970) Maximum structural response to seismic excitations. J Engrg Mech Div, ASCE 96(EM5):729–738
12. Iyengar RN, Manohar CS (1987) Nonstationary random critical seismic excitations. J Engrg Mech, ASCE 113(4):529–541
13. Manohar CS, Sarkar A (1995) Critical earthquake input power spectral density function models for engineering structures. Earthq Eng Struct Dyn 24:1549–1566
14. Abbas AM, Manohar CS (2002) Investigations into critical earthquake load models within deterministic and probabilistic frameworks. Earthq Eng Struct Dyn 31(4):813–832
15. Abbas AM, Manohar CS (2002) Critical spatially-varying earthquake load models for extended structures. J Struct Engrg (JoSE, India) 29(1):39–52
16. Abbas AM, Manohar CS (2007) Reliability-based vector nonstationary random critical earthquake excitations for parametrically excited systems. Struct Safety 29:32–48
17. Takewaki I (2001) A new method for nonstationary random critical excitation. Earthq Engrg Struct Dyn 30(4):519–535
18. Takewaki I (2002) Seismic critical excitation method for robust design: a review. J Struct Engrg ASCE 128(5):665–672
19. Takewaki I (2004) Critical envelope functions for non-stationary random earthquake input. Comput Struct 82(20–21):1671–1683
20. Takewaki I (2004) Bound of earthquake input energy. J Struct Engrg ASCE 30(9):1289–1297
21. Takewaki I (2006) Probabilistic critical excitation method for earthquake energy input rate. J Engrg Mech ASCE 132(9):990–1000
22. Takewaki I (2006) Critical excitation methods in earthquake engineering. Elsevier Science, Oxford
23. Sarkar A, Manohar CS (1996) Critical cross power spectral density functions and the highest response of multi-supported structures subjected to multi-component earthquake excitations. Earthq Eng Struct Dyn 25:303–315
24. Sarkar A, Manohar CS (1998) Critical seismic vector random excitations for multiply supported structures. J Sound Vib 212(3):525–546
25. Fujita K, Takewaki I (2010) Critical correlation of bi-directional horizontal ground motions. Eng Struct 32(1):261–272
26. Fujita K, Yoshitomi S, Tsuji M, Takewaki I (2008) Critical cross-correlation function of horizontal and vertical ground motions for uplift of rigid block. Eng Struct 30(5):1199–1213

Chapter 12
Optimal Placement of Visco-Elastic Dampers and Supporting Members Under Variable Critical Excitations

12.1 Introduction

The concept of performance-based design has recently been introduced and is well accepted in the current structural design practice of buildings. In earthquake-prone countries, the philosophy of earthquake-resistant design to resist ground shaking with sufficient stiffness and strength of a building itself has also been accepted as a relevant structural design concept for many years. On the other hand, a new strategy based on the concept of active and passive structural control has been introduced rather recently in order to provide structural designers with powerful tools for performance-based design.

In the early period of the research in passive structural control, the installation itself of supplemental dampers was the main objective. It appears natural that, after extensive developments of various damper systems, another target was refocused on the development of smart and effective use of such dampers.

Although the motivation was inspired and focused on smart and effective installation of dampers, the research on optimal damper placement has been very limited. The following studies may deal with this subject. Constantinou and Tadjbakhsh [1] derived the optimum damping coefficient for a damper placed on the first story of a shear building subjected to horizontal ground motions. Gurgoze and Muller [2] investigated a numerical optimal design method for a single viscous damper in a prescribed linear multi degree-of-freedom system. Zhang and Soong [3] presented a seismic design method for finding the optimal configuration of viscous dampers for a building with specified story stiffnesses. This study has been cited many times because the algorithm is very simple and extendable to further studies. Hahn and Sathiavageeswaran [4] performed parametric analyses on the effects of damper distribution on the earthquake response of buildings, and showed that, for a building of uniform story stiffnesses; dampers should be added to the lower half floors of the building. De Silva [5] presented a gradient algorithm for the optimal design of discrete dampers in the vibration control of a class of flexible systems.

I. Takewaki et al., *Improving the Earthquake Resilience of Buildings*,
Springer Series in Reliability Engineering, DOI: 10.1007/978-1-4471-4144-0_12,

Tsuji and Nakamura [6] proposed an algorithm to find both the optimal story stiffness distribution and the optimal damper distribution for a shear building model subjected to the spectrum-compatible ground motions. A series of the optimal designs for various lower bounds of damping coefficients has been searched.

In the second period of the research, Takewaki [7, 8] developed another optimal design method for the smart damper placement based on the concepts of inverse problem approaches and optimal criteria-based design approaches. He tackled a problem of optimal damper placement by deriving the optimality criteria first and then by developing an original incremental inverse problem approach. Subsequently, Takewaki et al. [9, 10] and Takewaki [11–13] devised another approach based on the concept of optimal sensitivity. The optimal quantity of passive dampers is obtained automatically together with the optimal placement through this innovative method. The essence of these approaches is summarized in the monograph [14].

After or parallel to these researches, many works have been developed around the world [15–40]. Most of them investigated new optimal design methods of supplemental dampers and proposed effective and useful methods. Some of the works are using the gradient-based approach proposed by Takewaki [7, 12].

In this chapter, an efficient method is explained for finding the optimal design of both dampers and their supporting members to minimize an objective function of a linear multi-story structure, modeled by a shear building model, subjected to resonant ground input. The objective function is expressed in terms of the sum of the mean squares of interstory drifts. A frequency-dependent visco-elastic damper including the supporting unit is taken into account. Due to the added stiffness by the visco-elastic damper, a resonant variable critical excitation [41, 42] needs to be updated in every phase of optimal damper placement. This difficulty does not exist in using viscous dampers without stiffness. Two different models of the whole damper unit are investigated. One is a detailed model called the "3N model" where the relative displacement between each component of damper unit can be defined. The other is a simpler model called the "N model" where the whole damper unit is converted to an equivalent frequency-dependent Kelvin–Voigt model. Numerical analyses are conducted and explained to show the ability of these different models and the validity of the proposed optimal design method.

12.2 Structural Model with Visco-Elastic Dampers and their Supporting Members

The building model is assumed to be a shear building model. This model is a fundamental model for multi-storied buildings and is known to be a good model for buildings with rather small aspect ratio (ratio of building height to building width). The characteristics of general visco-elastic dampers (VED) are dependent on frequency, temperature, and strain amplitude. Because of these complex

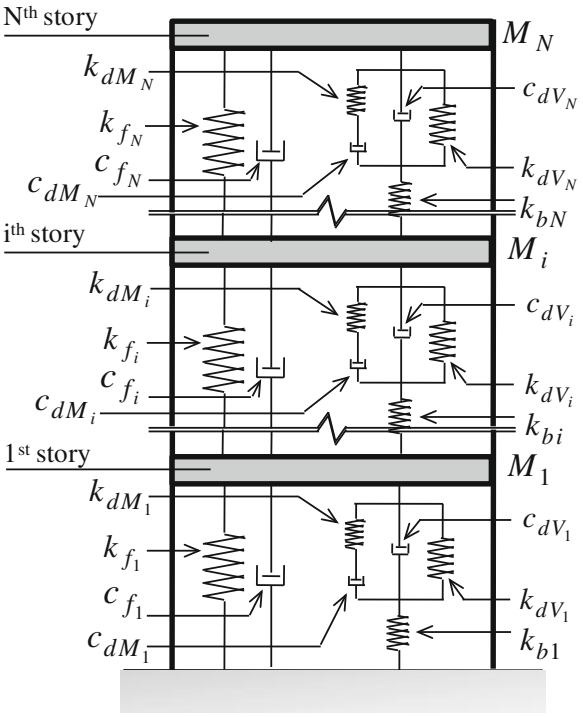

Fig. 12.1 Structural model with visco-elastic damper including supporting member (Fujita et al. [45] with permission from Techno Press)

features of VED, an appropriate VED model is necessary to describe these characteristics. In this chapter, consider an N-story planar building with frequency-dependent acrylic VED and their supporting members. The dependence on temperature and strain amplitude is ignored in this chapter. This acrylic VED is assumed to be described by a four-element model as shown in Fig. 12.1. $k_{\mathrm{M}i}$, $k_{\mathrm{V}i}$, $c_{\mathrm{M}i}$, and $c_{\mathrm{V}i}$ represent the stiffnesses and damping coefficients of each spring and dashpot in VED in the ith story. In order to take into account the stiffness of supporting members $k_{\mathrm{b}i}$, the four-element VED model is connected in series with another spring. This whole damper unit may be converted to two different models (Fig. 12.2).

The first model is a detailed model, as shown in Fig. 12.2a allocating small lumped masses between the components of spring and dashpot. Let U_i, u_{i1} and u_{i2} denote the ith story displacement relative to ground and the displacements of the lumped masses a and b relative to ground. This VED model has three DOF in each story and the structure with this VED model is called the "3N model". The stiffness and damping matrices of this VED model is independent of frequency. The components of stiffness and damping matrices $\mathbf{K}_{\mathrm{full}}$, $\mathbf{C}_{\mathrm{full}}$ are linear combinations of stiffness coefficients $k_{\mathrm{M}i}$, $k_{\mathrm{V}i}$, $k_{\mathrm{b}i}$, and damping coefficients $c_{\mathrm{M}i}$, $c_{\mathrm{V}i}$. Because of complex connection of each structural component, the overall stiffness matrix is not a simple one (not triple type matrix). For this reason, it may be

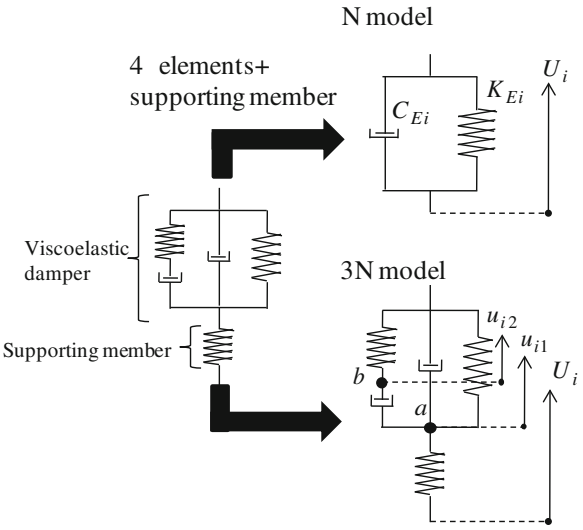

Fig. 12.2 Damper models simplified as "*N* model" and "3*N* model" (Fujita et al. [45] with permission from Techno Press)

disadvantageous to utilize the 3*N* model for a large-scale structure and a simpler VED model is needed.

The second VED model is called the "*N* model". In this VED model, the whole damper unit is converted to an equivalent frequency-dependent Kelvin–Voigt model. The equivalent stiffness and damping coefficients may be expressed by

$$K_{\mathrm{E}_i}(\omega, S_{\mathrm{d}_i}, k_{\mathrm{b}_i}) = \frac{(A - B\omega^2)(C - D\omega^2) + EF\omega^2}{(C - D\omega^2)^2 + F^2\omega^2} \tag{12.1}$$

$$C_{\mathrm{E}_i}(\omega, S_{\mathrm{d}_i}, k_{\mathrm{b}_i}) = \frac{(BF - DE)\omega^2 + CE - AF}{(C - D\omega^2)^2 + F^2\omega^2} \tag{12.2}$$

where the coefficients *A*–*F* are expressed as

$$\begin{aligned} A &= k_{\mathrm{b}_i} k_{\mathrm{M}_i} k_{\mathrm{V}_i} \\ B &= k_{\mathrm{b}_i} c_{\mathrm{M}_i} c_{\mathrm{V}_i} \\ C &= k_{\mathrm{b}_i} k_{\mathrm{M}_i} + k_{\mathrm{M}_i} k_{\mathrm{V}_i} \\ D &= c_{\mathrm{M}_i} c_{\mathrm{V}_i} \\ E &= k_{\mathrm{b}_i}(k_{\mathrm{V}_i} c_{\mathrm{M}_i} + k_{\mathrm{M}_i} c_{\mathrm{M}_i} + k_{\mathrm{M}_i} c_{\mathrm{V}_i}) \\ F &= c_{\mathrm{M}_i}(k_{\mathrm{b}_i} + k_{\mathrm{V}_i}) + k_{\mathrm{M}i}(c_{\mathrm{M}_i} + c_{\mathrm{V}_i}) \end{aligned} \tag{12.3a – f}$$

The detailed derivation of Eqs. (12.1) and (12.2) can be found in Appendix 1.

In this chapter, a detailed comparison is made between these two models (3*N* model and *N* model) for optimal damper placement.

12.3 Critical Excitation for Variable Design

In the seismic design of important structures, time history response analyses are often required for a set of recorded and/or simulated ground motions. However, it is well recognized that the ground motions include various uncertainties with various levels. In order to take into account these uncertainties, more reliable and robust structural design methods are desired and being investigated. The critical excitation method is adopted in this chapter. The critical excitation method was initiated by Drenick [43] and many subsequent researches have been accumulated [42].

Takewaki [41] introduced a concept of variable critical excitation which has a variable resonant circular frequency close to the natural circular frequency of the structure with varied stiffnesses of supplemental dampers. Based on this concept, a problem is posed such that the optimal placement of visco-elastic dampers is found together with the optimal stiffness distribution of supporting members.

Let $S_g(\omega)$ denotes the power spectral density (PSD) function of the input base acceleration $\ddot{u}_g(t)$. The constraints on $S_g(\omega)$ are the power, i.e., integration of the PSD function in frequency domain, described by

$$\int_{-\infty}^{\infty} S_g(\omega)\mathrm{d}\omega \le \bar{S} \tag{12.4}$$

and that of the intensity, i.e. maximum value of the PSD function, expressed by

$$\sup S_g(\omega) \le \bar{s} \tag{12.5}$$

$\bar{S}$ and $\bar{s}$ are the limits on power and intensity, respectively. These parameters characterizing the critical excitation are determined from the analysis of recorded ground motions. A shape of the PSD function as a solution to this problem is assumed to be a Dirac delta function (when $\bar{s}$ is infinite) or a band-limited white noise (when $\bar{s}$ is finite). The validity of this assumption has been demonstrated by Takewaki [42]. A band-limited white noise is explained in Fig. 12.3 where a frequency bandwidth Ω and upper and lower bounds ω_U, ω_L of frequency are obtained from given parameters $\bar{S}$ and $\bar{s}$.

In the following sections, the optimal placement of visco-elastic dampers is considered where the fundamental natural frequency of the structure with different damper placements may vary. In this case, ω_U, ω_L given for the critical excitation will change. This concept is the critical excitation for variable design [41, 42]. A similar concept has been developed in [12, 13]. However, it should be noted that, in [12, 13], a viscous damper has been treated and the variable design does not necessarily lead to the change of ω_U, ω_L.

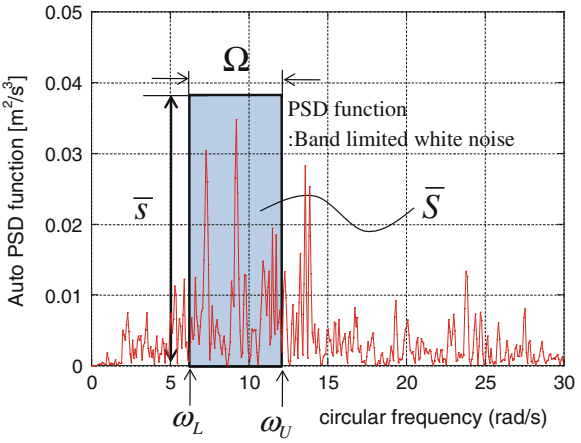

Fig. 12.3 Critical PSD function as a band-limited white noise compared with that of recorded ground motion (Fujita et al. [45] with permission from Techno Press)

12.4 Stochastic Response Evaluation in Frequency Domain

12.4.1 3N Model

Consider a $3N$ model first. Let $\mathbf{M}_{\text{full}}$, $\mathbf{r} = \{1, \ldots, 1\}^T$ denote the $(3N \times 3N)$ system mass matrix of the $3N$ model and the influence coefficient vector, respectively. The imaginary unit is denoted by $i = \sqrt{-1}$. The equations of motion of the building with passive dampers in frequency domain can be expressed by

$$(-\omega^2 \mathbf{M}_{\text{full}} + \mathrm{i}\omega \mathbf{C}_{\text{full}} + \mathbf{K}_{\text{full}})\mathbf{U}_{\text{full}}(\omega) = -\mathbf{M}_{\text{full}}\mathbf{r}\ddot{U}_{\text{g}}(\omega) \tag{12.6}$$

where $\mathbf{U}_{\text{full}}(\omega)$ and $\ddot{U}_{\text{g}}(\omega)$ are the Fourier transforms of the nodal displacements and the Fourier transform of the horizontal input acceleration $\ddot{u}_{\text{g}}(t)$. For simplicity of expression, Eq. (12.6) can be described as

$$\mathbf{A}_{\text{full}}\mathbf{U}_{\text{full}}(\omega) = \mathbf{B}_{\text{full}}\ddot{U}_{\text{g}}(\omega) \tag{12.7}$$

In Eq. (12.7) $\mathbf{A}_{\text{full}}$ and $\mathbf{B}_{\text{full}}$ are defined by

$$\mathbf{A}_{\text{full}} = -\omega^2 \mathbf{M}_{\text{full}} + \mathrm{i}\omega \mathbf{C}_{\text{full}} + \mathbf{K}_{\text{full}}, \mathbf{B}_{\text{full}} = -\mathbf{M}_{\text{full}}\mathbf{r} \tag{12.8a, b}$$

Fourier transforms $\mathbf{D}(\omega) = \{D_1, \ldots, D_N\}^T$ of the interstory drifts can be derived by

$$\mathbf{D}(\omega) = \mathbf{T}_{\text{full}}\mathbf{U}_{\text{full}}(\omega) \tag{12.9}$$

where $\mathbf{T}_{\text{full}}$ is a constant transformation matrix consisting of 1, −1, 0. By substituting Eq. (12.7) into Eq. (12.9), $\mathbf{D}(\omega)$ can be rewritten as

$$\mathbf{D}(\omega) = \mathbf{T}_{\text{full}}\mathbf{A}_{\text{full}}^{-1}\mathbf{B}_{\text{full}}\ddot{U}_{\text{g}}(\omega) \tag{12.10}$$

In Eq. (12.10), the transfer functions $\mathbf{H}_{\text{D}}^{\text{full}}(\omega) = \{H_{\text{D}_i}(\omega)\}$ of interstory drifts can be defined and expressed as

$$\mathbf{H}_{\text{D}}^{\text{full}}(\omega) = \mathbf{T}_{\text{full}}\mathbf{A}_{\text{full}}^{-1}\mathbf{B}_{\text{full}} \tag{12.11}$$

By using the resonant PSD function of the input, the objective function f_{3N} as the sum of the mean-squares response $\sigma_{\text{D}_i}^{\text{full}}$ of the ith interstory drift for the $3N$ model can be evaluated by

$$\begin{aligned} f_{3N} &= \sum_{i=1}^{N}\left(\sigma_{D_i}^{\text{full}}\right)^2 \\ &= \sum_{i=1}^{N}\int_{-\infty}^{\infty}\left|H_{\text{D}_{1+3(i-1)}}^{\text{full}}(\omega)\right|^2 S_{\text{g}}(\omega)\text{d}\omega \\ &= \sum_{i=1}^{N}\int_{-\infty}^{\infty}H_{\text{D}_{1+3(i-1)}}^{\text{full}}(\omega)H_{\text{D}_{1+3(i-1)}}^{\text{full}^*}(\omega)S_{\text{g}}(\omega)\text{d}\omega \end{aligned} \tag{12.12}$$

where $H_{\text{D}_i}^{\text{full}}(\omega)$ is the ith row vector of $\mathbf{H}_{\text{D}}^{\text{full}}(\omega)$ and $()^*$denotes the complex conjugate.

It is well recognized that the stiffness of supporting members should be strong enough to assure the effectiveness of the damper unit in the role of an energy dissipation system. For this reason, the stiffness $\mathbf{k}_{\text{b}} = \{k_{\text{b}_i}\}$ $(i = 1, \ldots, N)$ of each supporting member is treated as another design variable and the axial force of each supporting member is required not to exceed the upper limit (e.g., the yield force) determined from its material properties. In the $3N$ model, the maximum value of the axial force of the supporting member can be evaluated by

$$N_{\text{b}_i} = \rho k_{\text{b}_i}\sqrt{\int_{-\infty}^{\infty}\left|\mathbf{T}_{\text{b}}[\mathbf{H}_{\text{full}}(\omega)]_{2+3(i-1)}\right|^2 S_{\text{g}}(\omega)\text{d}\omega} \tag{12.13}$$

In Eq. (12.13), ρ is the peak factor for the maximum axial force of the supporting member. In order to evaluate the maximum axial force of the supporting member, the peak factor has been introduced. $\mathbf{T}_{\text{b}}$ is a transformation matrix from the nodal displacements to the relative displacements between both ends of supporting members (see Appendix 2).

12.4.2 N Model

Consider an N model next. Let $\mathbf{A}$, $\mathbf{B}$ denote the matrix and vector for the N model corresponding to Eq. (12.8a,b). The equations of motion for the N model in the frequency domain may be expressed simply by

$$\mathbf{A}\mathbf{U}(\omega) = \mathbf{B}\ddot{U}_{\mathrm{g}}(\omega) \tag{12.14}$$

The objective function can then be described by

$$f_{\mathrm{N}} = \sum_{i=1}^{N} \int_{-\infty}^{\infty} |H_{\delta_i}(\omega)|^2 S_{\mathrm{g}}(\omega)\mathrm{d}\omega \tag{12.15}$$

where $H_{\delta_i}(\omega)$ is the ith component of the interstory transfer function vector $\mathbf{T}\mathbf{A}^{-1}\mathbf{B}$ for the N model.

The axial force of the supporting member can be evaluated in the N model as the internal force of the frequency-dependent Kelvin–Voigt model.

$$N_{\mathrm{b}_i} = \rho \left(\int_{-\infty}^{\infty} |H_{\mathrm{Nb}_i}(\omega)|^2 S_{\mathrm{g}}(\omega)\mathrm{d}\omega \right)^{1/2} \tag{12.16}$$

where ρ and $H_{\mathrm{Nb}_i}(\omega)$ are the peak factor and the transfer function, respectively, of the axial force. The peak factor may be different from that for the $3N$ model in Eq. (12.13). The transfer function $H_{\mathrm{Nb}_i}(\omega)$ of the axial force can be expressed by

$$H_{\mathrm{Nb}_i}(\omega) = (K_{\mathrm{E}_i}(\omega) + \mathrm{i}\omega \mathrm{C}_{\mathrm{E}_i}(\omega))H_{\delta_i}(\omega) \tag{12.17}$$

where $K_{\mathrm{E}_i}(\omega) + \mathrm{i}\omega \mathrm{C}_{\mathrm{E}_i}(\omega)$ represents the complex stiffness of the equivalent Kelvin–Voigt model of the damper unit including a supporting member.

12.5 Optimal Design Problem

The problem of optimal damper placement of passive dampers and optimal stiffness selection of supporting members for the N-story shear building model subjected to variable critical excitation is stated as: find the distribution of both VED areas $\mathbf{S}_{\mathrm{d}} = \{S_{\mathrm{d}_1}, \ldots, S_{\mathrm{d}_N}\}$ and supporting member stiffnesses $\mathbf{k}_{\mathrm{b}} = \{k_{\mathrm{b}_1}, \ldots, k_{\mathrm{b}_N}\}$ subject to design constraints explained later.

The natural frequency ω_{c} of the building can vary according to the change of the damper unit (damper area and stiffness of supporting member). The property of the critical excitation $S_{\mathrm{g}}(\omega)$ is therefore dependent on the design variables $\mathbf{S}_{\mathrm{d}}$ and $\mathbf{k}_{\mathrm{b}}$. The objective function f defined in Eq. (12.15) can then be regarded as a function of ω_{c}, $\mathbf{S}_{\mathrm{d}}$, and $\mathbf{k}_{\mathrm{b}}$. In this case the objective function can be expressed explicitly as $f(\omega_{\mathrm{c}}, \mathbf{S}_{\mathrm{d}}, \mathbf{k}_{\mathrm{b}})$.

The first constraint on damper capacity is

$$\sum_{i=1}^{N} S_{\mathrm{d}_i} = \bar{W} \tag{12.18}$$

In Eq. (12.18) $\bar{W}$ is a specified total damper area. Additional constraints on the added damper's area in each story are described as

$$0 \le S_{\mathrm{d}_i} \le \bar{S}_{\mathrm{d}_i} \quad (i = 1, \ldots, N) \tag{12.19}$$

where $\bar{S}_{\mathrm{d}_i}$ is the upper bound of the damper area in the ith story.

On the other hand, the constraint on axial force of the supporting member may be described as

$$N_{\mathrm{b}_i}(\mathbf{S}_{\mathrm{d}}, \mathbf{k}_{\mathrm{b}}) \le \bar{P}_{\mathrm{y}_i}(k_{\mathrm{b}_i}) \quad (i = 1, 2, \ldots, N) \tag{12.20}$$

In Eq. (12.20), $\bar{P}_{\mathrm{y}_i}$ is the yield force of the supporting member and a function of k_{b_i}.

12.6 Optimality Conditions

The generalized Lagrangian L for the optimal design problem can be defined as

$$\begin{aligned} &L(\mathbf{S}_{\mathrm{d}}, \mathbf{k}_{\mathrm{b}}, \lambda, \boldsymbol{\mu}, \boldsymbol{\gamma}, \boldsymbol{\kappa}) \\ &= f + \lambda\Big(\sum_{i=1}^{N} S_{\mathrm{d}_i} - \bar{W}\Big) + \sum_{i=1}^{N} \mu_i(0 - S_{\mathrm{d}_i}) + \sum_{i=1}^{N} \gamma_i(S_{\mathrm{d}_i} - \bar{S}_{\mathrm{d}_i}) + \sum_{i=1}^{N} \kappa_i\big(N_{\mathrm{b}_i} - \bar{P}_{\mathrm{y}_i}\big) \end{aligned} \tag{12.21}$$

In Eq. (12.21) λ, $\boldsymbol{\mu} = \{\mu_i\}$ and $\boldsymbol{\kappa} = \{\kappa_i\}$ are the Lagrange multipliers. The principal optimality conditions for this problem without active upper and lower bound conditions on damper area and axial force of supporting member may be derived from the stationarity conditions of $L(\boldsymbol{\mu} = 0, \boldsymbol{\gamma} = 0, \boldsymbol{\kappa} = 0)$ with respect to $\mathbf{S}_{\mathrm{d}}$ and $\mathbf{k}_{\mathrm{b}}$.

$$f_{,j} + \lambda = 0 \text{ for } 0 < S_{\mathrm{d}_j} < \bar{S}_{\mathrm{d}_j},\ N_{\mathrm{b}_j} < \bar{P}_{\mathrm{y}_j} \quad (j = 1, \ldots, N) \tag{12.22}$$

$$f^{,j} = 0 \text{ for } N_{\mathrm{b}_j} < \bar{P}_{\mathrm{y}_j} \quad (j = 1, \ldots, N) \tag{12.23}$$

The symbols $(\ \ )_{,j}$ and $(\ \ )^{,j}$ denote the partial differentiation with respect to S_{d_j} and k_{b_j}, respectively.

In the process of allocating VED to each story, the axial force of the supporting member usually increases. When the constraint on axial force of the supporting member is active (satisfied with equality), the optimality conditions can be derived by the stationarity conditions of $L(\boldsymbol{\mu} = 0, \boldsymbol{\gamma} = 0)$ as follows:

$$f_{,j} + \lambda + \sum_{i=q_1}^{q_n} \kappa_i N_{\mathrm{b}_i,j} = 0 \text{ for } 0 < S_{\mathrm{d}_j} < \bar{S}_{\mathrm{d}_j} (j = 1, \ldots, N), N_{\mathrm{b}_i} = \bar{P}_{\mathrm{y}_i} (i = q_1, \ldots, q_n) \tag{12.24}$$

$$f^{,j} + \sum_{i=q_1}^{q_n} \kappa_i (N_{\mathrm{b}_i}^{,j} - \bar{P}_{\mathrm{y}_i}^{,j}) = 0 \text{ for } N_{\mathrm{b}_j} = \bar{P}_{\mathrm{y}_j} (j = q_1, \ldots, q_n) \tag{12.25}$$

where n and q_i denote the number of stories having active constraint on axial force of the supporting member and location (story number) of those stories, respectively. In Eq. (12.25), it is assumed that the partial differentiation of the ith story axial force N_{b_i} with respect to other story supporting member's stiffness k_{b_j} can be neglected ($N_{\mathrm{b}_i}^{,j} = 0 \quad (i \neq j)$). This assumption may be reasonable. In addition, the yield force of each supporting member $\bar{P}_{\mathrm{y}_j}$ is a function of only the stiffness k_{b_j} of the supporting member at that story. As a result, Eq. (12.25) can be replaced by

$$f^{,j} + \kappa_j \left(N_{\mathrm{b}_j}^{,j} - \bar{P}_{\mathrm{y}_j}^{,j} \right) = 0 \tag{12.26}$$

It is noted that the Lagrange multiplier κ_j can be evaluated directly from Eq. (12.26). This assumption facilitates the sensitivity expression of the objective function.

When the other constraints on upper and lower bounds of damper's area are active (satisfied with equality), the optimality conditions can be described by

$$f_{,j} + \lambda \geq 0 \text{ for } S_{\mathrm{d}_j} = 0 \tag{12.27}$$

$$f_{,j} + \lambda + \sum_{i=q_1}^{q_n} \kappa_i N_{\mathrm{b}_i,j} \leq 0 \text{ for } S_{\mathrm{d}_j} = \bar{S}_{\mathrm{d}_j}, N_{\mathrm{b}_i} = \bar{P}_{\mathrm{y}_i} \quad (i = q_1, \ldots, q_n) \tag{12.28}$$

If there is no VED where the axial force of supporting member attains its yield force, Eq. (12.28) should be replaced by

$$f_{,j} + \lambda \leq 0 \text{ for } S_{\mathrm{d}_j} = \bar{S}_{\mathrm{d}_j} \tag{12.29}$$

12.7 Algorithm for Optimal Damper Placement

12.7.1 Algorithm for Optimal Damper Placement and Optimal Design of Supporting Members

A gradient-based algorithm for the solution is introduced and explained for the problem of optimal damper placement. The flow chart of this solution algorithm is shown in Fig. 12.4. Furthermore, an instructive figure including the variation of design variables $\mathbf{S}_{\mathrm{d}}$ and $\mathbf{k}_{\mathrm{b}}$ in the optimal procedure is shown in Fig. 12.5.

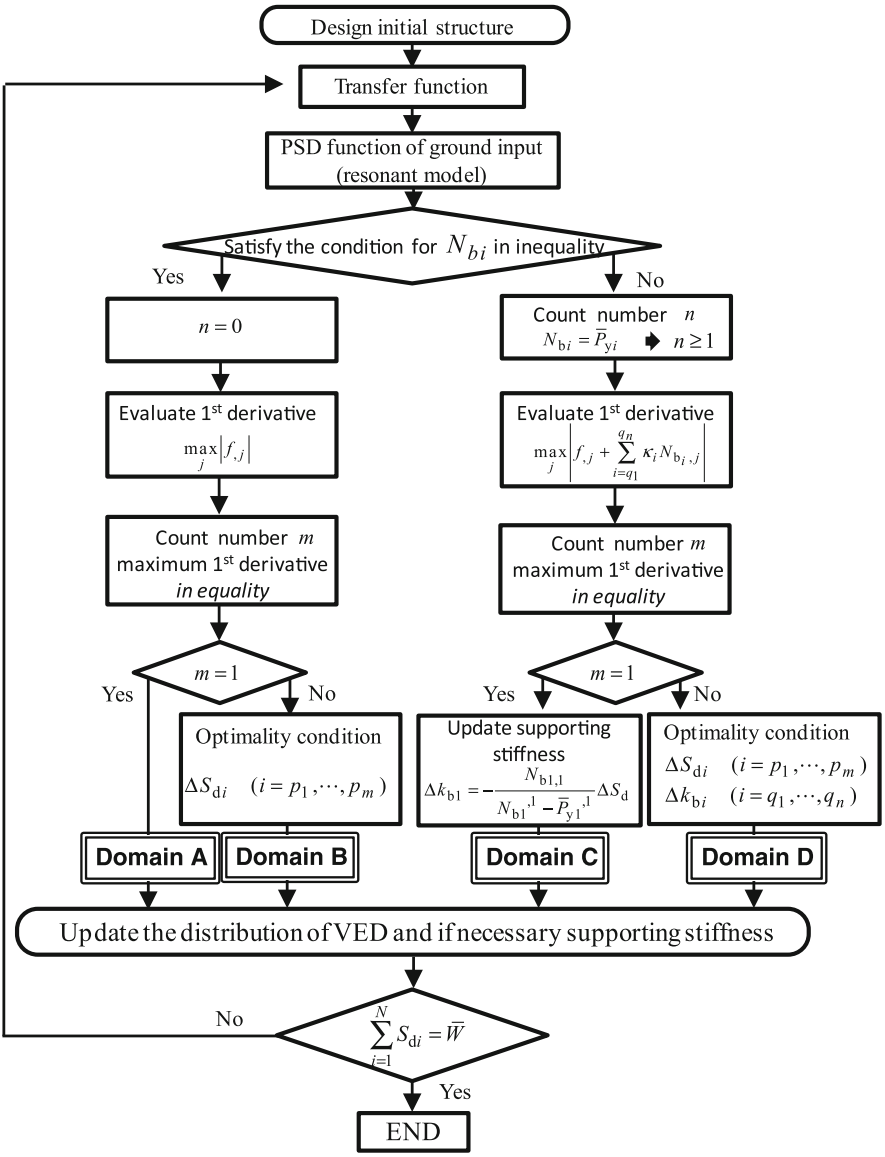

Fig. 12.4 Flowchart for optimal placement of visco-elastic dampers and supporting members (Fujita et al. [45] with permission from Techno Press)

The step-by-step solution procedure is summarized as follows:

Step 0 Design the structural model (stiffness of shear building model) without supplemental VED.
Step 1 Calculate the fundamental natural circular frequency ω_0 of the 3*N* model.

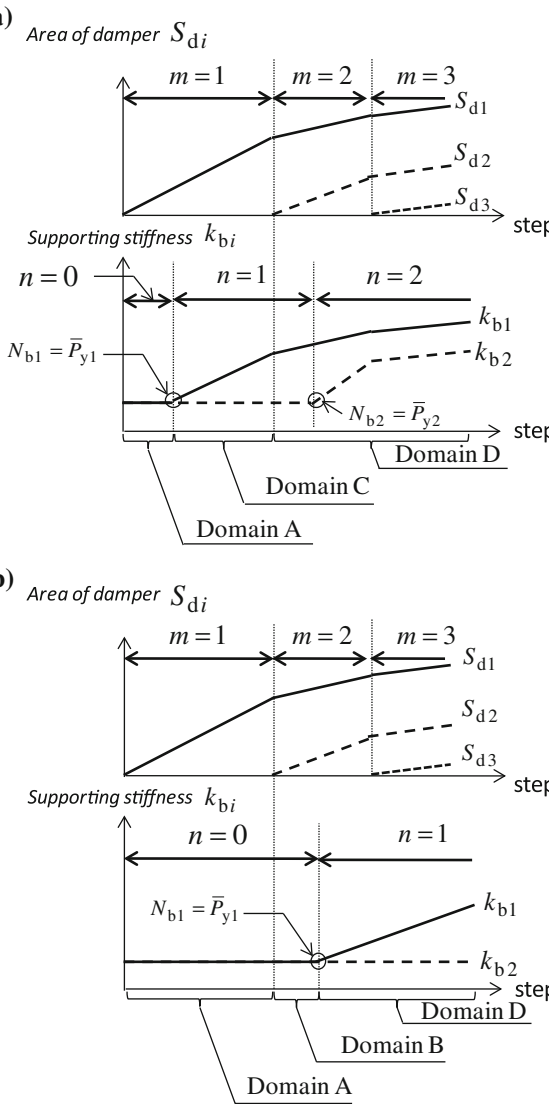

Fig. 12.5 Evolution of design variables by proposed optimization procedure. **a** Case including domains A, C, D. **b** Case including domains A, B, D (Fujita et al. [45] with permission from Techno Press)

Step 2 Create the critical PSD function $S_g(\omega)$ as a band-limited white noise which has a dominant frequency (central frequency) close to ω_0.
Step 3 Evaluate the axial force N_{b_i} of the supporting member and count the number n that N_{b_i} reaches its yield axial force N_{y_i}.
Step 4 Find the location of story where the absolute value of the first-order sensitivity of the objective function f reaches the maximum value along the story.
Step 5 Count the number m of stories where the maximum value of the absolute values of the first-order sensitivity of the objective function coincides.

Table 12.1 Optimality conditions in each domain (Fujita et al. [45] with permission from Techno Press)

Domain A ($m = 1$, $n = 0$)	p_1 Story	Other story	
	Eqs. (12.22), (12.23)	Eq. (12.27)	
Domain B ($m = 1$, $n = 1$)	$p_1(=q_1)$story Eqs. (12.24), (12.25)	Other story Eq. (12.27)	
Domain C ($m \geq 2, n \geq 1$)	$q_1 \sim q_n$story Eqs. (12.24), (12.25)	$p_{n+1} \sim p_m$story Eqs. (12.22), (12.23)	Other story Eq. (12.27)

This procedure can be classified into four domains, called A, B, C and D (see Fig. 12.5), by the combination of m and n. In order to find the optimal increment of $\mathbf{S}_\mathrm{d}$ and $\mathbf{k}_\mathrm{b}$, an appropriate combination of the optimality conditions should be selected from Eqs. (12.22)–(12.29). The relationship between the optimality conditions and each classified domain is shown in Table 12.1.

Step 6*A* The case of $m = 1$, $n = 0$ corresponds to the domain A. The increment ΔW of VED is added only to the specific story attaining $\max_j |f_{,j}|$.

Step 6*B* The case of $m \geq 2$, $n = 0$ corresponds to the domain B. When the multiple equality optimality conditions, Eq. (12.22), are satisfied, the optimal damper distribution $S_{\mathrm{d}i}$ has to be computed and updated to keep the coincidence of the multiple maximum first-order sensitivities.

Step 6*C* The case of $m = 1$, $n = 1$ corresponds to the domain C. The stiffness $k_{\mathrm{b}i}$ of the supporting member is increased to prevent $N_{\mathrm{b}i}$ from exceeding the yield axial force $\bar{P}_{\mathrm{y}i}$.

Step 6*D* The case of $m \geq 2, n \geq 1$ corresponds to the domain D. All the optimality conditions have to be satisfied. This corresponds to the conditions that the multiple maximum first-order sensitivities coincide due to Eq. (12.22) and the corresponding $k_{\mathrm{b}i}$ is increased to satisfy $N_{\mathrm{b}i} = \bar{P}_{\mathrm{y}i}$.

Step 7 Update design variables $\mathbf{S}_\mathrm{d}$ and $\mathbf{k}_\mathrm{b}$ according to the optimality conditions summarized in Table 12.1.

Step 8 Repeat Step 1 through Step 7 until the constraint Eq. (12.18), i.e., total area of supplemental VED, is satisfied.

The initial model is the model without supplemental VED, i.e. $S_{\mathrm{d}i} = 0 \ \ (i = 1, \ldots, N)$. An additional VED is distributed to each story via the steepest direction search algorithm [14]. The objective function is defined by the sum of the interstory drifts as shown in Eq. (12.12). Let $\Delta\mathbf{S}_\mathrm{d} = \{\Delta S_{\mathrm{d}i}\}$ and ΔW denote the increment of VED area in each story and the increment of the sum of VED area, respectively. When ΔW is given, we need to find the most effective placement of VED to decrease the objective function. For this purpose, the first- and second-order sensitivities of the objective function with respect to the design variables $\mathbf{S}_\mathrm{d}$ and $\mathbf{k}_\mathrm{b}$ are necessary. Those sensitivities $f_{,j}$, $f^{,j}$ (first-order), $f_{,jk}$, $f_{,}^{,k}$ and $f^{,jk}$ (second-order) can be derived by differentiating Eq. (12.15) by the design variables. Detailed expressions of the first and second-order sensitivities are shown later.

For clarification, the steps 6C and 6D are explained in more detail below.

(*Step 6C*) When $m = 1$, VED is added only to a single specific story. When $N_{\mathrm{b}j}$ attains its upper bound $\bar{P}_{\mathrm{y}j}$, $k_{\mathrm{b}j}$ has to be increased so as to keep the increment $\Delta N_{\mathrm{b}j}$ coinciding with $\Delta \bar{P}_{\mathrm{y}j}$. This condition requires

$$\mathrm{d}N_{\mathrm{b}j} = \mathrm{d}\bar{P}_{\mathrm{y}j} \Rightarrow \sum_{i=q_1}^{q_n} \left(N_{\mathrm{b}j,i}\Delta S_{\mathrm{d}i}\right) + N_{\mathrm{b}j}^{,j}\Delta k_{\mathrm{b}j} = \bar{P}_{\mathrm{y}j}^{,j}\Delta k_{\mathrm{b}j} \quad (j = q_1, \ldots, q_n) \tag{12.30}$$

Herein, the assumption discussed below Eq. (12.25) is employed again. When $n = 1$, the increment $\Delta k_{\mathrm{b}j}$ of the stiffness of the supporting member can be derived by

$$\Delta k_{\mathrm{b}q_1} = \frac{-N_{\mathrm{b}q_1}, q_1}{N_{\mathrm{b}q_1}^{,q_1} - \bar{P}_{\mathrm{y}q_1}^{,q_1}} \Delta S_{\mathrm{d}q_1} \tag{12.31}$$

(*Step 6D*) When $m \geq 2$, an appropriate distribution of VED to more than two stories should be employed for a given value of ΔW. In this case, the number of unknown variables is $m + n$. From Eq. (12.30), n equations with respect to $\mathbf{k}_{\mathrm{b}}$ can be derived. We, therefore, need more m equations.

Successive satisfaction of Eq. (12.24) requires that

$$\sum_{i=p_1}^{p_m} f_{,ji}\Delta S_{\mathrm{d}i} + \sum_{i=q_1}^{q_n} f_{,j}^{,i}\Delta k_{\mathrm{b}i} + \sum_{i=p_1}^{p_m}\sum_{k=q_1}^{q_n} \left(\kappa_k N_{\mathrm{b}k,j}\right)_{,i}\Delta S_{\mathrm{d}i} + \sum_{i=q_1}^{q_n}\sum_{k=q_1}^{q_n} \left(\kappa_k N_{\mathrm{b}k,j}\right)^{,i}\Delta k_{\mathrm{b}i} = 0 \quad (j = q_1, \ldots, q_n) \tag{12.32}$$

κ_k in Eq. (12.32) can be derived from Eq. (12.26) as

$$\kappa_k = \frac{-f^{,k}}{N_{\mathrm{b}k}^{,k} - \bar{P}_{\mathrm{y}k}^{,k}} \quad (k = q_1, \ldots, q_n) \tag{12.33}$$

It can be mentioned that, after the multiple optimality conditions are updated, the first-order sensitivities should continue to be satisfied. To achieve this, the following equation can be derived by substituting Eq. (12.33) into Eq. (12.32).

$$\sum_{i=p_1}^{p_m}\left[\left[f_{,ji} - \sum_{k=q_1}^{q_n}\left\{f^{,k}N_{\mathrm{b}k,j}/(N_{\mathrm{b}k}^{,k} - \bar{P}_{\mathrm{y}k}^{,k})\right\}_{,i}\right]\Delta S_{\mathrm{d}i}\right] + \sum_{i=q_1}^{q_n}\left[\left[f_{,j}^{,i} - \sum_{k=q_1}^{q_n}\left\{f^{,k}N_{\mathrm{b}k,j}/(N_{\mathrm{b}k}^{,k} - \bar{P}_{\mathrm{y}k}^{,k})\right\}^{,i}\right]\Delta k_{\mathrm{b}i}\right] = \text{const.} \quad (j = q_1, \ldots, q_n) \tag{12.34}$$

In case of using Eq. (12.22) in place of Eq. (12.24), the following equations should be employed.

$$\sum_{i=p_1}^{p_m} f_{,ji}\Delta S_{\mathrm{d}i} + \sum_{i=q_1}^{q_n} f_{,j}^{,i}\Delta k_{\mathrm{b}i} = \text{const.} \quad (j = p_{n+1}, \ldots, p_m) \tag{12.35}$$

After some manipulation in Eq. (12.34), we can derive $m-1$ equations to determine the optimal solution $\mathbf{S}_\mathrm{d}$ and $\mathbf{k}_\mathrm{b}$.

The last condition with respect to design variables $\mathbf{S}_\mathrm{d}$ is described by

$$\sum_{i=p_1}^{p_m} \Delta S_{\mathrm{d}i} = dW \tag{12.36}$$

where $p_i (i = 1, \cdots, m)$ denotes the ith story among multiple indices to be concerned.

From Eqs. (12.30), (12.34)–(12.36), we can derive the following set of the simultaneous linear equations for unknown design variables $\{\Delta S_{\mathrm{d}p_1} \cdots \Delta S_{\mathrm{d}p_m}\ \Delta k_{\mathrm{b}q_1} \cdots \Delta k_{\mathrm{d}q_n}\}$.

$$\begin{bmatrix} \alpha_{11} & \cdots & \alpha_{1m} & \beta_{11} & \cdots & \beta_{1n} \\ \vdots & \ddots & \vdots & \vdots & \ddots & \vdots \\ \alpha_{m-1,1} & \cdots & \alpha_{m-1,m} & \beta_{m-1,1} & \cdots & \beta_{m-1,n} \\ N_{\mathrm{b}q_1,p_1} & \cdots & N_{\mathrm{b}q_1,p_m} & N_{\mathrm{b}q_1}^{,q_1} - \bar{P}_{\mathrm{y}q_1}^{,q_1} & \cdots & N_{\mathrm{b}q_1}^{,q_n} - \bar{P}_{\mathrm{y}q_1}^{,q_n} \\ \vdots & \ddots & \vdots & \vdots & \ddots & \vdots \\ N_{\mathrm{b}q_n,p_1} & \cdots & N_{\mathrm{b}q_n,p_m} & N_{\mathrm{b}q_n}^{,q_1} - \bar{P}_{\mathrm{y}q_n}^{,q_1} & \cdots & N_{\mathrm{b}q_n}^{,q_n} - \bar{P}_{\mathrm{y}q_n}^{,q_n} \\ 1 & \cdots & 1 & 0 & \cdots & 0 \end{bmatrix} \begin{Bmatrix} \Delta S_{\mathrm{d}p_1} \\ \vdots \\ \Delta S_{\mathrm{d}p_m} \\ \Delta k_{\mathrm{b}q_1} \\ \vdots \\ \Delta k_{\mathrm{b}q_n} \end{Bmatrix} = \begin{Bmatrix} 0 \\ \vdots \\ \vdots \\ \vdots \\ 0 \\ dW \end{Bmatrix} \tag{12.37}$$

In Eq. (12.37) $\alpha_{ij} (i = 1, 2, \ldots, m-1;\ j = 1, 2, \ldots, m)$ and $\beta_{ij}\ (i = 1, 2, \ldots, m-1;\ j = 1, \ldots, n)$ are described by

$$\begin{aligned} \alpha_{ij} =& f_{,q_1p_j} - f_{,q_{i+1}p_j} \\ &+ \sum_{k=q_1}^{q_n} \frac{1}{N_{\mathrm{b}k}^{,k} - \bar{P}_{\mathrm{y}k}^{,k}} \begin{Bmatrix} -f_{,p_j}^{,k}(N_{\mathrm{b}k,q_1} - N_{\mathrm{b}k,q_i}) - f^{,k}(N_{\mathrm{b}k,q_1p_j} - N_{\mathrm{b}k,q_ip_j}) \\ +f^{,k}N_{\mathrm{b}k}^{\ ,k}{}_{,p_j}(N_{\mathrm{b}k,q_1} - f^{,k}N_{\mathrm{b}k,q_i})/(N_{\mathrm{b}k}^{\ ,k} - \bar{P}_{\mathrm{y}k}^{\ ,k}) \end{Bmatrix} \\ & \qquad (i = 1, \ldots, n-1 \quad j = 1, \ldots, m) \\ \alpha_{ij} =& f_{,p_np_j} - f_{,p_{i+1}p_j} \quad (i = n, \ldots, m-1 \quad j = 1, \ldots, m) \end{aligned} \tag{12.38a,b}$$

$$\begin{aligned} \beta_{ij} =& f_{,p_1}^{,q_j} - f_{,p_{i+1}}^{,q_j} \\ &+ \sum_{k=q_1}^{q_n} \frac{1}{N_{\mathrm{b}k}^{\ ,k} - \bar{P}_{\mathrm{y}k}^{\ ,k}} \begin{Bmatrix} -f^{,kq_j}(N_{\mathrm{b}k,q_1} - N_{\mathrm{b}k,q_{i+1}}) - f^{,k}(N_{\mathrm{b}k}^{\ ,q_j}{}_{,q_1} - N_{\mathrm{b}k}^{\ ,q_j}{}_{,q_{i+1}}) \\ +N_{\mathrm{b}k}^{\ ,kq_j}(f^{,k}N_{\mathrm{b}k,q_1} - f^{,k}N_{\mathrm{b}k,q_{i+1}})/(N_{\mathrm{b}k}^{\ ,k} - \bar{P}_{\mathrm{y}k}^{\ ,k}) \end{Bmatrix} \\ & \qquad (i = 1, \ldots, n-1 \quad j = 1, \ldots, n) \\ \beta_{ij} =& f_{,p_n}^{,q_j} - f_{,p_{i+1}}^{,q_j} \quad (i = n, \ldots, m-1 \quad j = 1, \ldots, n) \end{aligned} \tag{12.39a,b}$$

12.7.2 Sensitivity with Respect to Damper Area

The first- and second-order sensitivities of the objective function with respect to design variables $\mathbf{S}_\mathrm{d}$ and $\mathbf{k}_\mathrm{b}$ are explained and derived here.

The PSD function of the variable critical excitation has the power $\bar{S}$ only between ω_L and ω_U (like a band-limited white). The objective function in Eq. (12.15) can be replaced by

$$f(\mathbf{S}_\mathrm{d}, \mathbf{k}_\mathrm{b}) = \bar{S} \sum_{i=1}^{N} \{\Psi_{\delta_i}(\omega_U; \mathbf{S}_\mathrm{d}, \mathbf{k}_\mathrm{b}) - \Psi_{\delta_i}(\omega_L; \mathbf{S}_\mathrm{d}, \mathbf{k}_\mathrm{b})\} \tag{12.40}$$

where Ψ_{δ_i} is defined by

$$\Psi_{\delta_i}(\hat{\omega}; \mathbf{S}_\mathrm{d}, \mathbf{k}_\mathrm{b}) = \int_0^{\hat{\omega}} H_{\delta_i}(\omega) H_{\delta_i}^*(\omega) \mathrm{d}\omega \tag{12.41}$$

Note that ω_L and ω_U are dependent on the fundamental natural circular frequency ω_0 of the building with supplemental VED. For this reason, the objective function in Eq. (12.40) can be regarded as an implicit function of ω_0. The first- and second-order sensitivities with respect to $\mathbf{S}_\mathrm{d}$ can then be derived by

$$f_{,j} = 2\bar{S} \sum_{i=1}^{N} \left[\begin{array}{l} (\omega_0)_{,j} \{H_{\delta_i}(\omega_U) - H_{\delta_i}(\omega_L)\} \\ + \displaystyle\int_{\omega_L}^{\omega_U} \{H_{\delta_i}(\omega)\}_{,j} H_{\delta_i}^*(\omega) + H_{\delta_i}(\omega) \{H_{\delta_i}^*(\omega)\}_{,j} \mathrm{d}\omega \end{array} \right] \tag{12.42}$$

$$f_{,jk} = 2\bar{S} \sum_{i=1}^{N} \left[\begin{array}{l} (\omega_c)_{,jk} \{H_{\delta_i}(\omega_U) - H_{\delta_i}(\omega_L)\} \\ + (\omega_c)_{,j} \left\{ \begin{array}{l} (\omega_0)_{,k} (\partial H_{\delta_i}(\omega_U)/\partial\omega_0 - \partial H_{\delta_i}(\omega_L)/\partial\omega_0) \\ + H_{\delta_i}(\omega_U)_{,k} - H_{\delta_i}(\omega_L)_{,k} \end{array} \right\} \\ + (\omega_c)_{,k} \{H_{\delta_i}(\omega_U)_{,j} - H_{\delta_i}(\omega_L)_{,j}\} \\ + \displaystyle\int_{\omega_L}^{\omega_U} \left[\begin{array}{l} H_{\delta_i}(\omega)_{,jk} H_{\delta_i}^*(\omega) + H_{\delta_i}(\omega)_{,j} H_{\delta_i}^*(\omega)_{,k} \\ + H_{\delta_i}(\omega)_{,k} H_{\delta_i}^*(\omega)_{,j} + H_{\delta_i}(\omega) \{H_{\delta_i}^*(\omega)\}_{,jk} \end{array} \right] \mathrm{d}\omega \end{array} \right] \tag{12.43}$$

where the first and second sensitivities $H_{\delta_i}(\omega)_{,j}$ and $H_{\delta_i}(\omega)_{,jk}$ are derived as follows.

$$H_{\delta_i}(\omega)_{,j} = \mathbf{T}_i \left(\mathbf{A}^{-1}\right)_{,j} \mathbf{B} \tag{12.44}$$

$$H_{\delta_i}(\omega)_{,jk} = \mathbf{T}_i \left(\mathbf{A}^{-1}\right)_{,jk} \mathbf{B} \tag{12.45}$$

In Eq. (12.44), the first derivative of $\mathbf{A}^{-1}$ with respect to $\mathbf{S}_\mathrm{d}$ can be computed by

$$\begin{aligned}\mathbf{A}_{,j}^{-1} &= -\mathbf{A}^{-1}\mathbf{A}_{,j}\mathbf{A}^{-1} \\ &= -\mathbf{A}^{-1}\left(\mathbf{K}_{,j} + \mathrm{i}\omega\mathbf{C}_{,j}\right)\mathbf{A}^{-1}\end{aligned} \tag{12.46}$$

Furthermore $(\omega_0)_{,j}$ and $(\omega_0)_{,jk}$ are evaluated by using the method of Fox and Kapoor [44].

Referring to Eqs. (12.1) and (12.2), the first derivative of $\mathbf{K}$ and $\mathbf{C}$ with respect to S_{d_j} can be computed by the first derivative of the equivalent stiffness K_{E_i} and the damping coefficient C_{E_i} described by

$$K_{\mathrm{E}_i}(\omega, S_{\mathrm{d}_i}, k_{\mathrm{b}_i})_{,j} = k_{\mathrm{b}_i}^2 \frac{S_{\mathrm{d}_i}^2 c_1 c_2 + 2c_1 c_3 k_{\mathrm{b}_i} S_{\mathrm{d}_i} + c_2 c_3 k_{\mathrm{b}_i}^2}{(c_1 S_{\mathrm{d}_i}^2 + 2c_2 k_{\mathrm{b}_i} S_{\mathrm{d}_i} + c_3 k_{\mathrm{b}_i}^2)^2} \tag{12.47}$$

$$C_{\mathrm{E}_i}(\omega, S_{\mathrm{d}_i}, k_{\mathrm{b}_i})_{,j} = k_{\mathrm{b}_i}^2 \frac{c_4(c_1 S_{\mathrm{d}_i}^2 + c_3 k_{\mathrm{b}_i}^2)}{(c_1 S_{\mathrm{d}_i}^2 + 2c_2 k_{\mathrm{b}_i} S_{\mathrm{d}_i} + c_3 k_{\mathrm{b}_i}^2)^2} \tag{12.48}$$

Equations (12.1) and (12.2) have been rewritten in terms of the parameters $k_{\mathrm{dM}}, c_{\mathrm{dM}}, k_{\mathrm{dV}}, c_{\mathrm{dV}}$ without $\{S_{\mathrm{d}j}\}$. The coefficients $c_1 \sim c_4$ are defined as follows:

$$\begin{aligned}\varepsilon_1 &= k_{\mathrm{dM}} k_{\mathrm{dV}} - c_{\mathrm{dM}} c_{\mathrm{dV}} \omega^2 \\ \varepsilon_2 &= k_{\mathrm{dM}} c_{\mathrm{dM}} + k_{\mathrm{dV}} c_{\mathrm{dM}} + k_{\mathrm{dM}} c_{\mathrm{dV}} \\ c_1 &= \varepsilon_1^2 + \varepsilon_2^2 \omega^2 \\ c_2 &= k_{\mathrm{dM}} \varepsilon_1 + c_{\mathrm{dM}} \varepsilon_2 \omega^2 \\ c_3 &= k_{\mathrm{dM}}^2 + c_{\mathrm{dM}}^2 \omega^2 \\ c_4 &= -c_{\mathrm{dM}} \varepsilon_1 + k_{\mathrm{dM}} \varepsilon_2\end{aligned} \tag{12.49a – f}$$

On the other hand, in Eq. (12.45), the second derivative of $\mathbf{A}^{-1}$ with respect to $\mathbf{S}_{\mathrm{d}}$ can be computed by differentiating Eq. (12.46) with respect to S_{d_k}.

$$\mathbf{A}_{,jk}^{-1} = \mathbf{A}^{-1}\left(\mathbf{A}_{,j}\mathbf{A}^{-1}\mathbf{A}_{,k} + \mathbf{A}_{,k}\mathbf{A}^{-1}\mathbf{A}_{,j}\right)\mathbf{A}^{-1} - \mathbf{A}^{-1}\mathbf{A}_{,jk}\mathbf{A}^{-1} \tag{12.50}$$

In Eq. (12.50), it should be remarked that in case of using viscous damper or visco-elastic damper in a "3N model", $\mathbf{A}_{,jk} = 0$. This is because the stiffness and damping matrices consist of a linear combination of damper damping coefficients and stiffnesses, i.e., all the components of $\mathbf{A}_{,j}$ are constant values. On the other hand, in the case of using the frequency-dependent "N model", $\mathbf{A}_{,jk} \neq 0 \quad (j = k)$ because the first derivative of $\mathbf{A}$ contains Eqs. (12.47) and (12.48) which are also the functions of design variables $\mathbf{S}_{\mathrm{d}}$ and $\mathbf{k}_{\mathrm{b}}$.

The second-order sensitivities of the equivalent stiffness and damping coefficient with respect to damper area are shown in Appendix 3.

12.7.3 Sensitivity With Respect to Stiffness of Supporting Member

The sensitivity of the objective function with respect to $\mathbf{k}_{\mathrm{b}}$ is also needed to determine the optimal solution for the stiffness of supporting member. These sensitivities can be derived in almost the same form as Eqs. (12.42) and (12.43).

$$f^{,j} = 2\bar{S}\sum_{i=1}^{N}\left[\int_{\omega_L}^{\omega_U} H_{\delta_i}(\omega)^{,j}H_{\delta_i}^{*}(\omega)\mathrm{d}\omega + \int_{\omega_L}^{\omega_U} H_{\delta_i}(\omega)H_{\delta_i}^{*}(\omega)^{,j}\mathrm{d}\omega\right] \tag{12.51}$$

$$f^{,jk} = 2\bar{S}\sum_{i=1}^{N}\left[\begin{array}{l}\displaystyle\int_{\omega_L}^{\omega_U} H_{\delta_i}(\omega)^{,jk}H_{\delta_i}^{*}(\omega)\mathrm{d}\omega + \int_{\omega_L}^{\omega_U} H_{\delta_i}(\omega)^{,j}H_{\delta_i}^{*}(\omega)^{,k}\mathrm{d}\omega \\ \displaystyle + \int_{\omega_L}^{\omega_U} H_{\delta_i}(\omega)^{,k}H_{\delta_i}^{*}(\omega)^{,j}\mathrm{d}\omega + \int_{\omega_L}^{\omega_U} H_{\delta_i}(\omega)\{H_{\delta_i}^{*}(\omega)\}^{,jk}\mathrm{d}\omega\end{array}\right] \tag{12.52}$$

In Eqs. (12.51), (12.52) $H_{\delta_i}(\omega)^{,j} = \mathbf{T}_i\left(\mathbf{A}^{-1}\right)^{,j}\mathbf{B}$ and $H_{\delta_i}(\omega)^{,jk} = \mathbf{T}_i\left(\mathbf{A}^{-1}\right)^{,jk}\mathbf{B}$. The first derivative of $\mathbf{A}^{-1}$ with respect to $\mathbf{k}_{\mathrm{b}}$ can be computed by replacing $\mathbf{K}_j$ and $\mathbf{C}_j$ with $\mathbf{K}^{,j}$ and $\mathbf{C}^{,j}$ whose components consist of $K_{\mathrm{E}_i}^{j}$ and $C_{\mathrm{E}_i}^{j}$ described by

$$K_{\mathrm{E}_i}(\omega, S_{\mathrm{d}_i}, k_{\mathrm{b}_i})^{,j} = S_{\mathrm{d}_i}^2\frac{S_{\mathrm{d}_i}^2c_1^2 + 2c_1c_2k_{\mathrm{b}_i}S_{\mathrm{d}_i} + (2c_2^2 - c_1c_3)k_{\mathrm{b}_i}^2}{\left(c_1S_{\mathrm{d}_i}^2 + 2c_2k_{\mathrm{b}_i}S_{\mathrm{d}_i} + c_3k_{\mathrm{b}_i}^2\right)^2} \tag{12.53}$$

$$C_{\mathrm{E}_i}(\omega, S_{\mathrm{d}_i}, k_{\mathrm{b}_i})^{,j} = \frac{2S_{\mathrm{d}_i}^2k_{\mathrm{b}_i}c_4(k_{\mathrm{b}_i}c_2 + c_1S_{\mathrm{d}_i})}{\left(c_1S_{\mathrm{d}_i}^2 + 2c_2k_{\mathrm{b}_i}S_{\mathrm{d}_i} + c_3k_{\mathrm{b}_i}^2\right)^2} \tag{12.54}$$

Note that, the parameters K_{E_i} and C_{E_i} need to be evaluated only for $j = i$. In the same way, the second derivative of $\mathbf{A}^{-1}$ with respect to $\mathbf{k}_{\mathrm{b}}$ can be evaluated from $\mathbf{A}^{,j}$, $\mathbf{A}^{,jk}$ and $\mathbf{A}^{-1}$.

The second-order sensitivities of the equivalent stiffness and damping coefficient with respect to the stiffness of the supporting members are shown in Appendix 3.

12.7.4 Sensitivities of Axial Force of Supporting Member

The sensitivity of the axial force N_{b_i} of the supporting member with respect to $\mathbf{S}_{\mathrm{d}}$ can be derived as follows by differentiating Eq. (12.16).

$$N_{\mathrm{b}_i j} = \rho \sqrt{\frac{2\bar{S}}{\int_{\omega_L}^{\omega_U} |H_{\mathrm{N}_{\mathrm{b}i}}(\omega)|^2 \mathrm{d}\omega}} \int_{\omega_L}^{\omega_U} \mathrm{Re}\left[H_{\mathrm{N}_{\mathrm{b}i}}(\omega)_{,j} H^*_{\mathrm{N}_{\mathrm{b}i}}(\omega) \right] \mathrm{d}\omega \tag{12.55}$$

As defined before Eq. (12.17), $H_{\mathrm{N}_{\mathrm{b}i}}(\omega)$ is obtained from the complex stiffness of the equivalent "N model". In Eq. (12.55), the sensitivity of the axial force N_{b_i} of the supporting member with respect to $\mathbf{S}_{\mathrm{d}}$, i.e., $(H_{\mathrm{N}_{\mathrm{b}i}}(\omega))_{,j}$, can be derived from Eq. (12.17).

$$(H_{\mathrm{N}_{\mathrm{b}i}}(\omega))_{,j} = \begin{cases} \hat{K}_{\mathrm{E}_i} H_{\delta_i}(\omega)_{,j} + \hat{K}_{\mathrm{E}_i,j} H_{\delta_i}(\omega) & (i = j) \\ \hat{K}_{\mathrm{E}_i} H_{\delta_i}(\omega)_{,j} & (i \neq j) \end{cases} \tag{12.56}$$

In Eq. (12.56) $\hat{K}_{\mathrm{E}_i}$ is a complex stiffness of the equivalent whole damper unit as an "N model ", defined by $\hat{K}_{\mathrm{E}_i} = K_{\mathrm{E}_i} + \mathrm{i}C_{\mathrm{E}_i}$.

The sensitivity of N_{b_i} with respect to $\mathbf{k}_{\mathrm{b}}$ can be derived by replacing $H_{\mathrm{N}_{\mathrm{b}i}}(\omega)_{,j}$ in Eq. (12.55) with $H_{\mathrm{N}_{\mathrm{b}i}}(\omega)^{,j}$ computed by substituting $\hat{K}^{,j}_{\mathrm{E}_i}$, i.e. $K^{,j}_{\mathrm{E}_i} + \mathrm{i}C^{,j}_{\mathrm{E}_i}$, into Eq. (12.56) instead of $\hat{K}_{\mathrm{E}_i,j}$.

12.8 Numerical Examples

Numerical examples are presented for 3-story and 10-story building models to demonstrate the usefulness and validity of the explained optimal design method. In this chapter, two models, i.e., "3N model" and "N model" are proposed. Detailed comparison between these two different models is shown to demonstrate the validity of the explained models and method.

The structural parameters are shown in Table 12.2. The floor masses and frame story stiffnesses have the same values in all the stories. The structural damping ratio of the main frame is assumed to be 0.02 ($\mathbf{C}_{\mathbf{f}}$ is calculated as stiffness-proportional damping). The properties of each component in four elements of VED per unit VED area (thickness is fixed at 10 mm and area is 1 m^2) are shown in Table 12.3. The ratio $r_{\mathrm{s}} = k_{\mathrm{b}i}/k_{\mathrm{f}i}$ of the stiffness $k_{\mathrm{b}i}$ of the additional damper to the stiffness $k_{\mathrm{f}i}$ of the building frame is given from 0.5 to 3.0. The initial stiffness of the supporting member is given by selecting an appropriate ratio r_{s}. Total damper areas $\bar{W}$ in each example are given by $\bar{W} = 51.2\,\mathrm{m}^2$ for the 3-story building model and $\bar{W} = 400\,\mathrm{m}^2$ for the 10-story building model, respectively.

The critical PSD function of the ground motion defined as a variable critical excitation is computed to have the central circular frequency resonant to the fundamental natural circular frequency of the building model. In the process of optimal damper placement where the stiffness and damping matrices are updated according to the quantity of additional VED, eigenvalue analysis has to be

Table 12.2 Structural parameters of main frame (Fujita et al. [45] with permission from Techno Press)

	3-Story model	10-Story model
Floor mass (kg)	512×10^3	1024×10^3
Story stiffness (N/mm)	6.02×10^8	1.20×10^9
Natural circular frequency without damper (rad/s)	15.268	5.125
Natural period without damper (s)	0.411	1.225

Table 12.3 Properties of acrylic visco-elastic damper per unit area (Fujita et al. [45] with permission from Techno Press)

K_{dV}	2756.3 (N/m^3)	K_{dM}	5120.5 (N/m^3)
C_{dV}	221.7 (Ns/m^3)	C_{dM}	254.8 (Ns/m^3)

executed in every step. It should be remarked that the $3N$ model, whose components are independent of frequency, facilitates the computation of eigenvalues.

Figure 12.6a, b shows the variation of the first-order sensitivities of the objective function with respect to $\mathbf{S}_\mathrm{d} = \{S_{\mathrm{d}1}, \cdots, S_{\mathrm{d}N}\}$ for (a) 3-story and (b) 10-story models with $r_\mathrm{s}. = 1.0$. In the initial phase of the optimal solution which corresponds to the domain A, the maximum absolute value of the first derivative is attained only in the first story, i.e. $|f_{,1}|$. It is shown in Fig. 12.6 that, after the multiple coincidence of the maximum absolute value of the first derivatives in domain B, they continue to be satisfied in the optimal design process. This fact indicates a continuing satisfaction of the stationarity conditions of Lagrangian as the optimality conditions.

Figure 12.7a, b illustrates the distribution of the optimal areas $\mathbf{S}_\mathrm{d}$ of VED with respect to the varied total damper area and a variation of the lowest mode damping ratio. It can be observed that the passive dampers are placed optimally in the building model according to the variation of the first derivative of the objective function shown in Fig. 12.6. Figure 12.7a presents the comparison of this result by using different damper models, i.e., "N model" and "$3N$ model". From this figure, it can be observed that almost the same result can be obtained by using either of the two damper models. This supports the validity of the explained two VED models.

Figure 12.8a, b shows the variation of the stiffness and axial force of supporting members in the process of optimal damper placement. The initial yield force is also indicated in Fig. 12.8a. It can be observed that, after the axial force N_{b_i} coincides with the initial yield force, the stiffnesses $\mathbf{k}_\mathrm{b}$ of supporting members are updated according to the stationarity conditions.

Figure 12.9a, b presents the variation of the objective functions for the following three distributions. Case (1) optimal damper placement based on the explained method, Case (2) uniform placement, Case (3) first-story concentrated placement. It can be observed that the result of Case 1 perfectly coincides with that of Case 3 in the early stage of the optimization procedure. However, as the total damper area increases, the objective function is decreased most effectively by the optimal placement.

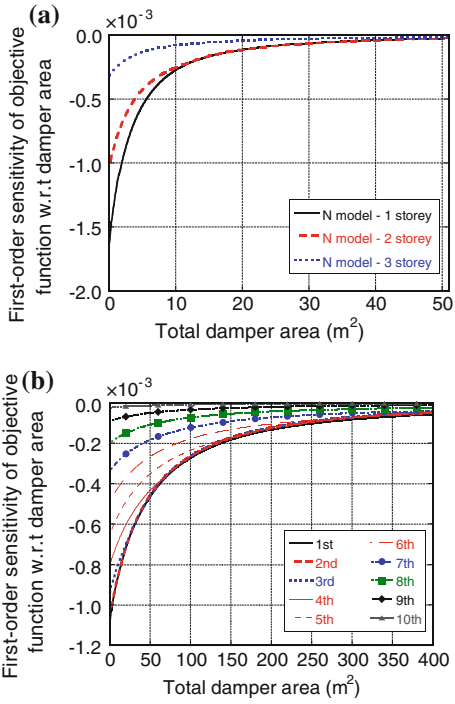

Fig. 12.6 First-order sensitivity of sum of mean-squares interstory drifts with respect to VED area. **a** 3-story model. **b** 10-story model (Fujita et al. [45] with permission from Techno Press)

12.9 Summary

The result explained in this chapter may be summarized as follows:

(1) An optimal placement and sizing method of visco-elastic dampers and supporting members has been explained. The critical earthquake ground motion is defined as the resonant input to the structure with visco-elastic dampers. As the size or quantity of visco-elastic dampers becomes large, the force acting on the supporting member increases and an appropriate cross-sectional size (stiffness and strength) of the supporting member is required. Simultaneous design of visco-elastic dampers and supporting members is a new aspect which has never been considered in the literature.

(2) The sum of the mean-squares of interstory drifts is taken as an objective function. The total quantity of visco-elastic dampers has been increased while the constraint on the member force of the supporting member is satisfied.

(3) Two models have been introduced and used in the modeling of the visco-elastic dampers. The first model is the four-element model of visco-elastic dampers including a supporting member. Two masses have been considered in this model. Then $3N$ degrees-of-freedom model for structural analysis has been employed in the first model. The second model is an equivalent Kelvin–Voigt model of visco-elastic dampers with a supporting member. There is no

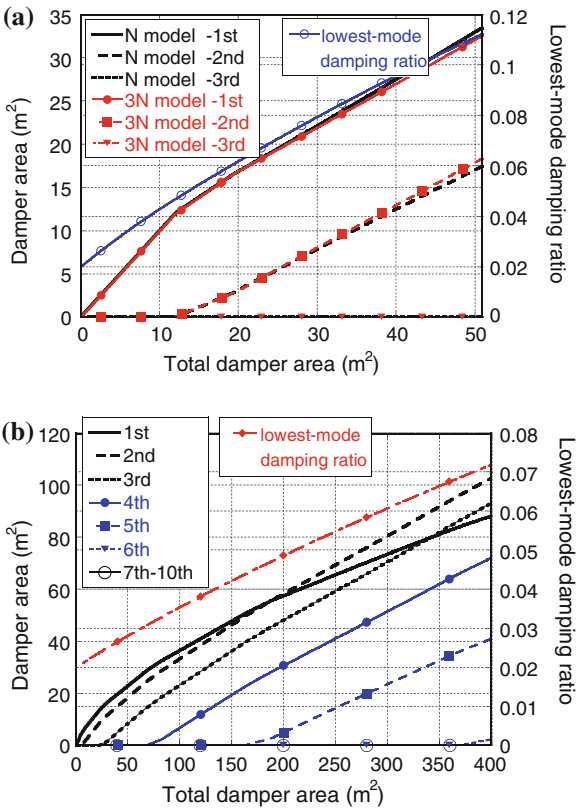

Fig. 12.7 Optimal damper placement and lowest-mode damping ratio. **a** 3-story model. **b** 10-story model (Fujita et al. [45] with permission from Techno Press)

additional mass in the model of the equivalent Kelvin–Voigt model. Then an N degrees-of-freedom model for structural analysis has been employed in the second model.

(4) A gradient-based evolutionary optimization technique using a Lagrange multiplier method was explained. Simultaneous satisfaction of the optimality criterion on placement of visco-elastic dampers and the constraint on forces of the supporting members has been shown to be guaranteed through numerical examples.

Appendix 1: Equivalent Stiffness and Damping Coefficient of Damper Unit Including Supporting Member in *N*-Model (Eqs. (12.1) and (12.2))

Let δ_{Fi}, δ_{1i}, δ_{2i} denote the interstory drift, the internal nodal displacement in the Maxwell model in Fig. 12.2 relative to the $(i-1)$th floor and the displacement of the node between the damper unit and the supporting member in the i-th story, i.e.

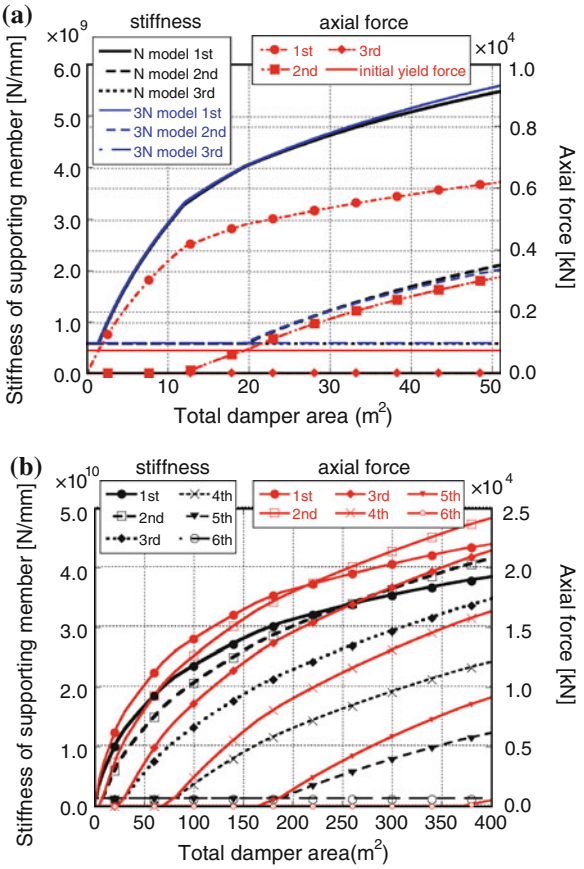

Fig. 12.8 Stiffness and axial force of supporting member. **a** 3-story model. **b** 10-story model (Fujita et al. [45] with permission from Techno Press)

$\delta_{\mathrm{F}i} = u_{\mathrm{F}i} - u_{\mathrm{F}(i-1)}$, $\delta_{1i} = u_{1i} - u_{\mathrm{F}(i-1)}$ and $\delta_{2i} = u_{2i} - u_{\mathrm{F}(i-1)}$. The equations of dynamic equilibrium of the $3N$ model can be derived as

$$k_{\mathrm{b}i}\delta_{2i} = p_i(t) \tag{12.57}$$

$$k_{\mathrm{M}i}(\delta_{1i} - \delta_{2i}) + k_{\mathrm{V}i}(\delta_{\mathrm{F}i} - \delta_{2i}) + c_{\mathrm{V}i}(\dot{\delta}_{\mathrm{F}i} - \dot{\delta}_{2i}) - k_{\mathrm{b}i}\delta_{2i} = 0 \tag{12.58}$$

$$c_{\mathrm{M}i}(\dot{\delta}_{\mathrm{F}i} - \dot{\delta}_{1i}) - k_{\mathrm{M}i}(\delta_{1i} - \delta_{2i}) = 0 \tag{12.59}$$

In Eq. (12.57) $p_i(t)$ denotes the internal force of the supporting member in the i-th story. Let $\Delta_{\mathrm{F}i}(\omega), \Delta_{1i}(\omega), \Delta_{2i}(\omega), P_i(\omega)$ denote the Fourier transforms of $\delta_{\mathrm{F}i}(t)$, $\delta_{1i}(t)$, $\delta_{2i}(t)$and $p_i(t)$. From Eq. (12.57), $\Delta_{2i}(\omega)$ can be described by $P_i(\omega)/k_{\mathrm{b}i}$. By substituting this equation into Eq. (12.59) expressed in frequency domain, we can obtain $\Delta_{1i}(\omega)$ as

$$\Delta_{1i}(\omega) = \frac{\mathrm{i}\omega k_{\mathrm{b}i}c_{\mathrm{M}i}\Delta_{\mathrm{F}i}(\omega) + k_{\mathrm{M}i}P_i(\omega)}{k_{\mathrm{b}i}(\mathrm{i}\omega c_{\mathrm{M}i} + k_{\mathrm{M}i})} \tag{12.60}$$

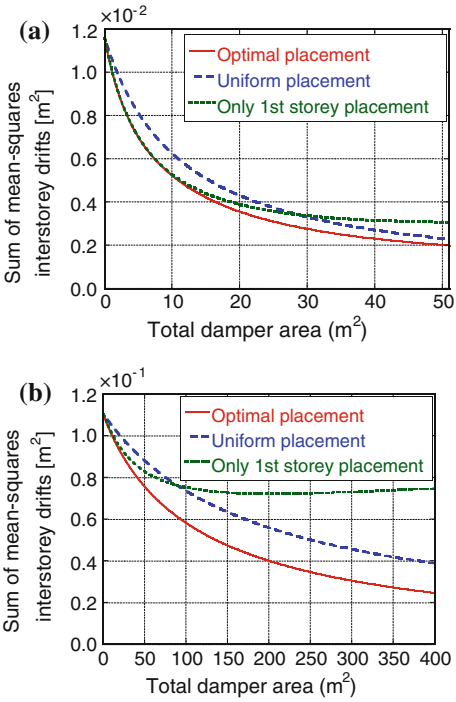

Fig. 12.9 Variation of objective function in optimal placement, uniform placement and first-story placement. **a** 3-story model. **b** 10-story model (Fujita et al. [45] with permission from Techno Press)

Substitution of these equations for $\Delta_{1i}(\omega)$ and $\Delta_{2i}(\omega)$ into Eq. (12.58) in frequency domain leads to the following relationship between $\Delta_{\mathrm{F}i}(\omega)$ and $P_i(\omega)$.

$$\begin{aligned}&\left(\frac{\mathrm{i}\omega k_{\mathrm{b}i}k_{\mathrm{M}i}c_{\mathrm{M}i}}{k_{\mathrm{M}i}+\mathrm{i}\omega c_{\mathrm{M}i}}+k_{\mathrm{b}i}k_{\mathrm{V}i}+\mathrm{i}\omega k_{\mathrm{b}i}c_{\mathrm{V}i}\right)\Delta_{\mathrm{F}i}(\omega)\\&=\left\{(k_{\mathrm{b}i}+k_{\mathrm{M}i}+k_{\mathrm{V}i}+\ \mathrm{i}\omega c_{\mathrm{V}i})-\frac{k_{\mathrm{M}i}^2}{k_{\mathrm{M}i}+\mathrm{i}\omega c_{\mathrm{M}i}}\right\}P_i(\omega)\end{aligned}\tag{12.61}$$

After some manipulations, Eq. (12.61) can be rewritten as

$$\begin{aligned}&\frac{k_{\mathrm{b}i}k_{\mathrm{V}i}k_{\mathrm{M}i}^2+\omega^2k_{\mathrm{b}i}c_{\mathrm{M}i}^2(k_{\mathrm{V}i}+k_{\mathrm{M}i})+\mathrm{i}\omega k_{\mathrm{b}i}\left\{k_{\mathrm{M}i}^2(c_{\mathrm{V}i}+c_{\mathrm{M}i})+\omega^2c_{\mathrm{V}i}c_{\mathrm{M}i}^2\right\}}{((k_{\mathrm{b}i}+k_{\mathrm{V}i})k_{\mathrm{M}i}^2+(k_{\mathrm{b}i}+k_{\mathrm{M}i}+k_{\mathrm{V}i})\omega^2c_{\mathrm{M}i}^2)+\ \mathrm{i}\omega\left\{k_{\mathrm{M}i}^2(c_{\mathrm{V}i}+c_{\mathrm{M}i})+\omega^2c_{\mathrm{V}i}c_{\mathrm{M}i}^2\right\}}\Delta_{\mathrm{F}i}(\omega)\\&=P_i(\omega)\end{aligned}\tag{12.62}$$

On the other hand, the force–displacement relation of the general Kelvin–Voigt model can be given by

$$(K_{\mathrm{E}i}+\mathrm{i}\omega C_{\mathrm{E}i})\Delta_{\mathrm{F}i}(\omega)=P_i(\omega)\tag{12.63}$$

where $K_{\mathrm{E}i}$ and $C_{\mathrm{E}i}$ are the equivalent stiffness and the damping coefficient of the frequency-dependent Kelvin–Voigt model in the i-th story defined by Eqs. (12.1) and (12.2). By comparing Eqs. (12.62) and (12.63), Eqs. (12.1) and (12.2) can be derived.

Appendix 2: Transformation Matrix from the Nodal Displacements to the Relative Displacements Between both Ends of Supporting Members

For evaluating the axial force of the supporting member, the relative displacements $\mathbf{u_b}$ between both ends of supporting members are expressed in terms of nodal displacements $\mathbf{u}_{\text{full}}$ by

$$\mathbf{u_b} = \mathbf{T_b}\mathbf{u}_{\text{full}} \tag{12.64}$$

In Eq. (12.64) $\mathbf{T_b}$ denotes the transformation matrix. In the case of the 3-story building model, $\mathbf{T_b}$ can be given by

$$\mathbf{T_b} = \begin{bmatrix} 0 & 0 & 0 & & & & & & \\ 0 & 1 & 0 & & [\mathbf{0}] & & & [\mathbf{0}] & \\ 0 & 0 & 0 & & & & & & \\ 0 & 0 & 0 & 0 & 0 & 0 & & & \\ -1 & 0 & 0 & 0 & 1 & 0 & & [\mathbf{0}] & \\ 0 & 0 & 0 & 0 & 0 & 0 & & & \\ & & & 0 & 0 & 0 & 0 & 0 & 0 \\ & [\mathbf{0}] & & -1 & 0 & 0 & 0 & 1 & 0 \\ & & & 0 & 0 & 0 & 0 & 0 & 0 \end{bmatrix} \tag{12.65}$$

Appendix 3: Second-Order Sensitivities of the Equivalent Stiffness and Damping Coefficient

The second-order sensitivities of the equivalent stiffness and damping coefficient for the N model can be derived as follows.

$$\begin{aligned} K_{\text{E}i,jk} &= -2k_{\text{b}i}^2 \frac{\left(c_1^2 c_2 S_{\text{d}i}^3 + 3c_1^2 c_3 k_{\text{b}i} S_{\text{d}i}^2 + 3c_1 c_2 c_3 k_{\text{b}i}^2 S_{\text{d}i} + c_3(2c_2^2 - c_1 c_3)k_{\text{b}i}^3\right)}{\left(c_1 S_{\text{d}i}^2 + 2c_2 k_{\text{b}i} S_{\text{d}i} + c_3 k_{\text{b}i}^2\right)^3} \\ K_{\text{E}i}^{jk} &= \left(S_{\text{d}i}^2/k_{\text{b}i}^2\right) K_{\text{E}i,jk} \\ K_{\text{E}i_{,j}}^{,k} &= 2k_{\text{b}i} S_{\text{d}i} \frac{c_1^2 c_2 S_{\text{d}i}^3 + 3c_1^2 c_3 k_{\text{b}i} S_{\text{d}i}^2 + 3c_1 c_2 c_3 k_{\text{b}i}^2 S_{\text{b}i} + \left(2c_2^2 c_3 - c_1 c_2^2\right) k_{\text{b}i}^2 S_{\text{d}i}}{\left(c_1 S_{\text{d}i}^2 + 2c_2 k_{\text{b}i} S_{\text{d}i} + c_3 k_{\text{b}i}^2\right)^3} \\ C_{\text{E}i,jk} &= -2k_{\text{b}i}^2 c_5 \frac{c_1 c_3 k_{\text{b}i}^2 S_{\text{d}i} + 2c_2 c_3 k_{\text{b}i}^3 + c_1^2 S_{\text{d}i}^3}{\left(c_1 S_{\text{d}i}^2 + 2c_2 k_{\text{b}i} S_{\text{d}i} + c_3 k_{\text{b}i}^2\right)^3} \\ C_{\text{E}i}^{jk} &= -2S_{\text{d}i}^2 c_5 \frac{3c_1 c_3 k_{\text{b}i}^2 S_{\text{d}i} + 2c_2 c_3 k_{\text{b}i}^3 - c_1^2 S_{\text{d}i}^3}{\left(c_1 S_{\text{d}i}^2 + 2c_2 k_{\text{b}i} S_{\text{d}i} + c_3 k_{\text{b}i}^2\right)^3} \\ C_{\text{E}i_{,j}}^{,k} &= -2k_{\text{b}i} S_{\text{d}i} c_5 \frac{2c_2 c_3 k_{\text{b}i}^3 + c_1 c_3 k_{\text{b}i}^2 S_{\text{d}i} + c_1^2 S_{\text{d}i}^3}{\left(c_1 S_{\text{d}i}^2 + 2c_2 k_{\text{b}i} S_{\text{d}i} + c_3 k_{\text{b}i}^2\right)^3} \end{aligned} \tag{12.66}$$

where c_1, c_2, c_3 are given by Eq. (12.49c, d, e).

References

1. Constantinou MC, Tadjbakhsh IG (1983) Optimum design of a first story damping system. Comput Struct 17(2):305–310
2. Gurgoze M, Muller PC (1992) Optimal positioning of dampers in multi-body systems. J Sound Vib 158(3):517–530
3. Zhang RH, Soong TT (1992) Seismic design of viscoelastic dampers for structural applications. J Struct Eng ASCE 118(5):1375–1392
4. Hahn GD, Sathiavageeswaran KR (1992) Effects of added-damper distribution on the seismic response of buildings. Comput Struct 43(5):941–950
5. De Silva CW (1981) An algorithm for the optimal design of passive vibration controllers for flexible systems. J Sound Vib 74(4):495–502
6. Tsuji M, Nakamura T (1996) Optimum viscous dampers for stiffness design of shear buildings. J Struct Des Tall Build 5:217–234
7. Takewaki I (1997) Optimal damper placement for minimum transfer functions. Earthq Eng Struct Dyn 26(11):1113–1124
8. Takewaki I (1999) Dynamic structural design: inverse problem approach. WIT Press, Southampton
9. Takewaki I, Yoshitomi S (1998) Effects of support stiffnesses on optimal damper placement for a planar building frame. J Struct Des Tall Build 7(4):323–336
10. Takewaki I, Yoshitomi S, Uetani K, Tsuji M (1999) Non-monotonic optimal damper placement via steepest direction search. Earthq Eng Struct Dyn 28(6):655–670
11. Takewaki I (1998) Optimal damper positioning in beams for minimum dynamic compliance. Comput Meth Appl Mech Eng 156(1–4):363–373
12. Takewaki I (2000) Optimal damper placement for planar building frames using transfer functions. Struct Multidisc Optim 20(4):280–287
13. Takewaki I (2000) Optimal damper placement for critical excitation. Probab Eng Mech 15(4):317–325
14. Takewaki I (2009) Building control with passive dampers: optimal performance-based design for earthquakes. John Wiley & Sons, Asia, Singapore
15. Lopez Garcia D (2001) A simple method for the design of optimal damper configurations in MDOF structures. Earthq Spectra 17(3):387–398
16. Lopez Garcia D, Soong TT (2002) Efficiency of a simple approach to damper allocation in MDOF structures. J Struct Control 9(1):19–30
17. Liu W, Tong M, Wu X, Lee G (2003) Object-oriented modeling of structural analysis and design with application to damping device configuration. J Comput Civ Eng ASCE 17(2):113–122
18. Singh MP, Moreschi LM (2001) Optimal seismic response control with dampers. Earthq Eng Struct Dyn 30(4):553–572
19. Singh MP, Moreschi LM (2002) Optimal placement of dampers for passive response control. Earthq Eng Struct Dyn 31(4):955–976
20. Kiu W, Tong M, Wu Y, Lee G (2004) Optimized damping device configuration design of a steel frame structure based on building performance indices. Earthq Spectra 20(1):67–89
21. Lavan O, Levy R (2005) Optimal design of supplemental viscous dampers for irregular shear-frames in the presence of yielding. Earthq Eng Struct Dyn 34(8):889–907
22. Lavan O, Levy R (2006) Optimal design of supplemental viscous dampers for linear framed structures. Earthq Eng Struct Dyn 35(3):337–356
23. Park J-H, Kim J, Min K-W (2004) Optimal design of added viscoelastic dampers and supporting braces. Earthq Eng Struct Dyn 33(4):465–484
24. Trombetti T, Silvestri S (2004) Added viscous dampers in shear-type structures: the effectiveness of mass proportional damping. J Earthq Eng 8(2):275–313
25. Uetani K, Tsuji M, Takewaki I (2003) Application of optimum design method to practical building frames with viscous dampers and hysteretic dampers. Eng Struct 25(5):579–592

26. Wongprasert N, Symans MD (2004) Application of a genetic algorithm for optimal damper distribution within the nonlinear seismic benchmark building. J Eng Mech ASCE 130(4):401–406
27. Xu ZD, Shen YP, Zhao HT (2003) A synthetic optimization analysis method on structures with viscoelastic dampers. Soil Dyn Earthq Eng 23:683–689
28. Xu ZD, Zhao HT, Li AQ (2004) Optimal analysis and experimental study on structures with viscoelastic dampers. J Sound Vib 273(3):607–618
29. Lavan O, Levy R (2006) Optimal peripheral drift control of 3D irregular framed structures using supplemental viscous dampers. J Earthq Eng 10(6):903–923
30. Silvestri S, Trombetti T (2007) Physical and numerical approaches for the optimal insertion of seismic viscous dampers in shear-type structures. J Earthq Eng 11(5):787–828
31. Levy R, Lavan O (2006) Fully stressed design of passive controllers in framed structures for seismic loadings. Struct Multidisc Optim 32(6):485–498
32. Liu W, Tong M, Lee G (2005) Optimization methodology for damper configuration based on building performance indices. J Struct Eng ASCE 131(11):1746–1756
33. Tan P, Dyke SJ, Richardson A, Abdullah M (2005) Integrated device placement and control design in civil structures using genetic algorithms. J Struct Eng ASCE 131(10):1489–1496
34. Marano GC, Trentadue F, Greco R (2007) Stochastic optimum design criterion for linear damper devices for seismic protection of building. Struct Multidisc Optim 33:441–455
35. Attard TL (2007) Controlling all interstory displacements in highly nonlinear steel buildings using optimal viscous damping. J Struct Eng ASCE 133(9):1331–1340
36. Aydin E, Boduroglub MH, Guney D (2007) Optimal damper distribution for seismic rehabilitation of planar building structures. Eng Struct 29:176–185
37. Cimellaro GP (2007) Simultaneous stiffness-damping optimization of structures with respect to acceleration, displacement and base shear. Eng Struct 29:2853–2870
38. Cimellaro GP, Retamales R (2007) Optimal softening and damping design for buildings. Struct Control Health Monit 14(6):831–857
39. Viola E, Guidi F (2008) Influence of the supporting braces on the dynamic control of buildings with added viscous dampers. Struct Control Health Monit 16(3):267–286
40. Wang Y, Dyke S (2008) Smart system design for a 3D base-isolated benchmark building. Struct Control Health Monit 30:939–957
41. Takewaki I (2002) Robust building stiffness design for variable critical excitations. J Struct Eng ASCE 128(12):1565–1574
42. Takewaki I (2006) Critical excitation methods in earthquake engineering. Elsevier Science, Amsterdam
43. Drenick RF (1970) Model-free design of aseismic structures. J Eng Mech Div ASCE 96(EM4):483–493
44. Fox RL, Kapoor MP (1968) Rates of change of eigenvalues and eigenvectors. AIAA J 6:2426–2429
45. Fujita K, Moustafa A, Takewaki I (2010) Optimal placement of viscoelastic dampers and supporting members under variable critical excitations. Earthq Struct 1(1):43–67

Chapter 13
Earthquake Response Bound Analysis of Uncertain Passively Controlled Buildings for Robustness Evaluation

13.1 Introduction

The structural control using passive dampers has a successful history in the field of mechanical and aerospace engineering. This may result from the characteristic that these fields usually deal with predictable external loading and environment with little uncertainty. On the other hand, in the field of civil engineering, it has a different situation and history [1–11]. Building and civil structures are often subjected to severe earthquake ground motions, wind disturbances, and other external loading with large uncertainties [12]. It is therefore inevitable to take into account of these uncertainties in their structural design and application to actual structures.

While the structural control is a promising and smart tool for sustainable building design [13, 14], it is also true that a lot of uncertainties should be quantified for reliable implementation of these techniques [15]. The sustainable building design under uncertain structural-parameter environment may be one of the most challenging issues in the building structural engineering. Even if all the design constraints are satisfied at the initial construction stage, some responses to external loadings (earthquakes, strong winds, etc.) during service life may violate such constraints due to various factors resulting from randomness, material deterioration, temperature dependence, etc. To overcome such difficulty, response evaluation methods for uncertain structural-parameter environments are desired. By predicting the response variability accurately, the elongation of service life of buildings may be possible.

In this chapter, it is shown that interval analysis (see, for example, [16–23]) in terms of uncertain structural parameters is an effective tool for evaluating the sustainability of buildings in earthquake-prone countries. All the combinations of uncertain structural parameters become huge numbers and this difficulty can be overcome by introducing the sensitivity or Taylor series expansion analysis.

I. Takewaki et al., *Improving the Earthquake Resilience of Buildings*,
Springer Series in Reliability Engineering, DOI: 10.1007/978-1-4471-4144-0_13,

In order to demonstrate the usefulness and reliability of the explained method [24], a shear building model including passive viscous dampers with supporting members is subjected to a set of scaled earthquake ground motions and the time-history response analysis is used for simulating the earthquake response. The critical combination of interval parameters is found by introducing an assumption of 'inclusion monotonic' and the sensitivity information by Taylor series expansion. It is demonstrated that the proposed method is actually useful for the development of the concept of sustainable building design under uncertain structural-parameter environments.

The design earthquake ground motions change from time to time when a new class of ground motions (e.g. long-period ground motions due to surface waves) is observed or a new type of damage appears during severe earthquakes. Because the explained method can easily add these earthquake ground motions, the flexibility of the explained method is expected to be high.

13.2 Concept of Sustainable Building Design Under Uncertain Structural-Parameter Environment

The concept of sustainable building design under uncertain structural-parameter environments is illustrated in Fig. 13.1 [24], where f, E and c_d denote a structural response as the objective function, Young's modulus and a damping coefficient, respectively. The member stiffness and strength of buildings are uncertain due to various factors resulting from randomness, material deterioration, temperature dependence, etc. The damping coefficients of structural members and/or passive dampers may also be uncertain [15]. The time variation of Young's modulus and damping coefficients are shown in Fig. 13.1 as representative examples. Karbhari and Lee [25] discusses the service life estimation and extension of civil engineering structures from the viewpoints of material deterioration. These member and/or damper uncertainties lead to response variability of buildings under earthquake ground motions. Efficient and reliable methods are desired for predicting the upper bound of such building response.

13.3 Interval Analysis Methods for Uncertain Structural Parameters

Figure 13.2 shows the relationship between the variation of the objective function f (response quantity) and a structural parameter combination for the cases of '*inclusion monotonic*' and '*inclusion non-monotonic*'. In the case of inclusion monotonic as shown in Fig. 13.2a where $\bar{X}_i, \underline{X}_i \ (i = 1, 2)$ denote the upper and lower bounds of uncertain parameters, the maximum and minimum points occur at

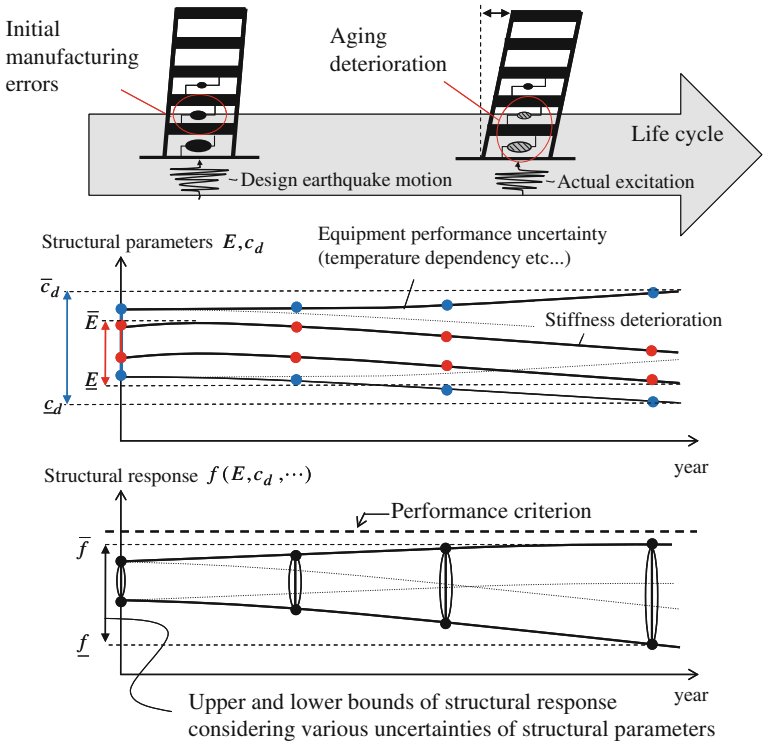

Fig. 13.1 Concept of sustainable design considering varied structural performance caused by various uncertainties of structural parameters [24]

the top left and bottom right corner points, respectively, and the check only for the corner points is sufficient. On the other hand, in the case of inclusion non-monotonic as shown in Fig. 13.2b where $\hat{X}_i^u$, $\hat{X}_i^l$ $(i = 1, 2)$ denote the uncertain parameters which maximize or minimize the objective function, the maximum and minimum points can occur in the inner region of uncertain parameters.

Based on the assumption of "*inclusion monotonic*", we can derive the upper and lower bounds of f by iterative calculations with all end-point combinations (2^{N_X} for N_X interval parameters), i.e. the upper and lower bounds of interval parameters. However, when the number N_X of interval parameters is extremely large, this primitive approach needs much computational time caused by a large combination number of interval parameters.

From the practical point of view, a more efficient methodology is desired which can estimate the upper and lower bounds of the objective function without a hard computational task. The interval analysis methodology using the approximation of Taylor series expansion has been developed so far [17, 18]. The formulation of Taylor series expansion in the interval analysis and the achievements of second-order Taylor series expansion proposed in [18] are explained in this section.

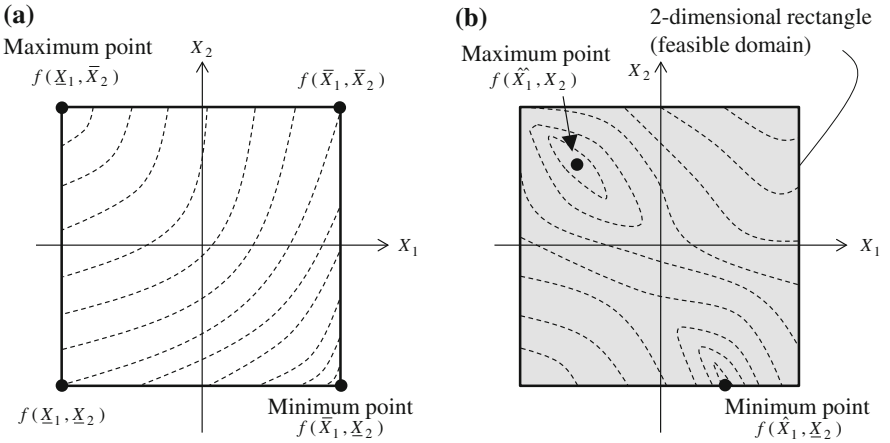

Fig. 13.2 Relationship between the variation of objective function and the structural parameter combination. **a** Example of 'inclusion monotonic'. **b** Example of 'inclusion non-monotonic' [24]

13.3.1 Interval Analysis Method Based on Approximation of First-Order Taylor Series Expansion

Let $\mathbf{X} = \{X_i\}, \mathbf{X}^c = \{X_i^c\}, \Delta\mathbf{X} = \{\Delta X_i\}$ denote the interval parameters, nominal parameter values, and half intervals. Let $(\ )^I$ and $[\ a\ ,\ \ b\ ]$ denote the definition of an interval parameter, where a and b are the lower and upper bounds of the interval parameter, respectively. Then $X_i^I = [X_i^c - \Delta X_i, X_i^c + \Delta X_i]$.

The upper and lower bounds $\bar{f}$, $\underline{f}$ of the objective function by the interval analysis method using first-order Taylor series expansion can be expressed as

$$\bar{f} \cong f(\mathbf{X}^c) + \sum_{i=1}^{N_X} \left| f_{,X_i} \Delta X_i \right| \tag{13.1}$$

$$\underline{f} \cong f(\mathbf{X}^c) - \sum_{i=1}^{N_X} \left| f_{,X_i} \Delta X_i \right| \tag{13.2}$$

where $(\ \ )_{,X_i}$ and N_X denote differentiation $\partial f(\mathbf{X})/\partial X_i|_{X_i = X_i^c}$ of the objective function at the nominal value and the number of uncertain parameters, respectively. Therefore $f_{,X_i}$ corresponds to a gradient of the objective function f with respect to ith interval parameter X_i for the nominal model.

13.3.2 Interval Analysis Method Based on Approximation of Second-Order Taylor Series Expansion

Although an approximation using first-order Taylor series expansion can be achieved without hard task, the result by this approximation may include a large error especially for a wide range of interval parameters. So as to enhance the accuracy of the interval analysis method, an approximation using second-order Taylor series expansion has been developed in [18]. An approximate objective function f^* using second-order Taylor series expansion around the nominal model can be described as

$$f^*(\mathbf{X}) = f(\mathbf{X}^c) + \sum_{i=1}^{N_X} f_{,X_i}\left(X_i - X_i^c\right) + \frac{1}{2}\sum_{i=1}^{N_X}\sum_{j=1}^{N_X} f_{,X_iX_j}\left(X_i - X_i^c\right)\left(X_j - X_j^c\right) \quad (13.3)$$

where $(\quad)_{,X_iX_j}$ denotes the second-order differentiation of the objective function at the nominal value. Therefore, $f_{,X_iX_j}$ corresponds to the Hessian matrix of the objective function f with respect to the ith and jth interval parameters X_i, X_j for the nominal model. Based on the general interval analysis method, the upper and lower bounds of Eq. (13.3) can be evaluated by calculating all the end point combinations of interval parameters and judging whether the objective function is the maximum or minimum value. The number of calculations in this approach is also 2^{N_X} which is the same number of calculation as that in the primitive interval analysis. However, the computational load for evaluating the objective function for each combination of interval parameters can be greatly reduced by using sensitivities around the nominal model.

By using the approximation of Taylor series expansion, iterative response analyses can be avoided. However, the computation of full elements of the Hessian matrix requires much time when N_X is large, especially for numerical sensitivity analysis, i.e. the finite difference analysis using gradient vectors. For this reason, a more simple approach has been proposed in [18] where the non-diagonal elements of the Hessian matrix are neglected. An approximate objective function f^{**} using second-order Taylor series expansion with only diagonal elements can be rewritten from Eq. (13.3) as

$$f^{**}(\mathbf{X}) = f(\mathbf{X}^c) + \sum_{i=1}^{N_X}\left\{f_{,X_i}\left(X_i - X_i^c\right) + \frac{1}{2}f_{,X_iX_i}\left(X_i - X_i^c\right)^2\right\} \quad (13.4)$$

From Eq. (13.4), we can evaluate the increment of the objective function by using first and second-order Taylor series expansion approximation as the sum of the increments of the objective function in the 1D domain. If we regard all interval parameters except X_i as nominal values in the incremental term in Eq. (13.4), the perturbation $\Delta f_i(\mathbf{X})$ of the objective function by the variation of X_i can be described as

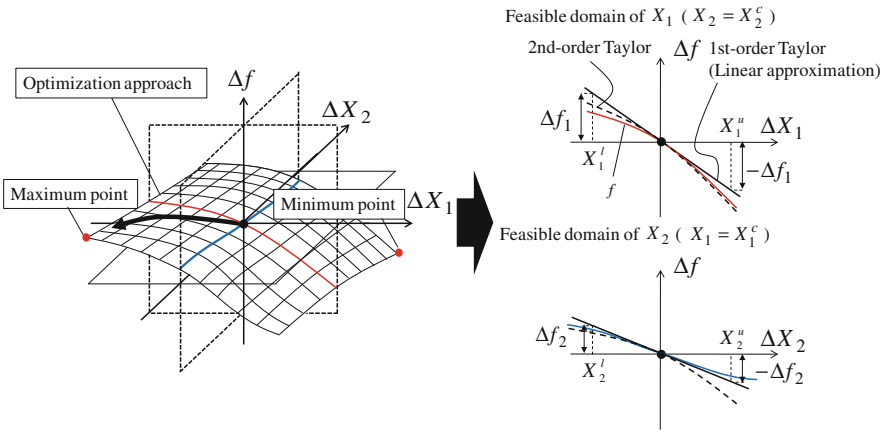

Fig. 13.3 Concept of interval analysis method using Taylor series approximation [24]

$$\Delta f_i\left(X_1^c,\cdots,X_{i-1}^c,X_i,X_{i+1}^c,\cdots,X_{N_X}^c\right)=f_{,X_i}\left(X_i-X_i^c\right)+\frac{1}{2}f_{,X_iX_i}\left(X_i-X_i^c\right)^2 \quad (13.5)$$

In Eq. (13.5), the interval extension Δf_i^I of the 1D perturbation can be derived as

$$\Delta f_i^I=\begin{bmatrix}\min\left[\Delta f_i\left(X_1^c,\cdots,\bar{X}_i,\cdots,X_{N_X}^c\right),\Delta f_i\left(X_1^c,\cdots,\underline{X}_i,\cdots,X_{N_X}^c\right)\right],\\ \max\left[\Delta f_i\left(X_1^c,\cdots,\bar{X}_i,\cdots,X_{N_X}^c\right),\Delta f_i\left(X_1^c,\cdots,\underline{X}_i,\cdots,X_{N_X}^c\right)\right]\end{bmatrix} \quad (13.6)$$

Finally, substituting Δf_i^I $(i=1,\cdots,N_X)$ into Eq. (13.4), the interval extension of the approximate objective function f^{**} can be obtained as

$$f\left(\mathbf{X}^I\right)\approx\left[f(\mathbf{X}^c)+\sum_{i=1}^{N_X}\underline{\Delta f_i}\left(X_i^I\right),f(\mathbf{X}^c)+\sum_{i=1}^{N_X}\overline{\Delta f_i}\left(X_i^I\right)\right] \quad (13.7)$$

It is remarkable that the number of calculations in Eq. (13.7) is reduced to $2\times N_X$ compared with 2^{N_X} in Eq. (13.3). For this reason, the computational load can be dramatically reduced by neglecting non-diagonal elements of the Hessian matrix. Figure 13.3 shows the concept of the interval analysis method using Taylor series approximation.

13.4 Advanced Interval Analysis Method Based on the Information of the Approximation of Taylor Series Expansion

When the degree of uncertainty of interval parameters is large, the result of the interval analysis applying the approximation of Taylor series expansion of the objective function may include numerical errors. On the other hand, a reliable result can be derived by reanalyzing the objective function with the obtained structural parameters. In this section, the advanced interval analysis method is presented using reanalysis based on the information of interval parameter set derived by the Taylor series approximation.

13.4.1 Reanalysis Approach Based on the Structural Parameter Set Derived by the Taylor Series Approximation

From Eqs. (13.5) and (13.6), the combination of the end points $\hat{\mathbf{X}}$ of the interval parameters $\mathbf{X}$ which maximizes the perturbation $\Delta f_i\left(X_1^c, \cdots, X_{i-1}^c, X_i, X_{i+1}^c, \cdots, X_{N_X}^c\right)$ $(i = 1, \cdots, N_X)$ of the objective function can be derived as

$$\hat{\mathbf{X}} = \{X_i \text{ so as to} \max[\Delta f_i(X_i)], i = 1, \cdots, N_X\} \tag{13.8}$$

The upper bound of the objective function can be evaluated using a reliable response analysis method (time-history response analysis) for a regenerated structural model with the critical combination of interval parameters set [Eq. (13.8)]. It should be mentioned that the objective function evaluated by the time-history response analysis method will not exceed the feasible domain of the objective function. The flowchart of this proposed methodology is as follows.

Step 1 Calculate the gradient vector $f_{,X_i}$ $(i = 1, \cdots, N_X)$ and diagonal element of Hessian matrix $f_{,X_iX_i}$ $(i = 1, \cdots, N_X)$ of the objective function for the nominal model.
Step 2 Evaluate Eq. (13.6) for the upper and lower bounds of the interval parameter X_i.
Step 3 Derive the target end point combinations $\hat{\mathbf{X}}$ of interval parameters corresponding to the upper bound of Eq. (13.6).
Step 4 Evaluate the objective function by the time-history response analysis for given structural parameters $\hat{\mathbf{X}}$.

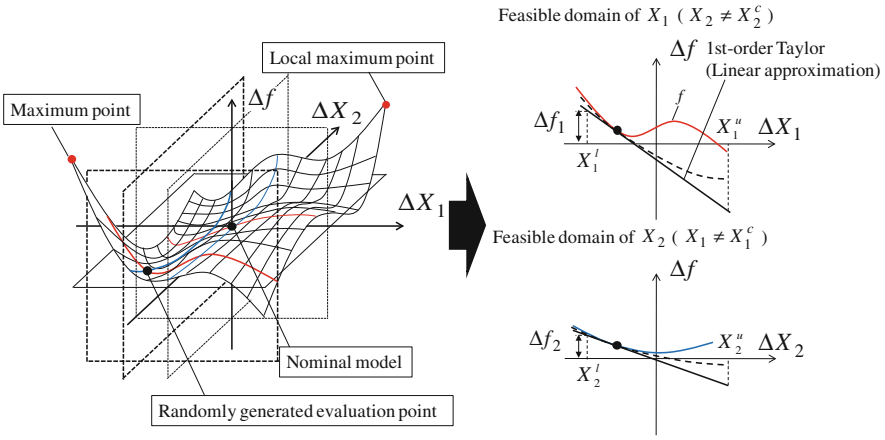

Fig. 13.4 Concept of advanced interval analysis method using Taylor series approximation and random search technique for initial evaluation point [24]

13.4.2 Varied Evaluation Point Method Considering the Influence of Initial Value Dependency

In order to obtain the reliable result of the response variability by using the proposed advanced interval analysis methodology in the previous section, it is important that the assumption of "*inclusion monotonic*" is satisfied for the objective function. If the objective function, e.g. the maximum interstory drift of a damped structure subjected to a ground motion as shown in the numerical examples (Sect. 13.5), has a property of non-monotonic variation for the variation of the interval parameters, the interval analysis method using the first and second-order sensitivities at the nominal model will not provide reliable response variability. To overcome this difficulty, an additional numerical procedure should be introduced to search for the evaluation point set for the evaluation of first and second-order sensitivities. In this chapter, it is shown in the later numerical example that the evaluation point selected randomly for the combination of the interval parameters is effective. This is called the varied evaluation point (VEP) method. Figure 13.4 shows the concept of the VEP method.

13.4.3 Search of the Exact Solution

In numerical examples, an approximate candidate of the exact solution of the maximum or minimum value of the objective function in a feasible domain of interval parameters is calculated by solving the original problem with the sequential quadratic programming (SQP) method. In this analysis for the exact

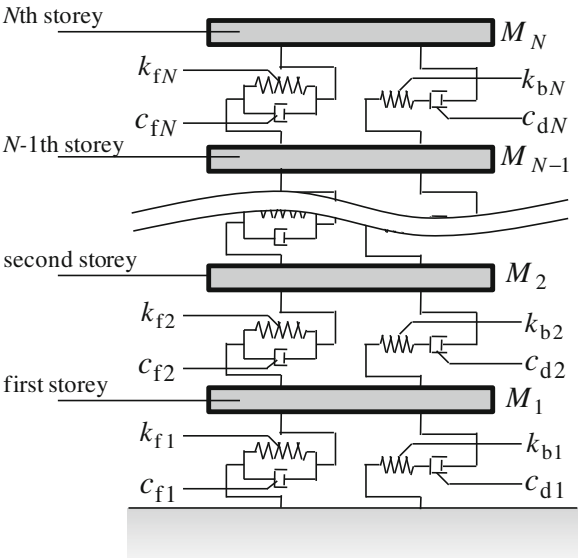

Fig. 13.5 Structural model with passive dampers including supporting members [24]

solution, the approximation by Taylor series expansion is not employed and the time-history response analysis for successive points of interval parameters is conducted. The problem of finding an approximate candidate of the exact solution of the maximum or minimum value of the objective function may be described by

$$\left.\begin{array}{l}\text{Find } \mathbf{X} = \{c_{d_1}, \ldots, c_{d_N}, k_{b_1}, \ldots, k_{b_N}, k_{f_1}, \ldots, k_{f_N}\}^T \\ \text{so as to maximize } f(\mathbf{X}) \\ \text{subject to } \mathbf{X} \in \mathbf{X}^I\end{array}\right\} \tag{13.9}$$

13.5 Numerical Examples

Numerical examples are presented for 20-story shear building models with passive viscous dampers to demonstrate the validity and accuracy of the proposed methodology. Figure 13.5 presents the shear building model with passive viscous dampers including supporting members. The properties of the nominal structural parameters are shown in Table 13.1. The floor masses are identical in all the storys. The frame stiffness distribution in the nominal model is given by Eq. (13.10) which can be derived from the straight-line shape of fundamental eigenmode of the main frame.

$$k_{f_i} = \frac{1}{2}\{N(N+1) - i(i-1)\}m\omega_1^2 \quad (i = 1, \cdots, N(= 20)) \tag{13.10}$$

Table 13.1 Structural parameters of main frame [24]

	20-storey building
Floor mass (kg)	1024×10^3
Storey stiffness (N/mm)	Eq. (13.10)
Damper capacity (Ns/mm)	2.250×10^7
Supporting member stiffness (N/mm)	Ratio 1.0 to frame storey stiffness
Structural damping ratio (stiffness-proportional damping)	0.02
Fundamental natural circular frequency[a] with damper (rad/s)	3.927

[a] Complex eigenvalue analysis

where ω_1 denotes the fundamental natural circular frequency of the frame and m is the floor mass. The nominal values of damping coefficients of passive viscous dampers are constant and are shown in Table 13.1. The ratio of the nominal value of supporting member stiffness to the nominal value of frame stiffness is assumed to be 1.0 in every story.

The structural parameters $\mathbf{c}_\mathrm{d}$, $\mathbf{k}_\mathrm{b}$ and $\mathbf{k}_\mathrm{f}$ are dealt with as interval parameters and the ratios of half the intervals to the nominal values are defined as follows.

$$\{\alpha_1, \ldots, \beta_1, \ldots, \gamma_1, \ldots\} = \left\{ \frac{\Delta c_{\mathrm{d}_1}}{c^c_{\mathrm{d}_1}}, \ldots, \frac{\Delta k_{\mathrm{b}_1}}{k^c_{\mathrm{b}_1}}, \cdots, \frac{\Delta k_{\mathrm{f}_1}}{k^c_{\mathrm{f}_1}}, \cdots \right\} \tag{13.11}$$

The degrees of uncertainties of interval parameters are given by $\alpha_i = \beta_i = 0.5$ and $\gamma_i = 0.3$ for all i. This means that the degree of performance of passive dampers may be rather large and that of mainframe may be relatively small.

Figure 13.6 shows representative recorded ground motions, El Centro NS 1940, Taft EW 1952, and Hachinohe NS 1968, whose maximum velocities are normalized by 50 cm/s. These earthquake ground motions are used for structural design (Level 2 of large earthquake ground motion) of high-rise and base-isolated buildings in Japan.

Figure 13.7 illustrates the comparison of evaluated bounds of the top horizontal displacement under uncertain structural parameters derived by Taylor series approximations with those derived by the SQP method. The SQP method has been applied to two cases. The first case has the nominal value as the initial value and the second case has randomly generated parameter combinations giving the top three maximum responses as the initial value. The second case has been introduced to guarantee the search of global optimum one. The first-order Taylor and reanalysis means that the critical combination is determined by the first-order Taylor series expansion and the upper bound of response is evaluated by the time-history response analysis for the determined combination. It can be observed from Fig. 13.7 that the first-order Taylor and reanalysis provides an accurate estimate for the maximum top horizontal displacement of all the three ground motions. Furthermore the result of the SQP method with the nominal value as the initial value coincides fairly well with that of the SQP method with randomly generated parameter combinations giving the top three maximum responses as the initial value.

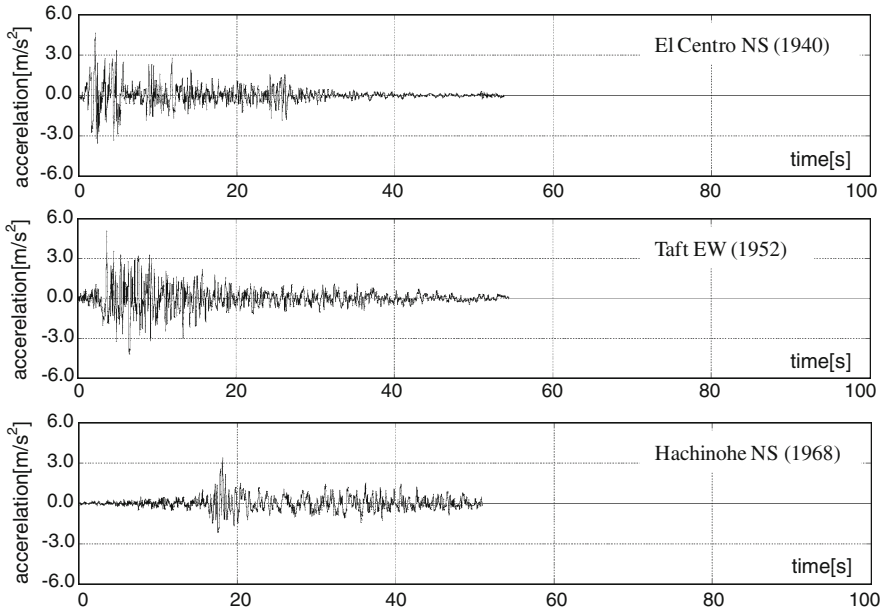

Fig. 13.6 Recorded ground motions whose maximum velocities are normalized by 50 cm/s [24]

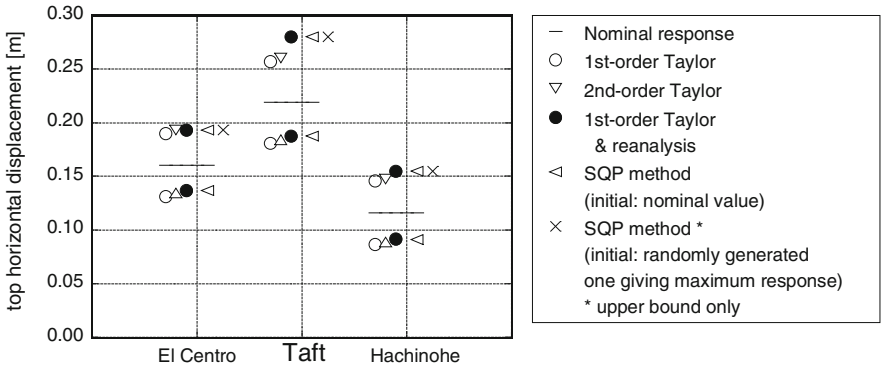

Fig. 13.7 Comparison of evaluated bounds of top horizontal displacement under uncertain structural parameters derived by Taylor series approximations with those derived by SQP method [24]

Figure 13.8 shows the comparison of critical interval parameters for the upper bound of the top horizontal displacement derived by the first-order approximation with those by the SQP method with the nominal value as the initial value. It can be observed that, while a little difference is seen for El Centro and Hachinohe, most parameters coincide well.

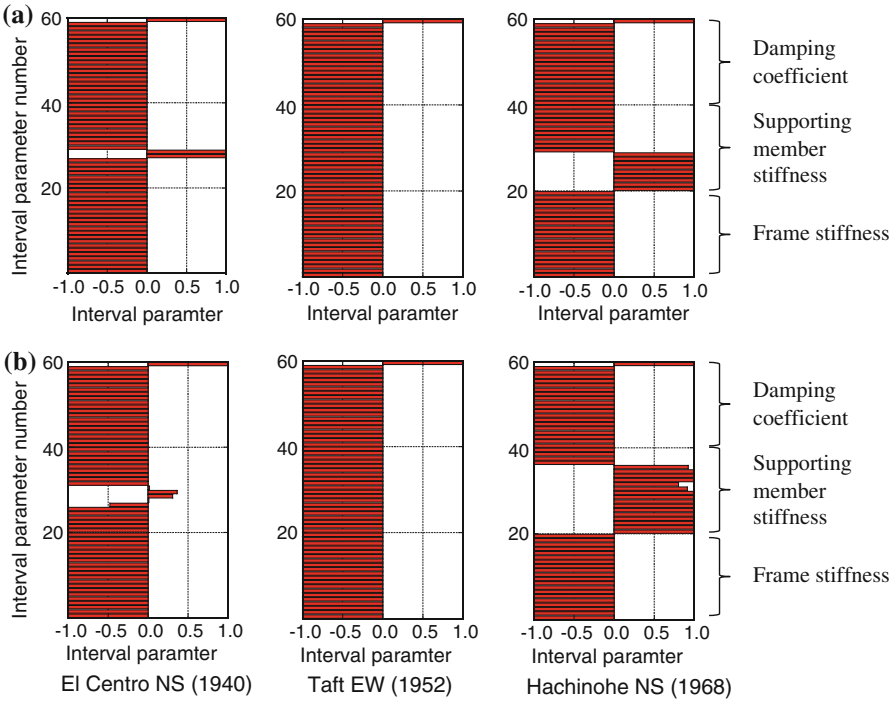

Fig. 13.8 Comparison of critical interval parameters for upper bound of top horizontal displacement derived by first-order approximation with those of exact solution. **a** First-order approximation. **b** SQP method with the nominal value as the initial value [24]

Figure 13.9 presents the comparison of evaluated bounds of the maximum interstory drift under uncertain structural parameters derived by Taylor series approximations and reanalysis method with those derived by the SQP method where the initial value is given by the nominal model. Furthermore, since the SQP method is known as the gradient-based optimization algorithm, the result by the SQP method may depend on the initial value and may attain a local maximum. For confirming whether the result by the SQP method is the global optimum solution or not as implemented in Fig. 13.7, the upper bound of the objective function for El Centro NS (1940) is derived by the SQP method where the initial value is given by three different randomly generated evaluation points making the objective function maximum (top three). It can be seen that the method with the nominal model as the initial model is not sufficient and another method is desired for the maximum interstory drift.

Figure 13.10 illustrates the comparison of critical interval parameters for the upper bound of the maximum interstory drift derived by the first-order approximation with those by the SQP method where the initial value is given by the nominal model. It can be observed from Fig. 13.10b that some critical structural parameters exist except at the end points of the interval. However, the critical

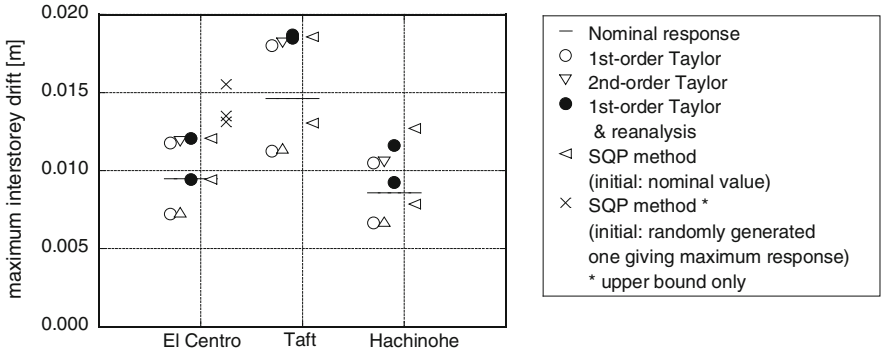

Fig. 13.9 Comparison of evaluated bounds of maximum interstory drift under uncertain structural parameters derived by Taylor series approximations with those derived by SQP method [24]

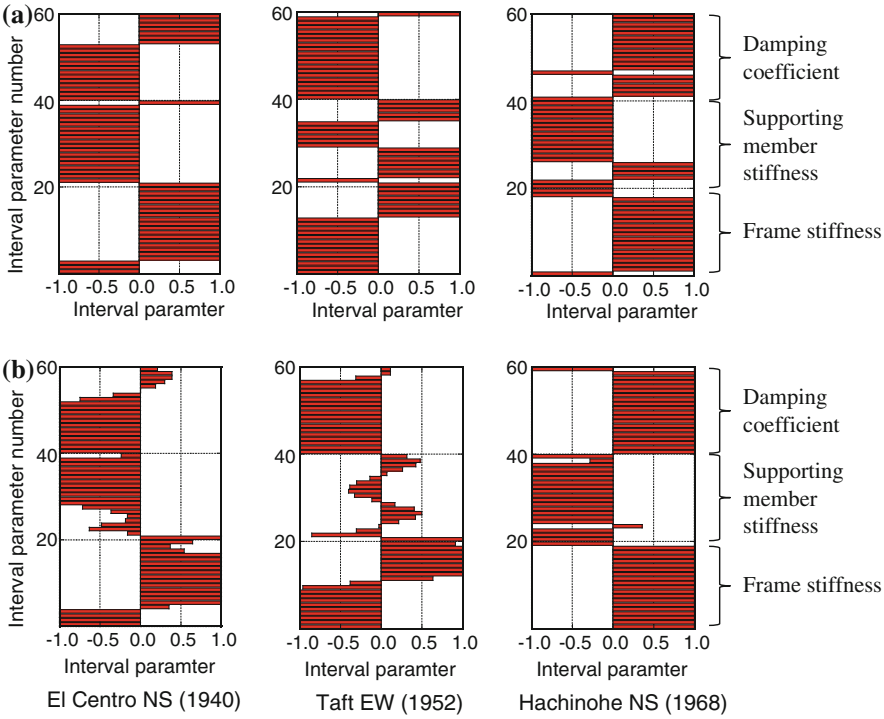

Fig. 13.10 Comparison of critical interval parameters for upper bound of maximum interstory drift derived by first-order approximation with those of exact solution. **a** First-order approximation. **b** SQP method [24]

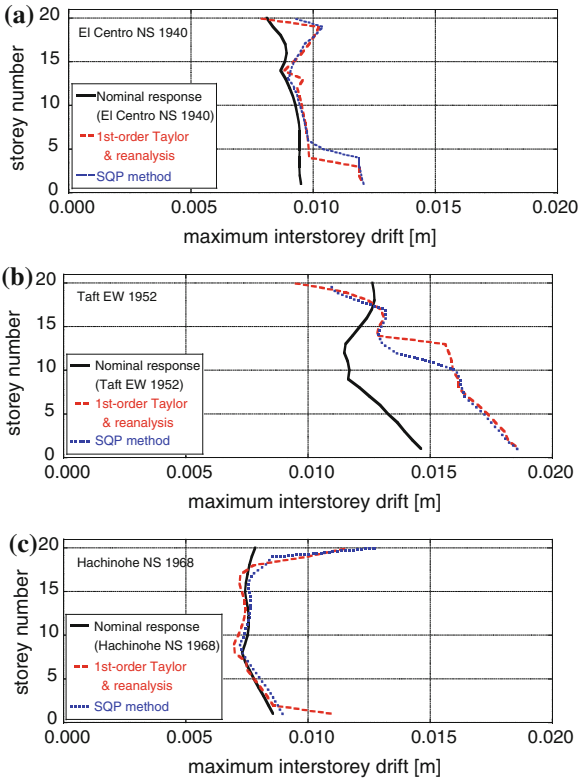

Fig. 13.11 Comparison of maximum interstory drifts under uncertain structural parameter sets derived by first-order Taylor approximation with those by SQP method. **a** El Centro NS 1940. **b** Taft EW 1952. **c** Hachinohe NS 1968 [24]

structural parameters by the first-order approximation with the nominal value as the initial value exhibit a distribution similar to those by the SQP method.

Figure 13.11 shows the comparison of the maximum interstory drifts under uncertain structural parameter sets derived by first-order Taylor series approximation with those by the SQP method employing the nominal model as the initial value combination for three ground motions, El Centro NS 1940, Taft EW 1952, and Hachinohe NS 1968. It can be observed that the maximum interstory drift of the nominal model occurs in the first storey for all the three ground motions. On the other hand, while the varied maximum interstory drift under uncertain structural parameters occurs in the first story for El Centro NS 1940 and Taft EW 1952, that occurs in the top story for Hachinohe NS 1968. In the case, where the story indicating the maximum interstory drift changes from the nominal model like Hachinohe NS 1968, the sensitivities of the objective function (maximum interstory drift in this case) with respect to uncertain parameters exhibit largely different values. This leads to large errors in evaluating the response variability (see Fig. 13.9).

It can also be understood from Fig. 13.11 that, although the story indicating the maximum interstory drift by first-order Taylor series approximation does not

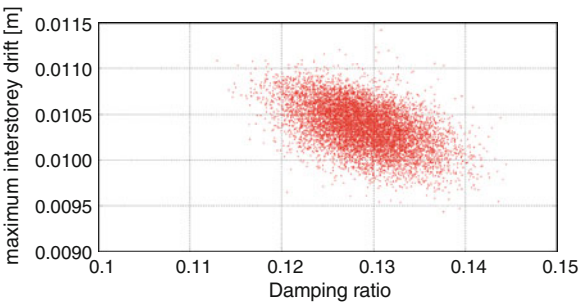

Fig. 13.12 Distribution of maximum interstory drift of damped structures given by randomly generated structural parameters (El Centro NS (1940)) [24]

change from that by the SQP method, the solution by the SQP method employing the nominal model as the initial value combination may drop into a local maximum. For such case, the VEP method introduced in Sect. 13.4.2 seems to be effective. A numerical example using the VEP method will be shown in the following.

Figure 13.12 shows the distribution of the maximum interstory drift for El Centro NS (1940) of damped structures given by randomly generated structural parameters. The horizontal axis indicates the lowest-mode damping ratio of the model with a respective set of randomly generated structural parameters. The number of samples is 10,000.

Figure 13.13a illustrates the comparison of interval parameters, i.e. initial structural parameters (randomly generated one giving maximum response), critical structural parameters by the VEP method (first-order Taylor approximation), and critical structural parameters by the SQP method for randomly generated combinations of uncertain structural parameters giving top three maximum interstory drifts. It can be observed that the critical structural parameters by the VEP method coincide fairly well with those by the SQP method. Figure 13.13b presents the result of the maximum interstory drifts by the VEP method and the SQP method. It can be seen that the maximum interstory drift by the VEP method coincides fairly well with that by the SQP method. This indicates the reliability and accuracy of the VEP method for the maximum interstory drift.

The degrees of uncertainties $\alpha_i = \beta_i = 0.5$ and $\gamma_i = 0.3$ are rather large and the present numerical examples seem to give the upper bounds of errors of the proposed method.

13.6 Summary

1. Interval analysis in terms of uncertain structural parameters is an effective tool for evaluating the response variability, bound, and the sustainability of buildings in earthquake-prone countries. A shear building model has been used including passive viscous dampers with supporting members for demonstrating

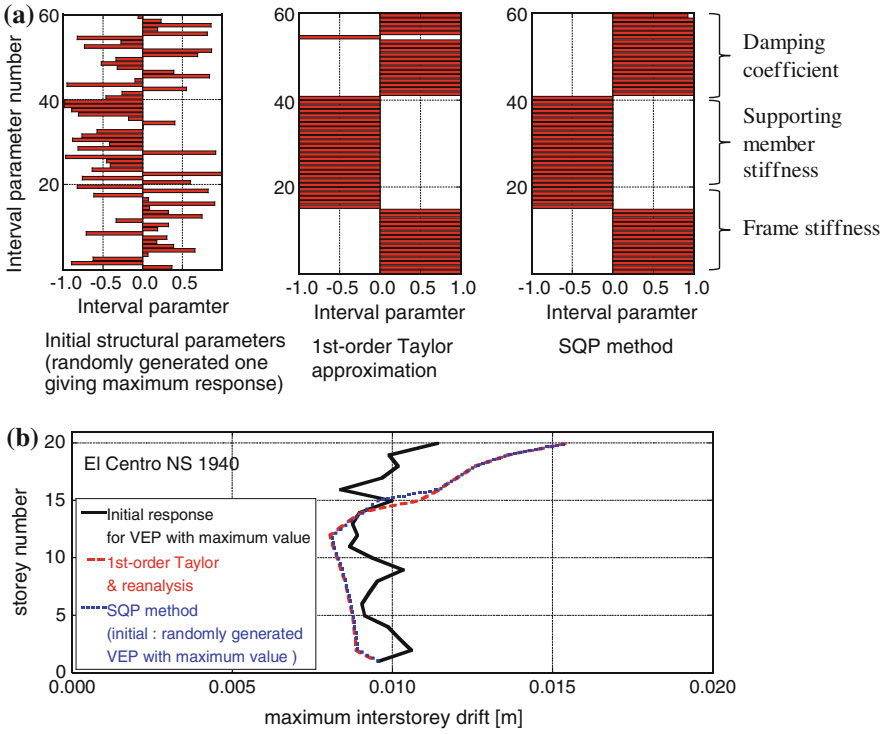

Fig. 13.13 VEP method for maximum interstory drift using initial structural parameter distribution derived by randomly generated one giving maximum response. **a** Comparison of interval parameters. **b** Comparison of maximum interstory drift [24]

the effectiveness and usefulness of the proposed interval analysis method. It has been made clear that the proposed method is actually useful for the development of the concept of sustainable building design under such uncertain structural-parameter environment.

2. All the combinations of end points of uncertain structural parameters lead to huge numbers and the evaluation of the upper and lower bounds of the objective function requires elaborate manipulation. It has been explained that this difficulty can be overcome by introducing the sensitivity or Taylor series expansion analysis.
3. If the objective function has a property of non-monotonic variation for the variation of the interval parameters, the interval analysis method using the first and second-order sensitivities at the nominal model will not provide reliable response variability. To overcome this difficulty, an additional numerical procedure has been introduced and explained for searching the evaluation point for the evaluation of first and second-order sensitivities by selecting randomly the combination of the interval parameters. This is called the VEP method. It has been explained and demonstrated that the VEP method is a reliable method

because the change of the evaluation point or the initial design point is necessary for search of the global solution.

4. The necessity of use of the VEP method depends on the objective function. When the objective function is a top floor displacement in the shear building model, it may not be necessary. When the objective function is an interstory drift, it appears necessary. It has been confirmed that the VEP method is an accurate and reliable method for the estimation of the maximum interstory drift of the shear building model under uncertain structural parameter environment.

References

1. Casciati F (ed) (2002) Proceedings of 3rd world conference on structural control. John Wiley & Sons, Como
2. Cheng FY, Jiang H, Lou K (2008) Smart structures: innovative systems for seismic response control. CRC Press, Boca Raton
3. Christopoulos C, Filiatrault A (2006) Principle of passive supplemental damping and seismic isolation. IUSS Press, University of Pavia, Italy
4. de Silva CW (ed) (2007) Vibration damping, control, and design, CRC Press, Boca Raton
5. Housner GW, Masri SF, Chassiakos AG (eds) (1994) Proceedings of 1st world conference on structural control. IASC, Los Angeles
6. Housner G et al (1997) Special issue, structural control: past, present, and future. J. Eng Mech ASCE 123(9):897–971
7. Johnson E, Smyth A (eds) (2006) Proceedings of 4th world conference on structural control and monitoring, (4WCSCM). IASC, San Diego
8. Kobori T, Inoue Y, Seto K, Iemura H, Nishitani A (eds) (1998) Proceedings of 2nd world conference on structural control. John Wiley & Sons, Kyoto
9. Soong TT, Dargush GF (1997) Passive energy dissipation systems in structural engineering. John Wiley & Sons, Chichester
10. Srinivasan AV, McFarland DM (2000) Smart structures: analysis and design. Cambridge University Press, Cambridge
11. Takewaki I (2009) Building control with passive dampers: optimal performance-based design for earthquakes. John Wiley & Sons Ltd., Asia, Singapore
12. Takewaki I (2007) Critical excitation methods in earthquake engineering. Elsevier, Amsterdam
13. Fujita K, Moustafa A, Takewaki I (2010) Optimal placement of viscoelastic dampers and supporting members under variable critical excitations. Earthq Struct 1(1):43–67
14. Takewaki I, Fujita K, Yamamoto K, Takabatake H (2011) Smart passive damper control for greater building earthquake resilience in sustainable cities. Sustain Cities and Soc 1(1):3–15
15. Takewaki I, Ben-Haim Y (2005) Info-gap robust design with load and model uncertainties. J. Sound Vib 288(3):551–570
16. Alefeld G, Herzberger J (1983) Introduction to interval computations. Academic Press, New York
17. Chen SH, Wu J (2004) Interval optimization of dynamic response for structures with interval parameters. Comp Struct 82:1–11
18. Chen SH, Ma L, Meng GW, Guo R (2009) An efficient method for evaluating the natural frequency of structures with uncertain-but-bounded parameters. Comp Struct 87:582–590

19. Koyluoglu HU, Elishakoff I (1998) A comparison of stochastic and interval finite elements applied to shear frames with uncertain stiffness properties. Comp Struct 67:91–98
20. Moore RE (1966) Interval analysis. Englewood Cliffs, Prentice-Hall, New Jersey
21. Qiu ZP (2003) Comparison of static response of structures using convex models and interval analysis method. Int J Numer Meth Eng 56:1735–1753
22. Qiu ZP, Chen SH, Song D (1996) The displacement bound estimation for structures with an interval description of uncertain parameters. C Numer Meth Eng 12:1–11
23. Mullen RL, Muhanna RL (1999) Bounds of structural response for all possible loading combinations. J Struct Eng ASCE 125:98–106
24. Fujita K, Takewaki I (2011) Sustainable building design under uncertain structural-parameter environment in seismic-prone countries. Sustain Cities and Soc 1(3):142–151
25. Karbhari VM, Lee LS (eds) (2010) Service life estimation and extension of civil engineering structures. Woodhead Publishing, Cambridge

Chapter 14
Earthquake Response Bound Analysis of Uncertain Base-Isolated Buildings for Robustness Evaluation

14.1 Introduction

An efficient methodology is explained to evaluate the robustness (variability of response) of an uncertain base-isolated building under various ground motions. It is well known that base-isolated buildings have large structural uncertainties due to wide variability of structural properties of base-isolation systems [1, 2]. The variability resulting from temperature and frequency dependences, manufacturing errors, and aging effect may be a representative one.

Under these circumstances, it is desired to evaluate the response variability caused by such structural variability [3–5]. The method based on the convex model may be one possibility [6]. Kanno and Takewaki [7] proposed an efficient and reliable method for evaluating the robustness of structures under uncertainties based on the concept of the robustness function [8, 9]. However, it does not seem that an efficient and reliable method for evaluating the robustness of structures has been proposed.

An interval analysis is believed to be one of the most efficient and reliable method to respond to this requirement. While a basic assumption of "inclusion monotonic" is introduced in usual interval analysis, the possibility is taken into account for occurrence of the extreme value of the objective function in an inner feasible domain of the interval parameters. It is shown that the critical combination of the structural parameters can be derived explicitly so as to maximize the approximate objective function by second-order Taylor series expansion. The Updated Reference-Point (URP) method is presented to obtain such critical combination of structural parameters [10].

In order to investigate the validity of the robustness evaluation methodologies, numerical analyses are conducted for 20-story base-isolated building models with natural rubber (NRB) isolators and passive dampers. The maximum displacement in the base-isolation story and the maximum acceleration at the building top floor

I. Takewaki et al., *Improving the Earthquake Resilience of Buildings*,
Springer Series in Reliability Engineering, DOI: 10.1007/978-1-4471-4144-0_14,

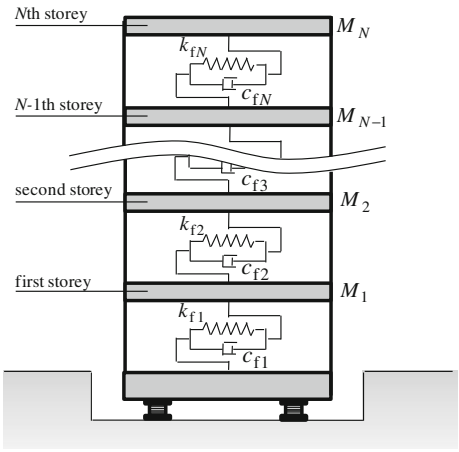

Fig. 14.1 *N*-story base-isolated building model [10]

are chosen as the objective function. By comparing the results with the exact solution and those by other conventional methods, it is shown that the URP method can provide a more accurate evaluation of response bounds without hard computational effort.

14.2 Modeling of Base-Isolated Buildings and Uncertainty of Isolators

Consider an *N*-story base-isolated shear building model as shown in Fig. 14.1. A simple model is used here to present an essential feature of the robustness evaluation method. The isolator consists of NRB and is described by a linear model as shown in Fig. 14.2. On the other hand, the damping is given by oil dampers.

It is necessary to take into account the response variability (robustness) of the building under earthquake ground motions due to the variability of isolators, dampers, and superstructural properties. As for temperature dependence of NRB, the shear modulus of NRB becomes 10 % larger in −10 degrees centigrade and several percent smaller in 40 degrees centigrade than the standard one in 20 centigrade. On the other hand, as for aging effect, it is known that about 10 % increase of shear modulus of NRB can be seen.

14.3 Past Work on Interval Analysis for Uncertain Input and Structural Parameters

Various methods have been proposed so far for evaluating the robustness of structures with uncertain parameters under uncertain disturbances. (for example, Ben-Haim [8], Takewaki and Ben-Haim [9], Zhao et al. [5], Rao and Berke [11],

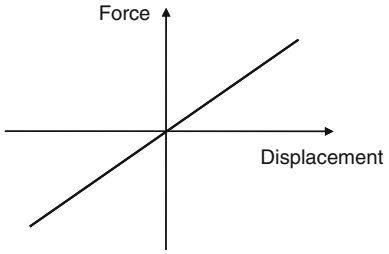

Fig. 14.2 Linear force–displacement relation of NRB isolator [10]

Qiu and Elishakoff [12], Qiu et al. [13], Chen et al. [14]). Among them, an interval analysis may be one of the most effective methods for the analysis under uncertainty. The interval analysis is aimed at finding the upper and lower bounds of the objective function for given widths of uncertain parameters.

Let $\mathbf{X}$ denote a set of uncertain parameters. The components of this set are referred to as interval variables and expressed as:

$$\mathbf{X}^I = \left\{ \left[X_i^c - \Delta \underline{X}_i, X_i^c + \Delta \bar{X}_i \right] \right\} \quad (i = 1, \ldots, N_x) \tag{14.1}$$

where $(\ )^I$ denotes an interval variable and $[a, b]$ indicates that a and b are the lower and upper bounds of the interval parameter. In Eq. (14.1), $(\ )^c$, $\Delta \bar{X}$, $\Delta \underline{X}$ and N_x indicate the nominal value, the upper side bandwidth, the lower side bandwidth, and the number of interval variables, respectively. The following representation of the objective function in terms of interval variables is called the interval extension.

$$f^I(\mathbf{X}) = f(\mathbf{X}^I) = f\left([X_1^c - \Delta \underline{X}_1, X_1^c + \Delta \bar{X}_1], \ldots, [X_{N_x}^c - \Delta \underline{X}_{N_x}, X_{N_x}^c + \Delta \bar{X}_{N_x}] \right) \tag{14.2}$$

Equation (14.2) implies to evaluate the upper and lower bounds of the objective function for all the combinations of end points of interval variables and defines the set of function values between these upper and lower bounds.

In usual interval analysis, a basic assumption of "inclusion monotonic" is introduced and the following relation is assumed.

$$\left\{ f(\mathbf{X}) : X_i \in X_i^I, i = 1, 2, \ldots, N_x \right\} \subseteq f(X_1^I, X_2^I, \ldots, X_{N_x}^I) \tag{14.3}$$

The right-hand side of Eq. (14.3) indicates the interval extension of the objective function as shown in Eq. (14.2). Equation (14.3) means that the maximum and minimum values of the objective function occur at the end points of interval variables.

Figure 14.3a and b presents two-variable examples of distribution of objective function for monotonic one and non-monotonic one. In the monotonic case (inclusion-monotonic assumption holds) as shown in Fig. 14.3a, an exact solution is included in the combination of end points of interval parameters. Therefore, an exact solution can be obtained by conducting the response analysis for all the

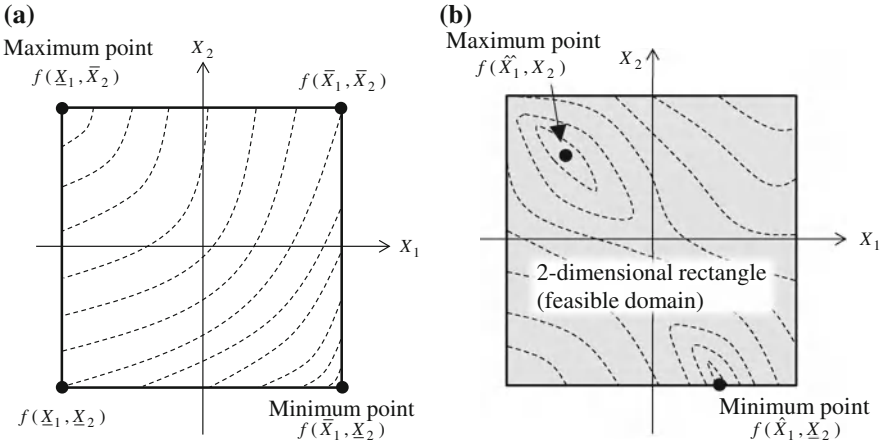

Fig. 14.3 Dependence of critical combination of uncertain parameters on properties of objective function, **a** inclusion monotonic, **b** non-monotonic [10]

combinations of end points $\bar{X}_i = X_i^c + \Delta\bar{X}_i$ and $\underline{X}_i = X_i^c - \Delta\underline{X}_i$ of interval parameters. The computational load (number of repetition) is given by 2^{N_x}. However, this repetition becomes huge for a large number of interval parameters. Furthermore, it is not appropriate to evaluate the objective function only at the end points of interval parameters when the objective function is not monotonic as shown in Fig. 14.3b.

In order to overcome this difficulty, some approaches have been proposed in the interval analysis, e.g., a method of approximating the inverse of the stiffness matrix by Neumann expansion, a method of approximating the objective function by converged series expansion. Furthermore, Chen et al. [14] proposed a method of using a first-order Taylor series expansion and a second-order Taylor series expansion with diagonal components only in approximating the objective function. However, when the objective function is nonmonotonic, a sequential quadratic programming (SQP) method or a response surface method has to be introduced in transforming the original problem of finding the upper and lower bounds of the objective function into an optimization problem. This procedure causes a large amount of computational work.

14.4 Interval Analysis Using Taylor Series Expansion

As stated before, it is often the case that the objective function becomes non-monotonic ones. A general problem of interval analysis may be stated as follows:

Find $\mathbf{X}$
so as to maximize or minimize

$$f(\mathbf{X}) \tag{14.4}$$

subject to $\mathbf{X} \in \mathbf{X}^I$

Equation (14.4) indicates a constrained optimization problem and various methods can be used to solve this. However, there are many difficulties in the computational time or convergence.

In this chapter, a new method is explained which can overcome the difficulty in problems with non-monotonic properties of objective functions. For preparing this, interval analysis using first- and second-order Taylor expansion is explained in Sects. 14.4.1 and 14.4.2.

14.4.1 Interval Analysis Using First-Order Taylor Expansion

The upper and lower bounds of the objective function by the first-order Taylor series expansion can be obtained as

$$\bar{f} = f(\mathbf{X}^c) + \sum_{i=1}^{N_x} \left| f_{,X_i} \Delta X_i \right|, \quad \underline{f} = f(\mathbf{X}^c) - \sum_{i=1}^{N_x} \left| f_{,X_i} \Delta X_i \right| \tag{14.5a, b}$$

where the first-order sensitivity of the objective function with respect to an interval parameter is to be evaluated numerically as

$$f_{,X_i} = \{ f(X_i^c + dX_i) - f(X_i^c) \} / dX_i \quad (i = 1, \ldots, N_x) \tag{14.6}$$

14.4.2 Interval Analysis Using Second-Order Taylor Expansion

An approximation of the objective function around the nominal value can be expressed as the second-order Taylor series expansion as follows:

$$f^*(\mathbf{X}) = f(\mathbf{X}^c) + \sum\nolimits_{i=1}^{N_x} f_{,X_i} \left(X_i - X_i^c \right) + \frac{1}{2} \sum\nolimits_{i=1}^{N_x} \sum\nolimits_{j=1}^{N_x} f_{,X_i X_j} \left(X_i - X_i^c \right) \left(X_j - X_j^c \right) \tag{14.7}$$

where the second-order sensitivity of the objective function with respect to interval parameter is to be evaluated numerically as

$$f_{,X_iX_j} = \begin{cases} \left\{ \begin{matrix} f(X_i^c + dX_i, X_j^c + dX_j) - f(X_i^c, X_j^c + dX_j) \\ -f(X_i^c + dX_i, X_j^c) + f(X_i^c, X_j^c) \end{matrix} \right\} / dX_i dX_j & (i \neq j) \\ \left\{ \hat{f}(X_i^c + 2dX_i) - 2\hat{f}(X_i^c + dX_i) + \hat{f}(X_i^c) \right\} / dX_i^2 & (i = j) \end{cases} \tag{14.8}$$

Following Chen et al. [14], let us approximate the objective function around the nominal value by the second-order Taylor series expansion with diagonal terms only.

$$f^{**}(\mathbf{X}) = f(\mathbf{X}^c) + \sum\nolimits_{i=1}^{N_x} \left\{ f_{,X_i}(X_i - X_i^c) + \frac{1}{2} f_{,X_iX_i}(X_i - X_i^c)^2 \right\} \tag{14.9}$$

In Eq. (14.9), each increment with each interval parameter is independent. For example, the increment with respect to X_1 may be expressed by

$$\Delta f_1\left(X_1, X_2^c, \ldots, X_{N_x}^c\right) = f_{,X_1}\left(X_1 - X_1^c\right) + \frac{1}{2} f_{,X_1X_1}\left(X_1 - X_1^c\right)^2 \tag{14.10}$$

In order to obtain the upper and lower bounds of the function of Eq. (14.9), it is necessary to evaluate the maximum and minimum values of Δf_i $(i = 1, \ldots, N_x)$ and sum up those values. For example, the upper and lower bounds of Δf_1 can be obtained as follows by doing the interval extension of Eq. (14.10).

$$\Delta f_1^I\left(X_1^I, X_2^c, \ldots, X_{N_x}^c\right) = \begin{bmatrix} \min\left[\Delta f_1\left(\bar{X}_1, X_2^c, \ldots, X_{N_x}^c\right), \Delta f_1\left(\underline{X}_1, X_2^c, \ldots, X_{N_x}^c\right)\right], \\ \max\left[\Delta f_1\left(\bar{X}_1, X_2^c, \ldots, X_{N_x}^c\right), \Delta f_1\left(\underline{X}_1, X_2^c, \ldots, X_{N_x}^c\right)\right] \end{bmatrix} \tag{14.11}$$

From Eq. (14.11), the computation of Δf_1 for the upper and lower bounds $\bar{X}_1$, $\underline{X}_1$ of X_1 can lead to the upper and lower bounds of Δf_1.

14.4.3 Interval Analysis Considering Non-Monotonic Property of Objective Function

In the method explained in the previous sections, the monotonic property of the objective function has been assumed. In other words, it was assumed that the maximum and minimum values of the objective function can be obtained at the end points of interval parameters. Furthermore, when the level of uncertainty is large, the approximation by Taylor series expansion may lead to large errors. In this section a method to overcome this difficulty will be shown.

If the critical combination of interval parameters maximizing the objective function can be predicted, it becomes possible to evaluate the robustness accurately. In this section, the Taylor series approximation with diagonal elements only is used to predict this critical combination.

As for the variation $\Delta f_i(dX_i)$ for X_i, let us regard $dX_i = X_i - X_i^c$ as a variable satisfying $-\Delta\underline{X}_i \le dX_i \le \Delta\bar{X}_i$. Then the variation $\Delta f_i(dX_i)$ can be expressed as

$$\Delta f_i(dX_i) = \frac{1}{2} f_{,X_iX_i}\left(dX_i + f_{,X_i}/f_{,X_iX_i}\right)^2 - f_{,X_i}^2/2f_{,X_iX_i} \tag{14.12}$$

This function is different from the function defined in Eq. (14.10). However, the same expression is used for simplicity. The function of Eq. (14.12) is a quadratic function and the value dX_i maximizing or minimizing Δf can be obtained explicitly. Consider the case $f_{,X_iX_i} < 0$. If the notation $\Delta\bar{X}_i = \Delta\underline{X}_i = \Delta X_i$ is used, the interval parameter giving $\max[\Delta f_i]$ can be obtained as follows:

$$\hat{X}_i = \begin{cases} X_i^c - f_{,X_i}/f_{,X_iX_i} & \left(\left|f_{,X_i}/f_{,X_iX_i}\right| \le \Delta X_i\right) \\ X_i^c + \Delta X_i & \left(-f_{,X_i}/f_{,X_iX_i} \ge 0,\ \left|f_{,X_i}/f_{,X_iX_i}\right| > \Delta X_i\right) \\ X_i^c - \Delta X_i & \left(-f_{,X_i}/f_{,X_iX_i} < 0,\ \left|f_{,X_i}/f_{,X_iX_i}\right| > \Delta X_i\right) \end{cases} \tag{14.13}$$

In order to determine dX_i from Eq. (14.13), it is necessary to evaluate the gradient $f_{,X_i}$ and Hessian (diagonal terms only) $f_{,X_iX_i}$. In computing $f_{,X_i}$ and $f_{,X_iX_i}$, the evaluation is usually made ordinary at the nominal model (reference point). It should be noted that the correlation among interval parameters is not taken into account.

In this chapter, a new method called the URP method is used. This method updates the reference point step-by-step. The algorithm for finding the upper bound of the objective function may be stated as follows:

Step 1 Compute the gradients $f_{,X_i}$ $(i = 1, \ldots, N_x)$ at the nominal model.

Step 2 Reorder the absolute values of the gradients $\left|f_{,X_i}\right|$ $(i = 1, \ldots, N_x)$ from the largest one. The corresponding interval variables are defined by $\mathbf{X}_\mathrm{A} = \{X_{\mathrm{A}1}, \ldots, X_{\mathrm{A}N_x}\}$. This procedure makes it possible to find the effective interval variables $\mathbf{X}$ affecting the objective function f.

Step 3 Compute the second-order sensitivities $f_{,X_{Ak}X_{Ak}}$ corresponding to X_{A_k}. For $k = 1$, the evaluation point is the reference point (nominal model). For $k \ge 2$, the evaluation point has been changed to an updated one. Then recompute $f_{,X_{Ak}}$ corresponding to X_{A_k}.

Step 4 Obtain $\hat{X}_{A_k}$ maximizing $\Delta f_k(X_{A_k})$.

Step 5 Update the interval; variable from X_{A_k} to $\hat{X}_{A_k}$ and update the evaluation (reference) point. Update also the damping and stiffness matrices $\mathbf{C}$, $\mathbf{K}$.

Step 6 Set $k = k + 1$ and repeat Steps 3–6 until $k = N_x$.

Step 7 After updating all the interval variables following the aforementioned procedure, conduct the response analysis for this model.

In case of finding the lower bound of the objective function, it is sufficient to find $\hat{X}_{A_k}$ minimizing $\Delta f_k(X_{A_k})$ in Step 4 and update the reference point. In the URP method, the interval variables corresponding to the upper and lower bounds of the

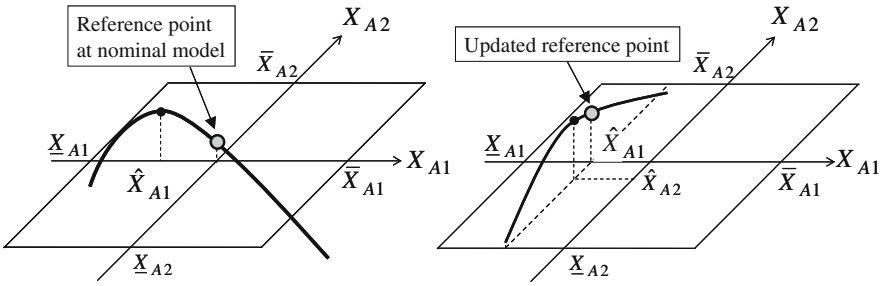

Fig. 14.4 Outline of URP method [10]

objective function are different. Therefore, the computational time in the URP method becomes about triple of that in Sect. 14.4.2. The overview of the URP method is shown in Fig. 14.4.

14.5 Numerical Verification of URP Method

Application of the URP method to the base-isolated building model treated in Sect. 14.2 is shown in this section. The usefulness of the URP method is demonstrated through the comparison with other methods (first-order Taylor approximation, second-order Taylor approximation, exact). The exact solution is replaced by the one obtained by using the SQP method. The SQP method does not necessarily provide the true exact one. However, it is regarded that a nearly or approximate exact solution can be found by the SQP by changing initial values.

The damping coefficient c_0 and the horizontal stiffness k_0 of the base-isolation story and the damping coefficient $\mathbf{c}_\mathrm{f}$ and the horizontal stiffness $\mathbf{k}_\mathrm{f}$ of the superstructure are treated as interval variables in this example. The set of interval variables is denoted by

$$\mathbf{X}^I = \left\{c_0^I, k_0^I, \mathbf{c}_\mathrm{f}^I, \mathbf{k}_\mathrm{f}^I\right\} \tag{14.14}$$

It may be appropriate to assign the same variability in each group of several stories in a building. The present formulation is applicable to such realistic case. Let us define the ratios of the upper and lower variations of interval variables to the corresponding nominal values as follows:

$$\bar{\alpha} = \left\{\frac{\Delta\bar{c}_0}{c_0^c}, \frac{\Delta\bar{k}_0}{k_0^c}, \frac{\Delta\bar{c}_{\mathrm{f}_1}}{c_{\mathrm{f}_1}^c}, \ldots, \frac{\Delta\bar{k}_{\mathrm{f}_1}}{k_{\mathrm{f}_1}^c}, \ldots\right\}, \quad \underline{\alpha} = \left\{\frac{\Delta\underline{c}_0}{c_0^c}, \frac{\Delta\underline{k}_0}{k_0^c}, \frac{\Delta\underline{c}_{\mathrm{f}_1}}{c_{\mathrm{f}_1}^c}, \ldots, \frac{\Delta\underline{k}_{\mathrm{f}_1}}{k_{\mathrm{f}_1}^c}, \ldots\right\} \tag{14.15a, b}$$

Table 14.1 Parameters of base-isolated building [10]

	Super-building	Base-isolation story
Mass ($\times 10^3$ kg)	1,024	3,072
Stiffness (N/m)	Eq. (14.16)	5.81×10^7
Damping coefficient (Ns/m)	Stiffness-proportional: lowest-mode damping ratio = 0.02	1.48×10^7

14.5.1 Property of Base-Isolated Building

Table 14.1 shows the parameters (superstructure and base-isolation story) of the 20-story base-isolated building ($N = 20$). The floor mass per story is $1{,}024 \times 10^3$ (kg). This corresponds to 32×32 m floor plan (1,000 kg/m^2). When the floor mass per story is denoted by m and the lowest mode of vibration of the super-building with fixed base-isolation story is given by a straight line, then the story stiffness can be expressed as

$$k_{f_i} = \frac{1}{2}\{N(N+1) - i(i-1)\}m\omega_1^2 \quad (i = 1, \ldots, N) \tag{14.16}$$

where ω_1 is the fundamental natural circular frequency of the super-building with fixed base-isolation story and is given by 3.93 rad/s (natural period = 1.6 s). The super-building is assumed to behave elastically.

The horizontal stiffness of the base-isolation story is given by specifying the natural circular frequency of the model with the rigid super-building as $\omega_0 = 1.57$ (natural period = 4.0 s). Then the horizontal stiffness of the base-isolation story k_0 is determined by

$$k_0 = \omega_0^2 W_E \tag{14.17}$$

For this model, the fundamental natural circular frequency is given by 1.5 rad/s (natural period = 4.19 s).

In the selection of the base isolator, the diameter, thickness, and shear modulus have to be determined. The required conditions are that (1) the stress under dead load is within an allowable value and (2) the deformation capacity and the fundamental natural period are appropriate. In the present numerical analysis, the horizontal stiffness of the base-isolation story is given by Eq. (14.17). Therefore it is required to satisfy the condition on the stress under dead load. When NRBs are used, the horizontal stiffness of the base-isolation story is determined by

$$k_0 = A_R G / T_R \tag{14.18}$$

where A_R, T_R, and G denote the cross-sectional area, the thickness, and shear modulus of the isolator. By equating Eqs. (4.17) and (4.18), the stress of the isolator under dead load can be expressed as

$$\sigma_R = gGT_R/\omega_0^2 \tag{14.19}$$

where g denotes the acceleration of gravity. By substituting $T_R = 0.2\,(\mathrm{m})$ and $G = 0.49(\mathrm{N/mm^2})$ in Eq. (14.19), $\sigma_R = 9.74\ (\mathrm{N/mm^2})$ can be derived. This is smaller than an allowable stress under dead load of ordinary NRBs. At the same time, the cross-sectional area of the isolators can be obtained from Eq. (14.18). In this example, the diameter of the isolators is given by ϕ 1,300 and 20 isolators are installed.

The damping coefficient of the dampers in the base-isolation story is given by specifying the damping ratio of the model with a rigid super-building as 0.2.

14.5.2 Input Ground Motions

Five ground motions are used in this example. Four recorded ground motions and one simulated motion both scaled to the same maximum ground velocity = 0.5 m/s are taken. Table 14.2 shows the parameters of the adopted five ground motions (ground motion number 1–5) and Fig. 14.5 presents those time histories.

14.5.3 Interval Analysis for Interstory Drift of Base-Isolation Story

The uncertainty analysis is shown here for the maximum interstory drift of base-isolation story. The level of variability in Eq. (14.15a, b) is given by

$$\bar{\alpha} = \begin{cases} 0.3 & (i=1) \\ 0.26 & (i=2) \\ 0.1 & (i=3,\ldots,N+2) \\ 0.05 & (i=N+3,\ldots,2N+2) \end{cases}, \quad \underline{\alpha} = \begin{cases} 0.3 & (i=1) \\ 0.15 & (i=2) \\ 0.1 & (i=3,\ldots,N+2) \\ 0.05 & (i=N+3,\ldots,2N+2) \end{cases} \tag{14.20a, b}$$

In Eq. (14.20a, b), i denotes the interval variable number. $i = 1$ corresponds to the damping coefficient of oil dampers in the base-isolation story and $i = 2$ corresponds to the horizontal stiffness k_0 of the base-isolation story. Here k_0 is treated as unsymmetrical in increasing and decreasing directions. This is due to the aging effect (hardening) of isolators [2]. Furthermore, $i = 3,\ldots,N+2$ corresponds to the damping coefficients $\mathbf{c}_\mathrm{f}$ of the super-building and $i = N+3,\ldots,2N+2$ corresponds to the story stiffness $\mathbf{k}_\mathrm{f}$ of the super-building.

Table 14.2 Properties of input ground motions [10]

	El Centro (1940)	Taft (1952)	Hachinohe (1968)	Tomakomai (2003)	BCJ L2
Maximum ground acceleration (m/s^2)	4.59	5.07	3.32	0.90	2.41
Ground motion no.	1	2	3	4	5

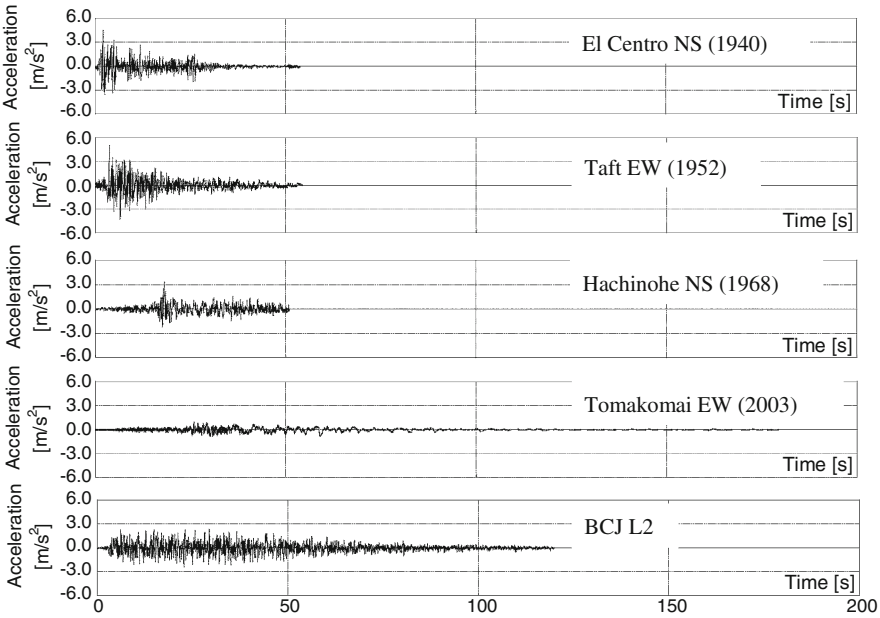

Fig. 14.5 Ground acceleration of input motions (maximum velocity = 0.5m/s) [10]

Figure 14.6 shows the results, i.e., the upper and lower bounds of the maximum interstory drift of base-isolation story, of interval analysis by various methods (first-order Taylor approximation, second-order Taylor approximation, URP method, exact). It can be observed that the result by the URP method coincides fairly well with the exact value and this indicates the usefulness and reliability of the URP method. From Fig. 14.6, it is also seen that, since Tomakomai motion (ground motion number 4) includes large components of long-period motion, the response is larger than those for other ground motions. Furthermore, the maximum interstory drift of base-isolation story becomes about 0.5 m when considering the variability of structural parameters and this value may exceed the upper limit. On the other hand, for other ground motions, the maximum interstory drift of base-isolation story does not exhibit much difference in the nominal model. However, it is also true that the level of variability of the response results due to the variability

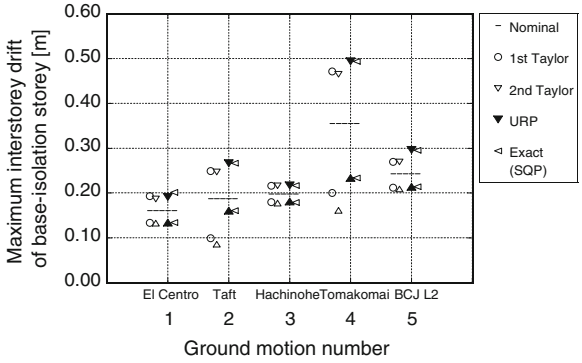

Fig. 14.6 Prediction of upper and lower bounds of maximum interstory drift of base-isolation story to five ground motions by various methods [10]

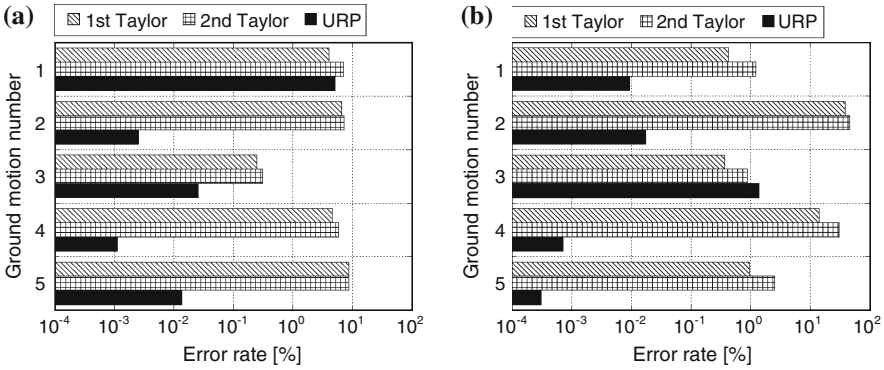

Fig. 14.7 Computational errors by various methods for maximum interstory drift of base-isolation story for five ground motions, **a** upper bound, **b** lower bound [10]

of structural parameters shows different properties depending on ground motions (ground motion number 1–3, 5). This may result from the fact that the effect of variability of structural properties is correlated complicatedly with the frequency contents of ground motions.

The accuracies of various interval analysis methods are compared. Figure 14.7 presents the errors of each method to the exact value. The difference of the result by each method from the exact value is divided by the exact value and the result is plotted in logarithmic scale. Although it may be said that the first-order and second-order Taylor expansion methods can simulate the upper and lower bounds approximately, the error attains 10 % in some ground motions. On the other hand, the error of the URP method is within 0.1 % in most cases and the maximum is within several percent at largest.

Figure 14.8 indicates the distribution of interval parameters for the second-order Taylor expansion, the URP method, and the exact value. The abscissa

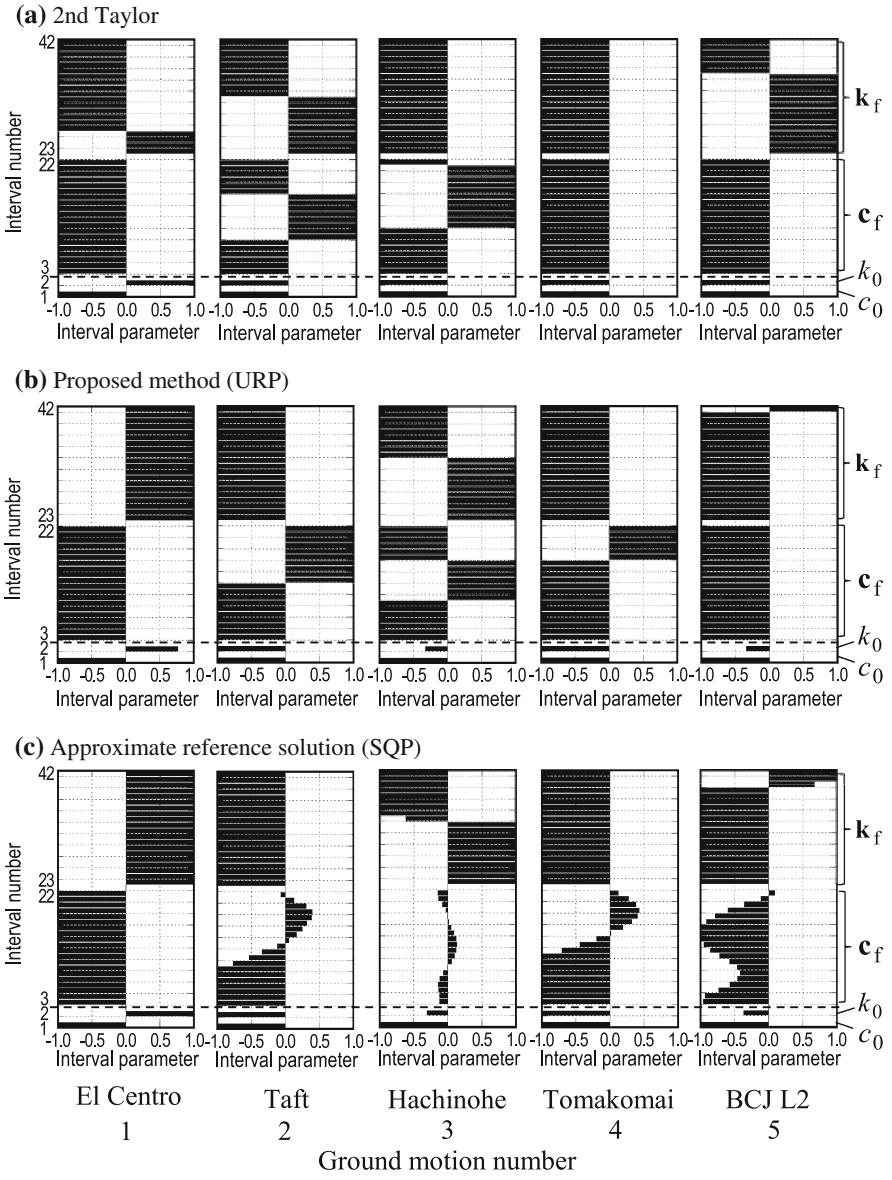

Fig. 14.8 Critical combination of uncertain parameters for maximum interstory drift of base-isolation story [10]

indicates the ratio of variability of interval parameters to the nominal value (-1 means the lower bound of interval parameter and 1 indicates the upper bound of interval parameter). On the other hand, the ordinate presents the interval parameter number defined in Eq. (14.14). $i = 1$ corresponds to the damping

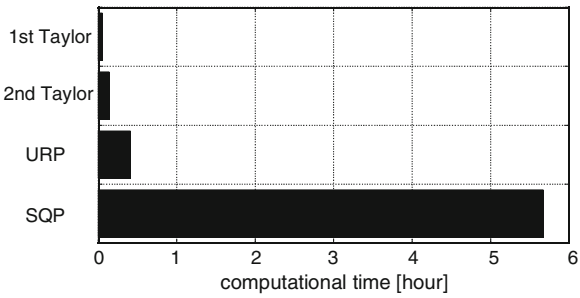

Fig. 14.9 Comparison of computational times by various methods [10]

coefficient of oil dampers in the base-isolation story and $i = 2$ corresponds to the horizontal stiffness k_0 of the base-isolation story. Furthermore, $i = 3, \ldots, 22$ corresponds to the damping coefficients $\mathbf{c}_f$ of the super-building and $i = 23, \ldots, 42$ corresponds to the story stiffness $\mathbf{k}_f$ of the super-building.

In the interval analysis method using the second-order Taylor expansion, the variation of the objective functions is evaluated for various combinations of end points of interval variables. For this reason, the critical interval parameters by the second-order Taylor expansion do not attain intermediate values between the upper and lower bounds of interval parameters. On the other hand, the critical interval parameters by the URP method and the exact value could exhibit intermediate values due to the non-monotonic properties of the objective function. It can be observed that the critical parameter of the damping coefficient of the base-isolation story corresponds to the lower bound of the interval parameter. On the other hand, the critical parameter of the horizontal stiffness of the base-isolation story can exist in intermediate regions for ground motions 1, 3, and 5. The results for ground motions 3 and 5 coincide fairly well with the exact value shown in Fig. 14.8c. Although some critical parameters in the super-building by the URP method are different from the exact one, this effect on the maximum interstory drift of base-isolation story is negligible. This means that the effect of the horizontal stiffness of the base-isolation story and the damping coefficient of the base-isolation story is significant.

Figure 14.9 shows the comparison of the computational times by various methods. The SQP method (approximately exact) depends largely on the initial values. Although the URP method requires slightly longer computational time compared to the first- and second-order Taylor series expansion methods, it may be said that the URP method can provide a reasonably accurate result with a reasonable computational time.

14.5.4 Interval Analysis for Top-Story Maximum Acceleration

Figure 14.10 presents the results, i.e., the upper and lower bounds of the maximum top-story floor acceleration, of interval analysis by various methods (first-order Taylor approximation, second-order Taylor approximation, URP method, exact).

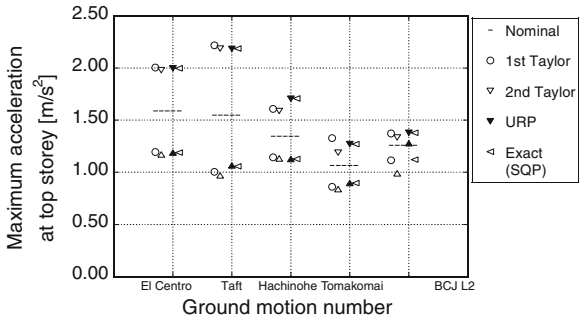

Fig. 14.10 Prediction of upper and lower bounds of maximum acceleration at top story to five ground motions by various methods [10]

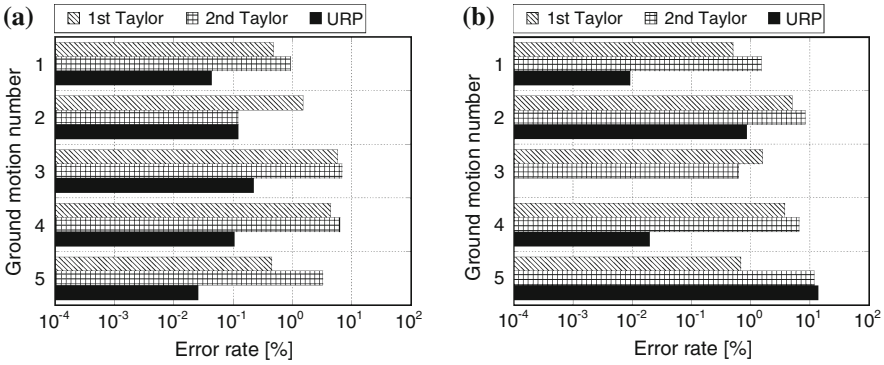

Fig. 14.11 Computational errors by various methods for maximum acceleration at top story for five ground motions, **a** upper bound, **b** lower bound [10]

It can be observed from Fig. 14.10 that the level of variability of the maximum value into the increasing side is the largest in ground motion number 2 and the ratio of that value to the nominal response is 1.43. There is no remarkable difference by any method for ground motion number 2. However, the first- and second-order Taylor approximations exhibit a smaller upper bound for some ground motions. On the other hand, the URP method provides a rather accurate evaluation. This indicates the usefulness and reliability of the URP method.

Figure 14.11a and b shows the errors of each method to the exact value as in Fig. 14.7. It can be observed that the error of the URP method is within 0.1 % in most cases of ground motions. For ground motion number 3 in Fig. 14.11b, the critical combination by the second-order Taylor approximation coincides perfectly with the exact result.

Figure 14.12 indicates the distribution of interval parameters for the second-order Taylor expansion, the URP method, and the exact value. It can be confirmed that the critical distribution by the URP method coincides well with that by the exact one. Figure 14.12b and c demonstrates that, since the URP method provides

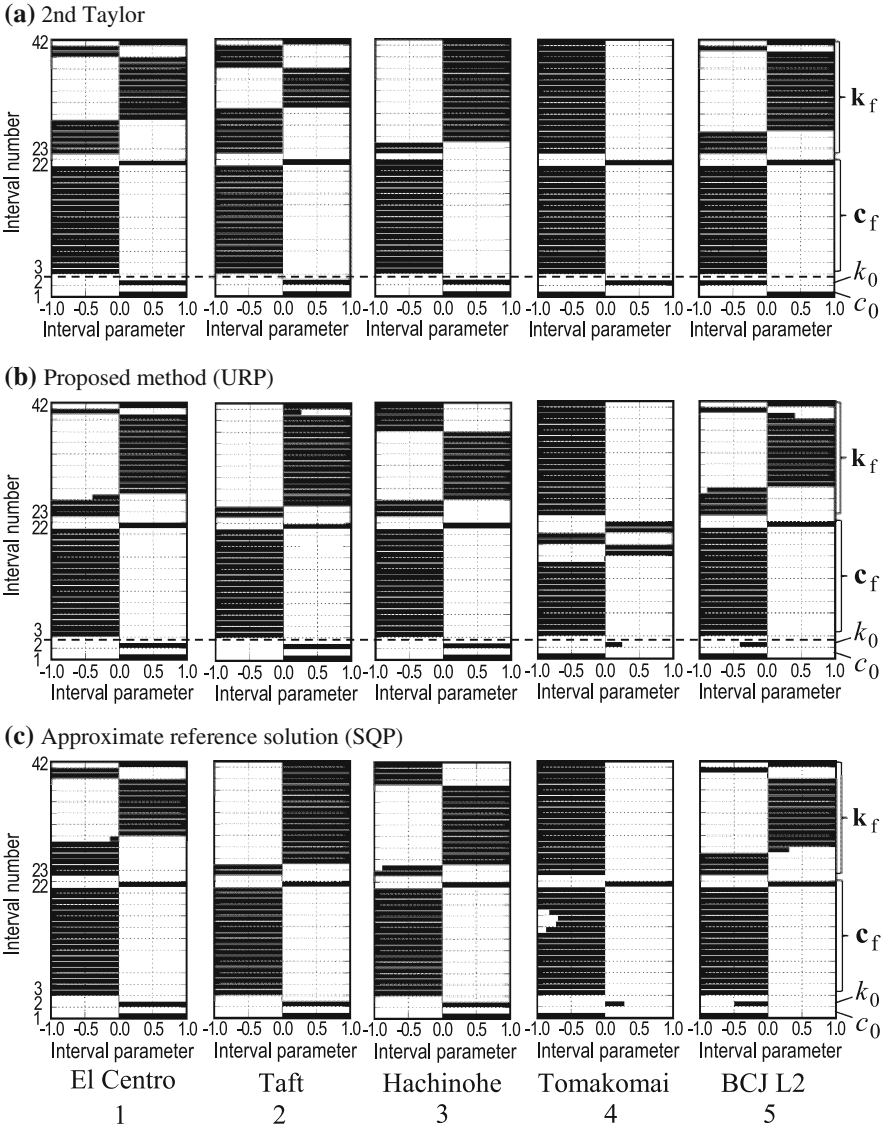

Fig. 14.12 Critical combination of uncertain parameters for maximum interstory drift of base-isolation story [10]

an accurate combination of critical parameters for the horizontal stiffness and damping coefficient of the base-isolation story, the URP method is reliable even for the maximum top-story floor acceleration.

While, in usual structural design of base-isolated buildings, the variability of base-isolation systems is often taken into account, the variability of super-building

parameters is not considered. As for the horizontal displacement of the base-isolation story, the variability of the base-isolation systems is essential. On the other hand, for the interstory drifts in super-buildings and top-story acceleration, the variability of super-building parameters is also significant. Therefore a detailed examination should be made carefully.

14.6 Summary

1. An efficient interval analysis methodology for robustness evaluation of a base-isolated building has been presented to find the upper and lower bounds of the dynamic response under several ground motions by using second-order Taylor series expansion. The objective function is defined by the maximum interstory drift of the base-isolation story or the maximum acceleration at the top story. Since the critical combination of interval parameters in a feasible domain, not only on the bounds but also in an inner domain of interval parameters, has been derived explicitly by evaluating the extreme value of the objective function via second-order Taylor series expansion, the upper and lower bounds of the objective function can be obtained straightforwardly for the predicted structural parameter set.
2. To evaluate the upper and lower bounds of the objective function more accurately within a reasonable task, a different method has been presented even for large intervals. The method is the URP method, where the reference point to calculate first- and second-order sensitivities has been updated according to the variation of structural parameters. By comparing the results by the proposed methodology with those by other methods, it has been shown that a more accurate solution of the bound of the objective function can be derived by the URP method.
3. Since several ground motions have been used as input motions, numerical sensitivities have to be used in the URP method. It has been demonstrated that this procedure can be feasible. By using these numerical sensitivities, the objective function can also be approximated by second-order Taylor series expansion including full elements. The SQP method has been applied to find the upper and lower bounds of the objective function by second-order Taylor series expansion with full elements.
4. Numerical examples of the robustness evaluation have been presented for a 20-story base-isolated shear building by applying the URP method, the method using first-order Taylor series expansion, the method using second-order Taylor series expansion with diagonal elements only (method due to Chen et al. [14]), the method using second-order Taylor series expansion with full elements solved by the SQP method, and the primitive interval analysis method.
5. Comparison of computational time for the robustness analysis by the explained methodology with those by various other methods has been conducted. It has been shown that, since the second-order Taylor series expansion is used in the

explained methodology to obtain a more accurate critical combination of interval parameters efficiently, the number of times for the response analysis can be reduced dramatically.

6. As for the maximum interstory drift of the base-isolation story, the long-period ground motion becomes a key input which amplifies the response of the nominal model. This is because the variation of natural period due to the change of structural parameters affects the response at base-isolation story sensitively. The critical response becomes 1.39 times the response of the model with nominal parameters to Tomakomai (2003).
7. As for the maximum acceleration at the top story, the response variation tends to become large to the ground motion with a large value of maximum ground acceleration. The critical response becomes 1.43 times the response of the model with nominal parameters to Taft (1952). It is often the case that a larger stiffness of the base-isolation story causes a larger value of maximum ground acceleration.

References

1. Architectural Institute of Japan (2001) Recommendation for design of base isolated buildings
2. Japan Society of Seismic Isolation (JSSI) (2010) Base-isolated structures—from fundamentals to design and practice (in Japanese)
3. Higashino M, Wada A (2009) A study on seismic isolation system with robustness for increasing ground motion level. J Struct Constr Eng 641:1233–1240 (in Japanese)
4. Takewaki I (2008) Robustness of base-isolated high-rise buildings under code-specified ground motions. Struct Design Tall Spec Buildings 17:257–271
5. Zhao Y, Ono T, Suzuki M (1997) Dynamic structural reliability evaluation considering parameter uncertainties. J Struct Constr Eng 497:33–38 (in Japanese)
6. Ben-Haim Y, Elishakoff I (1990) Convex models of uncertainty in applied mechanics. Elsevier, Amsterdam
7. Kanno Y, Takewaki I (2005) Approximation algorithm for robustness functions of trusses with uncertain stiffness under uncertain forces. J Struct Constr Eng 591:53–60 (in Japanese)
8. Ben-Haim Y (2001) Information-gap decision theory: decisions under severe uncertainty. Academic, San Diego
9. Takewaki I, Ben-Haim Y (2005) Info-gap robust design with load and model uncertainties, special issue: uncertainty in structural dynamics. J Sound Vib 288(3):551–570
10. Fujita K, Takewaki I (2011) Earthquake response bound analysis of uncertain base-isolated buildings for robustness evaluation. J Struct Constr Eng 666:1453–1460 (in Japanese)
11. Rao S, Berke L (1997) Analysis of uncertain structural systems using interval analysis. AIAA Journal 34(4):727–735
12. Qiu Z, Elishakoff I (1998) Antioptimization of structures with large uncertain-but-nonrandom parameters via interval analysis. Comput Methods Appl Mech Eng 152:361–372
13. Qiu Z, Chen S, Song D (1996) The displacement bound estimation for structures with an interval description of uncertain parameters. Commun Numer Methods Eng 12:1–11
14. Chen S, Ma L, Meng G, Guo R (2009) An efficient method for evaluating the natural frequency of structures with uncertain-but-bounded parameters. Comput Struct 87:582–590

Chapter 15
Future Directions

15.1 Earthquake Resilience

The word "resilience" may imply different meanings in each specific situation. In the engineering aspect, it represents the positive ability of a system to adapt itself to the consequences of a catastrophic failure caused by natural hazards (disasters), terrorism attacks or system faults, and so on. The Committee on National Earthquake Resilience Research, Implementation, and Outreach [1] defines resilience as "The capability of an asset, system, or network to maintain its function or recover from a terrorist attack or any other incident" [2].

Resilience is also defined as the capacity of a system, community, or society potentially exposed to hazards to adapt, by resisting or changing in order to reach and maintain an acceptable level of functioning and structure [3]. This is determined by the degree to which the social system is capable of organizing itself to increase this capacity for learning from past disasters for better future protection and to improve risk reduction measures.

Similarly, resilience is defined by the MCEER [4] as the ability of social units (e.g., organizations, communities) to mitigate risk and contain the effects of disasters, and carry out recovery activities in ways that minimize social disruption while also minimizing the effects of future disasters. Disaster Resilience may be characterized by reduced likelihood of damage to and failure of critical infrastructure, systems, and components; reduced injuries, lives lost, damage, and negative economic and social impacts; and reduced time required to restore a specific system or set of systems to normal or pre-disaster levels of functionality [4].

The catastrophic failure is generally followed by "progressive collapse." The progressive collapse is defined in Ref. [5, 6].

Spread of local damage, from an initiating event, from element to element resulting, eventually, in the collapse of an entire structure or a disproportionately large part of it; also known as disproportionate collapse (based on ASCE 7-05).

I. Takewaki et al., *Improving the Earthquake Resilience of Buildings*,
Springer Series in Reliability Engineering, DOI: 10.1007/978-1-4471-4144-0_15,

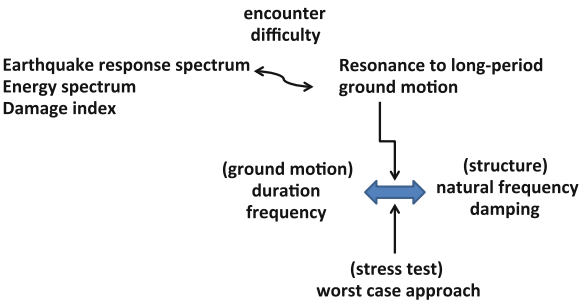

Fig. 15.1 Difficulty of conventional approaches in resonance of structures to *long-period* strong ground motions and role of worst case approach

15.2 Improving Earthquake Resilience Based on Redundancy and Robustness

It is well recognized that "redundancy" and "robustness" are two major concepts playing a central role in the upgrade of earthquake resilience [7–12]. To investigate the redundancy and robustness, various examinations are necessary. One of the effective examinations is the worst case approach [13–16]. The stress test in nuclear power plant facilities may be one of the examinations.

15.3 Resonant Response and Random Response

In the seismic resistant design of structures, the 2011 off the Pacific coast of Tohoku earthquake has shed light on a new structural design aspect, particularly for high-rise buildings [17]. Specifically, Takewaki et al. [17] have reported that a resonance phenomenon of high-rise buildings with long-period ground motions was observed during the 11 March 2011 off the Pacific coast of Tohoku earthquake. These authors concluded that the conventional methods of seismic loads specification, such as, the response spectrum method, the energy spectrum, and damage indexes, may have some difficulties in dealing with such resonance phenomenon. Uncertainties of duration and frequency in ground motions and those of natural frequency and damping in structures have properties different from those for random-type earthquake ground motions. With these uncertainties in mind, the worst case approach may provide a useful and effective tool for earthquake load specification for tall structures [18, 19]. Figure 15.1 explains schematically the limitation of conventional approaches in resonance of structures to long-period strong ground motions and the use of the worst case approach in this situation.

Figure 15.2 (Fig. 2.16) illustrates the comparison of the sensitivity of the response amplification of structures in the resonant case and nonresonant case with respect to damping reduction. It is useful to note that the amplification by damping can be expressed by

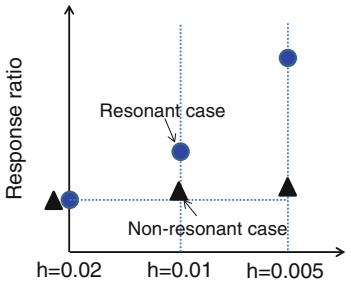

Fig. 15.2 Sensitivity of the response amplification for *high-rise* buildings in the resonant case and nonresonant case with respect to the value of the damping ratio

$$1/2h \quad \text{for resonant long-period ground motion} \tag{15.1a}$$

$$1.5/(1+10h) \quad \text{for non-resonant conventional ground motion (ratio to } h=0.05) \tag{15.1b}$$

This implies the high sensitivity of the structural response to damping in resonant long-period ground motions. Since the damping ratio in super high-rise buildings is generally small (smaller than 0.02) compared to low- and mid-rise buildings, this high sensitivity needs to be taken into consideration in the structural design of tall structures.

There is a report that a 55-story super high-rise building in Osaka [height = 256 m: $T_1 = 5.8$ s (long-span direction), 5.3 s (short-span direction)] was shaken severely regardless of the fact that Osaka is located about 800 km from the epicenter (about 600 km from the boundary of the fault region) and the JMA instrumental intensity was 3 in Osaka. Afterwards, the natural periods of the building were found to be longer than the design values reflecting the flexibility of pile-ground systems and the damage to nonstructural partition walls, etc. It should be pointed out that the level of velocity response spectra of ground motions observed here (first floor) is almost the same as that at the Shinjuku station (K-NET) in Tokyo and the top-story displacements are about 1.4 m (short-span direction) and 0.9 m (long-span direction). Figure 15.3 shows the ground acceleration, ground velocity, and top-story displacement recorded or numerically integrated in this building. It can be observed that a clear resonant phenomenon occurs during about eight cycles. It seems that such clear observation has never been reported in super high-rise buildings all over the world. This implies the need for consideration of long-period ground motions in the seismic resistant design of super high-rise buildings in mega cities even though the site is far from the epicenter.

Figure 15.4 illustrates the total input energy from the ground motion at Osaka bay area (NS) during the 2011 off the Pacific coast of Tohoku earthquake for various damping ratios together with the corresponding energy spectrum.

Figure 15.5 shows the mechanism of increase of credible bound of input energy [10] for the velocity power constraint due to uncertainties in input excitation duration (lengthening) and in structural damping ratio (decrease). As for

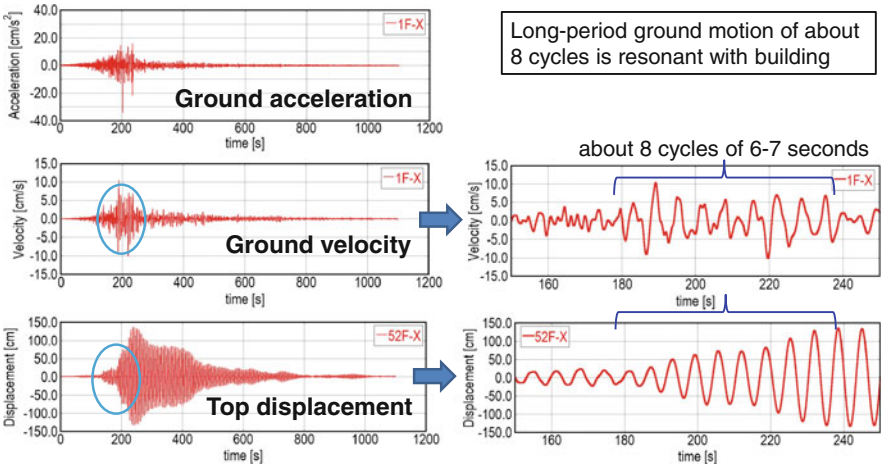

Fig. 15.3 Ground acceleration, velocity, and top-story displacement of a 55-story building in Osaka

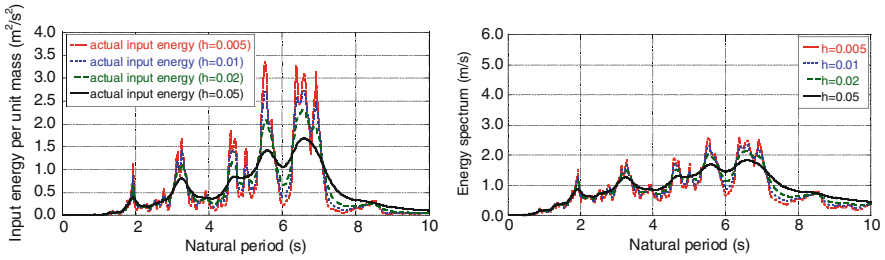

Fig. 15.4 Total earthquake input energy from ground motion at Osaka bay area (NS) for various damping ratios and energy spectrum

uncertainties in excitation predominant period and in natural period of a structure, the resonant case is critical.

15.4 Robustness Function for Seismic Performance

The convex models of uncertainty [20–22] and information-gap (info-gap) models of uncertainty developed by Ben-Haim provide a nonconventional approach for handling uncertainties compared to the probabilistic analysis of uncertainties using the probability theory. In the info-gap model [7], the uncertain structural parameters are assumed to be given by an interval model. The interval parameter X^I is defined by

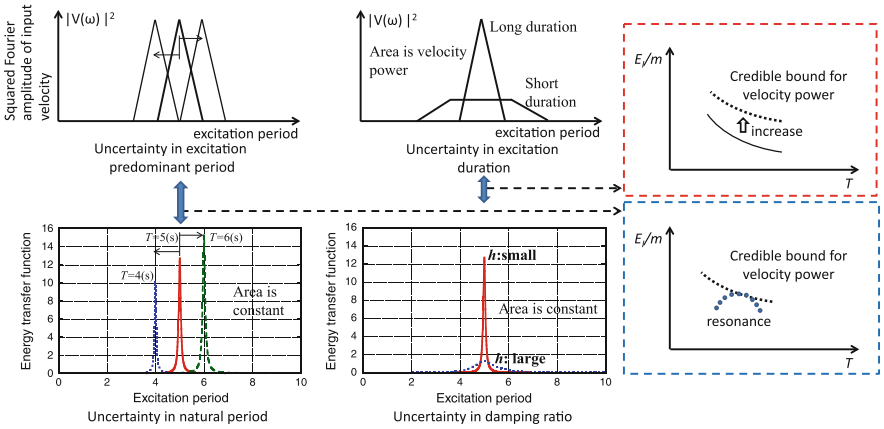

Fig. 15.5 Increase of credible bound of input energy for velocity power constraint due to lengthening of input excitation duration and *decrease* of damping ratio of structure

$$\mathbf{X}^I = \left\{ X_i^I \middle| [X_i^c - \Delta X_i, X_i^c + \Delta X_i], \quad i = 1, \ldots, N \right\} \tag{15.2}$$

In Eq. (15.2), $(\quad)^I$ and $[a\ b]$ denote the definition of an interval parameter where a and b are the lower and upper bounds of the interval parameter, respectively. Furthermore, $(\quad)^c$, $\Delta(\quad)$ and N denote the nominal value of an interval parameter, half the varied range of the interval parameter, and the number of interval parameters, respectively. When the uncertainty of structural parameters is given by the interval vector, the feasible domain of the interval parameters is constrained to an N-dimensional rectangle.

In the info-gap model, the level of uncertainty is defined by a single uncertain parameter α. Based on the definition of an uncertain parameter α in the info-gap model, the feasible domain of the interval parameter $\mathbf{X}^I$ can be regarded as an uncertainty set $\mathbf{X}^I(\alpha) \in R^N$ described by

$$\mathbf{X}^I(\alpha) = \left\{ X_i^I \middle| [X_i^c - \alpha\Delta X_i, X_i^c + \alpha\Delta X_i], \quad i = 1, \cdots, N \right\} \tag{15.3}$$

In Eq. (15.3), ΔX_i is a prescribed value of half the varied range of the interval parameters. Therefore, the uncertainty level of the uncertainty set $\mathbf{X}^I(\alpha)$ varies according to the variation of uncertain parameter α. Figure 15.6 shows the variation of 2D interval model with an uncertain parameter α. When $\alpha = 0$, the uncertainty set $\mathbf{X}^I(0)$ corresponds to a nominal vector of structural parameters.

The robustness function $\hat{\alpha}$ for the design constraint of the seismic performance can be defined as,

$$\hat{\alpha}(\mathbf{X}^c, f_c) = \max\{\alpha | f \leq f_c, \quad f \in U(\mathbf{X}^c, \alpha)\} \tag{15.4}$$

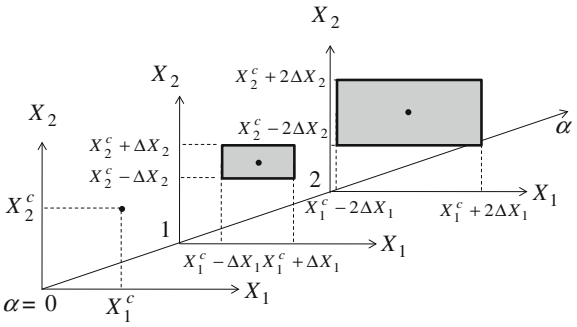

Fig. 15.6 Variation of uncertainty set of interval model

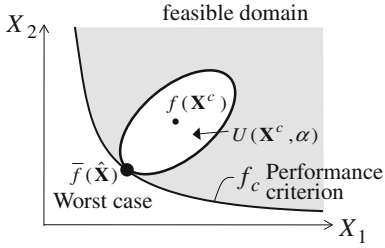

Fig. 15.7 Robustness function for a performance criterion

where f, f_c and $U(\mathbf{X}^c, \alpha)$ denote the objective function, the performance criterion value and the set of the possible structural responses in the domain of the uncertainty set $\mathbf{X}^I(\alpha)$. In Eq. (15.4), the robustness function $\hat{\alpha}$ is the maximum value of the uncertain parameter α which satisfies the performance criterion. If the nominal value $f(\mathbf{X}_c)$ of the objective function violates f_c or just coincides with f_c without considering a safety factor, the robustness function $\hat{\alpha}$ is regarded as zero, which means that no variability due to the uncertainty of structural parameters can be allowed. In the case of $\hat{\alpha}_1(\mathbf{X}_1^c, f_c) > \hat{\alpha}_2(\mathbf{X}_2^c, f_c)$, a design more robust than $\mathbf{X}_2^c$ can be achieved by $\mathbf{X}_1^c$.

Figure 15.7 illustrates the relationship between the robustness function and the allowable domain of structural design to satisfy the performance criterion f_c for 2D interval parameters. The robustness function $\hat{\alpha}$ is derived as the worst case of the objective function, for example, the upper bound of the objective function $\bar{f}$ in $U(\mathbf{X}^c, \hat{\alpha})$. However, when the number of the combinations of uncertain parameters is huge, it may be a hard task to evaluate the worst case of the objective function reliably. For this reason, an efficient uncertainty analysis method is desired which can evaluate the upper bound of the objective function considering the uncertainty of the structural parameters accurately and reliably.

The uncertainty of the structural response results from uncertainties involved in the seismic load and variability in the structural properties. As is well known, the uncertainty in the seismic load is relatively high compared to that in the structural properties. To minimize the uncertainty in the structural response or to achieve the

most accurate structural response, the structural engineer needs to accurately model uncertainties in the earthquake loads, and the structural model describing the behavior of the structure under seismic loads. Future research needs to focus more on large structures, to include effects of nonstructural elements on the structural response and to investigate the implication of different nonlinear models and damping models on the structural response.

A different problem that has emerged during the last decade owing to the accumulation of seismic data from recording networks (e.g. K-NET, KiK-net, COSMOS, PEER, SMART arrays, Guerrero Network) which was not considered in this book, is the selection and scaling of a proper earthquake records from a given large set of ground motions for a specific site and a given structure.

References

1. Committee on National Earthquake Resilience Research, Implementation, and Outreach (2011) Committee on seismology and geodynamics, national research council, national earthquake resilience: research, implementation, and outreach. The National Academy's Press, Washington
2. DHS (US Department of Homeland Security) (2006) National infrastructure protection program. Available at www.fas.org/irp/agency/dhs/nipp.pdf. Accessed 1 Jan 2012
3. UN ISDR (United Nations International Strategy for Disaster Reduction) (2006) Hyogo framework for action 2005–2015: Building the resilience of nations and communities to disasters. Extract from the final report of the world conference on disaster reduction (A/CONF.206/6), 16 Mar 2005. Available at www.unisdr.org/we/coordinate/hfa. Accessed 1 Jan 2012
4. MCEER (Multidisciplinary Center for Earthquake Engineering Research) (2008) MCEER research: enabling disaster-resilient communities. *Seismic waves*, Nov, pp. 1–2. Available at www.nehrp.gov/pdf/SeismicWavesNov08.pdf. Accessed 1 Jan 2012
5. Marjanishvili SM (2004) Progressive analysis procedure for progressive collapse. J Perf Construct Facil, ASCE 18(2):79–85
6. National Institute of Standard and Technology(NIST) (2007) Best practices for reducing the potential for progressive collapse in buildings. NISTIR 7396. Gaithersburg, MD
7. Ben-Haim Y (2002) Info-gap decision theory: decisions under severe uncertainty, 1&2 edn. Academic, London
8. Bertero RD, Bertero VV (1999) Redundancy in earthquake-resistant design. J.Struct Eng, ASCE 125(1):81–88
9. Kanno Y, Takewaki I (2006) Sequential semidefinite program for maximum robustness design of structures under load uncertainties. J Optim Theory Appl 130(2):265–287
10. Takewaki I (2008) Robustness of base-isolated high-rise buildings under code-specified ground motions. Struct Des Tall Spec Build 17(2):257–271
11. Takewaki I (2009) Building control with passive dampers: optimal performance-based design for earthquakes. Wiley, New York
12. Takewaki I, Ben-Haim Y (2005) Info-gap robust design with load and model uncertainties. J Sound Vib 288(3):551–570
13. Drenick RF (1970) Model-free design of aseismic structures. J Engrg Mech Div, ASCE 96(EM4):483–493
14. Shinozuka M (1970) Maximum structural response to seismic excitations. J Eng Mech, ASCE 96:729–738

15. Takewaki I (2002) Seismic critical excitation method for robust design: a review. J Struct Eng ASCE 128:665–672
16. Takewaki I (2007) Critical excitation methods in earthquake engineering. Elsevier, New York
17. Takewaki I, Murakami S, Fujita K, Yoshitomi S, Tsuji M (2011) The 2011 off the Pacific coast of Tohoku earthquake and response of high-rise buildings under long-period ground motions. Soil Dyn Earthq Eng 31(11):1511–1528
18. Fujita K, Takewaki I (2011) Sustainable building design under uncertain structural-parameter environment in seismic-prone countries. Sustain Cities Soc 1(3):142–151
19. Fujita K, Takewaki I (2011) An efficient methodology for robustness evaluation by advanced interval analysis using updated second-order Taylor series expansion. Eng Struct 33(12):3299–3310
20. Baratta A, Elishakoff I, Zuccaro G, Shinozuka M (1998) A generalization of the Drenick-Shinozuka model for bounds on the seismic response of a single-degree-of-freedom system. Earthq Eng Struct Dynam 27(5):423–437
21. Ben-Haim Y, Elishakoof I (1990) Convex models of uncertainty in applied mechanics. The Netherlands, Amsterdam
22. Elishakoff I, Ohsaki M (2010) Optimization and anti-optimization of structures under uncertainties. Imperial College Press, Singapore

Index

I. Takewaki et al., *Improving the Earthquake Resilience of Buildings*,
Springer Series in Reliability Engineering, DOI: 10.1007/978-1-4471-4144-0,